Transactions of the ASME®

Journal of Engineering for Gas Turbines and Power

Published Quarterly by The American Society of Mechanical Engineers

VOLUME 120 • NUMBER 1 • JANUARY 1998

TECHNICAL PAPERS

Advanced Energy Systems

Gas Turbines: Combustion and Fuels

Gas Turbines: Controls and Diagnostics

Gas Turbines: Electric Utilities

Manufacturing, Materials, and Metallurgy

(Contents continued on p. 247)

This journal is printed on acid-free paper, which exceeds the ANSI Z39.48-1992 specification for permanence of paper and library materials. ♾™

♻ **85% recycled content, including 10% post-consumer fibers.**

Technical Editor
H. L. JULIEN (1998)

Associate Technical Editors
Advanced Energy Systems
M. J. MORAN (1999)
Gas Turbine
D. COOKE (1999)
H. NELSON (1999)
J. PETERS (1999)
J. N. SHINN (1996)
Internal Combustion Engines
D. ASSANIS (1999)
Power
D. LOU (1998)

BOARD ON COMMUNICATIONS
Chairman and Vice President
R. MATES

OFFICERS OF THE ASME
President, **KEITH B. THAYER**

Executive Director, **D. L. BELDEN**

Treasurer, **J. A. MASON**

PUBLISHING STAFF
Managing Director, Engineering
CHARLES W. BEARDSLEY

Director, Technical Publishing
PHILIP DI VIETRO

Managing Editor, Technical Publishing
CYNTHIA B. CLARK

Managing Editor, Transactions
CORNELIA MONAHAN

Production Coordinator
VALERIE WINTERS

Production Assistant
MARISOL ANDINO

Transactions of the ASME, Journal of Engineering for Gas Turbines and Power (ISSN 0742-4795) is published quarterly (Jan., April, July, Oct.) for $185.00 per year by The American Society of Mechanical Engineers, 345 East 47th Street, New York, NY 10017. Periodicals postage paid at New York, NY and additional mailing offices. POSTMASTER: Send address changes to Transactions of the ASME, Journal of Engineering for Gas Turbines and Power, c/o THE AMERICAN SOCIETY OF MECHANICAL ENGINEERS, 22 Law Drive, Box 2300, Fairfield, NJ 07007-2300.

CHANGES OF ADDRESS must be received at Society headquarters seven weeks before they are to be effective. Please send old label and new address.

PRICES: To members, $40.00, annually: to nonmembers, $185.00. Add $40.00 for postage to countries outside the United States and Canada.

STATEMENT from By-Laws. The Society shall not be responsible for statements or opinions advanced in papers or . . . printed in its publications (B7.1, par. 3).

COPYRIGHT © 1998 by The American Society of Mechanical Engineers. Authorization to photocopy material for internal or personal use under circumstances not falling within the fair use provisions of the Copyright Act is granted by ASME to libraries and other users registered with the Copyright Clearance Center (CCC) Transactional Reporting Service provided that the base fee of $3.00 per article is paid directly to CCC, Inc., 222 Rosewood Dr., Danvers, MA 01923. Request for special permission or bulk copying should be addressed to Reprints/Permission Department.

INDEXED by Applied Mechanics Reviews and Engineering Information, Inc. Canadian Goods & Services Tax Registration #126148048

Downloaded 03 Jun 2010 to 171.66.16.159. Redistribution subject to ASME license or copyright; see http://www.asme.org/terms/Terms_Use.cfm

(Contents continued)

Gas Turbines: Structures and Dynamics

Gas Turbines: Vehicular

Internal Combustion Engines

TECHNICAL BRIEF

ANNOUNCEMENTS

Toward Automatic Process Simulators: Part I—Modular Numerical Procedures

E. Sciubba
Dipartimento di Meccanica ed Aeronautica,
Universita' di Roma 1—"La Sapienza,"
Rome, Italy

This paper presents a general design approach involving automatic, intelligent process simulation procedures. The aim is to derive a general set of design principles and methodologies that can be developed into computer-assisted procedures. This first part deals with numerical, quantitative calculations, i.e., with what commonly goes under the name of "Numerical Process Simulation." It is argued that the existing design methods can result in computer codes or packages that perform exactly (and deterministically) the numerical operations an engineer would perform. It is also shown that modularity in these codes is dictated by the necessity of automatically implementing numerical procedures that depend on the structure of the process under examination, rather than by user's convenience and ease of maintenance. An example of a modular, structure-oriented code (CAMEL) is given and discussed in detail, while numerical applications are discussed elsewhere [4]. The second part deals with the more complex qualitative approach to process design, i.e., with the possibility of implementing automatic "expert" procedures that perform the same conceptual tasks as human process engineers. It is shown that by means of Artificial Intelligence techniques it is possible to mimic (to an extent) the "thinking patterns" of a human expert, and to produce process schemes that are both acceptable and realistic. A general process synthesis package (COLOMBO) is described and some of its applications discussed. The main goal of the two parts of the paper is to show that the very complex activity of process design can be executed automatically, not only in principle, but in actual applications, and that both qualitative synthesis and quantitative calculations are possible with the present state of the art of our computational facilities.

1 Introduction

The first part of this paper presents an *explicit mapping* of the conceptual activities that constitute a "process design task" into a series of well-posed, complete, and general numerical procedures. In spite of the fact that there is a substantial number of "design manuals" (for thermal sciences, see e.g., [6]) and "design procedures" (see [1, 14]) that process engineers can consult to choose the most proper approach to a particular problem, there is on the one hand a remarkable lack of generality, in that for instance procedures that apply to the design of a wastewater treatment process cannot be used even in principle to design a fluidized bed system, and on the other hand an obvious repetition: All procedures involve mass and energy balances at some point. With the advance of numerical techniques, virtually every procedure has been "computerized," so that engineers can avail themselves of a multitude of "computer tools" in the majority of their process design activities. There is, however, a frustrating lack of coordination among different procedures, so that the potential user, however experienced, is usually confronted with a very confusing situation when searching for a general simulation tool. There are in fact many codes that perform nominally the same task, giving (sometimes substantially!) different results when applied to the very same problem; in addition, each code uses its own set of property tables, its own input/output format, etc. Finally, with very few exceptions, these codes are not mutually compatible, i.e., the output from any of them cannot be used as the input to any of the other, not only because of the respective formats, but rather because the quantities taken to represent a certain physical process are not the same in different codes.

The first part of this paper is aimed precisely at the bridging of this conceptual gap: detect all the similarities in known design procedures, construct a suitable knowledge base, and implement a general modular procedure that can assist the engineer in the largest possible number of process design calculations. The order of presentation of the material is historical/logical: It begins at the hand calculator level and proceeds toward a fully interactive and entirely modular process simulator. The path is made clear from the beginning: We are trying to extract from the various engineering activities all the essential knowledge that pertains to engineers, with the final goal of transferring this body of knowledge, in some form suitable to machine communication, to a "universal process simulator," that can then be applied with a high degree of confidence to a wide variety of particular process simulations.

2 How It Began: Process Simulation With Property Tables and Hand Calculator

Consider a relatively simple engineering problem: the design of a combined heat and power plant, featuring a gas turbine/generator set to produce the required electrical power P_{el} and a waste heat recovery boiler—fed by the gas turbine exhaust gas—to produce the required heat rate Q. The problem is properly formulated: Both P_{el} and Q are specified, and the additional design constraints are complete and congruent. The fuel is gas turbine oil with a known lower heating value (LHV). The maximum permissible pressure ratio and maximum safe turbine inlet temperature have been chosen. The design values for the air and water physical properties have been specified, and the emission limits properly set.

Contributed by the Advanced Energy Systems Division for publication in the JOURNAL OF ENGINEERING FOR GAS TURBINES AND POWER. Manuscript received by the Advanced Energy Systems Division December 15, 1996; revised manuscript received July 7, 1997. Associate Technical Editor: M. J. Moran.

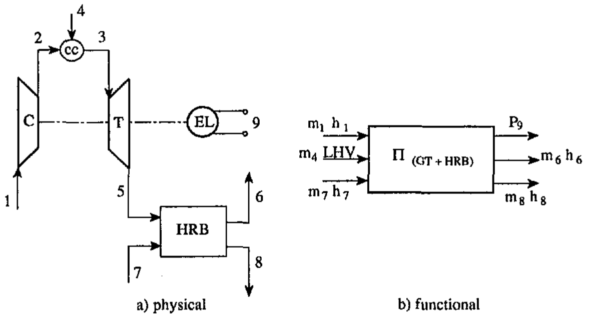

Fig. 1 Physical versus functional representation of a gas turbine/heat recovery process

Suppose we have no other computational means than a hand calculator and a (possibly graphic) set of air and combustion gas properties (like [2] and [13], for example). We might proceed through the following calculations, where the subscripts refer to Fig. 1:

(A) Compute the gas turbine cycle

step (1) Find T_2, the temperature of the compressed air entering the combustion chamber:

$$T_2 = f_1(T_1, p_2, p_1, k_{\text{air}}, \eta_{c,is}) \quad (1)$$

step (2) Find p_3, the pressure of the combustion gas exiting the combustion chamber:

$$p_3 = p_2 - \Delta p_{2-3} \quad (2)$$

step (3) Specify T_3, the maximum allowable gas temperature at turbine inlet:

$$T_3 = T_{\max} \quad (3)$$

step (4) Compute the fuel-to-air ratio:

$$\alpha = f_2(T_2, T_3, c_{p,2-3}, \eta_{cc}) \quad (4)$$

step (5) Compute T_5, the gas turbine exit temperature:

$$T_5 = f_3(T_3, p_3, p_5, k_3, \eta_{t,is}) \quad (5)$$

step (6) Compute the specific turbine work output:

$$w_t = (1 + \alpha)(h_3 - h_5) \approx (1 + \alpha)(c_{p,3}T_3 - c_{p,5}T_5) \quad (6)$$

step (7) Compute the specific compressor work requirements:

$$w_c = h_2 - h_1 \approx c_{p,2}T_2 - c_{p,1}T_1 \quad (7)$$

step (8) Compute the net specific electrical output:

$$w_{el} = (w_t - w_c)\eta_m\eta_{el} \quad (8)$$

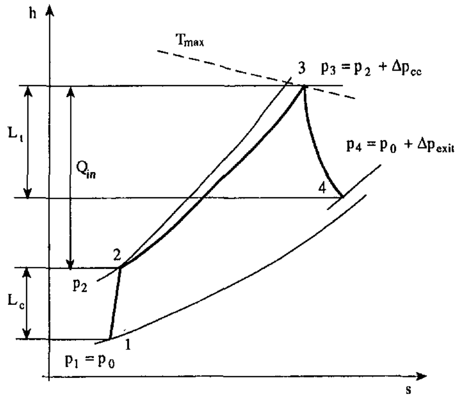

Fig. 2 Process diagram of the simple gas turbine cycle of Fig. 1

step (9) Compute the required mass flow rate of air:

$$m_1 = P/w_{el} \quad (9)$$

(B) Compute the steam generating process

step (1) Compute the maximum allowable steam temperature (ΔT_{pinch} is specified):

$$T_8 = T_5 - \Delta T_{\text{pinch}} \quad (10)$$

step (2) Compute the enthalpy of the water at boiler inlet:

$$h_7 = f_4(T_7, p_7) \quad (11)$$

step (3) Compute the enthalpy of the steam at the condenser inlet:

$$h_8 = f_5(T_8, p_8, x_8) \quad (12)$$

step (4) Compute the steam mass flow rate:

$$m_8 = Q/(h_8 - h_7) \quad (13)$$

step (5) Compute the gas temperature at stack inlet:

$$T_6 = \frac{1}{c_{p,6}}\left[c_{p,5}T_5 - \frac{Q}{\eta_{hrb}(1 + \alpha)m_1}\right] \quad (14)$$

In these equations, $f_1 \ldots f_5$ are thermodynamic relations involving the isentropic compressor and turbine efficiencies, the energy balance for the combustion chamber, the definition of enthalpy, etc.; they are well-known expressions and can be derived in closed form. However, if graphic property data are available for air and water, then Eqs. (1) and (5) can be replaced by an easy geometric construction (Fig. 2), Eqs. (6) and (7) can be directly read from the table, and Eqs. (11) and (12) can be entirely dispensed with, because enthalpies are directly read off the Mollier diagram.

Nomenclature

a = numerical underrelaxation factor
alt = alternator (electrical generator)
α = fuel-to-air mass ratio
β = compression or expansion ratio
c_p = specific heat at constant pressure, kJ/kgK
c_v = specific heat at constant volume, kJ/kgK
η = efficiency
h = specific enthalpy, kJ/kg
κ = steam-to-air mass ratio
k = ratio of specific heats = c_p/c_v
LHV = lower heating value, kJ/kg
m = mass flow rate, kg/s
p = pressure, Pa
P_{el} = electric power, kW
ps = power splitter
Q = heat flow, kW
t = time, s
T = temperature, K
w = specific work, kJ/kg

Subscripts

1, 2. . . = referred to states 1, 2, . . .
air = referred to air
c = compressor
cc = combustion chamber
el = electrical
hrb = heat recovery boiler
i = ideal
is = isentropic
m = mechanical
pinch = referred to a pinch point
t = turbine

With no lack of generality, the isentropic efficiencies, the ΔT's and Δp's can be thought of as "design constraints" and assumed as known. Notice that there are some intermediate checks that have to be recognized: for instance, if $w_c > w_t$, it will be necessary to iterate between steps (1) and (7) with different values of p_2. Or, if T_6 turns out to be lower than the minimum acceptable stack gas temperature, it will be necessary to lower T_8 or provide the heat recovery boiler with an afterburner.

The foregoing calculations are simple, and, with a minimum of engineering experience on the part of the designer, can result in a well-defined process scheme. This type of solution can be a very tedious task, however, especially if different sets of design values have to be considered. And, it is very much prone to human error ("miscalculations"). Note, in particular, that Eqs. (1), (4)–(7), (11), (12), (14) require property values that have to be extracted from the air and steam tables; both the numerical and graphical interpolations can be sources of errors. In any case, this calculation represents a proper *process calculation procedure,* and is an example of what we want to replace with an automatic, computer-assisted method.

3 The Notion Of "Process Simulation"

To limit the scope of the investigation and to make the goals more precise, let us give a general definition of the engineering activity that goes under the name of *Process Simulation* (of which an elementary example was given in Section 2). Denote by **P** an otherwise unspecified physical process and assume that the task is to calculate all the relevant quantities that identify **P** *for all practical engineering purposes.* This means that we will in general be concerned with problems that can be treated using the continuum hypothesis, the principles of engineering thermodynamics, etc. Processes that require a relativistic description or which by their nature defy the notion of continuum, etc., are not explicitly considered. However, such exceptions can be easily treated by relaxing some of the basic constraints.

Whatever the complexity of a process, it is always possible to break it down into subprocesses that are simpler, either because they are composed of a lower number of "elementary" thermodynamic transformations or because they refer to a smaller number of participating media. By repeating this splitting procedure as necessary, it is possible to reach a point at which the physical description of the single, complex process **P** can be shown to be equivalent to the description of several simpler interconnected subprocesses $\mathbf{P}_1 \ldots \mathbf{P}_n$. With no lack of generality, we will assume here that this decomposition has already been performed; and that, once the subprocesses have been simulated, it will be possible to re-assemble these $\mathbf{P}_i$'s into the original process **P**.

As shown in Fig. 3, the description of **P** can be in principle represented by an *operator* Π, which *acts on the inputs to produce the outputs.* Thus, "calculating" **P** means finding a suitable formal expression for Π (called the *transfer function* of **P**), applying it to the inputs $\mathbf{I}_j$ ($j = 1 \ldots f$) and deriving numerical computable formulae for the outputs $\mathbf{O}_k$ ($k = 1 \ldots p$), where **O** and **I** denote the output and input vector respectively:

$$\mathbf{O} = \Pi\langle \mathbf{I} \rangle \tag{15}$$

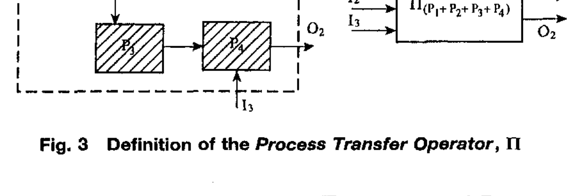

Fig. 3 **Definition of the *Process Transfer Operator*, Π**

In the most general case, Π is a nonlinear matrix operator linking *all* of the outputs with *all* of the inputs. No limit has been imposed on the form of operator Π: It can be algebraic, differential, integral-differential, steady or unsteady, etc. The form that Π takes will of course determine the number and type of necessary boundary (and/or initial) conditions, i.e., a certain number of design data, which quantitatively define some of the inputs or outputs.

On the basis of these considerations, we are now in a position to give an exact description of process simulation: Given a certain well-defined physical process, we aim to:

(*i*) devise a suitable representation for it in terms of its subprocesses, if necessary,
(*ii*) find a formal mathematical representation for its transfer function Π,
(*iii*) acquire all necessary boundary and initial conditions,
(*iv*) solve the system (15) for each subprocess, and
(*v*) assemble the partial solutions into the global solution.

In the following sections, each of the process simulation steps is analyzed with the objective of extracting a sufficient number of general principles that can be implemented in *automatic* numerical procedures, rather than by hand calculations such as described in Section 2, or by means of mathematical optimization techniques that, though definitely superior in their ability to locate actual optimal operating and design points, are not modular, and therefore not of general applicability [5, 15, 17].

4 Automatic Calculation of Material Properties

The first step to improve the approach of Section 1 might be to develop "material properties routines" that provide the thermodynamic quantities of interest (enthalpy, entropy, saturation values, steam quality in the wet region, specific heats, etc.). These calculations are carried out on the basis of interpolating formulae that can be *specific* for the particular fluid under consideration, or of *general validity* for a certain set of fluids.

Both types of routine are presently available, and both can be developed in such a way as to yield a high degree of accuracy while still retaining a relatively high degree of efficiency. Since deficient property routines can be very detrimental for the overall accuracy of the calculations, it is advisable to use only well-tested and well-documented packages (like [13], for example). These routines can be used either in "manual" mode, i.e., by plugging into them the values of the known parameters and deriving the outcome, or in "automatic" mode, i.e., by using them on some kind of calculator (for example, one of the handheld programmables). If a set of these routines is available, Eqs. (1) and (5), and consequently (6) and (7), can be directly computed in closed form, and the same applies to Eqs. (11) and (12). The advantages in terms of the repetitivity and of the accuracy of the solution are apparent; still, the entire procedure is essentially based on hand calculations that are time intensive and prone to error.

5 Automatic Calculation of Thermodynamic Relations

To devise a fully automatic procedure for the calculation of the gas turbine cycle of Section 2, let us now turn to the possibility of implementing a numerical procedure for the calculation of the thermodynamic relations, Eqs. (1)–(14). Here, we are immediately faced with a fundamental problem common to *all* numerical process calculators: It is not difficult to solve equations (1)–(14) sequentially (i.e., in the very same order in which they would be solved by a manual procedure) *but it is* *difficult to formulate a general procedure to solve Eq. (15) by direct inversion of the matrix* Π *without "knowing" in advance the structure of the process.* Let us explicitly compute Π for the present application. Referring again to Fig. 1, which shows clearly that m_1h_1, m_4 LHV, and m_7h_7 are the *inputs* and $P_{el} = m_1w_{le}$, $P_{\text{stack}} = m_1Q_{\text{stack}} = (m_1 + m_4)h_6$ and $Q_{st} = m_8h_8$ are the *outputs,* we can write Eq. (15) in its expanded dimensionless form, and obtain (both I and O being divided by m_1, and with $\alpha = m_4/m_1$, $\kappa = m_7/m_1$):

$$\begin{aligned} O_1 &= w_{el} = [(1+\alpha)(h_3 - h_5) - (h_2 - h_1)]\eta_{el} \\ O_2 &= q_{\text{stack}} = (1+\alpha)h_6 \\ O_3 &= q_{st} = \kappa(h_8 - h_7) \end{aligned} \tag{16}$$

which has the general structure indicated by Eq. (15):

$$\begin{aligned} O_1 &= \Pi_{11}I_1 + \Pi_{12}I_2 + \Pi_{13}I_3 \\ O_2 &= \Pi_{21}I_1 + \Pi_{22}I_2 + \Pi_{23}I_3 \\ O_3 &= \Pi_{31}I_1 + \Pi_{32}I_2 + \Pi_{33}I_3 \end{aligned} \tag{17}$$

and corresponds to the following form for Π (which is, as stated above, the transfer function of the process):

$$\pi = \begin{vmatrix} -\dfrac{(h_2 - h_1)\eta_{el}}{h_1} & \dfrac{(1+\alpha)(h_3 - h_5)\eta_{el}}{\alpha\text{LHV}} & 0 \\ 0 & \dfrac{(1+\alpha)h_6}{\alpha\text{LHV}} & 0 \\ 0 & \dfrac{(1+\alpha)(h_6 - h_5)}{\alpha\text{LHV}}\eta_{\text{hrb}} & 1 \end{vmatrix} \tag{18}$$

Notice that with the same approach it is possible to compute the mass and energy balances of a component or of a cycle. Actually, Eqs. (16) are just another way of writing an energy balance. In effect, we are making use here of the well-known black-box approach: The description of the generic process **P** given in Section 3 is exactly the same approach adopted in the input/output (or black-box) process representation.

Since $h_2(h_1, \beta, k_{12}, \eta_c)$ and all other thermodynamic relations cannot be computed unless they are expressed by explicit functions, one must augment the Π defined by the matrix (18) with a sufficient number of auxiliary equations of the type:

$$\begin{aligned} h_2 &= h_2(p_2, T_2) \\ h_5 &= h_5(p_5, T_5) \\ &\text{etc.} \end{aligned} \tag{19}$$

It can be shown [12] that a system in the form of Eqs. (17) can always be explicitly written for any process, and that it can always be derived using mass and energy balance equations in symbolic form (i.e., written without using any numerics, just in the same way in which an engineer would write them on a process sheet). These auxiliary equations make the calculation procedure *highly specialized* for the gas turbine process, so that *the same procedure cannot be employed to compute any other process (and not even similar processes with slightly different configurations, such as a regenerated or intercooled gas turbine cycle).* That is, *there are as many independently derived* Π*'s as the number of individual cycles or processes we wish to simulate; and these* Π*'s are in general different from each other.* This is actually the present situation: there are many codes for the process calculation of different processes or cycles, but they are very much application oriented and lack generality.

6 Toward a Modular Simulator

The conclusion that can be drawn from the foregoing considerations is this: *To develop a general process simulator, the difficult task is one of imparting to the code a flexible enough structure to be able to handle physically different processes automatically.* This is where the concept of a modular process simulator can help. If a number of elementary subprocesses $\mathbf{P}_i$ can be identified that can be used as building blocks for *any* process **P** of interest, a general process simulator can be constructed in principle by the following procedure:

(*i*) Create a *passive database* of elementary modules, each one of which simulates a process $\mathbf{P}_i$

(*ii*) Construct a user machine (software) interface capable of reproducing the physical interconnections among the various $\mathbf{P}_i$'s

(*iii*) Solve each $\mathbf{P}_i$ in turn under the proper assembly constraints, i.e., take into proper consideration the interactions of $\mathbf{P}_i$ with all other $\mathbf{P}_j$

(*iv*) Reassemble the solution under the global structure of **P**.

Such a process simulator will by necessity have a highly modular structure, consisting of: (1) a *core* that handles the *I/O* and implements the general solution strategy, (2) a series of subroutines (independent of each other), which are called in turn to solve a particular subprocess, and (3) a series of property tables in a database. The following sections describe the general features of the various portions of a possible code of this kind.

6.1 Translation of the Process Structure Into Machine-Readable Input. The physical structure of a process can be represented by a *process diagram* (Fig. 4), which displays the general layout of the system that implements the process. This diagram identifies the components and the fluxes of matter and energy that connect the components to each other, describes the exchanges of the system with its immediate surroundings, and contains essential quantitative information about the operating parameters of the process (pressures, mass and energy fluxes, enthalpies, etc.).

A numerical simulator cannot "read" the process diagram as a human does. It is, therefore, necessary to devise a "computer-readable" form of this diagram, which ought to be easily accessible by the code, but not too removed from the intuitive mathe-

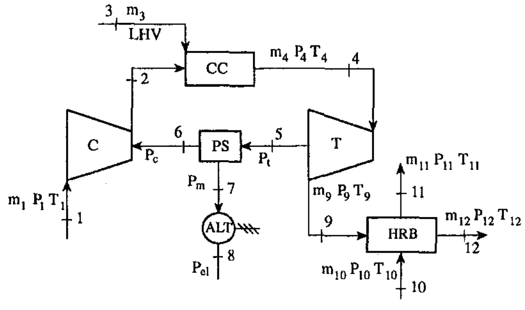

(a) Process scheme

	C	CC	T	PS	ALT	HRB
1-	1	0	0	0	0	0
2-	-1	1	0	0	0	0
3-	0	1	0	0	0	0
4-	0	-1	1	0	0	0
5-	0	0	-1	1	0	0
6-	1	0	0	-1	0	0
7-	0	0	0	-1	1	0
8-	0	0	0	0	-1	0
9-	0	0	-1	0	0	1
10-	0	0	0	0	0	1
11-	0	0	0	0	0	-1
12-	0	0	0	0	0	-1

(b) Interconnection matrix

Fig. 4 Process diagram of the gas turbine scheme of Fig. 1 and the corresponding interconnection matrix IM

matical comprehension of the user. The most suitable form is that of a matrix **IM**, defined as follows [4, 16]:

$IM_{i,j}$ is a character string that contains the *name of the component*

$IM_{i,1}$ is a character string that contains the *identifier of the flux*

$IM_{i,j}$ is $= 1$ if flux *i enters* component *j*

$IM_{i,j}$ is $= -1$ if flux *i exits* component *j*

$IM_{i,j}$ is $= 0$ otherwise

The matrix **IM** is the (augmented) matrix form of *the connectivity graph* of the system and, thus, is called the *interconnection (or structural) matrix.* This matrix is easy to construct once the structure of the system has been identified. An example of the "translation" of a process diagram into the corresponding **IM** is shown in Fig. 4 for the gas turbine plant of Fig. 1. Notice the different numbering of the flows in Fig. 1 and Fig. 4, due to the slightly different structure of the logical process scheme [4].

Besides constituting a synthetic way of describing the process structure, **IM** has another very important characteristic: *It allows a very efficient formal representation of the mass and energy balances of a system.* Consider again the process scheme of Fig. 2 and denote by m_1, m_2, etc., the mass flow rates in the sections 1, 2 . . . respectively. It will also be possible to define a "mass flow vector," **m**, whose entries are the various mass flow rates, with the additional stipulation that the fluxes which do not transport any mass (typically, as in this case, the "power" fluxes) are assigned a value 0.

The product:

$$IM*\mathbf{m} = \left|\begin{array}{cccccc} 1 & 0 & 0 & 0 & 0 & 0 \\ -1 & 1 & 0 & 0 & 0 & 0 \\ 0 & 1 & 0 & 0 & 0 & 0 \\ 0 & -1 & 1 & 0 & 0 & 0 \\ 0 & 0 & -1 & 1 & 0 & 0 \\ 1 & 0 & 0 & -1 & 0 & 0 \\ 0 & 0 & 0 & -1 & 1 & 0 \\ 0 & 0 & 0 & 0 & -1 & 0 \\ 0 & 0 & -1 & 0 & 0 & 1 \\ 0 & 0 & 0 & 0 & 0 & 1 \\ 0 & 0 & 0 & 0 & 0 & -1 \\ 0 & 0 & 0 & 0 & 0 & -1 \end{array}\right| \left|\begin{array}{c} m_1 \\ m_2 \\ m_3 \\ m_4 \\ m_5 \\ 0 \\ 0 \\ 0 \\ m_9 \\ m_{10} \\ m_{11} \\ m_{12} \end{array}\right|$$

is equal to the *mass balance vector:*

$$\begin{array}{l|c|} \text{comp} & m_1 - m_2 \\ cc & m_2 + m_3 - m_4 \\ \text{turb} & m_4 - m_9 \\ ps & 0 \\ \text{alt} & 0 \\ \text{hrb} & m_9 + m_{10} - m_{11} - m_{12} \end{array}$$

It is possible to show [8, 12] that a similar formalism applies to the energy balance as well. This fact has important consequences in the programming, because it makes possible the use of very compact and modular system assembly methods.

Since the balance equations constitute a nonlinear system, an iterative solution procedure is used. To begin with, an initial "state" of the system must be specified. This initial state does not need to be consistent (in the sense that the values of the assigned parameters may also *not* satisfy the balances) and usually contains design data and some additional information about known or guessed values for the process parameters. To impart these data to the code, it is necessary to assign *in the correct sequence* the various parameters (pressure, temperature, mass flow rate, composition, etc.) to the proper sections of the process diagram. This initialization can be done very efficiently by means of a series of specific subroutines that contain in a structured sequence relevant information about each component, its location in the system, and the working fluids through it. This "structure" is then used by the code to properly identify the data contained in the *input plant matrix,* **IPM**, and in the *output plant matrix,* **OPM**, which are in practice structured data tables. Both the **IM** and the **IPM** can be constructed with the aid of a specific utility; the **OPM** must be automatically generated by the code. For a detailed description of these matrices, see [4] and [8]. The **IPM** and **OPM** of the gas turbine case study considered here are reported in Fig. 5.

For unsteady state or transient simulations, the matrices **IPM** and **OPM** will in general be time dependent so that there will be an **IPM**(0) and an **OPM**(0), which will represent the *initial state* of the system just before the transient begins. If there are *n* time steps in the integrating procedure, there will be a series of *n* matrices **IPM**(t_1). . .**IPM**(t_n), **OPM**(t_1). . .**OPM**(t_n), which will contain all the process information needed at each timestep. It is important to remark at this point that the transient procedure just outlined rests on the assumption that any unsteady process can be represented via a quasi stationary approximation. This point will be discussed again in Section 7.

6.2 Solution of the Global System of Balance Equations. The nonlinear system of equations resulting from the application of the mass and energy balances to every component of the process does not constitute, except in trivial cases, a solvable system because its coefficient matrix is not square [12]. However, it is *always* possible to augment this coefficient matrix by the use of property relations (see Section 4) and by the imposition of the design specifications, which act as *constraints* on some of the degrees of freedom of the process. The final system has the form

$$\mathbf{CM}*\mathbf{x} = \mathbf{d} \tag{20}$$

where **CM** is the augmented coefficient matrix, **x** is the vector of unknowns, and **d** is a vector containing the design specifications and the constraints. Notice that the rank *r* of **CM** is *higher* than the number of components, because there is generally more than one equation per component. Furthermore, additional equations have been added to make the system solvable (i.e., **CM** invertible).

The system of equations (20) has two types of nonlinearities: One is explicit and is due to the fact that some of the equations (e.g., the isentropic relations) are nonlinear; and one is implicit, because the property relations [e.g., $c_p = f(T)$] are nonlinear.

```
        CAMEL: modular elemental plant calculation version 2.1
                Input for the calculations; matrix IPM
 1 -     447.00      100.00      300.00       .21     AIR
 2 -        .00         .00         .00       .00     FTU
 3 -        .00    41840.00         .00     14.20     FTU
 4 -        .00      832.00     1370.00       .00     FTU
 5 -        .00         .00         .00       .00     FTU
 6 -        .00         .00         .00       .00     FTU
 7 -        .00         .00         .00       .00     FTU
 8 -        .00         .00         .00       .00     FTU
 9 -        .00         .00         .00       .00     FTU
10 -      60.00      120.00      760.00      1.00     SHS
11 -        .00         .00      433.00       .00     WAT
12 -        .00     5290.00         .00       .00     FTU
```

```
        CAMEL: modular elemental plant calculation version 2.1
                Output for the calculations; matrix PM
 1 -     447.00      100.00      300.00       .21     AIR
 2 -     447.00      857.73      583.08       .21     AIR
 3 -      11.65    41840.00       38.34     14.20     FUE
 4 -     458.66      832.00     1370.00       .13     GAS
 5 - 253214.09         .00         .00       .00     POW
 6 - 131838.02         .00         .00       .00     POW
 7 - 121376.06         .00         .00       .00     POW
 8 - 115307.26         .00         .00       .00     POW
 9 -     458.66      120.00      791.15       .13     GAS
10 -      60.00     5131.00      760.00      1.00     SHS
11 -      60.00     5290.00      433.00       .00     WAT
12 -     458.66      116.00      458.67       .13     GAS
```

Fig. 5 Input (IPM) and output (OPM) matrices for the process schemes of Figs. 3 and 4

Therefore, a stable and robust iterative procedure must be employed to solve the system. There are several possible schemes available in the literature [7, 9, 10, 11].

6.3 The Selectively Segregated Approach for Steady-State Simulations. A different solution strategy for the system of equations (20) has been proposed recently [4]. The novelty of the approach consists of *solving one subprocess after the other in an order that is not predetermined, but rather dictated by the developing solution itself.* The algorithm has been called the Selective Segregated Solver ("SSS" in the following), and is described below. The attribute *segregated* (a name borrowed from the field of numerical fluid dynamics) has been given to this solver as a reminder of the fact that it solves only *some* of the equations at each step, and then uses the partial solutions to update the set of "known" variables sequentially.

After reading the initial data from the matrix **IPM**, the SSS scans the components sequentially, starting from the first column of the matrix **IM**, until it finds one for which there are as many unknown variables as there are independent equations. Let us assume that this jth component is a compressor. It will be identified by seven variables (m_1, p_1, T_1, m_2, p_2, T_2, L_c), four of which (m_1, p_1, T_1, p_2) are given in **IPM**. There are three equations available (the mass balance, the energy balance, and the polytropic compression equation). SSS will start an iterative procedure and drive it to convergence, thus completely specifying all values for the operating parameters of the compressor. SSS will then go on to the $(j + 1)$th component (combustion chamber) and determine that it has eight independent variables and only six available equations. Accordingly, SSS will *skip* this component and proceed to the $(j + 2)$th one, and so on, until one of two conclusions is reached: Either there are no more components to scan, and the **OPM** has still some undefined entries; or all the variables of the problem have been attributed a value. In the second case, the external iteration (extended to the entire system) is obviously completed; in the first case, it is not possible to solve the problem with the given data. More input data or more constraints are needed.

When the nth iteration has been completed, the resulting values are combined to those of the $(n - 1)$th step, to obtain the *corrected initial values for the* $(n + 1)$-th iteration. For the generic variable ξ, the following formula applies:

$$\xi^* = \alpha\xi_{n-1} + (1 - \alpha)\xi_n \tag{21}$$

where ξ^* is the initial value for the next iteration, and α is called the *underrelaxation factor.* Its function is to increase the stability of the numerical procedure by "damping" possible nonlinear oscillations in the solution. The range for α is 0.1 to 0.9, with 0.5 a commonly employed value. The lower the underrelaxation factor, the faster the solution will converge; but the less stable it will be. A flow chart of the steady-state procedure is shown in Fig. 6 [4]. It is important to remark that the segregated solution strategy represents an improvement over the conventional equation oriented solvers, that are difficult to control and that require computer resources exponentially growing with the number of components to solve for. At the same time, the SSS is much faster than the existing module oriented solvers, that employ a strictly sequential approach and do not "skip" components.

7 Unsteady Simulations: A Time-Marching Algorithm

The numerical simulation of unsteady processes is a very complex task, because it requires knowledge of a series of *instantaneous* data about the process:

(i) The variation of ALL of the inputs that contribute to the transient operation must be known at each time step;

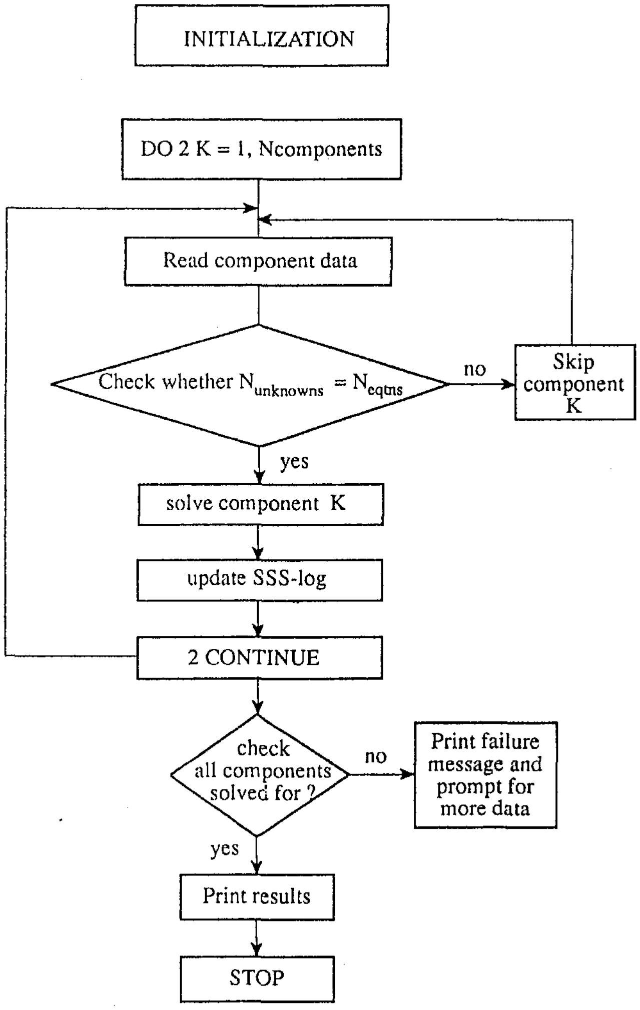

Fig. 6 Logical flow chart of the selective segregated solver

(ii) The transfer matrix (see Section 3) of each component of the process must also be known; if $\mathbf{O}_{k,j}$ is the kth output ($k = 1\ldots N$) of the jth component and $\mathbf{I}_{i,j}$ the ith input ($i = 1\ldots M$), the transfer matrix $\mathbf{F}$ is a $(N \times M)$ table, which contains the single transfer functions Π of the individual components and takes the general form:

$$\mathbf{F}_j = \begin{vmatrix} f_{1,1} & f_{1,2} & \cdots & f_{1,M} \\ f_{2,1} & f_{2,1} & \cdots & f_{2,1} \\ \cdots & \cdots & \cdots & \cdots \\ f_{N-1,1} & f_{N-1,1} & \cdots & f_{N-1,1} \\ f_{N,1} & f_{N,1} & \cdots & f_{N,1} \end{vmatrix} \tag{22}$$

where the individual entries are the coefficients of the general expression of the output–input relation [4, 12]:

$$O_{k,j} = \sum_{i=1}^{M} (f_{i,j} I_{i,j}) \quad (k = 1\ldots N) \tag{23}$$

where the time dependence is implicit in the f-coefficients (which in reality can be nonlinear functions of several $\mathbf{I}_{i,j}$). Notice that the system (22) can be directly related to the matrix **CM** defined in Section 5.

(iii) The time response of EACH component of the system must be known, so that the proper time shift can be inserted in the relevant f-coefficients. Except in relatively simple cases, a transient simulation can become a very cumbersome task. Furthermore, a procedure capable of performing *one specific* simulation would easily lack generality, i.e., it would be unsuitable for different processes or even for the same process undergoing a different transient. We will take here a simplified approach, by postulating that:

(a) The system proceeds from its *initial* to its *final* state through a succession of *local quasi-equilibrium states.* This means that, though the transfer matrix can be different at different time steps [i.e., $\mathbf{F}(t) \neq \mathbf{F}(t + \delta t)$], there is no *explicit* time dependence in the f-coefficients.
(b) It is always possible to choose a time step δt small enough that the response of every component is either instantaneous or displays a fixed delay in the vicinity of that δt: this means that the response can be computed in terms of $\Delta\mathbf{F}$ instead of $\partial\mathbf{F}/\partial t$.
(c) The transfer matrix $\mathbf{F}_j$ does not depend on the transfer matrix $\mathbf{F}_k$ of all other components possibly connected to component "j."

On the basis of the rather stringent assumptions given above, a time-marching procedure can be developed as follows: assume that the entire state of the process is known at time $t_0 = 0$; furthermore, for simplicity, let us prescribe a variation in only *one* of the process inputs. For each component, it is possible to compute the N outputs by either Eqs. (22) or (23). It is convenient to begin the time-marching from the component *"J," which is the recipient of the time-dependent input.* Provided the δt has been chosen properly, the time delay introduced by component J will either be zero or a finite (small) value τ_J. A linear response is assumed, i.e.,

$$O_J(t_0 + \delta t) = O_J(\tau_J) + \frac{\tau_J - \delta t}{\tau_J}[O_J(t_o) - O_J(t_o + \tau_J)] \quad (24)$$

Once $O_J(t_o + \delta t)$ has been computed, the algorithm will proceed as if the simulation was at steady state, and compute all the parameters that characterize the state of the system at the end of the first timestep. Then t is set to $t_o + 2\delta t$, and the process is repeated.

When using this procedure, the characteristic response of a component at a given time can be derived directly from its "performance chart," which is readily available for most components. Care is needed in regions where operation might be unsteady (e.g., near the choke or surge lines of a compressor) or where the characteristic response curve is steep. In both cases, it is possible that the search for a stable solution fails, because:

(1) Near unsteady operation regions, a possibility exists that one of the variations of an input (for example, a reduction of the inlet mass flow rate in a centrifugal compressor) brings the component into the unsteady region, in which, of course, the transfer matrix takes a different (and often unpredictable) form;
(2) If the characteristic curve is steep, a small variation of one of the inputs may correspond to a large variation of one or more of the outputs. The linear approximations employed here [Eqs. (23) and (24)] are poorly suited to follow such a behavior and Gibbs-type oscillations might appear in the solution, affecting the overall stability of the procedure and leading to numerical instability of the algorithm and divergence of the entire solution. A flow chart of the unsteady solution method is shown in Fig. 7.

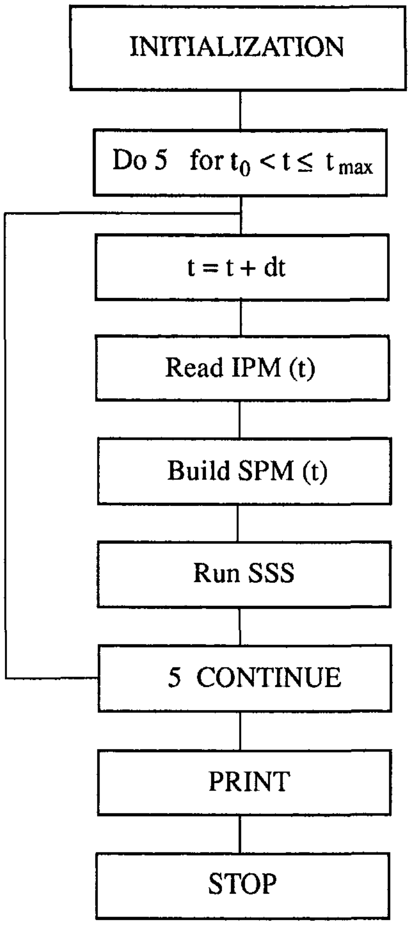

Fig. 7 Logical flow chart of the solution procedure for unsteady problems

8 Conclusions

This study was carried out with two objectives. The first was the search for a general process calculation procedure that can be applied to any process without need of extensive reprogramming if the process structure changes. The second was to exploit the idea that, since the nature of process engineering calculations is systematic and logically modular, a general algorithm can be always found to describe them properly. The arguments developed in this first part of the paper lead to the conclusion that both goals can be achieved. Indeed, a general, modular computer code, named CAMEL (from the Italian acronym of "Modular Elemental Computation"), has been developed that in its present version [4, 8] is capable of simulating the steady and unsteady behavior of gas turbine cycles, steam power cycles, combined gas and steam cycles, and heat exchanger networks. Several applications of the code have shown that it has the capabilities (flexibility, accuracy, numerical robustness) required for industrial process calculations. Work is under way to expand CAMEL's range of applications by increasing its subroutines library, i.e., expanding its capability to include different components and, therefore, different processes in the simulation. The code has completed its prototypal phase and is now in a demonstration stage. It is available from the authors for further development and refining.

References

Note: Commercial simulators cannot be included in a Reference List, because their Technical Manuals and Documentation do not constitute a reference proper. The interested reader can therefore consult directly the commercial information available for the existing Process Simulators. A necessarily incomplete listing of the most popular packages must include of course ASPEN+, followed by Speedup, Pro-Vision, Flowpack, Chemasim, GateCycle, P-sace. Recently, the "modular" approach described in this paper has brought some researchers to apply a general tool (like SIMULINK) to the simulation of transient processes.

1 A. Bejan, G. Tsatsaronis, and M. Moran, *Thermal Design and Optimization,* Wiley, 1995.

2 F. Bosniakovic, *Waermediagramme fuer Vergasung Verbrennung und Russbildung,* Springer Verlag, 1956.

3 L. F. Drbal, ed., *Black & Veatch Power Plant Engineering,* Chapman & Hall, 1996.

4 M. F. Falcetta and E. Sciubba, "A computational modular approach to the simulation of powerplants," *Heat Recovery Syst. & CHP,* Vol. 15, No. 2, 1995.

5 C. A. Frangopoulos, "Application of the thermoeconomic optimization method to the CGAM problem," *Energy,* Spec. Ed., Vol. 19, 1994.

6 E. Gyftopoulos, ed., *Industrial Energy Conservation Manuals,* MIT Press, 1982.

7 J. L. Kuester and H. Mize, *Optimization Techniques With FORTRAN,* McGraw-Hill, 1983.

8 R. Melli, B. Paoletti, and E. Sciubba, "SYSLAM: an interactive expert system approach to powerplant design and optimization," *IJEEE,* Vol. 2, No. 3, 1992.

9 P. Y. Papalambros and D. J. Wilde, *Principles of optimal design: Modeling and Computation,* Cambridge University Press, 1988.

10 W. C. Press, *Numerical Recipes,* McGraw-Hill, 1985.

11 G. V. Reklaitis, A. Ravindran, and K. M. Ragsdell, *Engineering Optimization,* Wiley, 1983.

12 M. Rettaroli and E. Sciubba, *MASAI: a code for the symbolic calculation of powerplants,* ASME PD/64/3, Proc. ESDA Conf., London 1994.

13 W. C. Reynolds, *Thermodynamic Properties in SI,* Stanford University Press, 1979.

14 W. F. Stoecker, *Design of Thermal Systems,* McGraw-Hill, 1980.

15 G. Tsatsaronis and J. Pisa, "Exergoeconomic evaluation and optimization of energy systems: application to the CGAM problem," *Energy,* Spec. Ed., Vol. 19, 1994.

16 A. Valero and C. Torres, *Algebraic Thermodynamic Analysis of Energy Systems,* ASME AES-Vol. 7, 1988.

17 M. R. von Spakovsky, M. R. Corti, and M. Banato, "The performance optimization of a gas turbine cogeneration/heat pump facility with thermal storage," ASME *JERT,* Vol. 117, No. 1, 1995.

Toward Automatic Process Simulators: Part II—An Expert System for Process Synthesis

E. Sciubba
Dipartimento di Meccanica ed Aeronautica,
Universita' di Roma 1—"La Sapienza,"
Rome, Italy

This paper presents an explicit mapping of the conceptual activities that constitute a "process design task" into a series of well-posed, complete, and general formal simulation procedures. Part I of this series of two papers dealt with numerical procedures for process simulation and showed that structure independence and modularity are two prerequisites for a general-purpose simulator. Part II approaches the problem from a completely different point of view and considers the question: Is it possible to derive a general set of design guidelines that can be implemented into a knowledge-based system and result in an automatic, computer-assisted process design procedure? This problem is different in character from that tackled in part I. First, it is by its own nature qualitative, i.e., it requires conceptual rather than numerical answers. Second, it is formulated at a higher level (in Artificial Intelligence terms, at a metalevel). Its solution is clearly in the domain of the logic of process design and, therefore, embeds (contains) all possible quantitative numerical schemes and does not depend on any of them for either its position or its solution. If the answer to this question is affirmative, the resulting code would be a sort of "Expert Assistant" to the engineer in the sense that it would suggest what process can be best[1] suited for the particular application under consideration. The study proceeds by trying to detect conceptual similarities in different design procedures, to construct a suitable knowledge base, and to implement a general macro-procedure that could automatically assist the engineer in the largest possible number of process design operations. The contention here is that the most recent developments of AI-based methods make it possible to extract from human experts all the essential knowledge that pertains to "engineering design," with the final goal of transferring this body of knowledge—in a form suitable to machine communication—to an "Expert System for Process Design," which can then be applied (interactively or on a stand-alone basis) with a high degree of confidence to a variety of particular process simulations. A prototype version of an Expert System Assistant is briefly discussed, and an application is analyzed in detail. The code is called COLOMBO and is available as a research tool from the author. Finally, Part II builds on Part I of this series of papers. In particular, it is assumed that a general, modular, numerical Process Simulation Package exists and that it is capable of executing the quantitative mass and energy balance operations described in Part I.

1 Process Optimization

1.1 General Problem Statement: "Direct" and "Inverse" Formulation. The term *optimization* is one of the most misused concepts in the field of engineering. When reading a technical report about some "optimization" performed on a process or a single component, it is often difficult to understand what has been optimized with respect to what, or what has been kept constant during the optimization procedure. Most disappointing though is the fact that in the quest for an idealized optimum point, frequently configuration, operation, and maintenance issues are entirely neglected or grossly underestimated, and the solution obtained via a purely mathematical procedure is presented as *the* solution to the given problem. Thus, neighboring "quasi-optima" are disregarded, that in real engineering applications often represent the most convenient solution. In this section we will consider what optimization means within the present context, and will make no attempt to describe in detail specific optimization techniques. Many excellent practical applications can be found in the current literature [1, 11–13].

Given an otherwise unspecified process (but the presentation applies as well to any engineering system[2]), its behavior will in general be described by a certain number n of *relevant variables* $\mathbf{x}$. These variables span a domain, called the *design domain* $\mathbf{D}$, that contains the range of operation of the process as a subdomain, $\mathbf{D}_o$. The *performance* of the process, however we wish to define it, will be expressed usually by a much smaller set of p *performance parameters* $\mathbf{w}$ ($p \ll n$) that individually and in possible combinations depend on the *operational* point identified in the subdomain $\mathbf{D}_o$ by m operational variables, and in $\mathbf{D}$ by the proper (n-m) design variables.

---

[1] Here "best" means exactly what it implies: the best solution among a limited number considered (in this case as defined or "constructed" by the Expert Assistant). Thus, "best" does not mean "optimal." For a given process and set of engineering assumptions, the *best* and the *optimal* solution may coincide but only coincidentally. The author wishes to express his thanks to the reviewer who brought up this very important point.

Contributed by the Advanced Energy Systems Division for publication in the JOURNAL OF ENGINEERING FOR GAS TURBINE AND POWER. Manuscript received by the Advanced Energy Systems Division December 15, 1996; revised version received July 7, 1997. Associate Technical Editor: M. J. Moran.

[2] A process here means a set of mechanical, chemical or thermal transformations whose goal is to transform some well-specified form and quantity of matter into a different thermodynamic state. An engineering system is a complex, interconnected set of components whose goal may or may not be that of realizing a process. As an example, a combined power plant constitutes, in the sense described here, a process: but it might also be regarded as a system. A city or any general portion of organized human structure (industrial or not) constitutes an engineering system; but it cannot be regarded as a process.

Let us define an *objective function* f as a real function of some or all of the $\mathbf{w}$'s. The context of each specific problem clarifies whether this "global performance index" $\mathbf{f}$ is to be minimized or maximized to achieve more satisfactory results.[3] The formulation of the problem also generally determines that there are a number v of constraints $\mathbf{c}$ that limit the range of variation of the $\mathbf{x}$'s in $\mathbf{D}$ either directly or indirectly. Optimization then consists in the following: *find the proper extremum of f, under the applicable set of constraints* $\mathbf{c}$, *for the* $\mathbf{x}$ *belonging to the design domain* $\mathbf{D}$.

In practice, there are two forms in which engineering optimization problems are encountered: *direct* and *inverse* problems. A direct problem has the following formulation: Given the process or system configuration, the proper description of all of its subprocesses (components) and the problem constraints, *find the operational point* $\mathbf{P}(\mathbf{x})$ *in the subdomain* $\mathbf{D}_o$ *such that* $\mathbf{f}$ *attains its extremal value.* An example of such a problem is when we seek the optimal pressure ratio of a gas turbine cycle that maximizes process efficiency. An inverse problem has a different formulation: Given the design objective and the process structure, *find the "optimal" design point* $\mathbf{P}(\mathbf{x})$ *in the domain* $\mathbf{D}$ *such that: (a) the design objective is attained for the specified operational range* $\mathbf{D}_o$, *and (b) the objective function* $\mathbf{f}$ *(in principle different from the one used in direct problems) attains an extremum.* An example of such a problem is the design of a subunit or of a component, when we seek the optimal design of, say, a compressor which, for the given inlet conditions, delivers a specified mass flow rate at a specified pressure *and* has the highest possible efficiency.

From a physical point of view, these two formulations are different. Yet, because they can be treated with a common mathematical approach, little attention is usually given (even by expert engineers) to the conceptual difference. An example immediately puts things in the proper perspective; for the "optimization" of a compressor, let us consider where the two approaches lead.

The direct formulation reads: "Given the geometry of the compressor, its performance curves, and the state of all thermodynamic quantities of interest, compute the operational point that corresponds to the maximum efficiency." It is clear that the search for the maximum efficiency is an easy task, which could actually be performed simply by inspecting the operational map of the compressor.

The inverse formulation reads: "For the prescribed values of the mass flow rate, m, and of the compression ratio, β, and for a given set of inlet conditions, find the (generally unique) set of geometric, kinematic, and dynamic quantities that, under the surge and choke constraints, deliver the specified flow rate at the specified pressure with the highest possible efficiency." It is immediately clear that this task is much more difficult than the previous one, for one thing because *the set of the independent variables included in the optimization routine is much larger here than in the direct problem,* and furthermore because *the direct problem requires an unconstrained maximixation (the only requirement is that the efficiency be at its maximum), whereas the inverse problem requires the optimization to be performed under a set of strong constraints.*

1.2 Process *Synthesis:* a More Difficult Optimization Problem.

In engineering practice, we are often faced with an optimization problem of a different sort: "Given a certain input, find the *optimal process scheme to deliver a certain output (possibly varying in time) and specify correspondingly the optimal design point as well as the optimal operational schedule.*[4] This is a higher level task than the direct and inverse optimization problems discussed above. Now, we introduce an additional variable space **SC** whose extent may *a priori* be unknown and, which contains *all of the technically possible embodiments of the process.* If we set equal to r the unknown number of these possible configurations, then the process synthesis and optimization problem can be thought of as an extremal problem whose solution is the locus of the r optima of each configuration. If the problem is nonlinear, there are very few examples of automatic approaches to its solution [4–7, 9, 15]. This consideration is reported here because, as discussed in the following section, Artificial Intelligence techniques are very well suited to tackle synthesis-and-optimization problems effectively.

2 Process Design: A Future for AI Methods

2.1 Artificial Intelligence and Expert Systems.

In Part I it was shown that in practice *all* process design calculations can, in one way or another, be performed by properly implemented automatic routines. Since process design is a highly labor intensive task and is by necessity performed by teams of specialists because of its inherent interdisciplinarity, it is usually also a very expensive task. Accordingly, there is a strong incentive to reduce this labor intensity (measured in man hours). The only task that has as of yet not been automated is the *conceptual* one: the choice of the type and of the characteristics of the process itself. In this section we discuss the possibility of *constructing an automatic procedure capable of choosing the most convenient process configuration for a given set of design goals and the possibility of its actual implementation in a code.*

This automation is facilitated by the application of a very powerful set of computational techniques, collectively known under the term *Artificial Intelligence* (AI), whose specific task is to make possible the codification of procedures that somehow mimic the thinking patterns of the human mind. There is a subset of these techniques, called Expert Systems ("ES" in the following), that can be used to reproduce the engineer's decisional path, which proceeds from the design data and constraints to possible process configurations.

Expert Systems are based on *relational languages* that use the symbolism of formal relational logic. They draw inferences from a number of *facts* stored in a particular database that is properly called a *knowledge base.* These facts can be design data, design rules, physical or logical constraints, etc. Each ES manipulates this knowledge in its own way, according to a logical procedure contained in its *inference engine.*

No attempt will be made here to give even a partial description of AI techniques. Interested readers are referred to some of the excellent monographic works on these topics [2, 14, 16] and for convenience to an introductory overview addressed to Process Engineers [10]. What is of interest here is that an ES can be constructed that performs in principle the following operations:

1 Acquires in machine-readable form a series of inputs that represent the knowledge of the state of the *universe* with which the ES will have to deal: design data, type and state of the environment, component specifications, state of the art of a certain technology, etc.;
2 Can be instructed by the user (with which it may interactively relate) about the logically and physically exact design goals, i.e., about some physical, logical, or numerical properties the solution must possess;
3 Manipulates the data contained in its knowledge-base according to a predetermined set of rules contained in its *inference engine,* a sort of built-in logical flowchart that instructs the ES on how to proceed in different situations;
4 Can call other numerical procedures if necessary. Of interest here is the fact that an ES can call any process calculation code, for example, the one discussed in Part I.

---

[3] Notice that $\mathbf{f}$ may also explicitly contain some of the $\mathbf{x}$'s.

[4] The problem can be further complicated by the requirement of finding the optimal process scheme for a certain set of *operational* points: but this will be not considered here.

2.2 General Knowledge Representation for Design Applications. Let us assume that the decision has been made to construct an ES for a certain design activity. What are the necessary steps that lead the engineer from design inception (definition of need, general engineering concept, see [1]) to the generation and technical description of one or more final designs? This section addresses this question. Of course, the more general the description (i.e., the higher the level of abstraction at which the procedure is described), the higher the danger of overgeneralization. It is left to the reader to fill in the gaps that may exist between the general method described here and particular applications.

The process of generating a design plan can be decomposed into three phases, roughly identifiable as *problem specification, functional analysis,* and *design plan generation* [10]. In the first phase, we try to identify and define the (physical and logical) parameters that constitute the design goal, those that constitute the data, and those that constitute the constraints. In the second phase, we investigate the functional relations that exist among those parameters and how they must be accounted for during design. The third phase consists of a mapping of the logical design algorithm onto a relational procedure that can be implemented in an application using one of the available AI languages and tools.

2.2.1 Problem Specification. The problem specification phase is divided into two subphases:

(*a*) *Problem identification and position.* This is a task that can be performed on the basis of an itemized identification list:

- Can the problem be decomposed into a set of smaller and easier (in some sense) *independent* or *loosely dependent* subproblems?
- Conversely, is the problem really a subproblem embedded in a higher-level problem for which a solution is already known?
- If the design problem consists of an assigned series of design steps, is it possible to ignore or skip those steps that are found to be either in conflict with others or superfluous for the general solution strategy?
- Is it possible to foresee the complete problem domain (its *universe*)?
- Is a single solution sought after, or is it necessary to produce and compare several different solutions?
- Is the assigned (or gathered) knowledge base self-consistent?
- Is it known from previous experience that the search for a solution requires a large body of knowledge, or is it sufficient to gather only problem-specific knowledge so as to somehow limit the solution space?
- Is the problem such that all of its knowledge base is well defined and unchanging, in which case the still-to-be-produced ES can run in batch mode, or is a portion of this knowledge base uncertain or variable so that it is imperative to chose a highly interactive ES?

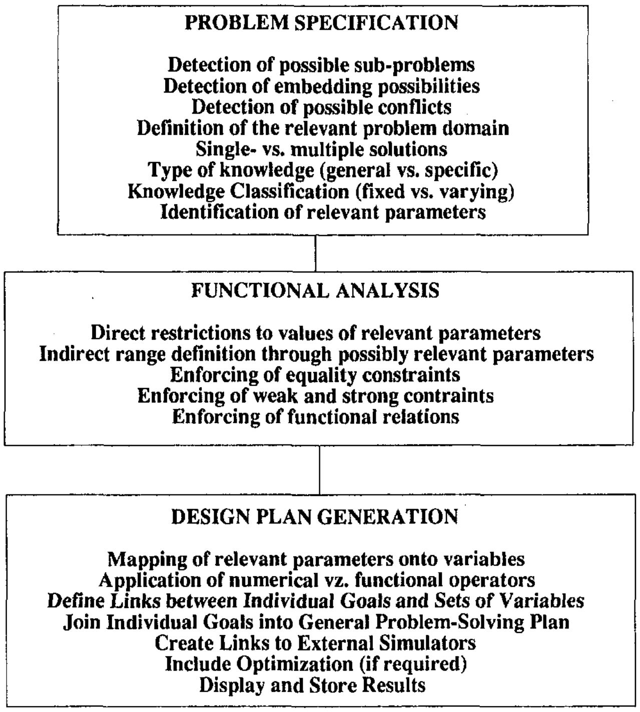

Fig. 1 Schematic representation of the generation of a design plan for an expert system

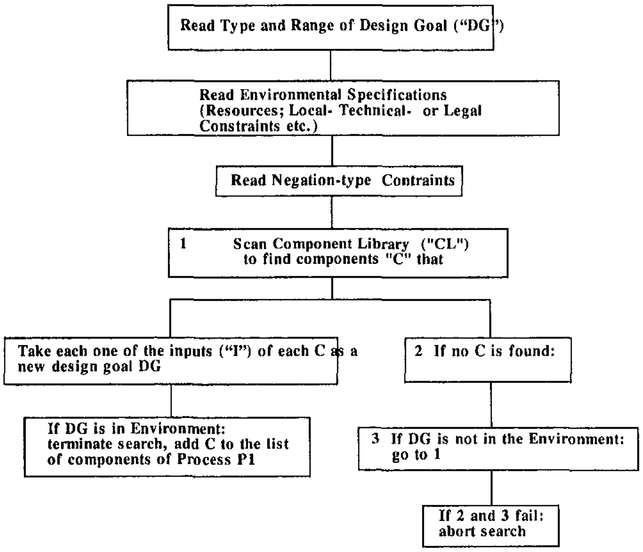

Fig. 2 Schematic representation of a possible inference engine for process synthesis

The answers to these questions result in a set of guidelines that will indicate which methods are likely to be more useful in solving the problem and will direct actual implementation of the code.

(*b*) *Identification of ''always-relevant'' parameters.* The conceptual structure of the general process configuration must be analyzed and ''decomposed'' to derive a fundamental set of parameters and define an initial set of relations linking them to each other and to the design data. In many instances, this step is unnecessary, because the related knowledge already exists and has been codified in numerous examples of prior successful designs. There can be ''always relevant'' and ''possibly relevant'' parameters and relations. The first type includes all those that capture important and essential aspects of the functionality of the final design product and that are always present in the basic set of similar design processes. The second type includes all parameters and relations that are either important for particular cases only or whose importance depends greatly on the design specifications and in either case vary from problem to problem.

2.2.2 Functional Analysis: Relations Between the Given Specifications and the Possibly Relevant Parameters The specifications (design data) may contain restrictions on a possibly relevant parameter p_p, either directly (by setting a range of acceptable values for it) or indirectly (by setting a range of accepted values for another parameter r that is somehow corre-

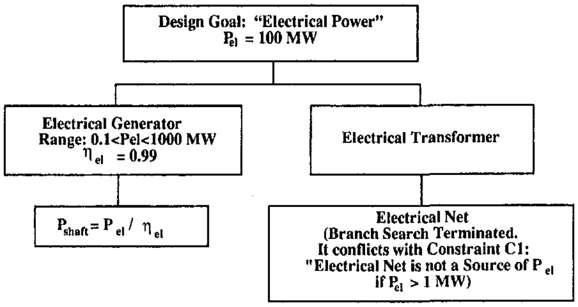

Fig. 3 Generation of electrical power: first step of the design decision

lated with p_p). In either case, p_p becomes *relevant;* and we will represent this by denoting it as $p_{r'}$. It becomes necessary, therefore, to establish and investigate the chain of functional relations that link all the p_r to each other (by definition, all the "always relevant" parameters p_a are also p_r). These functional relations f are the usual design relations: equality, constraint (weak and strong), polynomial dependence, etc., and constitute a sort of unstructured skeleton of functional links between different parameters.

2.2.3 Design Plan Generation. The Design Plan Generation Phase consists of the implementation of the skeleton plan produced in Phase 2 into a design plan. The relevant parameters are mapped onto (*set equal to*) the variables of a plan; the methods for assigning values are mapped onto (*developed into*) numerical or functional operators that act on the variables. The goals of the plan are then created, and the proper variable(s) are attached to them. Sets of variables corresponding to sets of tightly coupled parameters are attached to individual goals together with the applicable constraint(s). At the end of this process, all the elements of the design plan have been connected to each other in a network of goals that possesses (the network, and not necessarily the individual goals![5]) both the correct semantics of the original design problem, and the general rules of logical networks.

A design plan does not necessarily generate *a unique solution.* If the plan is correctly formulated, it will usually produce more than one feasible design. If needed, "optimization" procedures can be devised to choose, based on some criterion, the "best" one among different configurations proposed by the ES (but, see note 1 above). Notice that *additional information is needed to perform this extra task.* That is, each of the configurations proposed by the ES is feasible; but none is explicitly optimized at the time of its generation.

3 An Example of Automatic Process Design

Consider the most general problem that a designer can be faced with in the field of "energy systems": that of *choosing the most appropriate configuration to extract assigned amounts of exergy from a given resource base under some "environmental" as well as configurational constraints.* This apparently very complex problem turns out to have a relatively simple *qualitative* solution, but its complexity makes a *quantitative* solution difficult. The example discussed here consists of a procedure (called "COLOMBO" from "*CO* nstrained, *LO* gically *M*odified *B*oundaries *O*ptimization") [3, 8], that has been tested in several different realistic cases and has always proven to be capable of completely solving the problem, to be robust in consistently reaching acceptable solutions, and to be effective in its search of the solution space. The problem is posed in the following manner:

(A) Design data:

1 The required exergy rate(s) that must be specified both as to their *type* (electrical, mechanical, thermal) and their *amounts* (MW installed);

2 The type of *environment.* This comprises the following information:
- Type and amount of available resources (fuel, air, other materials that can take part in the process);
- Amount of water available (m^3/s);
- Any environmental characteristic that can be foreseen to influence the choice of the process (e.g., "station is mounted on a barge," or similar);
- All legal and/or technical constraints known to apply at the site under consideration.

3 A set of *negative* instances, i.e., of processes that cannot be accepted as a solution (e.g., "nuclear plant not acceptable").

(B) Components library (CL): for example, the procedure possesses its own default library (in the version used here, the library includes 27 components[6]):

back-pressure steam turbine
brine heater
combustion chamber
compressor
concentrated pressure loss
condenser
condensing steam turbine
contact (mixing) heat exchanger
distributed pressure loss
electric generator
electric motor
evaporator
feedwater heater
flow merger
flow splitter
fluidized bed combustor
fluidized bed heat exchanger
gas turbine
hydrostatic head
mechanical generator
power merger
power splitter
pump
separator
steam generator
surface heat exchanger
throttling valve

By adding new components, the list can obviously be expanded. A component is identified by a set of input and output streams (specifying the kind of working fluid, the type of power it adsorbs or delivers, and identifying which output streams are the "main" streams and which are the "byproducts"), the set of "design parameters" that uniquely identify it (inlet and outlet pressure, temperature, mass flow rate, power, etc.), and the set of mathematical rules that allow a complete specification of both the inlet and outlet streams given certain proper subsets of the design parameters.

A specific component is, in AI terms, an instance of a *class.* Such a class can be divided into *subclasses* according to some peculiar characteristic of each subclass. For example, if the

---

[5] There can be instances of conflicting goals (for example, minimum exchange area and maximum heat transfer in a heat exchanger) that are handled by the design plan in such a way that they result in an "optimal" heat exchanger configuration.

[6] Notice that some of the elements of the list are not actual components. They must be introduced though as such, because they *enact a process* (decrease the pressure of a stream, or partition a flow rate or power, etc.).

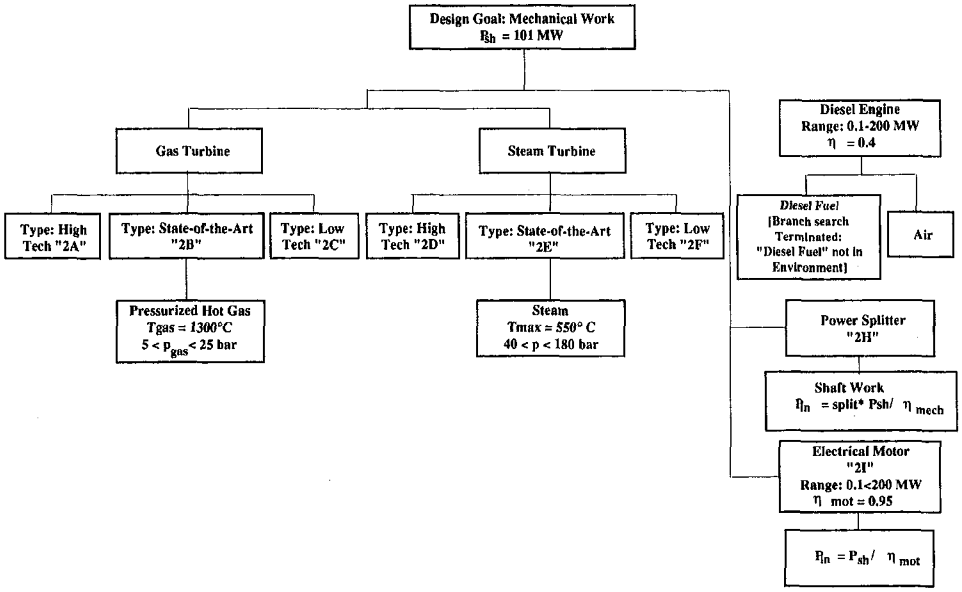

Fig. 4 Generation of shaft power: second step of the design decision

power range is chosen, the class "gas turbines" can be considered as comprising, say, four subclasses: "less than 5 MW," "between 5 and 30 MW," "between 30 and 100 MW," and "above 100 MW." These subclasses exhibit all properties of the class to which they belong (they are said to have *inherited* these properties) but can have different values (or ranges) of the design parameters. Each subclass is further divided (where feasible) into three types: "high tech," "state of the art" ("standard"), and "low tech." Again, this allows for different values of specific design parameters (in the case of a gas turbine, for instance, inlet gas temperatures will differ).

The procedure works *backward* (see Fig. 2), considering the design goal as an effect and trying to find its cause(s). Given the design goal, the inferential engine scans the component library to seek the components that would meet the goal (which is a given amount of thermal and/or mechanical and/or electrical power). The first component satisfying the goal is placed in the first slot of the working memory as the *last* component of a possible process P_1 that is still to be identified. If n components are found, there will be n possible "process trees" on which the procedure has to work. Then, for each P_i ($i = 1, \ldots n$), the inputs required by the component just found are taken to be the design goal, and the library is scanned again seeking for components whose outputs match the goal. The procedure is repeated until:

(*a*) All the required inputs are available from the class "environment" and the configuration developed so far meets all specified constraints. In this case, a process has been found, and is displayed to the user in a proper form (if more processes have been found, *all of them* are displayed);

(*b*) At a certain level in the process tree no match can be found (under the specified constraints) for the required inputs. The procedure is then aborted.

To "match" a design goal means that the output of the component under consideration must be of the same type as the design goal (mechanical power, etc.) and that the range attached to that subclass shares at least a subrange with the range required by the design goal. There are cases in which only the first of these two conditions is met, i.e., in which the output range of the component under consideration does not match the required input. In these cases, the component is added to the process, but the mismatch is recorded for future action. In fact, at each step the procedure checks whether there is the possibility that one or more "byproducts," or "secondary streams" can be used to force the match (for instance, increasing the temperature of the water flowing out of the condenser to match the boiler inlet temperature). A "relative cost" is attached to each of the constructed processes. This cost is a function of the number of components and of the number and amount of external resources used. So, for instance, a steam power plant with an externally fueled feedwater heater train will have a higher "cost" than the same process with regenerative feedwater heating.[7] COLOMBO, which is available on a UNIX platform but is almost universally portable being written in C++, displays the solution in the form of the interconnection matrix, **IM** (Section 6.1 of Part I of this series of papers). The design procedure can be directly "tested" by running it. Here, we give a detailed description of its structure by discussing a specific example: find the most appropriate plant of nameplate power P = 100 MW. Further design data are:

1 P has to be delivered in the form of electrical energy.
2 The environment is described by:
  - fuel: natural gas, of a given chemical composition, with LHV = 48000 kJ/kg, maximum available mass flow rate m_f = 70 kg/s;
  - air, of a standard chemical composition, at T_o = 32C and relative humidity φ_r = 50 percent;
  - no water available;
3 the following constraints apply:
  - plant factor P_f = 0.75 (6600 hours/year equivalent at nameplate load)
  - minimum conversion efficiency $\eta_{I,\text{process}}$ = 0.3

These data have to be given to the code in a proper form: COLOMBO needs a mix of numerical values (for the mass flow rates, for example) and propositional strings ("plant_output_is_electrical"). The specific format of the database can vary from case to case and also depends on the AI language chosen.

The logical steps of the inference process can best be described in the form of a decision tree. We will list here in the

---

[7] To avoid possible confusion, it must be stressed here that this "cost" may include monetary cost as well but is in general to be regarded as a sort of weighting or penalty function whose value is used by the search algorithm of COLOMBO to scan the decision tree more efficiently.

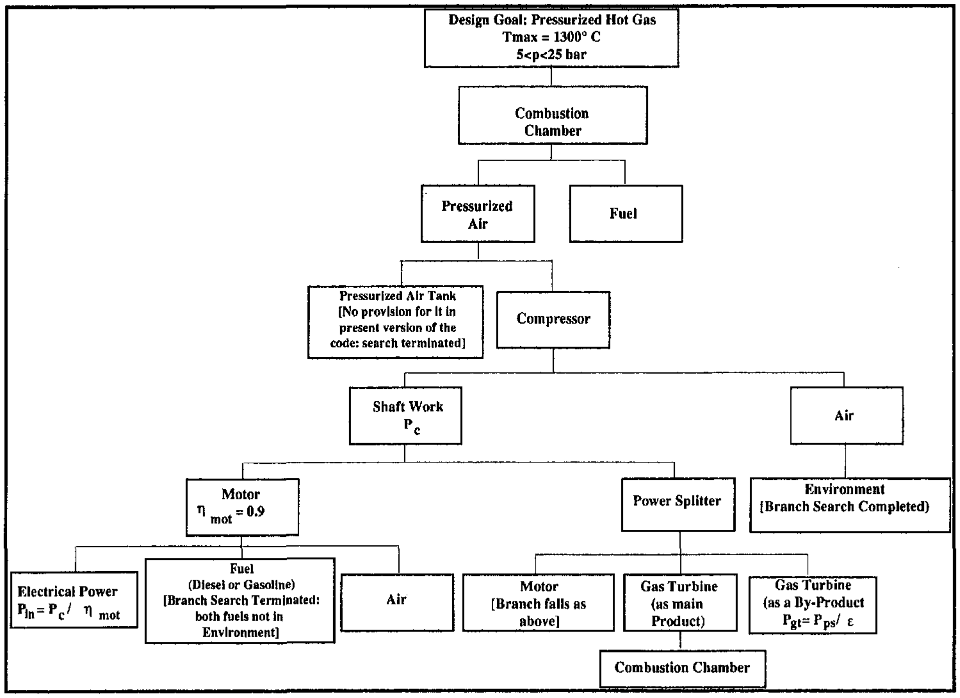

Fig. 5 Decision tree for gas turbine process selection and specification

proper order the decisional steps that have to be resolved and give for each of them its graphical representation in terms of nodes and branches [10]. ("CL" is COLOMBO's Component Library.)

- *1st design decision:* Find a component in CL capable of delivering 100 MW of electrical output. The search space is shown in Fig. 3. The result is "electrical generator," which needs a mechanical input of 101 MW.
- *2nd design decision:* Find a component in CL that delivers 101 MW of shaft work.

The pertinent portion of the search space is shown in Fig. 4. There are several possible choices:

gas turbine high-tech; input 2*A*: combustion gas at $T_{g,\max}$ = 1500°C
gas turbine standard; input 2*B*: combustion gas at $T_{g,\max}$ = 1300°C
gas turbine low-tech; input 2*C*: combustion gas at $T_{g,\max}$ = 1100°C
steam turbine high-tech; input 2*D*: steam at $T_{s,\max}$ = 650°C
steam turbine standard; input 2*E*: steam at $T_{s,\max}$ = 550°C
steam turbine low-tech; input 2*F*: steam at $T_{s,\max}$ = 450°C
diesel engine; input 2*G*: fuel oil, $m_{oil} \sim 6$ kg/s
power splitter; input 2*H*: shaft work P_{sh}
electrical motor; input 2*I*: electrical power P_{in}

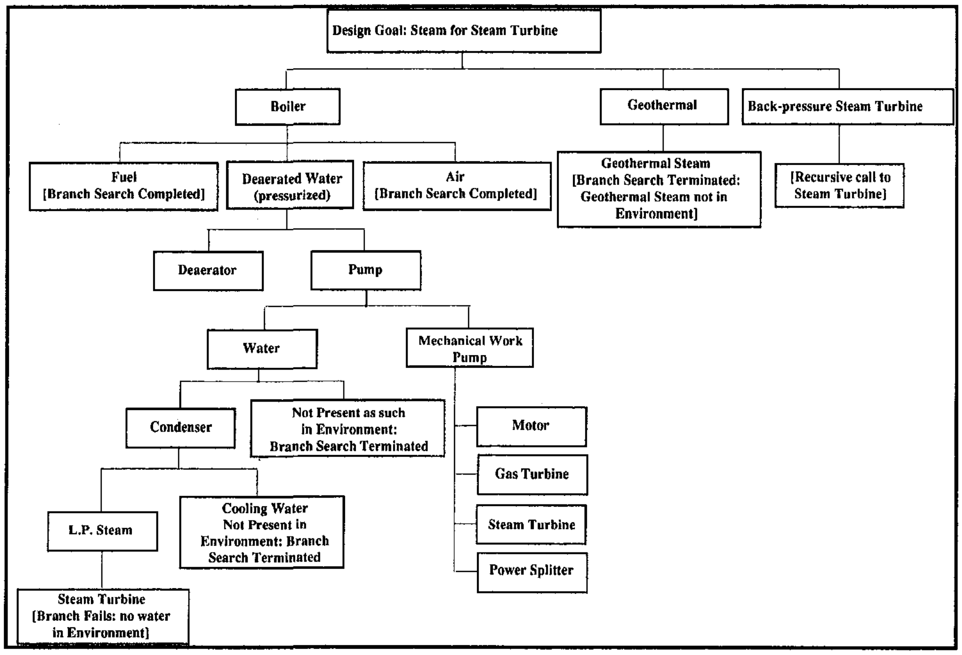

Fig. 6 Decision tree for steam generation process selection and specification

1st Process proposed by COLOMBO:

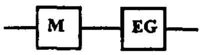

2nd Process proposed by COLOMBO:

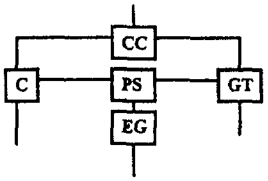

3rd Process proposed by COLOMBO:

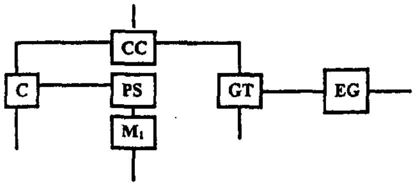

4th Process proposed by COLOMBO:

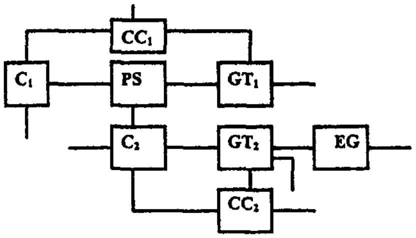

5th Process proposed by COLOMBO:

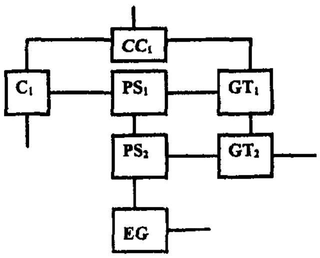

Fig. 7 The first five processes proposed by COLOMBO for electrical power generation

Notice that:

(*a*) The diesel engine is automatically discarded because its fuel ($2G$) is an input that is not available in the design environment;

(*b*) At this stage, we will not follow the "power-splitter" ($2H$) nor the "electrical motor" ($2I$) branches; but, as we will see, they are also capable of generating valid configurations;

(*c*) At this point, there are 6 "possible partial processes" and no constraint has been violated. For the sake of simplicity, we will follow goals $2B$ and $2E$ (see Fig. 4) and neglect the high- and low-tech possibilities.

- *3rd design decision:* Find all the components in CL that deliver inputs $2B$ and $2E$.

The pertinent portion of the search space is shown at the first level of the search trees of Fig. 5 for Goal $2B$ (the gas turbine) and in Fig. 6 for Goal $2E$ (the steam turbine). The available components are—quite obviously—combustion chambers that produce combustion gases and boilers that produce steam. Here, too, there would be three *types* of component for each class: high, standard, and low technology items. For the sake of simplicity, the type has not been explicitly included in the search shown in Figs. 5 and 6.

- *4th design decision:* consider $3A$ (combustion chamber) and find all components in CL that deliver "fuel" and/or "pressurized air."

The search space is shown at the second level of the search trees shown in Fig. 5. The "fuel" input is contained in the "environment." This portion of the branch search is terminated successfully. The "pressurized air" can be generated by a compressor, which needs air and shaft work as inputs.

- *5th design decision:* Find all components that deliver "air" and/or "shaft work."

The search space is shown in the lower portion of Fig. 5. "Air" is available from the environment. This portion of the branch search is terminated. "Shaft work" can be generated as the

- byproduct of a gas turbine
- main product of a gas turbine
- byproduct of a power splitter
- main product of a power splitter

- *6th design decision:* Try matching the required compressor input with the gas turbine output.

This is a constraint-checking activity. Since no constraints are violated and all inputs are available in the environment, a structured chain of components has been constructed that leads from the design goal (P_{el} = 100 MW). The corresponding process scheme is shown in Fig. 7.

- *7th design decision:* Try matching the compressor required input with the output of a power-splitter.

This is always possible; but, since a power splitter requires a work input, this procedure starts producing ever more complicated processes in which the compressor is powered by a gas turbine plant whose compressor is in turn powered by yet another gas turbine plant, and so on. However, there are specific built-in rules that avoid excessive recursivity (they cut the recursive procedures after, say, three or four steps). Some of the corresponding process schemes are shown in Fig. 7. Notice that the possibility for a power splitter to be fed by another power splitter is explicitly negated by the procedure in order to avoid useless looping.

- *8th design decision:* Consider $3D$ (steam generator) and find all components in CL that deliver "fuel" and/or "air" and/or "deaerated water."

The search space is shown at the second level of the search tree of Fig. 6. Both the "air" and the "fuel" inputs are contained in the "environment." This portion of the branch search is terminated successfully. The "deaerated water" can be generated by a deaerator that needs water and medium-pressure steam as inputs.

- *9th design decision:* Find all components that produce medium-pressure steam.

The search space is shown in the lower portion of Fig. 6. Since there is no cooling water available in the environment, and CL does not contain "air-cooled condensers," this branch search fails (for a detailed description of the successive attempts COLOMBO makes before failing, see [3]).

- *10th design decision:* Check if there are any unexplored branches.

This is a sort of a bookkeeping activity. Since no branch is found that has not been explored, the run is terminated.

A list of the first five configurations produced by the run described above is shown in Fig. 7. Notice that configuration 1 has been produced because the code has assumed—wrongly—that it can drive a 100 MW electrical motor directly from the net, since electricity is available from the net![8] This bug was detected in the first version of the code and amended, but it has been presented here to demonstrate the importance of working with a complete and exhaustive knowledge-base.

4 Conclusions

The possibility of implementing completely computer-assisted design procedures has been demonstrated in this series of two papers. In Part I, the highly systematic and modular numerical calculations that constitute the basis of quantitative process design have been translated into a completely process-independent computer code, which can be regarded as a ''general purpose numerical simulator.'' In Part II, the general theoretical steps that constitute the path from design inception to design realization have been analyzed with the purpose of extracting from the decisional patterns of a human process engineer the essential features that could be used to formulate a general Artificial Intelligence procedure capable of performing ''Process Synthesis.'' A prototype expert system has been implemented as a result of this analysis, and a first assessment of its capabilities has been attempted. A direct application to the generation of a process scheme for a power plant gives positive indications about the capability of the code to perform general process engineering tasks. Since the project has been coordinated in such a way that the two computational environments in which the two codes perform can be made to communicate at run time, COLOMBO and CAMEL can be run concurrently (the latter being a sort of mathematical subroutine to the former) and constitute an extremely powerful tool for automatic, entirely computer assisted process design.

References

1 A. Bejan, G. Tsatsaronis, and M. Moran, *Thermal Design and Optimization,* Wiley, 1995.

2 E. Charnak, and D. McDemmott, *Introduction to Artificial Intelligence,* Addison-Wesley, 1985.

3 M. De Marco, M. F. Falcetta, R. Melli, B. Paoletti, and E. Sciubba, ''COLOMBO: an expert system for process design of thermal powerplants,'' ASME AES-Vol. 1/10, 1993.

4 R. B. Evans, ''Thermoeconomic isolation and essergy analysis,'' *Energy,* Vol. 5, No. 8–9, 1980.

5 C. A. Frangopoulos, ''Intelligent functional approach: a method for analysis and optimal synthesis-design-operation of complex systems,'' *IJEEE,* Vol. 1, No. 4, 1991.

6 C. A. Frangopoulos, ''Optimal synthesis and operation of thermal systems by the thermoeconomic functional approach,'' ASME JOURNAL OF ENGINEERING FOR GAS TURBINES AND POWER, Vol. 114, Oct. 1992.

7 A. S. Kott, J. H. May, and C. C. Hwang, ''An autonomous Artificial Designer for thermal energy systems,'' ASME JOURNAL OF ENGINEERING FOR GAS TURBINES AND POWER, Vol. 111, Oct. 1989.

8 R. Melli, B. Paoletti, and E. Sciubba, ''SYSLAM: an interactive expert system approach to Powerplant design and optimization,'' *IJEEE,* Vol. 2, No. 3, 1992.

9 B. Olsommer, M. R. von Spakovsky, and D. Favrat, ''An approach for the time-dependent thermoeconomic modeling and optimization of energy system synthesis, design and operation,'' *Proc. TAIES'97,* World Publishing Co., Beijing, China, 1997.

10 B. Paoletti, and E. Sciubba, ''Artificial Intelligence in Thermal Systems Design: concepts and applications,'' in: *Developments in the Design of Thermal Systems,* R. Boehm ed., Cambridge Univ. Press, 1997.

11 P. Y. Papalambros, and D. J. Wilde, *Principles of optimal design: Modeling and Computation,* Cambridge University Press, 1988.

12 W. C. Press, *Numerical Recipes,* McGraw-Hill, 1985.

13 G. V. Reklaitis, A. Ravindran, and K. M. Ragsdell, *Engineering Optimization,* Wiley, 1983.

14 E. Rich, *Artificial Intelligence,* McGraw-Hill, 1983.

15 M. R. von Spakovsky and R. B. Evans, ''Engineering functional analysis,'' ASME *Journal of Energy Resources Technology,* Vol. 115, No. 2, 1993.

16 L. E. Widman, K. A. Loparo, and N. R. Nielsen, *Artificial Intelligence, Simulation and Modeling,* Wiley, 1989.

---

[8] The possibility of extracting electrical power from an electric net, if present, is of course included in COLOMBO's rules: The situation here negates it though, because this power would not be used to operate auxiliary equipment (as would be the case, for instance, in an electrically powered feedwater pump in a steam powerplant); but it would satisfy the main goal of the process (which is ''Generate 100 MW of electrical power'').

The Applicability of Jet-Shear-Layer Mixing and Effervescent Atomization for Low-NO_x Combustors

R. O. Colantonio
NASA Lewis Research Center,
21000 Brookpark Road,
Mail Stop 500-115,
Cleveland, OH 44135

An investigation has been conducted to develop appropriate technologies for a low-NO_x, liquid-fueled combustor. The combustor incorporates an effervescent atomizer used to inject fuel into a premixing duct. Only a fraction of the combustion air is used in the premixing process. This fuel-rich mixture is introduced into the remaining combustion air by a rapid jet-shear-layer mixing process involving radial fuel–air jets impinging on axial air jets in the primary combustion zone. Computational modeling was used as a tool to facilitate a parametric analysis appropriate to the design of an optimum low-NO_x combustor. A number of combustor configurations were studied to assess the key combustor technologies and to validate the three-dimensional modeling code. The results from the experimental testing and computational analysis indicate a low-NO_x potential for the jet-shear-layer combustor. Key features found to affect NO_x emissions are the primary combustion zone fuel–air ratio, the number of axial and radial jets, the aspect ratio and radial location of the axial air jets, and the radial jet inlet hole diameter. Each of these key parameters exhibits a low-NO_x point from which an optimized combustor was developed. Also demonstrated was the feasibility of utilizing an effervescent atomizer for combustor application. Further developments in the jet-shear-layer mixing scheme and effervescent atomizer design promise even lower NO_x with high combustion efficiency.

Introduction

Recent concerns on the destruction of the ozone layer brought on by pollutants have led to the development of low emission aircraft combustor concepts. One ozone-depleting pollutant created during the combustion process is oxides of nitrogen ($NO_x = NO + NO_2$). NO_x is a catalyst to the destruction of ozone. The formation of NO_x has been shown to be an exponential function of flame temperature. The temperature sensitivity of NO_x production is due to the fact that the reactions primarily involve atomic oxygen, which does not appear in large quantities at low temperatures. The chemical rate reactions are also sensitive to temperature. Therefore, the key to any successful low-NO_x combustor is to provide sufficient time and temperature for complete combustion but not enough time and temperature for high-NO_x emission levels. This has been accomplished by producing a nearly homogeneous fuel–air mixture and burning well away from stoichiometric conditions (lean or rich combustion).

Many combustor schemes have been designed and tested to reduce NO_x emissions. One scheme is Lean Direct Injection (LDI). The idea behind the LDI combustor is to provide a suitable fuel atomizer that will produce exceptionally small droplets. Current atomizers produce droplets that are too large for low-NO_x applications. Small droplet production is essential since large drops burn stoichiometrically via a diffusion-type mechanism and create local hot regions in the flow field. In the LDI concept, fuel droplets are injected into the primary combustion zone in such a way as to provide complete mixing, vaporization and burning. If this is not accomplished fully, some degree of fuel and air nonuniformity will occur and give rise to local hot regions (Lyons, 1981).

The present test program examines the effectiveness of an LDI combustor concept incorporating jet-shear-layer mixing for reducing NO_x emissions. A jet-shear-layer (JSL) mixing scheme, involving axial air jets impinging directly on radial fuel–air jets near the dome inside a flametube combustor, was shown by Abdul-Aziz and Andrews (1991), Abdul-Aziz et al. (1983), Abdul-Hussain and Andrews (1987, 1992), Abdul-Hussain et al. (1988a, b), Al-Dabbagh and Andrews (1981), and Al-Dabbagh et al. (1985) to provide rapid mixing with good combustion stability and low NO_x. They have demonstrated in one atmosphere the effectiveness of the JSL mixing scheme in combustor design. Water flow visualization tests were performed on axial and radial jet impingement showing mixing was 90 percent complete within five axial hole diameters and the jet spreading rate increasing to 90 deg as compared to 10 deg without radial jet interaction. The work done used both gaseous and liquid fuels. The use of liquid fuels has been shown to produce higher NO_x as compared to using gaseous fuels (Abdul-Aziz et al., 1987a, b; Abdul-Hussain and Andrews, 1989, 1990).

The goal of this study is to investigate whether the demonstrated low-NO_x potential of the JSL combustor when burning gaseous fuels is still present for liquid fuels. Two key features were added to the JSL combustor concept: a fuel–air premixing region and an effervescent atomizer. Premixing of all the fuel with some of the air prior to combustion permits greater fuel–air uniformity within the combustor and allows some degree of fuel droplet vaporization to take place (Anderson, 1973, 1975; Roffe and Ferri, 1975, 1976; Roffe, 1976). This fuel-rich, unignitable premixing region avoids the flashback problems encountered in some lean premixed combustor concepts.

To provide a minimal level of large, NO_x-producing fuel droplets, an effervescent fuel atomizer was used in the premixing region of the JSL combustor. In an effervescent atomizer, air bubbles are injected directly into the fuel upstream of

---

Contributed by the International Gas Turbine Institute for publication in the Journal of Engineering for Gas Turbines and Power. Manuscript received by the International Gas Turbine Institute October 22, 1995. Associate Technical Editor: G. S. Samuelsen.

the atomizer discharge orifice. Unlike some atomizers (e.g., air blast atomizers) only a small amount of air is needed for fuel atomization in an effervescent atomizer. It has been demonstrated (Roesler, 1988; Whitlow, 1990; Lefebvre, 1988) that these bubbles break up the fuel into ligaments, which are then ejected from the atomizer orifice at high velocities. The air bubbles explode upon exiting the orifice. These mechanisms all contribute to the production of small droplets (<20 μm Sauter mean diameter, SMD).

The simplicity and size of the JSL combustor make it an alternative to other low-NO_x combustors currently being developed. Therefore, for the present study it was hoped that successful, low-NO_x results could be achieved by incorporating an effervescent atomizer and partial premixing of the fuel and air into a JSL combustor using liquid fuels. To promote the highest degree of fuel-air mixing within the combustor a three-dimensional CFD code was used as a tool to facilitate a parametric analysis over a wide range of combustor operating conditions. This analysis led to an optimum configuration of a low-NO_x, JSL combustor. A number of combustor configurations were experimentally tested to demonstrate the low-NO_x potential of the liquid-fueled JSL combustor and to verify the CFD model.

Experimental

Various approaches to reducing NO_x were studied in some detail. Based on these reviews, an Allison T-56 combustor was modified to incorporate some key features of different experimental low-NO_x combustors. These key features include jet-shear-layer mixing in the primary zone, a premixed region upstream of the primary zone, and an effervescent atomizer.

The modified T-56 combustors are shown in Fig. 1. A summary of the JSL combustor configurations experimentally tested is listed in Tables 1 and 2. Airflow splits were calculated by using data obtained from measuring pressure drops (e.g., $\Delta P/P_3$ where P_3 is the combustor inlet pressure) across the combustor at various cold flow rates. Specific slots were blocked and pressure drops and flow rates were measured to determine the fraction of air going to each slot in the combustor. Most practical combustors have a cold flow pressure drop between 4 to 10 percent as compared to the 8 to 13 percent for the JSL combustor reported here. However, most of the combustor parameter changes were performed at 13 percent pressure drop so that their effect on emissions could be demonstrated. The combustors have a diameter of 0.138 m and an overall length of 0.432 m. The combustor liner length is 0.369 m. The combustor liner is a standard T-56 liner with all primary and dilution air holes on the liner blocked. Some cooling slots on the liner were still used to protect its structural integrity. The front dome sections of the T-56 combustors were removed and replaced by dome plates incorporating axial slots and a premixing duct from which radial jets eject a fuel and air mixture. All of the fuel and some of the air are premixed upstream of the primary combustion zone. Fuel is injected into the 38.1-mm-dia premixing duct via an effervescent atomizer, which can be moved axially to adjust the premixing length. The premixing duct is 0.102 m long.

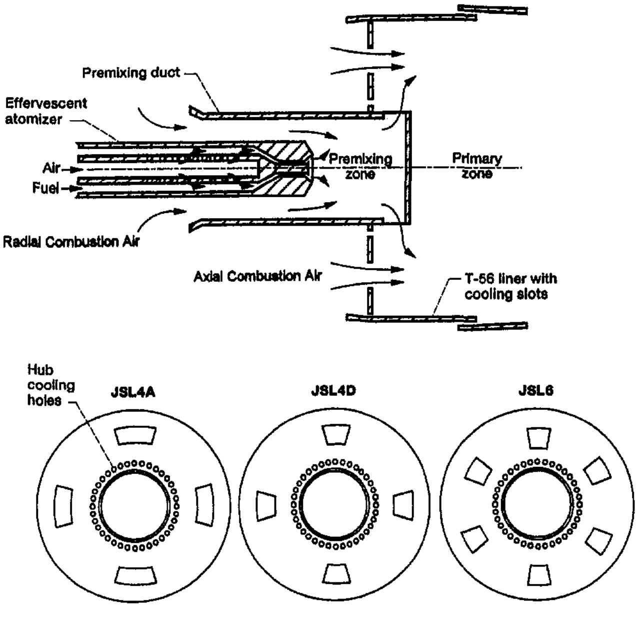

Fig. 1 Jet-shear-layer combustor configurations

Table 1 Airflow splits for JSL combustors

Air Slots	Combustor					
	JSL4A	JSL4B	JSL4C	JSL4D	JSL4E	JSL6
	Airflow splits, percentage of total airflow[a]					
Liner Cooling	50	40	25	25	25	25
Axial Combustion	32	39	48	48	47	48
Radial Combustion	14	16	20	20	22	20
Hub Cooling	4	5	7	7	6	7

[a] Nominal combustor airflow rate, 0.70 kg/s.

During the initial testing period, the central hub of the premixing duct that protrudes into the primary combustion zone partially ablated away. This was attributed to the central hub acting as a flameholder. To eliminate this problem, 36 2.54-mm-dia holes were drilled 10 deg apart around the outer perimeter of the hub (Fig. 1). These holes provide direct convective cooling to the hub. However, it should be noted that since the hub cooling jets are impinging on the radial jets, the radial jets will not be exactly 90 deg to the axial jets. Also, the radial jets may still have some residual axial velocity component stemming from the sharp 90 deg bend the premixed gas makes before exiting from the radial holes. This deviation from 90 deg will increase with larger radial location from the axial slots. This differs from past JSL flametube combustors tested by other researchers where the radial jet hole is longer to ensure a 90 deg impingement area.

The experimental combustor is configured in the test facility as shown in Fig. 2. The 0.635-m-long test section that houses the combustor tapers in diameter from 0.191 to 0.140 m. Flow straighteners are located upstream of the test section to smooth out the air flow. Downstream of the flow straighteners are two concentric diffusers used to expand the air to the 191-mm-dia test section inlet. Inlet temperature and pressure are monitored by a chromel/alumel thermocouple and a pressure tap, respectively, located in the test section housing. A traversing gas sampling probe, located directly downstream of the test section housing, is used to collect gaseous emissions. A description of

Table 2 Configurations for JSL combustors

Combustor	Axial Slot Centerline, r/R	Axial Slot Aspect Ratio, AR	Pairs of Axial/Radial Slots	Radial Hole Diameter, mm	$\Delta P/P_3$,%[a]
JSL4A	0.72	2.49	4	14.7	8
JSL4B	0.72	2.49	4	14.7	10
JSL4C	0.72	2.49	4	14.7	13
JSL4D	0.72	1.00	4	14.7	13
JSL4E	0.72	1.00	4	17.5	13
JSL6	0.72	1.00	6	12.3	13

[a] Cold flow pressure drop only.

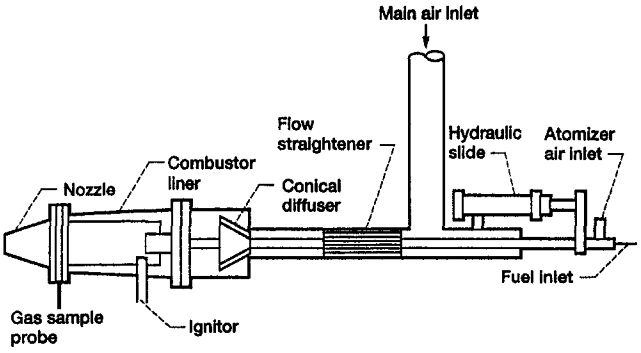

Fig. 2 Test section configuration

the gas sampling system is given elsewhere (Colantonio, 1993). This report also contains a full description of the methods employed in sampling and measuring NO_x, CO, CO_2 and unburned hydrocarbons. Essentially a single-point, water-cooled traversing probe was used to sample emissions on one radial axis of the combustor exit. A 4.76-mm-dia Iconel gas sampling collection tube was located 102 mm downstream of the combustor exit. Gas flows through an electrically heated sampling line maintained at 505 K up to the gas analyzers. The combustion exhaust gases exit the test section into a fixed-geometry converging nozzle, which governs back pressure at a given flow condition. The exhaust gases are then expelled to the atmosphere.

The effervescent atomizer used in this research program is shown in Fig. 1. Its geometry and flow characteristics are based on work done by Whitlow (1990). For the atomizer air–fuel ratio of 0.2 (by mass) used for this testing the Sauter mean diameter and drop size distribution parameter were experimentally determined to be 20 μm and 1.8, respectively. The atomizer consists of two concentric tubes, 25.4 mm and 12.7 mm in diameter. The inner tube supplies effervescent air to the annular gap region where fuel is flowing. Thirteen sets of 0.79-mm-dia holes, spaced 3.18 mm apart in the inner tube, are used to inject air bubbles into the fuel. The pintle gap width is 0.51 mm and produces a spray having an included angle of 90 deg. No variations in atomizer characteristics other than fuel and atomizer air flow rates were performed in this test program.

Computational

An advanced CFD package (CFD Research Corporation, 1990), REFLEQS (Reactive Flow Equation Solver), was used to model the primary combustion zone of the JSL combustor and incorporated the effects of liner cooling air. REFLEQS solves the full three-dimensional Navier–Stokes equations for fluid flow in a generalized coordinate system. For reactive flows, additional energy and species concentration equation are solved. The main features used in REFLEQS are the one-step instantaneous burning of propane (C_3H_8), a standard $k-\epsilon$ turbulence model, upwind differencing scheme, standard JANNAF thermodynamic properties and stoichiometric relations and a simple Zeldovich reaction scheme for calculating NO_x emissions. REFLEQS is a well-documented program and has been validated by many users. Over 30 validation cases have been performed and good-to-excellent agreement between benchmark data and predictions has been shown (Ratcliff and Smith, 1989; Smith et al., 1988).

Boundary conditions selected for REFLEQS are based on reviews of previous combustor modeling and testing and on data obtained from preliminary JSL combustor testing. A full description of the boundary conditions used can be found from Colantonio (1993). Although liquid Jet-A fuel was used in the experimental program, the chemical complexity of Jet-A combined with the unavailability of a fuel droplet vaporization and burning model in REFLEQS confined the present CFD work to a gaseous fuel, namely propane. Due to the incorporation of an effervescent atomizer and a premixing duct, the assumption of complete fuel vaporization was considered valid for a parametric study of the JSL combustor configuration. Combustor wall temperature boundaries were estimated from thermal indicating paint applied to the outside of the combustor and also from empirical relations for film-cooling combustor liners.

The NO_x model assumes NO_x reaction does not contribute to the overall heat release in the combustor and NO_x concentration itself is small compared to those of other species. Also, prompt NO is ignored in the model. This assumption allows NO_x reactions to be decoupled from the heat release reactions. NO_x is calculated as a passive scalar after the computation of the reacting flow field.

A simple Zeldovich reaction scheme was used to model NO_x formation. According to the mechanism, NO can be expressed by:

$$N_2 + O \rightarrow NO + N$$

$$O_2 + N \rightarrow NO + O$$

The first reaction is much slower than the second one and hence controls the rate of NO formation. If the concentration of NO is much smaller than the corresponding equilibrium value, the rate equation for NO can be written as:

$$\partial(NO)/\partial t = K(N_2)(O)$$

The rate coefficient, K, has been experimentally determined to be an exponential function of temperature. Approximating the concentrations of N_2 and O by the local equilibrium values, the rate equation is given by

$$\partial(NO)/\partial t = A \exp(-E/RT)(N_2)(O_2)^{1/2}$$

where A is an experimentally determined constant, E is the activation energy in joules per mole, R is the universal gas constant, and T is the gas temperature in degrees Kelvin. Due to the one-step instantaneous chemical kinetics model, REFLEQS does not take into account combustion inefficiency and chemical dissociation, both of which will lower the actual adiabatic flame temperature within the combustor and hence, over-estimate the NO_x emissions. Therefore, the NO_x model in REFLEQS was calibrated against experimental data shown in Fig. 3 over a wide range of fuel–air ratios by adjusting the A and E/R terms. Even with these simplifying assumptions REFLEQS provides

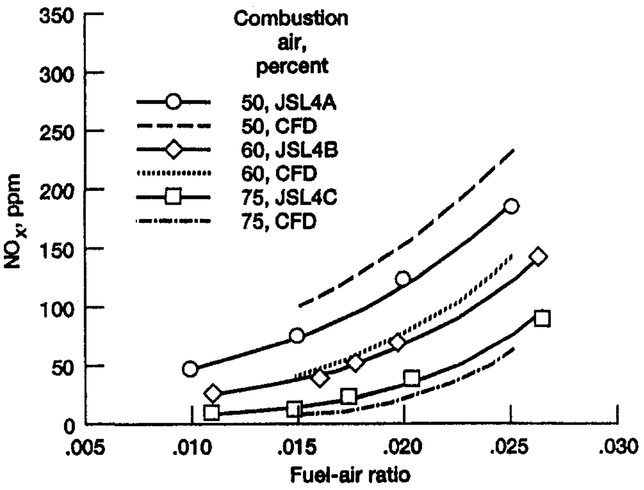

Fig. 3 Effects of fuel–air ratio and combustion air quantity on NO_x emissions; T_A = 551 K; P_A = 0.48 MPa

an unique means to optimize combustor parameters for low NO_x and substantiates the experimental results.

Results

In order to simulate an Allison T-56 combustor at cruise conditions the inlet combustor pressure, P_A, and inlet temperature, T_A, for both the experimental testing and computational analysis were 0.480 MPa and 551 K, respectively. The fuel–air ratios ranged from 0.012 to 0.025 for experimental testing and from 0.015 to 0.025 for CFD analysis. The nominal air flow rate was 0.70 kg/s. The nominal air flow rate for a T-56 combustor at cruise condition is 1.17 kg/s. However, this higher flow rate includes additional liner cooling, dilution, and secondary air not used in the present JSL combustor. Also, the air flow rate at a given inlet pressure is controlled by the fixed converging nozzle downstream of the combustor exit. The nominal air/fuel ratio (by mass) of the effervescent atomizer was 0.20. The premixing length was kept constant at 76.2 mm. In all experimental testing Jet-A fuel was used.

Each of the air flows within the JSL combustor is governed by pressure differential across the air slots. Therefore, a decrease in liner cooling air necessarily results in increases in the axial, radial, and hub cooling air flows. It is assumed that all the axial, radial, and hub cooling air flows participate in combustion, with negligible liner cooling air interaction. As combustion air is increased (by blocking liner cooling slots) for a fixed fuel–air ratio, the primary combustion zone burns leaner, resulting in lower predicted NO_x emissions (Fig. 3). Also, with higher combustion air come higher air slot velocities, which could increase the degree of fuel–air mixing from the greater momentum transfer between impinging jets. Combustor efficiency suffers slightly from increasing the combustion air (Fig. 4), which is attributed to higher unburned hydrocarbons emanating from a cooler combustion zone.

It has been determined through CFD analysis that the radial location of the axial air slots has a direct effect on NO_x emissions. This was also shown in the work of Abdul-Hussain et al. (1988a, b). The axial slot position was varied from radially inward, toward the central premixing duct, to radially outward, toward the combustor liner wall. The maximum and minimum radial positions in the CFD analysis were limited due to the axial slot thickness and the position of the hub cooling holes. Therefore, the radial position of an axial slot, having an aspect ratio, AR, of 2.49, was varied from an r/R of 0.58 to 0.88 where r is the radial location within the combustor of radius R.

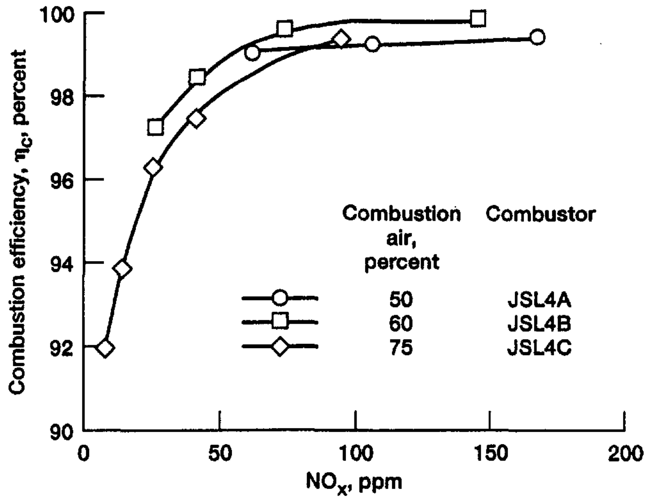

Fig. 4 Experimental results showing the effects of combustion efficiency and combustion air quantity on NO_x emissions (fuel-to-air ratio is varying); T_A = 551 K; P_A = 0.48 MPa

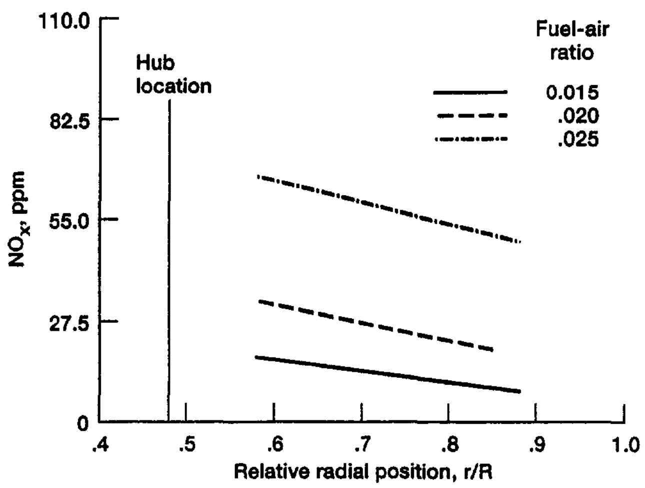

Fig. 5 CFD predictions of the effects of axial slot radial position and fuel–air ratio on NO_x emissions; T_A = 551 K; P_A = 0.48 MPa

The AR is defined as the slot arc length divided by the slot width. The arc length is calculated from the slot's circumferential centerline as indicated in Table 2.

A fuel-rich radial jet intercepting an axial air jet produces a nominally fuel-lean jet downstream of the interception region. However, jet expansion into the combustor volume is critical for thoroughly mixing all the fuel with the axial air. The gaps between the adjacent axial jets increases with a more outward axial slot. As this gap decreases with a more inward axial slot, the jets are confined to expand and mix in the circumferential direction. As the axial slot is moved radially outward, the axial jet is less confined and can expand freely into the combustor volume in both the circumferential and radial directions. Figure 5 shows the CFD predictions of the effect of axial slot radial position on NO_x emissions for a four-slotted JSL combustor using 75 percent combustion air. Lower NO_x is produced with axial slots closer to the liner wall as compared to the central hub.

The AR was varied from 0.61 to 5.22 while maintaining the axial slot area constant. The outer radius of the axial slots was held at an r/R of 0.82. Figure 6 shows the CFD predictions of NO_x emissions as axial slot AR is varied for a four-slotted JSL combustor with 75 percent combustion air. The lowest NO_x is produced with an AR close to unity. This suggests that round axial holes might be superior to rectangular axial slots. Any change in AR away from unity increases NO_x. From CFD-

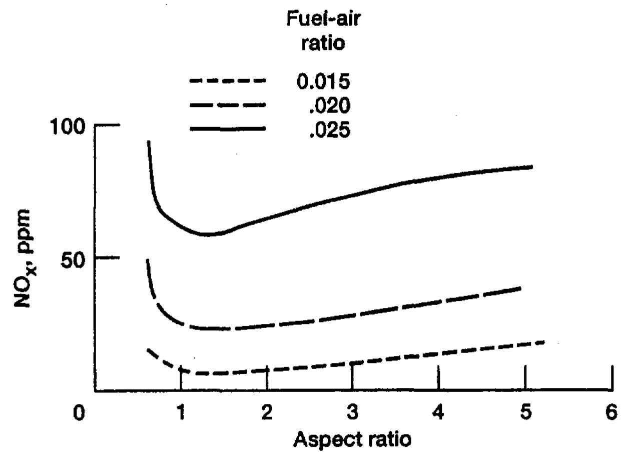

Fig. 6 CFD predictions of the effects of axial slot aspect ratio and fuel–air ratio on NO_x emissions; T_A, = 551 K; P_A = 0.48 MPa

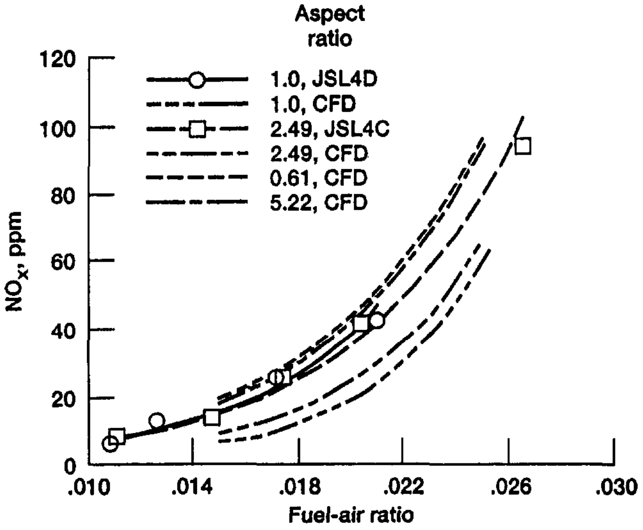

Fig. 7 Effects of fuel–air ratio and axial slot aspect ratio on NO$_x$ emissions; T_A = 551 K; P_A = 0.48 MPa

generated temperature profiles within the combustor (Colantonio, 1993) a circumferentially thin axial jet appears to act like a wedge for the incoming fuel-rich radial jets, preventing the radial jet from breaking up the axial jet adequately. Instead, the radial jet only partially breaks up the bottom portion of the axial jet, with high-temperature combustion occurring at the sides of the axial jet. A higher AR restricts the axial jet from expanding and mixing circumferentially into the combustor volume. Figures 7 and 8 show the experimental results obtained for a four-slotted JSL combustors having ARs of 1.0 and 2.4, respectively. The higher AR yielded a slightly lower NO$_x$. However, the combustion efficiency for an AR of 1.0 is greater than that for an AR of 2.4.

The axial and radial jet pairs were varied from 3 to 6. In each case the axial and radial slot areas remained constant. Also, the AR of the axial slot was kept constant at 1.00. The gap between adjacent axial jets decreases with an increase in number of in-line jets. As this gap becomes narrower, the axial jets cannot expand and mix adequately into the combustor volume without interfering with adjacent jets. Figure 9 shows the CFD predictions of number of in-line jets on NO$_x$ emissions. Lower NO$_x$ was produced with fewer in-line jets. Figures 9 and 10 show the experimental results obtained from JSL combustors having four and six pairs of in-line jets, respectively. The four-slotted combustor produced lower NO$_x$ emissions with higher combustion efficiency as compared to the six-slotted combustor. These results verify the CFD trends in varying the number of in-line jets.

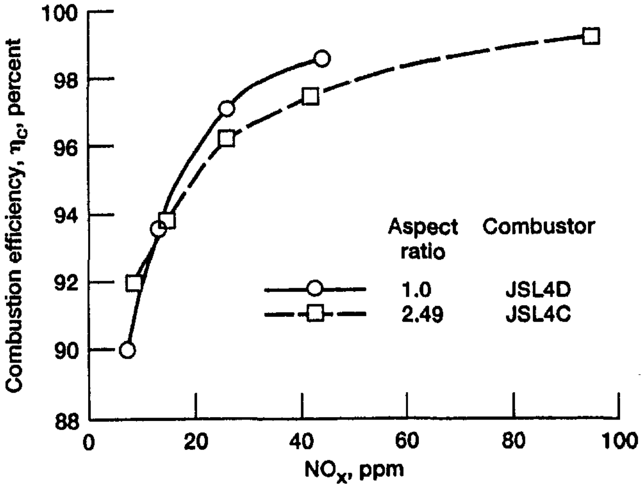

Fig. 8 Experimental results showing the effects of combustion efficiency and axial slot aspect ratio on NO$_x$ emissions (fuel-to-air ratio is varying); T_A = 551 K; P_A = 0.48 MPa

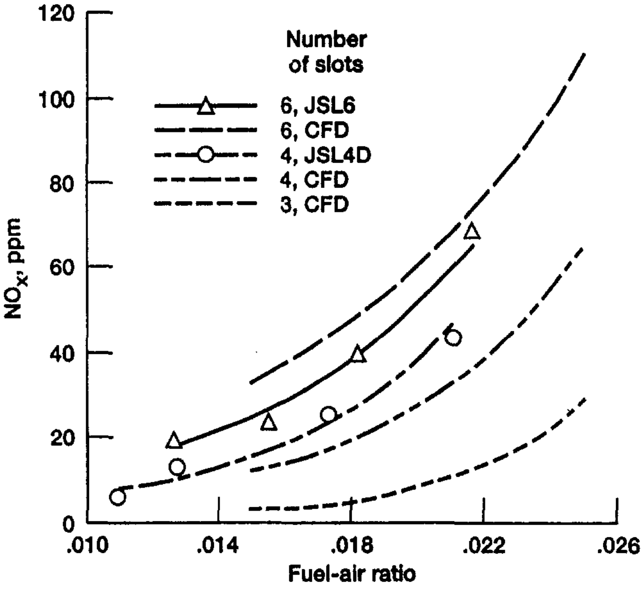

Fig. 9 Effects of fuel–air ratio and number of in-line jets on NO$_x$ emissions; T_A = 551 K; P_A = 0.48 MPa

It has also been determined from experimental and CFD results that the radial jet hole diameter has a direct effect on NO$_x$ emissions. The radial hole size was varied from 9.93 to 17.46 mm. Increases in premixing air lower NO$_x$ emissions. However, an increase in radial hole size does not, in all cases, decrease NO$_x$ emissions. The flow through all the air ports in the combustor is governed by pressure differential, hole area, and discharge coefficients. The annular gap cross-sectional area between the effervescent atomizer and the inner wall of the premixing duct is fixed (Fig. 1). If the total radial jet hole area is greater than the total annular gap area, then the air flow through the premixing tube will be controlled by the annular gap region. As the hole diameter is continually increased, a critical radial hole diameter is reached where further increases in hole diameter cannot increase the premixing flow rate. At this point, the flow rate will be metered by the annular gap region and the radial jet velocity is reduced.

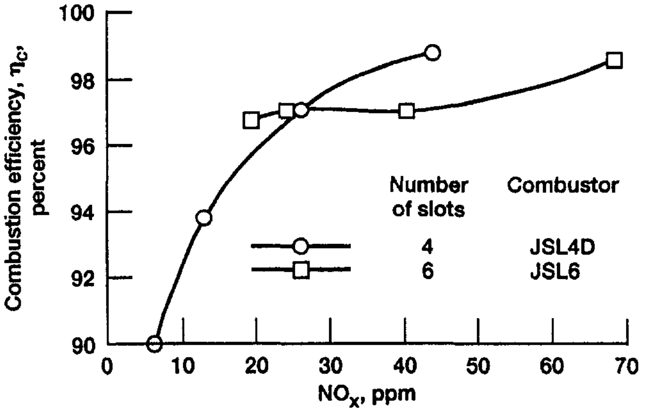

Fig. 10 Experimental results showing the effects of combustion efficiency and number of in-line jets on NO$_x$ emissions (fuel-to-air ratio is varying); T_A = 551 K; P_A = 0.48 MPa

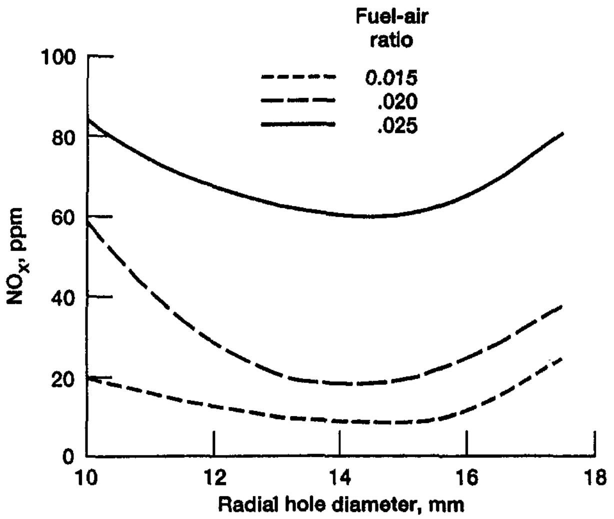

Fig. 11 CFD predictions of the effects of radial hole diameter and fuel-air ratio on NO_x emissions; T_A = 551 K; P_A = 0.48 MPa

Figure 11 shows the CFD predictions of radial hole diameter on NO_x. The lowest NO_x was produced with a radial hole diameter around 15 mm and increases for smaller and larger diameter holes. For small-diameter holes, higher NO_x is caused by low premixing air flow. For large diameter holes, higher NO_x is caused by the low velocity radial jets not mixing adequately with the axial jet air.

Figures 12 and 13 show the experimental results obtained for the JSL combustor having an axial slot AR of unity. Experimental results verify the NO_x trends of the CFD results, but the quantitative agreement of the NO_x prediction was poor. The large holes produce high NO_x emissions and low combustion efficiency. From this parametric study it appears that the radial hole diameter is critical for a given premixing duct size. No attempt was made to optimize the effervescent atomizer. A smaller diameter atomizer should be designed to allow more premixing air and a resulting higher radial jet velocity.

Conclusions

By incorporating an effervescent atomizer in a fuel–air premixing duct and using a three-dimensional CFD code to optimize the mixing in the primary combustion zone, a low-NO_x, liquid-fueled JSL combustor was successfully developed and tested. The CFD code was used as a tool to facilitate a parametric analysis that led to optimum fuel–air mixing and low NO_x production within the combustor. From the experimental and CFD analysis it was found that the percentage of total air employed in combustion had the strongest effect on NO_x emissions. A high combustion air quantity leads to a cooler primary zone temperature. Optimum fuel–air mixing was demonstrated by varying a number of geometric features of the basic JSL configuration. It was found that a low number of in-line jets and an outboard axial air slot having an aspect ratio of near unity produced the highest degree of fuel–air mixing within the combustor. An optimum radial hole diameter was also found to provide the largest amount of fuel–air premixing with the highest radial jet velocity for a given JSL geometry. NO_x emission between the baseline combustor, JSL4A, and the optimized combustor, JSL4D, was reduced by a factor of three with the combustion efficiency increasing slightly. NO_x emissions were over three times lower for the JSL4D combustor as compared to a conventional T-56 combustor at equivalent operating conditions. Small differences in combustion efficiency were noted: For the JSL4D and T-56 combustors the efficiencies were 98 and 99 percent, respectively. Further combustor development and effervescent atomizer optimization promises even lower NO_x while maintaining high combustion efficiency, thus making it highly competitive with other low-NO_x combustor concepts.

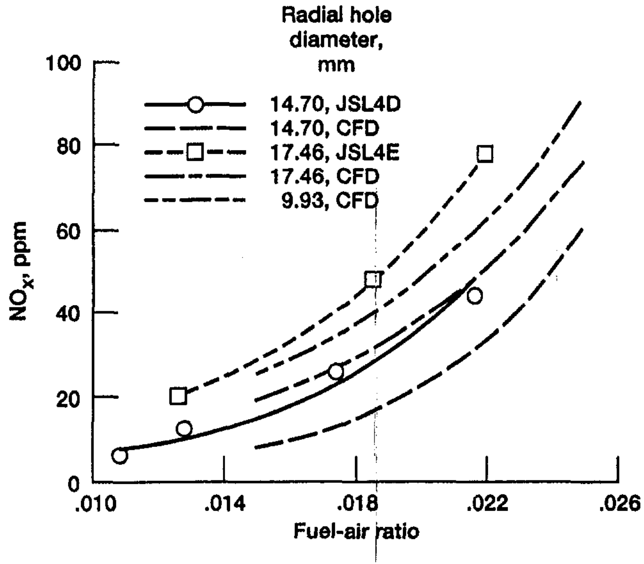

Fig. 12 Effects of fuel–air ratio and radial hole diameter on NO_x emissions; T_A = 551 K; P_A = 0.48 MPa

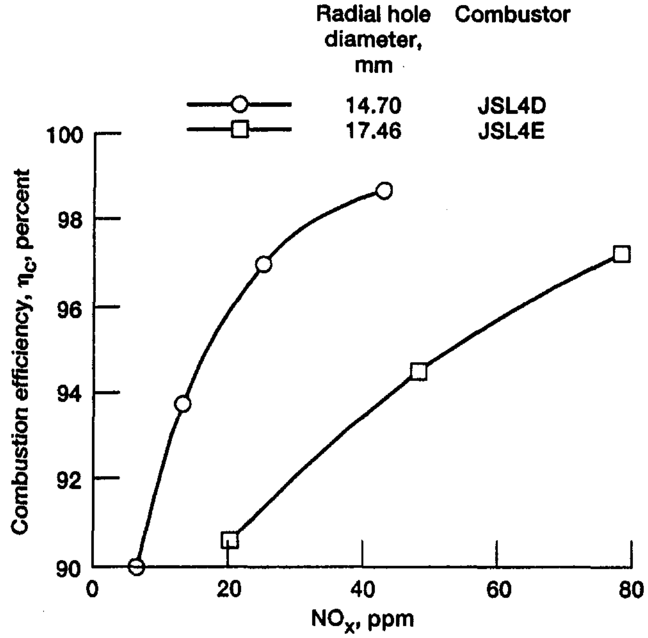

Fig. 13 Experimental results showing the effects of combustion efficiency and radial hole diameter on NO_x emissions (fuel-to-air ratio is varying); T_A = 551 K; P_A = 0.48 MPa

Acknowledgments

This research effort was funded under a grant from the Combustion Technology Branch of the NASA Lewis Research Center. The test facility used, the Thermal Sciences and Propulsion Center (TSPC), is located at Purdue University. The author sincerely appreciates the advice and support provided by Dr. Arthur Lefebvre and Dr. J. S. Chin. Recognition is also due to the CFD Research Corporation, Huntsville, Alabama, for providing usage of their REFLEQS modeling code.

References

Abdul-Aziz, M. M., Abdul-Hussain, U. S., Al-Dabbagh, N. A., and Andrews, G. E., 1987a, "The Influence of Flame Stabilizer Pressure Loss on Fuel Atomization, Mixing and Combustion Performance," *Proc. Eighth International Symposium on Air Breathing Engines,* AIAA, pp. 721–729.

Abdul-Aziz, M. M., Abdul-Hussain, U. S., Al-Dabbagh, N. A., Andrews, G. E., and Shahabadi, A. R., 1987b, "Lean Primary Zones: Pressure Loss and Residence Time Influences on Combustion Performance and NO_x Emissions," presented at the International Gas Turbine Congress, Tokyo.

Abdul-Aziz, M. M., Al-Dabbagh, N. A., and Andrews, G. E., 1983, "Mixing and Fuel Atomization Effects on Premixed Combustion Performance," ASME Paper No. 83-GT-55.

Abdul-Aziz, M. M., and Andrews, G. E., 1991, "Jet Mixing Shear Layers for the Lean Combustion of Liquid Fuels With Low NO_x at Gas Turbine Primary Zone Conditions," presented at the Japanese International Gas Turbine Congress, Yokohama, Japan.

Abdul-Aziz, M. M., and Andrews, G. E., 1985, "Smoke Emissions From Lean Well Mixed Gas Turbine Primary Zones," ASME Paper No. 85-IGT-117.

Abdul-Hussain, U. S., and Andrews, G. E., 1990, "Air Blast Atomization as a Function of Pressure Loss for Large Air Flow Rates," ASME Paper No. 90-GT-277.

Abdul-Hussain, U. S., and Andrews, G. E., 1989, "Air Blast Atomization Using Large Flow Rates," presented at the The Ninth International Symposium on Air Breathing Engines, Athens, AIAA, Washington, pp. 954–962.

Abdul-Hussain, U. S., and Andrews, G. E., 1987, "Concentration Fluctuations in a Turbulent Cross Jet," *NATO Advance Study Institute on Instrumentation for Combustion and Flow in Engines,* Portugal, pp. P2-1–P2-14.

Abdul-Hussain, U. S., and Andrews, G. E., 1992, "Concentration Fluctuations in Turbulent Cross Jet Mixing," ASME Paper No. 92-GT-346.

Abdul-Hussain, U. S., Andrews, G. E., Cheung, W. G., and Shahabadi, A. R., 1988a, "Jet Mixing Shear Layer Combustion: An Ultra-Low NO_x System for Natural Gas Fired Gas Turbines," *Proc. IMechE, Conference on Combustion in Engines,* C68/88, pp. 246–252, MEP.

Abdul-Hussain, U. S., Andrews, G. E., Cheung, W. G., and Shahabadi, A. R., 1988b, "Low NO_x Primary Zones Using Jet Shear Layer Combustion," ASME Paper No. 88-GT-308.

Al-Dabbagh, N. A., and Andrews, G. E., 1981, "The Influence of Premixed Combustion Flame Stabilizer Geometry on Flame Stability and Emissions," ASME JOURNAL OF ENGINEERING FOR POWER, Vol. 103, p. 749.

Al-Dabbagh, N. A., Andrews, G. E., and Shahabadi, A. R., 1985, "Combustion and Emissions Performance of a Rapid Fuel and Air Mixing Combustor," *Seventh International Conference on Air Breathing Engines,* AIAA, pp. 804–812.

Anderson, D., 1975, "Effects of Equivalence Ratio and Dwell Time on Exhaust Emissions From an Experimental Premixing Prevaporizing Burner," NASA TMX-715925.

Anderson, D., 1973, "Effects of Premixing on Nitric Oxide Formation," NASA TMX-68220.

CFD Research Corporation, 1990, "REFLEQS-3D: A Computer Program for Turbulent Flows With and Without Chemical Reactions—Vol. 1: User's Manual, Version 1.2," Huntsville, AL.

Colantonio, R. O., 1993, "Application of Jet-Shear-Layer Mixing and Effervescent Atomization to the Development of a Low-NO_x Combustor," NASA TM 105888.

Lefebvre, A. H., 1988, "A Novel Method of Atomization With Potential Gas Turbine Application," *Def. Sci. J.,* Vol. 38 (4), p. 353.

Lyons, V. J., 1981, "Fuel/Air Nonuniformity-Effect on Nitric Oxide Emissions," *AIAA Journal,* Vol. 20 (5), p. 660.

Ratcliff, M. L., and Smith, C. E., 1989, "REFLEQS-2D: A Computer Program for Turbulent Flows With and Without Chemical Reaction, Vol. 2: Validation Manual," CFD Research Corporation, Huntsville, AL.

Roesler, T. C., 1988, "An Experimental Study of Aerated-Liquid Atomization," Ph.D. Thesis, Purdue University, West Lafayette, IN.

Roffe, G., 1976, "Effect of Inlet Temperature and Pressure on Emissions From a Premixing Gas Turbine Primary Zone Combustor," NASA CR-2740.

Roffe, G., and Ferri, A., 1976, "Effect of Premixing Quality on Oxides of Nitrogen in Gas Turbine Combustors," NASA CR-2657.

Roffe, G., and Ferri, A., 1975, "Prevaporization and Premixing to Obtain Low Oxides of Nitrogen in Gas Turbine Combustors," NASA CR-2495.

Smith, C. E., Ratcliff, M. L., Przekwas, A. J., Habchi, S. D., and Singhal, A. K., 1988, "Validation of an Advanced Turbulent Combustion Code: REFLEQS," presented at the 7th Space Shuttle Main Engine CFD Workshop, NASA MSFC, Huntsville, AL.

Whitlow, J. D., 1990, "An Experimental Investigation of Internal-Mixing Twin-Fluid Atomizers," MSME Thesis, Purdue University, West Lafayette, IN.

An Experimental/Computational Study of Airflow in the Combustor–Diffuser System of a Gas Turbine for Power Generation[1]

A. K. Agrawal
School of Aerospace and
Mechanical Engineering,
University of Oklahoma,
Norman, OK 73019

J. S. Kapat
MMAE Department,
University of Central Florida,
Orlando, FL 32816

T. T. Yang
Department of Mechanical Engineering,
Clemson University,
Clemson, SC 29630

This paper presents an experimental/computational study of cold flow in the combustor–diffuser system of industrial gas turbines employing can-annular combustors and impingement-cooled transition pieces. The primary objectives were to determine flow interactions between the prediffuser and dump chamber, to evaluate circumferential flow nonuniformities around transition pieces and combustors, and to identify the pressure loss mechanisms. Flow experiments were conducted in an approximately one-third geometric scale, 360-deg annular test model simulating practical details of the prototype including the support struts, transition pieces, impingement sleeves, and can-annular combustors. Wall static pressures and velocity profiles were measured at selected locations in the test model. A three-dimensional computational fluid dynamic analysis employing a multidomain procedure was performed to supplement the flow measurements. The complex geometric features of the test model were included in the analysis. The measured data correlated well with the computations. The results revealed strong interactions between the prediffuser and dump chamber flows. The prediffuser exit flow was distorted, indicating that the uniform exit conditions typically assumed in the diffuser design were violated. The pressure varied circumferentially around the combustor casing and impingement sleeve. The circumferential flow nonuniformities increased toward the inlet of the turbine expander. A venturi effect causing flow to accelerate and decelerate in the dump chamber was also identified. This venturi effect could adversely affect impingement cooling of the transition piece in the prototype. The dump chamber contained several recirculation regions contributing to the losses. Approximately 1.2 dynamic head at the prediffuser inlet was lost in the combustor–diffuser, much of it in the dump chamber where the fluid passed though narrow pathways. A realistic test model and three-dimensional analysis used in this study provided new insight into the flow characteristics of practical combustor–diffuser systems.

Introduction

Gas turbine engines employ a diffuser system between the compressor discharge and combustor(s). The primary functions of this system are to decelerate the compressor discharge flow and to distribute air evenly to various holes on the combustor liner. The diffusion process must be accomplished with a low total pressure loss because losses have an adverse impact on the thermal efficiency. The flow uniformity around the liner is important to achieve stable and efficient combustion, to prevent liner hot spots, and to provide an acceptable combustor exit pattern factor. Basic configurations and design considerations for the combustor diffusers are discussed by Lefebvre (1983). A recent review by Klein (1995) elaborates on flow characteristics of the combustor diffusers. A commonly used combustor–diffuser in aircraft engines is the dump diffuser configuration, wherein the compressor discharge air is decelerated in a short, conventional prediffuser and then "dumped" into a large chamber, which divides flow to the flame tube and to the inner and outer annuli around the combustor liner. The sudden expansion at the prediffuser exit causes flow recirculation in the dump, which helps to maintain a stable flow pattern rather insensitive to changes in the engine operating conditions. The sudden expansion incurs pressure losses. However, the required diffusion is accomplished in a short length. Most of the loss occurs in the dump chamber, while nearly all of the static pressure recovery occurs in the prediffuser (Klein, 1995).

The dump diffuser system has been studied experimentally and computationally by several investigators. Fishenden and Stevens (1977) and Stevens et al. (1978) experimentally found that the liner location had a marked effect on the performance and stability of flow in the diffuser. They emphasized the need for careful matching of the geometries of the diffuser, the liner, and the surrounding annuli for optimal performance and flow stability. Recent experiments by Srinivasan et al. (1990a, b) and Carrotte et al. (1994) have reached a similar conclusion. Because the experiments provide only a limited amount of data, computational fluid dynamic calculations have been used in recent years to yield the detailed flow characteristics. Adkins et al. (1992) used a combination of empirical data, simplified and detailed analyses, and model tests to develop, evaluate, and qualify an annular combustor–diffuser with a 180-deg bend accompanied with air extraction for turbine blade cooling. Koutmos and McGuirk (1989) modeled flow in the axisymmetric configuration tested by Fishenden and Stevens (1977) and

---

[1] This work was performed at Clemson University, Clemson, SC.

Contributed by the International Gas Turbine Institute and presented at the 41st International Gas Turbine and Aeroengine Congress and Exhibition, Birmingham, United Kingdom, June 10–13, 1996. Manuscript received at ASME Headquarters February 1996. Paper No. 96-GT-454. Associate Technical Editor: J. E. Peters.

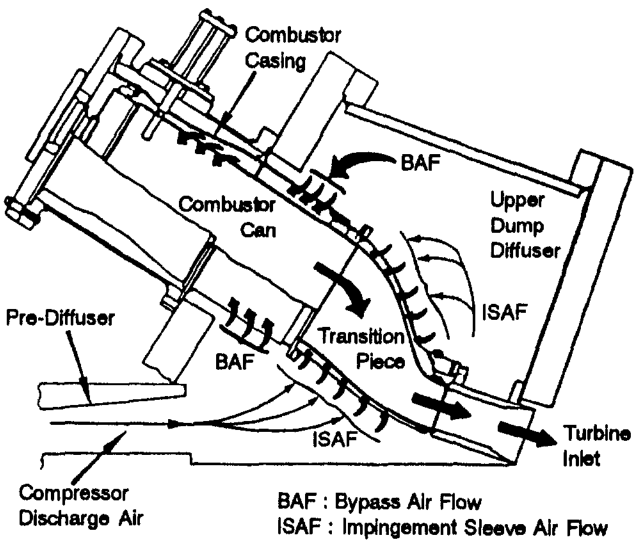

Fig. 1 Combustor–diffuser system of typical industrial gas turbines

found the predictions to be of sufficient accuracy for engineering purposes. Similar studies by Shyy (1985) and Little and Manners (1993) indicate that the gross features of the flow field are predicted very well. However, the accuracy of the results is limited by the grid resolution, the numerical scheme, and the turbulence model. For example, the $\kappa-\epsilon$ model of turbulence has known shortcomings in predicting flows with adverse pressure gradients and strong streamline curvature.

The studies reviewed above provided flow characteristics of the dump diffuser without the practical details such as the support struts, fuel nozzles, and liner ports. Thus, the flow geometry was axisymmetric. Geometric details were incorporated by Karki et al. (1992) in three-dimensional simulation of airflow in a 45-deg sector of the combustor–diffuser. The computations showed that the fuel nozzles caused (*i*) a significant slow-down of the flow discharged from the prediffuser, (*ii*) a severe change in flow direction as the flow approached the stem, and (*iii*) a stronger lower than upper recirculation zone. Also, the strut produced a back flow, which generated recirculation zones within the dome region and a flow exiting from it. Clearly, the three-dimensional effects not observed in simplified axisymmetric configurations have a significant influence on flow distribution in practical combustor–diffuser systems.

The focus of this paper is on the combustor–diffuser system of a power-generating gas turbine, illustrated in Fig. 1. The main features of this system include a prediffuser to recover the kinetic energy of the compressor discharge air and a dump chamber to distribute air uniformly to the combustor liners. The present configuration, however, differs from the typical dump diffuser in several aspects: (1) Combustors in power-generating gas turbines are located radially outward from the compressor discharge. Unlike the dump diffuser where the prediffuser discharge flow splits into the inner and outer annuli around the combustor liner and the dome region, all of the prediffuser discharge flow in the present system turns radially outward. (2) Unlike an annular combustor typically used in aircraft engines, the power-generating gas turbines employ several can-annular combustors. The air for combustion, cooling, and dilution is supplied by the dump chamber through an annulus around the combustor can. Each can-annular combustor unit is supported by a strut, which extends to the inner wall of the dump chamber. (3) Circular-to-annular sector transition pieces are used to connect combustors to the inlet of the turbine expander. The current trend toward high turbine inlet temperature places stringent demands on cooling of the transition piece. A typical approach involves a perforated sleeve, which forms an impingement shell around the transition piece. In this transition piece–impingement sleeve assembly, the sleeve causes jets of a portion of the compressor discharge air to be directed onto the transition piece core.

The air flow path in the present diffuser system can now be described as follows: The air exiting the compressor is decelerated in an annular prediffuser before it is discharged into a dump chamber. Then, a portion of the discharge air flows through holes on the impingement sleeve into the annular space between the sleeve and transition piece, thereby cooling the transition piece. This air then flows through the annular space toward the annulus of the combustor liner where it joins the remainder of the air coming directly from the dump chamber through bypass holes on the combustor casing. Finally, all of the air reaches the combustor through primary, secondary, dilution, and cooling holes on the liner. The design requirements for the diffuser system are: (1) high-pressure recovery in the prediffuser and low-pressure losses in the dump chamber to maximize the turbine efficiency, (2) uniform flow distribution around the impingement sleeve to prevent hot spots on the transition piece, and (3) a uniform flow in the combustor annulus to ensure stable and efficient combustion. These later requirements of flow uniformity are increasingly important at high turbine inlet temperatures necessary to improve the gas turbine thermal efficiency.

The flow characteristics in the combustor–diffuser of industrial gas turbines using can-annular combustors and impingement-cooled transition pieces are investigated in this paper. An aerodynamic evaluation of such systems is needed to minimize parasitic losses and to ensure safety of the components in the hot gas flow path. A review of the open literature revealed neither the experimental nor any analytical investigation of such systems except that similar work has continued at Clemson University (Kapat et al., 1996; Zhou et al., 1996). The key focus of the present experimental/computational study is on the flow characteristics in the prediffuser and dump chamber. Thus, the flow distribution within the combustor was not considered. Because this was the first attempt, the results are presented without an effort to parameterize or optimize the complex flow system.

Technical Approach

This study was initiated with cold-flow experiments in a scale model of the combustor–diffuser system. The preliminary results showed trends not explained by the measured data. Thus, a three-dimensional computational fluid dynamic model was developed, validated, and used to identify the global features of the flow. The following sections provide details of the experimental and computational components of the study.

Experimental. A scale model simulating the combustor–diffuser system was designed and built for cold flow experiments in a suction type wind tunnel facility. The measurements were taken by wall pressure taps and hot-wire anemometry.

Test Model and Flow System. Figure 2 shows a cross-sectional view of the test model simulating the gas turbine section between the compressor discharge and inlet of the turbine expander. The main features of this test model, also used by Kapat et al. (1996) to investigate air extraction in gas turbines for integrated gasification combined cycle, include: (1) approximately one-third geometric scale, (2) annular with 360 degrees in circumference, and (3) practical three-dimensional geometric details. The geometric scale was chosen to provide reasonable measurement accuracy in the prediffuser. In the model, the radius ratio at the prediffuser inlet was 0.84, the prediffuser area ratio was 1.6, and the prediffuser height (H) to length (L) ratio was 4.2. The outer diameter of the dump chamber was approximately 1.4 m and the total length of the test section was 0.75 m. Although two-dimensional and annular sector models

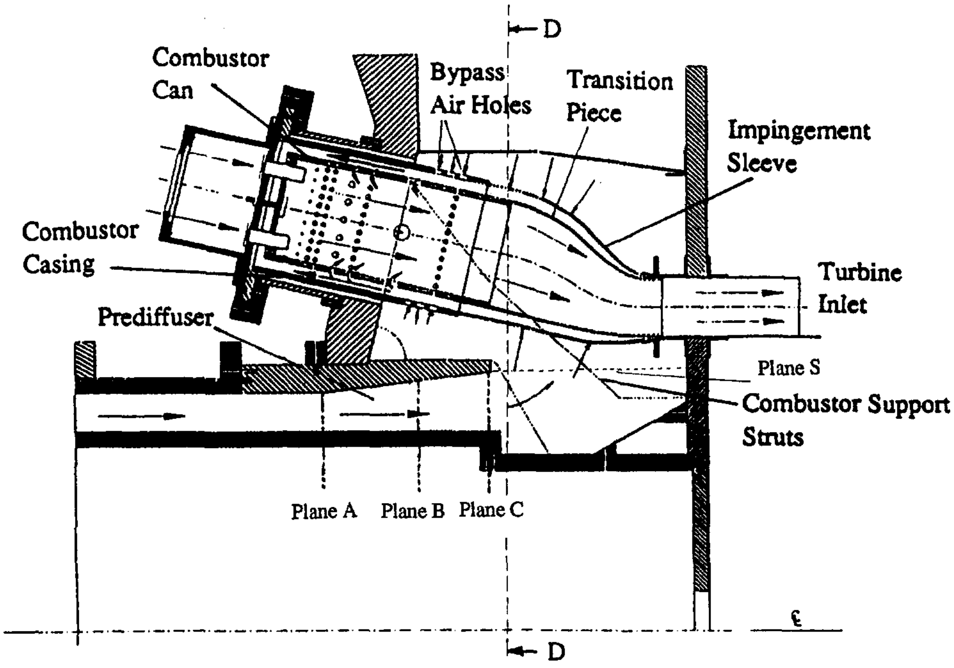

Fig. 2 Cross section of the test model between the combustor support struts

are common, a 360-deg annular model was used in this work. Little and Manners (1993) have shown that the boundary layers growing along the side walls and the secondary flows created by them have considerable influence even for two-dimensional models with aspect ratios in excess of 10, and 90-deg annular sectors. The test model simulated three-dimensional geometric features of the prototype, including the support struts, impingement sleeves, transition pieces, and can-annular combustors with dilution, cooling and combustion air holes. Klein (1995) pointed out that experiments on combustor diffusers are rare where the test setup comprised the original combustion chamber with all its flows through the dome and liners. The present model, inherently more complex than the combustor–diffuser of aircraft engines, represents a significant step forward in simulating practical systems. The complexity of the test model, however, limited access to the flow region and hence, to the amount of data that could be obtained.

The desired airflow through the test model was provided by a suction-type wind tunnel shown schematically in Fig. 3. The ambient air entered through a square bell mouth inlet lip, the filters, a 90 deg bend, and a honeycomb, followed by transition sections, which guided airflow to an annular flow developing section. A nose cone at the upstream end of the inner pipe of this 1-m-long flow developing section allowed a gradual flow transition while sealing the inside of the inner pipe. The exit of the flow developing section was attached to the inlet of the test model. The airflow exiting the test model discharged into a 1.2-m-long, 2.1-m-wide, and 1.6-m-high plenum to isolate the test model from oscillations of the suction fan located downstream. The plenum also allowed physical access to the interior of the test section necessary to install probes and automated traverse systems. The suction fan was belt driven by a 150 kW, three-phase, constant-speed electrical motor, and the airflow was regulated by a set of computer-controlled louvers at the fan inlet. The maximum average axial velocity at the test section inlet was 50 m/s, corresponding to a volumetric flow rate of 4.0 m^3/s.

Instrumentation. Pressure was recorded by a 96-channel pressure scanning system, Scanivalve MSS-48C, with two pressure sensors (±0.17 bar and ±0.34 bar range). Each pressure measurement consisted of 20 readings in 6 seconds. The velocity was measured by a single-wire, hot-film anemometer at longitudinal planes with symmetry in the circumferential direction. This was the key requirement in measuring the radial and axial velocities by the single-wire, hot-film probe. At each point of measurement, the voltage output from the probe was measured for two orientations of the film sensor 90 deg apart. At these orientations, one of the two velocity components was normal to the wire and the other component was normal to the wire in one orientation (called the normal orientation) and parallel to the wire in the other orientation (called the tangential orientation). The hot-film was calibrated in a blowing-type wind tunnel for the two different orientations to yield relationships between (*i*) the voltage output and effective cooling velocity, and (*ii*) the yaw coefficient and tangential velocity. The hot-wire operation was controlled by a TSI IFA-100 thermal anemometer. The voltage output was digitized by a Metrabyte DAS-20 board on a microcomputer.

Computational. Three-dimensional computational fluid dynamic (CFD) analysis was necessary to supplement the experiments, especially in the dump chamber around impingement sleeves where only limited measurements could be made. Klein's (1995) review reported only one three-dimensional computational study of the combustor–diffuser (Karki et al., 1992) although similar works have appeared in recent years (e.g., Chen and Reynolds, 1993; Zhou et al., 1996). The flow in the combustor–diffuser involves regions of flow recirculation, adverse pressure gradients, strong streamline curvature, developing boundary layers and impingement. These features coupled with complex three-dimensional geometry make accurate numerical simulations extremely difficult and perhaps impossible at this time. Thus, the present approach was to employ numerical features similar to those used by Karki et al. (1992) and Tolpadi and Braaten (1992) to achieve reasonable accuracy. These include fully elliptic, three-dimensional body-fitted computational fluid dynamics code, finite volume approach with velocity-pressure coupling (Patankar, 1980), and multiple block grid calculations. The turbulence was modeled using the standard $\kappa-\epsilon$ model along with the wall function treatment for near-wall regions. The density was assumed constant because the Mach number at the prediffuser inlet was less than 0.2. A

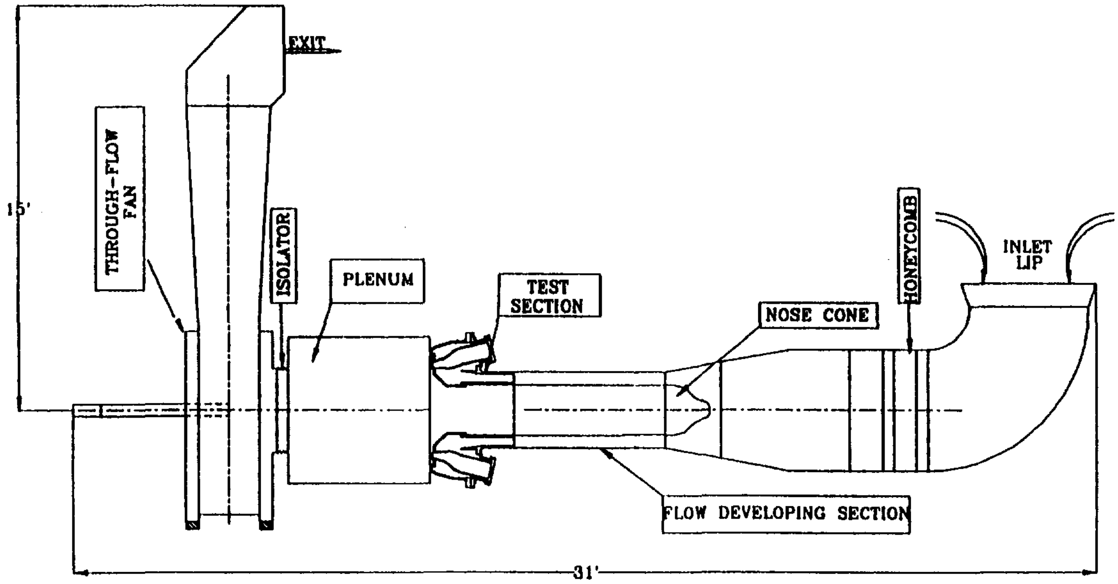

Fig. 3 Layout of the suction type wind-tunnel

single grid code was modified for this work to allow the multiple block calculations. The computations allowed flow interactions among the prediffuser, dump chamber, impingement sleeve, and combustor casing. The flow inside the combustor was not considered. The important details of the computational procedure are given below.

Governing Equations. The fully elliptic form of the three-dimensional conservation equations may be written in general for a conserved variable ϕ in the Cartesian coordinates as:

$$\frac{\partial(\rho u\phi)}{\partial x}+\frac{\partial(\rho v\phi)}{\partial y}+\frac{\partial(\rho w\phi)}{\partial z}=\frac{\partial}{\partial x}\left(\Gamma_\phi\frac{\partial\phi}{\partial x}\right)+\frac{\partial}{\partial y}\left(\Gamma_\phi\frac{\partial\phi}{\partial y}\right)+\frac{\partial}{\partial y}\left(\Gamma_\phi\frac{\partial\phi}{\partial y}\right)+S_\phi(x,y,z) \quad (1)$$

where Γ_ϕ is the effective viscosity. S_ϕ is the source term, which depends on the equation being considered. Six equations representing the velocity components u, v, and w, pressure correction derived from the continuity equation, turbulent kinetic energy κ, and turbulent dissipation ϵ were solved at each control volume in the transformed body-fitted coordinates.

Domain Decomposition. In this inherently three-dimensional configuration, the can-annular combustors, impingement sleeves, and support struts repeated periodically in the circumferential direction. Additionally, these components were symmetric about their respective midplanes. Therefore, only one-half of the periodic distance in the circumferential direction was necessary for computations. The computational domain included the prediffuser and dump chamber. The velocity profiles at the prediffuser inlet were taken from the experiments. The inlet turbulence intensity was taken as 10 percent and the inlet turbulent energy dissipation was $[C_d^{0.75}\kappa^{1.5}/l]$ where $C_d = 0.16$ and the length scale l was the annulus height at the prediffuser inlet. A uniform pressure was imposed at the end of the combustor annulus. This later assumption was justified because the flow in the combustor was not considered and the end of the combustor annulus was farther downstream from the dump chamber.

The complex geometry of the combustor–diffuser presented difficulties in generating an acceptable structured grid. It was found necessary to employ a multiblock procedure wherein the computational region was divided into two parts: (1) an inner block consisting of the prediffuser and inner dump chamber directly facing the prediffuser exit, and (2) an outer block representing the outer dump chamber with impingement sleeve and combustor casing. The support strut was split between the blocks. The two blocks shared an interface through which boundary condition data were communicated and updated during calculations. The domain decomposition procedure was similar to that used by Tolpadi and Braaten (1992) and Agrawal et al. (1993). The computational steps to implement this procedure were as follows: (1) Prescribe a pressure distribution at the exit of the inner block (or the interface). (2) Compute flow field in the inner block. (3) Compute flow field in the outer block. The flow solution in the inner block provided inlet boundary conditions for the outer block. (4) Return to step (2) with an updated pressure distribution at the interface obtained from solution in the outer block. Continue iterations until pressure distribution at the interface no longer changed. The global residuals of the conservation equations were reduced by several orders of magnitude during the iteration process.

It was necessary to underrelax changes in pressure at the interface to prevent numerical oscillations. An underrelaxation factor of 0.2 was found to be acceptable in this work. The computations proceeded serially on a single CPU. Thus, at the end of the computations in a block, the flow field data were saved on disk files before computations were initiated for the other block. Each trial took approximately 120 flow iterations. The flow field calculated for an earlier trial served as the initial guess for the new trial. The overall flow field converged in about 10 trials. Each trial took 12 to 15 cpu hours on a Sun Sparkstation 10 Model 30. Implementation on a parallel processor would reduce the CPU requirements such that the analysis could be used effectively for combustor system design.

Grid Generation. Generating a suitable structured grid in the combustor–diffuser required substantial effort (several hundred hours), although subsequent geometry changes could be made in a short time. The problem was complicated by the following factors: (1) the orientation and three-dimensional shape of the impingement sleeve changing from a circular cross section to an annular sector, (2) the location and extent of the support strut, and (3) the size and shape of the dump chamber. A grid-generation program was used to create structured three-dimensional grids with embedded obstacles. The objective was

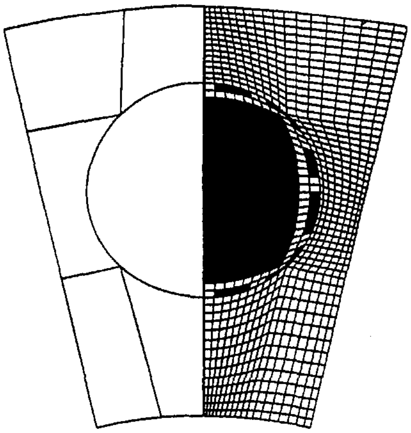

Fig. 4(*a*) Computational grid in the upper block at a plane near the combustor can

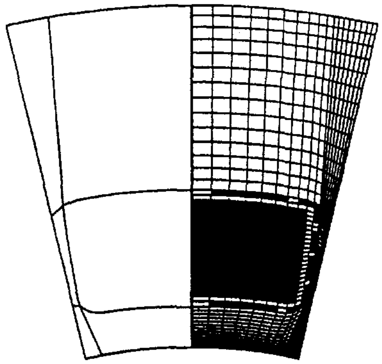

Fig. 4(*b*) Computational grid in the upper block at a plane near the turbine expander

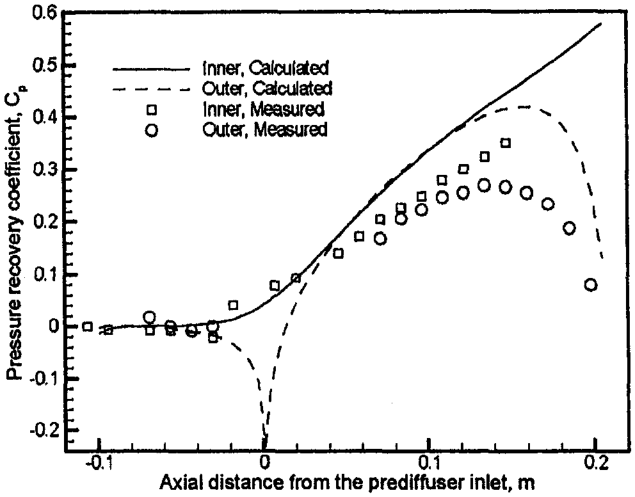

Fig. 6 Prediffuser wall static pressure recovery coefficient

to represent the geometry correctly while minimizing grid nonorthogonalities, aspect ratios, and expansion ratios. The three-dimensional grid was formed by stacking a series of two-dimensional grids, one for each cross section. Each cross section, in turn, was divided into subsections representing specific objects. A two-dimensional grid was generated independently within each subsection to allow grid refinement and an accurate representation of the embedded obstacles. The subsections (left side) and grid (right side) are shown in Figs 4(*a*,*b*), respectively, at planes next to the combustor exit and near the inlet of the turbine expander. The central shaded region in Fig. 4 represents the transition piece while the outer shaded strip corresponds to the surface of the impingement sleeve. Figure 4 also demonstrates how the cooling holes and the complex geometry of the sleeve (and the transition piece) were captured by the three-dimensional grid. The combustor casing had three rows of bypass holes and each of the rows consisted of several discrete holes equally spaced in the circumferential direction. The impingement sleeve had several rows of cooling holes. The finite grid in the present analysis could not precisely and indivisibly resolve the large number of cooling holes. Therefore, only 12 holes were considered in each row. These holes were distributed nearly uniformly in the circumferential direction. Although the exact shape and orientation of the holes in a row could differ, the area of each hole was kept the same. If the actual number of holes in a row exceeded 12, then the total area of these 12 holes was made equal to the actual total area of holes in that row. Each hole contained of one or more grids. When the area of a grid exceeded the area of the hole it represents, the grid was partially blocked to the flow.

Figure 5 shows grids in the two blocks at a longitudinal plane between the support struts (also the midplane of the combustor or sleeve). The shaded grids in Fig. 5 represent the embedded obstacles. The stair-stepped boundaries in Fig. 5 mimic the structural features of the prototype. A total of 125,856 grid nodes were used for computations. There were 62,208 grid

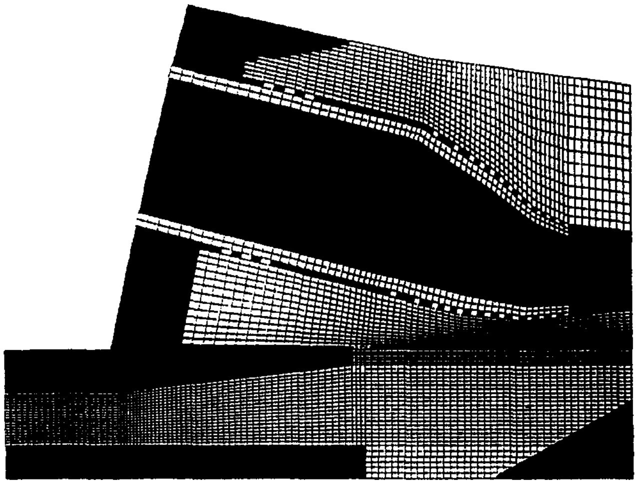

Fig. 5 Computational grid in the blocks at plane between the combustor support struts

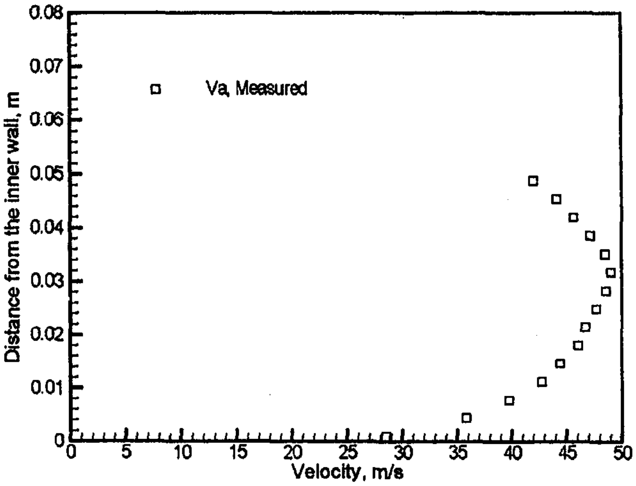

Fig. 7 Measured axial velocity profile at the prediffuser inlet plane *ABC*

nodes in the inner block; 18 grid lines were used in the circumferential direction, 32 in the radial direction, and 108 in the axial direction. The outer block consisted of 63,648 grid nodes; 18 grid lines were used in the circumferential direction, 52 in the radial direction, and 68 in the axial direction.

Results and Discussion

Experimental and computational results are presented for a Reynolds number of 1.5×10^5 based on the prediffuser inlet height. This Reynolds number is lower than that in the prototype by an order of magnitude. However, the differences in flow behavior are expected to be of second order in nature because the flow was turbulent in both the test model and prototype. Measurements were taken mainly in the prediffuser and inner dump chamber. The velocity profiles were obtained only at the two symmetry planes: (1) between the support struts or midplane of the combustors, and (2) between the combustors or midplane of the support struts.

Flow Characteristics. Measured and computed pressure recovery coefficients, $Cp\,[=(p-\bar{p}_a)/h_D]$, where p is the static pressure, a refers to the prediffuser inlet, the overbar denotes the mass-averaged value, and h_D is the dynamic head at the prediffuser inlet, are shown in Fig. 6 for the prediffuser inner and outer walls. Experimental data and computed results show similar trends, although the measured values were lower. The static pressure increased linearly along the inner wall of the prediffuser. Measured and computed Cp values at the last measurement location on the inner wall were 0.35 and 0.45, respectively. This compared well with a Cp of about 0.4 measured by Sovran and Klomp (1967). An unexpected result in Fig. 6, shown by measurements as well as computations, was the sudden decrease in the outer wall pressure at the prediffuser exit. This pressure decrease, suggesting flow acceleration, reduced the prediffuser outer wall Cp to only 0.1. The nonuniform pressure indicated by Fig. 6 signified a strong influence of the dump chamber on the prediffuser exit flow.

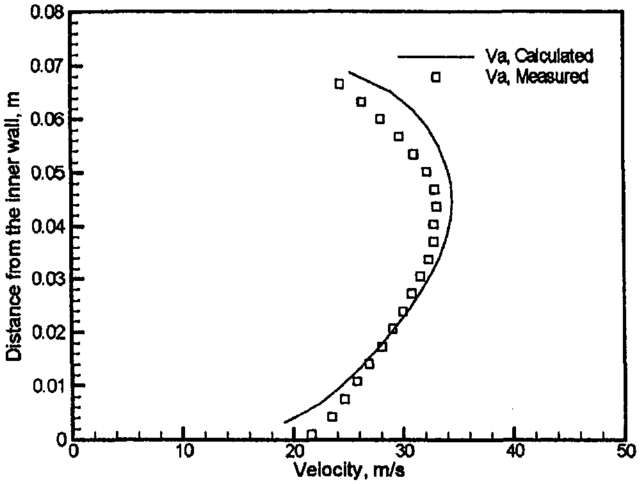

Fig. 8(*a*) Axial velocity profiles at station *BBC*

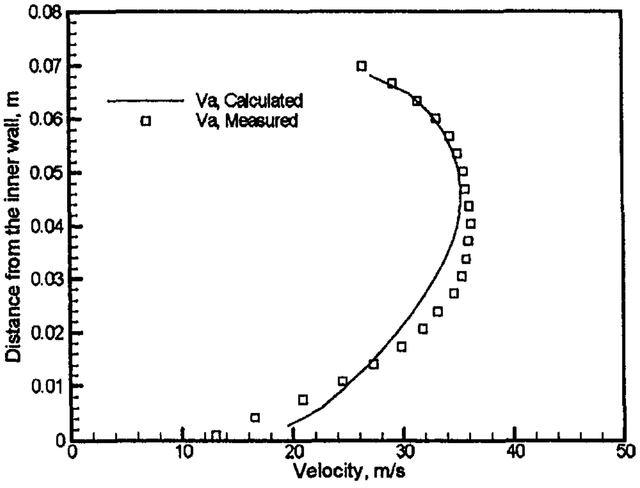

Fig. 8(*b*) Axial velocity profiles at station *BBS*

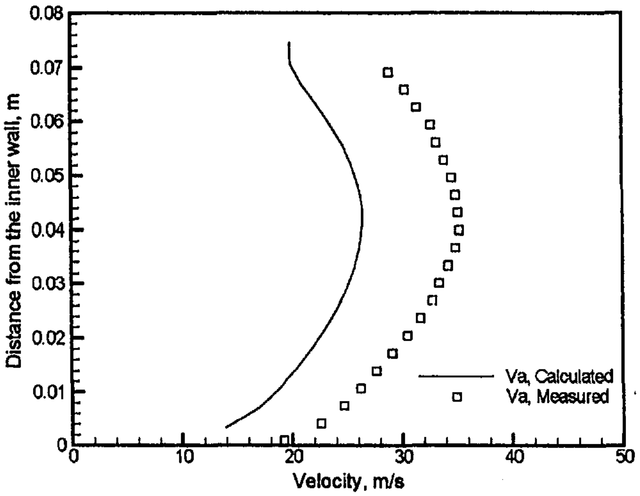

Fig. 9(*a*) Axial velocity profiles at station *CBC*

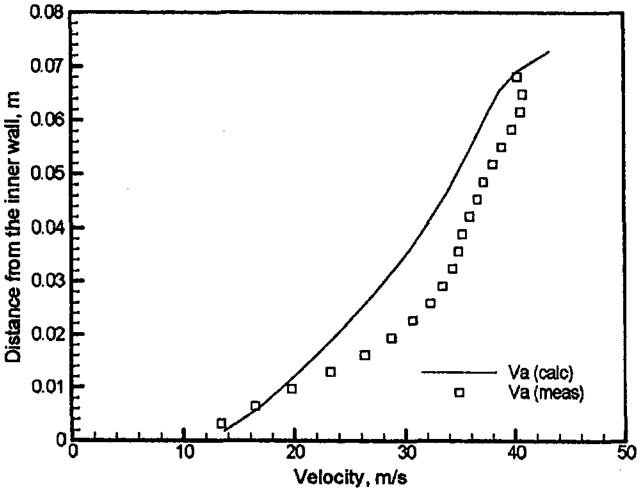

Fig. 9(*b*) Axial velocity profiles at station *CBS*

The velocity profiles are presented next at the five measurement planes *A*, *B*, *C*, *D*, and *S*, identified in Fig. 2. Planes *A*, *B*, and *C* were, respectively, at the prediffuser inlet, midway, and exit. Plane *D* was in the dump chamber immediately downstream of the prediffuser exit, and the axial plane *S* was under the impingement sleeve, coinciding with the interface in the block computations. Because the measurement locations were not directly accessible from the outside, the probes were mounted on computer-controlled traverse systems located inside the test model. Each profile location is identified by three characters. The first character refers to the plane and the next two characters specify the circumferential location: *BC* stands for *B*etween *C*ombustors and *BS* stands for *B*etween support *S*truts. Figure 7 shows the measured axial velocity (*Va*) profile at the prediffuser inlet, also used as input for the computations. The axial velocity profiles at stations *BBC* and *BBS* in the prediffuser, shown in Figs. 8(*a*, *b*), reflect a good agreement between

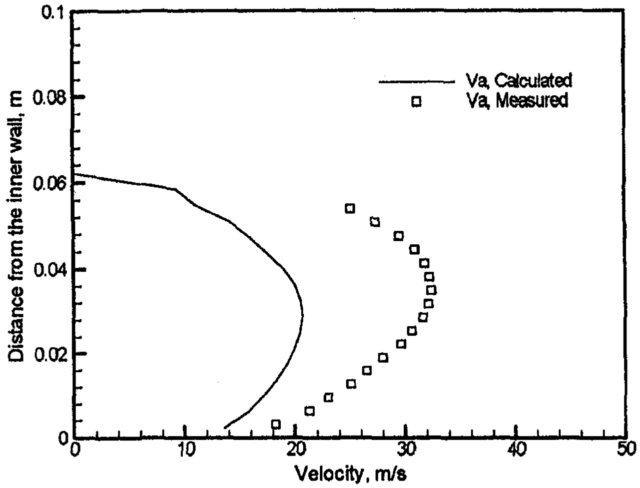

Fig. 10(*a*) Velocity profiles at station *DBC*

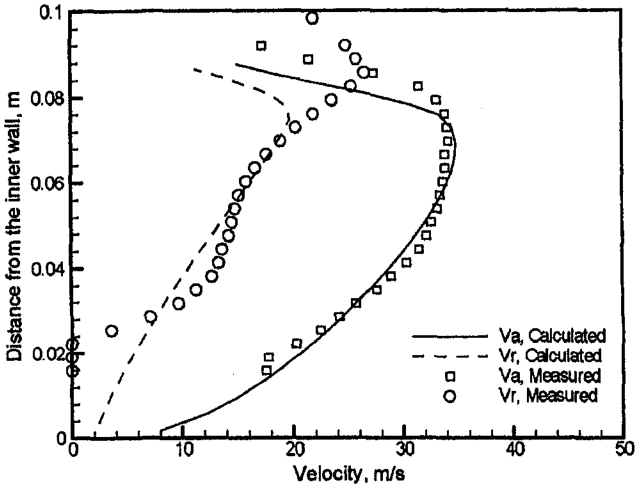

Fig. 10(*b*) Velocity profiles at station *DBS*

measurements and computations. Velocity profiles at the two circumferential locations were similar, indicating that the flow was nearly axisymmetric midway in the prediffuser. The axial velocity profiles at the prediffuser exit plane *C* are shown in Figs. 9(*a*, *b*). Unlike plane *B*, the velocity profiles at plane *C* are different at the two circumferential locations. This three-dimensional flow behavior at the prediffuser exit was attributed to the support struts located downstream in the dump chamber. Between struts, the flow accelerated near the outer wall of the prediffuser exit, as shown in Fig. 9(*b*). This explained the decrease in Cp at the prediffuser's outer wall. The flow acceleration was not apparent between the combustors because of the blockage by the support strut. The experimental and computational results were consistent with each other.

The three-dimensional nature of the flow at plane *D* in the inner dump chamber is apparent from the velocity profiles shown in Figs. 10(*a*, *b*). At location *DBC*, the computed and measured axial velocity profiles showed a similar trend, although the predicted values were smaller than the measured data. A possible explanation for this difference might be a misalignment of the support struts in the test model. The measured axial velocity would be higher if the hot-wire probe did not coincide with the symmetry plane. Figure 10(*b*) shows excellent correlation between measurements and computations at location *DBS*. An outer peak in the axial velocity profile was consistent with flow acceleration at the prediffuser exit. Figure 10(*b*) also shows large radial (Vr) velocities in the outer regions. These observations suggested a sharp flow turning at the prediffuser exit. The axial and radial velocity profiles at location *SBS*, shown in Fig. 11, substantiated flow turning at the predif-

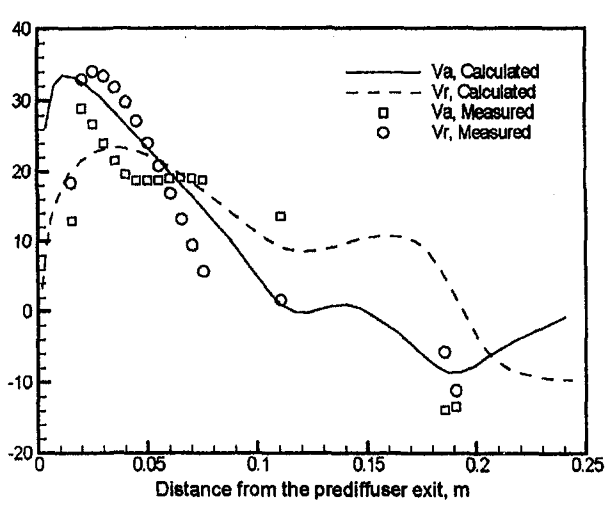

Fig. 11 Velocity profiles at station *SBS*

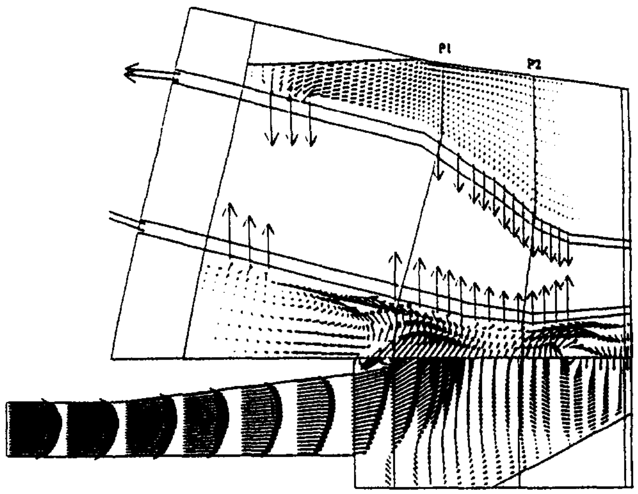

Fig. 12(*a*) Projected velocity vectors at a plane between the combustor support struts

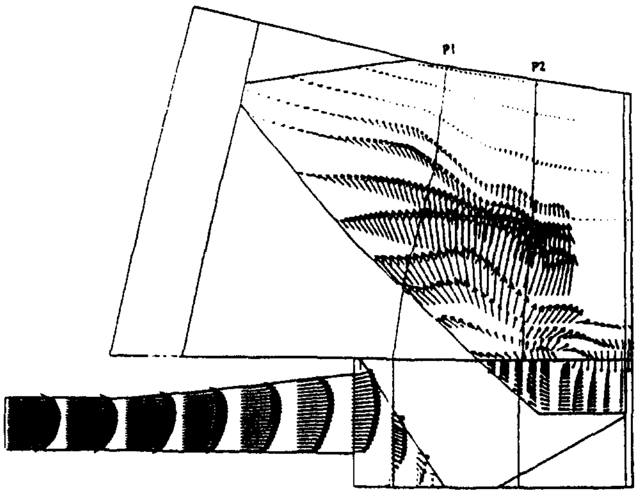

Fig. 12(*b*) Projected velocity vectors at a plane between the combustors fuser exit. The measurements indicated a sharper turning than the predictions, since the measured peak in the radial velocity was higher and narrower than predicted. Another observation in Fig. 11 was the reverse flow along more than half of the plane *S*. This implied a stagnant region directly underneath the impingement sleeve.

In this study, the circumferential velocity was assumed to be zero at the measuring stations. However, misalignment in the test rig or probe orientation and probe vibrations could introduce three-dimensional effects, and thus influence the measurements. Because of the large computational requirements, a check for the grid size convergence with successively finer grids could not be pursued in the present analysis. Furthermore, the turbulence parameters at the prediffuser inlet and the turbulence model itself are subjected to considerable uncertainties. Finer grids, detailed turbulence measurements, and improved turbulence models might be necessary for accurate predictions. Accounting for the present limitations, the correlation reached between the measurements and computations was considered as reasonable for engineering purposes.

Flow Interactions. Results discussed in the previous section implied flow interactions between the prediffuser and dump chamber. The limited measurement locations, however, were inadequate to construct a comprehensive description of the flow field. Thus, the computational results were used in this section to describe the flow interactions. This approach is justified because a reasonable agreement was reached between the measurements and predictions. Figures 12(*a*, *b*) show projected views of velocity vectors at selected locations in the midplanes of the combustor and support strut, respectively. Velocity vectors in the inner block were hidden at the interface because of the manual overlapping of results from the two blocks. The flow field at the two circumferential locations was nearly the same within the prediffuser. However, the three-dimensional effects of the support strut were apparent at the prediffuser exit. Between support struts, the prediffuser exit flow turned radially outward (Fig. 12(*a*)) in contrast with the radially inward flow and circumferential turning in the presence of the strut (Fig. 12(*b*)). Figure 12(*a*) shows how the prediffuser exit flow divided among combustor bypass holes and impingement cooling holes. The air at the bypass holes came directly from the outer region of the prediffuser, while the inner part of the prediffuser supplied air to the sleeve next to the turbine expander. Most of the inner dump chamber contained recirculation regions with velocities comparable to those at the prediffuser exit. The flow separated in the dump chamber at the tip of the prediffuser's outer wall and in space between the combustor casing and the prediffuser's outer wall. However, the size and strength of these eddies were relatively small. The flow features identified in the previous section, i.e., the flow acceleration and turning at the prediffuser exit and flow reversal in the inner dump chamber, are apparent in Fig. 12.

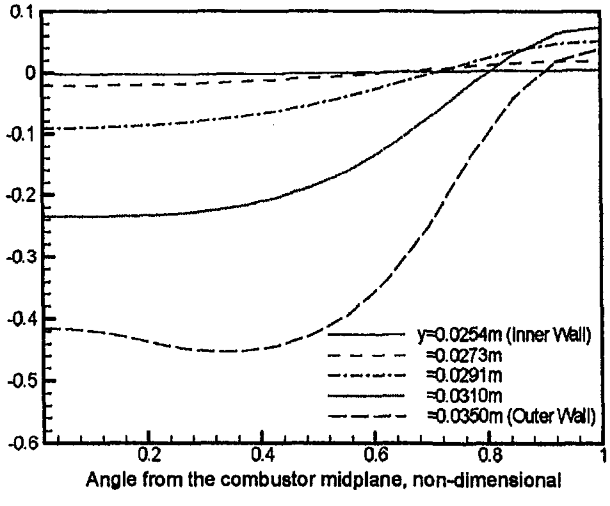

Fig. 13 Static pressure distributions at the prediffuser exit plane

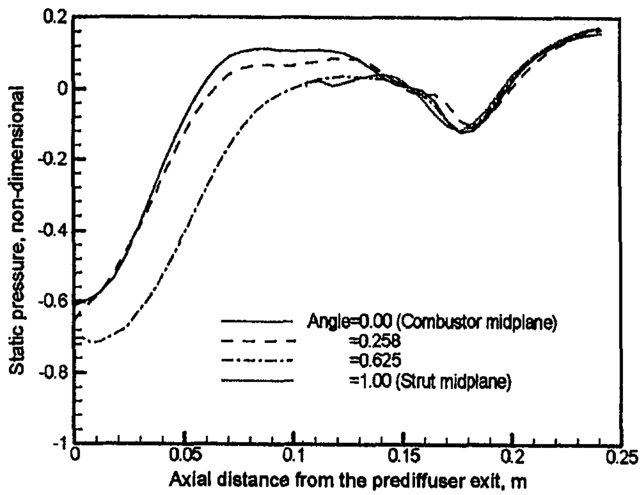

Fig. 14 Static pressure distributions at the interface plane S

Figure 13 shows the computed profiles of static pressure in the circumferential direction for several radial locations at the prediffuser exit plane *C*. The pressure is given with reference to the pressure at the exit of the prediffuser inner wall and normalized by the prediffuser inlet dynamic head. The angle in the circumferential direction was normalized by the angle between the two symmetry planes. The three-dimensional nature of the prediffuser exit flow is evident in Fig. 13. The pressure was constant at the inner wall and reached the lowest value at the outer wall. The difference in the inner and outer wall pressures was nearly 50 percent of the inlet dynamic head. The pressure varied only radially in the first half of the circumferential plane, indicating that the three-dimensional effects of the strut were localized. Another indication of the flow nonuniformities is given by Fig. 14, which shows computed profiles of static pressure for several circumferential locations at the interface plane *S*. The pressure was normalized in a manner similar to that in Fig. 13. It is seen that the pressure variation in the axial direction was significant compared to that in the circumferential direction. Static pressure near the turbine expander was close to that at the prediffuser inner wall. In agreement with Fig. 13, a low-pressure region was observed near the prediffuser exit. The difference between the minimum and maximum pressures was nearly one prediffuser inlet dynamic head.

The low pressure at the prediffuser exit was attributed to the bypass holes on the combustor casing. The prediffuser exit flow divided among bypass holes and cooling holes. The airflow directly from the prediffuser exit to the bypass holes corresponded to the path of the least resistance. Alternatively, the air must pass through the narrow space between sleeves, the cooling holes and then, the annulus between the sleeve and transition piece. The low pressure at the bypass holes altered the pressure distribution at the prediffuser exit, resulting in short-circuiting of the flow in the dump chamber. This observed behavior was termed as the "sink effect" of the combustor bypass holes (Yang, 1993).

Flow Distribution. The flow interactions examined in the previous section determined the prediffuser flow split between the sleeve and combustor casing. The emphasis in this section is on flow distribution around the sleeve, which determines cooling of the transition piece. Figures 15(*a*, *b*) show projections of selected velocity vectors at axial planes P1 and P2,

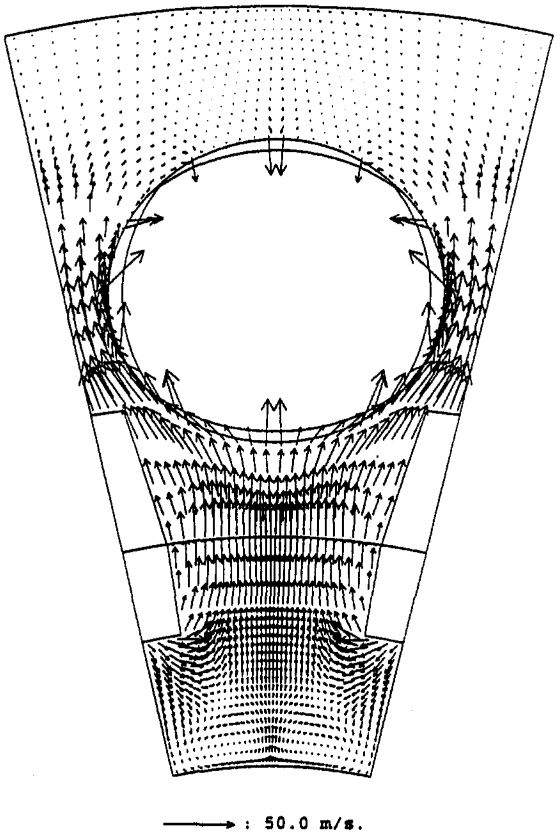

Fig. 15(*a*) Projected velocity vectors at the azimuthal plane P1

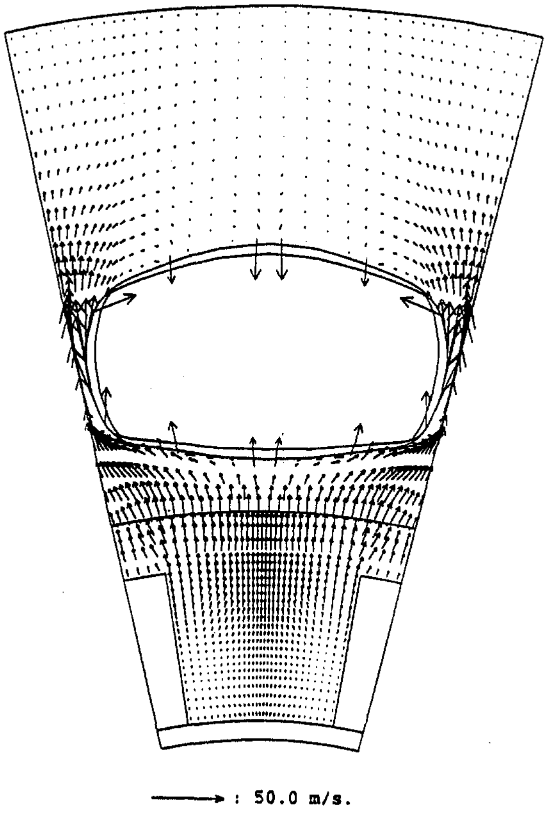

Fig. 15(*b*) Projected velocity vectors at the azimuthal plane P2

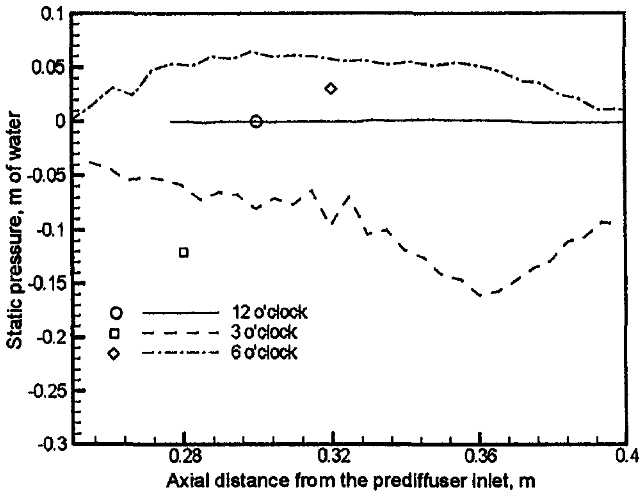

Fig. 16 Static pressure distribution along the impingement sleeve

identified in Fig. 12. At plane P1, next to the prediffuser exit, the support strut incurred a large flow blockage, and the sleeve was nearly circular in cross section (see Fig. 15(*a*)). The fluid directed inward by the strut turned azimuthally before joining the unblocked fluid flowing radially toward the sleeve. The flow around the sleeve was highly nonuniform with the highest flow velocities near the side panels (i.e., 3 or 9 o'clock positions) and the lowest flow velocities at the 12 o'clock position. The fluid accelerated near the side panels because of the narrow space between the sleeves, and then decelerated into the periphery of the dump chamber. The observed flow acceleration and deceleration around the sleeve was termed the "venturi effect." At plane P2, the blockage by the strut was reduced, the sleeve was nearly rectangular in cross section, and the sleeves were closer to each other. The flow field, shown in Fig. 15(*b*), was similar to that at plane P1 except that the venturi effect was more pronounced. This venturi effect caused reverse flow at the side panels, wherein the air exited from the transition piece into the dump chamber through holes on the sleeve.

Figure 16 shows axial distributions of static pressure around the sleeve at three circumferential locations (i.e., 12, 3, and 6 o'clock). The reference pressure was taken as the static pressure at the 12 o'clock position. Figure 16 also shows wall static pressures measured at one of the axial locations. In agreement with the measurements, the pressure was highest at the 6 o'clock position and lowest at the 3 o'clock position. The single location measurements agreed qualitatively with the computations. At the 12 o'clock position, the pressure was nearly constant along the length of the sleeve. At the 3 o'clock position, the pressure along the sleeve decreased toward the turbine expander because of the increased venturi effect. Figure 16 indicated a decrease in the circumferential pressure variation near the prediffuser inlet or the combustor casing. This latter result, attributed to the increased space between casings and hence to the reduced venturi effect, also agreed with the wall pressure measurements at the combustor casing (not shown in the figure).

Total Pressure Loss. The measured total pressure loss coefficients in the prediffuser, $\lambda_{ac}[=(Pa - Pc)/h_D]$, where P is the mass-averaged total pressure, and a and c refer to the planes, was 0.02 at a plane between the combustors (*ABC* to *CBC*) and it was 0.12 at a plane between the struts (*ABS* to *CBS*). The measured loss coefficients were different at the two planes because the mass flows at the prediffuser exit were different. The computed loss coefficient in the prediffuser was 0.04, within the bounds established from the measurements. Both the measurements and computations indicated that approximately 1.2 dynamic head at the prediffuser inlet was lost in the combustor–diffuser. Approximately 80 percent of this loss occurred in the outer dump chamber where the fluid passed through the narrow space between sleeves. The prediffuser's contribution to the total loss was only 3 percent.

Conclusions

The flow field in the combustor–diffuser of power-generating gas turbines with an impingement-cooled transition piece was investigated. The prediffuser exit flow in this system was divided among bypass holes on the combustor casing and cooling holes on the impingement sleeve around the transition piece. The bypass holes exerted a strong upstream influence, referred to as the sink effect, causing the prediffuser exit flow to accelerate and turn sharply toward the bypass holes. This short-circuiting of the prediffuser flow resulted in flow recirculations in the inner dump chamber. The static pressure at the prediffuser exit was highly nonuniform, indicating that the uniform exit flow conditions typically assumed in the diffuser design were violated and the prediffuser was ineffective in adequately diffusing the flow. This study also examined circumferential flow distribution around the impingement sleeve and combustor casing. The circumferential nonuniformities were small near the combustor casing but increased at the sleeve toward the turbine expander. This was attributed to the space between sleeves, which narrowed near the turbine expander. The narrow space led to the venturi effect, wherein the flow accelerated between sleeves prior to decelerating into the periphery of the dump chamber. The venturi effect also resulted in flow exiting from the transition piece into the dump chamber at certain locations. This could adversely affect the impingement cooling of the transition piece in the prototype. The results showed that approximately 1.2 dynamic head at the prediffuser inlet was lost in the combustor–diffuser. Most of this loss occurred in the outer dump chamber where the fluid passed through the narrow passages. The study pointed to the need for design improvements to reduce the total pressure loss and to minimize the flow nonuniformities. For example, the sink effect could be minimized by redistributing area of the bypass holes to the cooling holes. The circumferential flow nonuniformities could be reduced using variable size cooling holes around the sleeve. Because of the strong flow interactions observed, this study concludes that the individual components of the combustor–diffuser could not be studied in isolation. The realistic test model and three-dimensional analysis used in this work provided new insight into flow characteristics of practical combustor–diffuser systems.

Acknowledgments

This work was performed under the Morgantown Energy Technology Center, Department of Energy contract number DE-AC21-89MC26041, and with assistance from Mr. Thomas Ekstrom at the General Electric Gas Turbine Technology Department, Schenectady, New York. Mr. Leland E. Paulson was the METC project manager.

References

Adkins, R. C., Benin, A. C., Escher, P. C., Hellat, J., and Koenig, W. M., 1992, "A Combustor Diffuser of Annular Configuration Suitable for Industrial Gas Turbines," ASME Paper No. 92-GT-41.

Agrawal, A. K., Krishnan, S., and Yang, T. T., 1993, "Use of Subdomain for Inverse Problems in Branching Flow Passages," ASME *Journal of Fluids Engineering,* Vol. 115, pp. 227–232.

Chen, D. Y., and Reynolds, R. S., 1993, "3-D CFD Modeling of Gas Turbine Combustor-Integral Bleed Flow Interaction," *Proc. 5th Thermal and Fluids Analysis Workshop,* NASA CP 10122, pp. 359–380.

Carrotte, J. F., Denman, P. A., Wray, A. P., and Fry, P., 1994, "Detailed Performance Comparison of a Dump and Short Faired Combustor Diffuser System," ASME JOURNAL OF ENGINEERING FOR GAS TURBINES AND POWER, Vol. 116, pp. 517–526.

Fishenden, C. R., and Stevens, S. J., 1977, "Performance of Annular Combustor-Dump Diffusers," *Journal of Aircraft,* Vol. 14, pp. 60–67.

Kapat, J. S., Agrawal, A. K., and Yang, T.-t., 1997, "Air Extraction in Gas Turbines for Integrated Gasification Combined Cycle (IGCC): Experiments and Analysis," ASME JOURNAL OF ENGINEERING FOR GAS TURBINES AND POWER, Vol. 119, pp. 20–26.

Kapat, J. S., Wang, T., Ryan, W. R., Diakunchak, I. S., and Bannister, R. L., 1996, "Cold Flow Experiments in a Sub-scale Model of the Diffuser-Combustor Section of an Industrial Gas Turbine," ASME Paper No. 96-GT-518.

Karki, K. C., Oechsle, V. L., and Mongia, H. C., 1992, "A Computational Procedure for Diffuser-Combustor Flow Interaction Analysis," ASME JOURNAL OF ENGINEERING FOR GAS TURBINES AND POWER, Vol. 114, pp. 1–7.

Klein, A., 1995, "Characteristics of Combustor Diffusers," *Proceedings of the Aerospace Science,* Vol. 31, pp. 171–271.

Koutmas, P., and McGuirk, J. J., 1989, "Numerical Calculations of the Flow in Annular Combustor Dump Diffuser Geometries," *Proc. Instn. Mech. Engrs: Part C,* Vol. 203, pp. 319–331.

Lefebvre, A. H., 1983, *Gas Turbine Combustion,* Taylor and Francis.

Little, A. R., and Manners, A. P., 1993, "Predictions of the Pressure Losses in 2D and 3D Model Dump Diffusers," ASME Paper No. 93-GT-184.

Patankar, S. V., 1980, *Numerical Heat Transfer and Fluid Flow,* McGraw-Hill, Washington, DC.

Shyy, W., 1985, "A Numerical Study of Annular Dump Diffuser Flows," *Computer Methods in Applied Mechanics and Engineering,* Vol. 53, pp. 45–65.

Sovran, G., and Klomp, E. D., 1967, "Experimentally Determined Optimum Geometries for Rectilinear Diffusers With Rectangular, Conical or Annular Cross-Sections," in: *Fluid Mechanics of Internal Flows,* Elsevier, New York.

Srinivasan, R., Freeman, W. G., Mozumdar, S., and Grahmann, J. W., 1990a, "Measurements in an Annular Combustor-Diffuser System," AIAA Paper No. 90-2162.

Srinivasan, R., Freeman, W. G., Grahmann, J., and Coleman, E., 1990b, "Parametric Evaluation of the Aerodynamic Performance of an Annular Combustor-Diffuser System," AIAA Paper No. 90-2163.

Stevens, S. J., Nayak, U. S. L., Preston, J. F., Robinson, P. J., and Scrivener, C. T. J., 1978, "Influence of Compressor Exit Conditions on Diffuser Performance," *Journal of Aircraft,* Vol. 15, pp. 482–488.

Tolpadi, A. K., and Braaten, M. E., 1992, "Study of Branched Turboprop Inlet Ducts Using a Multiple Block Grid Calculation Procedure," ASME *Journal of Fluids Engineering,* Vol. 114, pp. 379–385.

Yang, T.-t., 1993, private communication with Morgantown Energy Technology Center, US Department of Energy.

Zhou, D., Wang, T., and Ryan, W. R., 1996, "Cold Flow Computations for the Diffuser-Combustor Section of an Industrial Gas Turbine," ASME Paper No. 96-GT-513.

W. Konrad

N. Brehm

Combustion Department,
BMW Rolls-Royce AeroEngines,
Dahlewitz, Germany

F. Kameier

Turbomachinery Department,
BMW Rolls-Royce AeroEngines,
Dahlewitz, Germany

C. Freeman

Advanced Propulsion Systems,
Rolls-Royce plc,
Derby, United Kingdom

I. J. Day

Whittle Laboratory,
Cambridge University,
Cambridge, United Kingdom

Combustion Instability Investigations on the BR710 Jet Engine

During the development of the BR710 jet engine, audible combustor instabilities (termed "rumble") occurred. Amplitudes measured with test cell microphones were up to 130 dB at around 100 Hz. Disturbances of this amplitude are clearly undesirable, even if only present during start-up, and a research program was initiated to eliminate the problem. Presented here is the methodical and structured approach used to identify, understand, and remove the instability. Some reference is made to theory, which was used for guidance, but the focus of the work is on the research done to find the cause of the problem and to correct it. The investigation followed two separate, but parallel, paths—one looking in detail at individual components of the engine to identify possible involvement in the instability and the other looking at the pressure signals from various parts of a complete engine to help pinpoint the source of the disturbance. The main cause of the BR710 combustor rumble was found to be a self-excited aerodynamic instability arising from the design of the fuel injector head. In the end, minor modifications lead to spray pattern changes, which greatly reduced the combustor noise. As a result of this work, new recommendations are made for reducing the risk of combustion instabilities in jet engines.

Introduction

"Rumble" is an audible noise generated by unsteady pressure fluctuations in the combustor. The rumble frequency is generally in the range of about 100 Hz. Combustor rumble is usually not a certification issue and is only important if it coincides with a mechanical resonance. However, rumble elimination is of major importance for customer satisfaction, even more so when the engine is attached to a corporate business jet, as in the case of the BR710 engine.

Here, the fluctuating combustor pressures result from unsteady heat release, i.e., unsteady air–fuel ratio. Both mass flow and fuel flow fluctuations can lead to unsteady air–fuel ratio. Two kinds of rumble have been identified, having different frequencies and driving mechanisms. There are axial modes, driven by the fuel system or the injector aerodynamics, and circumferential modes resulting from combustor geometry. The axial modes are associated with frequencies that depend on the flame physics, combustor geometry, and acoustic boundary conditions. Circumferential modes travel with the speed of sound and hence frequencies are determined by geometry only. Typical frequencies for circumferential modes of modern gas turbine engines are 200–500 Hz.

In cases where the unsteadiness is restricted to the combustor, self-excitation can lead to combustor rumble. Such self-excited vibrations are often amplified by compressibilities in the fuel path. Amplification is possible when the fluctuating pressure in the combustor feeds back into the fuel injector or fuel system, thus inducing a vibration of the fuel column. A combustion system can also suffer from external excitation, for example when the fuel system or the compressor are part of a larger unstable system. Generally, unsteady combustion can be caused or amplified by:

- Vibrating fuel columns due to compressibilities in the fuel system
- Mechanical vibration of the fuel manifold
- Fuel storage in cavities in the fuel injector
- Circumferential maldistribution of fuel
- Combustion inefficiency fluctuations
- Poor fuel injector performance, i.e., poor atomization
- Unsteady air flow due to low compressor efficiency, e.g., stall
- Large-scale fluctuations due to injector aerodynamics.

The work reported below concerns the steps taken to identify which of these possible sources of instability were to blame for the rumble problem in the BR710 engine.

Stability Theory

Extensive literature exists on the subject of combustion instabilities, e.g., Kenworthy et al. (1988), a more recent publication being that of Culick et al. (1996). In the early years when rockets were the prime interest of combustion engineers, the time lag theory was established by Crocco and Cheng (1956). They postulated that a combustion instability can only occur when a time lag t exists between fuel injection and heat release. Such a lag is, of course, always present in diffusion flames and instability is thus always possible when the correct phasing of that time lag is established. The phasing leading to unstable burning can be determined with the Rayleigh (1878) stability criterion, as modified by Putnam (1971):

$$\int_{t_0}^{t_0+T} \tilde{\dot{Q}}(t) \cdot \tilde{p}(t) dt > 0.$$

If we take $\tilde{\dot{Q}}(t) = \hat{\dot{Q}} \cos(\omega t - \omega \tau)$ and $\tilde{p}(t) = \hat{p} \cos \omega t$, we find that

$$\int_{t_0}^{t_0+T} \tilde{\dot{Q}}(t) \cdot \tilde{p}(t) dt = \hat{\dot{Q}} \cdot \hat{p} \cdot \frac{T}{2} \cos \omega \tau > 0$$

For $0 < \tau < \frac{1}{4}T, \frac{3}{4}T < \tau < \frac{5}{4}T$, etc. unsteady burning is possible.

Note that Rayleigh's original formulation involved only the product of heat release and pressure fluctuation. Although the

---

Contributed by the International Gas Turbine Institute and presented at Turbo Asia '96, Jakarta, Indonesia, November 5–7, 1996. Manuscript received at ASME Headquarters July 1996. Associate Technical Editor: J. W. Shinn. Paper No. 96-TA-36.

Table 1 Combustor can standards

Standard	Concept
Can 1	Conventional
Can 2	Low NO_x

Table 2 Fuel injector standards (airblast)

Standard	Spray angle	Air streams
Injector 1	narrow-cone	2-stream
Injector 2	wide-cone	3-stream
Injector 3	narrow-cone	3-stream

Table 3 Combustor standards

Standard	Can	Injector
Combustor 1	1	1
Combustor 2	2	1
Combustor 3	2	2
Combustor 4	2	3

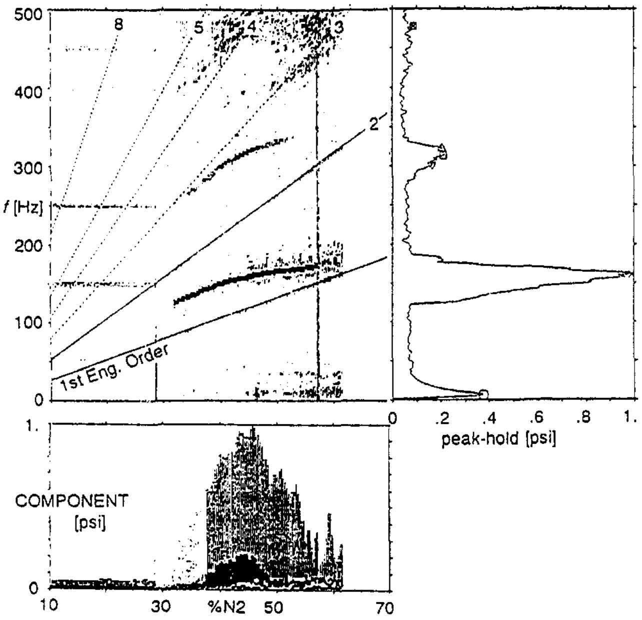

Fig. 1 Combustor 2 noise

formulation is quite simple, important conclusions can be drawn from it:

- long homogeneously burning flames are less susceptible to combustion instabilities because they embrace regions where the unsteadiness is amplified as well as regions where damping prevails,
- stabilizing a short flame in a different location could move it into a phase that is more stable.

Unstable burning may be restricted to local flameouts, especially in typical gas turbine combustors. In essence, any change to the flame structure can change the physics such that the Rayleigh criterion, necessary for instability, is not satisfied anymore. A good example of the application of the stability criterion to a laboratory flame was given by Hermann et al. (1995).

BR710 Rumble History

A number of combinations of can and fuel injector standards were tested during the development program. These standards are summarized in Tables 1 and 2, respectively.

The design of Can 1 followed traditional practice, e.g., Lefebvre (1983). Can 2 was aimed at minimizing NO_x emissions, naturally at the expense of increasing UHC and CO emissions at low power.

The fuel injector standards are primarily identified by the spray angle, which is established by the amount and distribution of swirl in the air streams. A further main design feature is the number of air streams, where all designs atomize fuel between an inner and an outer air stream while the three-stream design allows for placing air in a third dome swirler such that high weak extinction is achieved. The combinations of cans and fuel injectors are listed in Table 3.

During initial engine runs with Combustor 1, fluctuating combustor pressures were recorded, but rumble was not audible in the acoustically treated test cell to cause concern. Development of a low-NO_x combustor led to the implementation of Combustor 2, the new Can 2 being necessary to achieve low emissions. In parallel, Injector 2 was developed to achieve high weak extinction and high mechanical integrity. Audible rumble on the BR710 was first noticed after the introduction of Injector 2 into Can 2. Noise was present during start-up, steady-state low idle, and during acceleration from low to high idle. It was loudest during cold starts and always returned after the engine was decelerated from full power to low idle.

For comparison purpose, the Campbell plots in Figs. 1 and 2 show the pressure data in the combustor annulus for Combustors 2 and 3. The data are plotted versus speed because for a given combustor standard the frequency characteristics were reproducible for different runs and engine configurations. In Fig. 1 the frequency varies broadly as high pressure compressor speed N2, i.e., the rumble frequency lies about 25 percent above N2 from light-up to idle. The frequency increases as the gas temperature and flow increase.

Figure 2 shows the same engine after a test bed change to Injector 2. The characteristic changed drastically, the frequency drops with increasing speed, amplitudes are much increased, and even the third harmonic can clearly be seen. The noise sets in after light-up, follows first engine order, drops in frequency, stays at a frequency of about 75–80 Hz up to 46 percent N2, at higher than 46 percent N2 the frequency drops slightly and then increases again but remains less than first engine order at steady-state idle. The signature of the characteristic is such that the frequencies do not follow the trend with temperature and vary significantly with fuel–air ratio.

The noise produced by Injector 2 was unacceptable but the weak extinction of this injector was much improved over Injector 1. Minor modifications to Injector 2 did not succeed in

Nomenclature

AFR = air–fuel ratio
f = frequency
$N1$ = low-pressure spool speed
$N2$ = high-pressure spool speed
p = pressure
$\tilde{p}$ = fluctuating part of pressure
$\hat{p}$ = amplitude of pressure
P30 = combustor entry pressure
$\tilde{\dot{Q}}$ = fluctuating part of heat release
$\hat{\dot{Q}}$ = amplitude of fluctuating part of heat release
t = time
T = period, temperature
T30 = combustor entry temperature
τ = time lag
ω = angular frequency

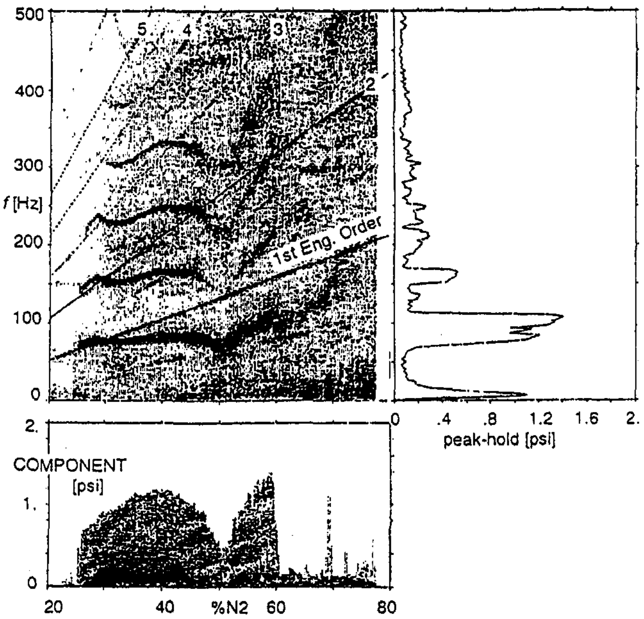

Fig. 2 (Low NO_x) combustor 3 noise

reducing the noise and so it was decided to introduce a plan that would reduce noise to an acceptable level while keeping all performance aspects of the combustor standard. The combustor geometry is shown in Fig. 3.

Experimental Investigation

It became clear that the simple observations would not lead to an understanding of the cause of the instability and that tuning external components was insufficient. A more sophisticated approach was necessary to understand combustor rumble. This approach involves variation of engine parameters with extensive dynamic instrumentation on a running engine. Simultaneously other test vehicles were used to reduce the jet engine to smaller, less complex units to try to isolate the cause of the instability. Because the instability problem occurred during the development program it was possible to carry out experiments and diagnostic tests on a complete twin-spool engine, a core engine, a full annular combustion rig, a compressor rig, and individual fuel injectors. In the following two sections, first tests on the individual components are reported and then the full engine measurements are analyzed.

Component Investigations

Fuel System. A potential problem in the fuel system is the inclusion or release of air bubbles. Bubbles can agglomerate to form air pockets and introduce compressibility into the fuel system, thus providing spring effects. Figure 4 shows a simplified layout of the fuel system. Upstream of the fuel metering unit, pressures are too high to cause concern. Downstream of the fuel metering unit the splitter unit generates a constant 70 psi pressure drop, while the split manifold compensates for head effects at low power. The flow number of the fuel injectors was 2.2 in Imperial units.

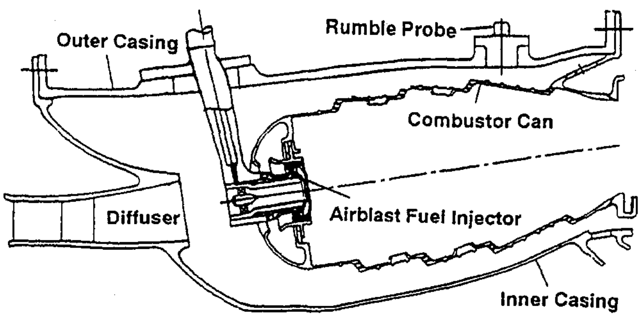

Fig. 3 Combustor geometry

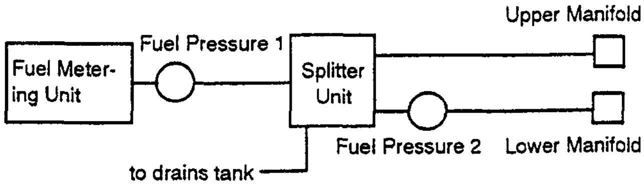

Fig. 4 Fuel system

After shutdown of the engine a drain pipe (cf. Fig. 4) leads the fuel remaining in the manifolds back to the fuel tank. It was thought possible that in this pipe not all the air is vented during start-up to idle and thus compressible effects may lead to unsteady fuel supply. An attempt on an engine to improve the situation by eliminating the drain pipe did not, however, show any improvement.

The fuel splitter unit was also checked as a possible source of unsteadiness in the fuel supply system. During a core engine test the splitter unit was replaced with a simple T-adaptor and during engine fuel spiking tests the splitter unit was removed. Neither test yielded any improvement.

It was considered that at low fuel flows and after manifold filling during start-up, air pockets could exist in the fuel pipes. To isolate the fuel pipes, the stiffness of the system was increased by replacing the trim restrictors in the fuel injectors. Even a sixfold increase of the pressure drop across the fuel injectors did not show any sign of noise reduction. The general conclusion was that the fuel system itself was unlikely to be the source of the instability problem.

High-Pressure Compressor. Several attempts were made to use the variable guide vane schedule to improve the rumble. The guide vane angles were changed both individually in the core engine and as a group on the whole engine. None of the changes showed any improvement. During the adjustment of the engine to the new operating point, rumble disappeared but reappeared immediately after establishing the new steady operating point.

Axial compressors may run inefficiently during start-up to idle when operation is at off-design conditions. For example, rotating stall can occur with a frequency at about 50 percent of first engine order. Rotating stall gives rise to a disturbance that rotates at less than high-pressure compressor speed and has its peak amplitude at the front of the compressor.

A high-pressure compressor test rig was run with dynamic instrumentation to understand the off-design behavior. Figure 5 shows the correlation of compressor wall pressures at Rotor 1 and Rotor 10 at 50 percent N2 speed (133 Hz). Sufficient coherence exists to trace disturbances from upstream of Rotor 1 to upstream of Rotor 10, i.e., close to the combustor inlet. These disturbances, however, are all at frequencies sufficiently above the combustion instability frequency to rule out any correlation.

Combustor Can. The influence of the combustor can design on the rumble was deduced from tests on different engines. Tests were run with Can 1 and Can 2. Not surprisingly, Can 2 generated more noise because its design is associated with higher UHC and CO emissions, i.e., lower efficiency at low power. While low efficiency can induce rumble, it was later demonstrated that Can 2 was not in itself the source of the instability.

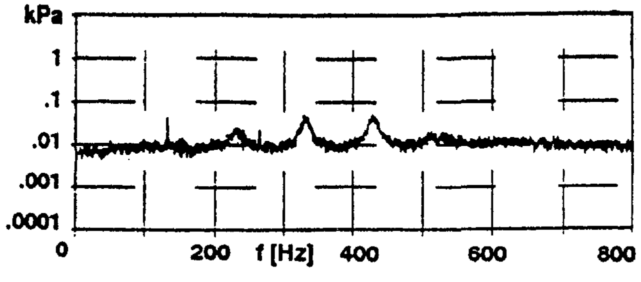

Wall Pressure (upstream HPC Rotor 1)

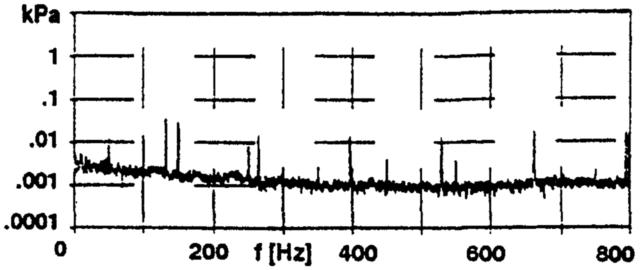

Wall Pressure (upstream HPC Rotor 10)

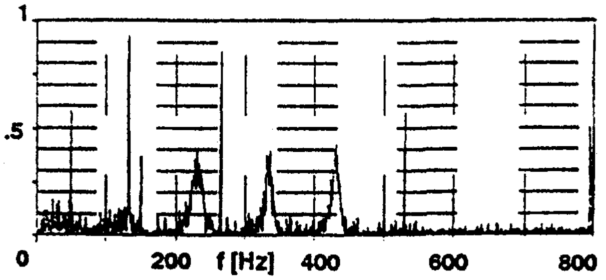

Coherence (Rotor 1 / Rotor 10)

Fig. 5 Correlation of HP compressor wall pressures

Fuel Injector. Based on negative results from the compressor rig and the fuel system diagnostic tests, it was postulated that the fuel injector itself may be the cause of the problem. A series of investigative tests was then introduced, the first to assess the possible effects of air pockets in the injector itself. A drastic increase in noise amplitude was noted when fuel injectors were tested with insulating internal air cavities. Fuel could enter the air cavity and the compressible air acted as a spring, further driving the pressure fluctuation in the combustor. Eliminating the air cavity, however, did not stop the noise.

Annular combustion rig tests were also run to isolate the effect of the fuel injector. Injector 2 was first tested because it produced the loudest noise in the engine and it was most likely also to show instability in a combustor rig. Rumble was reproduced at 103 Hz with an amplitude of about 4 kPa. Steady-state test conditions were P30 = 324 kPa, T30 = 451 K, and AFR = 37. After a test bed change to Injector 1, no rumble was found at or near the established rumble conditions of Injector 2.

With the insight gained from the annular combustor tests, it was decided to set up a well-defined, simple experiment with an isolated airblast-type fuel injector. At the Whittle Laboratory in Cambridge, experimental experience on fuel injector tests as well as equipment were readily available. Spray tests were carried out on a twice-size model of Injector 2. The purpose of the tests was to examine the fluid mechanics of spray generation at low fuel flow rates and to investigate the possibility of modifying the internal geometry of the injector to reduce self-excited instabilities. The use of water rather than fuel was considered adequate for the tests where small differences in viscosity and density will not greatly influence the basic fluid mechanics and the effect of surface tension was known.

A twice-size model was selected because of the difficulty of building a 1:1 scale model in which the position of the fuel metering ring could easily be changed. Working on a larger scale made it possible to have a sliding metering ring held in position by very small grub screws. A further simplification was introduced by making the spray head axisymmetric, thus avoiding the complicated shape of the injector stem. Figure 6 shows the injector model components. The ''fuel'' supply to the model was achieved via three radial pipes connected to an annular chamber upstream of the fuel distribution slots. The model was mounted at the end of an air supply tube, which has a diameter three times greater than the model itself. The head of the model protruded from the end of the pipe so that the spray cone was essentially a free jet unconstrained by adjacent walls.

The tests were conducted at low air and fuel ratios to simulate the conditions at which start-up rumble occurred. From the beginning, it was visibly obvious that under certain flow conditions the ''fuel'' delivery rate was unsteady. The flow appeared to pulsate as if the fuel were being supplied in spurts. There did not seem to be a fixed frequency associated with the pulsing, rather a sporadic pulsing of the flow in the region of 5 to 8 Hz. These frequencies are lower than those encountered in the engine during rumble, but this may be due to the fact that the dimensions of the model are larger than those of the actual injectors and that the flame characteristics define the harmonic oscillation in the combustor. Video pictures suggest that the pulsing was not axisymmetric and that an element of rotation exists as the fuel breaks away from the nozzle lip.

Tests were carried out to establish the range of operating conditions over which unstable behavior occurred. First the fuel flow was held steady while the air flow rate was varied and then the air supply was held steady while the fuel was increased. The results showed that the nozzle behavior is not unstable at all operating conditions, only in a specific range of fuel and air flow rates. This gave rise to the idea that the unsteadiness might be associated with water being stripped in bursts or globules from the fuel cavity lip. If this were correct it was reasoned that the sporadic stripping of water from the lip would create unsteady pressures in the fuel cavity.

The pressure in the cavity midway between the fuel metering ring and the mouth of the nozzle was measured. A fast response pressure transducer was used and care was taken to position the measuring point midway between the jets from the six fuel metering slots. Air pressure drop was held at 400 mm water.

The pressure signals from the transducer were very unsteady and no specific frequency could be identified. The dominant disturbances were in the 0–10 Hz range, thus supporting the observed pulsations in the fuel spray. The measurements of the unsteadiness in the cavity are shown in Fig. 7, where the peak in unsteadiness coincides with the center of the unsteady operating regime.

The mean pressure levels in the cavity are also of particular interest and these are shown in Fig. 8. In the fuel flow range corresponding to the unstable behavior, i.e., from 0.1 to 0.7

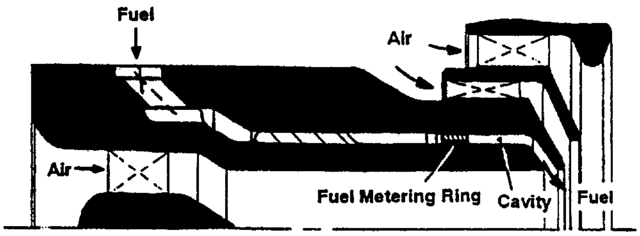

Fig. 6 Fuel injector model for spray tests

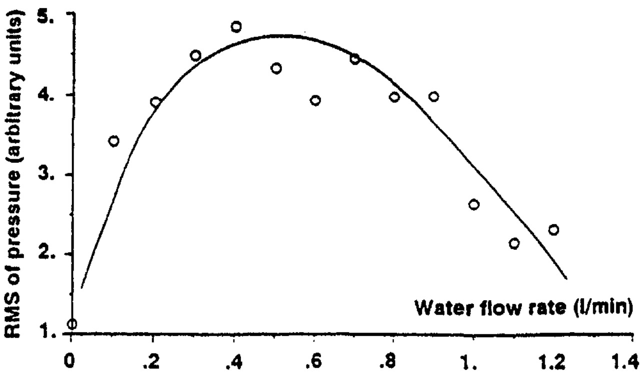

Fig. 7 The rms unsteadiness in the cavity

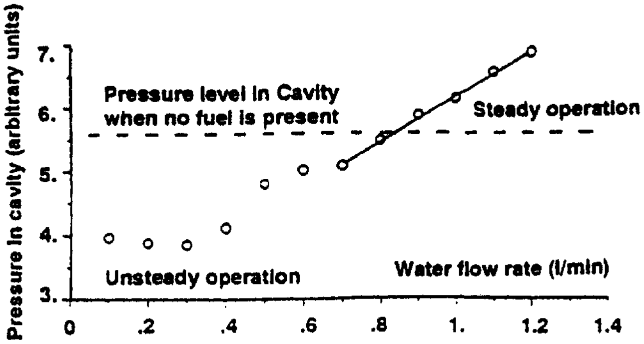

Fig. 8 Mean fuel pressure in the cavity

liters/minute, the pressure in the cavity is lower than the level when no fuel is present. This means that when fuel arrives at the lip of the nozzle, it is stripped away by the passing air giving rise to a partial vacuum in the cavity. As the fuel flow rate is increased, the cavity fills up and the pressure then begins to rise linearly with the increase in fuel supply. When this happens, the fuel release rate is steady because fuel is being forced out of the mouth of the nozzle in a continuous process rather than being dragged out in sporadic bursts.

An important part of the current tests was to establish what the effect would be of moving the metering ring closer to the exit plane of the nozzle. If this could be done without disturbing the spray pattern, the cavity volume in the nozzle would be reduced, thereby reducing the possibility of fuel instabilities. In moving the ring to the farthest downstream position, a particular concern was that spokes might appear in the spray cone due to the fact that there are six narrow channels in the metering ring through which all fuel passes.

The tests with the metering ring in the downstream position did not show any sign of spoking in the spray cone. In fact, moving the ring to either side of the design position had little noticeable effect on the spray. The unsteady pulsing of the fuel flow was detected with the ring in all three positions. It was found, however, that the range over which pulsating occurred was reduced when the metering ring was moved closer to the mouth of the nozzle, i.e., when the fuel cavity volume was reduced. Thus, moving the metering ring downstream reduced fuel flow instabilities without disturbing the spray pattern.

The work at the Whittle Laboratory thus identified a self-excited unsteadiness in the fuel spray mechanism at low flow rates as a possible source of the rumble. The work also suggested that a reduction in the volume of the fuel cavity downstream of the metering ring may be one way of reducing the problem.

Engine Measurements. In parallel to the above diagnostic component tests described above, simultaneous unsteady measurements were carried out on a full engine with extensive dynamic instrumentation. The engine under investigation had Combustor 3 installed.

Experimental Setup. Simultaneous dynamic measurements of pressure fluctuations in the fuel system, the high-pressure compressor, and the combustor were carried out to locate the source of disturbances that could be responsible for the rumble phenomenon. A cross-correlation was found very useful for determining the propagation directions of tonal frequency components (Bendat and Piersol, 1993). For this work, several fast response pressure transducers were mounted in the fuel system and in the compressor and combustor casings. The following data were recorded:

- core mass flow and fuel flow
- combustion noise (three Kistlers 120 deg apart)
- fuel pressures (Kulites up- and downstream of the splitter unit)
- engine shaft speeds N1 and N2
- combustion total pressure
- low pressure turbine inlet temperature
- engine noise (microphones in the test cell)
- compressor pressures upstream Rotor 1 (three Kulites 120 deg apart) and upstream Rotor 2 (one Kulite).

Diagnostic Investigations. The instrumented engine underwent a series of starts to idle and beyond. To investigate the effect of fuel–air ratio, compressor stall, etc., the engine was tested over a range of acceleration rates, compressor speeds, guide vane, and bleed valve settings.

The slope of the fuel ramp after light-up was once doubled and once halved. While the amplitudes of the sub-idle rumble remained approximately constant, the duration of the noise significantly decreased for steeper fuel ramps: 25 s for slope halfed, 12 s nominal, and 8 s when the slope was doubled. The data are shown in Fig. 9.

The opening and closing of the bleed valve changes the frequency of the steady-state rumble. Opening the bleed valve increases fuel flow and decreases combustor air flow by about 10 percent, thereby lowering air–fuel ratio. The transient bleed valve follows logic that detects changes in engine speed. Upon maneuvering the engine, the bleed valve opens and the rumble frequency goes down.

While the fuel ramp and bleed valve changes showed that rumble could be influenced in frequency and duration the amplitude of the rumble could not be decreased. Especially at steady-state idle operation the engine remained very noisy.

Dynamic Data Analysis. Standard data analyses using these measurements were performed for:

- combustion pressure fluctuation on a time-frequency plot
- air–fuel ratio
- estimated combustor efficiency
- cross-spectra of combustor/compressor/fuel pressures.

Standard phase relationships were analyzed for the compressor/combustor/fuel system. The phase relationships were used to determine the interaction between the various engine components. Figure 10 shows power spectrum, coherence, and phase between two combustor casing pressures for one speed. At the speed the data were taken rumble was at about 76 Hz, coherence is nearly 1, and the phase difference is zero. Consequently, the rumble seen here is a purely axial phenomenon. Phase analyses at other speeds and probe references confirmed that only axial modes were present.

The transfer function between the compressor Kulites and the rumble probes was also computed. In Fig. 11 power spectrum, coherence, and phase are plotted for the compressor Kulite up-

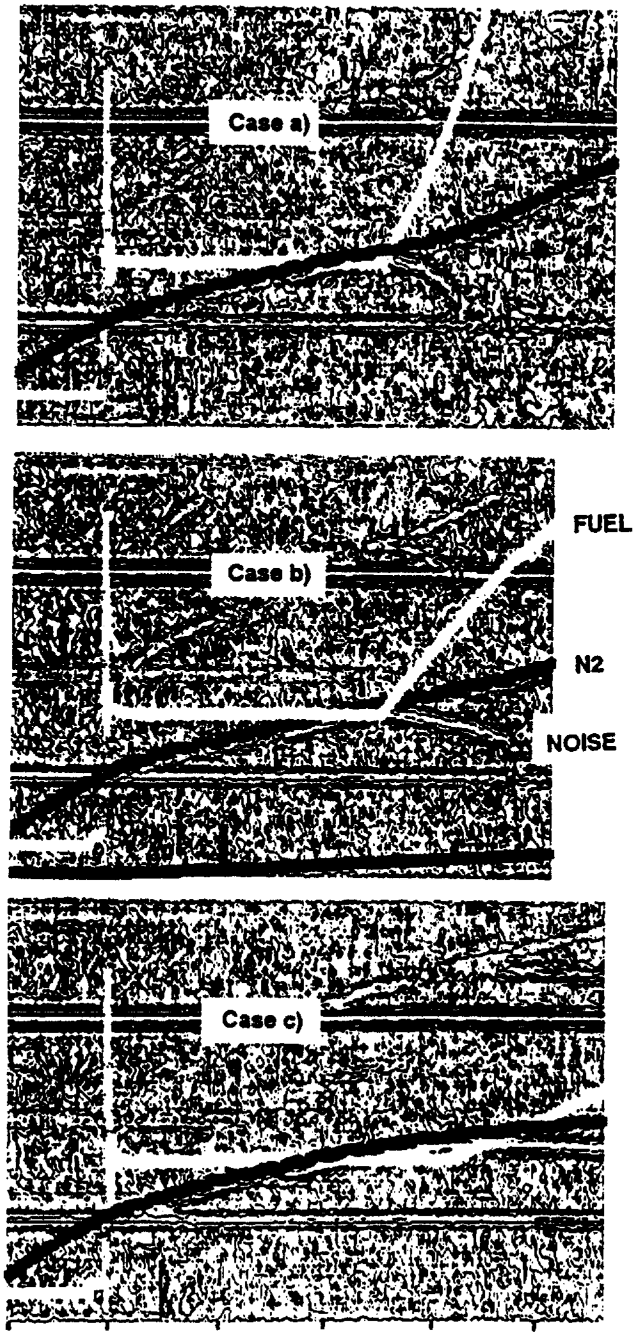

Fig. 9 Variation of fuel ramp after startup: (*a*) 200 percent ramp, (*b*) nominal, (*c*) 50 percent ramp

stream Rotor 1 with respect to combustor pressure. The compressor lags the combustor at the rumble frequency, hence the compressor does not play a part in the instability, it only "listens." High coherence is observed at the frequency of interest.

Similar analyses were carried out for the correlation of fuel system/combustor pressures and the two pressures measured in the fuel system. Phase changes were observed but careful analysis revealed that they were due to the characteristic of the splitter unit. The fuel system only picked up the combustor pressure fluctuations but did not play a role in the unstable behavior of the engine.

From the analysis of the engine data it was concluded that the exclusive source of the noise was contained within the combustion module of the engine. As the analysis was conducted in parallel to the component investigations and the injector spray tests the required action became very clear: The injector had to be modified.

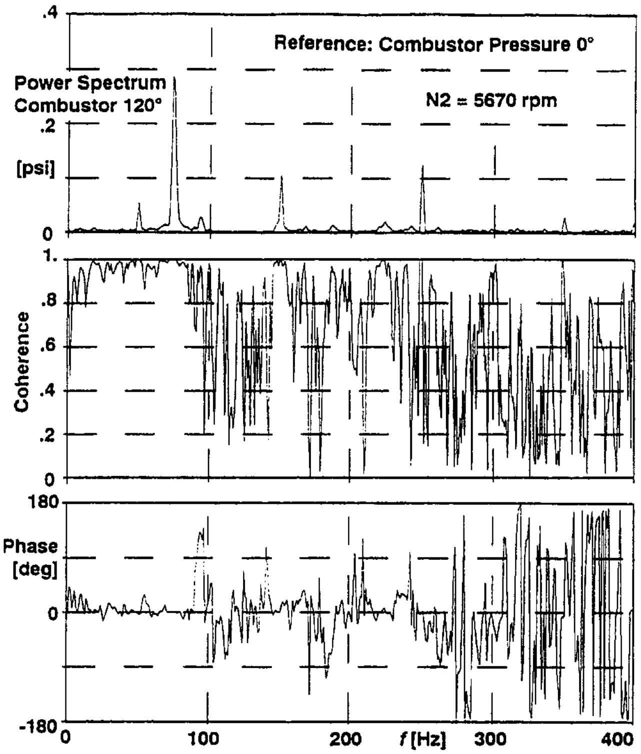

Fig. 10 Cross-correlation of combustion pressures showing one-dimensional characteristic

Elimination of the Instability

To meet the weak extinction requirements and to avoid overheating of the fuel injector shrouds, Injector 1 was not a reliable

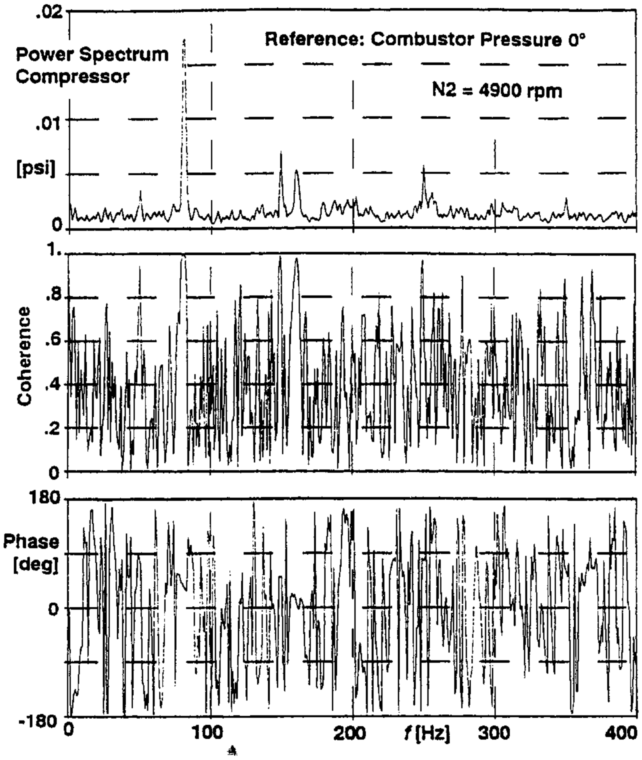

Fig. 11 Cross-correlation compressor/combustor pressures

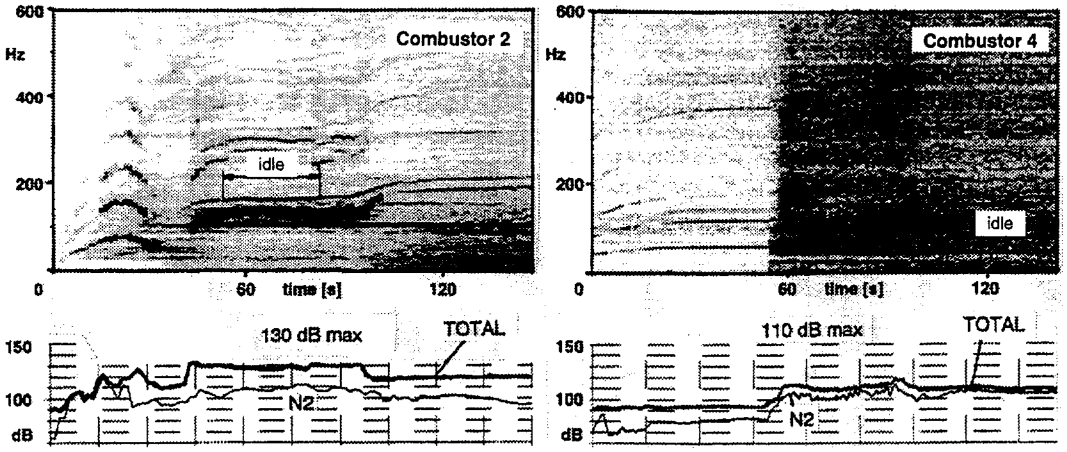

Fig. 12 Microphone data comparison of old and improved standards

choice for certification. Injector 2, on the other hand, was shown to be the source of the rumble. It was decided that Injector 2 should be modified while trying to keep its good weak extinction and thermal characteristics.

One of the main differences between the injectors is the spray angle, which is a function of swirl strength and distribution. Several improvements were tested and the best results in terms of spray and cooling characteristics were found when the swirl was decreased in the outermost air stream. Initial tests were conducted in a 90 deg sector rig to check for emissions, weak extinction, and integrity. The best candidate, Injector 3, having a narrow-cone fuel spray closer to the characteristics of the Injector 1 design was tested in the full annular rig with good results; no rumble was detected.

The final test was carried out in a full engine. Figure 12 shows microphone data from an early flight engine with the old combustor and for comparison an engine with the improved fuel injector. Recorded data are shown versus time up to high idle. It is clear that the old combustor rumbled during startup, at idle, and during acceleration from low to high idle. Amplitudes were up to 130 dB. The improved combustor does not rumble after ignition and overall noise is about equal to first engine order noise (about 110 dB). At idle rumble is gone and it does not reappear during acceleration from low to high idle.

Conclusions

On the BR710 jet engine combustor rumble was noticed after a test bed change of the fuel injector. A systematic search was undertaken to identify the source of the combustion instability. With measurements performed on a development engine and on component test rigs, it was demonstrated that the rumble was due to a self-excited instability associated with the fuel injector design. Detailed studies of the injector revealed a possible mechanism for unsteady fuel delivery and subsequent design changes eliminated the rumble noise.

As a result of the work described here it is possible to make the following recommendations:

- avoid internal air pockets in the injector
- avoid unstable high swirl aerodynamics
- take most of the pressure drop across the fuel injector tip
- minimize the cavity downstream of the fuel metering ring
- ensure good atomization at sub-idle conditions by appropriate swirl distribution.

References

Bendat, J. S., and Piersol, A. G., 1993, *Engineering Applications of Correlation and Spectral Analysis*, 2nd ed., Wiley, New York.

Crocco, L., and Cheng, S. I., 1956, *Theory of Combustion Instability in Liquid Propellant Rocket Motors*, AGARDograph 8, Butterworths.

Culick, F., Heitor, M. V., and Whitelaw, J. H., 1996, *Unsteady Combustion*, NATO ASI Series, Serie E: Applied Sciences 306.

Hermann, J., Zangl, P., Gleis, S., and Vortmeyer, D., 1995, *Untersuchung der Anregungsmechanismen selbsterregter Verbrennungsschwingungen an einem Verbrennungssystem für Flüssigkraftstoff*, VDI Berichte No. 1193, Deutscher Flammentag.

Kenworthy, M. J., Bahr, D., Mungur, P., Burrus, D. L., and Mehta, J. M., 1988, *Dynamic Instability Characteristics of Aircraft Turbine Engine Combustors*, AGARD CP-450.

Lefebvre, A. H., 1983, *Gas Turbine Combustion*, McGraw-Hill, New York.

Putnam, A. A., 1971, *Combustion-Driven Oscillations in Industry*, Elsevier, New York.

Rayleigh, J., 1878, *The Explanation of Certain Acoustical Phenomena*, Nature, July 18, pp. 319–321.

Development of a Dry Ultra-Low NO_X Double Swirler Staged Gas Turbine Combustor

H. Sato

M. Mori

T. Nakamura

Energy Technology Research Institute,
Tokyo Gas Co., Ltd.,
Tokyo, Japan

This paper describes the development of an ultra-low NO_x gas turbine combustor for cogeneration systems. The combustor, called a double swirler staged combustor, utilizes three-staged premixed combustion for low NO_x emission. The unique feature of the combustor is its tertiary premix nozzles located downstream of the double swirler premixing nozzles around the combustor liner. Engine output is controlled by simply varying the fuel gas flow, and therefore employs no complex variable geometries for air flow control. Atmospheric combustion tests have demonstrated the superior performance of the combustor. NO_x level is maintained at less than 3 ppm (O_2 = 15 percent) over the range of engine output between 50 and 100 percent. Assuming the general relationship that NO_x emission is proportional to the square root of operating pressure, the NO_x level is estimated at less than 9 ppm (O_2 = 15 percent) at the actual pressure of 0.91 MPa (abs.). Atmospheric tests have also shown high combustion efficiency; more than 99.9 percent over the range of engine output between 60 and 100 percent. Emissions of CO and UHC are maintained at 0 and 1 ppm (O_2 = 15 percent), respectively, at the full engine load.

Introduction

The number of cogeneration systems using a gas turbine as the prime mover has been increasing in Japan because of their high total thermal efficiency. Cogeneration systems are subject to strict NO_x regulations since air pollution in big cities such as Tokyo shows no sign of improvement. Gas turbines have generally employed the water/steam injection or the selective catalytic reduction methods to reduce NO_x emission. Both methods increase costs, thereby discouraging the wider use of cogeneration systems. A simple NO_x reduction method with low running and initial costs is urgently required.

Lean premixed combustion is believed to be one of the most promising methods to reduce NO_x emission from gas turbine combustors. A number of gas turbine manufacturers have applied lean premixed combustion technology to develop dry low NO_x combustors (Willis et al., 1993; Smith, 1992; McLeroy et al., 1995; Puri et al., 1995; Kitajima et al., 1995). Tokyo Gas has focused on the development of dry low NO_x combustors for cogeneration systems with electricity output in the range of 1 to 4 MW. Engine output is controlled by varying the fuel gas flow and therefore uses no complex variable geometries for air flow control. The combustors are also expected to replace existing gas turbine combustors without remodeling the gas turbine system.

Phase 1 of the development produced a double swirler combustor (Mori et al., 1993; Ishizuka et al., 1993). Atmospheric combustion tests showed promising results. NO_x emission is expected to be less than 17 ppm (O_2 = 15 percent) at the actual operating pressure while maintaining higher than 99 percent combustion efficiency between 75 and 100 percent of engine load. Ishikawajima-Harima Heavy Industries Co., Ltd. has employed the combustor for a 2 MW class gas turbine for a cogeneration system. Engine tests currently being conducted have successfully confirmed the low NO_x emission of the combustor.

Phase 2 has produced a double swirler staged combustor that achieves much lower NO_x emission. Atmospheric combustion tests have demonstrated the superior performance of the double swirler staged combustor. This report describes the results of atmospheric bench tests of the double swirler staged combustor.

Theoretical Considerations of Lean Premixed Staged Combustion

While it is expected to be one of the most effective methods to reduce NO_x emission, lean premixed combustion achieves low NO_x emission with stable combustion only in a narrow combustion range. A low excess air ratio close to the stoichiometric value allows stable combustion but results in very high thermal NO_x emission due to high flame temperature. A high excess air ratio, which achieves very low NO_x emission, often leads to high emission of CO and UHC with low flame stability. Both the excess air ratio and the flame temperature need to be maintained within an appropriate range to achieve low NO_x while minimizing CO and UHC. The behavior of thermal NO formation as well as the oxidation of CO and UHC need to be carefully considered.

Figure 1 shows calculated NO_x levels against the excess air ratio and adiabatic flame temperature of an air–natural gas mixture (Hase et al., 1991; Hase and Kori, 1994). Natural gas supplied in Japan is considered (CH_4 88.5 percent, C_2H_6 4.6 percent, C_3H_8 5.4 percent, C_4H_{10} 1.5 percent). The calculation assumes atmospheric pressure and temperature for the premixture. The calculation is designed to simulate NO_x levels in a test combustor with a residence time of between 20 and 25 ms depending on the excess air ratio. The calculation takes into account the effect of the mixing of the air and fuel gas on NO_x emission. Partial mixing means that premixed combustion takes place before the mixing between the air and fuel gas is completed to the molecular level. Partial mixing assumes Gaussian distribution in terms of the excess air ratio. The standard deviation is set at 11 percent of excess air ratio; a typical degree of the fluctuation of excess air ratio observed in practical premixed combustors. With theoretically ideal perfect mixing, low NO_x emission requires the flame temperature to be less than 1800 K. With partial mixing, a much lower flame temperature is

---

Contributed by the International Gas Turbine Institute and presented at the 41st International Gas Turbine and Aeroengine Congress and Exhibition, Birmingham, United Kingdom, June 10–13, 1996. Manuscript received at ASME Headquarters February 1996. Paper No. 96-GT-134. Associate Technical Editor: J. N. Shinn.

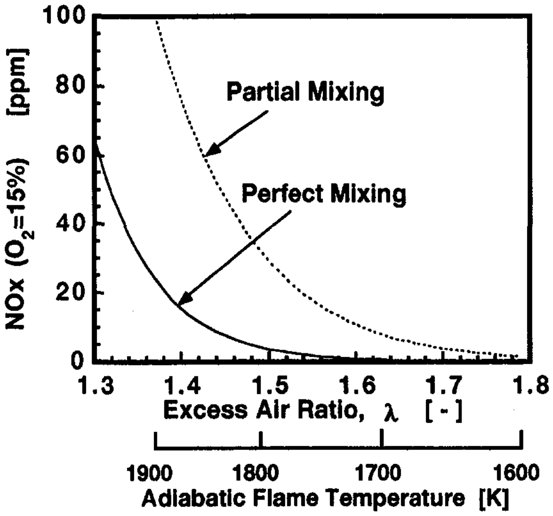

Fig. 1 Predicted thermal NO_x levels against excess air ratio and adiabatic flame temperature (Hase and Kori, 1994)

needed; roughly lower than 1650 K. A much lower flame temperature than the theoretical value appears to be necessary in practice to reduce thermal NO_x from actual gas turbine combustors.

It is difficult, however, to maintain complete, stable combustion of the premixed air fuel mixture with a flame temperature in a range under 1650 K. Two or multistaged combustion is one of most suitable methods to sustain stable combustion. In two-stage premixed combustion as shown in Fig. 2, the secondary premixture ignites and burns while mixing with the primary hot combustion products generated by the stable primary combustion. The secondary premixture is critically lean, often out of the flammability limit. Extensive study has been made to investigate the oxidation behavior of the secondary ultra-lean premixture (Fujisaki et al., 1995). Along with experiments, the study made theoretical investigation using the "CHEMKIN" code, which was developed by Sandia National Laboratories in the U.S. (Kee et al., 1988) The oxidation behavior of methane and CO was investigated.

Figure 3 shows the relation between the mixture temperature and the time required for 90 percent of the methane to be oxidized. Here, the mixture temperature is defined as the temperature of the instantaneous mixture consisting of the primary combustion products and the unburned secondary premixture prior to the oxidation. Enthalpy balance along with the dependency of specific heat capacity on temperature is taken into account to calculate the mixture temperature. The oxidation of methane depends predominantly on the mixture temperature and is almost independent of the excess air ratio of the secondary premixture. The mixture temperature needs to be higher than 1250 K to oxidize methane in less than 1 ms, a residence time short enough for the flame zone of a gas turbine combustor. The mixture temperature needs to be at least 1200 K to oxidize the secondary premixture in less than 2 ms, a typical residence time given to the flame zone.

Figure 4 shows the relation between the mixture temperature and the time required for CO to be oxidized down to 500 ppm. CO oxidation is influenced by the secondary excess air ratio of the secondary premixture as well as the mixture temperature. A high secondary excess air ratio requires a higher mixture temperature to oxidize the secondary premixture in the same residence time. A high secondary excess air ratio leads to a stronger effect of the mixture temperature on CO oxidation. When the secondary excess air ratio is lower than 6, the effect of the mixture temperature is marginal and 1300 K is enough to oxidize CO in less than 2 ms. When the secondary excess air ratio is higher than 10, the effect of the mixture temperature is strong and the mixture temperature needs to be higher than 1400 K. A low secondary excess air ratio or relatively rich secondary premixture is preferred for the oxidation of CO.

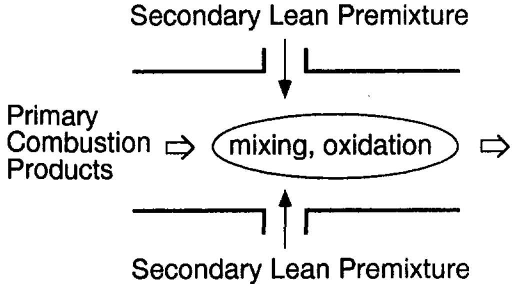

Fig. 2 Schematic of two-stage combustion

Based on these considerations, staged combustion needs to generate a flame temperature lower than 1650 K to minimize NO_x emission. To achieve high combustion efficiency, staged combustion needs to maintain the mixture temperature of the primary combustion products and the secondary premixture at more than 1400 K for a wide range of secondary excess air ratios. The mixture temperature can be higher than 1250 K if the secondary excess air ratio is maintained at less than 6.

Double Swirler Staged Combustor

The double swirler staged combustor has been developed based on the considerations outlined in the previous section. Figure 5 shows the concept of the double swirler staged combustor. The unique feature of the combustor is a set of tertiary premix nozzles located around the combustor liner downstream of the double swirler premixing nozzles. The double swirler premixing nozzles consist of two coaxial annular nozzles, primary and secondary, with radial swirlers. A pilot nozzle with an axial swirler is installed in the center of the double swirler premixing nozzles. Since it generates a diffusion flame rather than a perfect premixed flame, the pilot nozzle is expected to stabilize lean premixed flames generated by the other premix nozzles adequately. All the swirlers generate swirling flows of the same rotation.

The double swirler staged combustor has four separate fuel lines leading to the pilot, primary, secondary, and tertiary nozzles. Figure 6 shows the fuel supply schedule to the nozzles. The fuel supply schedule maintains the excess air ratio of the pilot nozzle (hereafter λ_{pil}) and the excess air ratio of the primary nozzle (hereafter λ_{pri}) as a constant over the whole engine load to generate a stable combustion with low NO_x emission. In the low mode, when the engine load is between 0 and approximately 30–40 percent, the schedule supplies fuel only to the secondary nozzle, with no fuel to the tertiary nozzles. The secondary fuel is controlled to meet the engine load. The fuel–air premixture created in the secondary nozzle is essentially very lean with its excess air ratio (hereafter λ_{sec}) being a minimum of 2.0, thereby igniting and oxidizing while directly contacting

Nomenclature

λ_{pil} = pilot nozzle excess air ratio
λ_{pri} = primary nozzle excess air ratio
λ_{sec} = secondary nozzle excess air ratio
λ_{ter} = tertiary nozzles excess air ratio
λ_{tot} = total excess air ratio

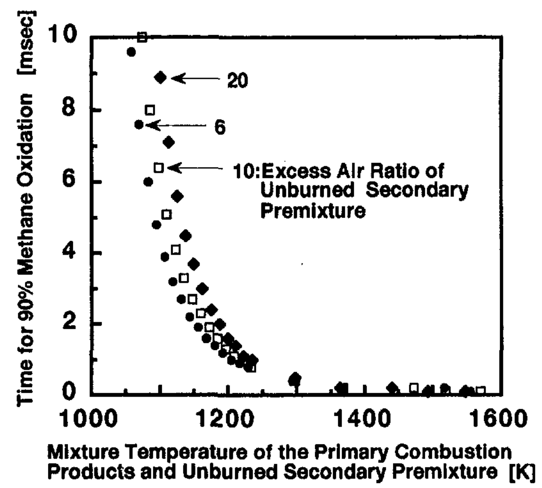

Fig. 3 Methane oxidation time (Fujisaki et al., 1995)

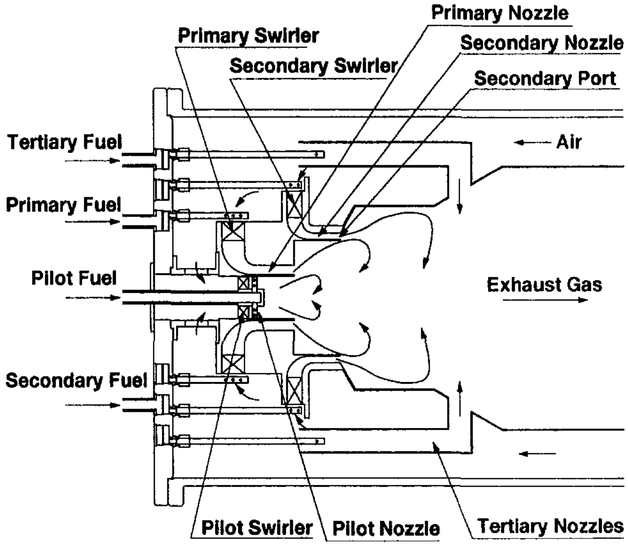

Fig. 5 Double swirler staged combustor

the stable primary combustion products generated by the pilot and primary nozzles. Since its flame temperature is kept low with excessively high excess air ratio, the secondary flame is expected to produce almost no thermal NO_x. In the high mode in which the engine load is up to 100 percent, fuel is supplied to the tertiary premix nozzles. All the other fuel flows to the pilot, primary, and secondary nozzles, are maintained constant at the maximum levels. Similar to the ignition behavior of the secondary fuel, the tertiary premixture is expected to mix with the combustion products generated by the pilot, primary, and secondary nozzles and finally oxidizes in a few milliseconds. The excess air ratio of the tertiary nozzles (hereafter λ_{ter}) is also kept high so that almost no NO_x is produced.

The double swirler staged combustor, with its ability to control the fuel flow of the tertiary as well as secondary nozzles, is expected to allow a wider turn-down ratio than the original double swirler combustor. Since it minimizes the proportion of fuel to the pilot and primary nozzles, which are considered to be the main NO_x source, the double swirler staged combustor is also expected to reduce NO_x emission substantially.

Operating Conditions and Target Performance

The operating conditions and target performance of the combustor were determined to meet the general requirements for gas turbine combustors for cogeneration systems. Table 1 shows the operating conditions and target performance. The target NO_x level is 9 ppm at engine load between 50 and 100 percent, the normal operating range of gas turbines for cogeneration. At less than 50 percent engine load, the target NO_x level is 25 ppm, which is a general low NO_x combustor target. These target NO_x levels are converted to 3.0 and 8.3 ppm under atmospheric pressure assuming the general relationship that NO_x emission is proportional to the square root of operating pressure. NO_x emission is reported to be slightly less than proportional to the square root of operating pressure for lean premixed combustion (Willis et al., 1993; Correa, 1992). Therefore, these target NO_x levels under atmospheric pressure appear to be on the reasonably safe side. It should be noted, however, that further consideration is necessary to determine precisely the effect of pressure on NO_x in the range of 5–10 ppm along with the effect of prompt NO that might be generated by the pilot diffusion flame.

The target combustion efficiency is higher than 99 percent, preferably nearing the 99.9 percent level, under normal operation between 50 and 100 percent engine load. Higher than 95 percent efficiency is required below 50 percent load to provide moderate engine operation.

Figure 7 shows the schematic of a prototype combustor. Table 2 shows the open area ratios of the combustor nozzles.

Test Facility

A schematic of the test facility is shown in Fig. 8. The test facility comprises an air blower, an air preheater, test combus-

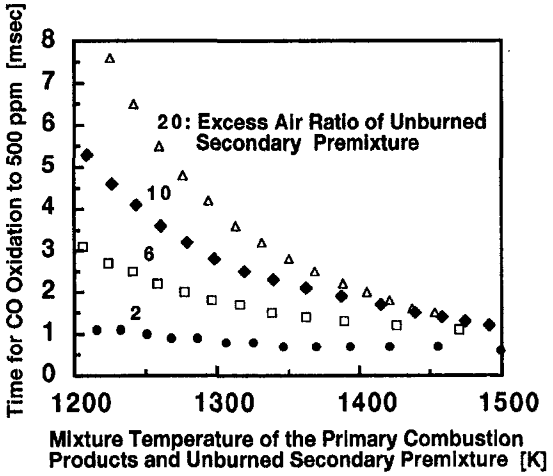

Fig. 4 CO oxidation time (Fujisaki et al., 1995)

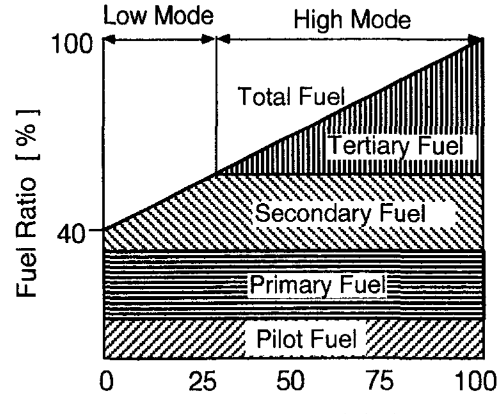

Fig. 6 Schematic of fuel gas supply schedule

Table 1 Target performance and operating conditions

Combustor Inlet Air Pressure	0.91 MPa (abs)
Combustor Inlet Air Temperature	640 K
Full Load Combustor Outlet Gas Temperature	1473 K
Full Load Excess Air Ratio	2.7
Fuel (LHV)	Natural Gas (41.6MJ/Nm^3)
NOx Target (50-100% Engine Load) (0-50% Engine Load)	 < 9 ppm (O_2=15%) < 25 ppm (O_2=15%)
Combustion Efficiency Target (50-100% Engine Load) (0-50% Engine Load)	 > 99% > 95%
Pattern Factor Limit	< 0.15
Combustor Pressure Drop	3 %

Table 2 Open area ratios of combustor nozzles

Pilot Nozzle	7.2 %
Primary Nozzle	14.3 %
Secondary Nozzle	17.1 %
Tertiary Nozzles	36.6 %
Sub Total	75.2 %
Cooling Air	7.0 %
Dilution Air	17.8 %

tors, a measurement section, and an exhaust gas cooler. The air was preheated to the required temperature by the heat exchanger. After being rectified in the rectifying tank, the air was introduced into the test combustor. Natural gas supplied in Japan (CH_4 88.5 percent, C_2H_6 4.6 percent, C_3H_8 5.4 percent, C_4H_{10} 1.5 percent) was used as a fuel. The flow rates of the fuel gas were measured with roots-type volumetric flow meters (Gas Oval, accuracy ±1 percent of the full scale). Combustion exhaust gas was sampled with a five-point water-cooled probe positioned 450 mm downstream from the combustor outlet. The sampled gas was introduced into gas analyzers through a Teflon tube heated at 390 K. Five major components of O_2, CO, CO_2, NO_x, and UHC were analyzed. Of these components, O_2 was analyzed with a magnetic analyzer, CO and CO_2 with a nondispersive infrared analyzer, NO_x with a chemiluminescence analyzer, and UHC with a flame ionization detector. The temperature distribution at the combustor outlet was measured at nearly the same axial position as the gas sampling probe. The distribution was measured with type *K* thermocouples (diameter 3.2 mm) at 24 stationary positions to obtain the pattern factor. Through the inspection window located at the end of the combustion chamber, the flame was continuously monitored by a TV camera.

The total flow rate of the process air was calculated from exhaust gas composition and measured total fuel flow. The flow rate to each nozzle was calculated by assuming that the total air flow was split proportional to the open area of the respective air nozzle as shown in Table 2. The excess air ratio of each nozzle was finally calculated from the calculated air flow and measured fuel flow rate at each nozzle. The effective flow areas of each nozzle were not calculated or measured to estimate the air flow splits accurately, and thus the excess air ratios of each nozzle. Since the present combustor is a prototype combustor tested under atmospheric pressure to identify the effect of multistaged combustion, accurate estimation of the air splits seemed unnecessary. It should be noted, however, that the tertiary nozzle, with a long duct and a sharp elbow, may have relatively large pressure loss than the other nozzles. Air flow through the tertiary nozzle may be lower than based on the open area.

Combustion Characteristics

Figures 9, 10, 11, and 12 show a typical combustion performance of the combustor. The effects of the total excess air ratio (hereafter λ_{tot}) on NO_x, combustion efficiency, CO, and UHC are shown separately. Total excess air ratio, λ_{tot}, was calculated from the composition of exhaust gas measured at the exit of the combustor. Engine loads of 100, 50, and 0 percent correspond to 2.7, 3.9, and 6.8 of λ_{tot} in the figure if 0 percent engine load requires 40 percent of the full-load fuel flow, the amount necessary to drive the compressor. λ_{pil} was maintained at 2.0. The combustor employed two levels of λ_{pri}, 1.6 and 1.8, each of which was held constant over the whole engine load.

NO_x Characteristics. Figure 9 shows the behavior of NO_x emission. NO_x level is greatly influenced by the high/low mode along with λ_{tot}. In the low mode, when the engine load is small, λ_{tot} is varied by controlling the secondary fuel, with no fuel into the tertiary nozzles. When λ_{tot} is between 8.0 and 6.0 the NO_x level remains low at approximately 1.5 and 2.9 ppm for λ_{pri} of

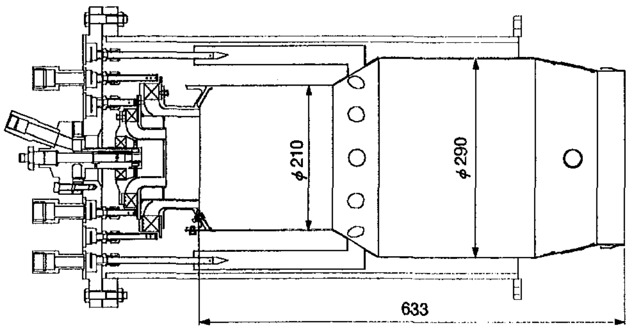

Fig. 7 Schematic of double swirler staged combustor

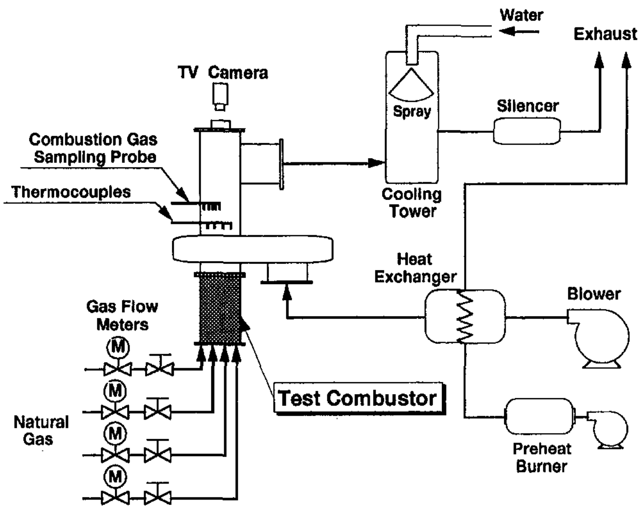

Fig. 8 Schematic of test facility

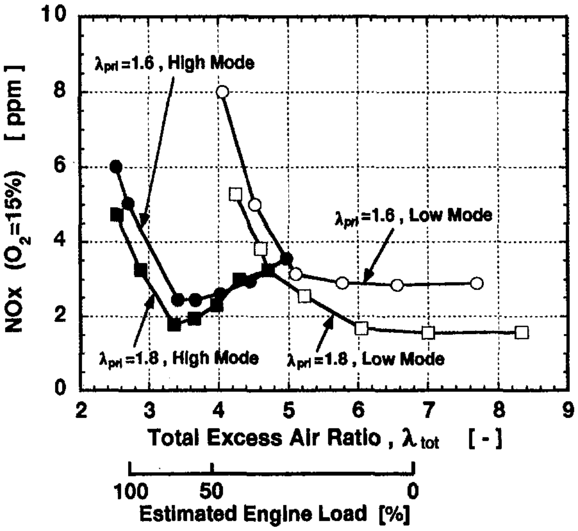

Fig. 9 Effect of total excess air ratio on NO_x emission

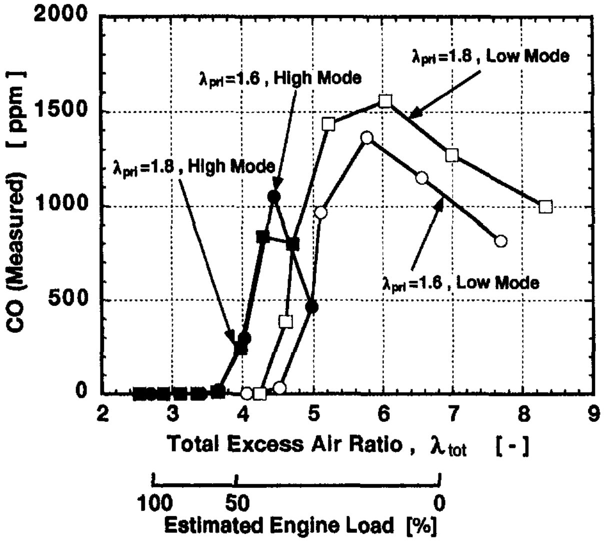

Fig. 11 Effect of total excess air ratio on CO

1.6 and 1.8, respectively. The secondary flame appears to produce virtually no NO_x in this range of λ_{tot}. A sharp increase in NO_x level is observed when λ_{tot} decreases from 5.0 to 4.0. The NO_x level reaches as high as 8 ppm for λ_{tot} of 4.0 and λ_{pri} of 1.6. When λ_{tot} is 4.0 with λ_{pri} of 1.6, λ_{sec} is as low as 1.5, lower than λ_{pri} of 1.6. Very low λ_{sec}, and thus high secondary flame temperature, appears to cause the sharp increase in thermal NO_x production. A theoretical consideration of adiabatic flame temperature, as shown in Fig. 1, may explain this phenomenon. The calculated adiabatic flame temperature of the mixture of the pilot, primary, and secondary flames is 1598, 1691, and 1780 K at λ_{tot} of 5.1, 4.5 and 4.1, respectively, so a high level of NO_x is expected at λ_{tot} of 4.1 and 4.5.

Considering the behavior of NO_x level in the low mode, the change in the combustion mode from low to high was initiated at λ_{tot} of approximately 5.0. In the high mode, the combustor supplied and controlled the tertiary fuel while maintaining the secondary fuel constant at the level at which the combustion mode changes. A marginal decrease in NO_x level is observed when λ_{tot} decreases from 5.0 to 3.5. With its sufficiently high excess air ratio, the tertiary flame appears to produce almost no NO_x in this range of λ_{tot}. Lower λ_{tot} eventually leads to lower converted NO_x emission since the tertiary flame consumes more oxygen without producing NO_x. When λ_{tot} decreases below 3.5, a sharp increase in NO_x level is again observed. Similar to the effect of λ_{sec} in the low mode, a low level of λ_{ter} and thus high temperature of the tertiary flame appears to allow a sharp increase in thermal NO production. When λ_{pri} is set at 1.6, the calculated adiabatic flame temperature of the tertiary flames is 1248, 1653, and 1778 K at λ_{tot} of 3.4, 2.7, and 2.5, respectively, so a high level of NO_x is expected at λ_{tot} of 2.7 and 2.5.

The effect of λ_{pri} is straightforward. Higher λ_{pri} results in lower NO_x level. At λ_{tot} of 2.7, i.e., the full engine load, λ_{pri} of 1.8 generated approximately 1 ppm lower NO_x than that of λ_{pri} 1.6. The NO_x level of approximately 4–5 ppm at λ_{tot} of 2.7, i.e., full engine load, does not appear to satisfy the target value of 3 ppm under the atmospheric combustion test. Either λ_{pil} or λ_{pri} should be increased.

Combustion Efficiency. Figures 10, 11, and 12 show the behavior of combustion efficiency, CO, and UHC, respectively. In Fig. 10, the high mode shows high combustion efficiency, in particular at λ_{tot} less than 4.0. Loss of combustion efficiency is observed at λ_{tot} around 4.5. Figures 11 and 12 reveal that this loss is mainly due to a large increase in unburned CO rather than UHC. At λ_{tot} of 4.5 and λ_{pri} of 1.6, λ_{ter} is calculated to be

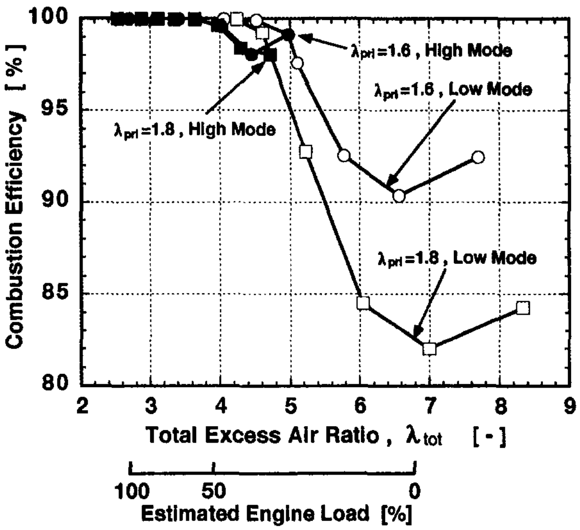

Fig. 10 Effect of total excess air ratio on combustion efficiency

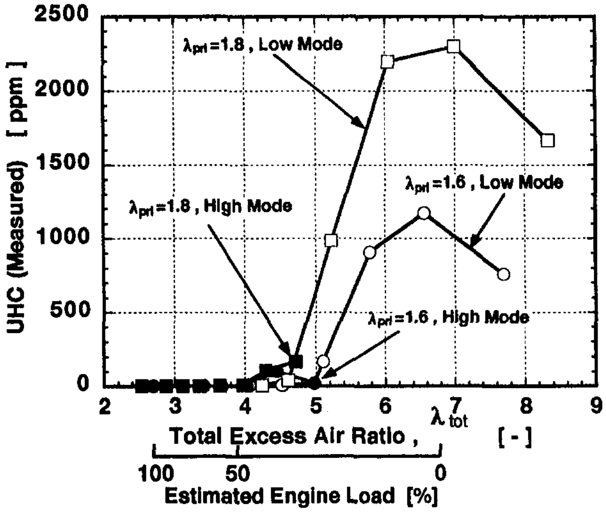

Fig. 12 Effect of total excess air ratio on UHC

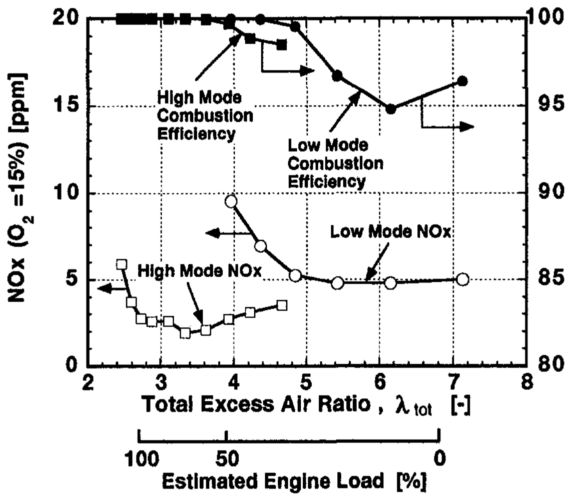

Fig. 13 Optimized performance of the combustor

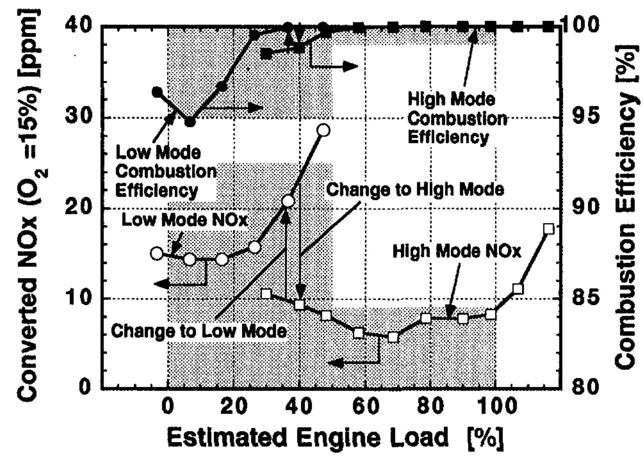

Fig. 15 Estimated actual engine performance

approximately 16, with the mixture temperature of the combustion products from the pilot, primary, and secondary flames and the tertiary premixture being 1264 K. While this level of the mixture temperature is high enough for the oxidation of methane as shown in Fig. 3, the high level of λ_{ter} requires excessively long residence time for CO oxidation, thereby leaving a substantial amount of CO unburned, as explained by Fig. 4.

In the low mode, high emission of CO and UHC, and thus a large loss of combustion efficiency, is observed when λ_{tot} is greater than 4.5. Higher λ_{pri} results in lower combustion efficiency. The primary flame appears to have a great effect on combustion efficiency. The calculated adiabatic flame temperature of the mixture of the pilot and primary flames is 1887 and 1806 K, for λ_{pri} of 1.6 and 1.8, respectively. The temperature of the instantaneous mixture of the combustion products from the pilot and primary flames and the secondary lean premixture is 1297 and 1250 K, for λ_{pri} of 1.6 and 1.8, respectively. This 47 K difference in the mixture temperature appears to have resulted in the great difference in combustion efficiency. In the theoretical consideration shown in Fig. 3, a minimum mixture temperature of 1250 K is needed to oxidize the secondary lean premixture in less than 1 ms if the mixing process between the primary combustion product and the secondary premixture is instantaneous. A sharp increase in the oxidation time is expected when the temperature of the mixture decreases below 1200 K. It appears that for the practical combustor in this research, the mixing process between the pilot and primary flame and the secondary premixture may not necessarily be instantaneous, and thus the required temperature for methane oxidation may be higher depending on the degree of the mixing.

Combustion efficiency is minimized at λ_{tot} of approximately 7.0, with the highest emission of UHC. At λ_{tot} of 7.0 and 6.6, λ_{sec} becomes excessively high, over 7.2 and 7.3 for λ_{pri} of 1.8 and 1.6, respectively. The oxidation of CO and the secondary fuel gas is hardly expected. Combustion efficiency recovers as λ_{tot} increases to its maximum level. This is due to the fact that at the maximum λ_{tot} the combustor supplies virtually no secondary fuel. The combustion efficiency and the emission of UHC and CO at the maximum λ_{tot} is therefore from the combination of the pilot and the primary flames. As λ_{tot} increases from about 7.0 to its maximum level, the secondary flame produces less UHC and CO as the secondary gas flow itself is reduced, thereby improving the overall combustion efficiency ultimately to that of the combination of the pilot and primary flames. Similar phenomena of increased combustion efficiency are also observed in high mode combustion, when λ_{tot} increases from 4.5 to 5.0. In the high mode, the tertiary flame appears to act as the secondary flame does in the low mode.

It is very important to identify whether the pilot or the primary flame produces UHC and CO at the maximum λ_{tot} when no secondary fuel is supplied. Considering that the pilot burner is designed to generate a stabilized diffusion flame, the majority of UHC and CO appears to come from the premixed primary flame, the stabilization of which depends on the pilot flame. Unlike the pilot flame, the primary flame has a direct mixing with the secondary air flow when no fuel is supplied to the secondary nozzle. The outer side of the swirling primary flame, in particular, has a very limited residence time, approximately

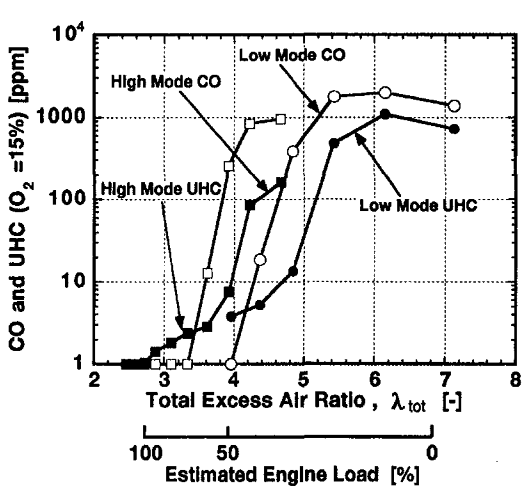

Fig. 14 CO and UHC performance of the combustor

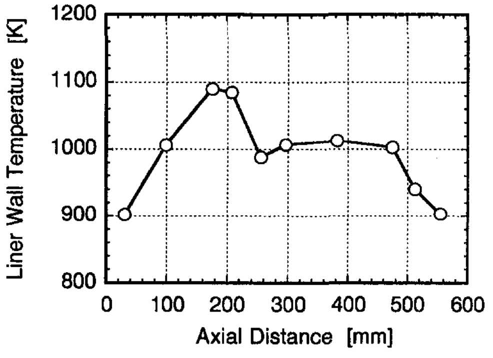

Fig. 16 Liner wall temperature (at full-load operation)

1 ms, before it mixes with the secondary air flow, presumably resulting in high emission of UHC and CO.

Optimization of the Combustor

The previous chapter suggests various strategies to optimize the combustor. To improve the combustion efficiency in the low mode and to reduce NO_x level in the high mode, λ_{pil} and λ_{pri} have been modified. Two different levels of λ_{pri} have been set depending on the combustion modes, 1.4 in the low mode and 1.8 in the high mode. λ_{pil} has been reduced and maintained at 2.2 over the whole engine load to further reduce NO_x emission. The results are shown in Figs. 13 and 14. The optimized levels of λ_{pri} substantially improve NO_x emission in the high mode and combustion efficiency in the low mode. At λ_{tot} of 2.7, i.e., the full engine load, 2.8 ppm NO_x, 0 ppm CO and 1 ppm UHC are obtained. At λ_{tot} of 3.6, i.e., the 60 percent engine load, 2.1 ppm NO_x, 13 ppm CO, and 3 ppm UHC are obtained.

Figure 15 shows the estimated performance of the actual engine if the present combustor is used at the actual operating pressure of 0.91 MPa (abs.). In actual engine operation, the combustion mode should be changed preferably at engine load of 40 percent. A NO_x level of 9 ppm converted empirically to the actual operating pressure and higher than 99 percent combustion efficiency is expected for engine load between 50 and 100 percent, the normal operating range. Higher than 99.9 percent combustion efficiency is expected for engine load between 60 and 100 percent. In the range of less than 50 percent engine load, usually observed at start-up and shut down, less than 25 ppm NO_x and more than 95 percent combustion efficiency are expected.

Figure 16 shows the axial temperature distribution of the liner wall at the full engine load. The axial distance starts from the secondary nozzle port (see Fig. 4). Type K thermocouples (diameter 1.0 mm) were used. The liner utilizes little cooling air to prevent excessive cooling air from quenching lean combustion. Relatively hot points are observed around 200 mm position, the liner temperature is maintained reasonably low.

Figure 17 shows the distribution of exhaust gas temperature at the full engine load measured by 24 stationary thermocouples. So far as the 24 measuring points are concerned, no hot spots are identified. Considering that the combustor is a single can in which the flow is in nature an axisymmetric strong swirling flow with large internal recirculation in the vicinity of the primary and secondary nozzles, the temperature distribution appears to be reasonably uniform. A very good pattern factor of 0.014 has been achieved. The exhaust gas in practice led to the turbine through the scroll, suggesting that better distribution of exhaust gas temperature is expected at the turbine inlet.

Pressure loss at the full engine load is acceptable at approximately 3.9 percent.

Conclusion

A double swirler staged combustor has been successfully developed at atmospheric pressure. This combustor has a simple geometry, which covers the whole range of engine load simply by controlling fuel gas flow. Atmospheric bench tests showed that the double swirler staged combustor offers superior performance; less than 3 ppm NO_x emission ($O_2 = 15$ percent) between 50 and 100 percent of engine load and more than 99.9 percent combustion efficiency between 60 and 100 percent of engine load. The NO_x emission level is estimated at less than 9 ppm ($O_2 = 15$ percent) if converted empirically to the actual operating pressure. The liner wall temperature and pattern factor of the exhaust gas temperature are maintained satisfactorily.

After further improvement, a series of engine tests will be conducted to establish the practical performance of the combustor.

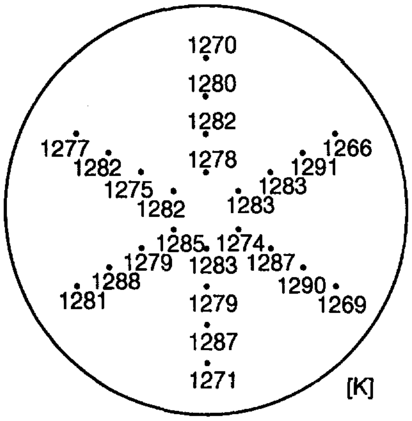

Fig. 17 Exhaust gas temperature distribution (at full-load operation)

References

Correa, M. S., 1992, "A Review of NO_x Formation Under Gas-Turbine Combustion," *Combustion Science and Technology*, Vol. 87.

Fujisaki, W., Takei, M., Amano, T., and Hase, K., 1995, "Combustion Characteristics of an Ultra Low NO_x Two-Stage Premixed Combustor," *The Proc. 8th International Symposium on Transport Phenomena in Combustion*, San Francisco.

Hase, K., Ohgi, K., and Kori, Y., 1991, "Effect of Air–Fuel Ratio Fluctuation on Nitrogen Oxides," *Proc. First International Conference on Combustion Technologies for a Clean Environment*, Vilamoura, Portugal.

Hase, K., and Kori, Y., 1994, "Effect of Premixing of Fuel and Air on NO_x Formation," *Proc. Pacific Rim International Conference on Environmental Control of Combustion Processes*, AFRC/JFRC Joint Conf., Hawaii.

Ishizuka, A., Mori, M., Miyahara, M., and Kuwabara, S., 1993, "Development of a Dry Low NO_x Combustor for Cogeneration Gas Turbine," *Proc. First International Conference on Combustion & Emissions Control*, The Institute of Energy, Cardiff.

Kee, J. R., Grcar, F. J., Smooke, D. M., and Miller, A. J., 1988, Sandia Report, SAND85-8240.

Kitajima, J., Kimura, T., Sasaki, T., Okuto, A., Kajita, A., Ohga, S., and Ogata, M., 1995, "Development of a Second Generation Dry Low NO_x Combustor for 1.5MW Gas Turbine," ASME Paper No. 95-GT-255.

McLeroy, J. T., Smith, D. A., and Razdan, M. K., 1995, "Development and Engine Testing of a Dry Low Emissions Combustor for Allison 501-K Industrial Gas Turbine Engines," ASME Paper No. 95-GT-335.

Mori, M., Ishizuka, A., Miyahara, M., and Kuwabara, S., 1993, "Development of Double Swirler Low NO_x Combustor for Gas Turbine," *Proc. 20th CIMAC G03*, London.

Puri, R., Stansel, D. M., Smith, D. A., and Razdan, M. K., 1995, "Dry Ultra-Low NO_x 'Green Thumb' Combustor for Allison 501-K Series Industrial Engines," ASME Paper No. 95-GT-406.

Smith, K. O., 1992, "Engine Testing of a Prototype Low NO_x Gas Turbine Combustor," ASME Paper No. 92-GT-116.

Willis, D. J., Toon, J. I., Schweiger, T., and Owen, D. A., 1993, "Industrial RB211 Dry Low Emission Combustion," ASME Paper No. 93-GT-391.

NO_x-Abatement Potential of Lean-Premixed GT Combustors

T. Sattelmayer
Technical University Munich,
D-85748 Garching, Germany

W. Polifke

D. Winkler

K. Döbbeling

ABB Corporate Research,
CH-5405 Baden-Dättwil, Switzerland

The influence of the structure of perfectly premixed flames on NO_x formation is investigated theoretically. Since a network of reaction kinetics modules and model flames is used for this purpose, the results obtained are independent of specific burner geometries. Calculations are presented for a mixture temperature of 630 K, an adiabatic flame temperature of 1840 K, and 1 and 15 bars combustor pressure. In particular, the following effects are studied separately from each other:

- *molecular diffusion of temperature and species*
- *flame strain*
- *local quench in highly strained flames and subsequent reignition*
- *turbulent diffusion (no preferential diffusion)*
- *small scale mixing (stirring) in the flame front*

Either no relevant influence or an increase in NO_x production over that of the one-dimensional laminar flame is found. As a consequence, besides the improvement of mixing quality, a future target for the development of low-NO_x burners is to avoid excessive turbulent stirring in the flame front. Turbulent flames that exhibit locally and instantaneously near laminar structures (''flamelets'') appear to be optimal. Using the same methodology, the scope of the investigation is extended to lean–lean staging, since a higher NO_x-abatement potential can be expected in principle. As long as the chemical reactions of the second stage take place in the boundary between the fresh mixture of the second stage and the combustion products from upstream, no advantage can be expected from lean–lean staging. Only if the primary burner exhibits much poorer mixing than the second stage can lean–lean staging be beneficial. In contrast, if full mixing between the two stages prior to afterburning can be achieved (lean-mix-lean technique), the combustor outlet temperature can in principle be increased somewhat without NO penalty. However, the complexity of such a system with a larger flame tube area to be cooled will increase the reaction zone temperatures, so that the full advantage cannot be realized in an engine. Of greater technical relevance is the potential of a lean-mix-lean combustion system within an improved thermodynamic cycle. A reheat process with sequential combustion is perfectly suited for this purpose, since, first, the required low inlet temperature of the second stage is automatically generated after partial expansion in the high pressure turbine, second, the efficiency of the thermodynamic cycle has its maximum and, third, high exhaust temperatures are generated, which can drive a powerful Rankine cycle. The higher thermodynamic efficiency of this technique leads to an additional drop in NO_x emissions per power produced.

Introduction

Due to its outstanding NO_x abatement potential, lean-premixed combustion has become the prevailing combustion technique of gas-fired land-based gas turbines within the last decade. Furthermore, progress has been made recently in the extension of the fuel spectrum toward liquid fuels as well as syngas from gasification processes. Since at high air pressures and temperatures lean premixing exhibits inherent flashback problems, compromises in regard to mixing quality had to be made until now in the design of reliable gas turbine burners, which result in elevated NO_x levels. However, improvements of the fuel–air mixing technique will lead to gas turbine burners that are free of these shortcomings in the near future. As a consequence, it becomes increasingly important to investigate how far the NO_x production of lean, perfectly premixed turbulent flames can be lowered.

The minimum attainable level for the unstaged process is influenced by the interaction of turbulence with chemistry. Modeling this interaction in sufficient depth would require a direct numerical simulation with detailed chemistry in order to capture the important influences on NO_x formation. Such numerical simulations up to now have been restricted to very simple flows and low turbulent Reynolds numbers. The computation of flows with a higher technical relevance, like combustor flows in our case, requires turbulence modeling and other crude simplifications with respect to the chemical reaction, so that the generation of a detailed understanding of the underlying phenomena cannot be expected.

Fortunately, the influence of turbulence-chemistry interaction on NO_x formation can be studied in sufficient detail as long as the minimum NO_x level is of technical interest. Since the local characteristics of premixed flames can be characterized by similarity numbers, a phenomenological description of effects that potentially may govern the NO_x formation can be given and the phenomena can be explored on the basis of model flames and reactor models, which are accessible for a full numerical modeling without excessive difficulty. This approach not only provides information about the NO formation of a turbulent flame front but, in addition, reveals the potential of lean and staged combustion methods.

The nitrogen chemistry as such is well enough understood for present purposes. As long as only clean fuels without fuel-

---

Contributed by the International Gas Turbine Institute and presented at Turbo Asia '96, Jakarta, Indonesia, November 5–7, 1996. Manuscript received at ASME Headquarters July 1996. Associate Technical Editor: J. W. Shinn. Paper No. 96-TA-21.

bound nitrogen are considered, three NO_x-formation paths, i.e., the so-called Zel'dovich, nitrous oxide (N_2O), and prompt mechanisms, contribute to the formation of NO in lean premixed combustion. The prompt mechanism, based on available rate data, exerts a negligible-to-weak effect in high pressure, lean flames. For the flame zone of atmospheric, lean, premixed combustors, the mechanism can be significant and has to be considered. As the excess air and/or the pressure increases, the ratio of NO formed by the Zel'dovich mechanism to NO formed by the nitrous oxide mechanism decreases. This is due to the high activation energy of the Zel'dovich mechanism and the pressure sensitivity of the N_2O formation. Under the conditions of greatest interest for gas turbine combustion, namely near lean extinction and at high pressures, the nitrous oxide mechanism is predominant and can account for essentially all of the NO formed [1]. Since the NO formation through all three paths strongly depends on the concentration of the radicals of the oxyhydrogen pool, the NO is formed mainly in the flame zone, where super-equilibrium concentrations are observed. Farther downstream, after the breakdown of the fuel and the consumption of the intermediates is completed, the NO production drops to the rate given by the Zel'dovich mechanism at O-equilibrium. As a consequence, for primary zone temperatures below approximately 1750 K no significant dependence of the NO_x emissions on the combustor residence time is found.

Although some differences in the NO_x-formation rates predicted from different reaction mechanisms are found in the literature, only the results computed on the basis of the mechanism for methane proposed by Miller and Bowman [2] will be presented throughout the paper. It is important to note that the findings presented subsequently were not altered qualitatively when using different models. Combustion process parameters are chosen to represent current development targets for utility heavy-duty gas turbines.

Flame Structures of Gas Turbine Burners

Turbulent processes in flames are characterised by a broad range of time and length scales. In swirling flows, the size of the largest vortices with the turbulent macroscale L_t is strongly linked to the burner size. Perturbations with long wavelengths generate large vortices, which subsequently interact with each other and form a cascade of smaller and smaller vortices of increasing frequency [3]. The turbulent kinetic energy, which is mainly concentrated in the motion of the large vortices, is finally dissipated at vortex sizes below the Kolmogorov scale.

In order to characterize the interaction between turbulence and chemistry, similarity parameters can be defined. The governing parameters can be grouped within a set of essentially five dimensionless numbers. The ratio u'/s_l and the ratio L_t/δ_l relate properties of the large-scale turbulence to parameters that characterize a one-dimensional laminar flame. In addition, the turbulent Reynolds number Re_t relates the transport by large turbulent vortices ("turbulent diffusion") to molecular transport (diffusion), whereas the Damköhler number Da compares the mixing time due to the large-scale vortex motion to the characteristic chemical time scale of a laminar one-dimensional flame. The Karlovitz number Ka relates this chemical time scale to the mixing time of the smallest vortices in the turbulent energy cascade. Different definitions for Ka are found in the literature based either on the Taylor scale λ or on the Kolmogorov microscale η and with a variety of constants proposed. Interestingly, the Karlovitz number is also a measure for the volumetric heat release, since it relates the chemical time scale of the flame front to the generation of flame surface in the turbulent case. Implicitly, in defining the Damköhler number and the Karlovitz number, it is assumed that the mixing time within turbulent eddies correlates well with the time for eddy rotation. This might not be fully justified at least for low turbulent Reynolds numbers [4]. The five parameters mentioned are not independent from each other but can be coupled via the relationships of the turbulent cascade of isotropic turbulence. (A summary of the most important relationships as well as the aforementioned definitions are listed in Appendix A). When the turbulent Reynolds number Re_t, the Damköhler number Da, and the Karlovitz number Ka are expressed as a function of u'/s_l and L_t/δ_l, turbulent flames can be characterized in the so called Borghi diagram [5] (Fig. 1).

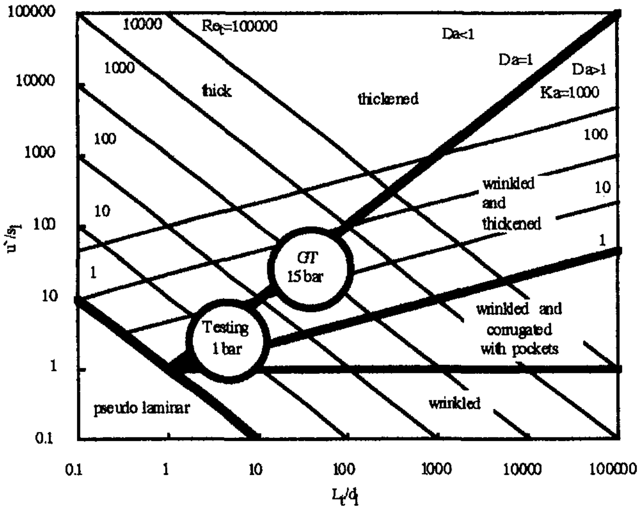

Fig. 1 Turbulent combustion diagram

The two marked spots in the diagram represent the conditions for typical premixed gas turbine burners in an engine and at atmospheric test conditions, respectively. The highest Karlovitz numbers appear at the maximum air preheat and represent operating points near the lean blowout limit (the burner rating is 5–10 MW thermal output at 15 bar combustor pressure, turbulent length scales were obtained by LDA measurements, and the laminar flame speed and flame thickness were computed with a one-dimensional premixed flame model).

Nomenclature

a = thermal diffusivity, m^2/s
a = strain rate, s^{-1}
A = area, m^2
D = diffusion coefficient (species), m^2/s
Da = Damköhler number
Da_{mix} = mixing Damköhler number = τ_{mix}/τ_{chem}
ϵ = turbulent dissipation rate, m^2/s^3
δ_l = laminar flame thickness, m
η = Kolmogorov scale, m
k = turbulent kinetic energy, m^2/s^2
Ka = Karlovitz number
L_t = turbulent macroscale, m
Le = Lewis number = a/D
λ = Taylor scale, m
λ = thermal conductivity, W/m/K
ν = kinematic viscosity, m^2/s
p = pressure, N/m^2
Re_t = turbulent Reynolds number
s_l = laminar flame speed, m/s
t = time, s
$t_{burnout}$ = burnout time (99.9 percent reaction progress), s
t_{res} = residence time, s
T = local temperature, K
T_{ad} = adiabatic flame temperature, K
T_{in} = reactant temperature at inlet, K
τ = characteristic time scale, s
u' = rms of turbulent fluctuations, m/s
X = mole fraction

A set of borderlines can be defined, where turbulent flames change their appearance due to changes in the interaction of turbulence with chemistry. However, since the methodology depends on the comparison of two phenomena competing with each other with subsequent neglecting of the influences of the weaker partner as well as on the validity of relationships of isotropic turbulence, a sharp transition cannot be expected when such a borderline is crossed. Turbulent premixed flames have been a major research field for a long time and many detailed investigations of particular effects present in turbulent flames have been published. Subsequently, a brief overview of the current knowledge will be given. In interpreting the results from the review, an attempt is made to develop an understanding of the phenomena governing the structure of turbulent flames with respect to the properties of the underlying flow field. The following flame types can be defined.

"Pseudo" Laminar Flames. In flows with local laminar flame structure, the turbulent Reynolds number of all possible vortex sizes must be less than unity. This condition is satisfied if $Re_t < 1$. Since the viscous dissipation is strong in comparison with the turbulent transport, this leads to immediate dissipation, so that the character of the flame is well represented by the relationships of a one-dimensional laminar flame.

Wrinkled Flames. Reacting flows with low turbulence intensity and turbulent length scales, which are considerably greater than the thickness of the flame front, generate a wrinkling of the reactive layer with an increase in total flame area and volumetric heat release. As long as u' remains smaller than the laminar flame speed s_1, the flame front exhibits a connected surface.

Wrinkled, Corrugated Flames With Pockets. Turbulent structures with intensities u' above the laminar flame speed s_1 cause a disruption of the flame surface. Zones of high velocity can, for example, bend the local flame zone so strongly that locally Ω-shaped bulges of products are generated and finally separated from the main flame front (pockets) after the reaction at the link to the main flame front has been quenched.

Flames of the three aforementioned types have been subject to a large number of detailed investigations. Although the global appearance of the flame front is strongly influenced by turbulence, it is commonly understood that with respect to NO production no major deviations from the mechanisms found in one-dimensional flames can be expected. As long as the laminar flame is faster than the turbulent velocity u' and the flame is much thinner than the size of all turbulent eddies, it can be concluded that the combustion process is locally well represented by the laminar flame theory. In comparison to this so-called (unstrained) flamelet regime, the current understanding of premixed, highly turbulent flames is much less consistent. Stirring of the flame front by turbulent eddies, the increase of the diffusion due to turbulence as well as the local stretching of flame fronts during flame–vortex interaction with subsequent quenching and re-ignition may affect the NO production of premixed flames.

Thickened, Wrinkled Flames. As soon as the Karlovitz number exceeds unity, the dissipation of turbulent kinetic energy will require a drop in the turnover time of the smallest eddies below the reaction time of the laminar flame front. It is postulated in the literature [6] that the smallest eddies of the turbulent flow field will produce stirring in the reacting layer and will alter the appearance of the flame front. The turbulent scales smaller than the flame thickness produce a thickening of the reactive layer due to enhanced (turbulent) diffusion of temperature and species, whereas the larger scales wrinkle the thickened flame front. The increase in heat release is attributed to the generation of flame area (wrinkling) as well as to an increase of flame speed. It is important to keep in mind that the mixing process in the flame front, which finally leads to thickening, is generated by the rotational motion of vortices. Since this kind of stirring produces continuously backward and forward mixing, it leads to the mixing of media with different levels of reaction progress during the combustion process. It has to be expected that the relationship between the concentration of radicals governing NO formation and the average reaction progress is altered with respect to the laminar case. It is somewhat unclear presently how quickly flame thickening occurs when the Karlovitz number is increased above unity.

Thickened (Thick) Flames. Increasing the Karlovitz number further shifts the critical vortex size, which separates the regime of flame thickening from that of flame wrinkling, toward the largest vortices of the turbulent flow field ($Da = 1$). Above that limit ($Da < 1$) even the turnover time of the largest vortices is shorter than the chemical time scale. As a consequence, the wrinkled flame structure is lost entirely and the flame front appears as a thick reacting layer, which progresses with high turbulent flame speed. The reacting layer between reactants and products can be interpreted as an ensemble of stirred spots with a wide range of sizes, which promote the diffusion of temperature and species. The continuous transition (time average) from reactants to products implies directly that the characteristic size of the stirred spots does not exceed the thickness of the reaction zone. A widely used classical model of a highly stirred flame is the perfectly stirred reactor (PSR). However, the PSR does not fulfill the constraint that the characteristic size of the stirred spots does not exceed the thickness of the reaction zone because the homogeneous reaction volume cannot be subdivided in areas of different time-averaged reaction progress. Since the homogeneous reaction volume is obtained at the expense of a discontinuity at the inlet of the reactor, fundamental differences between the reaction in highly turbulent flames and stirred reactors exist.

Stretched Flames. Besides flame front stirring and enhanced diffusion due to turbulence, flame stretch might alter the radical pool during reaction. As already mentioned, the ensemble of turbulent vortices produces fluctuating strain to which the flame front is exposed while it propagates against the flow direction. A flame is locally stretched when in a frame of reference moving with the flame the velocity normal to the flame front undergoes deceleration toward the reaction zone. At the same time, a velocity component parallel to the flame front develops. In contrast to the unstrained one-dimensional flame, which consumes all the reactants it has previously preheated, the strained flame is characterized by a continuous convective loss of reactants during preheat. Flame zones of high strain are found, e.g., where a counterflow from opposite sides toward a point of stagnation occurs [7]. The case of a counterflow of reactants from one side and products from the second side is of particular interest for strained premixed flames. At very low strain rates the flame front is located far from the stagnation point. The velocity gradient is low when compared to the flame thickness and no fundamental difference is found with respect to laminar flames. At high strain rates, however, the reaction zone is remarkably influenced by the convective/diffusive transport of products and temperature toward the flame front from the side beyond the stagnation point. Strain increases the gradients of species and temperature and, as a consequence, diffusive fluxes. Near the point of stagnation itself the transport is dominated by diffusion alone. The combined diffusion and convection of products and temperature toward the reactive layer leads to an enhanced heating and a dilution of the reactants with products.

The NO concentration is composed of one contribution that originates from the reaction and a second share that is transported with the counterflowing products toward the reactive layer. This makes the comparison of the NO emissions from strained and unstrained flames difficult. A special procedure described in Appendix B can be used to separate the NO generated in the flame from the amount that originates from the product side.

The disturbance of the balance between the heat release and the diffusion as well as the convection of temperature and species alters the flame front characteristics considerably. The generation of strain can be accomplished by vortices of all sizes. Since vortices at the lower end of the turbulent energy cascade produce the highest strain (see Appendix A), a Karlovitz number on the order of unity, the so-called Klimov–Williams limit, is of special interest. On the other hand, the interaction time of the smallest vortices might be insufficient to influence the flame strongly enough. A number of investigations [7–11], which cover the more generic case of single vortices and assume that a superposition of effects from different vortex sizes is permissible, consistently predict a limit for local quenching at Karlovitz numbers above unity. An efficiency function can be calculated that takes into account that the smallest vortices cannot maintain flame stretch long enough. The interesting result that vortices of a medium size in between the turbulent microscale and macroscale are most effective is found (valid for flames with $L_t/\delta_l > 5-10$).

Re-ignition and Afterburning. In highly strained flames, a certain share of the reactants cannot react immediately despite the existence of an interface between reactants and products. The understanding of this phenomenon, how complete combustion is finally achieved, is not very well developed yet. Usually, the description that subsequent reaction takes place in ''distributed reaction zones'' is found in the literature without detailed definition.

The enhanced convective/diffusive fluxes in strained zones lead to a velocity component parallel to the flame front and a loss of matter sideways. Counterflows of reactants and products with high strain rates are characterized by huge convective/diffusive fluxes with respect to the heat release in the flame front. Asymptotically, a pure mixing process is approached for infinite strain rates. It is important to mention that, although the temperature and species concentration change due to chemical reaction might be negligible for excessive strain rates, a breakdown of the combustion process does not occur for a counterflow of reactants and products. As the result of the mixing process, a wide range of mixture ratios of reactants and products are generated, which will undergo an afterburning process in zones of lower local strain. As long as no temperature increase due to diffusion takes place, zones of high reactant concentration will either assume temperatures below the self-ignition limit, or temperatures that require long induction times for the onset of chemical reaction. In contrast, zones of higher product concentration will exhibit a higher temperature in the adiabatic case. A massive drop of the local strain rate will directly lead to a smaller ratio between convective/diffusive fluxes and heat release. Thus, structures similar to those of an unstrained flame will appear and ''re-ignition'' will mainly progress via the diffusion of temperature and species from the hotter zones toward the zones of higher reactant content. Although it is somewhat unclear whether the self-ignition of isolated pockets of mixtures is of evidence in addition, a model that assumes ''the distributed reaction zones'' to be a local sudden combustion without any diffusive transport is certainly unrealistic. If one assumes that the formation of flame fronts, which propagate diffusion-driven into a mixture of reactants and products, represents the reality more adequately, the (unstrained or weakly strained) combustion of mixtures of reactants and products, a kind of local exhaust gas recirculation, can be defined as a simplified model for the afterburning process. A model can be constructed that depicts highly turbulent flames as an ensemble of highly strained flame zones complemented by weakly strained zones of combusting reactant/product mixtures. However, the transition toward the highly stirred (thick) flame regime or the well-stirred reactor can not be described adequately as long as stirring caused by the turbulent eddies is excluded.

In general it has to be mentioned that detailed investigations on stretched flames reported in the literature were restricted to the generic case of single vortices. Effects due to the coexistence of vortices of different sizes were not covered. So, stirring effects by smaller vortex sizes were beyond the scope of those investigations. Furthermore, local flame quenching was not easy to monitor experimentally or needed crude assumptions like massive radiative heat loss in order to become visible in numerical investigations.

In summary, the current knowledge does not provide a full understanding for Karlovitz numbers above unity. Besides known effects like flame stretch and afterburning in distributed reaction zones, turbulent mixing in the flame front has to be considered in order to generate a consistent understanding of the structure of turbulent flames over a wide range of turbulence intensities and length scales.

Modeling the Effect of Turbulence on NO Generation. Figure 1 reveals that the flame structure of gas turbine burners cannot be universally characterized by one single turbulent flame regime. Burners operated very close to lean extinction (1650–1750 K) are represented by Karlovitz numbers between 10 and 100 and Damköhler numbers near unity, whereas an increase of the flame temperature toward 1900–2000 K will reduce the Karlovitz number remarkably. In terms of the turbulent flame structure, it has to be expected that this will be accompanied by a change from a highly stirred and stretched flame toward flamelet structures. In order to assess whether turbulence affects the NO emissions of perfectly premixed flames from gas turbine combustors, a number of simplified models will be defined.

The reference case is the one-dimensional laminar flame, which represents not only the laminar but also the moderately turbulent (unstrained flamelet) regime. The computations of the freely propagating flames presented in this paper are accomplished by the widely used Sandia codes [12]. NO formation in laminar flames is influenced by the diffusion of species. Diffusion is complex, since each species has its own individual diffusion coefficient, which depends on all other species and on the temperature field.

A model that is widely used in NO studies is the combination of a stirred reactor and a plug flow reactor. Although the flame stabilization of turbulent flames due to the diffusion of temperature and species is not well represented by a PSR, the combination PSR–PFR is useful when the PSR volume is minimized. The need for the PSR as an ''artificial'' ignition zone, which compensates for the missing flame holding capability of the PFR, does not constrain too severely the investigation of NO formation, which happens mainly in the mid and high-temperature regime. Usually, only small amounts of NO are produced at the exit of the PSR and the further formation can be studied in the absence of diffusive transport.

Turbulent diffusion, which is in reality generated by vortex motion, is often strongly simplified for the purpose of flow modeling. The transport term is modeled largely similar to the laminar case, with the major difference that the diffusion coefficient depends on turbulent quantities of the flow field and is no longer species or temperature dependent. Thickening of flame fronts due to turbulence enhanced diffusion can be studied using the laminar flame code when the matrix of the diffusion coefficients is replaced by one ''turbulent'' value and the strength of the transport of temperature with respect to the transport of species is predetermined by the selection of the Lewis number Le. In order to compute the one-dimensional flame with turbulent diffusion coefficients, the laminar flame code was modified accordingly. The benefit of this model is threefold: First, the influence of turbulent diffusion, which is usually at least an order of magnitude higher than in the laminar case, can be studied and, second, the impact of preferential diffusion of species on NO formation can be quantified. Third, the sensitivity of the NO production on the balance between the diffusion of temperature and the diffusion of species can be quantified, if the Lewis number is varied. It can be shown analytically from the underlying equations that the propagation velocity of the flame as well as the flame thickness δ are both proportional to the square root of the diffusivity of temperature and species and, as a consequence, the reaction progress with respect to time is *not* a function of the diffusivity. In other words, the local turbulence level and the turbulent macroscale will influence the flame propagation and the volumetric heat release but not the time scale of the chemical reaction and not the formation of NO. A particle that crosses the flame front will not experience any difference when the diffusion coefficients a and D are similarly scaled (i.e., to maintain a constant Lewis number).

The representation of the turbulent interactions with the flame by turbulent diffusion has the shortfall that the character of stirring by vortex motion, namely to mix media of different reaction progress continuously in the flame front, is not accounted for. A number of advanced models have been proposed in the past that account for stirring (e.g., "Interaction by Exchange with the Mean" model [13], "Coalescence-Dispersion" model [14, 15]). Simply speaking, in these models the flow volume under consideration is divided into a number of subvolumes ("particles") with homogeneous mixture in each of them. The mixture in each subvolume reacts according to a full kinetics scheme. The particles travel randomly from the inlet of the apparatus to the exit and interact with each other according to the assumptions of the particular model. The results obtained generally deliver NO emissions below those computed for a PSR as an upper limit. Flame stabilization in such models without diffusive transport requires backmixing of "older" to "younger" material when the incoming mixture is too cold to undergo self-ignition. Although promising agreement with reactor experiments has been obtained, it appears to be difficult to specify the model constants and assumptions so that turbulent flame fronts are well represented. Hence, for our purpose we restrict the investigation to the classical PSR–PFR combination mentioned above and vary the PSR volume in order to account for stirring. It is worth mentioning that the PSR is an extreme (asymptotic) assumption for the modeling of the turbulent stirring in a flame front. The intense stirring, which is enabled by the existence of the reactor confinement and high velocities, is generally not achieved in propagating flames as long as the burner pressure loss is, as usual, only a small fraction of the system pressure. Therefore, the PSR will overpredict effects on NO formation considerably.

A flame front that propagates in a turbulent flow field is continuously exposed to fluctuating strain produced by turbulent eddies. Using the code of Rogg [16, 17] for a counterflow flame, the influence of flame stretch on NO formation is calculated. The study focuses on the counterflow of premixed reactants and products since this is more relevant for highly turbulent flames than the counterflow of reactants on both sides.

In order to assess the importance of afterburning in zones that have previously undergone mixing without significant heat release due to locally high strain rates, the one-dimensional unstrained laminar flame of mixtures of reactants and products has been additionally investigated. At higher product concentration in the mixture, the self-ignition temperature is exceeded and the well-known problem of defining the cold boundary arises. This difficulty has been overcome in calculating a burner-stabilized flame instead of a freely propagating one. In increasing the flow rate toward the point of liftoff the heat loss to the "burner" was almost fully suppressed and adiabatic conditions were established. For the sake of simplicity, the products mixed with the reactants were free of NO. As far as lean combustion is concerned, it can easily be shown that the NO content of the primary mixture does not influence the NO generation of the afterburning process and that no significant reburning of the NO from the first combustion will happen during afterburning. As a consequence, the NO production of the afterburning can be separated from that of the primary process and a superposition is allowed.

Results for the Unstaged Flame

Laminar flame propagation is governed by the diffusion of temperature (heat conduction) from the hot products toward the cold reactants. The boundary between the preheat zone, which absorbs more heat than it generates, and the reaction zone is located near the turning point of the temperature curve. At 1 bar (Fig. 2) heat release starts at approximately 25 percent temperature rise (900 K) and peaks at approximately 70 percent. In addition to heat conduction, the diffusion of species influences the appearance of the flame front considerably. For example, the fuel concentration has dropped to approximately 50 percent of the initial value due to diffusion before the heat release starts, and at the point of maximum heat release the fuel has already been fully converted to intermediates. Diffusion also widens the area where intermediates like CO are found and transports products toward zones of low temperature. Increasing the pressure to gas turbine conditions leads to significant changes. As the thermal conductivity λ is independent of pressure, the thermal diffusivity $a = \lambda/(c_p\rho)$ is inversely proportional to the pressure p. Due to the higher thermal capacity of the reactants with increasing pressure, the transport of temperature is slowed down and the reaction rate is increased. Both effects generate steeper gradients in the flame front and the flame becomes thinner and slower. The heat release is

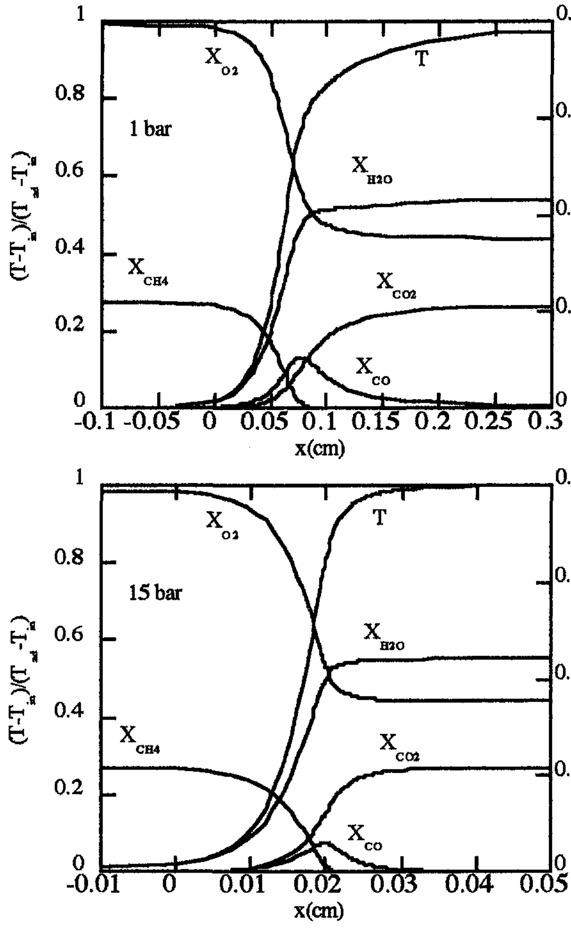

Fig. 2 Pressure effects on laminar flame fronts

shifted toward higher temperatures and peaks at 85 percent temperature rise (15 bar).

In order to demonstrate the dependence of important species, key radicals, the NO concentration, and the NO production rate from temperature, a reaction progress variable $(T_{ad} - T)/(T_{ad} - T_{in})$ is introduced (Fig. 3), which describes the temperature deficit with respect to the final state T_{ad} (1 = reactant temperature T_{in}, 0 = adiabatic flame temperature T_{ad}). As long as the prompt NO formation is of minor importance, an assessment of the NO formation can be made solely on the basis of the O, H, and OH radical concentrations with respect to temperature (and a characteristic reaction time). Since it can be shown for all cases under consideration that OH as well as H concentrations are closely linked to the O radical, only the latter will be presented in the graphs as a measure for the generation of NO in the flame. With increasing pressure, the recombination of radicals is enhanced and the O radical concentration drops. The pressure sensitivity of the NO formation paths as well as the altered diffusion lead to higher NO concentrations at low temperatures. The comparison of the NO mole fraction and the NO production rate reveals that the NO concentrations seen at low temperatures are due to diffusion from downstream (Fig. 3). At high pressure, the NO production rate is negative below 40 percent reaction progress due to the shift of NO to NO_2. This high-pressure effect is responsible for the undesired formation of yellow smoke from gas turbine combustors at low load. Fortunately, the NO_2 is fully converted back to NO in the high-temperature regime of adiabatic premixed flames.

At first, the missing pressure influence on the NO concentration appears surprising for the adiabatic flame temperature under consideration (1840 K), which is beyond the threshold of the pressure-sensitive thermal NO formation. At higher T_{ad}, the NO concentration at 99.9 percent reaction progress even drops when the pressure is increased. As Fig. 4 shows, the reaction becomes much shorter at high pressure. A comparison of the two cases for the same residence time would reveal a considerably higher NO level for the high-pressure case. If the burnout time at 1 bar is selected for the comparison (e.g., 99.9 percent reaction progress), this corresponds to holding the high-pressure case for a long time after burnout at T_{ad}. Even at the equilibrium concentration of the O radical, the pressure-dependent thermal NO formation route produces significant additional postflame NO.

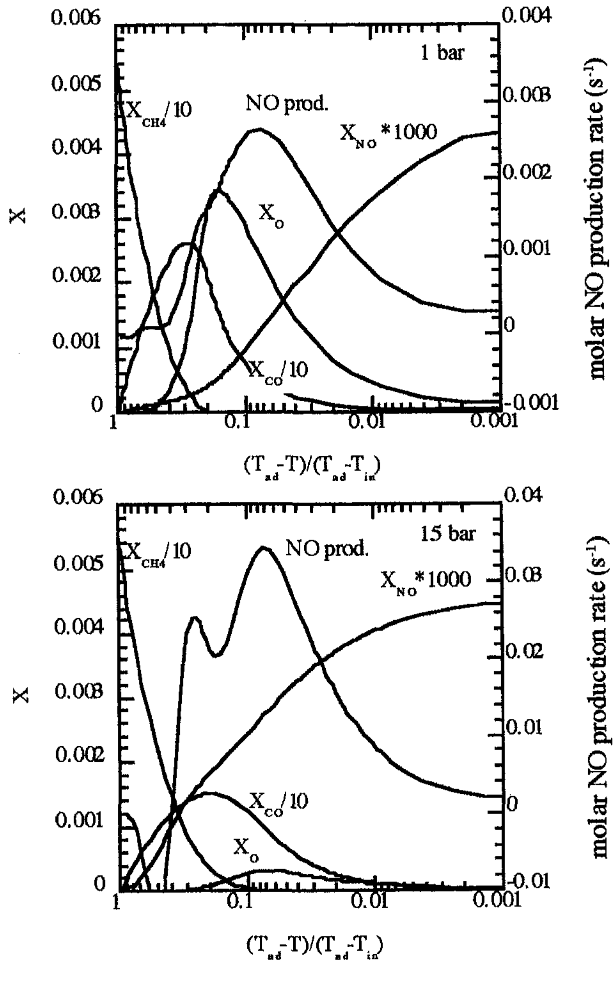

Fig. 3 NO formation in laminar flame fronts

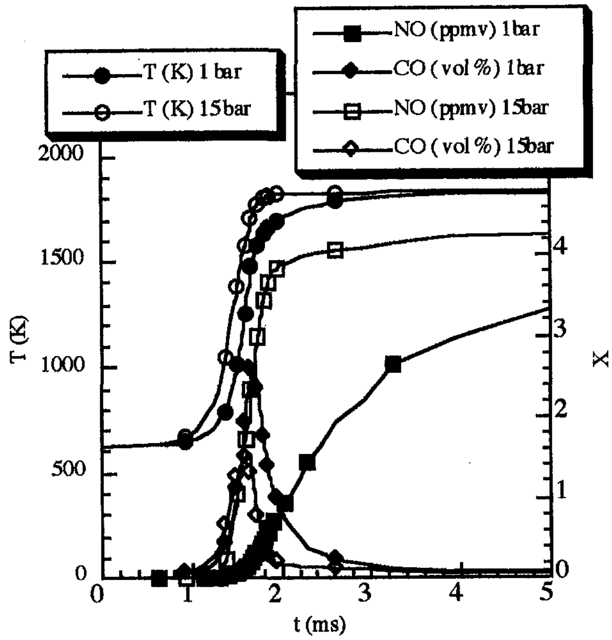

Fig. 4 Pressure influence on reaction progress of laminar flame fronts

Diffusion influences the relationship between key radicals and temperature, e.g., the diffusive radical transport into hotter zones enhances the NO formation. The effects can be quantified, if combustion is accomplished in the diffusion-free environment of a plug flow reactor PFR. At 1 bar, the PSR at incipient extinction provides 70 percent of reaction progress and heat release (Fig. 5). It is easy to understand that radical concentrations at the PSR exit are higher when compared to the laminar flame, since a higher share of the chemically bound energy has been released already. Although only 30 percent of the heat is released in the PFR, the radical concentrations quickly progress toward the values found in the laminar flame front. The lower slope of the NO curve is due to the quicker reaction progress, which reaches approximately twice the speed of the laminar case. This acceleration is caused by the fact that the temperature rise in the PFR is not damped by the diffusive heat loss toward the preheat zones. The lower NO concentrations of the PSR–PFR combination with respect to the laminar case were found similarly for both pressures and the whole range of flame temperatures investigated ($T_{ad} < 2000$ K). In summary, it can be concluded that the somewhat unphysical absence of the diffusive transport did not change the NO emissions more than a change in adiabatic flame temperature of 20–60 K.

The transition from the laminar flame to a flame with "turbulent" gradient diffusion leads to a relative reduction of the diffusion of the lighter species with respect to those with a higher molecular weight. As shown in Fig. 6 for a Lewis number of unity, the peak concentration of the NO-generating O radical is higher than in the laminar case. The same applies to the H

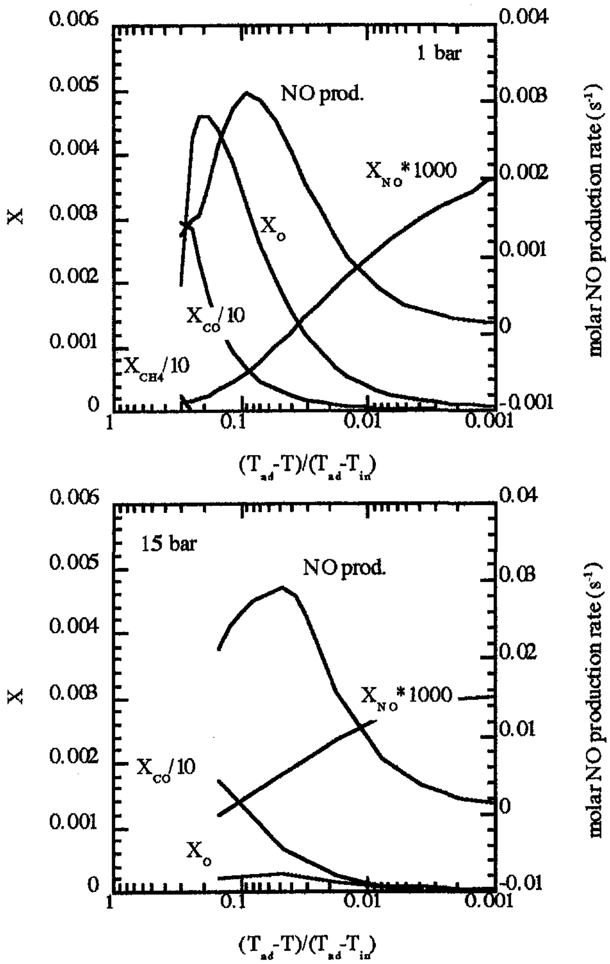

Fig. 5 NO formation of a PSR-PFR combination

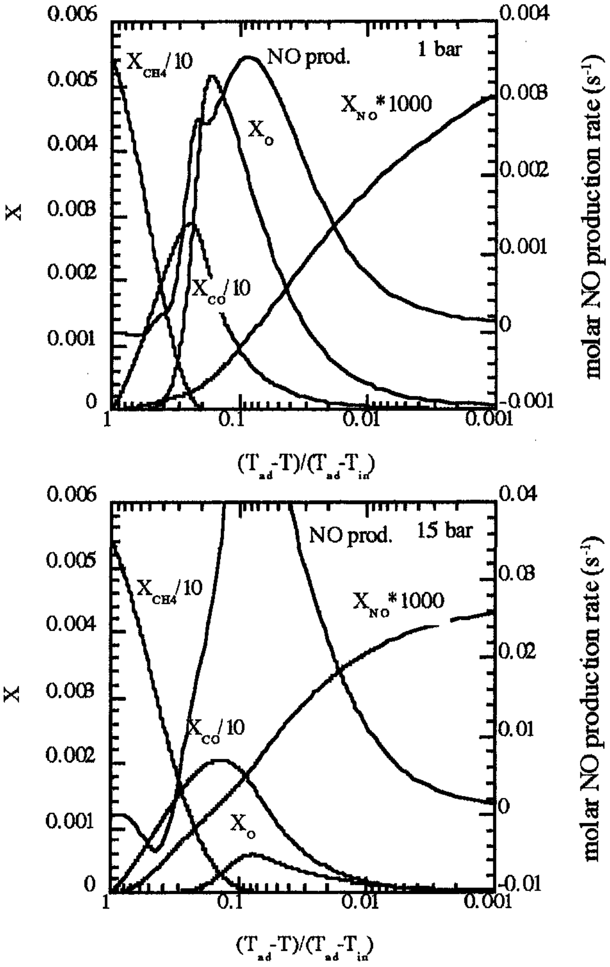

Fig. 6 NO formation of a one-dimensional flame with "turbulent" diffusion

radical (not shown here). In spite of the higher radical concentration, the final NO level is not considerably altered. This has to be attributed to the drop in reaction time, which goes along with the transition to the turbulent diffusion concept. It can be concluded that the preferential diffusion of the species in a laminar flame does not remarkably influence the NO generation.

A useful feature of the concept of turbulent diffusion is that the strength of species diffusion with respect to the diffusion of temperature can easily be altered. The case of high Lewis numbers (low species diffusion) is of particular interest, since the extent to which the propagation and reaction density of a premixed flame front depend on the diffusion of species can be studied. When the diffusion of fuel as well as of radicals is impeded, no significant radical attack from the reaction zone toward the preheat zone will take place. This results in a strong preheating of the reactants before the reaction is initiated. For Le = 5 and 1 bar, the heat release peaks at 1666 K (200 K higher than in the laminar case). The higher effective preheat temperature at the starting point of the reaction goes along with a stronger heat loss from the reaction zone. Due to the importance of the Zel'dovich mechanism at 1 bar, the NO emission is increased by approximately 30 percent. A similar effect is not found at 15 bar, since the N_2O mechanism, which dominates at high pressures, does not respond to the shift of the reaction toward higher temperatures in the same way. Increasing the species diffusion (Le = 0.07) will enhance the transport of fuel into the reaction zone strongly and all radical concentrations are much lower than in the other cases, whereas no significant effect on the NO levels was found. Figure 7 shows the heat release pattern of four cases, namely the laminar flame and the flame with turbulent diffusion and three different Lewis numbers (Le = 0.07, 1, 5). The global increase of species diffusion lowers the reaction progress considerably. Decreasing species diffusion results in a very quick heat release and a steep temperature rise. Effects of preferential diffusion of light species, which are an essential characteristics of laminar flames, lead to a less intense heat release than the Le = 1 case. The calculations reveal that the NO emission of one-dimensional flames exhibits

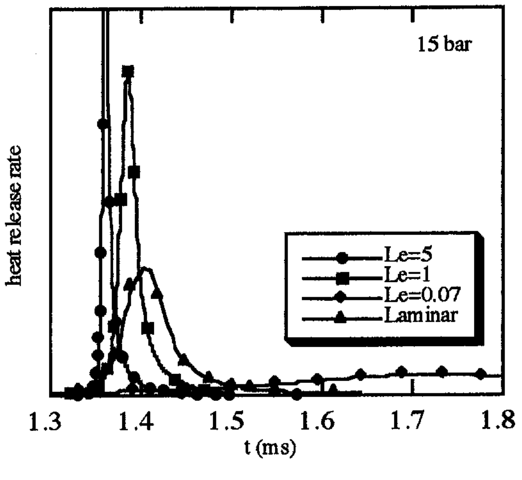

Fig. 7 Lewis number effects on one-dimensional flame fronts

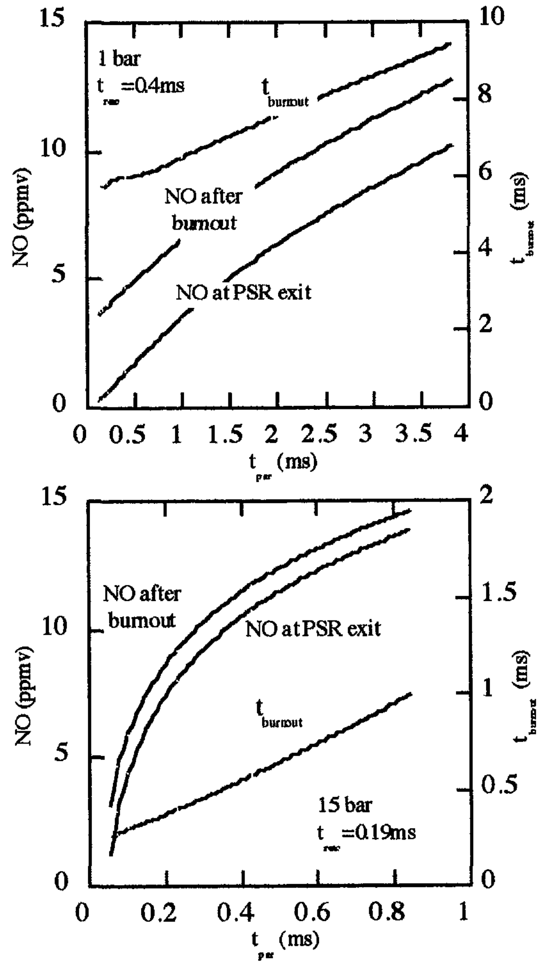

Fig. 8 Effect of stirring on the NO emission

a remarkably low sensitivity to even crude and unphysical manipulations of the diffusive transport.

As already mentioned, the goal of modeling the influence of turbulent eddies on the flame front realistically by a gradient formulation cannot be achieved, since the effect of stirring is not adequately represented. In order to obtain an estimate for the strength of the effect of stirring on NO, Fig. 8 presents the NO emissions (99.9 percent reaction progress) of the PSR–PFR combination and a wide range of residence times (PSR reactor volume). The comparison with the characteristic chemical time scale t_{reac}, which has been derived from the temperature profiles of the laminar flame, is of particular interest, since it allows one to assess in principle how strongly stirring can effect the NO formation. At 1 bar, changing the residence time in the PSR (below t_{reac}) will not substantially influence the NO emission, whereas the NO slope is steep at 15 bar. At 1 bar, as a consequence, in order for a major impact of stirring on NO formation to occur, a strongly overproportional thickening of the flame front with respect to the propagation velocity would be required, which cannot be seen in gas turbine burner investigations [18]. At high pressures, however, a significant impact of stirring on NO can be expected. Although it is difficult to draw quantitative conclusions from Fig. 8, the statement might be accepted for 15 bar, that the potential increase in the NO emission due to stirring is on the order of the NO emission of the unstirred flame.

An influence of strain on the NO emission of strained flames can be expected when the strain rate is of the order of the inverse of the reaction time. Computations were performed at 1 bar pressure and strain rates between $1000\ 1/s < a < 10{,}000\ 1/s$ as well as at 15 bar pressure and strain rates between 2000 and 20,000 1/s. In Fig. 9 the NO concentrations are plotted over the reaction progress variable $(T_{ad} - T)/(T_{ad} - T_{in})$. A direct comparison of the NO generation in the strained case with the unstrained case cannot be immediately made, since a fixed value has to be set at the product inlet of the computational domain [17], which then influences the NO value at the right boundary $(T_{ad} - T)/(T_{ad} - T_{in}) = 0.001$ of Fig. 9. In the computations shown in Fig. 9 the NO concentrations of the corresponding unstrained flames (99.9 percent reaction progress) were specified for the NO concentration in the product stream.

The remarkable influence of the strain rate can only be seen at low pressures. When compared to the unstrained flames, higher NO concentrations are generally found at low temperatures. By virtue of the data reduction technique described in Appendix B, the mole fraction X_{products} of the species, which originate from the product side, are calculated. For the highest strain rates a proportionality between X_{products} and the reaction progress is approached (Fig. 10). Consequently, it can be concluded that at high strain rates, mixing of cold reactants and hot products have a strong impact on temperature changes due to chemical reaction. Since it is not observed that the volumetric heat release rate is influenced by strain (not shown here), the effect is caused by the increase of the convective/diffusive

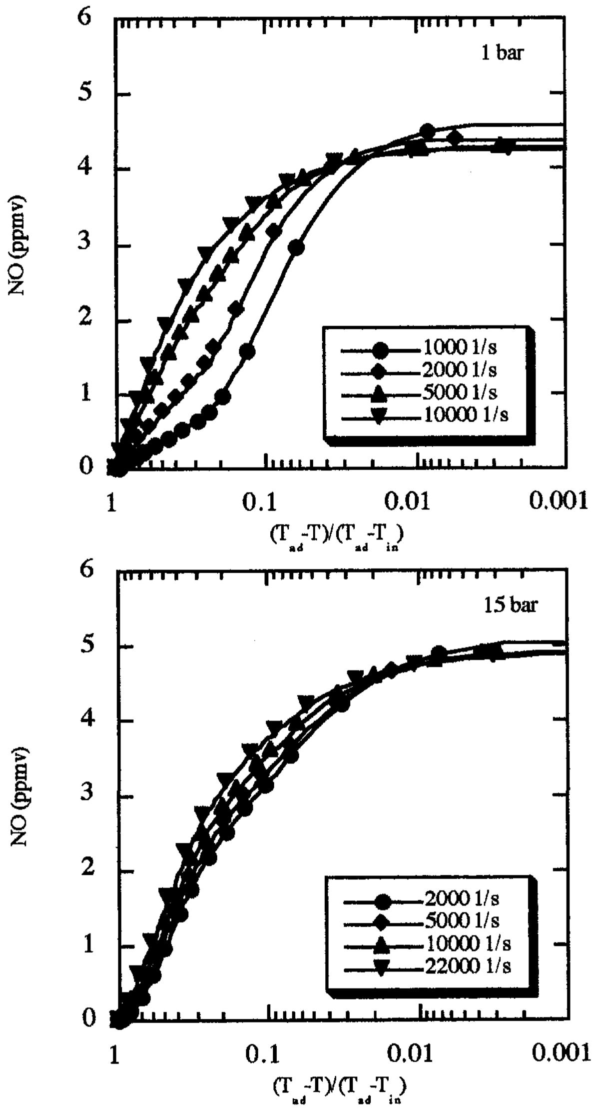

Fig. 9 NO concentration in strained flames

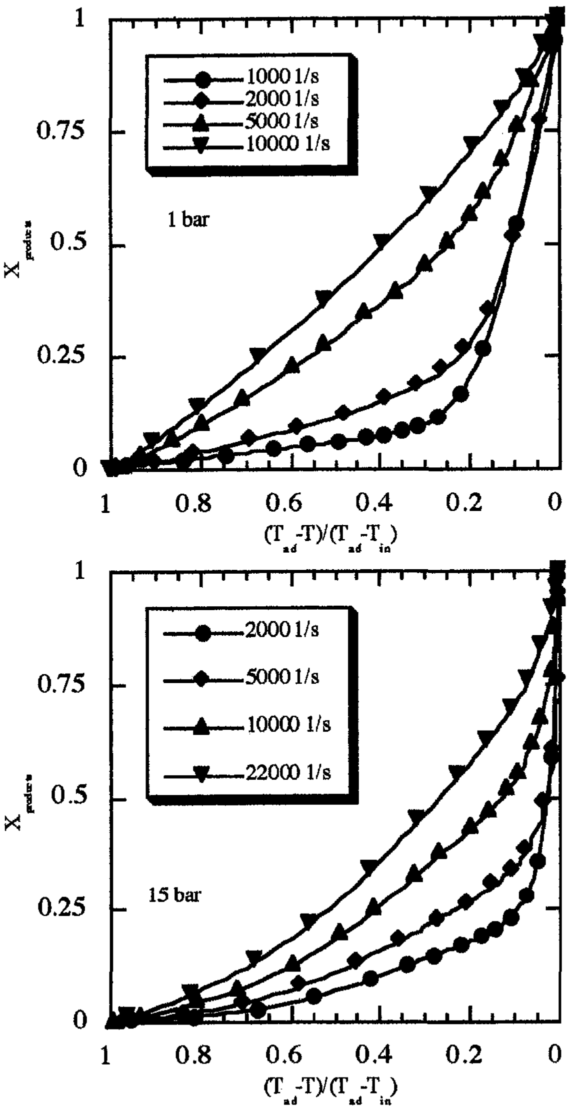

Fig. 10 Mixing of products with reactants in strained flames

fluxes at high strain rates. Interestingly, a sudden extinguishing of the flame (quench) is not observed, because the product side represents an infinite source of heat. Due to the decrease of the diffusivities a and D with pressure, the regime, where considerable "product" concentrations X_{products} are found at low strain rates, is restricted at 15 bar to $(T_{ad} - T)/(T_{ad} - T_{in}) < 0.1$ (>90 percent reaction progress), whereas the influence is extended down to approximately 70 percent reaction progress at atmospheric pressure. After the separation of the NO, which originates from the product inlet, from the flame-generated NO (Appendix B), Fig. 11 is obtained. High flame stretch has an NO-reducing effect. The same results yields Fig. 12, where the NO-production rate is shown for comparison.

The distribution of strain rates in turbulent flows can be obtained on the basis of isotropic turbulence [3]. It can be shown that very high strain rates occur relatively seldom and that the global NO emission of a flame front is dominated by regimes exposed to low to medium strain. Consequently, it cannot be expected that the calculated effect of locally high strain on NO generation will remarkably reduce the NO emissions from gas turbine burners.

The flame zones with high local strain that generate unburned mixtures of reactants and products will undergo an afterburning process after the strain strength has been released. In Fig. 13 the results for the mixture temperature of 1273 K, which corresponds to a ratio of approximately unity of reactant mixture to product mixture, are presented. Surprisingly, the radical concentrations recover the level seen in the case of the combustion of pure reactants (Fig. 3) very quickly, despite the fact that the fuel concentration is lowered by 50 percent. NO emissions at 1 bar are also almost identical due to the Zel'dovich mechanism, which is characterized by the NO generation in the high-temperature regime of the reactive layer. Per quantity fuel, almost twice as much NO has been generated. In contrast, at high pressure a start of the afterburning at higher temperature reaction is beneficial due to the characteristics of the predominant N_2O path. With the assumption that the products, which are mixed with the reactants upstream of the flame, contain NO according to an unstrained flame ($=NO_{\text{unstrained}}$) at $(T_{ad} - T)/(T_{ad} - T_{in}) = 0.001$ (99.9 percent reaction progress), the results of a set of calculations with different ratios of reactants and products are summarized in Fig. 14. At 1 bar afterburning stimulates total NO formation clearly, whereas at 15 bar no net effect can be detected. In addition, Fig. 14 shows that the same result is found on the basis of a PSR-PFR/PFR model. It can be concluded that high local flame strain, which leads to lower NO,

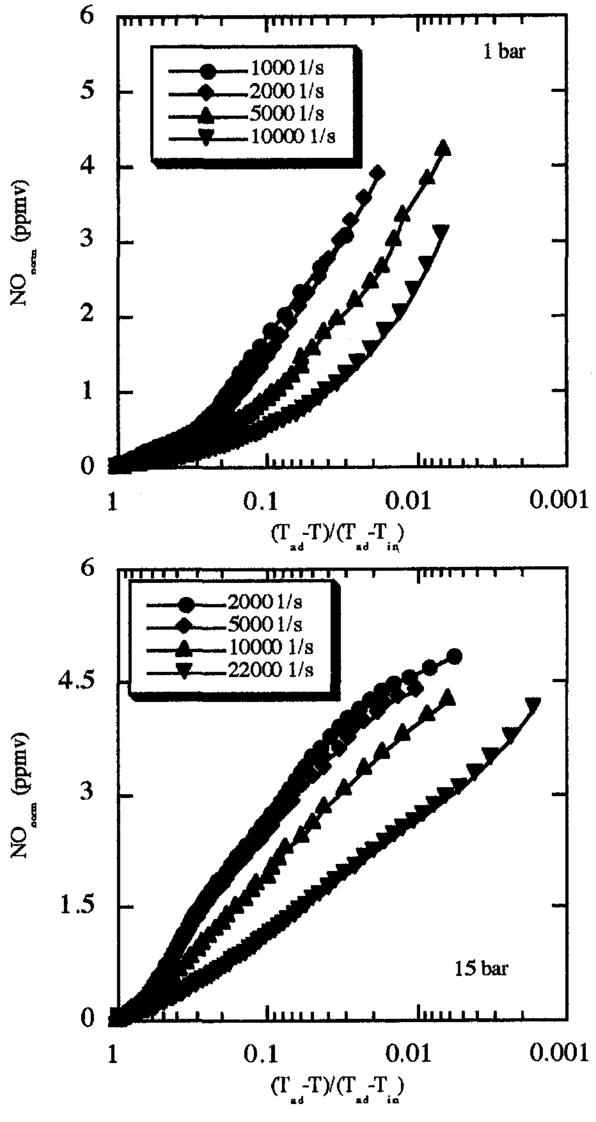

Fig. 11 Flame-generated NO in strained flames

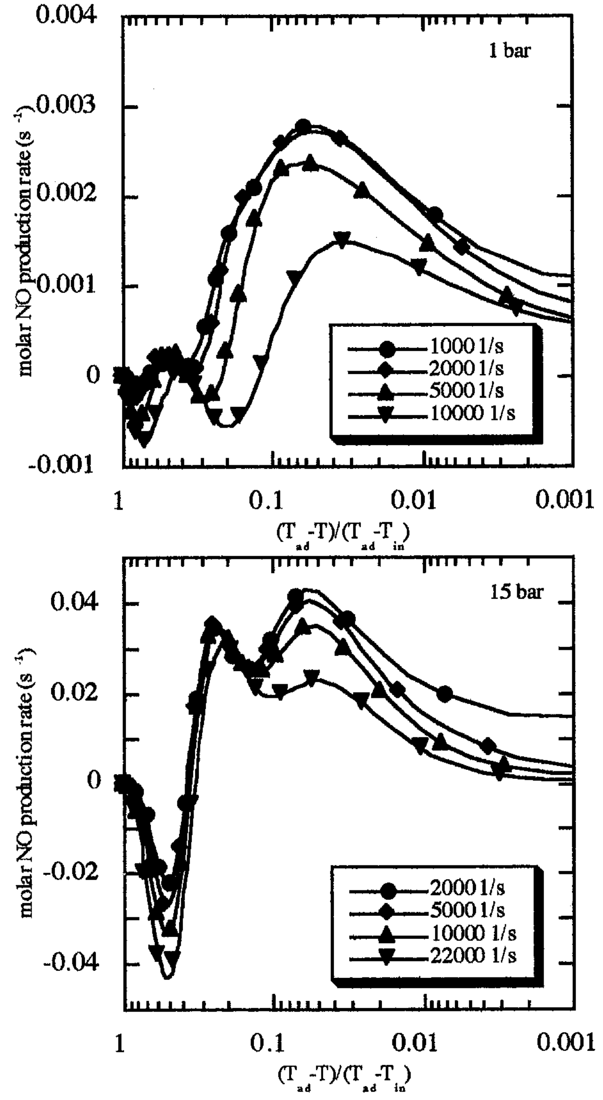

Fig. 12 NO production rate in strained flames

is accompanied by an afterburning process of diluted reactants, which has an adverse effect on NO as long as the pressure is low.

Staging Effects

If the reactants of a second stage are fed into the exhaust of a first stage, which has previously approached the adiabatic flame temperature, no significant difference to the aforementioned effects in the unstaged flame is to be expected. The reactive layer between the media of both stages exhibits a structure according to the corresponding turbulent combustion regime. Of greater interest is the following scenario: In a first very lean (or catalytic) stage nearly NO-free exhaust gas is generated, which is diluted with air until the desired temperature is achieved. This temperature is selected low enough to permit enough mixing time for fuel injection in a second stage (or a richer fuel–air mixture) before the second ignition takes place. The final temperature (of 1840 K) is reached after the completion of the burnout of the secondary fuel. Figure 15 depicts the NO emissions of such a lean-mix-lean process. The mixing Damköhler number Da_{mix} has been derived from engine experience. Only in the region below unity can perfect fuel admixing be reached (mixing element size realistic for gas turbine application) before the reaction is initiated in the second stage. It is evident that at 1 bar even for NO free exhaust from a first stage no considerable benefit exists, whereas at 15 bar a reduction of NO by 50 percent seems to be the limit.

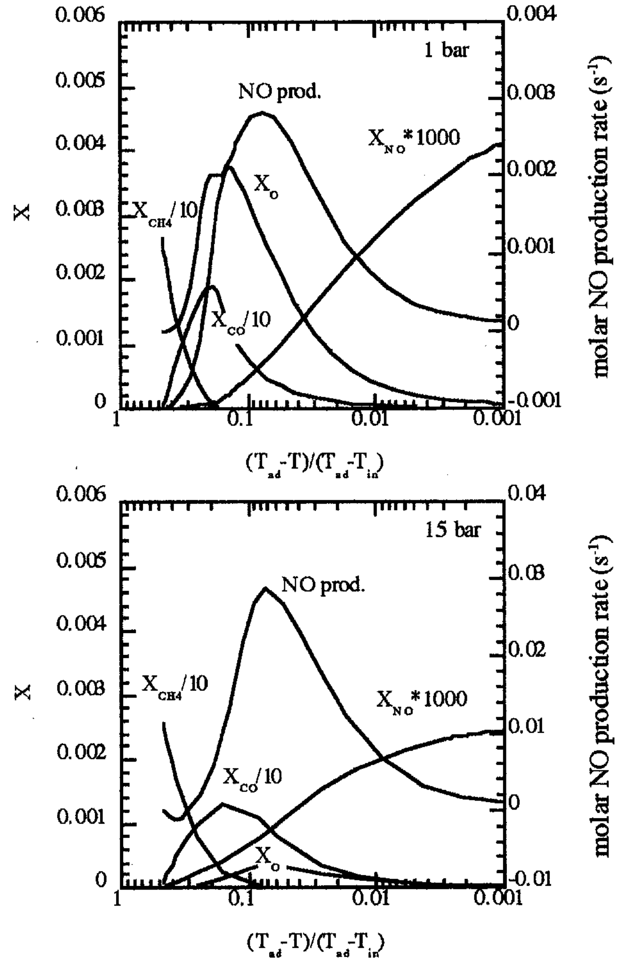

Fig. 13 NO from the unstrained combustion of a NO free mixture of products and reactants

However, the assumption that no NO in the first stage is generated is unrealistic: For perfectly premixed, aerodynami-

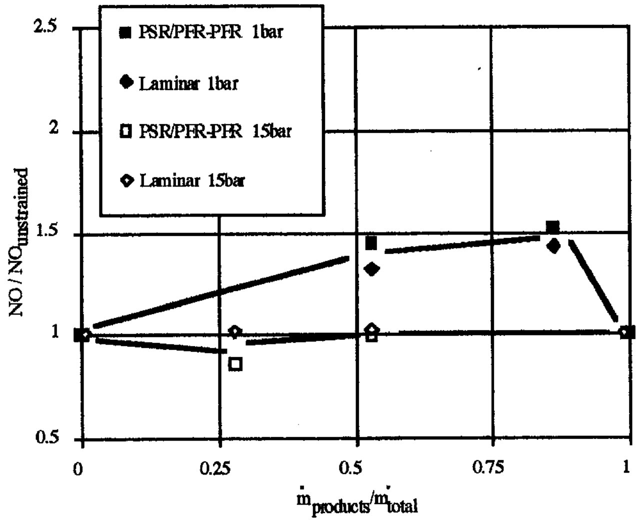

Fig. 14 Influence of afterburning on NO

cally stabilized flames, lean blowout temperatures below approximately 1700 K are difficult to achieve with sufficient blowout margin. Since this limits the NO concentration from the first stage to approximately 2 ppm (one-dimensional laminar flame results for 1700 K), the net effect of staging will be considerably smaller. It is questionable whether any advantage remains, when the larger liner surface of a staged system, which has to be cooled and reduces the air available for combustion, is taken into consideration. In contrast, the characteristics of lean-mix-lean systems match very well the requirements of modern gas turbine reheat cycles, which provide ideal inlet temperatures in the second stage due to the partial expansion in a high-pressure turbine after primary combustion. In these cases a reduction of NO is achieved primarily due to the higher thermodynamic efficiency. The ABB gas turbine family GT24/26 comprises the first implementation of this ultralow NO_x reheat principle.

Conclusions

The study of model flames with full chemistry reveals that the one-dimensional flame represents a good model for gas turbine burners at moderate turbulence levels. The NO abatement potential of a moderately turbulent combustor is shown in Fig. 16 (Miller and Bowman mechanism). The importance of residence time for high adiabatic flame temperatures is apparent. Residence times below 10 ms are difficult to achieve with current designs, since the mixing time exceeds by far the chemical time. Burners with a high number of small-scale elements offer a promising way to minimize residence time in the future.

Excessive stirring within the reactive layer of the flame enhances NO production and should be avoided in the design of high-pressure gas turbine burners.

Flame strain locally lowers NO formation. However, a strong influence on the emissions from burners cannot be expected because of the strain distributions found in turbulent flow fields.

Afterburning of previously "quenched" flame zones leads only at low pressures to higher NO formation.

The NO generation of premixed flames is remarkably insensitive to changes in the diffusive transport of temperature and species or the absence of diffusive transport.

Staged combustion will only have an influence on NO emissions when mixing between the stages occurs before the second reaction is initiated. The NO reduction potential is moderate and might be lost due to the bigger volume and higher complexity of a staged combustor.

Staged (sequential) lean–lean combustion is attractive for reheat cycles, since higher thermodynamic efficiencies can be achieved.

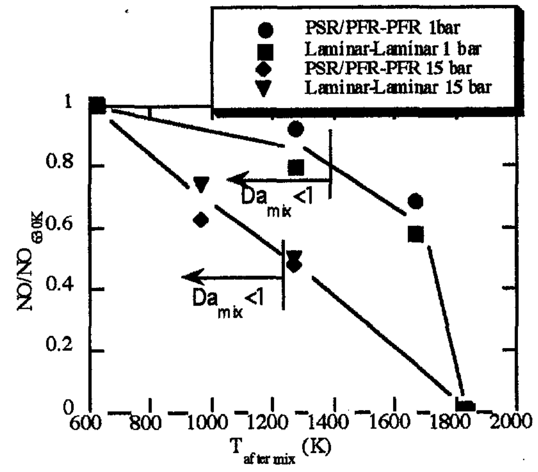

Fig. 15 NO emissions from a lean-mix-lean process

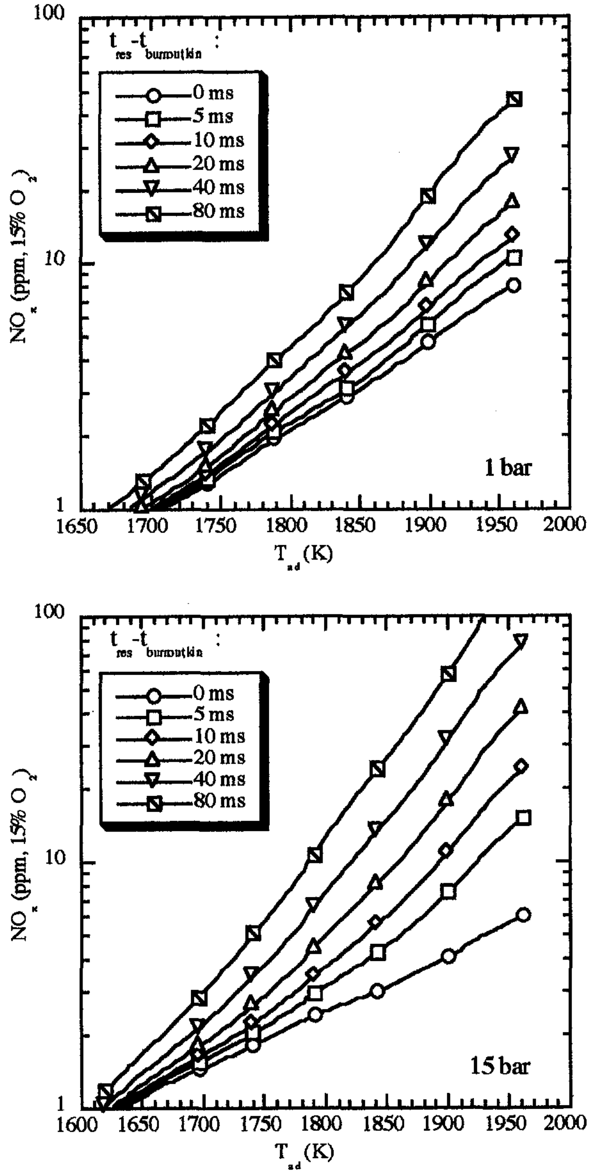

Fig. 16 NO abatement potential of kinetically controlled gas turbine combustors

References

1 Nicol, D. G., Steele, R. C., Marinov, N. M., and Malte, P. C., "The Importance of the Nitrous Oxide Pathway to NO_x in Lean-Premixed Combustion," ASME JOURNAL OF ENGINEERING FOR GAS TURBINES AND POWER, Vol. 117, 1995, pp. 100–111.

2 Miller, J. A., and Bowman, C. T., "Mechanisms and Modeling of Nitrogen Chemistry in Combustion," *Prog. Energy Combustion Sci.*, Vol. 15, 1989, pp. 287–338.

3 Tennekes, H., and Lumley, J. L., *A First Course in Turbulence*, MIT Press, 1985.

4 Koochesfaharni, M. M., and Dimotakis, P. E., "Mixing and Chemical Reactions in a Turbulent Mixing Layer," *LFM*, Vol. 170, 1986, pp. 83–112.

5 Borghi, R., "Turbulent Combustion Modeling," *Prog. Energy Combustion Sci.*, Vol. 14, 1988, pp. 245–292.

6 Zimont, V. L., "Theory of Turbulent Combustion of a Homogeneous Fuel Mixture at High Reynolds Numbers," *Combust. Expl. and Shock Waves*, 1979, pp. 305–311.

7 Meneveau, C., Poinsot, T., "Stretching and Quenching of Flamelets in Premixed Turbulent Combustion," *Combustion and Flame*, Vol. 86, 1991, pp. 311–332.

8 Poinsot, T., Veynante, D., and Candel, S., "Diagrams of Premixed Turbulent Combustion Based on Direct Simulation," *23rd Symp. (Int.) on Combustion*, 1993, pp. 613–619.

9 Roberts, W. L., Driscoll, J. F., Drake, M. C., and Goss, L. P., "Images of the Quenching of a Flame by a Vortex to Quantify Regimes of Turbulent Combustion," *Combustion and Flame*, Vol. 94, 1993, pp. 58–69.

10 Abdel Gayed, R. G., and Bradley, D., "Criteria for Turbulent Propagation Limits of Premixed Flames," *Combustion and Flame,* Vol. 62, 1985, pp. 61–68.

11 Abdel Gayed, R. G., and Bradley, D., "Combustion Regimes and the Straining of Turbulent Premixed Flames," *Combustion and Flame,* Vol. 76, 1989, pp. 213–218.

12 Kee, R. J., Grcar, J. F., Smooke, M. D., and Miller, J. A., "A Fortran Program for Modeling Steady Laminar One-Dimensional Premixed Flames (Chemkin Manual)," Sandia Report SAND85-8240, 1985.

13 Correa, S. M., "Turbulence-Chemistry Interactions in the Intermediate Regime of Premixed Combustion," *Combustion and Flame,* Vol. 93, 1993, pp. 41–60.

14 Curl, R. L., "Dispersed Phase Mixing: Theory and Effects in Simple Reactors," *AIChE J.,* Vol. 9, pp. 175–181.

15 Tonouchi, J. H., Pratt, D. T., "A Finite-Rate Macromixing, Finite-Rate Micromixing Model for Premixed Combustion," The Combustion Institute Fall Meeting, 1995, Stanford University, Paper 95F-167.

16 Rogg, B., "Response and Flamelet Structure of Stretched Premixed Methane–Air Flames," *Combustion and Flame,* Vol. 73, 1988, pp. 45–65.

17 Rogg, B., "RUN-1DL; The Cambridge Universal Laminar Flamelet Computer Code," *Reduced Kinetic Mechanisms for Applications in Combustion Systems,* Springer, 1993.

18 Kampmann, S., Leipertz, A., Döbbeling, K., Haumann, J., and Sattelmayer, T., "Two Dimensional Temperature Measurements in a Technical Combustor With Laser Rayleigh Scattering," *Applied Optics,* Vol. 32, No. 30, Oct. 1993, pp. 6167–6172.

APPENDIX A

Relationships of Isotropic Turbulence and Definitions

Inertial range (Kolmogorov):

$$\epsilon \propto \frac{u^3_{\text{vortex}}}{l_{\text{vortex}}} \propto \frac{l^2_{\text{vortex}}}{t^3_{\text{vortex}}} \propto \text{const}$$

Vortex characteristic velocity:

$$u_{\text{vortex}} \propto l^{1/3}_{\text{vortex}}$$

Vortex turnover time:

$$\tau_{\text{vortex}} \propto l^{2/3}_{\text{vortex}}$$

Strain rate:

$$\tau_{\text{vortex}} = \tau_s$$

$$a = \frac{1}{\tau_s} = \frac{dA_{\text{flame}}/dt}{A_{\text{flame}}} = \frac{u_{\text{vortex}}}{l_{\text{vortex}}} \propto 1/l^{2/3}_{\text{vortex}}$$

Macroscale:

$$L_t \propto \frac{u'^3}{\epsilon} \qquad \tau_{L_t} \propto \frac{u'^2}{\epsilon} \approx \frac{k}{\epsilon}$$

Taylor scale:

$$\lambda \propto L_t/\text{Re}_t^{1/2} \propto \nu \cdot \frac{u'^2}{\epsilon} \propto \nu \cdot \frac{k}{\epsilon}$$

Microscale:

$$\eta \approx \left(\frac{\nu^3}{\epsilon}\right)^{1/4} \approx L_t/\text{Re}_t^{3/4} \qquad \tau_\eta \approx \left(\frac{\nu}{\epsilon}\right)^{1/2} \approx \tau_{L_t}/\text{Re}_t^{1/2}$$

$$u_\eta \approx (\nu \cdot \epsilon)^{1/4} \approx u'/\text{Re}_t^{1/4}$$

Turbulent Reynolds number:

$$\text{Re}_t = \frac{u' \cdot L_t}{\nu}$$

Turbulent Damköhler number:

$$\text{Da} = \frac{\tau_{L_t}}{\tau_c} \approx \frac{L_t/u'}{\delta_l/s_l}$$

Karlovitz number:

$$\text{Ka} = \frac{\tau_c}{\tau_\eta} \approx \frac{\delta_l/s_l}{\eta/u_\eta} \propto \frac{\tau_c}{\tau_\lambda} \approx \frac{\delta_l/s_l}{\lambda/u'}$$

$$\text{Ka} = \frac{\tau_c}{\tau_s} = \frac{\delta_l/s_l}{A_{\text{flame}}/(dA_{\text{flame}}/dt)}$$

APPENDIX B

Evaluation of NO From Strained Flames

In order to separate the NO generated in a strained counterflow flame of reactants and products from that originating from the product inflow, two computations are made for the flame under consideration. In the first run products with a reasonable NO content (e.g., that of an unstrained flame) are specified, whereas in the second run the products are free of NO. As a result two curves

$$\text{NO}_{\text{tot}} = f\left(\frac{T_{ad} - T}{T_{ad} - T_{in}}\right)$$

and

$$\text{NO}_{\text{reactants}} = f\left(\frac{T_{ad} - T}{\text{T}_{ad} - T_{in}}\right)$$

are obtained. The difference between the two curves is due to the transport from the product inlet:

$$\text{NO}_{\text{products}} = \text{NO}_{\text{tot}} - \text{NO}_{\text{reactants}}$$

$\text{NO}_{\text{products}}$ can serve as a "tracer" for the diffusion of products toward the reactants, since the diffusivity of NO is similar to the diffusivity of the products. As a consequence, the concentration of products from the product inlet diffusing toward the reactants can be found:

$$X_{\text{products}} = K_{\text{NO}} \cdot \frac{\text{NO}_{\text{products}}}{\text{NO}_{\text{productsinlet}}}$$

K_{NO} represents the thermal NO formation of the products on their way from the inlet toward the reactants. If thermal NO formation is neglected, K_{NO} is set to unity.

Since the products from the combustion of the reactants are diluted with products from the product inlet, the NO concentration is finally normalized:

$$X_{\text{reactants}} = 1 - X_{\text{products}}$$

$$\text{NO}_{\text{reactants,corrected}} = \text{NO}_{\text{reactants}}/X_{\text{reactants}}$$

Numerical Studies on Trapped-Vortex Concepts for Stable Combustion

V. R. Katta
Innovative Scientific Solutions, Inc.,
Dayton, OH 45430

W. M. Roquemore
Wright Laboratory,
Wright-Patterson Air Force Base, OH 45433

Spatially locked vortices in the cavities of a combustor aid in stabilizing the flames. On the other hand, these stationary vortices also restrict the entrainment of the main air into the cavity. For obtaining good performance characteristics in a trapped-vortex combustor, a sufficient amount of fuel and air must be injected directly into the cavity. This paper describes a numerical investigation performed to understand better the entrainment and residence-time characteristics of cavity flows for different cavity and spindle sizes. A third-order-accurate time-dependent Computational Fluid Dynamics with Chemistry (CFDC) code was used for simulating the dynamic flows associated with forebody-spindle-disk geometry. It was found from the nonreacting flow simulations that the drag coefficient decreases with cavity length and that an optimum size exists for achieving a minimum value. These observations support the earlier experimental findings of Little and Whipkey (1979). At the optimum disk location, the vortices inside the cavity and behind the disk are spatially locked. It was also found that for cavity sizes slightly larger than the optimum, even though the vortices are spatially locked, the drag coefficient increases significantly. Entrainment of the main flow was observed to be greater into the smaller-than-optimum cavities. The reacting-flow calculations indicate that the dynamic vortices developed inside the cavity with the injection of fuel and air do not shed, even though the cavity size was determined based on cold-flow conditions.

Introduction

A revolutionary advancement in the development of a simple, compact, and efficient method of combustion was recently proposed by Hsu et al. (1995). This new combustor concept employs a vortex that is trapped in a cavity to stabilize the flame, and hence, is referred as the Trapped-Vortex (TV) concept. Even though the idea of trapping a vortex for flame stabilization purposes is a novel one, interest in the utilization of vortex motion to aerodynamic advantage has intrigued aerodynamicists for many years. The experiments of Rohsenow et al. (1951) have shown that when two circular orifices are placed in series in a pipe, in certain circumstances, a large recovery of pressure may occur across the second orifice; hence, the overall pressure drop is considerably less for the two orifices than for a single one having the same flow. In ribbed diffusers, Migay (1963) found that balancing the fluid removed by entrainment and the fluid entering the cavity by reversed flow ensures that the flow outside the cavities will follow the ribs fairly closely and a good pressure recovery will be obtained. By mounting a disk behind the base of a blunt body, Mair (1965) has shown that the afterbody drag of the blunt object will be reduced. Using similar concepts, Roshko and Koenig (1976) have reported a reduction in drag of blunt forebodies when disks are placed on spindles ahead of the body.

In order to understand the aerodynamics associated with minimum-drag conditions, Little and Whipkey (1979) conducted extensive investigations on the dynamic nature of flows over bluff bodies using smoke-flow-visualization and laser-velocimetry techniques. Because of the limitations of the smoke tunnel, they used reduced flow conditions (~0.3 m/s) and half-scaled geometries for the flow-visualization studies and full-scale geometries and turbulent flows (~30 m/s) for the time-averaged drag measurements. Based on these reduced and full-scale experiments, they correlated the afterbody drag and the motion of the vortex in the wake region and postulated that a minimum-drag condition was established when the wake vortices are locked between two disks mounted in series on a spindle. They also suggested that the cavity formed between the disk and the bluff body should be of such dimensions that the locked vortex effectively fills the cavity. Since these dynamic flow results were obtained for velocities lower by nearly two orders of magnitude than those used in the full-size wind-tunnel experiments, these conclusions are open to question. And also, in practical combustors, partial burning takes place in the recirculation zones and in the cavity vortices, which could alter the vortex dynamics. As a result, it might be expected that the criterion for trapping a vortex in a combustor would be different from that observed in cold flows.

Performing experimental studies on vortex dynamics inside the cavities in a combusting environment is extremely difficult mainly because of (1) limited access to the bright, hot cavity flow and (2) problems arising from the use of moving parts. On the other hand, recent progress in Direct-Numerical-Simulation techniques (Grinstein and Kailasanath, 1995; Veynante et al., 1994) has led to a growing interest in investigating dynamic flows computationally.

In the present investigation the trapped-vortex concepts were studied numerically using a third-order-accurate time-dependent Computational Fluid Dynamics with Chemistry (CFDC) code. Results obtained for cold flows with different cavity sizes were analyzed to gain an understanding of the dynamic nature, entrainment, and residence-time characteristics of the cavity flow. Calculations were also performed for the reacting flow in the center-body trapped-vortex combustor using a fast-chemistry assumption.

Modeling

A time-dependent, axisymmetric mathematical model that solves for axial- and radial-momentum equations, continuity,

---

Contributed by the International Gas Turbine Institute and presented at Turbo Asia '96, Jakarta, Indonesia, November 5–7, 1996. Manuscript received at ASME Headquarters July 1996. Paper No. 96-TA-19. Associate Technical Editor: J. W. Shinn.

and enthalpy- and species-conservation equations is used to simulate the flowfields in the trapped-vortex combustor. Density is obtained by solving the state equation, while the pressure field at every time step is determined from pressure Poisson equations. For the cases in which turbulent-flow characteristics were modeled, the time-dependent equations for turbulent energy (k) and turbulent-energy dissipation (ϵ) are also solved, along with the other governing equations. The standard isotropic $k-\epsilon$ turbulence model is incorporated in those cases. Even though all the governing equations are solved in an uncoupled manner, the turbulence and species-conservation equations are coupled through the source terms during the solution process to improve the stability of the algorithm.

In the present analysis of reacting flows, the simple global-chemical-kinetics model involving propane, oxygen, water, carbon dioxide, and nitrogen used is expressed as follows:

$$C_3H_8 + 5\ O_2 + N_2 \Rightarrow 3\ CO_2 + 4\ H_2O + N_2.$$

The specific reaction rate for this equation is written in Arrhenius form, with an activation energy of 1000 cal/mole and pre-exponential of 1.0×10^{16} m^6/mole^2/s to yield very high reaction rates at all temperatures. These numbers for reaction rate are obtained from a trial-and-error calculations on turbulent free jets (Katta and Roquemore, 1996).

An orthogonal, staggered-grid system with varying cell sizes in both the x and r directions is utilized. The momentum equations are integrated using an implicit QUICKEST (Quadratic Upstream Interpolation for Convective Kinematics with Estimated Streaming Terms) numerical scheme (Katta et al., 1994a; Leonard, 1979) which is third-order accurate in both space and time and has a very low numerical diffusion error. On the other hand, the species, enthalpy, and turbulence-energy conservation equations, which have relatively large source terms, are integrated using the hybrid scheme of Spalding (1972). By rearrangement of the terms, the finite-difference form of each governing equation at all grid points is written as a system of algebraic equations which is then solved using the Alternative-Direction-Implicit (ADI) technique. The time increment, Δt, is determined from the stability constraint and maintained as a constant during the entire calculation. The pressure field at every time step is accurately calculated by simultaneously solving the system of algebraic pressure Poisson equations at all grid points using the LU (Lower–Upper) decomposition technique.

Temperature- and species-dependent thermodynamic and transport properties are used in this formulation. The enthalpy of each species is calculated from polynomial curve fits, while the viscosity, thermal conductivity, and diffusion coefficients of the species are estimated from the Lennard–Jones potentials.

Flat velocity profiles are used at the fuel and air inflow boundaries. A simple extrapolation procedure (Katta et al., 1994b) with weighted zero- and first-order terms was used to estimate the flow variables at the out-flow boundary. The usual no-slip, adiabatic, and chemically inert boundary conditions were applied at the walls. Wall functions were used for determining the gradients of the flow variables near the walls in the cases where turbulence was modeled.

Results and Discussion

The geometry chosen for the study of fluid-dynamics effects on a bluff forebody is very similar to that used by Little and Whipkey (1979) in their experimental investigations on locked vortices. It consists of a 100-mm-dia flat cylindrical forebody enclosed in an annular cylindrical tube having a 200-mm I.D. An afterbody disk having a diameter and thickness of 75 and 2 mm, respectively, is attached to the forebody using spindles. Two sizes of spindle (9- and 28-mm diameter) are used. The size of the cavity formed between the forebody and the disk is varied by moving the disk toward or away from the forebody. Airflow over this body develops vortices inside the cavity and behind the disk; normally these vortices shed, and the flow becomes dynamic in nature. The velocity of the air used in the annular gap between the forebody and the surrounding tube is 30 m/s. Axisymmetric calculations are made for different cavity sizes using a 301 × 91 grid system. The geometry and the grid system used are shown in Fig. 1. Varying grid spacing was adopted in both the axial (x) and radial (r) directions to cluster the grid points in the cavity and near the walls.

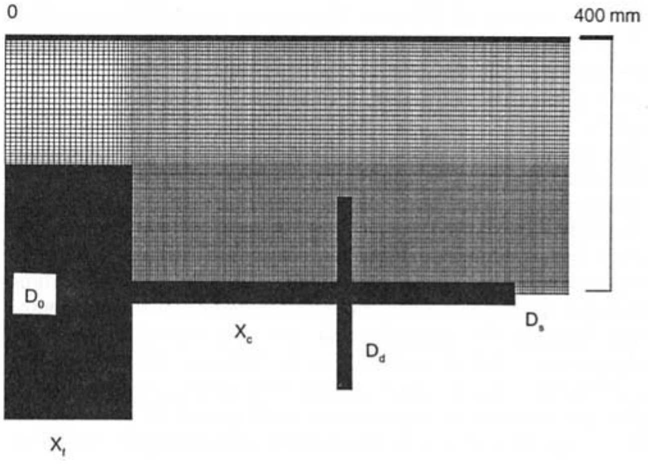

Fig. 1 Geometry of the forebody-spindle-disk combination used for the study of trapped-vortex concepts in cold and combustion environments. Grid system employed for the direct simulation of large-scale structures is also shown.

Starting from an uniform initial flowfield around the forebody-spindle-afterbody combination, direct numerical simulations are made for different cavity sizes using the model described earlier. Turbulence modeling was not used for these cold-flow cases. In order to obtain results that are not biased by the initial uniform flowfield, initial calculations for 25,000 time steps (corresponding to 0.675 s of real time) were discarded prior to the recording of the dynamic solutions. Calculations were then continued for another 5000 time steps for data-analysis purposes.

Drag on Forebody-Spindle-Afterbody Combination. The total time-averaged drag coefficient (C_D) on the forebody-spindle-disk combination for each case is computed from the unsteady data using the expression

$$\begin{aligned} C_D &= \int_0^{t_c} (c_p + c_w)dt \\ &= \frac{1}{\rho_\infty V_\infty^2} \int_0^{t_c} \left[\int (p_w - p_0)dA + \int \tau_w dA \right] dt \end{aligned}$$

Here, p_w and p_0 correspond to wall and inlet pressures, respectively; τ_w is the wall shear stress; and c_p and c_w are the pressure-drag and skin-friction coefficients, respectively. Time t_c corresponds to the calculated time. For investigating the drag increase or decrease resulting from the cavity formed between the forebody and the disk, calculations are first made for the forebody-spindle combination alone. These calculations are made without the use of a turbulence model. The total drag coefficients (C_D) obtained for the large (28-mm) and small (9-mm) spindles are 0.125 and 0.151, respectively. The corresponding values measured by Little and Whipkey are 0.179 and 0.186, respectively. Considering the fact that surface roughness and small-scale turbulence near the walls may contribute additional drag in the experiments, the values predicted by the model that neglected these effects seem to be reasonably good.

Calculations were performed on an afterbody-spindle-forebody combination for different cavity sizes and for the annular airflow velocity of 30 m/s. The direct simulation using 301 × 91 grid points resulted in dynamic flows with a degree of unsteadiness related to the cavity size. Time-averaged quantities from these calculations were obtained by averaging the data over a period of 135 ms (5000 time steps). Calculations were also made incorporating $k-\epsilon$ turbulence model. Even though the same fine grid having 301 × 91 points was used in these simulations, use of the $k-\epsilon$ turbulence model yielded steady flowfields for all the cavity sizes. The drag coefficient obtained from the direct simulations and from the calculations made using the $k-\epsilon$ turbulence model for different cavity sizes indicate that the drag coefficient decreases initially with the separation between the forebody and disk and increases for large separations—which is similar to the behavior observed in the experiments. Quantitative comparisons with the experimental data are made for changes in drag coefficient (ΔC_D) for different cavity sizes which are obtained by subtracting the base drag coefficient (without disk) from that obtained with the disk.

Computed results in the form of drag reduction obtained for different cavity sizes are compared with the experimentally measured ones in Fig. 2(*a*) and 2(*b*) for small- and large-spindle cases, respectively. Both the calculations and the experimental data show that drag reduction is maximum when the disk is placed 50 to 60 mm downstream of the forebody. Interestingly, even though the simulations with the $k-\epsilon$ turbulence model did not result in the dynamic flows observed in the experiments, the drag coefficients compare favorably with those from the experiment. On the other hand, the direct simulations obtained by solving Navier–Stokes equations without incorporating any turbulence models yielded dynamic flows similar to those observed in the experiment. It is known that the 30-m/s airflow would result in turbulent flow in the channel created by the annular tube and the forebody-spindle-disk combination. However, the higher-order-accurate algorithms used for solving the momentum and pressure Poisson equations are expected to simulate flow structures that are comparable to the grid system utilized. In the present study, the grid spacing in the cavity region varies from 0.8 to 0.92 mm, and a time step equal to 0.027 ms was chosen. With the use of this model, flow structures of 6-mm size (an order of magnitude smaller than the cavity height) can be resolved. The reasonably good agreement seen in Fig. 2 suggests that the drag force associated with this geometry is dominated by the large-scale motion of the fluid and that the small scales (turbulent scales) are playing a secondary role. For both spindle sizes, a maximum drop in drag coefficient occurs for approximately the same cavity length.

The calculated drag-coefficient profile for the small-spindle ($D_s/D_0 = 0.0938$) case [Fig. 2(*a*)] indicates that the drag coefficient decreases monotonically to a minimum value and then increases for cavity lengths greater than 60 mm. On the other hand, for a larger spindle ($D_s/D_0 = 0.281$), it should be noted that the drag coefficient increases significantly for cavity lengths between 40 and 60 mm before reaching the minimum value [Fig. 2(*b*)]. Turbulent-flow calculations with the $k-\epsilon$ model yielded no spikes in drag coefficient for either spindle size. Detailed analysis of the time-dependent data obtained for a cavity length of 50 mm indicated that the vortices inside the cavity became quite unsteady, resulting in more shedding of vortices from the cavity and, hence, a higher drag coefficient. Experiments showed no such spikes for the large-spindle case; however, interestingly, a large spike in the drag-coefficient profile was observed for the small-spindle case, indicating that for some smaller-than-optimum size cavities, the drag coefficient could increase drastically. Calculations have captured this phenomenon, but for a different spindle size. The discrepancy noted between the calculations and the experimental results regarding the occurrence of drag spike is believed to result from geometric parameters such as rounded corners and surface roughness and flow quantities such as inlet profiles and fluctuations that are inherent in the experiments. Additional work is needed in the modeling and experimental aspects to allow better comparisons; however, since the present model is reasonably predicting the drag-coefficient Vs cavity-length profile and spikes in the drag coefficient for certain cavity sizes, the model results could be used with confidence to obtain a qualitative understanding of the physical process that result in such effects.

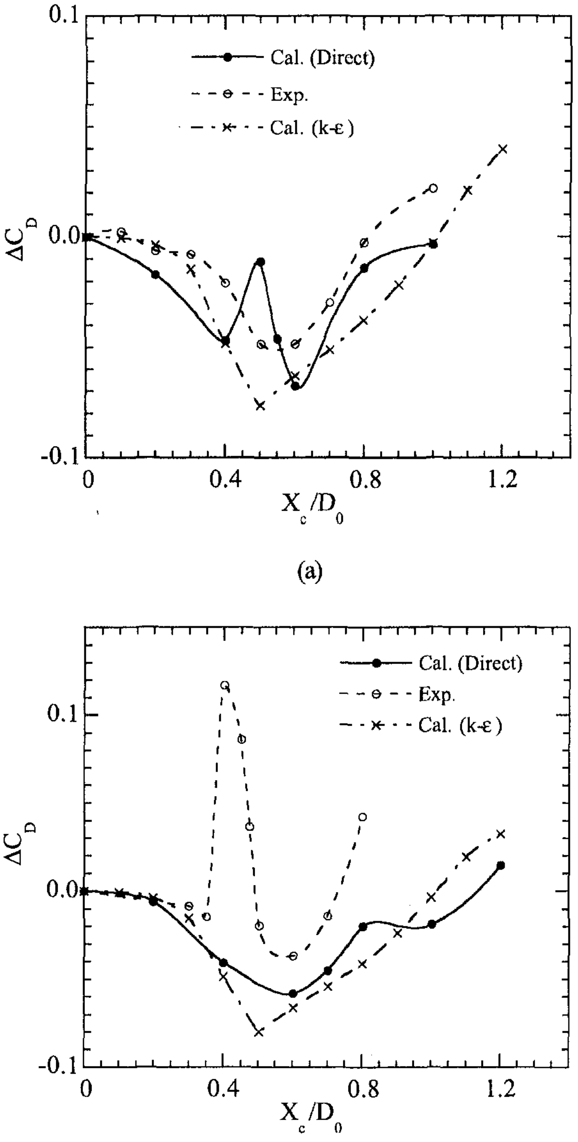

(a)

(b)

Fig. 2 Change in drag coefficient resulting from the addition of disk to forebody-spindle geometry obtained for different cavity lengths: (*a*) small-spindle (D_s/D_0 = 0.281) case

Flow Structures. The instantaneous solution obtained for the forebody-spindle combination (without the disk) is shown in Fig. 3 in the form of velocity vectors in the upper half and particle traces in the lower half. This solution represents data obtained at the end of the 30,000-time-step calculation. The flowfield is nearly at steady state, with a large recirculation zone being created downstream of the forebody and extending up to z = 160 mm. A small vortex has also developed in the corner of the forebody and spindle. For visualizing the dynamic nature of the flow, the instantaneous positions of the particles that were continuously released from locations near the entrance region are shown in Fig. 3. The solid triangles represent the locations of the particles that were released in the free stream and close

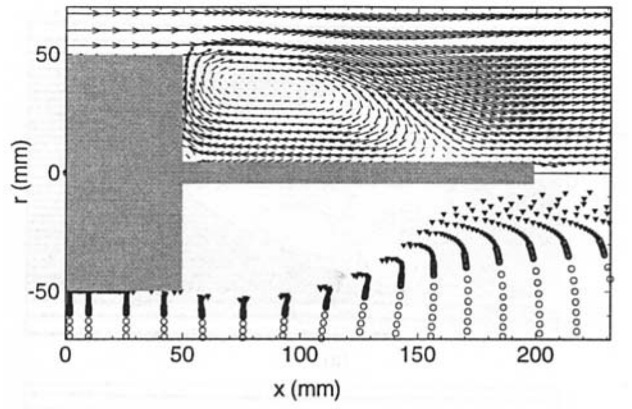

Fig. 3 Nonreacting flow around the geometry formed with 100-mm-dia forebody and a spindle of $D_s/D_0 = 0.0938$. Velocity vectors and particle distributions are shown in the upper and lower halves, respectively.

to the forebody, whereas the open circles represent the locations of the particles that were released away ($r > 60$ mm) from the forebody. The steady nature of the flowfield in the absence of the afterbody disk (Fig. 3) is evident from the separate streaks of particles. Note that none of the particles injected into the free stream entered the recirculation region formed behind the forebody. On the other hand, the particles that were injected into the recirculation zone (not shown in the figure for clarity) remained within the recirculation region.

Perturbation to the steady flow that developed over the forebody-spindle geometry is studied by placing a disk on the spindle. The instantaneous flowfields obtained with the disk located at different distances from the forebody are shown in Figs. 4(*a*)–4(*d*). The plotting scheme used for these figures is identical to that used in Fig. 3. In general, vortices are formed in the cavity and downstream of the disk in all cases. When the cavity formed between the forebody and disk is small [Fig. 4(*a*)], several vortices are developed within the cavity, and the flow is dominated by two counterrotating vortices. Note that the largest vortex in the cavity is rotating in the direction opposite that of the recirculating vortex seen in Fig. 3. The unsteady nature of these cavity vortices triggers shedding of the large recirculating vortex formed behind the disk. The dynamics of the flow may be visualized readily from the particle traces (or streak-lines) shown on the lower half of each plot in Fig. 4. A significant number of particles represented by solid triangles has entered the cavity and the vortex behind the disk in the case of $X_c/D_0 = 0.4$, which indicates the intense mixing resulting from the dynamic flow structures.

When the disk was located at $X_c/D_0 = 0.6$, the cavity flow became steady; as a result, the flow behind the disk also became nearly steady [Fig. 4(*b*)]. The total drag under this condition reached a minimum value. Well-defined corner vortices have formed in this case. Interestingly, the direction of rotation of the fluid in the cavity follows that observed for the no-disk case (Fig. 3). The steady vortices in the cavity and behind the disk in this optimum case seem to be the split parts of the steady vortex computed without the disk, and the velocity vectors at the tip of the disk show that the fluid is passing around the disk smoothly. However, the location of the main-flow re-attachment point on the spindle has shifted from 110 to 125 mm from the forebody with the addition of the disk. This increase in the reattachment distance was also observed in the flow-visualization experiments of Little and Whipkey (1979). Simulations made for $X_c/D_0 = 0.7$ [Fig. 4(*c*)] yielded perfectly steady vortices within the cavity and behind the disk. The flow structure is similar to that observed for the $X_c/D_0 = 0.6$ case.

For cavity sizes greater than $X_c/D_0 > 0.7$, flow in the cavity and behind the disk became unsteady [Fig. 4(*d*)], resulting an increase in the drag coefficient. Unlike in the smaller-than-optimum-cavity case [Fig. 4(*a*)], only one dominating vortex was formed in the cavity and a multiple-vortex structure was established behind the disk. The vortex in this larger-than-optimum-cavity case is not shedding. However, since the size of the cavity in this case is larger than the optimum one, the trapped vortex rotates within the cavity. This is evident from the particle traces plotted in the bottom half of Fig. 4(*d*). At this instant the solid-triangle particles are pulled into the cavity

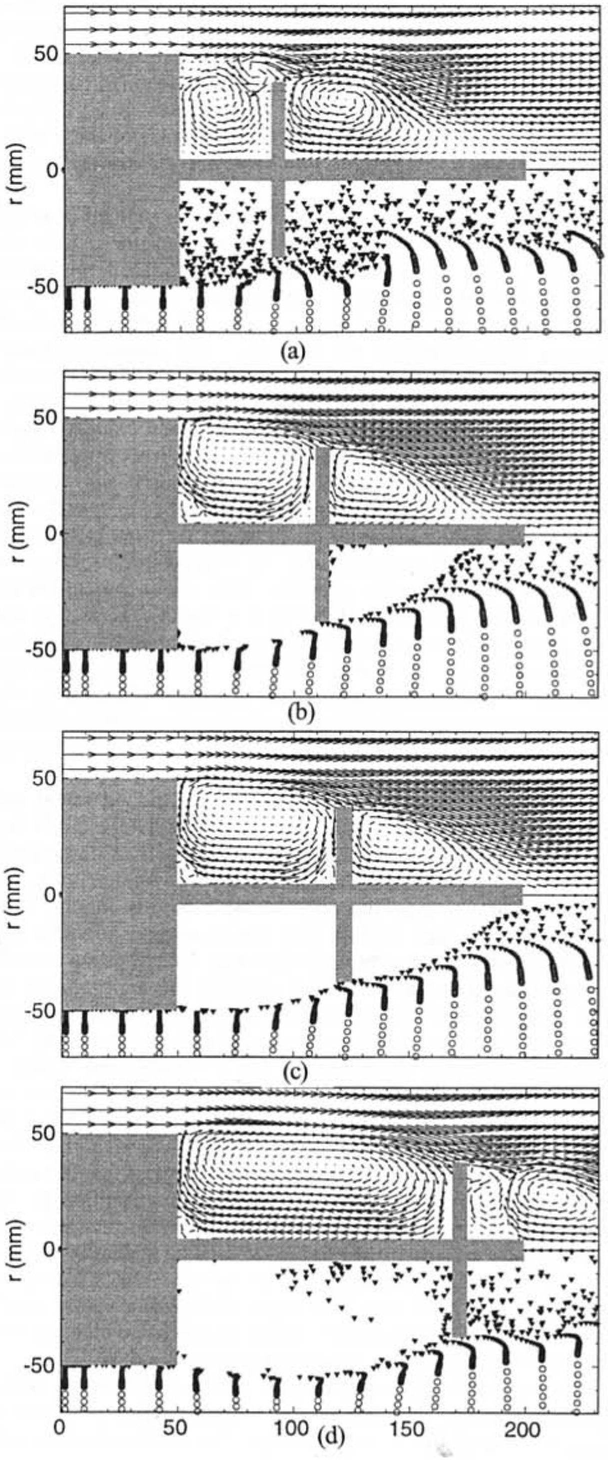

Fig. 4 Instantaneous flowfields obtained using direct numerical simulations for forebody-spindle-disk combination for various disk locations. X_c/D_0 = (*a*) 0.4, (*b*) 0.6, (*c*) 0.7, and (*d*) 1.2. Velocity vectors and particle distributions are shown in upper and lower halves, respectively.

since the vortex is closer to the disk; at other instants these particles pass over the disk when the vortex is pushed toward the forebody. The distribution of particles in this figure also indicates that particles lump together while moving around the center of the cavity; when that lump approaches the edge of the afterbody, a fraction of particles leaves the cavity. This implies that particles are entrained into the cavity vortex during a certain phase and then exit the cavity during a different phase, leading to periodic accumulation of particles in the cavity.

Calculations for the forebody-spindle-afterbody geometries are also made using the $k-\epsilon$ turbulence model. For these calculations grid, time-step, and flow conditions utilized are the same as those used for the direct simulations. Interestingly, for every cavity size, the simulation with the turbulence model quickly converged to steady-state flowfield. Results obtained for cavity sizes $X_c/D_0 = 0.4$, 0.6, 0.7, and 1.2 are shown in Figs. 5(*a*), 5(*b*), 5(*c*), and 5(*d*), respectively. Since each of these solutions represents a steady-state flowfield, streamlines are plotted rather than particle traces.

In general, the turbulent-flow calculations yielded a single vortex in the cavity region and another behind the disk. In the case of $X_c/D_0 = 0.4$, the direction of rotation of the cavity vortex is normal (clockwise). On the other hand, as shown in Fig. 4(*a*), the direct simulations resulted in a multiple-vortex structure with the largest one rotating in the counterclockwise direction, which compares well with the experimental data obtained by Little and Whipkey (1979). The flow structure downstream of the disk captured by $k-\epsilon$ turbulence calculations is also quite different from that captured by direct simulations. The vortex in the former is squeezed toward the spindle, whereas that in the latter is pushed away from the spindle. For the near optimum-size-cavity cases where the flow is at steady state, turbulent and direct calculations yielded similar solutions. The turbulent calculations predicted flow reattachment on the spindle at $x = 175$ and 192 mm for the $X_c/D_0 = 0.6$ and 0.7 cases, respectively, while the direct simulations predicted reattachment at $x = 175$ and 186 mm, respectively. However, some minor differences exist in the solutions obtained by the turbulent and direct calculations for these cases. The turbulence model seems to dissipate the corner vortices that are observed in the direct simulations.

The cavity flow structures predicted by the turbulent and direct simulations for the $X_c/D_0 = 1.2$ case [Figs. 5(*d*) and 4(*d*), respectively] are similar in nature, even though the latter is dynamically oscillating within the cavity. Interestingly, the streamline drawn from the edge of the forebody in Fig. 5(*d*) shows that flow dips slightly into the cavity near the disk and then flows back around the tip of the disk. This dividing streamline also suggests that no flow is entering the recirculation region. The dynamic flow structure downstream of the disk predicted by the direct simulations is quite different from the single-vortex structure obtained with the $k-\epsilon$ turbulence model.

In general, results obtained for the larger-spindle case are similar to those shown in Figs. 4 and 5. Calculations were also made for different disk sizes, and similar dynamic flow structures were found. These calculations suggest that the minimum-drag-coefficient condition seems to be coupled to the steadiness of the vortex trapped in the cavity formed between the forebody and disk. Multiple vortices form in the smaller cavities and periodically shed, which, in turn, makes the vortex behind the disk shed also. The single dominating vortex established in larger cavities rotates within the cavity, which, in turn, develops multiple vortex structures behind the disk.

The drag coefficient computed as a function of time for different disk locations for smaller and larger spindles is shown in Figs. 6(*a*) and 6(*b*), respectively. The time-averaged data shown in Fig. 2 correspond to the instantaneous data given in Fig. 6(*a*). Data for the optimum cavity sizes are shown with solid circles. Overall, the frequency for fluctuations in ΔC_D is found to be inversely related to the cavity size. For cavities smaller than the optimum size, calculations have always yielded fluctuating drag coefficients. On the other hand, for larger-than-optimum cavities, fluctuations in the drag coefficient are observed only for significantly larger cavities. Interestingly, the near-steady drag coefficient for $X_c/D_0 = 0.7$ in the case of the smaller spindle [Fig. 6(*a*)] and for $X_c/D_0 = 0.8$ in the case of the larger spindle [Fig. 6(*b*)] is significantly higher than the respective values obtained with the optimum cavity sizes. This

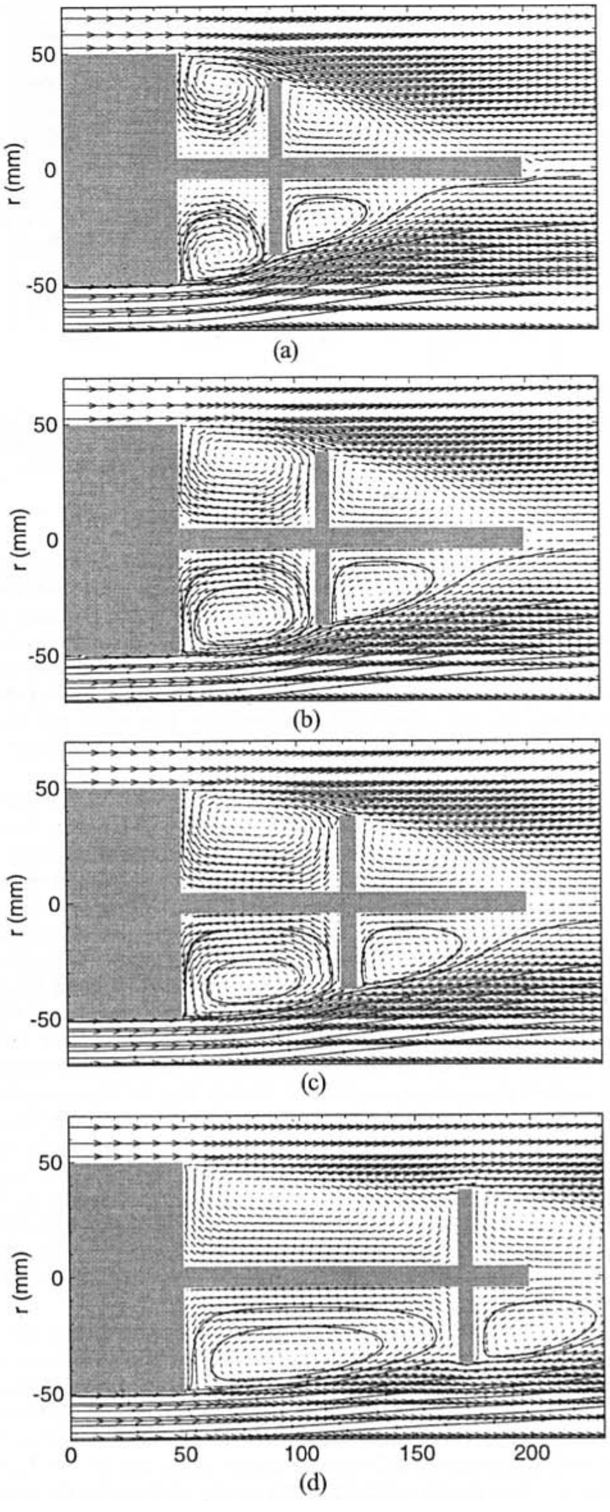

Fig. 5 Steady-state flowfields obtained using $k-\epsilon$ turbulence model for the forebody-spindle-disk combination. X_c/D_0 = (*a*) 0.4, (*b*) 0.6, (*c*) 0.7, and (*d*) 1.2.

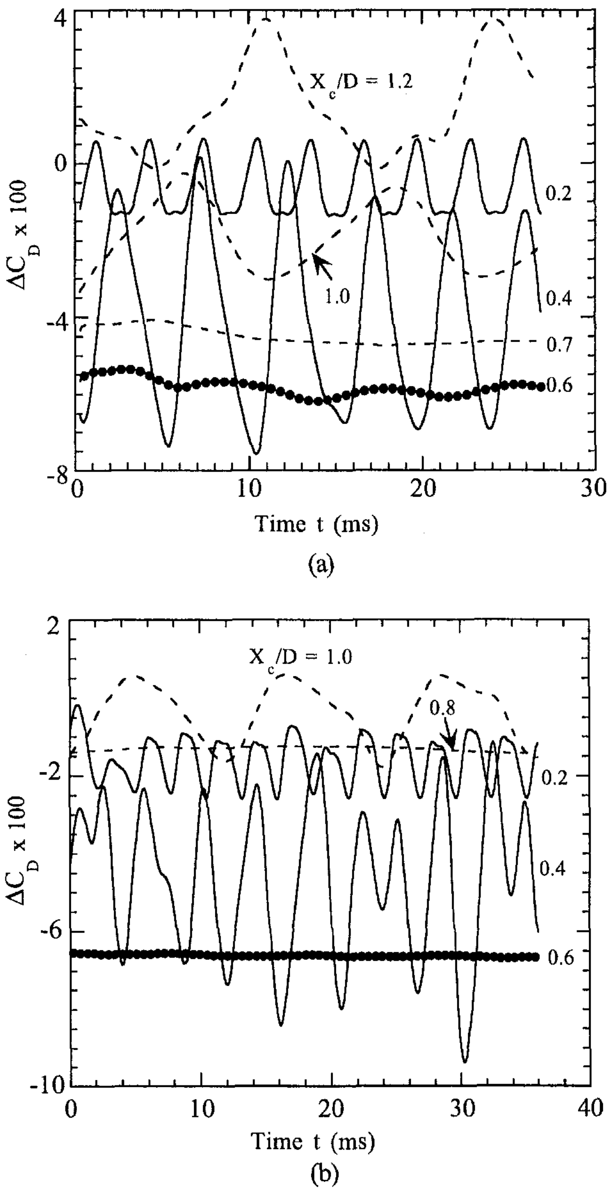

Fig. 6 Change in drag coefficient with time resulting from the addition of the disk to the forebody-spindle geometry obtained for different cavity lengths: (*a*) small-spindle case; (*b*) large-spindle case

indicates that even though under minimum-drag conditions the vortices in the cavity and behind the disk are locked spatially, the converse—locked vortices yielding minimum drag—is not always true.

Residence Time and Entrainment in the Cavity. With the proper choice of cavity dimensions such as length and height, the vortex/vortices in the cavity can be made stationary. On the other hand, a stationary vortex yields minimum mass exchange between the vortex and the main flow (flow in the annular gap). In a combustor, this implies that the transport of the oxidizer from the main flow into the cavity will be minimum when the vortices in the cavity are locked. Since locked vortices help to stabilize the flames in the combustor, for accommodating the decrease in the oxidizer entrainment into the cavity, additional air must be fed into the cavity directly to obtain better performance from the trapped-vortex combustor. Therefore, it is important to understand the residence time and entrainment characteristics of cavity flows for different cavity sizes.

A quantitative estimation of entrainment is difficult in a dynamic-flow system since entrainment resulting from vortex motion and fluid transported from the molecular and/or turbulent diffusion are tightly coupled. The concentration of tracer fluid, which represents the net transport from entrainment and diffusion, cannot yield the entrainment characteristics of a dynamic flow. Therefore, in the present study, estimations for the residence time and entrainment resulting from the dynamic motion of vortices in the cavity are made by following a unique approach based on particle distribution. Two sets of massless particles were injected into the combustor—one set in the cavity region close to the forebody (Location A) and the other into the air flow at the entrance (Location B). Both sets of particles were injected into the flowfield with a time interval of 0.27 ms. The fraction of the mass that originated in the cavity and remained in the cavity after *t* ms is obtained by summing the particles that were released from Location A at a time *t* ms prior and are still laying within the cavity. The decay of injected fluid in the cavity at different times for different cavity sizes is shown in Fig. 7(*a*). Since the residence time for the fluid that is injected into the cavity is inversely proportional to the decay time, Fig. 7(*a*) also represents the residence-time characteristics

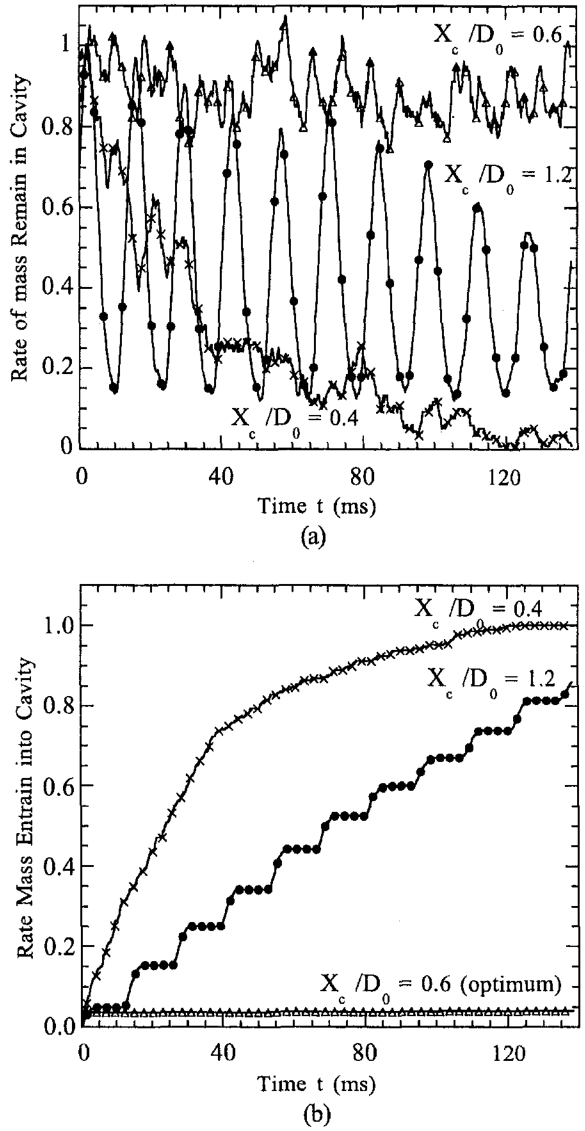

Fig. 7 Residence-time and entrainment characteristics obtained from particle distributions for different cavity lengths: (*a*) ratio of rate of decrease in cavity mass and rate of injection of mass into cavity; (*b*) ratio of rate of increase in cavity mass and rate of injection of mass outside cavity

for different cavity sizes. The observations made from Fig. 7(*a*) are as follows: (1) When the vortices in the cavity become stable (0.6 case), the injected fluid remains in the cavity. The small fluctuations obviously indicate that the vortices in the cavity are not perfectly locked. (2) For the case of X_c/D_0 = 0.4, the injected fluid leaves the cavity with time. Interestingly, the fluid decay in this case is not a linear function of time. Figure 7(*a*) indicates that the initial 80 percent of the fluid left the cavity in about 40 ms, whereas the remaining 20 percent fluid required ~80 ms to leave the cavity. This variation in residence time results from the differences in the dynamic characteristic of the vortices in the cavity. The vortices in the upper half seem to shed from the cavity, whereas the ones in the lower half move within the cavity itself. Therefore, the particles (or mass) injected into the vortices in the upper half have less residence time, and the particles injected into the lower-half vortices remain in the cavity for longer periods of time. Because of the difference in the residence times of the mass injected from different locations within the cavity, evenly distributed combustion within the cavity can be achieved by injecting fuel and air into the cavity at multiple locations with varying flow rates.

Flow within the cavity becomes dynamic also for the cases where the length of cavity is greater than that of the optimum one. As a result, the mass of the fluid remaining in the cavity decreases with time [Fig. 7(*a*)]. However, unlike in the case of the shorter-than-optimum cavity, fluid fluctuates at a near-constant frequency (72 Hz). These fluctuations result either from entrainment of particles into the cavity that had left earlier or from accumulation of particles resulting from a phase lag between the injection and ejection times. A close look at the cavity-flow structure in Fig. 5(*d*) suggests that vortices are *not* shedding from the cavity; hence, entrainment of cavity particles back into the cavity may be ruled out. The particle distribution in this figure also indicates that particles lump together while moving around the center of the cavity and when that lump comes closer to the edge of the afterbody, a fraction of particles leaves the cavity. This implies that the particles injected into the cavity vortex at a certain phase leave the cavity quickly [corresponds to the maxima in the X_c/D_0 = 1.2 curve in Fig. 7(*a*)]; on the other hand, those injected at other phases tend to remain in the cavity for longer periods of time (corresponds to the minima). This scenario can be confirmed by considering the relationship between the time period for one cycle (~14 ms) and the distance traveled by the particle lump (~340 mm, obtained from the cavity dimensions), which yields a velocity of 24 m/s—close to the jet velocity or the recirculating flow velocity in the cavity. These insights into the vortex dynamics and particle accumulation in the cavity aid in determining the injection pattern for providing longer or shorter residence times for the fuel–air mixture to obtain better combustion and pollutant management.

For bringing the main air/fuel into the cavity, it is important to know the entrainment characteristics of the vortices for different cavity sizes. Such characteristics for three cavity sizes were obtained by calculating the number of particles injected in the main flow and entrained into the cavity. Entrainment rates from the particle count are shown in Fig. 7(*b*). As expected, when the vortex is trapped in the optimally designed cavity, very little main flow is entrained into the cavity. This emphasizes the important aspect of the trapped-vortex combustor—that under optimum design conditions, the fuel and air necessary for efficient combustion in the cavity should be directly injected into the cavity without relying on entrainment from the main flow. On the other hand, when the cavity is smaller than the optimum one, as in the case of X_c/D_0 = 0.4, the entrainment rate initially increased linearly up to t = 40 ms and later slowly reached a saturated value. The balance between entrainment into and shedding from the cavity resulted in a saturated level for the main-flow particles in the cavity. In the case of the larger-than-optimum cavity [X_c/D_0 = 1.2 case in Fig. 7(*b*)], particles that were injected into the main flow entered the cavity in a stepwise fashion. As discussed earlier, a maximum number of particles enters the cavity during a certain period of the vortex evolution. The gradual decrease in the step height with time indicates that the entrainment rate is approaching a saturated value.

Combusting Flow. Considering the advantages of locked vortices for stable combustion, Hsu et al. (1995) have developed a laboratory combustor that can operate over a wide range of flow-rate conditions. The geometry of the center-body combustor designed by Hsu et al. (1995) is similar to that studied by Little and Whipkey (1979) for nonreacting flows. For investigating the vortex characteristics in the cavity under combusting-flow environment, calculations were made for the simulation of reacting flow for the combustor of Hsu et al. (1995). This combustor consists of a forebody and an afterbody of diameters 70 and 50.8 mm, respectively. The combustor is enclosed in a 80-mm-dia Pyrex annular tube. Main air is delivered through the annular gap between the Pyrex tube and the forebody at a velocity of 42 m/s. Primary air and fuel (propane) are injected into the cavity from the afterbody. Fuel and air are carried to the afterbody through a central tube that connects the afterbody to the forebody. Figure 8(*a*), obtained using a normal photographic camera with long exposure time, shows the flame and the combustor geometry for operation under a primary equivalence ratio (defined as fuel-to-air ratio injected into the cavity relative to the ratio required for stoichiometric combustion) of 4.4.

Calculations were made for this fuel-rich condition using a 251 × 101 grid system. Fuel and air in the experiment were injected into the cavity through three coannular rows of holes drilled on the face of the afterbody. The fuel holes were sandwiched between the air holes. The symmetric distribution of holes is assumed to provide only weak three-dimensional effects. For performing axisymmetric calculations on this near-symmetric combusting flow, the fuel and air holes were replaced with annular slots of 1-mm width in the model. The flat velocities of 12.4 and 5 m/s at the exits of air and fuel slots gave the measured flow rates of 56 and 25 slpm, respectively.

The instantaneous flow computed with a fast-chemistry assumption is shown in Fig. 8(*b*) by plotting iso-temperature contours and velocity vectors in the upper and lower halves, respectively. Computed flow in the cavity has a large vortex generated by the high-speed annulus air flow and several small vortices that are primarily developed from the interaction of fuel and air jets injected into the cavity. Figure 8(*b*) also indicates that the flow of combustion products from the cavity over the disk is associated with only weak shedding. This was confirmed by making an animation of the time-dependent solution. The weak vortex shedding from the cavity suggests that the global vortex structure in the cavity represents a locked vortex. Note that the design strategy used by Hsu et al. (1995) for determining the cavity size was based on the conditions for obtaining locked vortices in cold flows without primary injection. For this cavity size, cold-flow calculations also showed locked vortices within the cavity and behind the afterbody. Absence of strong vortex shedding from the cavity, noted from the reacting flow calculations made with primary injection (Fig. 8), suggests that the locked-vortex criterion obtained using cold annular flow yields locked vortices (overall) in the reacting flow case also. Additional calculations must be performed with different cavity sizes before a general conclusion can be reached regarding locked vortices in cold and reacting flows.

The overall flow structure and the temperature field are obtained from direct numerical simulations by time averaging the 8000 instantaneous solutions over a period of 40 ms. The results are shown in Fig. 8(*c*). The dominating cavity vortex and the near steady-state wake vortex noted in the instantaneous solutions [e.g., Fig. 8(*b*)] have appeared in the time-averaged data

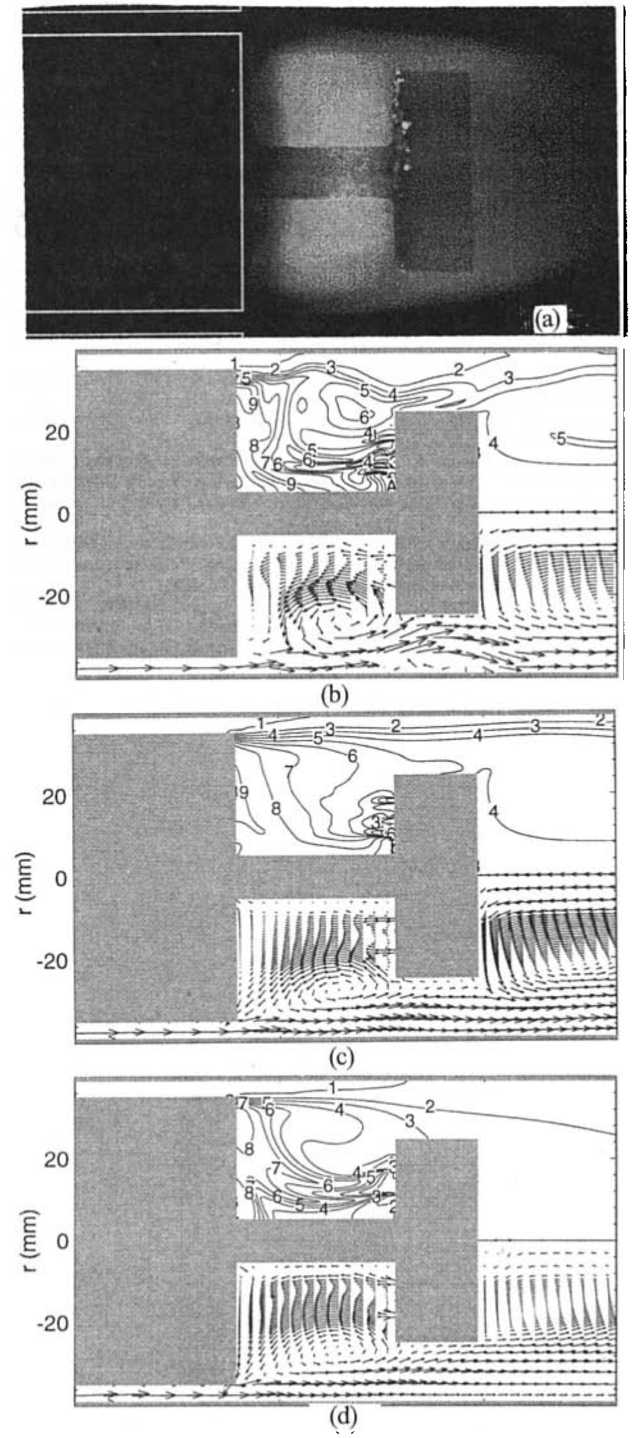

Fig. 8 Reacting flow inside trapped-vortex combustor for primary equivalence ratio of 4.4: (*a*) direct photograph of flame, (*b*) instantaneous flowfield obtained with direct numerical simulation, (*c*) flame obtained by averaging several instantaneous solutions, and (*d*) steady-state flame simulated using $k-\epsilon$ turbulence model. Iso-temperature contours are plotted with 150-K interval from 300 K.

as stable recirculation regions. A small recirculation region in the corner of the spindle and disk may also be noted in Fig. 8(*c*). Time averaging has also eliminated the temperatures that are greater than 1600 K [absence of Contour No. A in Fig. 8(*c*)].

The computed peak temperature (time-averaged) of 1600 K is lower than that measured (~1900 K) in the experiment. In fact, even the instantaneous temperature never exceeded 1750 K in the direct numerical simulations. Since a fast-chemistry model was used in the present simulations, the lower computed temperature could be resulting from the mixing-limited environment in the cavity. It is known that even though large-scale flow structures play a major role in the mixing of fuel and air, small scales are important for mixing on a local level. The present simulations predict only the large-scale vortical structures in the cavity. The lower predicted temperature could then be due to the absence of small-scale vortices in the calculations. For verifying this, calculations were made by including the $k-\epsilon$ model for turbulence. Computations resulted in a steady flow and the predicted temperature field is shown in Fig. 8(*d*). Note that the same 251×101 grid system utilized in direct numerical simulations was employed for these calculations also. Surprisingly, the peak temperature obtained in Fig. 8(*d*) was only 1500 K—lower than that obtained without the turbulence model. This suggests that the combustion in the cavity is not limited by the small-scale mixing.

In experiments, primary fuel and air are passed through the central tube and afterbody before being injected into the cavity. Since both the center tube and afterbody are surrounded by the hot combustion products, their wall temperatures are expected to be higher than the temperature of the incoming fuel and air, which, in turn, heats the fuel and air. On the other hand, even though the walls of the afterbody and center tube were treated as adiabatic walls in the present simulations, fuel and air were injected in the cavity at room temperature since flow inside the tubes was not considered. It is believed that the hotter fuel and air injected into the cavity leads to the higher temperatures in the experiment.

A comparison between the time-averaged flow field [Fig. 8(*c*)] and the steady-state solution resulted from $k-\epsilon$ model [Fig. 8(*d*)] reveals significant similarities. Mainly, the recirculation zone observed in the time-averaged data matches well with that obtained with $k-\epsilon$ model. On the other hand, the wake vortex behind the disk and the corner vortex of the spindle and disk predicted with $k-\epsilon$ turbulence model are weaker than those obtained from the time-averaged direct-numerical-simulations data. The temperature distributions in Figs. 8(*c*) and 8(*d*) are also quite different. Simulations with the $k-\epsilon$ model yielded jet-flame structures in the cavity following the fuel and air injections, whereas, more uniform temperature distributions are obtained with direct numerical simulations.

Summary

Vortex shedding behind a bluff forebody leads to a higher drag coefficient. It is known that by trapping these wake vortices using disks, the drag coefficient of the forebody-spindle-disk combination can be decreased. The dynamics of the vortices formed inside the cavity and behind the forebody were studied using a time-dependent, axisymmetric Computational Fluid Dynamics with Chemistry (CFDC) code. A large number of grid points with ΔX and $\Delta r \sim 0.9$ mm was used to capture the large-scale structures whose physical size is up to an order of magnitude smaller than the cavity height. The important conclusions reached from the calculations made with different cavity sizes, spindle diameters, and disks are that (1) changes in drag coefficient can be predicted from the simulation of large-scale structures alone, (2) for the optimum cavity length at which the drag coefficient becomes minimum, the vortices in the cavity and behind the disk are locked spatially; however, the converse—locked vortices correspond to a minimum-drag condition—is not always true, (3) more than one dominant vortex is developed in smaller-than-optimum cavities and vortex shedding always occurs from these cavities, (4) a single dominating vortex formed within a larger-than-optimum cavity moves within the cavity and shedding is not associated, and (5) because of the cavity-vortex shedding, entrainment into the cavity is greater and residence time is lower in the smaller-than-optimum cases compared to those in the larger-than-optimum ones. These findings are useful in determining the locations for injecting primary air and fuel into the cavities for trapped-vortex-combustor applications.

Calculations were also performed for the reacting flow in the trapped-vortex combustor designed by Hsu et al. (1995) using the fast-chemistry model. Preliminary results suggest that the optimum cavity length determined from the nonreacting annular flow seems to yield nonshedding cavity flows, even with combustion and primary injection into the cavities. Additional calculations must be performed to verify this conclusion for different-geometry combustors.

Acknowledgments

This work was supported, in part, by Air Force Contract No. F33615-95-C-2507 and the Air Force Office of Scientific Research. The authors would like to thank Dr. Mark Hsu for stimulating discussions and allowing us to use Fig. 8(*a*) and Mrs. Marian Whitaker for the editorial help.

References

Grinstein, F. F., and Kailasanath K., 1995, "Three-Dimensional Numerical Simulations of Unsteady Reactive Square Jets," *Proc. 25th International Symposium on Combustion,* Combustion Institute, Pittsburgh, PA.

Hsu, K. Y., Goss, L. P., Trump, D. D., and Roquemore, W. M., 1995, "Performance of a Trapped-Vortex Combustor," AIAA Paper No. 95-0810.

Katta, V. R., Goss, L. P., and Roquemore, W. M., 1994a, "Numerical Investigations of Transitional H2/N2 Jet Diffusion Flames," *AIAA Journal,* Vol. 32, pp. 84–94.

Katta, V. R., Goss, L. P., and Roquemore, W. M., 1994b, "Simulation of Vortical Structures in a Jet Diffusion Flame," *Int. J. Num. Meth. Heat Fluid Flow,* Vol. 4, p. 413.

Katta, V. R., and Roquemore, W. M., 1996, "Numerical Studies on Trapped-Vortex Combustor," AIAA Paper No. 96-2660.

Leonard, B. P., 1979, "A Stable and Accurate Convective Modeling Procedure Based on Quadratic Upstream Interpolation," *Computer Methods in Applied Mech. and Engineer.,* Vol. 19, p. 59.

Little, B. H., and Whipkey, R. R., 1979, "Locked Vortex Afterbodies," *Journal of Aircraft,* Vol. 16, No. 5.

Mair, W. A., 1965, "The Effect of a Rear-Mounted Disc on the Drag of a Blunt-Based Body of Revolution," *The Aeronautical Quarterly,* Nov., pp. 350–360.

Migay, V. K., 1963, "Study of Ribbed Diffusers" [in Russian], *Toploenergetika,* No. 10, 1962, English translation issued as A.R.C. Paper 25,382.

Rohsenow, W. M., Fink, C. H., and Pollis, S. R., 1951, "Flow Through Two Orifices in Series," ASME Paper No. 51-A-87.

Roshko, A., and Koenig, K., 1976, "Interaction Effects on the Drag of Bluff Bodies in Tandem," presented at the symposium on Aerodynamic Drag Mechanisms of Bluff Bodies and Road Vehicles, General Motors Research Laboratories, Sept. 27–28.

Spalding, D. B., 1972, "A Novel Finite Difference Formulation for Difference Expressions Involving Both First and Second Derivatives," *International Journal for Numerical Methods in Engineering,* Vol. 4, pp. 551–559.

Veynante, D., Vervisch, L., Poinsot, T., Linan, A., and Ruetsch, G., 1994, "Triple Flame Structure and Diffusion Flame Stabilization," *Proc. Summer Program 1994,* Center for Turbulent Research, NASA Ames/Stanford University, CA, pp. 55–73.

Optical Measurement of Gas Turbine Engine Soot Particle Effluents

R. J. Litchford
Mem. ASME

F. Sun

ERC Incorporated,
1940 Elk River Dam Road,
Tullahoma, TN 37388

J. D. Few

J. W. L. Lewis

Center for Laser Applications,
University of Tennessee Space Institute,
B. H. Goethert Parkway,
Tullahoma, TN 37388

This paper addresses optical-based techniques for measuring soot particulate loading in the exhaust stream of gas turbine engines. The multi-angle scattering and multi-wavelength extinction of light beams by ensembles of submicrometer soot particles was investigated as a diagnostic means of inferring particle field characteristics. That is, the particle size distribution function and particle number density were deduced using an innovative downhill simplex inversion algorithm for fitting the deconvolved Mie-based scattering/extinction integral to the measured scattering/extinction signals. In this work, the particle size distribution was characterized by the widely accepted two-parameter log-normal distribution function, which is fully defined with the specification of the mean particle diameter and the standard deviation of the distribution. The accuracy and precision of the algorithm were evaluated for soot particle applications by applying the technique to noise-perturbed synthetic data in which the signal noise component is obtained by Monte Carlo sampling of Gaussian distributed experimental errors of 4, 6, and 10 percent. The algorithm was shown to yield results having an inaccuracy of less than 10 percent for the highest noise levels and an imprecision equal to or less than the experimental error. Multi-wavelength extinction experiments with a laboratory bench-top burner yielded a mean particle diameter of 0.039 μm and indicated that molecular absorption by organic vapor-phase molecules in the ultraviolet region should not significantly influence the measurements. A field demonstration test was conducted on one of the JT-12D engines of a Sabre Liner jet aircraft. This experiment yielded mean diameters of 0.040 μm and 0.036 μm and standard deviations of 0.032 μm and 0.001 μm for scattering and extinction methods, respectively. The total particulate mass flow rate at idle was estimated to be 0.54 kg/h.

Introduction

Accurate measurement of soot particle effluents from aircraft gas turbine engines is required for several engineering applications, including management of internal heat transfer loads, prediction and modification of plume visibility and infrared emission signatures, and quantification and control of both low-altitude and high-altitude pollutant emissions. Many of these performance parameters are equally relevant to stationary gas turbine engines. For these applications it is believed that the mean soot particle diameter falls in the range of 0.03–1 μm, and a new class of instrument is needed to access this small particle domain. In view of recent findings on the seriousness of small particle impacts on health, it is certain that new regulations concerning small particle pollution are on the horizon. As such, it will be necessary to develop new measurement standards for gas turbine particulate emissions.

To define fully the influence of soot particle effluents on the performance parameters of interest, it is necessary to determine accurately both the Particle Size Distribution Function (PSDF) and the particle number density. The current standard pertaining to gas turbine engine exhaust particulates is the SAE Smoke Number. Unfortunately, measurement of the Smoke Number entails a recipe-based procedure with little scientific basis. As such, it is useful for comparing the relative particulate output between engines, but it does not provide a reliable quantitative measure of the combustion particulate emission rate. Furthermore, the SAE procedure is disadvantageous in terms of the costs and time expenditures associated with implementation. Reliable alternative methods are needed.

In the past, workers in this field have relied primarily on sample extraction probes inserted into the exhaust plume to obtain such quantitative data. For example, the widely used Electrostatic Aerosol Analyzer (EAA) consists of an insertion probe and a remotely located sensor, which sorts the sample particles as they pass through an applied electrostatic field. The reliability of results obtained by such techniques is, however, somewhat suspect. Extraction probes perturb the local flow field, are prone to sampling bias errors, which can translate into significant measurement uncertainty, and have poor time/spatial resolution. Furthermore, the cost associated with fully mapping the exhaust stream cross section is prohibitive in terms of the excessive test times required.

Because of these limitations, nonintrusive optical methods are more attractive in terms of their ability to provide remote in-situ measurement of exhaust stream particulates. These techniques, which can be categorized as either single-particle optical probes or ensemble optical probes, measure the interaction between small particles and known light sources to infer particle properties on a very small spatial scale (van de Hulst, 1957; Kerker 1969; Borhen and Huffman, 1983). In general, the single-particle and ensemble categories are distinguished by the average size and number density in the particulate field. Single particle counting is suited to large particles (diameters greater than 20 μm) with a relatively low number density, whereas ensemble techniques are suited to high concentrations of small particles (diameters less than 1 μm). Because of varying light source intensities and detector sensitivities, the terms large and small are relative. However, a rough rule of thumb may be given for optical wavelengths. That is, if the particle's dimensions are

---

Contributed by the International Gas Turbine Institute for publication in the JOURNAL OF ENGINEERING FOR GAS TURBINES AND POWER. Manuscript received by the International Gas Turbine Institute February 20, 1997. Associate Technical Editor: J. E. Peters.

somewhat larger than the wavelength of scattered light, the particle can in most instances be individually detected. On the other hand, if the particle's dimensions are somewhat less than the wavelength of scattered light, individual detection becomes difficult. Soot particles fall into the submicrometer size range, and ensemble probes are generally required based on sensitivity and measurement speed considerations.

The two major optical strategies for making ensemble measurements of the PSDF and particle number density are multi-angle scattering and multi-wavelength extinction of a directed beam of light. Because these techniques have a solid theoretical underpinning, they offer the promise of remotely operated, nonperturbative probing with high spatial and temporal resolution. They can also be readily adapted for near-real-time analysis and monitoring during normal engine operation. Whereas scattering techniques can be implemented as either single-particle probes or ensemble probes, wavelength-dependent extinction of a light beam is applicable only to ensembles of small particles since the extinction produced by a large particle is very difficult to measure. Single particle scattering systems such as the dual-beam Laser-Doppler Velocimeter (LDV) and the Phase-Doppler Particle Analyzer (PDPA) are highly developed and commercially available; however, systems for ensemble optical measurements, as required for soot-laden exhaust streams, are not yet fully developed. The central objective of this work was to advance the development of ensemble optical probe techniques with application to gas turbine engine exhausts.

The work in this paper describes the application of combined multi-angle scattering and multi-wavelength extinction measurements for deducing (1) the mean and standard deviation parameters of an assumed log-normal PSDF, (2) the soot particle number density, and (3) the mass flux of soot particles in the exhaust of an aircraft gas turbine engine. Numerical evaluations, as well as laboratory and field tests, were performed to demonstrate the innovative downhill simplex deconvolution algorithm of Sun and Lewis (1995) for this application.

Theoretical Background

In implementing ensemble optical probe techniques, a beam of light is projected through the particle field and particle size information is extracted from (1) the angular dependent scattering signals from a finite probe volume along the beam and/or (2) the wavelength-dependent extinction of the light beam integrated along its path through the particle field. The former technique most often employs a monochromatic light source (e.g., laser) and particle size is inferred from the angular distribution of scattered light. The latter technique requires a broadband CW light source extending well into the ultraviolet (UV) in order to detect the full range of soot particle sizes. Throughout the forgoing analysis, the particulate field is idealized as a composition of spherical, homogeneous particles having a number density size distribution $n(r) = Np(r)$ where N is the total number density and $p(r)$ is the normalized, relative PSDF for the particle radius r.

The incident light beam of power P_0, intensity I_0, and wavelength λ interacts with the particles having a complex index of refraction $m = \eta(\lambda) + i\kappa(\lambda)$ to produce a scattering signal of intensity:

$$I_s(\Omega_0, \lambda, m) = P_0 N L_s \int_0^\infty C_s(\Omega_0, \lambda, r, m) p(r) dr \quad (1)$$

where C_s is the differential scattering cross section integrated over the subtended solid angle Ω_0 of the detector at the polar and azimuthal scattering angles θ and φ, and L_s is the effective scattering length of the probe volume. The scattering probe volume is defined by the input and collection optics and it is sized to contain a sufficient number of particles for accurately representing the PSDF.

When the incident light beam of intensity I_0 passes through the particle field, it is attenuated by scattering and absorption effects and the transmitted beam exits with intensity $I(\lambda)$ according to the extinction equation:

$$I(\lambda) = I_0 \exp(-\tau) \quad (2)$$

The transmissivity of the medium, τ, is a measure of its optical depth and is defined by

$$\tau = N L_e \int_0^\infty C_e(\lambda, r, m) p(r) dr \quad (3)$$

where L_e is the path length of interaction and C_e is the extinction cross section. Through Eq. (3), the variation of the extinction cross section with λ dominates the variation of transmission with λ. That is, the determination of the size distribution $p(r)$ comes primarily from the variation of τ with λ.

For interaction of a planar electromagnetic wave with a spherical object, the scattering and extinction cross sections C_s and C_e are defined by classical Mie theory. Although the soot particles are in actuality nonspherical agglomerated fractal chains, Few et al. (1990) have demonstrated that the scattering and extinction characteristics of an ensemble of randomly oriented nonspherical absorbing particles are adequately approximated by Mie theory if the average particle size is sufficiently small and the Mie sphere diameter is chosen to have the same volume as the nonspherical particle according to the Purcell–Pennypacker scattering model. It is also known that the sensitivity of Mie-based techniques decreases as the particle diameter D decreases. Specifically, as the ratio $\pi D|m - 1|/\lambda$ becomes much less than unity, the size-specific information content of scattering and extinction data vanishes (Bohren and Huffman, 1983). This implies a lower limit for detectable particle diameters of about 0.02 μm. However, previous measurements using Diffusion Broadening Spectroscopy (DBS), which is known to have sufficient sensitivity for detecting particle diameters down to 0.005 μm, have indicated that the mean soot particle diameter is generally greater than 0.03 μm, thereby confirming the validity of Mie-based techniques for this application (Bernard, 1988; Petrovic, 1991). Detailed procedures for computing the Mie cross sections are described by Kerker (1969), Wiscombe (1979), and Bohren and Huffman (1983).

We now note that Eqs. (1) and (3) governing the multi-wavelength extinction and multi-angle scattering signals share the common form of a Fredholm integral equation of the first kind:

$$g(\alpha_i) = \int_0^{r_{\max}} K(\alpha_i, r) p(r) dr, \quad i = 1, 2, \ldots, n \quad (4)$$

where α_i denotes the set of n angles Ω_i or n wavelengths λ_i at which measured scattering or transmissivity signals $g(\alpha_i)$ are obtained. For simplicity, the theoretically unimportant parameters, such as laser power, have been suppressed and $r_{\max}$ represents the numerical cut-off radius of computation. The function $K(\alpha_i, r)$ is the kernel function, and recovery of the PSDF, $p(r)$, for particles of radius r requires the generally difficult deconvolution of Eq. (4). The Mie cross section in the kernel K is a strong function of particle diameter, and it has a wavelength dependence from two sources, the first being the particle-size parameter $x = 2\pi r/\lambda$, which is the argument of the Mie equations, and the second being the normally weaker dependence produced by the spectral variation of the index of refraction. In general, certain simplifying approximations can be invoked in the evaluation of K when x is much less than or much greater than unity. That is, approximations for K effect Fourier ($x \ll 1$) and Mellon ($x \gg 1$) transformations, thereby determining $p(r)$ (Shimizu and Ishimaru, 1990; Box and Viera, 1990). For general size parameters, however, Mie theory must be used for the evaluation of the kernels and the deconvolution. In this work, the Mie kernels were calculated with the Wiscombe

(1979) code, and a Gaussian quadrature was used for the numerical integration (Press et al., 1989).

Deconvolution algorithms for recovering $p(r)$ are generally based on a linear vector space representation of the Fredholm integral equation of the first kind

$$g(\alpha_i) = \sum_{j=1}^{m} K(\alpha_i, r_j)p(r_j), \quad i = 1, 2, \ldots, n \tag{5}$$

which may be written in matrix form as:

$$\mathbf{g} = \mathbf{K}\cdot\mathbf{p} \tag{6}$$

where $\mathbf{g}$ is an $n \times 1$ column matrix, $\mathbf{p}$ is an $m \times 1$ column matrix, and $\mathbf{K}$ is an $n \times m$ matrix, which may include numerical quadrature coefficients. Multiplying through by $\mathbf{K}^T$ and inverting yields the PSDF, $\mathbf{p} = (\mathbf{K}^T\mathbf{K})^{-1}\cdot\mathbf{K}^T\cdot\mathbf{g}$. Unfortunately, this linear inversion is subject to instability because of the ill-conditioned Mie kernels and because the kernels may exhibit linear dependence (Twomey, 1977; Jones et al., 1994). Given a finite measurement error ϵ, Twomey (1977) showed that the resulting error in $\mathbf{p}$ would be:

$$|\delta p(r)| = \sum_{i=1}^{n} \frac{\epsilon_i^2}{\lambda_i} \tag{7}$$

where λ_i is the ith eigenvalue of the covariance matrix defined by the product $\mathbf{KK}^T$. For relatively large off-diagonal terms, the eigenvalues can be extremely small and a finite measurement error $\boldsymbol{\epsilon}$ can lead to a large error in $\mathbf{p}$.

A promising alternative algorithm that avoids these numerical problems has been proposed by Sun and Lewis (1995). Their method poses a multi-parameter functional form $\mathbf{f}$ for the PSDF from which a trial data vector $\mathbf{t}$ is calculated as:

$$\mathbf{t} = \mathbf{K}\cdot\mathbf{f} \tag{8}$$

With the experimental data vector $\mathbf{g}_e = \mathbf{g} + \boldsymbol{\epsilon}$, which includes the measurement error, it then becomes possible to form the square difference χ^2 as:

$$\chi^2 = |\mathbf{t} - \mathbf{g}_e|^2 \tag{9}$$

The fitting parameter χ^2 is then minimized by adjusting the parameters of the assumed PSDF $\mathbf{f}$ where the minimization process is accomplished using the downhill simplex (DHS) method (Nelder and Mead, 1965; Press et al., 1989; Sun, 1994). The uncertainty of the DHS method was estimated to be (Sun and Lewis, 1995):

$$\langle(\mathbf{f} - \mathbf{p})^2\rangle \approx \langle\boldsymbol{\epsilon}^2\rangle \tag{10}$$

which compares well with the error estimate for the conventional unconstrained linear-inversion method, Eq. (7).

The simplest forms for $\mathbf{f}$ are one-parameter distribution functions such as the Gaussian, Rayleigh, or Boltzman distributions, but the more accepted practice is to use two-parameter forms such as the log-normal, gamma, or Weibull distributions. In this work, the soot particles of number density N_0 are characterized by a log-normal distribution with a mean diameter D_0 and a standard deviation V_0:

$$p(D = 2r) = \frac{1}{\sigma D\sqrt{2\pi}} \exp\left\{-\frac{1}{2\sigma^2}[\ln D - \mu]^2\right\} \tag{11}$$

where $\mu = \ln D_0 - \sigma^2/2$ and $\sigma^2 = \ln[1 + (V_0/D_0)^2]$. Note that the log-normal distribution is defined only for $D > 0$.

There remains some degree of uncertainty in the literature as to the appropriate index of refraction for soot. The most applicable data appear to be those reported by Dalzell and Sarofim (1969) and by Lee and Tien (1981). We have relied on both of these distinctly different indices of refraction throughout this work.

Accuracy and Precision Evaluations

Issues of accuracy and precision are important considerations for any diagnostic measurement, and quantitative measures of experimental error propagation are desirable. In this application, the major questions of import were:

(*a*) How do the ever-present experimental errors propagate through the deconvolution algorithm and affect the results of D_0, V_0, and N, and how precise must the data be to achieve the desired precision in the results?

(*b*) How does one best represent this uncertainty in the results to convey a measure of the confidence limits, or goodness, of the results?

(*c*) How does one predict the number and location of the α_i's, that is, the wavelengths and angles, that one should use to achieve the desired goodness of fit?

To address these issues, deconvolutions were performed with the downhill simplex algorithm using noise contaminated synthetic data for soot size particles. In this evaluation, the synthetic soot PSDF was contaminated with data errors obtained through Monte Carlo sampling of a Gaussian distribution having a predefined noise level. This provided a sample data set for determining the associated uncertainty in D_0, V_0, and N. With each set of sampled input data, multiple starting points were also used for the simplex deconvolution process, so that each deconvolved set of (D_0, V_0, N) would be characterized by uncertainty values. The repetition of this process yields probability distribution functions (pdf) for the predicted mean diameter, variance, and number density. Narrow pdf's imply precise deconvolutions. Figure 1 illustrates this numerical process.

The synthetic soot sample was defined by a log-normal distribution of mean diameter $D_0 = 0.05$ μm, standard deviation $V_0 = 0.02$ μm, and number density–path length product $NL = 1.1 \times 10^{10}$ cm^2. The simulated, or synthetic, input data were assumed to be provided by 17 wavelength extinction points and 7 angular scattering data points (located at the scattering angles of 4, 7, 15, 90, 160, 165, and 170 deg). Gaussian distributed experimental errors of 4, 6, and 10 percent were sampled to introduce measurement uncertainties into the synthetic data vector, and the resulting PSDF parameters D_0, V_0, and NL were determined for each sample using the downhill simplex deconvolution algorithm outlined in the previous section. The accumulated statistics yielded probability distribution functions (pdf) for the measurement uncertainty in the PSDF parameters.

Figures 2, 3, and 4 show the Gaussian fitted pdf results for D_0, V_0, and NL, respectively, with 4, 6, and 10 percent noise. It is noted from these figures that the downhill simplex deconvolutions predict the PSDF parameters with an inaccuracy of less

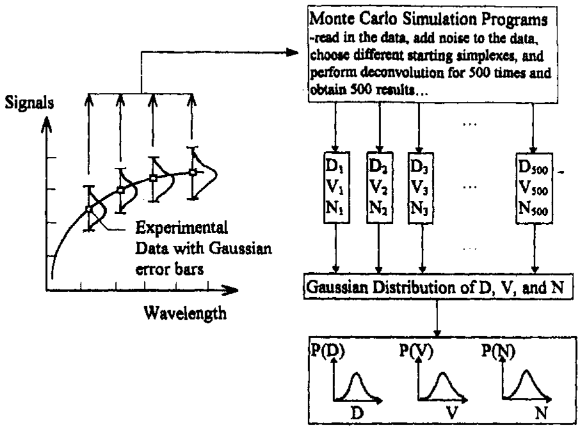

Fig. 1 Diagram illustrating the Monte Carlo numerical procedure for evaluating experimental error propagation through the downhill simplex deconvolution algorithm

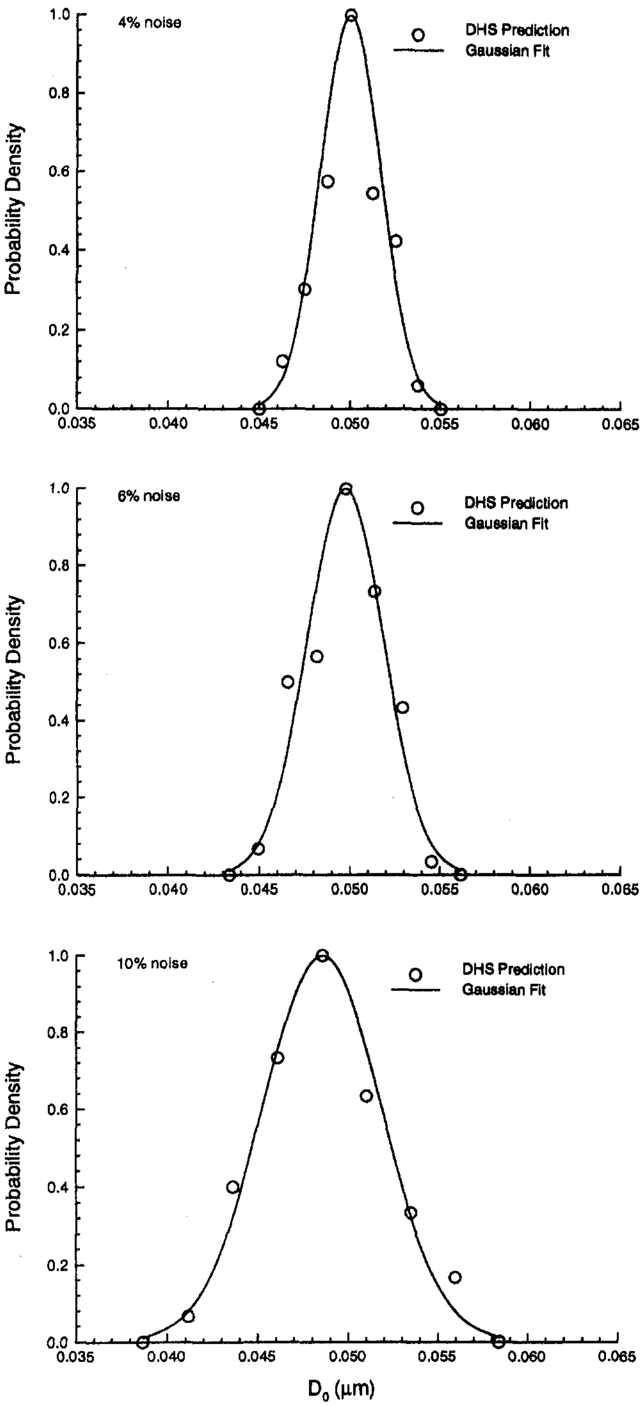

Fig. 2 Gaussian fitted pdf results for D_0 with 4, 6, and 10 percent experimental error

than 10 percent and with an imprecision that is equal to or less than the assumed level of experimental error. It was found in general that the nonlinear simplex approach was more tolerant of data channels with little information and plentiful noise than the commonly used constrained linear inversion techniques. This assertion is supported by further evaluations with an increased number (i.e., 10) of scattering angles in which we were unable to find any significant deviation in the results. That is, no additional information content was provided by an increase in the number of data inputs beyond the original configuration.

Deconvolutions of the synthetic extinction data for the distinctly different indices of refraction of Dalzell and Sarofim (1969) and Lee and Tien (1981) yielded only slight variations in the predicted PSDF parameters as indicated by the results of Table 1. This result may not be obtained for soot samples of smaller mean diameters because the ultraviolet (UV) wavelength region possesses more information content and assumes more importance than the visible region. The greatest differences in the index of refraction occur in the UV region and the general validity of the result given above is questionable.

Laboratory Burner Results

Multi-wavelength extinction data were acquired from a bench-top laboratory burner to support the development of the soot particle measurement diagnostic. In addition to measuring the PSDF parameters of the soot particle effluents, it was desired

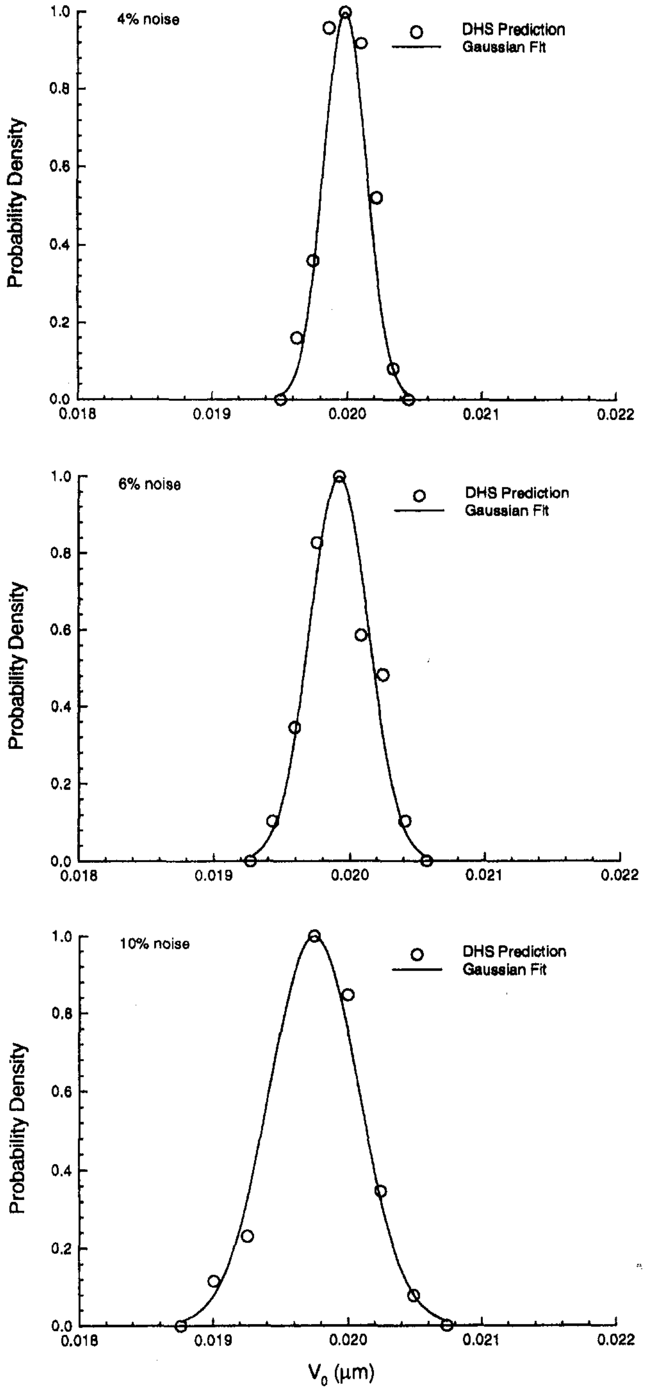

Fig. 3 Gaussian fitted pdf results for V_0 with 4, 6, and 10 percent experimental error

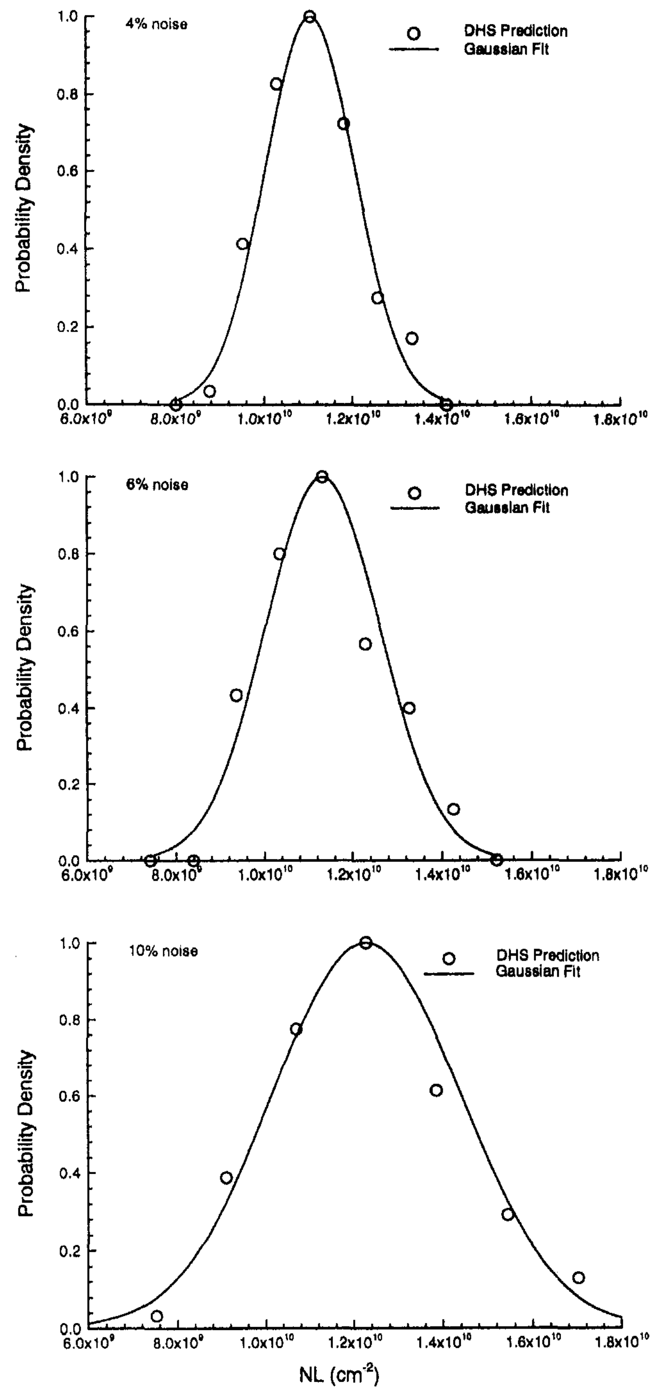

Fig. 4 Gaussian fitted pdf results for NL with 4, 6, and 10 percent experimental error

to determine whether organic vapor-phase molecules exhibit sufficient absorption to perturb PSDF measurements. Of particular interest was the UV region of $\lambda \leq 320$ nm where various organic species in fuel-rich flames are likely to exhibit absorption features.

The desired data were obtained from a laminar-flow CH_4/O_2 diffusion-flame produced by a Wolfhard–Parker burner. The burner was operated with a fuel/oxygen ratio of 0.413 and a linear flow speed of 35 cm/s. Absorption data were acquired using a 0.5 m focal length JACO spectrometer and a deuterium lamp source. The spectrometer grating was 1200 groove/mm and the unilateral, gaged entrance and exit slits were set at 400 μm. The effective bandpass of the instrument was 0.6 nm.

Table 1 Comparison of predicted log-normal PSDF parameters for the complex index of refraction data of Dalzell and Sarofim (1969) and Lee and Tien (1981). Calculations based on downhill simplex deconvolutions of noise-contaminated synthetic extinction data.

Index of Refraction	Dalzell and Sarofim (1969)			Lee and Tien (1981)		
PSDF Parameter	$\langle D_0 \rangle$ (μm)	$\langle V_0 \rangle$ (μm)	$\langle NL \rangle$ (cm^{-2})	$\langle D_0 \rangle$ (μm)	$\langle V_0 \rangle$ (μm)	$\langle NL \rangle$ (cm^{-2})
4% Noise	4.9406×10^{-2}	1.9957×10^{-2}	1.1424×10^{10}	4.9509×10^{-2}	1.9964×10^{-2}	1.1357×10^{10}
6% Noise	4.9347×10^{-2}	1.9908×10^{-2}	1.1603×10^{10}	4.9042×10^{-2}	1.9935×10^{-2}	1.1699×10^{10}
10% Noise	5.0806×10^{-2}	2.0025×10^{-2}	1.0633×10^{10}	5.0048×10^{-2}	1.9971×10^{-2}	1.1329×10^{10}

Data were acquired over the wavelength range of 200–450 nm, and no significant features of molecular absorption were noted that would place realistic limits on the use of this technique to determine the PSDF. We also concluded that such flame sources would be suitable for supporting the future development of these optical-based measurement diagnostics. A downhill simplex fit to the multi-wavelength extinction data, as shown in Fig. 5, yielded the following log-normal PSDF parameters: $D_0 = 0.039$ μm, $V_0 = 0.008$ μm, and $N = 3.2 \times 10^9$ cm^{-3}. The scatter in the data is due to insufficient averaging. The predicted log-normal PSDF is shown in Fig. 6.

Field Test Results

A field test demonstration for combined multi-wavelength extinction and multi-angle scattering measurements using the downhill simplex deconvolution algorithm was conducted in the engine exhaust plume of a Sabre Liner jet aircraft. Each of the aircraft's twin JT-12D engines is rated at 3000 lb of thrust with an exhaust duct exit diameter of 33 cm (13 in.). This engine was previously investigated in 1992 using only multi-wavelength extinction measurements, yielding a mean soot particle diameter of approximately 0.04 μm and a particulate loading of 15.4 mg/SCM. The experimental configuration for the scattering and extinction measurements reported in this work is shown in Fig. 7.

The scattering system projects a mechanically chopped argon-ion laser beam (25 mW @ 546 nm) through the plume cross section, and the scattering signals are collected by photomultiplier tube (PMT) optical detectors located at various forward and backward scattering angles. In this field test, seven scattering detectors were located at 4, 7, 15, 90, 160, 165, and 170 deg with respect to the beam path. All scattering detectors lie on a common radius, and they are apertured to focus on a common probe volume at the center of the plume. The detector

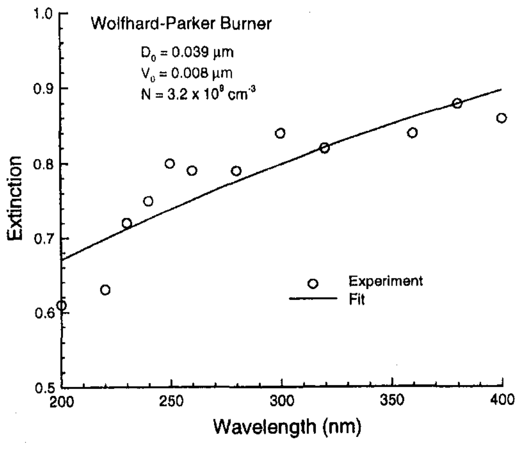

Fig. 5 Downhill simplex fit to the multi-wavelength extinction data for the Wolfhard–Parker laboratory burner. The experimentally acquired spectrums were ensemble-averaged at each selected wavelength of the fit.

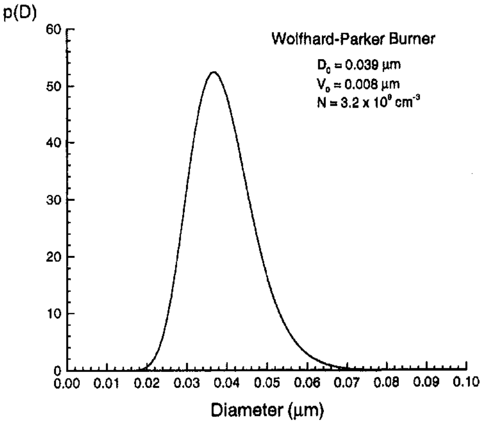

Fig. 6 Predicted log-normal PSDF for the Wolfhard–Parker laboratory burner flame

signals are phase-locked to the optical chopper frequency to improve the signal-to-noise ratio, and the signals are recorded on a remote PC-based data acquisition system. The multi-wavelength extinction system uses a deuterium lamp as a UV radiation source, and it is collimated and passed through the engine exhaust stream. This beam was folded and passed through the exhaust plume five times in order to achieve the required level of sensitivity. The beam is then collected in a fiber optic coupling, which is connected to an array detector spectrometer having the same configuration used in the laboratory experiments. Spectroscopic data are acquired over a wavelength interval of 250 to 500 nm with an Optical Multichannel Analyzer (OMA) and stored for analysis. The optical plane of interrogation is located at a plume cross section 16 cm downstream from the exhaust duct exit.

The geometry of the collection optics for the scattering signals is illustrated in Fig. 8. The detectors use optical collection lenses having the same focal length and magnification ratio at all angles, and different aperture sizes are required so that each detector sees the same scattering probe volume. Given a scattering probe length L_s we know that the projected probe length at the angle α is defined by $L_s \sin(\alpha)$. Thus, for a constant magnification ratio β, the aperture slit width δ along the beam's length can be determined for any angle from the relation:

$$\frac{\delta}{L_s \sin(\alpha)} = \frac{1}{\beta} \tag{12}$$

The length of the slit in a direction perpendicular to the beam is fixed at a value larger than the beam diameter. Using a slit width of 0.5 mm at a scattering angle of 4 deg and a magnification ratio of 2.7 yields the scattering length for this experiment as $L_s = (0.5\ \text{mm})\,(2.7)/\sin(4\ \text{deg}) = 19.35$ mm. The slit widths for all other angles are now determined from Eq. (12) holding L_s and β constant. In these experiments, the laser beam was polarized perpendicular to the detector plane to simplify definition of the Mie scattering kernels.

The experimental results reported here are for engine idle conditions only. Attempts to make measurements at midpower and full-power conditions were not successful due to excessive vibration in the optical support structure. Based on our experiences, we believe that acoustically driven vibrations can cause severe perturbations in the optical-based measurements and that considerable effort will be required to develop a suitable support structure for a practical instrumentation system.

Examples of the downhill simplex fitted scattering and extinction data are shown in Figs. 9 and 10, respectively. The downhill simplex deconvolution results for the log-normal PSDF parameters were as follows: $D_0 = 0.040\ \mu$m and $V_0 = 0.032\ \mu$m for scattering data; $D_0 = 0.036\ \mu$m and $V_0 = 0.001\ \mu$m for extinction data. The extinction data also yielded a soot particle number density of $N = 3.5 \times 10^8\ \text{cm}^{-3}$. The volumetric fraction of particulates, f_V, was converted to a mass loading of the plume, $m = \rho_s v A f_V$, where ρ_s is the density of soot, v is the exhaust velocity of the engine, and A is the cross-sectional area of the plume. The total particulate mass flow rate from the engine at

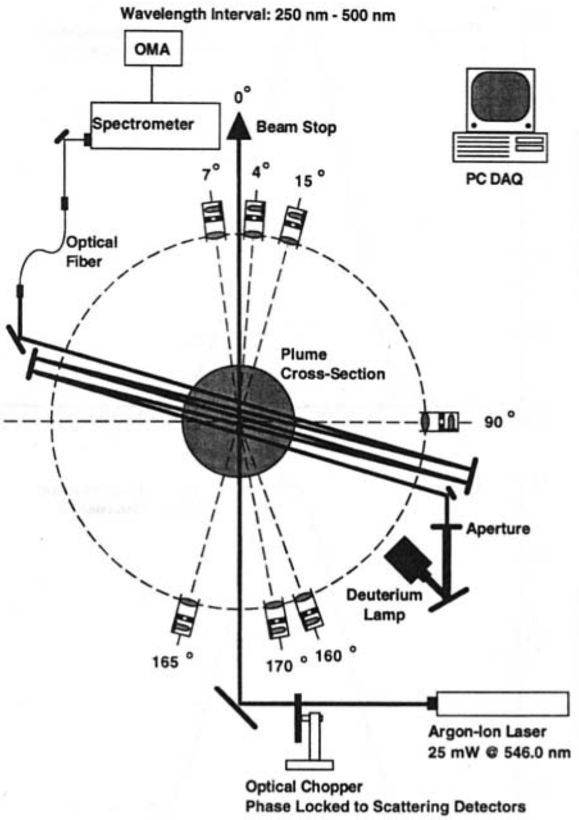

Fig. 7 Field test experimental configuration for combined scattering and extinction measurements in the exhaust plume of a JT-12D jet aircraft engine

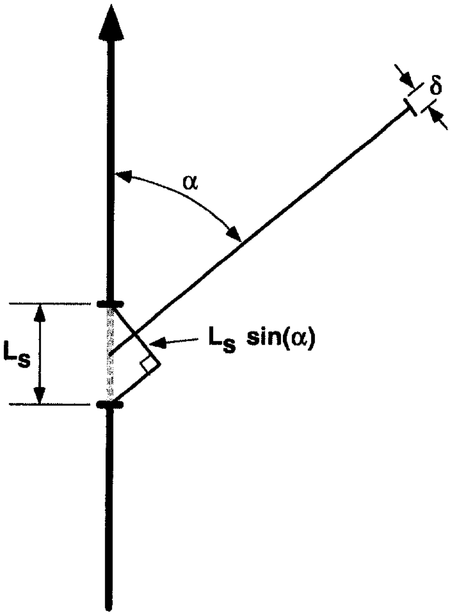

Fig. 8 Diagram illustrating the collection optics geometry for the scattering detectors

idle was estimated to be 0.54 kg/h. The agreement for the mean soot particle diameter is acceptable, but the scattering measurements indicate a broader distribution in particle sizes than that implied from the extinction measurements. Our preference is for the extinction results. We believe that the discrepancy may be due to the different probe volumes of the two techniques. Unless the soot size distribution and number density are homogeneous across the entire plume, one should not expect the size distributions to match. In addition, part of the discrepancy may be attributed to our inability to maintain good optical alignment in the high-intensity acoustical cone of the engine exhaust plume. We encountered particular difficulty with acoustically induced vibration of the collection optics for the small angle scattering detectors.

Conclusions

The research and development work reported in this paper was directed at the resolution of technical feasibility issues associated with optical-based measurement of soot particle effluents from gas turbine engines. This was accomplished through computer simulations, bench-top laboratory tests, and a field test on a jet aircraft engine exhaust. The field test was conducted with general purpose research equipment and instrumentation to provide a preliminary demonstration of an innovative particle measurement technology under practical conditions. The results of this work are summarized as follows:

1. No more than 17 wavelength extinction points and 7 angular scattering angles are needed to approach the maximum accuracy and precision of the downhill simplex deconvolution algorithm.
2. Deconvolution results using distinctly different indices of refraction from Dalzell and Sarofim (1969) and Lee and Tien (1981) for soot yielded only slight variations in the log normal PSDF parameters; however, this result may not be valid for particles with very small mean diameter. In this case, the ultraviolet (UV) wavelength range possesses more information content and assumes more importance.
3. Experiments using a bench-top laboratory flame indicated that absorption by vapor-phase organic molecules will not significantly perturb PSDF measurements and that such flame sources are suitable for supporting future activities related to development of an integrated instrumentation system.
4. Demonstration field tests were successfully conducted on a Sabre Liner JT-12D jet aircraft engine. Preliminary analysis of the data yielded acceptable agreement between the scattering and extinction measurements. The total particulate mass flow rate from the engine at idle was measured to be 0.54 kg/h.

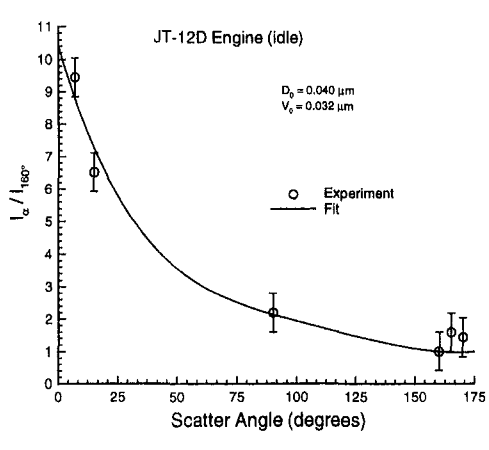

Fig. 9 Downhill simplex fit to the multi-angle scattering data in the JT-12D engine exhaust plume. Experimental signals were time-averaged at each detector position and then normalized by the signal intensity measured at a scattering angle of 160 deg.

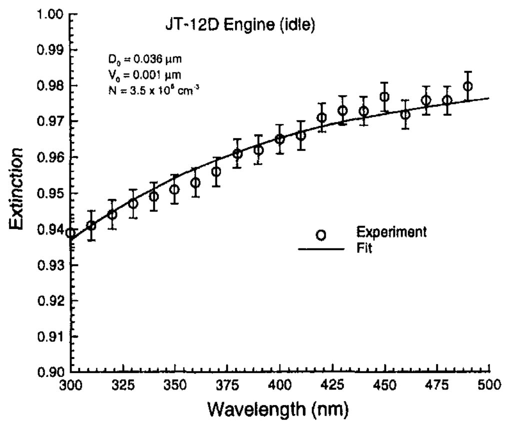

Fig. 10 Downhill simplex fit to the multi-wavelength extinction data in the JT-12D engine exhaust plume. The experimentally acquired spectrums were ensemble-averaged at each selected wavelength of the fit.

5. The field test demonstrated that acoustically driven vibrations of the optical support structure can cause severe perturbations in the measurement results. Thus, controlling and damping these vibrations is a critical development issue with respect to the practical implementation of this technology.
6. Increased particulate information can be obtained through the combined application of scattering and extinction optical probing techniques. Furthermore, the ensemble measurement approach offers a considerable improvement in speed over intrusive probe point measurements with the possibility of near real-time analysis as compared to conventional post-test analysis.
7. Because the mean particle diameter is so close to the lower limit of detection of the scattering and extinction measurement methods, it would be advantageous to extend the dynamic range of the total instrumentation system by including a diffusion broadening spectroscopy module. This would permit detection of soot particle diameters down to 0.005 μm and improve resolution of the PSDF low-end tail.

Acknowledgments

This work was supported by the U.S. Navy Small Business Innovation Research (SBIR) program, Aircraft Environmental Support Office, Naval Air Station, San Diego, CA under Contract No. N00244-95-C-5528 to ERC Incorporated, Tullahoma, TN (Contract Monitor: Mr. Everett L. Douglas).

References

Bernard, J. M., 1988, "Particle Sizing in Combustion Systems Using Scattered Laser Light," *Journal of Quantitative Spectroscopy and Radiative Transfer,* Vol. 40, pp. 321–330.

Bohren, C. F., and Huffman, D. R., 1983, *Absorption and Scattering of Light by Small Particles,* Wiley, New York.

Box, M. A., and Viera, G., 1990, "Information-Content Analysis of Aureole Inversion Methods: Differential Kernel Versus Normal," *Journal of the Optical Society of America A,* Vol. 7, pp. 1015–1018.

Dalzell, W. H., and Sarofim, A. F., 1969, "Optical Constants of Soot and Their Application to Heat Flux Calculation," ASME *Journal of Heat Transfer,* Vol. 91, pp. 100–104.

Few, J. D., Lewis, J. W. L., and Hornkohl, J. O., 1990, "Measurement and Prediction of Jet Engine Effluents," Report No. NAPC-PE-195C, Naval Air Propulsion Center, Trenton, NJ.

Jones, M. R., Curry, B. P., Brewster, M. Q., and Leong, K. H., 1994, "Inversion of Light-Scattering Measurements for Particle Size and Optical Constants: Theoretical Study," *Applied Optics,* Vol. 33, pp. 4025–4034.

Kerker, M., 1969, *The Scattering of Light and Other Electromagnetic Radiation,* Academic, New York.

Lee, S. C., and Tien, C. L., 1981, "Optical Constants of Soot in Hydrocarbon Flames," *Proc. 18th Symposium (International) on Combustion,* The Combustion Institute.

Nelder, J. A., and Mead, R., 1965, "A Simplex Method for Function Minimization," *Journal of Computation,* Vol. 7, pp. 308–313.

Petrovic, D., 1991, "Optical Determination of Hydrocarbon Particle Sizes Produced by Pyrolysis of Acetylene," Ph.D. Dissertation, Department of Physics, University of Tennessee, Knoxville, TN.

Press, W. H., Flannery, B. P., and Teukolsky, S. A., 1989, *Numerical Recipes,* Cambridge University Press, Cambridge.

Shimizu, K., and Ishimaru, A., 1990, "Differential Fourier Transform Technique for the Inversion Scattering Problem," *Applied Optics,* Vol. 29, pp. 3428–3433.

Sun, F., 1994, "Optical Measurement of Particle Size Distribution Function Using Downhill Simplex Method: Theory and Experiment," Ph.D. Dissertation, Department of Physics, University of Tennessee, Knoxville, TN.

Sun, F., and Lewis, J. W. L., 1995, "Simplex Deconvolutions of Particle-Size Distribution Functions From Optical Measurements," *Applied Optics,* Vol. 34, pp. 8437–8446.

Twomey, S., 1977, *Introduction to the Mathematics of Inversion in Remote Sensing and Indirect Measurements,* American Elsevier, New York.

Van der Hulst, H. C., 1957, *Light Scattering by Small Particles,* Wiley, New York.

Wiscombe, W. J., 1979, "Mie Scattering Calculation; Advanced in Technique and Fast Vector-Speed Computer Codes," NCAR Technical Note NCAR/TN-140+STR, National Center for Atmospheric Research, Boulder, CO.

M. Kurreck

M. Willmann

S. Wittig

Lehrstuhl und Institut für Thermische
Strömungsmaschinen,
Universität Karlsruhe (T.H.),
Karlsruhe, Federal Republic of Germany

Prediction of the Three-Dimensional Reacting Two-Phase Flow Within a Jet-Stabilized Combustor

Numerical calculations of the two-phase flow in an experimentally well-investigated research combustor are presented. The comparison between measurements and calculations demonstrates the capabilities of the state-of-the-art Euler/Lagrange method for calculating two-phase flows, when applied to a complex reacting liquid-fueled combustor. The governing equations for gaseous and liquid phase are presented, with special emphasis on the control of the coupling process between the two phases. The relaxation method employed, together with a convergence history, shows a suitable way to achieve a fast and accurate solution for the strongly coupled two-phase flow under investigation. Furthermore, methods are presented to simulate the stochastic behavior of the atomization process caused by an air-blast atomizer. In addition to the numerical methods, experimental techniques are presented that deliver detailed information about droplet starting conditions.

Introduction

High efficiency–low emission combustor development requires a detailed knowledge about the physical phenomena taking place in evaporating, reacting fuel sprays. Numerical methods give a closer insight into the mechanisms of spray propagation and evaporation and therefore serve as an important tool for the design of gas turbine combustors.

The Euler/Lagrangian Method for calculating two-phase flows in combustors has been well known for several years (Gosman and Ioannides, 1983), and improved by several authors (Kneer et al., 1993; Milojevic, 1990). Nevertheless, due to the enormous expenditure, only few detailed comparisons between measurements and calculations for complex combustor flows are found in literature. At the Institut für Thermische Strömungsmaschinen (ITS) at Karlsruhe University, a three-dimensional combustor flow was investigated in detail recently (Bauer et al., 1995; Koch et al., 1994; Jeckel and Wittig, 1993; Jeckel et al., 1992; Kurreck et al., 1993). This research combustor was fired alternatively with gaseous propane or liquid diesel oil. In this paper the liquid-fueled case was selected as a test case for the validation of a two-phase flow simulation code developed at the ITS. In addition to the comparison between measurements and calculations, a method is presented to achieve a fast and accurate solution for complex, strongly coupled two-phase flows in gas turbine combustors.

Numerical Method

Gaseous Phase. Three-dimensional turbulent flows are governed by the set of continuity equations, the Navier–Stokes equations, and the two transport equations of the k–ϵ turbulence model (Launder and Spalding, 1974). The heat release is described by the "eddy-dissipation" concept (Magnussen and Hjertager, 1977). Therefore, two additional transport equations for fuel and oxidizer have to be solved. Temperature distribution is deduced from the enthalpy field, also solved from a transport equation. Density is calculated by an equation of state for an ideal mixture. All the transport equations formulated in cylindrical coordinates can be written in the following form:

$$\mathrm{div}(\rho\vec{c}\phi) = \mathrm{div}(\Gamma_\phi \cdot \mathrm{grad}\phi) + S_\phi . \qquad (1)$$

Γ_ϕ is an effective diffusion coefficient and S_ϕ denotes the source term.

The transport equations are discretized by the finite-volume method. Therefore, the computational domain is subdivided into a number of control volumes. The diffusive fluxes and the source terms are discretized by the central-difference scheme. In contrast, a second-order bounded scheme called Monotonized Linear Upwind (MLU) is applied for the discretization of the convective fluxes (Noll, 1992). This scheme is introduced via the well-known "deferred correction" approach. Boundedness of the high-order scheme is essential in order to avoid negative values for the species concentrations.

Pressure field is determined by the SIMPLEC pressure correction algorithm on nonstaggered grids (Van Doormal and Raithby, 1984). Septdiagonal matrices for all transport equations arise:

$$a_P\phi_P = \sum_{ab} a_{ab}\phi_{ab} + S_\phi \quad nb = E, W, N, S, H, L \qquad (2)$$

The linear systems of algebraic equations are solved by iterative conjugate gradient solvers (Noll and Wittig, 1991). The solution steps within the solver are called inner iterations. Outer iterations are performed in order to take into account the nonlinearity of the equations.

Liquid Phase. A Lagrangian approach is used to describe the turbulent flow of the liquid droplet phase. From a balance of momentum and heat and mass transfer at the surface of single droplets the ordinary differential equations for position, velocity, diameter, and temperature are obtained. For turbulence modeling the eddy-life time concept is applied, where lifetime,

---

Contributed by the International Gas Turbine Institute and presented at the 41st International Gas Turbine and Aeroengine Congress and Exhibition, Birmingham, United Kingdom, June 10–13, 1996. Manuscript received at ASME Headquarters February 1996. Paper No. 96-GT-468. Associate Technical Editor: J. N. Shinn.

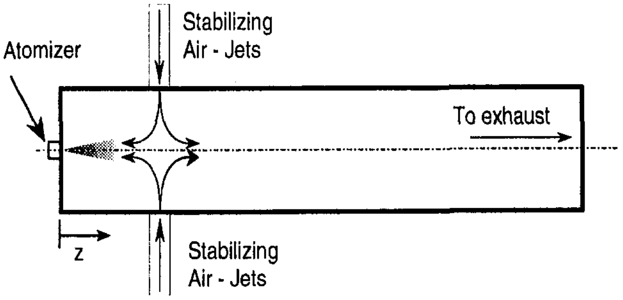

Fig. 1 Research combustor configuration

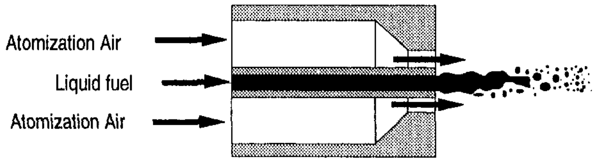

Fig. 2 Air-blast atomizer

extension, and velocity of single eddies are determined from local values for k and ϵ of the gas phase turbulence model (Gosman and Ioannides, 1983). Single droplets interact with these randomly produced eddies and by averaging several droplet trajectories, the solution for the liquid phase is obtained. Applying this method, three-dimensional turbulent dispersion is calculated in the 45 deg segment grid used for the gas phase calculation (Fig. 1). The well-known uniform temperature model is used to calculate droplet evaporation. Based on the assumption of fast mixing inside the droplet, the transport of heat and mass inside the droplet is neglected. A single component fuel is used instead of the experimentally employed multicomponent diesel oil. This substitute has typical data close to tetradecane. In comparison to the more complex approaches of Kneer et al. (1993), reasonable results can be obtained from this model in adequate calculation time.

Coupling of the Phases. For the prediction of coupled two-phase flows with an Eulerian/Lagrangian approach, each of the phases is calculated alternatively. The phases are coupled via an exchange of mass, momentum, enthalpy, and turbulence. In this study the repercussion of the droplets on the turbulence field of the gaseous phase was not taken into account.

The influence of the gaseous phase on the droplets is considered by using local gas phase data when tracking single particles through the flow field. As far as the interaction between droplets and gaseous phase is concerned, the source terms calculated by the liquid phase part are included in the right-hand side of the algebraic transport equations. First of all the vapor source is introduced in the pressure correction equation and the transport equation of the fuel:

$$a_P p'_P = \sum_{nb} a_{nb} p'_{nb} + S_{p'} + C_{vp} \qquad (3)$$

$$a_P Y_{f,P} = \sum_{nb} a_{nb} Y_{f,nb} + S_{Y_f} + C_{vp} \qquad (4)$$

The loss or gain of momentum is taken into account in the momentum equations as:

$$a_P \phi_P = \sum_{nb} a_{nb} \phi_{nb} + S_\phi + C_\phi \quad \phi = u, v, w \qquad (5)$$

Finally the phases are coupled via an exchange of enthalpy:

$$a_P h_P = \sum_{nb} a_{nb} h_{nb} + C_h \qquad (6)$$

With the exception of the pressure correction equation, the coefficients a_p are corrected with the additional source term of the continuity equation:

$$a_P = \sum_{nb} a_{nb} - S'_\phi + C_{vp} \qquad (7)$$

Due to the strong coupling of both phases considering evaporating sprays and flows with heat release, the source terms have to be relaxed. Otherwise the strong influence of the sources and sinks leads to divergence of the overall process.

The relaxation is done in the following way:

$$C_\psi = \alpha_\psi \cdot C_\psi^N + (1 - \alpha_\psi) \cdot C_\psi^0 \quad \psi = vp, u, v, w, h \qquad (8)$$

C_ψ^N denotes the source term of the last droplet calculation and C_ψ^0 is the relaxed source term applied for the last prediction of the gaseous phase. The relaxation factor α_ψ is chosen between zero and one. While the gaseous phase is solved, the droplet source terms are held constant.

Due to the completely different frames of reference, two separate codes for gaseous and liquid phase have been developed. The data exchange between both programs is done with external files. In summary, the solution strategy including the most important steps is as follows:

1 Calculate the gaseous phase without droplet source terms
2 Calculate the liquid phase and the source terms
3 Repeat step 1 including the droplet sources
4 Repetition of steps 3 and 2 until convergence is achieved

Boundary Conditions. Gaseous phase boundary conditions are obtained from detailed experimental results documented in Bauer et al. (1995). For the liquid phase it is of essential importance, especially for the atmospheric case, to select suitable droplet starting conditions, since the solution of

Nomenclature

a = transport coefficient
$\vec{c}$ = velocity, m/s
C_ϕ = source term
$D_{10\%}$, $D_{50\%}$, $D_{90\%}$ = char. diameters (vol. based), μm
$\dot{m}_{\text{air nozzle}}$ = atomizer air mass flow, kg/h
$\dot{m}_{\text{air jet}}$ = jet air mass flow, kg/h
$\dot{m}_{\text{fuel}}$ = fuel mass flow, kg/h
N_{CI} =number of coupling itererations
p = pressure, Pa
r = radial coordinate, mm
S_ϕ = source term
S'_ϕ = linearized part of S_ϕ
T = temperature, K
v = radial velocity, m/s
w = axial velocity, m/s
Y = mass fraction
z = axial position, mm
α = relaxation factor
ρ = density, kg/m^3
ϕ = transport variable
Γ_ϕ = effective diffusion coefficient
E, W, N, S, H, L = east, west, north, south, high, low
f = fuel
h = enthalpy
nb = neighbor
O, N = old, new
P = point
vp = vapor

Table 1 Combustor operating conditions

Secondary air (Four Jets)	
$\dot{m}_{air\ jet}$	32.3 kg/h
Atomization air	
$\dot{m}_{air\ nozzle}$	1.2 kg/h
Liquid fuel	
$\dot{m}_{fuel}$	1.0 kg/h

the calculation is strongly influenced by these values. In order to come up with the random process of atomization of the employed type of atomizer, a Monte-Carlo simulation has to be applied for starting position and starting velocity. Adequate modeling of the atomization process is very time consuming and with reasonable accuracy for a technical application currently not available. Therefore, it is of essential importance to obtain all information about droplet diameter spectrum, starting position, starting velocities, and temperatures from experimental data.

Results

Experimental Setup. The research combustor under investigation has a tubular design with an inner diameter of 80 mm. The flame is stabilized in the front part of the combustor by four perpendicular arranged air jets at a plane 60 mm downstream the combustor head as shown in Fig. 1. The total length of the tubular test section is more than ten times of tube diameter in order to avoid disturbances from downstream flow.

The combustor casing has a modular design, allowing to put in window flanches, temperature or pressure probe holders or quartz-glass tube units, which gives the possibility to employ all necessary combustion diagnostic techniques.

The air-blast atomizer shown in Fig. 2 is fixed in the center of the combustor head. High-velocity atomization air is used to desintegrate the liquid core in the center of the atomizer. The ring channel for the atomization air has an outer diameter of 3.0 mm and an inner diameter of 1.0 mm; the liquid fuel supply has a diameter of 0.7 mm.

Operating conditions of the combustor are listed in Table 1. Jets, atomizer air, and liquid fuel are measured by temperature and pressure-controlled rotameter.

Starting Conditions for the Liquid Phase. Two different techniques are applied to obtain suitable starting conditions for the droplet phase calculation. In the first step visualization of the atomization process gives details about droplet starting conditions such as liquid ligament length or radial extension close to the atomizer.

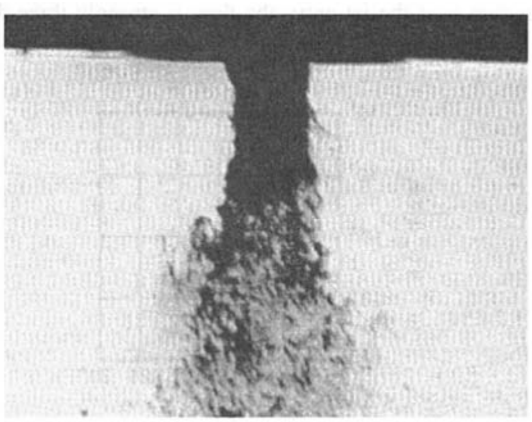

Fig. 3 Visualization of atomization process (frame 6 × 4.5 mm)

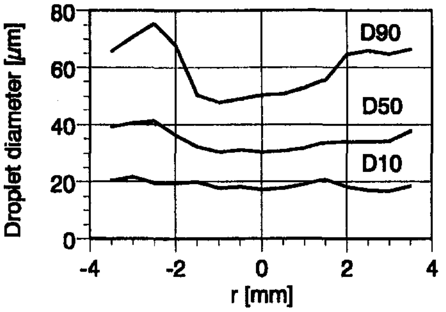

Fig. 4 Droplet diameter distribution (z = 11 mm)

The two-phase flow visualization in Fig. 3 achieved by flash-light shadowgraphy clearly shows the disintegration process of the liquid core. This core penetrates into the gas flow up to a length of about 1.5 mm, until it is desintegrated by the surrounding high-velocity air flow.

Since phase-Doppler particle sizing is based on the presence of spherical droplets, measurements can only be taken in a certain distance from this liquid core breakdown. Therefore, first, detailed measurements, which are shown in the following, were taken at a distance of z = 11 mm.

The measured droplet diameter distributions in Fig. 4 clearly indicate typical effects observed in atmospheric sprays. The main core of the spray shows a uniform radial droplet size distribution with typical values for $D_{10\%}$ of 20 μm, $D_{50\%}$ of 32 μm, and $D_{90\%}$ of 50 μm. At the spray edges an increase of droplet size is observed, which is typical for atmospheric sprays, where large droplets leave the core flow due to their inertia and in difference to the smaller droplets do not follow the main gas flow.

The mean axial droplet velocities for different droplet size classes in Fig. 5 confirm the observed behavior. In the core region small droplets are strongly accelerated by the gaseous phase, where larger droplets show a lower axial velocity due to their inertia. In the outer range, on the other hand, the larger droplets show higher axial velocities, since they are accelerated in the core flow, and in difference to the smaller droplets are not decelerated by the surrounding gas of low velocity.

The measured droplet radial velocities in Fig. 6 show the radial dispersion of the spray and indicate, that especially the large droplets show high radial components in the outer spray range due to their typical bullet-like behavior.

A very important value for the spray characterization is the droplet volume flux shown in Fig. 7. The figure clearly indicates that the main droplet volume can be observed on the atomizer axis. The spray cone at the measured axial position shows an outer radius of about 3 mm, with a strong decrease in volume flux to the spray edges.

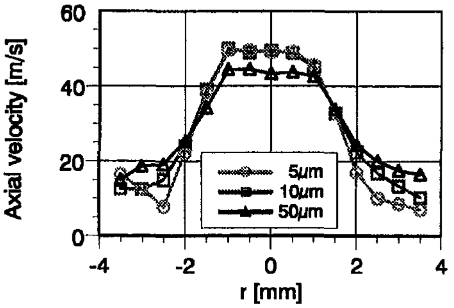

Fig. 5 Mean axial droplet velocity (z = 11 mm)

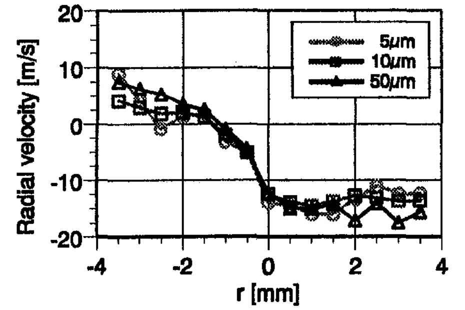

Fig. 6 Mean radial droplet velocity (z = 11 mm)

Table 2 Spray boundary conditions

Diameter distribution	$D_{10\%} = 20\mu m$, $D_{50\%} = 32\mu m$, $D_{90\%} = 50\mu m$
Axial starting velocity	w = 10 m/s ± 0.5 m/s
Radial starting velocity	v = 0 m/s ± 0.5 m/s
Axial starting position	z = 1.5 mm ± 0.5 mm
Radial starting position	r = 0 mm ± 0.5 mm

From the results of these experimental investigations boundary conditions for the spray simulation can be obtained. These droplet starting conditions were found in an iterative process using the measurements at the z = 11 mm downstream location as reference.

The axial starting position for the droplets is fixed by a constant distribution in the range of 1 to 2 mm behind the atomizer exit, as a result from visualization. Also as a result from Figs. 3 and 7 the radial starting position is obtained from a Gaussian normal distribution with a mean value of r = 0 mm and a standard deviation of r_{RMS} = 0.5 mm. The diameter distribution of the spray is taken from the core measurements, since the main droplet volume flux is observed there. Spray edge effects observed in the measurements are not simulated explicitly, but result from calculations with the selected boundary conditions. Droplet starting velocities are obtained from a comparison and adjustment between measurements and calculations at the measured downstream position.

Convergence Analysis. In this subsection, an analysis of the convergence history of the overall solution process is presented. The prediction of strongly coupled two-phase flows requires the convergence of each phase and of the coupling process itself. Because of the fact that no general convergence criteria, either for single phase or for two-phase flows, are known until now, the following variables are considered: the changes of the droplet source terms C_i and of the gaseous phase variables between two subsequent coupling iterations. For the prediction of the two-phase flow within the combustion chamber, 25 coupling iterations were performed. Each coupling iteration consisted of about 800 outer iterations for the gaseous phase and the tracking of 14,000 droplet trajectories.

The changes of the vapor concentration source term versus the number of coupling iterations are presented first in order to demonstrate the convergence history. These values are very sensitive to convergence because they are additionaly influenced by the exchange of momentum and heat. The vapor concentration is determined by the trajectories of the droplets driven by the velocity and the turbulence field of the gaseous phase. Furthermore, vapor concentration is influenced by the temperature field. In Fig. 8 the normalized changes versus the number of coupling iterations are shown.

For the first coupling iteration a strong overshoot can be found. This is caused by the evaporation of the droplets in the vicinity of the atomizer for the first two coupling iterations. Because of fuel-rich conditions, no combustion takes place, and therefore the droplets erroneously grow due to condensation of the gaseous fuel. This condensation process leads to large negative vapor source terms within the third coupling iteration. After 15 coupling iterations, the changes of the vapour source terms remain constant at a level of approximately 6×10^{-3}.

Figure 10 shows the gaseous phase temperature T and the axial velocity w versus the number of coupling iterations at two significant positions within the chamber. First position $P1$ ($z = 0.02$; $r = 0.02$) is located in the main reaction zone and the second position $P2$ ($z = 0.5$; $r = 0.02$) is chosen at the combustor exit. Both variables reach their final level for both locations after ten coupling iterations and show only small deviations after 25 coupling iterations.

Finally, the relative changes of the temperature between the 24th and the 25th coupling iteration in the plane $\varphi = 0$ deg are displayed in Fig. 9. In most parts of the plane the changes are smaller than 5 percent. Only in the vicinity of the atomizer values of 10 percent can be found. In this region the spray is very dense. Therefore, large gradients in the source term distributions occur. These gradients are slightly shifted in space from one coupling iteration to another due to the statistical way of predicting the liquid phase. This leads to the relatively large changes of the temperature.

The results of the convergence analysis clearly indicate that the solution can be considered to be convergent with an engineering accuracy. Except for the region near the atomizer the changes of the variables between two subsequent coupling iterations are comparatively small. Therefore, it can be concluded that 25 coupling iterations are sufficient for that test case.

Comparison of Numerical and Experimental Data. In the region near the jet entry the flow is strongly three-dimensional. In contrast to this, upstream and downstream of this

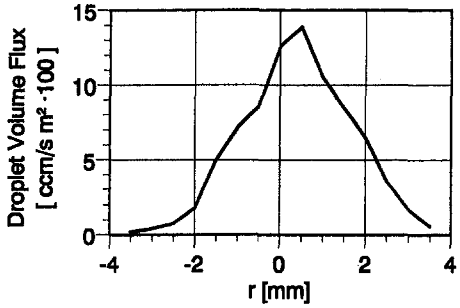

Fig. 7 Particle volume flux (z = 11 mm)

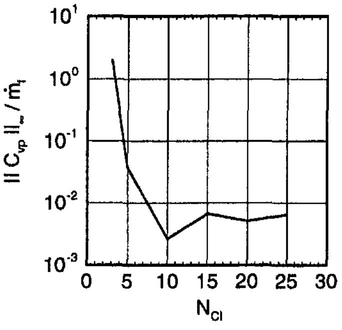

Fig. 8 Normalized changes of vapor source terms

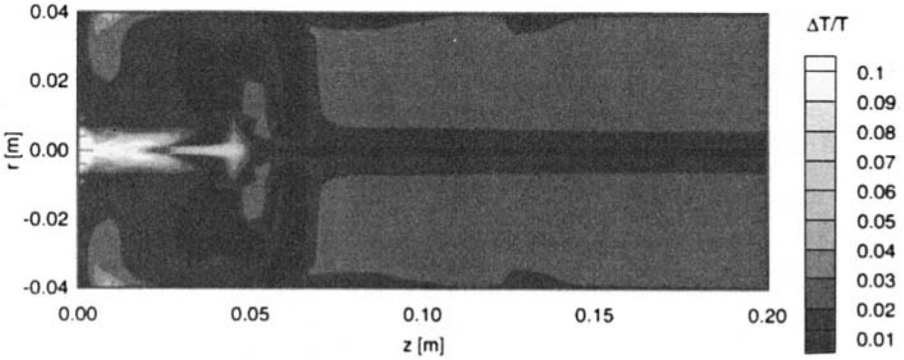

Fig. 9 Relative changes of temperature (φ = 0 deg)

plane, the flow structure does not strongly depend on the circumferential position. This is due to the large amount of turbulence produced. Therefore, the results are shown and compared in the plane $\varphi = 0$ deg.

The velocity distribution predicted is shown in Fig. 11. In radial direction every second velocity vector is skipped. The jets subdivide the flow in the chamber into two parts: the main reaction zone where the flame is stabilized and the region downstream of the jet entry. In the stabilization region a toroidal recirculation zone is established. Because of high velocity the air flow of the atomizer influences the flow to the axial position where the jets enter the chamber. The axial velocity decay of the air fuel mixture along the axis of the combustor in the region between the atomizer and the jet entry is in good qualitative agreement with the theoretical data given by Abramovich (1964). At an axial position two diameters downstream of the jet inlet the flow becomes uniform and parabolic. As it can be seen from the temperature distribution (cf. Fig. 12) the highest values of about 2200 K are located within the toroidal recirculation zone near the jets. Hot combustion air as well as liquid fuel is transported downstream of the jets and therefore a second maximum of the temperature field is established there.

In the vicinity of the atomizer at the boundary of the liquid fuel spray, high temperatures occur due to stoichiometric conditions.

In contrast to this, the core of the spray is relatively cold. The temperature decreases because of the evaporation of the droplets. Similar to the velocity field, the temperature distribution is equalized at an axial position two diameters downstream of the jet entry.

The droplet trajectory plots in Fig. 13 clearly show the effect of droplet size on the spray propagation and evaporation behavior. The left diagram shows trajectories from droplets with a starting diameter of $D = 30$ μm. These droplets evaporate or are radially deflected, before they reach the jet stabilization plane. The larger droplets in the right diagram ($D = 50$ μm) show a different behavior. They follow similar trajectories upstream of the jet plane, but then penetrate the plane due to their inertia and evaporate in the downstream region.

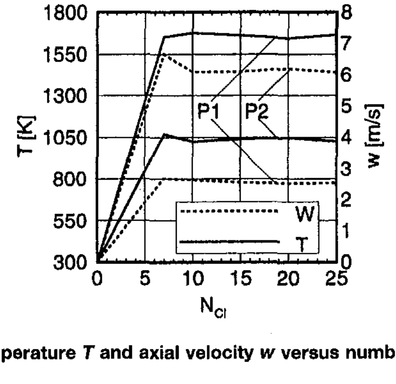

Fig. 10 Temperature *T* and axial velocity *w* versus number of coupling iterations

It is obvious that droplets smaller than $D = 30$ μm, which hold the main fuel volume, evaporate in the primary zone and therefore reaction upstream of the jet plane is achieved. Considering larger diameters, a penetration of droplets into the secondary zone is observed. Therefore, a high amount of gaseous fuel evaporated from these droplets will not enter the main reaction zone and elevated emissions of carbon monoxide and unburned hydrocarbones have to be expected. Since the cumulative volume of the few droplets penetrating the stabilazation plane is low in the case investigated here, they do not significantly influence the overall reaction. However, the increase of CO and UHC has been detected in the measurements of Bauer et al. (1995).

Circumferential and axial components of the velocity were measured by the laser-Doppler technique. Prediction and measurement showed that the circumferential velocities are small in most parts of the chamber. The assumption of symmetric boundary conditions in circumferential direction of the chamber was confirmed. Therefore, only a sector of 45 deg was discretized and the number of grid points could be reduced. (25 × 14 × 59 grid points: r, φ, z) This is important especially for the prediction of two-phase flows, requiring a large amount of computing time due to the iterative coupling procedure. Velocity and temperature profiles at different locations are given in Figs. 15 and 14. In general good agreement could be accomplished. Especially the shapes of the velocity profiles within the main reaction zone ($z = 22$ mm) are very similar. This indicates that the complex structure of the flow in this part of the chamber has been predicted well. High turbulence intensities in the downstream region of the chamber lead to a flattening of the measured profiles. The predicted velocities are too large at the center and too small at the wall indicating that the strong exchange of momentum has not been predicted well enough.

Temperatures could not be measured in the main reaction zone ($z = 22$ mm), due to the large amount of liquid fuel. Therefore, a comparison of measured and predicted temperatures is given downstream of the jet inlet. As for the velocity profiles, the predicted temperatures are in qualitative agreement with the measurements. In general the predicted temperatures are higher compared to the measurements. One reason for this may be radiative losses of the temperature probe, especially in the main reaction zone. Another reason is the assumption of complete reaction in the underlying model for the heat release.

Conclusion

Numerical calculations of the reacting two-phase flow in a research combustor were presented. The coupling methods pro-

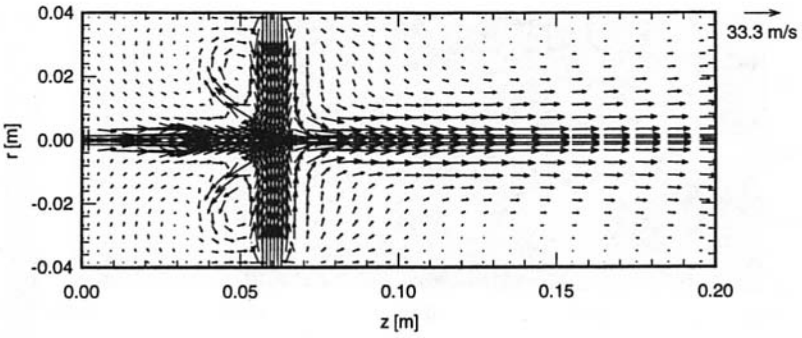

Fig. 11 Velocity vectors (φ = 0 deg)

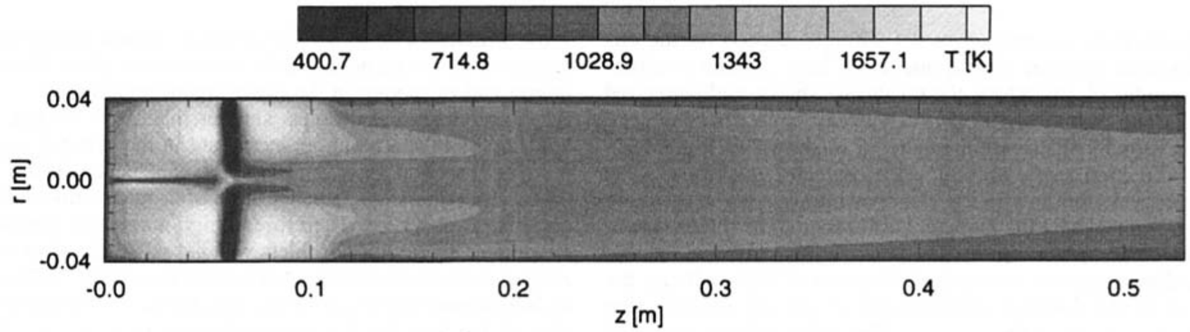

Fig. 12 Temperature contours (φ = 0 deg)

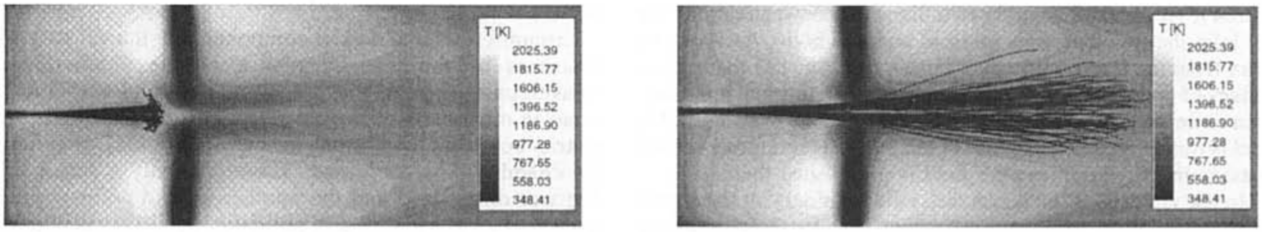

Fig. 13 Droplet trajectories (left side: D = 30 μm, right side: D = 50 μm)

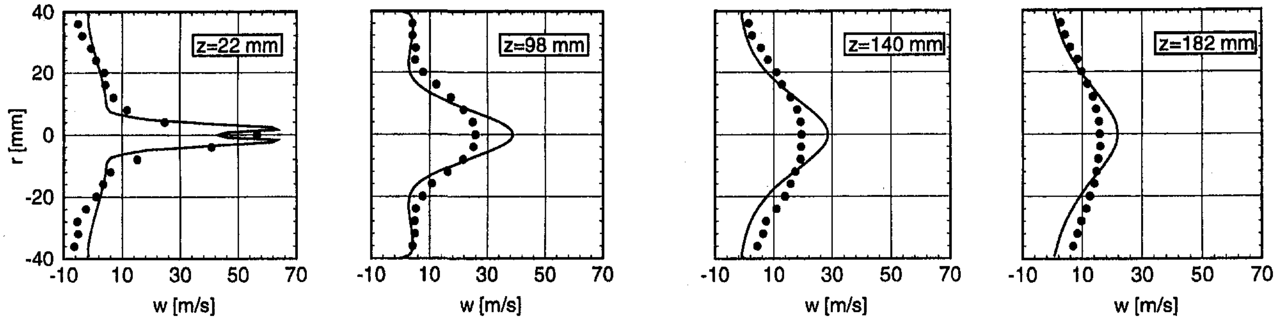

Fig. 14 Temperature profiles (φ = 0 deg; −calculation; • measurement)

posed indicate a possibility to get a fast and accurate solution for this complex and strongly coupled flow.

The comparison between measurements and calculations shows a good agreement especially for the velocity field. The measured temperature field was not reproduced with a similar accuracy due to several reasons in the experimental as well as in the modeling part. On the experimental side, recently performed CARS measurements should give a better representation of the actual temperatur field, since existing measurements come from thermocouple probes. On the modeling side, more detailed evaporation models as well as improved models for the chemical reaction should give better results.

However, with the suggested methods for coupling the two phases the Euler/Lagrangian method is a suitable tool to calculate two-phase combustor flows. The position of the main reaction zone in the research combustor was localized by the calculations, velocity fields were well reproduced and it was possible to analyze important phenomena within the evaporating spray.

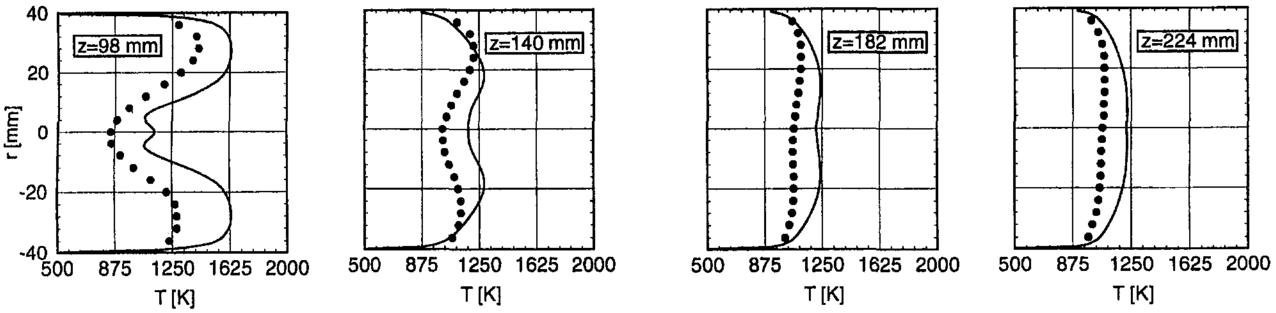

Fig. 15 Axial velocity profiles (φ = 0 deg; −calculation; · measurement)

Acknowledgments

The study presented was supported by grant from AG TURBO (Arbeitsgemeinschaft Hochtemperatur Gasturbine) sponsored by the Bundesministerium für Bildung und Forschung (BMBF) and by grant from "Sonderforschungsbereich 167—Hochbelastete Brennräume" sponsored by the "Deutsche Forschungsgemeinschaft (DFG)," which is gratefully acknowledged.

References

Abramovich, G. H., 1963, *The Theory of Turbulent Jets*, The M.I.T. Press, Mass. Inst. for Techn., Cambridge, MA.

Bauer, H. J., Eigenmann, L., Scherrer, B., and Wittig, S., 1995, "Local Measurements in a Three Dimensional Jet Stabilized Model Combustor," ASME Paper No. 95-GT-71.

Gosman, A. D., and Ioannides, E., 1983, "Aspects of Computer Simulation of Liquid-Fueled Combustors," *Journal of Energy*, Vol. 7, No. 6, pp. 482–490.

Jeckel R., and Wittig S., 1993, "Time-Resolved Measurements in a Three Dimensional Model Combustor," presented at the AGARD-PEP 81st Symposium on Fuel and Combustion Technology for Advanced Aircraft Engines, Colleferro, Roma, Italy, May 10–14.

Jeckel, R., Noll, B., and Wittig, S., 1992, "Three Dimensional Time-Resolved Velocity Measurements in a Model Combustor," presented at the 6th International Symposium on the Application of Laser Techniques to Fluid Mechanics; Lisbon, Portugal, July 20–23.

Kneer, R., Schneider, M., Noll, B., and Wittig, S., 1993, "Diffusion Controled Evaporation of a Multicomponent Droplet: Theoretical Studies on the Importance of Variable Liquid Properties," *Int. J. Heat and Mass Transfer*, Vol. 36, pp. 2403–2415.

Koch, R., Krebs W., Jeckel R., Ganz B., and Wittig S., 1994, "Spectral and Time Resolved Radiation Measurements in a Model Gas Turbine Combustor," ASME Paper No. 94-GT-403.

Kurreck, M., Jeckel R., Koch R., Scheurlen M., and Wittig S., 1993, "Einflußparameter der strahlstabilisierten Brennkammer—Numerische und experimentelle Analyse," VDI-Berichte No. 1090, pp. 251–261.

Launder, B. E., and Spalding, D. B., 1974, "The Numerical Computation of Turbulent Flows," *Computer Methods in Applied Mechanics and Engineering*, Vol. 3, pp. 269–289.

Magnussen, B. F., and Hjertager, B. H., 1977, "On Mathematical Modelling of Turbulent Combustion with Special Emphasis on Soot Formation and Combustion," *16th Int. Symp. on Combustion*, pp. 719–729.

Milojevic, D., 1990, "Lagrangian Stochastic-Deterministic (LSD) Predictions of Particle Dispersion in Turbulence," *Part. Part. Syst. Charact.*, Vol. 7, pp. 181–190.

Noll, B., and Wittig, S., 1991, "Generalized Conjugate Gradient Method for the Efficient Solution of Three-Dimensional Fluid Flow Problems," *Numerical Heat Transfer*, Part B, Vol. 20; pp. 207–221.

Noll, B., 1992, "Evaluation of a High-Resolution Scheme for Combustor Flow Computations," *AIAA Journal*, Vol. 30, 1, pp. 64–69.

Van Doormal, J. P., and Raithby, G. D., 1984, "Enhancement of the SIMPLE Method for Predicting Incompressible Fluid Flows," *Numerical Heat Transfer*, Vol. 7, pp. 147–163.

Control System for a 373 kW, Intercooled, Two-Spool Gas Turbine Engine Powering a Hybrid Electric World Sports Car Class Vehicle

C. C. Shortlidge
Senior Engineer,
SatCon Technology Corporation,
161 First St.,
Cambridge, MA 02142

SatCon Technology Corporation has completed design, fabrication, and the first round of test of a 373 kW (500 hp), two-spool, intercooled gas turbine engine with integral induction type alternators. This turbine alternator is the prime mover for a World Sports Car class hybrid electric vehicle under development by Chrysler Corporation. The complete hybrid electric vehicle propulsion system features the 373 kW (500 hp) turbine alternator unit, a 373 kW (500 hp) 3.25 kW-h (4.36 hp-h) flywheel, a 559 kW (750 hp) traction motor, and the propulsion system control system. This paper presents and discusses the major attributes of the control system associated with the turbine alternator unit. Also discussed is the role and operational requirements of the turbine alternator unit as part of the complete hybrid electric vehicle propulsion system.

Introduction

SatCon is currently testing a 373 kW (500 hp), twin-spool, intercooled gas turbine alternator for the Chrysler hybrid electric World Sports Car class race car "Patriot." Each spool of the Patriot power plant consists of an integrated compressor, turbine, and three-phase induction motor/generator with 186 kW (250 hp) electric power output capability. As shown in Figs. 1 and 2, an intercooler is used between the compressor stages, and the engine combustor is located between the high-speed, high-pressure compressor and turbine. The turbine alternator supplies electric power to both a 373 kW (500 hp) mechanical battery (i.e., flywheel) and a 559 kW (750 hp) rated traction motor.

Propulsion System Architecture

The 373 kW (500 hp) turbine alternator, 373 kW (500 hp) flywheel, 559 kW (750 hp) rated traction motor, and a 9000 μF capacitor bank are electrically coupled via an 800 VDC power bus, as shown in Fig. 3. Power may flow electrically to/from any propulsion system component to/from any other component. Power flows are controlled by a microprocessor-based controller operating on an IGBT-based power electronics architecture.

The capacitor bank is present to reject the highest frequency bus voltage disturbances. The controller associated with the flywheel permanent magnet motor is designed to yield the next highest bandwidth power flow capability in the entire system. The flywheel controller acts as a bus voltage regulator, in the presence of disturbances introduced to the bus voltage by the traction motor drawing power during vehicle accelerations and generating power during regenerative vehicle braking. The turbine alternator unit (TAU) consumes power during starting and during closed-loop rotor speed control at or near idle. The TAU provides the longer time scale averaged power flow from the propulsion system to the vehicle final drive.

The flywheel provides the higher bandwidth output power response capability of the system, while the power-dense turbine alternator provides a low-bandwidth, high-efficiency power flow response characteristic. The turbine alternator is essentially charged with appropriately maintaining the flywheel state-of-charge. Detailed analysis shows that good power management is consistent with maintaining the total kinetic energy associated with the vehicle at a relatively constant level. The flywheel state-of-charge should be high when the vehicle is stationary or traveling at low speed. The flywheel state-of-charge should be low when the vehicle is traveling at high speed, thus accommodating a large inflow of power to the flywheel during a large-scale regenerative braking maneuvre.

A detailed model of propulsion system power flows over a typical vehicle lap profile at LeMans, France, yields a rational estimate of required turbine alternator performance for good overall propulsion system performance. Turbine alternator power output demand for this model simulation is shown in Fig. 4. The system design accordingly calls for the turbine alternator to be capable of modulating electrical output power in the range of 224–373 kW (300–500 hp) with a power flow slew rate capability of ±37 kW/s (±50 hp/s).

The Turbine Alternator

The 373 kW (500 hp) Patriot TAU consists of a high-speed (100,000 rpm) and a low-speed (60,000 rpm) spool. The nominal pressure ratios are 4.6 and 3.1 for the low-speed and high-speed compressors, respectively. The intercooler cools 1.45 kg/s (3.2 lb_m/s) of air from 205°C (400°F) to 94°C (200°F), rejecting 0.145 W (153 Btu/s) of heat. The cooling water flow rate is 2.27 kg/s (5 lb_m/s), with inlet and outlet temperatures of 68°C (154°F) and 85°C (185°F), respectively.

The Patriot TAU operates on an open Brayton cycle, with no recuperator or regenerator. The inlet temperature to the high-pressure turbine is 1038°C (1900°F), the crossover point is at 760°C (1400°F), and the low-pressure exhaust is at 477°C (890°F). Both spools have the same physical arrangement, as shown in Figs. 1 and 2.

Contributed by the International Gas Turbine Institute and presented at Turbo Asia '96, Jakarta, Indonesia, November 5–7, 1996. Manuscript received at ASME Headquarters July 1996. Paper No. 96-TA-38. Associate Technical Editor: J. W. Shinn.

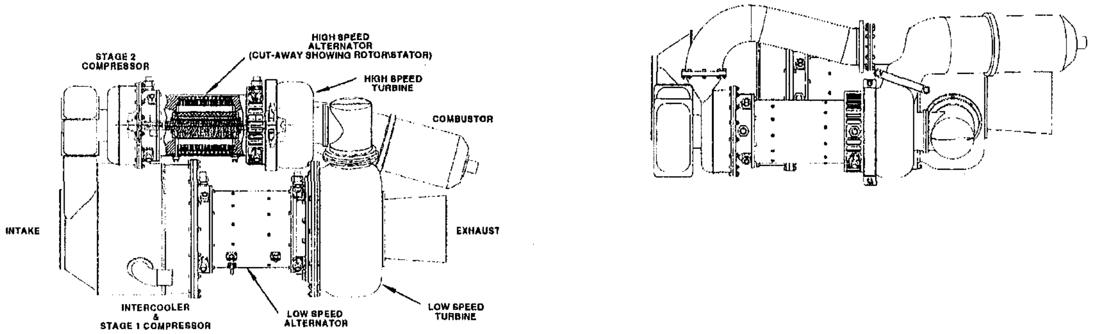

Fig. 1 Twin-spool 373 kW "Patriot" turbine alternator (two views)

The alternator is centered between fluid film flexure pad bearings, with the compressor overhanging on one end of the shaft and the turbine on the other. Both rotor systems operate supercritically with the low-pressure spool operating between the first and second criticals and the high-speed spool operating between the third and fourth criticals.

Both radial bearings and the thrust bearing, located at the compressor end, are water lubricated. The water also serves as a coolant for the bearings as well as for the alternators. The alternator stator is cooled by an outer water jacket, while the rotor includes a proprietary internal cooling system developed for use with high-speed, high-power density alternators.

The race car application requires a design that maximizes power density and minimizes overall weight. Table 1 lists the materials used for the main engine components. The high-speed alternator rotor and turbine diameters are 0.0635 m (2.5 in.) and 0.112 m (4.4 in.), respectively, while the corresponding low-speed dimensions are 0.109 m (4.3 in.) and 0.185 m (7.3 in.).

The high-pressure turbine design features uncooled rotor blades consistent with transitioning the developed technology to low-cost, high-volume manufacturing of commercial automotive components.

The Patriot engine is designed to burn natural gas (lower heating value of 4.742×10^6 J/kg (20,400 Btu/$\mathrm{lb_m}$)), which is stored as a cryogenic liquid and vaporized in a separate unit prior to entering the combustor. The nominal design point specific fuel consumption is 0.27 kg/(kW-h) (0.45 $\mathrm{lb_m}$/(hp-h)). No change to the turbine alternator, other than the combustor, would be required to operate with a different fuel. The turbine alternator unit is fueled by methane for the development phase of the program. This choice of fuel type facilitates purchase of small quantities of fuel and also yields a tighter tolerance on fuel heating value, which is important for performance measurement.

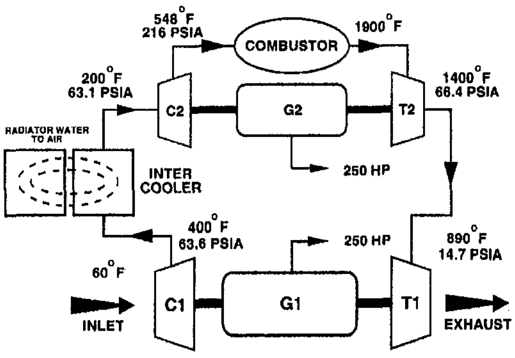

C_1 Low-speed compressor
T_1 Low-speed turbine
G_1 Alternator running off low-speed turbine
C_2 High-speed compressor
T_2 High-speed turbine
G_2 Alternator running off high-speed turbine

Fig. 2 Cycle diagram for the Patriot turbine alternator

The Power Electronics

The power electronics associated with the turbine alternator induction type alternators consists of a three-phase inverter with a sine wave pulse width modulated (PWM) drive. The high-speed induction motor is one-pole, while the low-speed alternator is two-pole.

The power electronics has an associated microprocessor based controller. The controller combined with the power electronics effects a closed-loop speed control for each of the TAU spools. The control loop effectively modulates alternator slip to achieve a target speed reference. Implementation of this slip control algorithm is shown schematically in Fig. 5.

The power electronics commutes excitation of the alternator stator phases relative to a measured rotor position to achieve a desired stator to rotor slip:

$$\sigma = (f_{\mathrm{stator}} - f_{\mathrm{rotor}})/f_{\mathrm{stator}}$$

The resultant electrical torque associated with the machine is governed by a characteristic electrical torque versus slip characteristic for a given induction machine hardware design. The characteristics for the Patriot TAU low-speed and high-speed alternator designs are shown in Figs. 6 and 7. Strictly speaking, the machine slip characteristic is valid for a given level of rotor magnetic flux. Closed-loop control of the rotor flux is difficult to implement in practice; instrumentation of the machine for accurate measurement of rotor flux while minimizing rotor air gap is not a realistic proposition. Alternatively, one may control rotor flux open loop by maintaining constant application of the ratio of stator phase voltage to stator frequency,

$$\nu = V_{\mathrm{stator}}/f_{\mathrm{stator}}$$

For improved control of rotor flux, the stator IR loss may be modeled for biasing the applied stator voltage.

The slip controller power electronics operates using a 16 kHz PWM frequency. The PWM frequency is synchronized with the inverter switching for improved attenuation of subharmonics and low-order harmonics, specifically the 3rd, 5th, and 11th harmonics. The speed control loop is closed in software with a minor frame frequency of 4 kHz. The software runs on a Texas Instruments C40 50 MHz DSP. The interface between the PWM and the encoder is implemented using a field programmable gate array (FPGA).

The speed control loop design is optimized for high-frequency (high rotor speed) operation. Furthermore, implementation requires relatively low resolution on rotor position; the low-

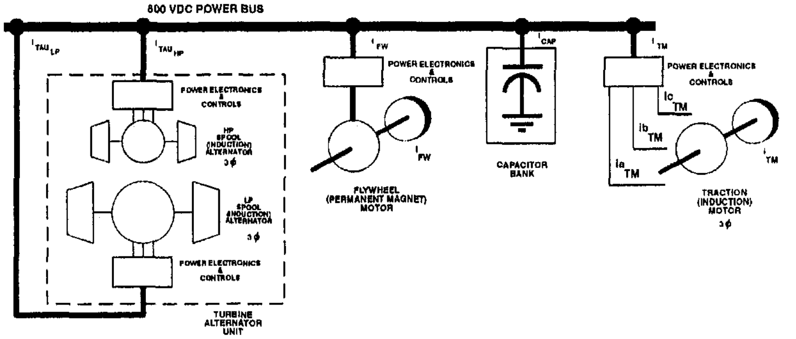

Fig. 3 Patriot vehicle propulsion system power flow architecture

speed and high-speed modules use two tachometer type sensors operating in quadrature for a net resolution of 3.75 and 7.5 deg, respectively.

The rotor speed control loop operates closed loop with a time constant of

$$\tau = 0.150 \text{ s}$$

The Fuel System

The turbine alternator burns gaseous methane (CH_4) delivered to the combustor at 66°C (150°F) and a static pressure that matches the high-pressure compressor discharge pressure. The fuel for the Patriot race car is stored cryogenically at −162°C (−260°F). A three-stage G-rotor type pump is submerged in the liquid phase methane and supplies liquid methane to a vaporizor as a function of pump speed.

The vaporizor is constructed essentially as a helical coil passing methane through the inner diameter of the coil while comparatively hot water (Tin = 70°C (158°F)) flows in a cross-counterflow arrangement. The heat transfer from the water to the methane proceeds according to a convection–conduction–convection type network with the controlling heat transfer surface being the inner methane surface. The methane proceeds into the vaporizor as a liquid until the boundary layer temperature approaches the saturation temperature for methane at the local fuel system pressure. Heat transfer in this section of the vaporizor is much higher than in the entrance region due to the two phase boiling flow regime, as suggested by Fig. 8. Note that Fig. 8 is presented for water and suggests the relevant effect of two-phased boiling for methane in the gas turbine fuel system vaporizer. Once the methane changes state from liquid to gas, the gas is then superheated in the remainder of the vaporizor section. The vaporizor is significantly oversized relative to the surface area, or length required to vaporize the liquid. Accordingly, there is little chance of liquid phase methane passing through the fuel system during rough road racing conditions. Also, the oversized design ensures that the methane gas leaves the vaporizor essentially at the water side bulk temperature, 69°C (156°F), which is desirable for stable combustion.

The gaseous methane is delivered to an ASME elliptic type metering nozzle. The temperature, T_1, and pressure, P_1, of the gas upstream of the nozzle, and the pressure, P_2, downstream of the nozzle is measured in real time. These data and the nozzle geometry are used to compute the mass flow to the engine in real time according to the compressible gas flow equation:

$$M = 8.02C_v A(\text{sqrt}((P_1/RT_1)((k/(k-1))((P_2/P_1)^{2/k} - (P_2/P_1)^{(k+1)/k})))/(\text{sqrt}(1-(A_2/A_1)^2(P_2/P_1)^{2/k})))$$

where A is the nozzle throat area (in.^{2}), R is the gas constant for methane, pressures are measured in lb_f/in^2, temperature is measured in R, and the flow coefficient $C_v < 1$ represents the boundary layer and vena contracta effects on the flow field in the region of the nozzle throat.

The mass flow to the engine is nominally controlled by modulating pump speed. A high-order model of the heat transfer and fluid flow associated with the fuel system from the cryogenic storage system to the combustion zone was created to, among other things, select a suitable set of controller gains for closed-loop control. A simulation result for a large scale change in fuel flow is shown in Fig. 9.

Detailed component level testing of the vaporizer and the vaporizer/pump subsystem is now under way to validate the modeling and component level designs.

The turbine alternator is currently being tested using the described speed control loops and a fuel system consisting of the nominal race car fuel metering hardware and an array of high-pressure bottled methane throttled down to 24.1 bar (350 lb_f/in^2). The 24.1 bar methane is buffered into a 0.757 m^3 (200 U.S. gal) holding tank. Mass flow from the holding tank through the fuel metering hardware is controlled by modulating the position of a throttling valve directly upstream of the ASME metering nozzle. The nozzle is close-coupled to the combustor.

The modified control system is being used to extensively test the turbine alternator for endurance characteristics. Upon

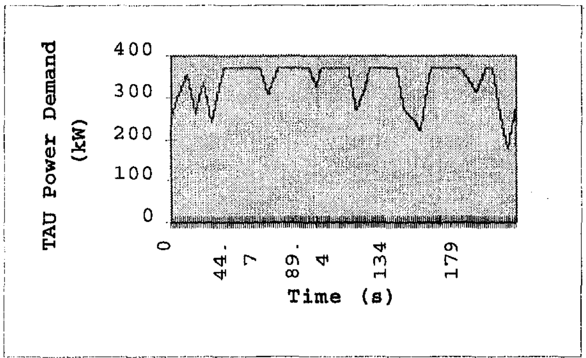

Fig. 4 Turbine alternator power output demand for typical LeMans lap profile

Table 1 Main "Patriot" engine component materials

	High-Speed	Low-Speed
Turbine	Inconel 100	Inconel 100
Turbine Shroud	Inconel 100	Inconel 718
Compressor	Titanium	Titanium
Compressor Shroud	303 Stainless	304 Stainless
Rotor	AerMet 100	AerMet 100
Rotor Housing	Carbon Composite	Carbon Composite
Intercooler Housing	304 Stainless	

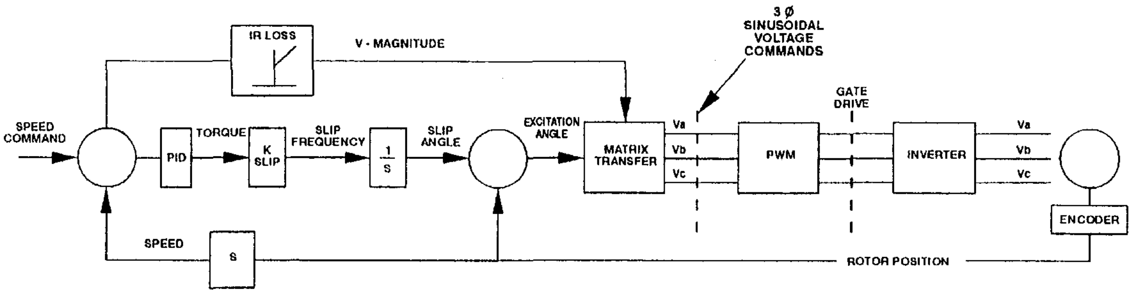

Fig. 5 Turbine alternator speed control loop architecture

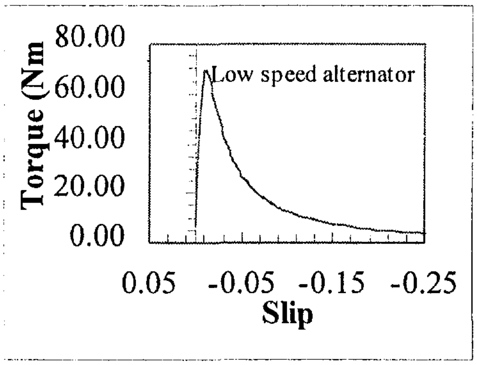

Fig. 6 Low-speed alternator torque versus slip

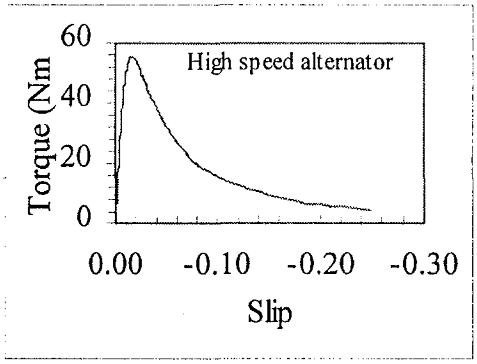

Fig. 7 High-speed alternator torque versus slip

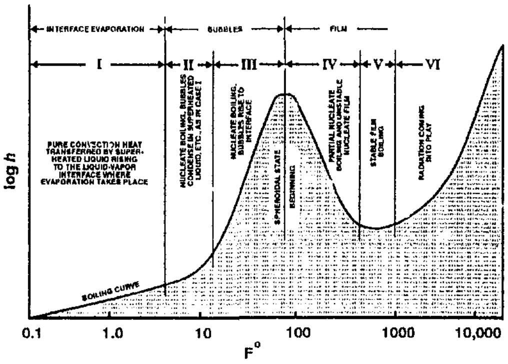

Fig. 8 Heat flux from an electrically heated platinum wire, from Farber and Scorah [1]

completion of turbine alternator testing, the TAU will be shipped to Chrysler for integration into stationary testing of the full-up propulsion system using the cryogenic fuel system.

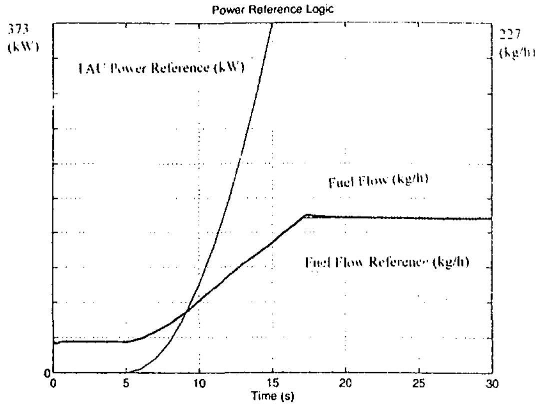

Fig. 9 Simulated large scale fuel flow transient

Top Level Control System Architecture

The vehicle implements a distributed hierarchical control system design, as shown in Fig. 10. Three subsystems are directly relevant to control of the TAU: the vehicle management computer (VMC), the power electronics controller (PC), and the TAU fuel system controller (TAUC). The VMC generates software commands based on driver control inputs such as throttle and brake position. The PC receives commands from the vehicle management computer via an optical serial data link. The power electronics controller and the TAU controller are linked similarly by an optical serial data link. Commands from the VMC to effect changes in the TAU power setting are relayed by the power electronics controller.

Turbine Alternator Control Modes

The turbine alternator is nominally controlled by modulating fuel flow, low-pressure spool alternator torque, and high-pressure spool alternator torque. The primary control mode is implemented to achieve a requested engine power level by slewing the fuel flow servo loop reference in the desired direction. A

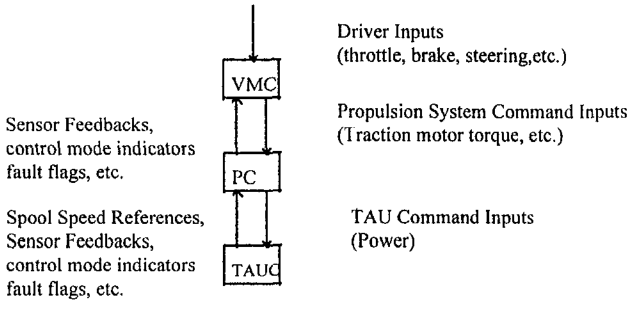

Fig. 10 Top level control system architecture

slew rate limit is applied in software to the fuel flow servo loop reference according to the turbine alternator power slew rate specification identified above. Actual or sensed fuel flow is used to compute Lp and Hp spool speed references. These references are passed to the high bandwidth slip type induction alternator speed controllers. Slip is modulated to achieve the desired speed references. The alternator speed control loops are closed at a significantly higher bandwidth than the fuel flow servo loop. Accordingly, the speed loops are able to follow the speed references accurately during the relatively slower fuel flow transients.

A consequence of the primary control mode is that the TAU is constantly operating on a predefined steady-state map of fuel flow, Lp spool speed, and Hp spool speed. The map is specified in the TAU controller software in terms of corrected parameters. The corrected parameters are unwrapped according to engine inlet conditions and Hp compressor inlet temperature to yield real-time specification of physical speed references used by the alternator speed control loops. Since power transients are slow, thermal energy storage or "heat soak" has a negligible effect on the engine thermodynamic cycle operating point.

In addition to this primary control mode, the TAUC sequences actuation of a fuel shutoff valve and a combustor ignitor to achieve a TAU start and nominal shutdown. The TAUC also continuously monitors the engine sensor set and invokes a rapid emergency shutdown if a critical engine parameter measurement such as a spool speed or high-pressure turbine inlet temperature goes out of limits.

Conclusions

The system level design for the Patriot race car propulsion system requires low bandwidth power modulation from the turbine alternator. High-bandwidth rotor speed control loops are achievable using the integral induction alternators and associated power electronics. Consequently, the fuel flow servo loop associated with the cryogenic fuel system is designed as a single-input single-output loop with a break frequency to meet the overall power flow bandwidth requirement. Setting high bandwidths for the speed loops avoids the need for a complex, multi-variable control system design; the system dynamic design may be achieved using multiple SISO loops with ample bandwidth separation for effective dynamic decoupling. Local to the TAU, the fuel flow and spool speed servo loops have characteristic time constants of

$$\tau_{\text{fuel flow}} = 3.0 \text{ s}$$

$$\tau_{\text{spool speed}} = 0.15 \text{ s}$$

yielding greater than a decade of bandwidth separation.

Active control of both the low-pressure and the high-pressure spool speeds enables precise coordination of the compressor operating points. Compressor variable geometry is not required to rematch the compressor during fast accels or decels, since there is a negligible speed-speed mismatch.

Testing of the TAU and other Patriot propulsion components continues. Data characterizing measured performance of the TAU and the TAU control system are currently under review and will be shared with the engineering community in future technical papers on the subject.

Reference

Farber, E. A., and Scorah, E. L., 1948, "Heat Transfer to Water Boiling Under Pressure," *Trans. ASME,* Vol. 70, p. 369.

R. A. Van den Braembussche
von Karman Institute for Fluid Dynamics,
Waterloosesteenweg, 72,
1640, Sint-Genesius-Rode, Belgium

H. Malys
Technip,
Tour Technip,
92090, Paris La Defense, France

Dynamic Stability of a Water Brake Dynamometer

A lumped parameter model to predict the high frequency pressure oscillations observed in a water brake dynamometer is presented. It explains how the measured low frequency variations of the torque are a consequence of the variation in amplitude of the high frequency flow oscillations. Based on this model, geometrical modifications were defined, aiming to suppress the oscillations while maintaining mechanical integrity of the device. An experimental verification demonstrated the validity of the model and showed a very stable operation of the modified dynamometer even at very low torque.

The Water Brake Dynamometer

Vaned rotor and perforated disk hydraulic dynamometers can be very compact because they dissipate energy by intensive agitation and high turbulence of the fluid. However, they suffer from cavitation erosion at high rpm, which can result in a complete destruction of the power element in a few hundred hours. The need for reliable high-speed water brake dynamometers for modern gas turbine testing has therefore resulted in smooth disk dynamometers, in which the drag is created by viscous shear on smooth surfaces. The lower drag per disk is compensated by an increase of the number and size of the disks and, as smooth disks are not susceptible to cavitation, by an increase of the peripheral speed. They are available for power up to 180 MW and speeds over 30,000 rpm (Deblon, 1978).

The smooth disk dynamometer consists of a number of tapered disks, rotating in a cavity, partially filled with water. The water enters the cavity at the root radius and accelerates by friction on the rotor wall to the rotor peripheral velocity by which it is centrifuged outward (Fig. 1) (Chew and Vaughan, 1988; Kurokawa and Sakuma, 1988; Karaskiewicz, 1995).

The fluid on the stator wall has a zero peripheral velocity and is pushed inward by the radial pressure gradient resulting from the average peripheral velocity in the cavity. This results in a ring of water near the outer radius of the cavity in which a swirling flow absorbs kinetic energy on the rotor side and dissipates it on the stator. The dissipated mechanical energy is converted into heat by fluid friction and removed with the water leaving the chamber at the outer radius.

The torque resulting from friction on the rotor counteracts the rotor rotation like a brake. The same torque, but of opposite sign, acts on the stator wall where it can be measured by a load cell if the stator is mounted in a pendulum fashion.

A cross-sectional view on the smooth disk water brake dynamometer, on which the actual study has been performed, is shown in Fig. 2. It contains six disks and is designed for maximum 16,000 hp, 11,500 Nm torque, and a maximum of 11,000 rpm. The different cavities are connected by channels to an outlet plenum with a single control valve. A perspective view on only two disks is shown in Fig. 3. A schematic view on two disks and the connecting channel is shown in Fig. 4. Symbols defining the dimensions of a cavity and disk are explained in Fig. 5.

The steady torque resulting from the friction on the disks is calculated by integrating the shear forces on each disk surface (Daily and Nece, 1960)

$$T_o = \int_{R_1}^{R_2} 2\pi R^2 \tau_w dR$$

where τ_w can be approximated by

$$\tau_w = C_f \rho \frac{U^2}{2} = \frac{5}{8\pi} C_m \rho \Omega^2 R^2$$

Since the density of the air is three orders of magnitude smaller than that of water, one can neglect its influence and limit the calculation to the area between R_i and R_2, occupied by the water (Fig. 5).

Integration results in

$$T_o = \frac{C_m}{4} \rho \Omega^2 (R_2^5 - R_i^5) \qquad (1)$$

and the power absorbed by the two sides of Z disks is

$$E = 2Z T_o \Omega = \frac{C_m}{2} Z \rho \Omega^3 (R_2^5 - R_i^5) \qquad (2)$$

The momentum coefficient C_m depends on the type of flow between the disk and the stator wall (laminar or turbulent, fully developed viscous flow, or two separate boundary layers), which in turn depends on the Reynolds number, roughness, and distance between rotor and stator wall (Daily and Nece, 1960; Nece and Daily, 1960).

The amount of water required to evacuate the heat resulting from friction is controlled by an outlet valve. The energy dissipation depends on R_i and is adjusted by changing the amount of water Q inside the cavity by means of the inlet valve.

The variation of the torque with rotor speed is shown by the curves T_o in Fig. 6 for different values of R_i. A typical variation of the turbine torque with speed is shown by curve T_u and the operating points are defined by the intersection of the T_o and T_u curves. Stability analysis shows that stable operation is assured if the T_o curves have a larger slope than the T_u ones, which is the case for a dynamometer–turbine combination. Smooth disk dynamometers are therefore well suited to control turbines.

Steady operation can be perturbed if the amount of water in the cavities changes under the influence of the external conditions, such as variation of the water supply pressure, control valve oscillations, or load variations. These variations can be remediated or at least reduced by a closed-loop control system, adjusting the control valve position to compensate for the changing external conditions.

However, an unstable operation has been observed at constant inlet pressure and fixed valve positions, as illustrated by the experimental data shown in Fig. 7. These results are obtained on the dynamometer shown in Fig. 2 at 6000 rpm and low load.

Contributed by the International Gas Turbine Institute for publication in the Journal of Engineering for Gas Turbines and Power. Manuscript received by the International Gas Turbine Institute August 16, 1996. Associate Technical Editor: D. H. Cooke.

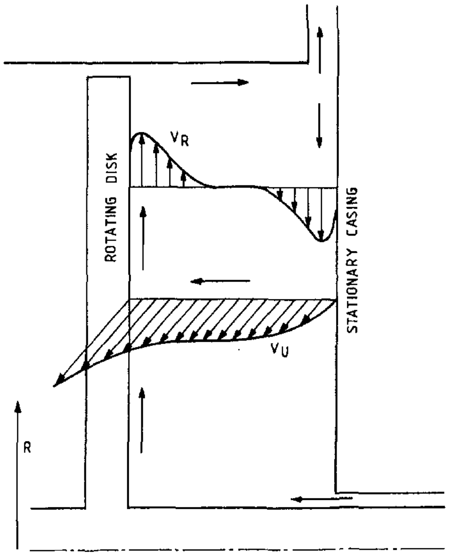

Fig. 1 Flow in a cavity with rotating disk

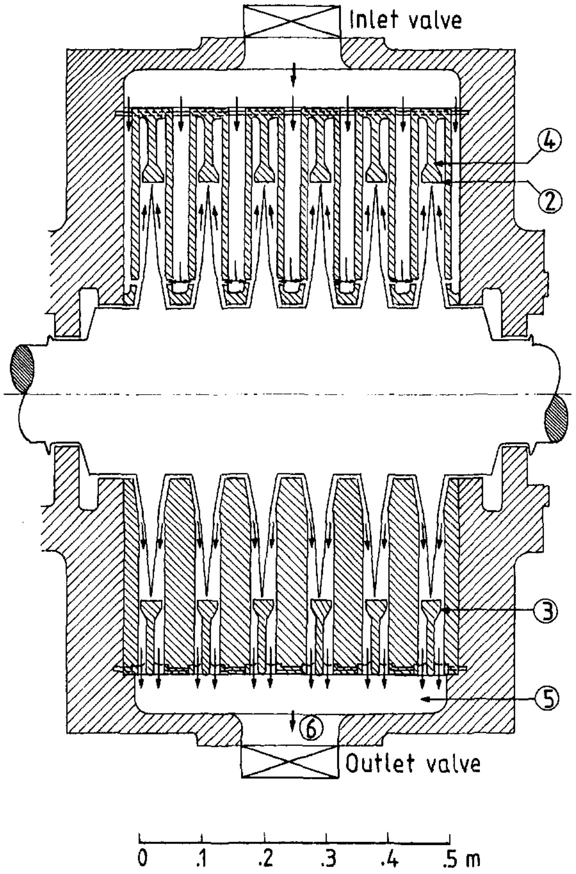

Fig. 2 Cross section of the smooth disk dynamometer used in the present study

The torque and the water pressure, upstream of the control valve, show high-frequency oscillations (at ≈10 Hz) and low-frequency variations of the average value (at ≈0.3 Hz). The rpm measurements show only low-frequency variations with a 90 deg phase delay when compared with the torque measurements. The rpm increases as long as the dynamometer torque values are below average, and decreases when the torque is above average. This indicates that the variations of rpm are due to a change in load and not a consequence of a variation in turbine torque. An increase of torque due to the driving turbine would result in an increase in rpm.

In order to verify that the unsteadiness results from the instabilities inside the torquemeter and not from the turbine, the same measurements have been repeated on a test stand where the torquemeter was driven by an electric motor. Results indicated the same type of large-amplitude oscillations of torque and pressure.

Experimental results at different load conditions show that the amplitude of these instabilities increases with decreasing quantity of water in the brake (lower torque operating conditions). This nonnegligible variation of the torque and rpm is undesirable as it prevents a stable operation of the driving turbine.

This paper first presents a lumped parameter model that predicts the high-frequency pressure oscillations and explains how the low-frequency variations of the torque are a consequence of the variation in amplitude of the high-frequency oscillations. The paper continues with a description of the geometric modifications that have been made to suppress the oscillations and the results of the experimental verifications.

Unsteady Flow Model

This model describes a periodic variation of the water flow inside the brake at constant external conditions and valve positions. The flow is split into a steady flow through each cavity, required to evacuate the heat, and, superimposed on it, a cyclic movement of the fluid from one cavity to another through the connecting channels (Figs. 3 and 4). The instabilities resulting from the latter one can not be remediated by any external control

Nomenclature

a = acceleration
A = cross-sectional area
b = fence or cavity width
C = cross-sectional contour length
C_f = friction coefficient
C_F = approximated friction coefficient, m/s
C_m = momentum coefficient = $(4\pi/5)C_f$
$\mathcal{D}_H$ = equivalent hydraulic diameter
E = power
$\vec{f}$ = friction force per unit mass
K = velocity coefficient
l = length along a streamline
$\mathcal{L}$ = equivalent length
P = pressure
Q = quantity of water in a cavity
R = radius
t = time
T_o = dynamometer torque
T_u = torque of driving device
U = peripheral velocity
V = velocity
Z = number of disks
Δ = amplitude of time-varying difference
Δ' = instantaneous difference
ρ = density of water
τ = time delay between volume increase and pressure rise
τ_w = wall shear force
Ω = disk rotational speed

Subscripts

1, 2, . . = position in dynamometer (Figs. 3 and 4)
i = water ring inner radius (Fig. 5)
R = radial component
U = tangential component

Superscripts

$\bar{\ }$ = time or mass-averaged value
$\bar{\bar{\ }}$ = time and mass-averaged value
$\vec{\ }$ = vector
$'$ = time-varying quantity

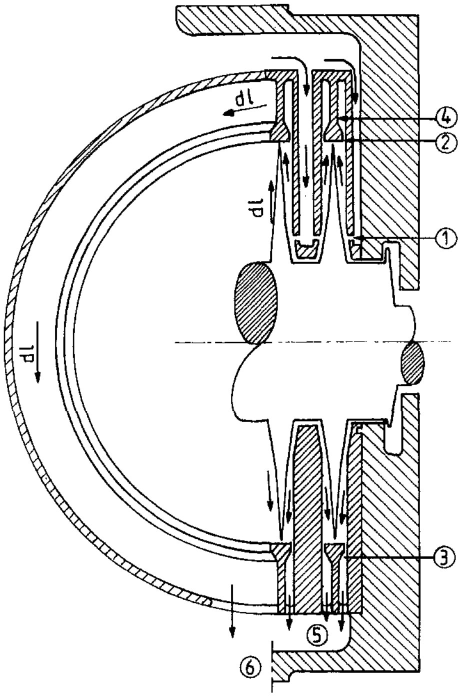

Fig. 3 Perspective view on two disks of the dynamometer and definition of positions

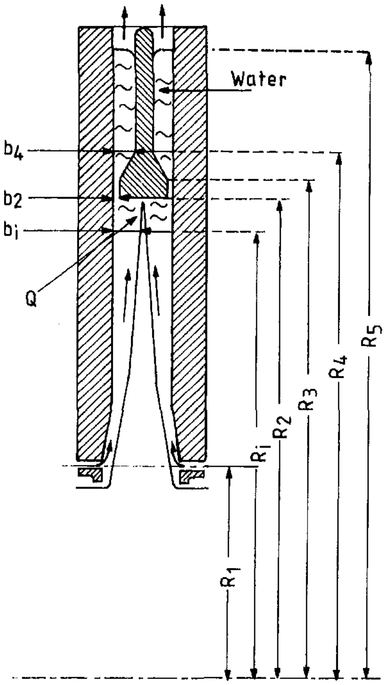

Fig. 5 Definition of water ring in the dynamometer and notations of overall dimensions used in the calculation

system. It is assumed that both steady and unsteady flows can be studied separately, and we will concentrate here on the oscillating motion that is at the origin of the unsteady operation.

Unsteady Flow Equations. The acceleration of the fluid in the channels, connecting the cavities (L) and (R), is a function of the pressure gradient, friction, and gravity forces. It is defined by:

$$\vec{a} = -\frac{\nabla P}{\rho} + \vec{f} - \nabla(g\vec{z}) \tag{3}$$

Replacing the acceleration by the total derivative of the fluid velocity V:

$$\vec{a} = \frac{D\vec{V}}{\partial t} = \frac{\partial \vec{V}}{\partial t} + \vec{V}\cdot\nabla\vec{V} \tag{4}$$

and neglecting the gravity forces, the integration of the terms along a streamline between the (L) and the (R) cavity results in:

$$\int_L^R \frac{\partial \vec{V}}{\partial t}\cdot d\vec{l} = \int_L^R \vec{f}\cdot d\vec{l} - \left|\frac{P}{\rho} + \frac{V^2}{2}\right|_L^R \tag{5}$$

This equation expresses the acceleration of the fluid (left-hand side), contained in the connecting channels, under the influence of friction in the channel and the difference in total pressure between the two cavities (right-hand side). The integrals have to be made along a streamline starting at the outlet fence (2) of one cavity going through the connecting channels to the outlet fence of the other cavity.

Integration of the first term is possible by taking into account the change in cross section of the connecting channel (Fig. 4). Assuming a uniform velocity in each cross section, the local velocity can be defined from continuity:

$$V = \frac{A_2 V_{R2}}{A} \tag{6}$$

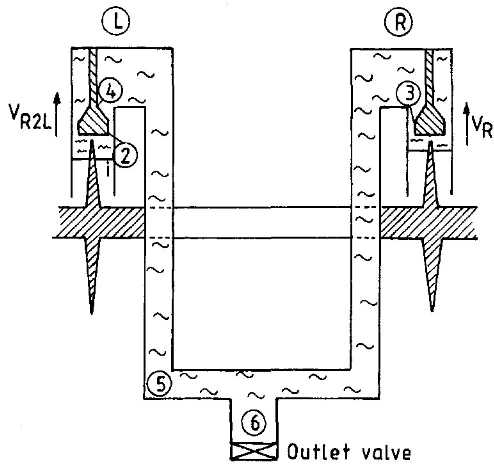

Fig. 4 Schematic presentation of dynamometer geometry with two disks and definition of positions

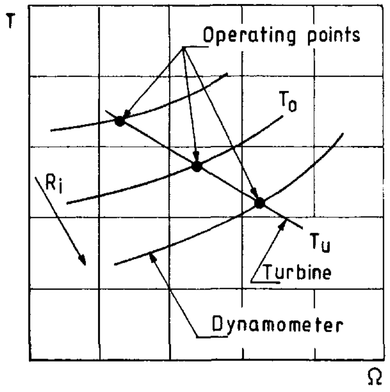

Fig. 6 Variation of torque in function of rotor speed of the turbine (T_u) and dynamometer (T_o)

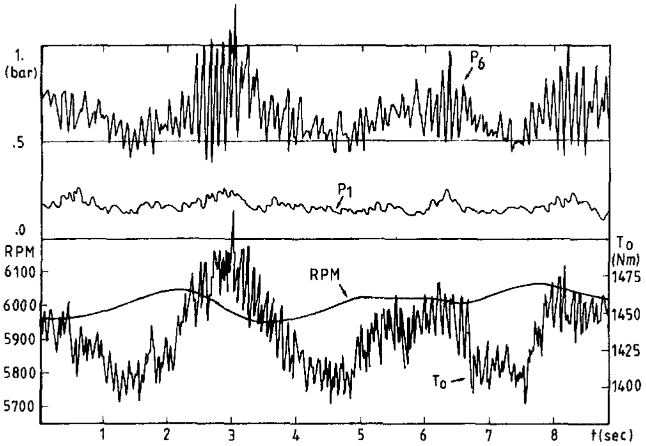

Fig. 7 Measured variation of inlet and outlet pressure, torque, and rpm during unsteady operation of the dynamometer

The left-hand side of Eq. (5) can then be written as follows:

$$\int_L^R \frac{\partial \vec{V}}{\partial t}\cdot d\vec{l} = \frac{\partial V_{R2}}{\partial t}\int_L^R \frac{A_2}{A}\,dl = \frac{\partial V_{R2}}{\partial t}\mathcal{L} \tag{7}$$

where $\mathcal{L}$ is the equivalent length of the connecting channel. Its value is defined by Eq. (7) and calculated in the appendix.

The second term of Eq. (5) accounts for energy dissipation at sudden enlargements of the connecting channel and by friction on the walls. Its main effect is a damping of the oscillation amplitude by a force opposite to the fluid motion. It can be approximated by:

$$\int_L^R \vec{f}\cdot d\vec{l} = -\int_L^R \frac{C_f V\vec{V}}{A}\,C d\vec{l}$$

where C_f is a friction coefficient, depending on Reynolds number and roughness, and C is the contour length of the cross section, so that $Cd\vec{l}$ is the surface on which the friction takes place.

In order to simplify the equations, without compromising the generality of the model, we introduce the following linearized expression

$$\int_L^R \vec{f}\cdot d\vec{l} = -\int_L^R C_F \frac{C}{A}\vec{V}\cdot d\vec{l}$$

After substitution of the hydraulic diameter

$$D_H = \frac{4A}{C}$$

and taking into account continuity, Eq. (6), one obtains:

$$\int_L^R \vec{f}\cdot d\vec{l} = -4C_F V_{R2}\frac{\mathcal{L}}{\mathcal{D}_H} \tag{8}$$

where $\mathcal{D}_H$ is an equivalent hydraulic diameter defined by:

$$\frac{\mathcal{L}}{\mathcal{D}_H} = \int_L^R \frac{A_2}{AD_H}\,dl$$

The third term of Eq. (5) expresses the instantaneous total pressure difference between the cavities (L) and (R). Neglecting the velocity difference that may exist in the two cavities, this term reduces to the difference in pressure rise in each cavity. The latter one is calculated by integrating in each cavity the radial pressure gradient due to the centrifugal forces resulting from the mass-averaged peripheral velocity in the cavity:

$$\frac{\partial P}{\partial R} = \rho\frac{V_U^2}{R} \tag{9}$$

Representing the average peripheral velocity V_U as a fraction of the rotor peripheral velocity as done by Due (1966)—$V_U = K\Omega R$—and integrating the corresponding pressure gradient over the radial extend of the water ring, results in a pressure at the outlet of the cavity defined by:

$$P_2 - P_i = \rho\frac{K^2\Omega^2(R_2^2 - R_i^2)}{2} \tag{10}$$

The amount of water in the cavity

$$Q = \pi b_i(R_2^2 - R_i^2)$$

allows the following simple expression for the pressure rise in each cavity:

$$P_2 - P_i = \rho\frac{K^2\Omega^2 Q}{2\pi b_i} \tag{11}$$

As the cavities have a drain to the atmosphere, one can assume $P_i = P_{\text{atm}}$, and the pressure difference between the cavity (L) and (R) is given by:

$$P_{2(L)} - P_{2(R)} = \rho\frac{K^2\Omega^2(Q_{(L)} - Q_{(R)})}{2\pi b_i} \tag{12}$$

Values of K are around 0.5, as experimentally defined by Due (1966), who also shows a dependence of K on the axial width of the cavity, the fluid properties, and the flow coefficient V_{R2}/U_2 (Fig. 8).

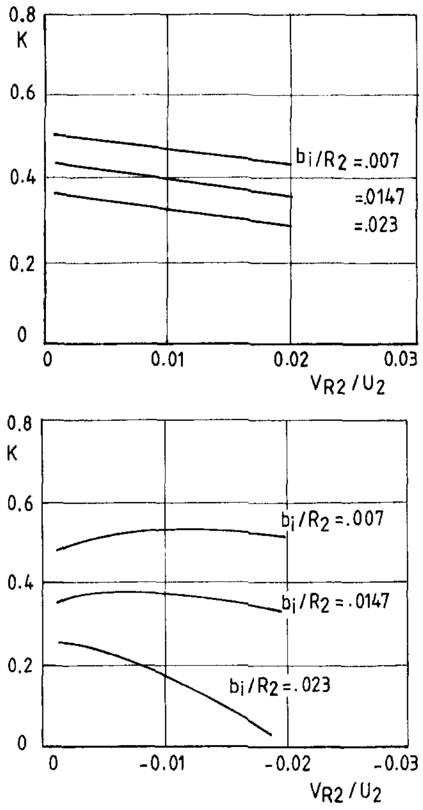

Fig. 8 Variation of velocity ratio in function of cavity width for outgoing ($V_{R2}/U_2 > 0$) and incoming fluid ($V_{R2}/U_2 < 0$) according to Due (1966)

Unsteady Fluid Forces. At stable operation, the amount of water inside each cavity adjusts itself until the pressure rise in each cavity is in equilibrium with the pressure drop over the outlet valve (Fig. 4).

Assume that for some reason the amount of water in cavity (L) is temporarily larger than in cavity (R) $(R_{i(L)} < R_{i(R)})$. This results in a pressure difference defined by

$$P_{2(L)} - P_{2(R)} = \rho \frac{K^2\Omega^2(R_{i(R)}^2 - R_{i(L)}^2)}{2} \tag{13}$$

and the amount of water in the connecting channels is pushed from the high pressure (L) to the low pressure (R) cavity until the pressures are equal again.

Because of the inertia of the fluid in the connecting channels, this movement will continue also after the pressure has been equalized, so that $Q_{(R)}$ will become larger than $Q_{(L)}$ and the pressure difference will be inverted. The fluid is then pushed backward to the cavity (L), whereafter the movement from the (L) to (R) cavity may start again. The changing pressure force is proportional to the displacement of the fluid in a way similar to the alternating forces by a spring attached to an oscillating mass. The amplitude of such a movement is normally damped out by viscous dissipation and the fluid returns to its equilibrium position after a few oscillations.

The oscillating motion can be sustained if the damping force, which opposes the velocity, is counteracted by a force acting on the fluid in the direction of the movement. The later one adds energy to the system and is often called negative damping. The amplitude of the oscillation will grow under its influence, until the added energy is compensated for by the increased damping due to increased dissipation and friction on the walls.

The origin of such a force is found in the experimental data of Due (1966) (Fig. 8). The curves applicable to the present geometry are the lower ones because the clearance in the dynamometer ($b_i/R_2 = 0.06$) is larger than the highest clearance on the figure. One observes only a small decrease in K with increasing positive values of V_{R2}/U_2, indicating that the average swirl velocity remains almost constant when the flow is leaving the cavity. A very large decrease of K is observed for negative values of V_{R2}/U_2, even going to zero for incoming radial velocities in excess of 2 percent of the peripheral velocity.

As a consequence, the pressure difference between the cavity (L), where the amount of water is decreasing, and the pressure rise in the cavity (R), where the water is entering, is larger than the one estimated in Eq. (13). This gives rise to an extra force in the direction of the movement. The pressure difference $P_{(L)} - P_{(R)}$ continues to exist even after the quantity of water has become equal in both cavities, and the pressure force will be inverted only after $Q_{(R)}$ has become larger than $Q_{(L)}$.

The change of K with the sign of V_{R2} can be explained as follows: The fluid leaving the cavity near the nonrotating wall has a small peripheral velocity and is not contributing much to the pressure rise in that cavity. As a consequence the pressure is not decreasing in proportion to the decreasing amount of water (increasing R_i) because the average peripheral velocity has increased. The fluid entering the low-pressure cavity through the fence has a zero tangential velocity and does not contribute to the pressure rise in that cavity. It may even perturb the circumferential motion that is responsible for the pressure rise.

Introducing the measured values of K into the theory would not change the conclusions, but one prefers to model them as follows: Assume it takes a time interval τ before the fluid entering the cavity has migrated along the fixed wall up to $R = R_i$ where it gains a tangential velocity by friction on the rotating disk. Its contribution to the pressure rise in the cavity is delayed over the same period, during which the kinetic energy of the fluid in the cavity remains unchanged:

$$\rho Q \bar{V}_U^2 = \rho(Q + \Delta Q)(\bar{\bar{V}}_U + \Delta \bar{V}_U)^2 \tag{14}$$

Further analysis will show that any positive value of τ decreases stability. Although its absolute value is not directly needed for the present discussion, one can quantify it by substituting experimental values of K (Fig. 8) into Eq. (18).

In a similar way one can assume that some amount of fluid ΔQ can leave the cavity near the fixed wall before the total kinetic energy starts decreasing by additional friction on the fixed wall.

One can conclude from Eq. (14) that a change of the quantity of water in a cavity by an amount $\Delta Q \lesseqgtr 0$ results in an opposite change of average peripheral velocity ($\Delta \bar{V}_U \gtrless 0$) and as a consequence in a variation of K defined by:

$$\frac{(\bar{K} + \Delta K)^2}{\bar{K}^2} = \frac{(\bar{\bar{V}}_U + \Delta \bar{V}_U)^2}{\bar{\bar{V}}_U^2} = \frac{Q}{Q + \Delta Q} \tag{15}$$

or

$$\frac{(\bar{K} + \Delta K)^2}{\bar{K}^2} \approx 1 - \frac{\Delta Q}{Q} \tag{16}$$

Expressing the change of Q in function of the radial velocity in the fence

$$-2\pi R_2 b_2 V_{R2} = \frac{\partial Q}{\partial t} \tag{17}$$

the instantaneous value of K^2 can be approximated by

$$K^2 = \bar{K}^2\left(1 - \frac{\partial Q}{\partial t}\frac{\tau}{Q}\right) = \bar{K}^2\left(1 + \frac{2\pi R_2 b_2 V_{R2}\tau}{Q}\right) \tag{18}$$

where $\bar{K}$ is the average value corresponding to the steady flow operation ($\partial Q/\partial t = 0$).

This formulation is probably not the most rigorous one, but has been selected because it is based on a physical model and predicts a dependence of K on the amplitude and sign of V_{R2}, which is similar to the one measured by Due (1966). It also shows that the influence of V_{R2} on the variation of $\bar{V}_U$ or K decreases with increasing values of Q.

This decrease of K in the cavity where $V_{R2} < 0$ and the increase of K in the cavity where $V_{R2} > 0$ creates a difference between $K_{(R)}$ and $K_{(L)}$. This results in an extra pressure force in the direction of the fluid motion and adds energy to the oscillatory movement.

Substituting Eqs. (7), (8), and (12) into Eq. (5) and taking into account the difference between $K_{(L)}$ and $K_{(R)}$ (Eq. (18)) results in the following approximate equation describing the unsteady flow in the water brake:

$$\frac{\partial V_{R2}}{\partial t}\mathcal{L} = \frac{-4\mathcal{L}C_F}{\mathcal{D}_H}V_{R2} + \frac{\bar{K}^2\Omega^2}{2\pi b_i}(Q_{(L)} - Q_{(R)} + 4\pi R_2 b_2 V_{R2}\tau) \tag{19}$$

Substituting Eq. (17) and its time derivative

$$-\frac{\partial V_{R2}}{\partial t} = \frac{1}{2\pi R_2 b_2}\frac{\partial^2 Q}{\partial t^2}$$

into Eq. (19) and grouping the terms in Q, $\partial Q/\partial t$, and $\partial^2 Q/\partial t^2$, one obtains:

$$\frac{\mathcal{L}}{2\pi R_2 b_2}\frac{\partial^2 \Delta' Q}{\partial t^2} + \left(\frac{2C_F\mathcal{L}}{\pi R_2 b_2 \mathcal{D}_H} - \frac{\bar{K}^2\Omega^2\tau}{\pi b_i}\right)\frac{\partial \Delta' Q}{\partial t} + \frac{\bar{K}^2\Omega^2}{\pi b_i}\Delta' Q = 0 \tag{20}$$

where $\Delta' Q = (Q_L - Q_R)/2$ is the difference between the instantaneous quantity of water Q in each cavity.

As $\mathcal{L}/\pi R_2 b_2$ cannot be negative, the system becomes unstable when the coefficient of $\partial\Delta' Q/\partial t$ in Eq. (20) is negative:

$$\left(\frac{2C_F\mathcal{L}}{\pi R_2 b_2 \mathcal{D}_H} - \frac{\bar{K}^2\Omega^2\tau}{\pi b_i}\right) < 0 \tag{21}$$

or when the damping force (proportional to C_F) is smaller than the excitation force (proportional to $\bar{K}^2\Omega^2\tau$). The later one is a direct consequence of the time delay τ between the increase of water volume in a cavity and the corresponding pressure rise.

The undamped natural frequency of the unsteady motion is easily defined from Eq. (20) for the situation where the excitation forces and damping forces compensate for each other. It is given by:

$$\omega = \sqrt{\frac{\bar{K}^2\Omega^2 2R_2b_2}{b_i\mathcal{L}}} \tag{22}$$

Substituting the dimensions of the water brake and the value of $\mathcal{L}$ (defined in the appendix) into Eq. (22), a value of ω = 25.5 rad/s is predicted. This corresponds to a periodic variation of the water quantity in each cavity at 4.06 Hz.

Experimental Results

Pressure Variations. The pressure measured at the control valve, halfway between the two cavities, shows a periodic variation at ≈10 Hz. This is about twice the frequency predicted by the theoretical model for each cavity. However, one should keep in mind that the control valve will feel the pressure pulses coming from all cavities. The pressure variation in the middle between the (L) and (R) cavity can be estimated by calculating the average of P_L and P_R.

Assume that the amount of water in each cavity changes in a periodic way with amplitude ΔQ

$$Q = \bar{Q} \pm \Delta Q \sin(\omega t) \tag{23}$$

where ± stands for the (L) and (R) cavity. After substitution of Q into Eq. (11) and into the definition of K (Eq. (18)), one obtains the following value for the pressure at the control valve:

$$\frac{P_{2(L)} + P_{2(R)}}{2} = \bar{P}_2 + \frac{\rho\Omega^2\Delta Q^2\bar{K}^2\omega\tau}{2\pi b_i Q}\sin(2\omega t)$$

This pressure variation at 2ω is in quite good agreement with the frequency of the measured pressure oscillation (≈10 Hz).

It is not yet clear what the origin is of the periodic change in amplitude of the pressure oscillations. A first explanation is an interaction between different pairs of cavities at different distances. As a consequence, oscillations occur at slightly different frequencies, which results in amplitude modulation.

It is also possible that the amplitude ΔQ of the oscillations grows until the amount of fluctuating water is larger than the average amount of water in the cavity. This means that the cavity is temporarily emptied during an oscillation and pockets of air are aspirated in the connecting channel where they have a stabilizing influence.

Torque Variations. The experimental results in Fig. 7 show an increase of the torque each time the amplitude of the pressure oscillations gets larger. This increase of the torque is then compensated for by the control system opening the exit control valve or closing the inlet valve to decrease the amount of water in the cavities, which in term results in a proportional decreases of the exit pressure. This increase of torque also takes place at constant total fluid in the dynamometer, and can be explained as follows.

Each time the fluid leaves one cavity through the fence, it completely dissipates its swirl velocity by friction in the connecting channel. It enters the cavity on the other side with zero tangential velocity where it is reaccelerated, resulting in an increase of the friction on that disk. This dissipation and reenergization of the fluid at each period of the oscillation results in an increase of the torque.

The increase of torque is proportional to the amount of oscillating fluid, which also defines the amplitude of the pressure changes in the outlet channel. It can be calculated in the following way. The amount of energy per unit volume required to increase the tangential velocity from zero, when it enters the cavity at the fence, to its average tangential velocity in the cavity at radius R_i, is given by:

$$\frac{\rho\bar{V}_{Ui}^2}{2} = \frac{\rho\bar{K}^2\Omega^2\bar{R}_i^2}{2}$$

The extra power required to re-energize the incoming volume flow $\partial Q/\partial t$ into a cavity (L) or (R) allows the calculation of the instantaneous variation of the torque

$$\Delta' E = \Omega\Delta' T_o = \frac{\rho\bar{K}^2\Omega^2 R_i^2}{2}\left|\frac{\partial Q}{\partial t}\right| \tag{24}$$

$\Delta' T_o$ quantifies the instantaneous increase of torque by friction on the disks for a given fluid flow entering a cavity.

Dividing Eq. (24) by Eq. (1), one obtains the relative variation of the torque per cavity:

$$\frac{\Delta' T_o}{T_o} \approx \frac{\bar{K}^2 R_i^2}{C_m\Omega(R_2^5 - R_i^5)}\left|\frac{\partial Q}{\partial t}\right| \tag{25}$$

This does not allow the conclusion that $\Delta' T_o/T$ is proportional to $1/\Omega$, because $\partial Q/\partial t$ is not independent of Ω.

Taking the time derivative of Q (Eq. (23)) and taking into account that $\Delta Q = -2\pi\bar{R}_i b_i\Delta R_i$, one obtains:

$$\frac{\partial Q}{\partial t} = 2\pi\bar{R}_i b_i\Delta R_i\omega|\cos\omega t| \tag{26}$$

After substitution of ω (Eq. (22)) one obtains:

$$\frac{\Delta' T_o}{T_o} = Cte\,\frac{\bar{R}_i^3 b_i}{(R_2^5 - R_i^5)}\,\Delta R_i|\cos\omega t|$$

where

$$Cte = \frac{4\pi\bar{K}^3}{C_m}\sqrt{\frac{2R_2b_2}{b_i\mathcal{L}}}$$

and the time-averaged increase in torque is given by:

$$\frac{\overline{\Delta T_o}}{T_o} = Cte\,\frac{2}{\pi}\,\frac{\bar{R}_i^3 b_i}{(R_2^5 - R_i^5)}\,\Delta R_i \tag{27}$$

This relation between the amplitude of the torque variation and the average amount of fluid $\bar{Q}$ in the cavities (function of $R_2 - R_i$) is shown in Fig. 9. It expresses the sensitivity of the brake to fluid oscillations between the cavities of two different disks of amplitude ΔR_i. One observes that the brake is more stable for larger values of $\bar{Q}$ (larger values of $(R_2^5 - R_i^5)$), which according to Eq. (1) corresponds to larger values of the average torque.

At constant power E of the driving turbine or electric motor, a variation of the torque results in a variation of the rotational speed defined by:

$$\frac{\Delta T_o}{T_o} \approx -\frac{\Delta rpm}{rpm}$$

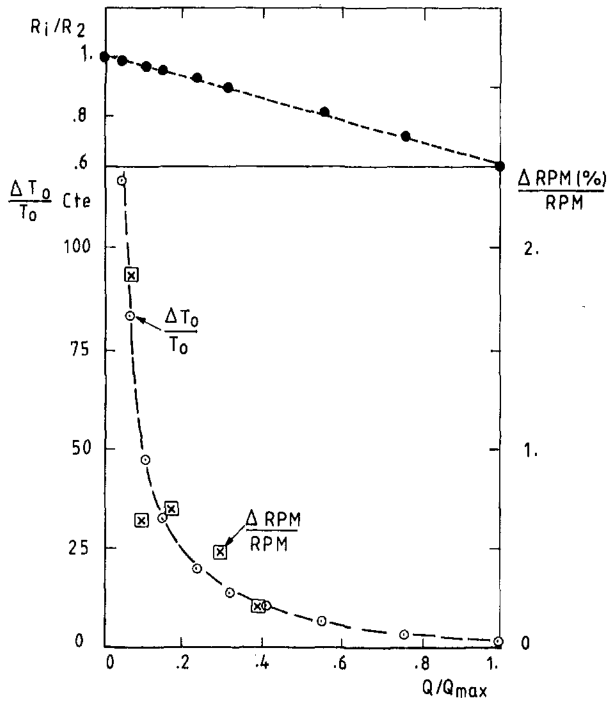

Fig. 9 Calculated amplitude of torque variations and measured variation of rotational speed, as a function of the average amount of water in the cavity

Experimental values of $-(\Delta rpm/rpm)$, also indicated in Fig. 9, show a variation that is in good agreement with the theoretical predictions of $\Delta T_o/T_o$ by this model.

Stabilization of Dynamometer

Some modifications have been made to the dynamometer in order to enhance its stability at all operating points between high and low torque and high and low rpm. The first modification intends to separate the different cavities in order to prevent the fluctuating motion just described. For this purpose the common outlet section and the single control valve have been replaced by a separate collector and control valve for each disk. The only possible oscillation that could still exist after this modification is one between the cavities on both sides of the same disk.

However, such an oscillation can be excluded on the basis of following arguments. A motion whereby the fluid is leaving one cavity through the radial fence at position 2 (Fig. 4) and returning to the neighboring cavity of the same disk after it has passed through the connecting channel is very unlikely. This would involve much more dissipation than when going from one side to the other side of the same disk, through the gap between the casing and the tip of the disk. However, the frequency of the latter oscillation would be much higher than the one observed, because the corresponding equivalent length $\mathcal{L}$ in Eq. (22) is very short. It would also not give rise to a sustained oscillation and an increase in torque because the fluid would not loose its tangential velocity component $\overline{V_U}$ when going through the rotor tip gap at R_2. As it would not require any re-energization, when entering the other cavity, it would also not influence the torque.

In addition to the previous modification, the amount of water in the cavities has also been increased, in order to increase the value of $(R_2^5 - R_i^5)$, which according to Eq. (27) reduces the value of $\Delta T_o/T_o$. This means that the number of cavities filled with water must be reduced in order not to increase the torque. This is easily achieved by closing the water supply valves of some cavities in which the disks rotate now in air without any pressure build up in the cavity. Special mechanical reinforcements of the water brake are therefore required in order to prevent deformation of the walls separating the cavities under the large pressure difference between the cavities partially filled with water and those filled only with air. As can be evaluated by Eq. (10) these pressures can attain more than 5.0 bar when operating the dynamometer at high rpm and maximum torque (large amount of water). For the present dynamometer this would result in a total lateral force of 250,000 N on the walls separating the cavities.

When controlling the flow in each cavity with a separate valve, one must make sure that they operate in the same way to assure nearly equal pressures in each cavity. Any accidental opening of one valve would result in a large pressure drop in the corresponding cavity and a large pressure force on the wall between the cavities in operation. It was therefore decided to link the valves mechanically.

The modified water brake has only two cavities filled with water, each of them having a separate control valve. It has been tested under the same conditions as the original one and showed a much more stable operation. Both the high and low-frequency pressure and torque variations have been reduced by two orders of magnitude (from 500 Nm to 4 Nm).

Reducing the number of disks from six to two requires nearly three times more water in each cavity, to obtain the same overall torque. According to Eq. (27), this results in an equivalent reduction of the torque oscillations. However, measurements show a larger reduction of the torque variations, confirming that also the oscillations between the different cavities have been suppressed.

The modified dynamometer allows a stable operation of the driving turbine and an accurate measurement of the torque up to very low values.

Conclusions

The paper demonstrates that a lumped parameter model allows a correct description of the unsteady flow in smooth disk dynamometers. It explains the basic mechanism responsible for sustained oscillations of the flow between the different cavities and how they are responsible for large fluctuations of the pressure and torque:

- Comparisons with experimental results show that the frequencies of the pressure oscillations are accurately predicted.
- The relation between the amplitude of the high-frequency pressure variations and the low-frequency torque variations is explained.
- The amplitude of the torque variations is correctly correlated to the amount of water in the cavities.

The model has been successfully used to evaluate possible modifications intended to stabilize the dynamometer and to verify their impact on mechanical integrity. Its validity was confirmed during a second series of experiments in which only 2 cavities were filled with water, each of them controlled separately by a valve. The torque variations have been reduced by two orders of magnitude.

References

Chew, J. W., and Vaughan, C. M., 1988, "Numerical Predictions for the Flow Induced by an Enclosed Rotating Disc," ASME Paper No. 88-GT-127.

Daily, J. W., and Nece, R. E., 1960, "Chamber Dimension Effects on Induced Flow and Frictional Resistance of Enclosed Rotating Disks," ASME *Journal of Basic Engineering,* Vol. 82, pp. 217–232.

Deblon, B., 1978, "Full Load Tests of the 80-MW Gas Turbine V93.2 Using a Water Brake," ASME Paper No. 78-GT-68.

Due, H. F., 1966, "An Empirical Method for Calculating Radial Pressure Distribution on Rotating Disks," ASME JOURNAL OF ENGINEERING FOR POWER, Vol. 88, pp. 188–196.

Karaskiewicz, K., 1995, "Turbulent Flow Along Enclosed Rotating Disk," VDI Berichte No. 1186, pp. 79–90.

Kurokawa, J., and Sakuma, M., 1988, "Flow in a Narrow Gap Along an Enclosed Rotating Disk With Through-Flow," *JSME International Journal*, Series II, Vol. 31, No. 2, pp. 243–251.

Nece, R. E., and Daily, J. W., 1960, "Roughness Effects on Frictional Resistance of Enclosed Rotating Disks," ASME *Journal of Basic Engineering*, Vol. 82, pp. 553–562.

APPENDIX

Calculation of Equivalent Length

Figures 3–5 define the geometry, positions, and dimensions used in the calculation of $\mathcal{L}$. The total equivalent length is calculated by summing up the equivalent length of the different components:

$$\mathcal{L} = \int_{(L)}^{(R)} \frac{A_2}{A}\, dl = 2 \int_2^6 \frac{A_2}{A}\, dl$$

$$= 2 \int_2^3 \frac{A_2}{A}\, dl + 2 \int_3^4 \frac{A_2}{A}\, dl + \ldots + 2 \int_5^6 \frac{A_2}{A}\, dl$$

The first two components have a simple geometry and the corresponding $\mathcal{L}$ is easily calculated:

$$\mathcal{L}_{2,3} = \int_2^3 \frac{2\pi R_2 b_2}{2\pi R b_2}\, dR = \ln \frac{R_3}{R_2} = 0.0118 \text{ m.}$$

$$\mathcal{L}_{3,4} = \int_3^4 \frac{2\pi R_2 b_2}{2\pi R(b_2 + b_4)/2}\, dR = \frac{2b_2 R_2}{b_2 + b_4} \ln \frac{R_4}{R_3} = 0.00834 \text{ m}$$

The value of $\mathcal{L}_{4,5}$ is more difficult to calculate because it concerns the flow in a circumferential channel where the mass flow increases linearly along the circumference over a distance $\bar{R}_4\pi$, between the top and the bottom of the device (Fig. 5). The easiest way to calculate this equivalent length is by going back to the definition (7)

$$\mathcal{L} = \frac{\int_o^\pi \frac{\partial V}{\partial t}\, dl}{\frac{\partial V_{R2}}{\partial t}}$$

taking into account that the mass flow increases uniformly around the circumference (entering at R_4), the local velocity variation at each circumferential position can be estimated from:

$$A \frac{\partial V}{\partial t} = A_2 \frac{\partial V_{R2}}{\partial t} \frac{\alpha}{2\pi}$$

Substitution into the definition of $\mathcal{L}$, with $dl = \bar{R} d\alpha$ and taking into account that the total cross-sectional area is $2A$ because the flow moves on both sides from 0. to π, results in

$$\mathcal{L}_{4,5} = \int_0^\pi \frac{A_2}{2A} \frac{\alpha}{2\pi} \bar{R}\, d\alpha = 3.86 \text{ m.}$$

The equivalent length $\mathcal{L}_{5,6}$ between position 5 and the middle of the dynamometer (position 6), is

$$\mathcal{L}_{5,6} = \int_5^6 \frac{A_2}{h_6 b_6}\, dl = 0.599 \text{ m}$$

taking for $l_{5,6} = .092$ m (half the axial distance between three rotors).

The total length to be used in the calculation of the frequency (Eq. (22)) is

$$\mathcal{L} = 2(\mathcal{L}_{23} + \mathcal{L}_{34} + \mathcal{L}_{45} + \mathcal{L}_{56}) = 8.96 \text{ m}$$

By far the largest contribution to $\mathcal{L}$ is the equivalent length $\mathcal{L}_{4,5}$ of the circumferential channel. The axial distance $\mathcal{L}_{5,6}$ has only a minor contribution to the equivalent length so that one can conclude that it is not important to find out exactly which disks are oscillating. $\mathcal{L}_{1,2}$ and $\mathcal{L}_{2,3}$ are negligible.

One can also conclude from this that the measured frequency cannot result from an oscillation through the rotor tip gap of the fluid between two cavities at each side of a rotor.

F. Caruel

S. Bourguignon

B. Lallement

S. Fargeas

A. DeBussac

SNECMA,
Gennevilliers and Evry,
France

K. Harris

G. L. Erickson

J. B. Wahl

Cannon-Muskegon Corporation,
[SPS Technologies, Inc.],
Muskegon, MI 49443

SNECMA Experience With Cost-Effective DS Airfoil Technology Applied Using CM 186 LC® Alloy

From a cost point of view SNECMA has found DS columnar grain manufacturing technology to be highly attractive compared to single crystal. CM 186 LC[1] *alloy exhibits enhanced mechanical and environmental properties and temperature capability compared to MAR M*[2] *200 Hf alloy; these properties are close to first-generation single crystal alloys up to 982°C (1800°F). The alloy is shown to be amenable to various coating and brazing high-temperature processes. The longer term creep-rupture/phase stability data base on the alloy has now been extended out to 8300 hours at 1038°C (1900°F). Castings for engine test have been produced using CM 186 LC alloy.*

Introduction

The efficiency of gas turbines is dependent on thermodynamic criteria such as overall pressure ratio and turbine inlet temperature. During the last 30 years, turbine inlet temperatures have increased by about 450°C (810°F). About 70 percent of this increase is due to more efficient design of air cooling for turbine blades and vanes, particularly the advent of serpentine convection cooling with turbulators and pin fins and film cooling and thermal barrier ceramic coatings, while the other 30 percent is due to improved superalloys and casting processes. The greatest advances in metal temperature, stress, and environmental capability for turbine airfoils have been the result of the development of directionally solidified, columnar grain (DS) and single crystal (SX) superalloy casting process and engine application technology pioneered by Pratt and Whitney Aircraft.

DS manufacturing technology (casting, solution heat treatment, and inspection) can be less expensive than single crystal and the production of single or multi-airfoil vanes with large platforms can be more straightforward. MAR M 200 Hf alloy has been widely used for DS columnar grain airfoils and SNECMA has had good experience with the alloy in complex shape vanes and blades, in particular those with extended platforms. These comments relate to both manufacturing experience and turbine engine service performance.

However, the temperature and environmental conditions in new engine designs are becoming more severe, not only for vanes but also for the longer, low-pressure (LP) turbine blades. This brings about the need for improved second-generation DS superalloys. This class of alloy generally contains 3 percent Re, offers improved creep and oxidation performance but at the expense of some increased density. The second-generation alloy studied in the paper is CM 186 LC [3], which is a nickel-base alloy containing 3 percent Re, 1.4 percent Hf and 67 percent of the coherent γ' precipitate strengthening phase.

The following were investigated for this work:

- heat treatment evaluation
- initial environmental and mechanical property characterization
- industrialization
- a thermal fatigue technological test, and engine testing with a M53-P2 military engine used as a test vehicle.

This work is typical of a new alloy evaluation program at SNECMA. The data offer to design engineering the possibility of designing turbine airfoils with an alloy that may be useful for future engines.

Chemical Composition and Heat Treatment

Chemical Composition. The nominal composition of CM 186 LC is shown in Table 1, in comparison with René 142, PWA 1426, and MAR M 200 Hf, all of which are Ni-based DS superalloys.

The first three alloys contain 3 percent Re. They are designated second-generation DS superalloys whereas MAR M 200 Hf is a first-generation DS superalloy. Re is known to partition mainly to the γ matrix (roughly 80 percent), and retard coarsening of the γ' strengthening phase because it slows diffusion and increases γ/γ' misfit. Small Re clusters, detected in the γ matrix, act as efficient obstacles against dislocation movement. The remaining 20 percent of the Re partitions to the γ' thereby strengthen that phase [3]. These features provide significant

---

[1] CM 186 LC®, CM 247 LC®, CMSX-2®, CMSX-3® and CMSX-4® are registered trademarks of the Cannon-Muskegon Corporation.

[2] MAR M is a registered trademark of the Martin Marietta Corporation.

[3] Hastealloy® and Haynes® are registered trademarks of Haynes International.

Contributed by the International Gas Turbine Institute and presented at the 41st International Gas Turbine and Aeroengine Congress and Exhibition, Birmingham, United Kingdom, June 10–13, 1996. Manuscript received at ASME Headquarters February 1996. Paper No. 96-GT-493. Associate Technical Editor: J. N. Shinn.

Table 1 Chemical composition (wt%)

	C	Cr	Co	Mo	W	Ta	Re	Al	Ti	B	Nb	Zr	Hf	Ni	
CM 186 LC®	0.07	6	9	0.5	8.4	3.4	3	5.7	0.7	0.015	–	0.005	1.4	bal.	8.70
René 142	0.12	6.8	12	1.5	4.9	6.4	2.8	6.2	–	0.015	–	0.02	1.5	bal.	8.6
PWA 1426	0.10	6.5	12	1.7	6.5	4	3	6	–	0.015	–	0.03	1.5	bal.	8.6
MAR M 200 Hf	0.13	8	10	–	12	–	–	5	2	0.015	0.9	0.02	1.75	bal.	8.5

Density (kg/dm³)

improvement to mechanical and environmental properties. Re, Cr, and Mo decrease metal fluidity during the casting operation. CM 186 LC has the lowest Re + Cr + Mo content.

All the alloys contain Hf to strengthen and improve the ductility of grain boundaries, thus improving transverse properties. This is particularly important for vane shrouds [4]. However, Hf is highly reactive with shells and ceramic cores and can be responsible for oxide inclusions in DS airfoil components.

The second-generation alloys contain less W than MAR M 200 Hf. This element provides some improvement in high-temperature mechanical properties but can be responsible for freckles, which are chains of small equiaxed grains formed during solidification of the DS airfoils, and instability problems in relationship with Hf. (The occurrence of platelets during HCF tests has led SNECMA to decrease Hf content from 2.1 to 1.75 percent in MAR M 200 Hf.) Re-containing alloys can be sensitive to freckles. The (W + Re) content of CM 186 LC is slightly lower than the W content of MAR M 200 Hf, and CM 186 LC contains 3.4 percent Ta, which is beneficial in relation to propensity to freckling. High W also adversely affects oxidation and hot corrosion resistance.

Interestingly from a cost point of view, CM 186 LC is a derivative of the CMSX®-2/-3/-4 family of single crystal alloys. This ensures the possibility of melting from virgin/CMSX-2/-3/-4 foundry revert blends [3]. Table 2 compares chemical compositions of two heats: one from 100 percent virgin material and another with 50 percent recycled CMSX®-4 foundry revert material.

These alloy features confirm SNECMA's strategy to evaluate CM 186 LC for future turbine engine applications.

In this paper, CM 186 LC alloy is directly compared to MAR M 200 Hf, which features 1.75 percent Hf and improved solutioning at 1240°C (2264°F) (5°C below the incipient melting temperature). This specific heat treatment for MAR M 200 Hf results in a 10°C creep temperature capability improvement and also offers a significant decrease in property scatter compared to the original property performance of the alloy.

Heat Treatment

Solutioning. The majority of DS and SX alloys need a solutioning heat treatment to give a uniform precipitation of optimized 0.45 μm cubic γ′ on subsequent aging to maximize creep-rupture properties. MAR M 200 Hf and René 142 require extensive solutioning to optimize their mechanical properties [1]. PWA 1426 has been developed to offer the mechanical properties of single-crystal PWA 1480 while having higher casting yields normally achieved with DS alloys. This has been achieved with only partial solutioning [50 percent] of the γ′ precipitates [2].

Table 2 Chemical composition of CM 186 LC alloy heats with or without recycled material (wt%, *ppm)

	C	Si	Mn	S*	Al	B	Bi*	Nb	Co	Cr	Cu	Fe	Hf
100% virgin	0.069	<0.02	<.001	4	5.68	0.015	<.2	<.05	9.4	6	<.001	0.027	1.4
50% recycled	0.07	<0.02	.001	2	5.7	0.014	<.2	<.05	9.4	6	<.001	0.047	1.4

	Mg*	Mo	N_2*	O_2*	Ta	Ti	W	Zr	Re
100% virgin	<80	.5	1	1	3.4	0.74	8.4	0.005	2.9
50% recycled	<80	.49	1	1	3.4	0.74	8.4	0.006	2.9

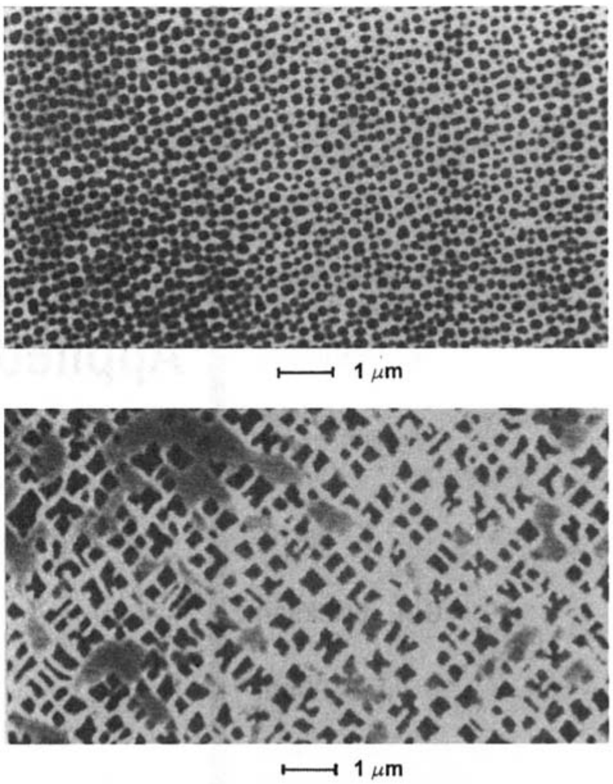

Fig. 1 γ′ morphology in the as-cast condition

The development program goal of CM 186 LC was to provide longitudinal creep rupture properties in the as-cast plus double aged condition better than DS CM 247 LC® [5–6] and equivalent to CMSX-2/-3 [7] single crystals alloys up to 980°C (1796°F). This is interesting for vane applications since solutioning can result in recrystallization due to high residual casting stresses in transition areas between thick and thin sections of the part (for example, trailing edge areas near the shroud of an integrally cast, shrouded vane segment). Nevertheless, the possibility of improving the mechanical properties by performing a solutioning treatment has been investigated.

Liquidus, solidus, and γ′ solvus have been determined for CM 186 LC using a Differential Thermal Analysis method with a high-temperature calorimeter. The liquidus is 1388°C (2530°F) and the solidus is 1326°C (2418°F). The γ′ solvus

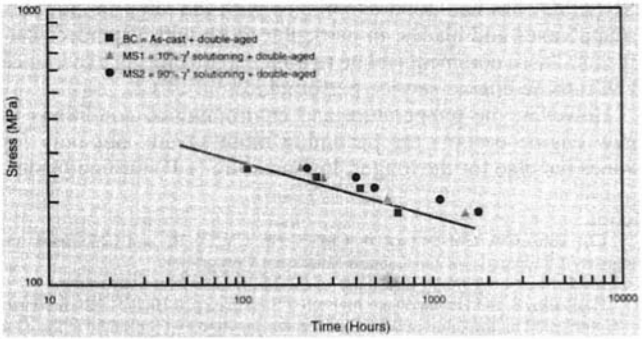

Fig. 2 Stress rupture at 950°C (1742°F) of CM 186 LC partially or completely solutioned compared to as-cast and double-aged condition

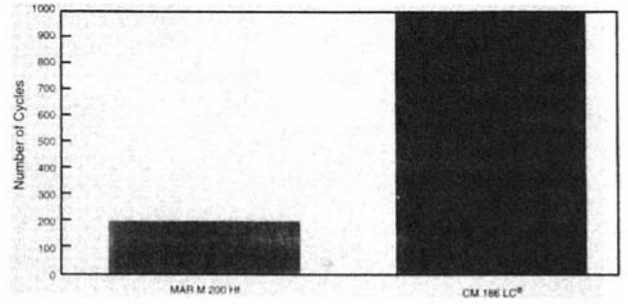

Fig. 3 Oxidation resistance at 1100°C of CM 186 LC and MAR M 200 Hf

is 1250°C (2282°F). In fact, SEM examination of samples treated at different temperatures showed that γ' solutioning begins at 1220°C (2228°F).

In the as-cast condition, SEM examination has shown appreciable areas of γ/γ' eutectic phase (Fig. 1). The γ' precipitates have a rather irregular cubic morphology: 0.5 to 0.75 μm. Interdendritic areas have been found where the γ' is rather globular. This can be a result of microsegregation.

The first goal was to determine the incipient melting point. Samples in the as-cast condition were placed in a furnace at temperatures between 1250°C (2282°F) and 1300°C (2372°F). Incipient melting appears at 1275°C (2325°F), which is 20°C (36°F) higher than MAR M 200 Hf.

Different solutioning heat treatments have been tested and a solutioning ratio determined for each of them. Up to 90 percent of the γ/γ' eutectic phase could be solutioned. Stress-rupture tests were performed on samples in the as-cast plus double-aged condition, ''partially'' solutioned (10 percent of γ/γ' eutectic phase) plus double-aged condition and ''completely'' solutioned (90 percent of γ/γ' eutectic phase) plus double-aged condition. Test results are presented in Fig. 2.

Effect of Aging on Carbide Stability. The effects of aging in the range 1050°C (1922°F)–1200°C (2192°F) have been studied to address standard brazing and coating process thermal cycles. Image analysis techniques have been extensively used to study the effect of high-temperature aging on carbide morphology and size.

In the as-cast condition, there are two types of carbide:

- ''Chinese script'' type, that is fine carbides whose morphology appears like chinese script [MC_1]
- Blocky carbides [MC_2]

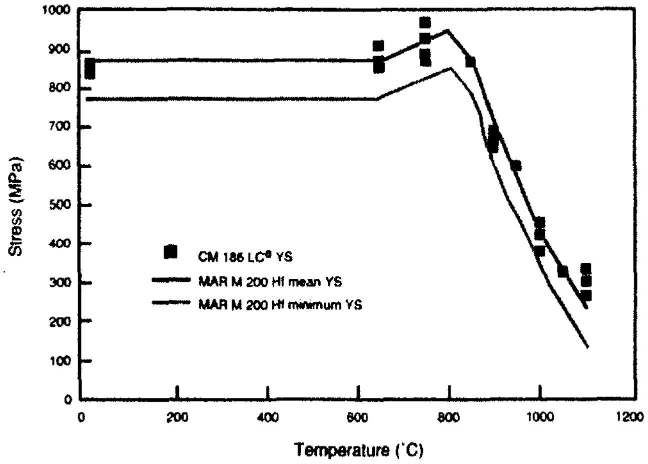

Fig. 5 Tensile yield strength

The first type contains Ti, Hf, and Ta, whereas the second type contains only Hf and Ta.

At 1050°C (1922°F), there is no modification on carbides up to 10 h. For longer times, fine dispersed carbides form along grain boundaries and small lenticular and acicular carbides appear, which contain Hf and Ta [MC_2]. At 1150°C (2102°F), grain boundary and ''Chinese script'' carbides disappear after 10 h and the lenticular and acicular carbides continue to develop. The same phenomenon occurs at 1200°C (2192°F) but at a faster rate.

Standard Condition Characterization

The standard study of cast superalloys for turbine airfoils at SNECMA consists of oxidation/corrosion testing to find whether the alloy is suitable for jet engine applications and determine the type of coating needed. This is followed by physical and mechanical properties characterization.

Oxidation and Hot Corrosion (Sulfidation) Resistance. CM 186 LC, DS bare specimens have been tested in oxidation and hot corrosion (sulfidation). In oxidation, plates and bulk specimens of CM 186 LC have been tested at 1100°C (2012°F). The second-generation alloy is much better than MAR M 200 Hf. Figure 3 shows the results in terms of number of cycles before catastrophic mass loss. Those tests also showed that CM 186 LC is sensitive to spalling at the edges of the specimens and life is dependent on geometry. It confirms that CM 186 LC needs a coating to avoid problems particularly at leading and

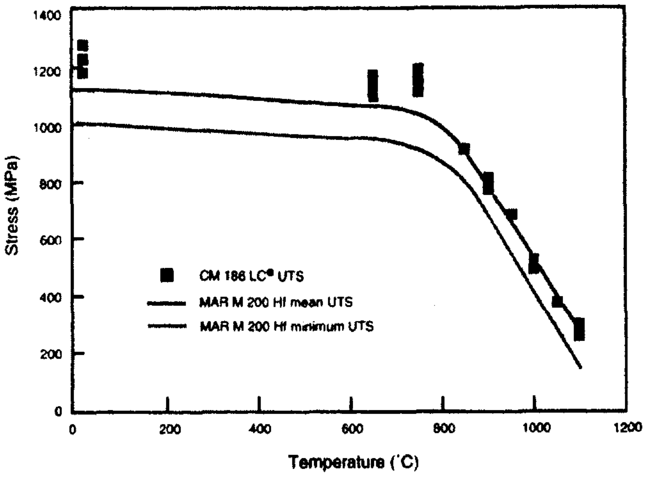

Fig. 4 Ultimate tensile strength

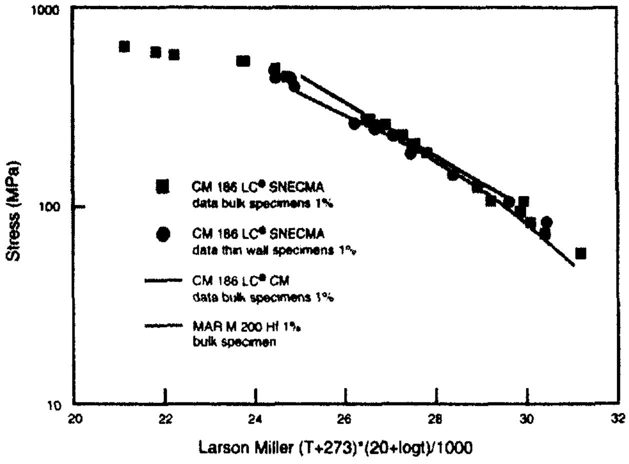

Fig. 6 DS Longitudinal 1 percent creep properties

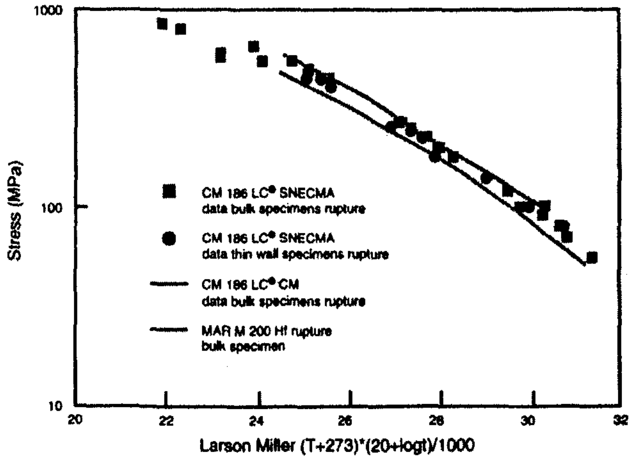

Fig. 7 DS Longitudinal stress-rupture properties

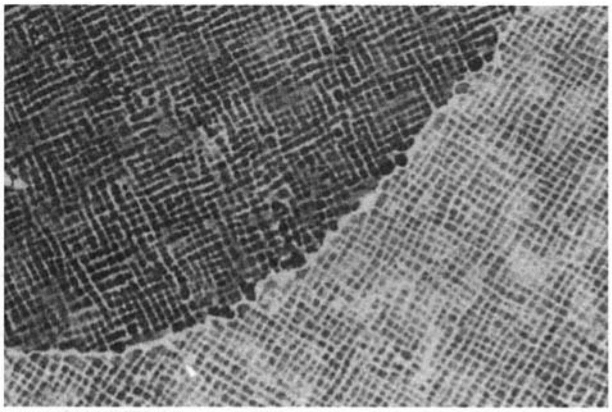

(a) MAR M 200 Hf

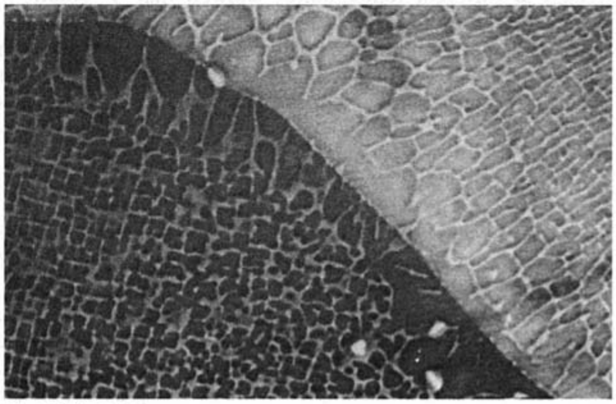

(b) CM 186 LC

Fig. 9 Grain boundary structure of (*a*) MAR M 200 Hf and (*b*) CM 186 LC

trailing edges. At 850°C (1562°F) and 900°C (1652°F) in standard sulfidizing conditions, hot corrosion resistance of the two alloys are very similar. This fact led us to the conclusion that a C1A coating, consisting of chromizing and aluminizing, is necessary for turbine engine service.

Mechanical Properties. Since CM 186 LC is likely to need a coating, it was decided to conduct mechanical testing on samples with the following heat treatment: as-cast +1100°C (2012°F)/10 h + 870°C (1598°F)/16 h. The first part of the treatment simulates a normal C1A coating diffusion, which is the most frequently used at SNECMA for DS or single-crystal alloys. In fact, process parameters will be defined later, but then it will be necessary to evaluate the alloy's sensitivity to heat treatment. In all cases, it was necessary to characterize the mechanical properties in this condition.

Tensile Tests. Tensile tests have been performed at 20°C (68°F), 750°C (1382°F), 850°C (1562°F), 950°C (1742°F), 1050°C (1922°F), and 1100°C (2012°F) (Figs. 4 and 5). They show that the yield strength of CM 186 LC is similar to MAR M 200 Hf. A significant improvement is obtained for ultimate tensile strength.

Creep Tests. Longitudinal creep and stress rupture tests show marginal effects of heat treatment between the SNECMA heat treatment and the Cannon-Muskegon double age of 1079°C (1975°F)/4 h + 871°C (1600°F)/20 h (Figs. 6 and 7). Tests performed on thin-wall specimens show no drop in mechanical properties. All these results confirm that even in the SNECMA standard condition, i.e., no solution heat treatment, CM 186 LC offers a creep temperature capability improvement of 20°C (36°F) compared to MAR M 200 Hf up to 1050°C (1922°F) and even more at higher temperatures. It seems that CM 186 LC is not very sensitive to aging heat treatment conditions. This beneficial feature is probably due to Re, which slows γ' coarsening that occurs during the coating simulation heat treatment. The longer term creep-rupture/phase stability data base on the alloy has now been extended out to 8328 h at 1038°C (1900°F) with maintenance of the linear log stress-log stress-rupture life relationship.

Creep and rupture tests with stress perpendicular to grain boundaries on bulk specimens have been performed to test the transverse properties (Fig. 8). The results obtained are consistent with Cannon-Muskegon transverse creep data. Metallographic analysis was performed to compare the grain boundary grain microstructure of MAR M 200 Hf and CM 186 LC (Fig.

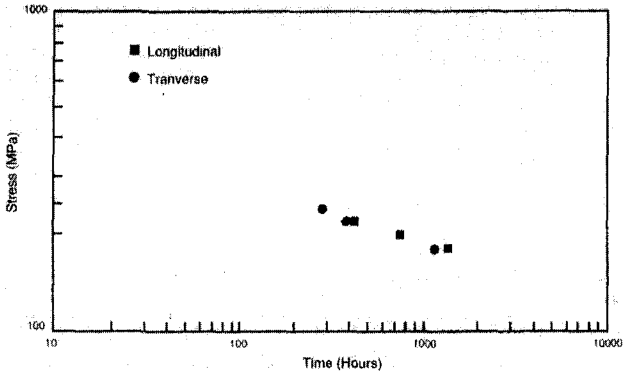

Fig. 8 DS Transverse stress-rupture properties at 950°C (1742°F)

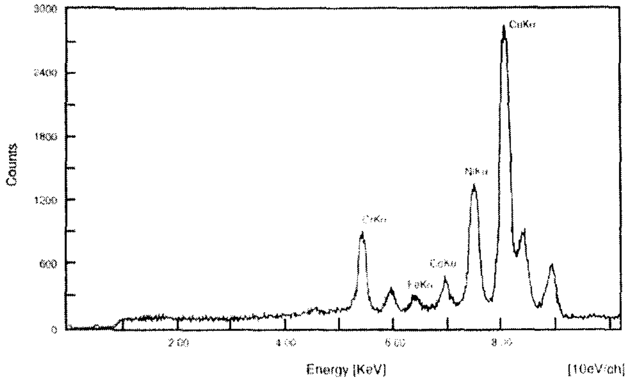

Fig. 10 Carbide analysis of MAR M 200 Hf

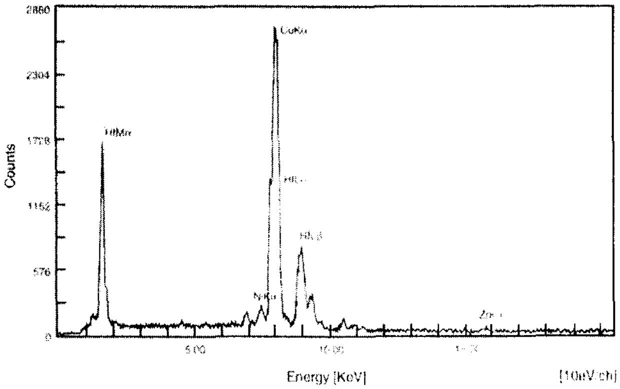

Fig. 11 Carbide analysis of CM 186 LC

Table 3 Tensile properties

Specimen	Yield strength (MPa)	UTS (MPa)*	A%
CM 186 LC/Hastelloy X (300μm)	138	147	6.8
Hastelloy X minimum		105	
CM 186 LC/Haynes Alloy 25 (300μm)	209	236	9.5
CM 186 LC//Haynes Alloy 25 (40μm)	209	230	9.5
Haynes Alloy 25 minimum	125	230	

(*UTS=Ultimate Tensile Strength)

9). The carbide distribution for MAR M 200 Hf is more continuous compared to CM 186 LC, which contains coarse γ' along the grain boundaries. Microchemical analyses using transmission electron microscopy with energy dispersive spectroscopy determined that the carbides in MAR M 200 Hf are $Cr_{23}C_6$ and are HfC in CM 186 LC (Figs. 10 and 11, respectively). The copper identified is due to the maintaining grid in the TEM.

Low Cycle Fatigue Tests. Low cycle fatigue testing is also in progress. Results were not available at time of publication.

Industrialization

In this section, the results of studies used to determine the manufacturing process parameters and the alloy sensitivity to processes needed for vane production will be presented.

Castability. Solidus and liquidus temperatures for CM 186 LC are 30°C (54°F) higher than for MAR M 200 Hf, but the castability range (liquidus-solidus) is wider in the case of MAR M 200 Hf (75°C (135°F) versus 52°C (94°F) for CM 186 LC).

Samples of CM 186 LC have been melted under vacuum at 1530°C (2786°F) in two ceramic crucibles, which represent the shell mold compositions that are used at SNECMA. The same trials have been performed with MAR M 200 Hf. Each button and crucible have been characterized visually and by chemical analysis of their surfaces and of a section in order to choose the most suitable ceramic system from a reactivity point of view. The reactivity behavior of the two alloys are very similar.

A few molds of CM 247 LC, CM 186 LC and René 142 have been cast to evaluate the alloys' DS castability. The parts cast were:

- LP turbine blade of CFM56-5C commercial engine.
- HP turbine blade of M53-P2 military engine.
- HP turbine vane of M53-P2 military engine.

For each mold, the normal DS casting parameters used for MAR M 200 Hf have been used. Fluorescent dye penetrant macroetch and X-ray inspection were performed. The results showed little porosity and good columnar grain morphology.

In view of the in-depth CM 186 LC evaluation, it was necessary to produce half a set of M53-P2 HP turbine vanes. Four molds have been cast to define casting parameters. The defects encountered have been freckles and grain morphology defects. No problems of reactivity or inclusions has appeared in production, but problems with freckles and grain morphology were confirmed. These problems are probably due to lack of experience and part geometry: The vane segment has a wide chord and is complex with large shrouds (Fig. 12).

Brazing. This study included parameter determination and mechanical property characterization. HP turbine vanes are assembled with Hastelloy® Alloy X cooling inserts and Haynes® Alloy 25 caps. Two filler metals can be used, depending on the gaps: one for gaps greater than 100 μm and another for less than 100 μm. The configurations tested are the following:

CM 186 LC—Hastelloy Alloy X with a 300 μm gap
CM 186 LC—Haynes Alloy 25 with a 300 and 40 μm gap

Process parameters currently used for MAR M 200 Hf parts were first tested. The process is the following:

- brazing of cooling inserts
- visual and X-ray inspection
- brazing of external parts
- diffusion.

The parameter selection has been made by means of SEM examination of samples brazed and heat treated in order to take

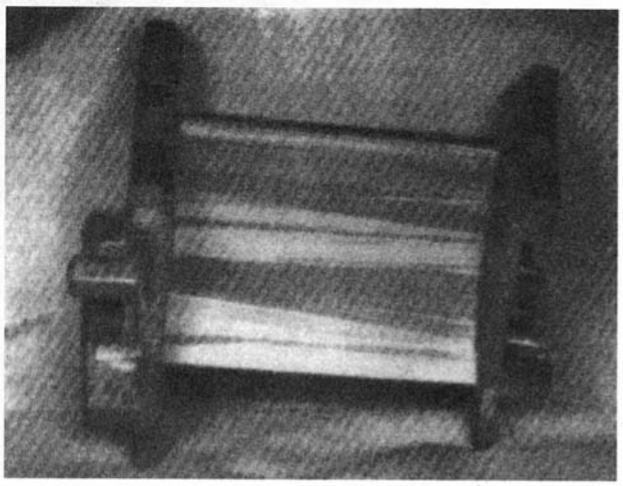

Fig. 12 M53-P2 HP turbine vane

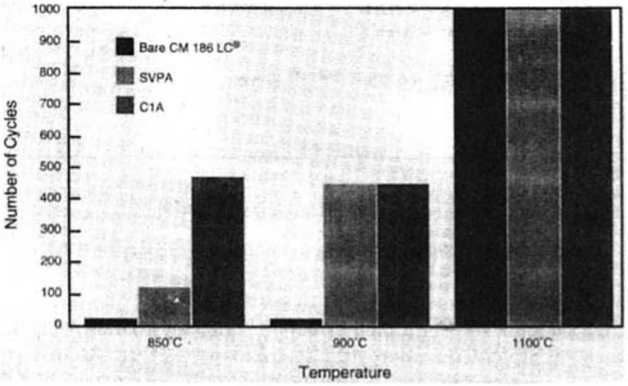

Fig. 13 Corrosion and oxidation tests at 850°C (1562°F), 900°C (1562°F), and 1100°C (2012°F)

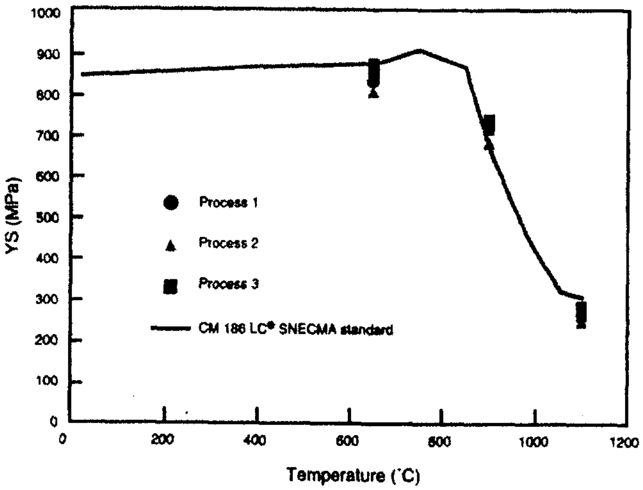

Fig. 14 Yield strength

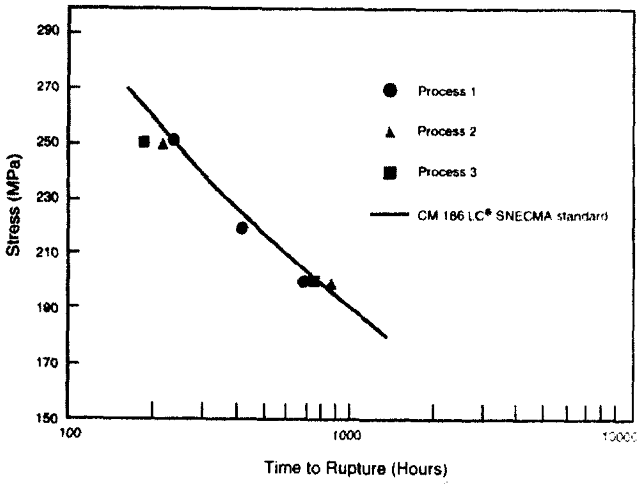

Fig. 17 Stress-rupture 950°C (1742°F)

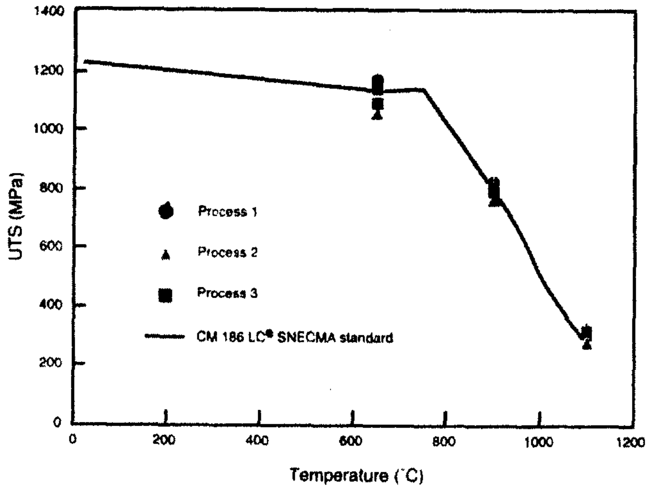

Fig. 15 Ultimate tensile strength

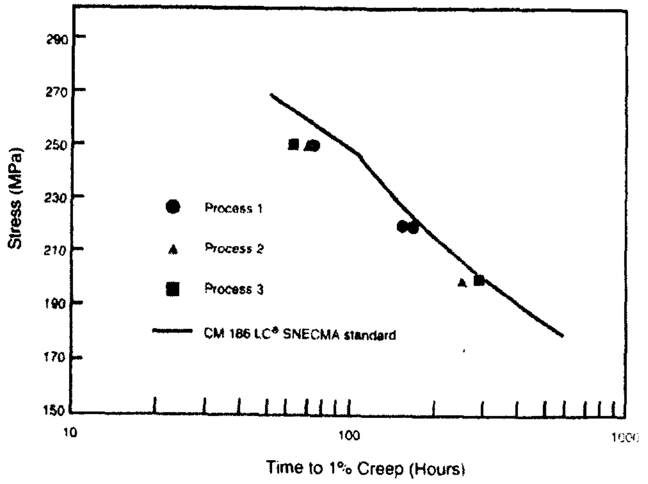

Fig. 16 1 percent creep 950°C (1742°F)

into account the combined effects of brazing, coating, and final heat treatment on microstructure and properties. At this moment, it is not known which coating will be chosen, but the potential damage is due to microstructural changes, which are controlled by process temperatures. Consequently, it was decided to coat at 1150°C (2102°F) for 3 h, which is the highest temperature that could be attained, and then age at 870°C (1598°F) for 16 h.

The micrographic examination revealed that:

- all gaps have been filled in
- no chemical reactions with the coating were apparent
- for high clearances, no eutectic phases have been met in the bonding area
- no major metallurgical transformations were seen in CM 186 LC.

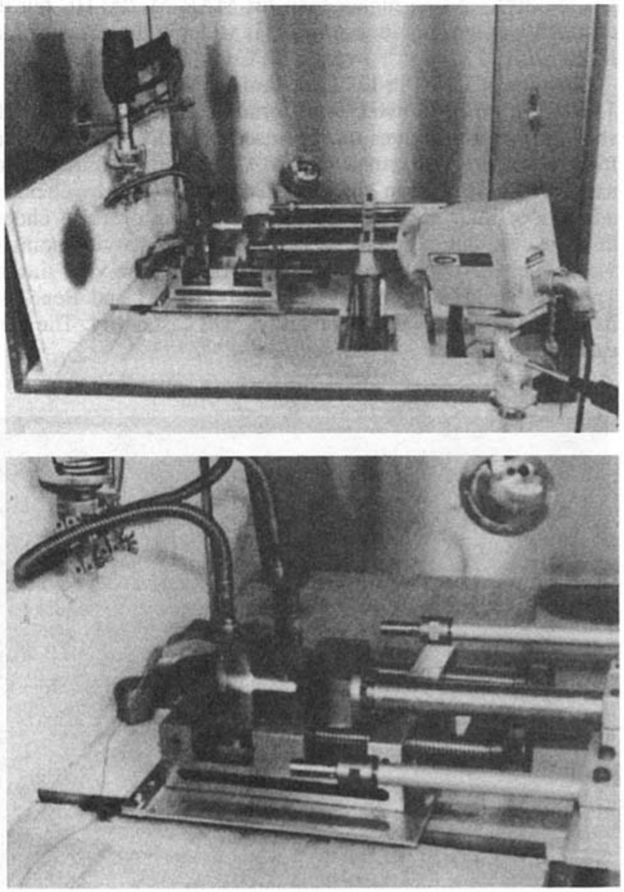

Fig. 18 Test facility and configuration

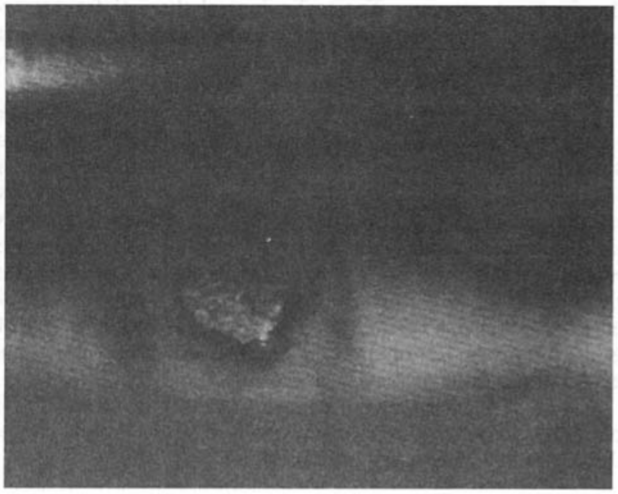

(a) MAR M 200 HF

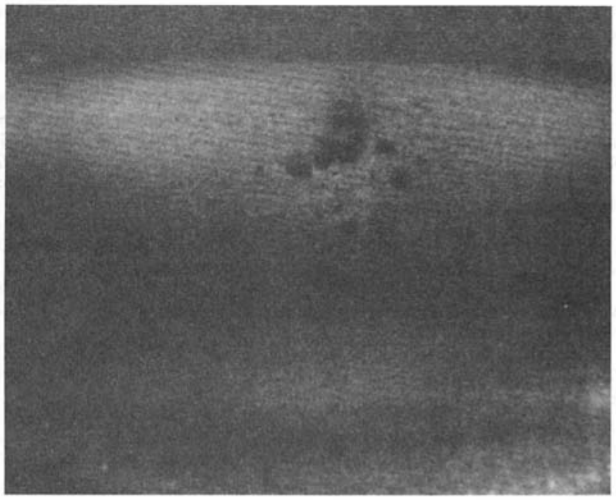

(b) CM 186 LC

Fig. 19 Leading edge damage from technological thermal fatigue test (*a*) MAR M 200 Hf (*b*) CM 186 LC

Tensile tests have been performed on brazed specimens following the process described earlier. The results are reported in Table 3. These mechanical property results are excellent.

Coating. The process parameters were to be chosen among the following possibilities:

- aluminizing by a SNECMA process (SVPA)
- C1A (chromizing and aluminizing)

Micrographic examinations have been performed but didn't show any major differences between the different coating processes. Due to this fact, the only way to select the best process was to test specimens coated in the different conditions in oxidation at 1100°C (2012°F) and hot corrosion at 850°C (1562°F) and 900°C (1652°F) (Fig. 13). The performance of CM 186 LC in the oxidation test was so good that no improvement from standard coatings was observed. The corrosion test showed that C1A was clearly better at 850°C (1562°F); both coatings performed the same at 900°C (1652°F).

Process Effects on Mechanical Properties. The goal of this study was to compare tensile and creep properties of CM 186 LC heat treated following three different vane processes to standard CM 186 LC properties:

- Process 1: brazing-diffusion-SVPA 1100°C (2012°F)/5 h
- Process 2: brazing-diffusion-C1A 1100°C (2012°F)/10 h
- Process 3: brazing-diffusion-C1A 1100°C (2012°F)/5 h + 1150°C (2102°F)/3 h.

All these parameters are possible for engine application. In addition, the test material from each process was aged at 870°C (1598°F)/16 h prior to testing.

The tests conducted were tensile test at 650°C (1202°F), 900°C (1652°F), and 1100°C (2012°F), and creep test at 950°C (1742°F). The results are shown in Figs. 14–17.

No significant drop in the mechanical properties has been observed except in creep. Metallurgical changes in γ' morphology have been observed after the treatment at 1100°C (2012°F)/5 h + 1150°C (2102°F)/3 h. So despite the fact that we didn't see any clear mechanical improvement of 1100°C (2012°F)/10 h compared to 1100°C (2012°F)/5 h + 1150°C (2102°F)/3 h, the chosen process is the following:

- Brazing
- Diffusion
- Chromizing 1100°C (2012°F)/5 h C1A coating
- SVPA 1100°C (2012°F)/5 h
- Aging 870°C (1598°F)/16 h

Technological Thermal Fatigue and Engine Test

Technological Thermal Fatigue Test. Since the thermal fatigue properties of DS alloys are highly dependent on their crystallographic orientation because of elastic anisotropy, it was interesting to test MAR M 200 Hf and CM 186 LC in conditions as close to reality as possible (except for environment). The

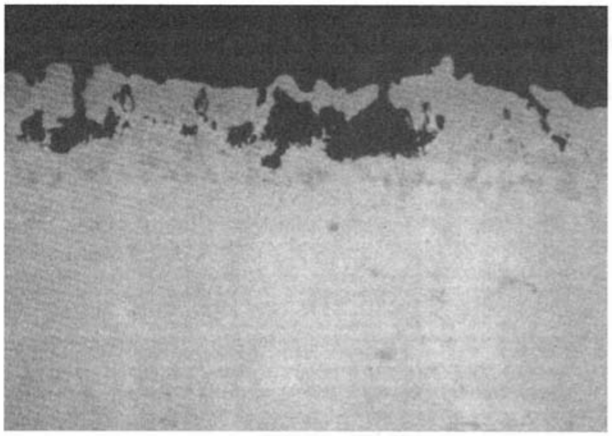

(a) MAR M 200 Hf

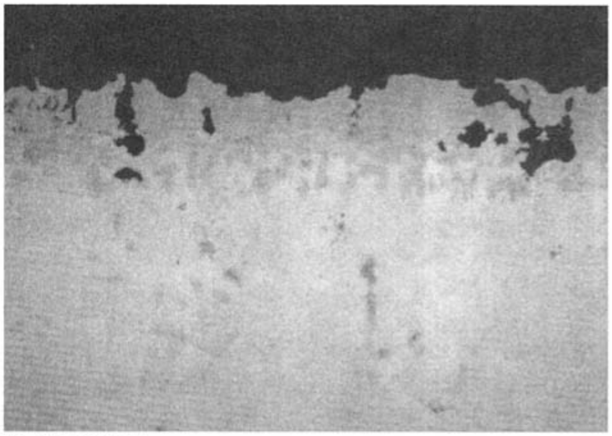

(b) CM 186 LC

Fig. 20 Oxidation pattern at leading edge from technological thermal fatigue test: (*a*) MAR M 200 Hf; (*b*) CM 186 LC intent is to evaluate, by comparison with engine test results, the importance in service of high-temperature properties and oxidation/hot corrosion resistance.

The test configuration is shown in Fig. 18. Two vanes are tested at the same time: one each of MAR M 200 Hf and CM 186 LC. The vanes were processed to the conditions chosen in the previous section (i.e., C1A-coated). The temperature was determined by an optical pyrometer, which had been checked with two other parts containing thermocouples. The cooling air inside the vanes was 100°C (212°F). The cycle, as measured by the optical pyrometer at the leading edge of the MAR M 200 Hf part, was 670°C (1238°F) to >1150°C (2102°F) in 10 s, 1150°C (2102°F) to 670°C (1238°F) in 10 s. There was no hold time in the heating and cooling cycle.

Because of air flow heterogeneity in the test facility, the maximum temperature seen by CM 186 LC was 1180°C (2156°F). The two parts have been submitted to 5000 cycles. Figure 19 shows the induced damages, and Fig. 20 compares the oxidation effects near the major defect on each part. It can be seen that the interface between the coating and the part is much more oxidized for MAR M 200 Hf. Since oxides have a greater volume than normal constituents, they force the coating to crack, which explains the larger defect on MAR M 200 Hf.

Engine Test. An endurance test on a M53-P2, a military engine, will be completed by mid 1996. Three HP turbine vane materials will be tested: MAR M 509, MAR M 200 Hf, and CM 186 LC. The results of this test were not available at the time of publication.

Conclusions

Mechanical, oxidation, and hot corrosion tests of CM 186 LC in SNECMA standard conditions show that this alloy is a good candidate for applications in future engines.

All the processes for vane and blade production have been developed (brazing and coating) to save time in an engine development program. The technological thermal fatigue test has confirmed the improved properties of CM 186 LC in oxidation and thermal fatigue and that C1A coating is well suited for CM 186 LC. Engine testing will be performed this year.

DS airfoils using CM 186 LC could be a cost-effective alternative to single-crystal components for many high-temperature applications in advanced turbine engines. Although Re-containing second generation DS alloys offer only a small raw material cost reduction compared to first-generation single-crystal alloys, DS castings are easier to produce and have lower manufacturing costs. In the foundry process, grain defect rejections are lower and production of vanes with large platforms is easier. Elimination of solution heat treatment with CM 186 LC is an important advantage compared to other DS alloys and avoids the risk of recrystallization.

For all of these reasons, CM 186 LC can find application in parts that do not require single crystal properties, but do exceed the capability of first generation DS alloys.

References

1 Ross, E. W., and O'Hara, K. S., "René 142: A High Strength, Oxidation Resistant DS Turbine Airfoil Alloy," *Superalloys*, 1992.

2 Cetel, A. D., and Duhl, D. N., "Second Generation Columnar Grain Nickel Base Superalloy," *Superalloys*, 1992.

3 Harris, K., Erickson, G. L., Sikkenga, S. L., Brentnall, W. D., Aurrecoechea, J. M., and Kubaryck, K. G., "Development of the Rhenium Containing Superalloys CMSX-4 and CM 186 LC for Single Crystal Blade and Directionally Solidified Vane Application in Advanced Turbine Engines," *Superalloys*, 1992.

4 Holt, R. T., and Wallace, W., "Impurities and Trace Elements in Nickel-Base Superalloys," *International Metal Review*, Mar. 1976.

5 Harris, K., Erickson, G. L., and Schwer, R. E., "MAR M 247 Derivations—CM 247 LC DS Alloy, CMSX Single Crystal Alloys, Properties and Performance," *Proc. 5th Symposium on Superalloys*, Seven Springs, 1984.

6 Erickson, G. L., Harris, K., and Schwer, R. E., "DS CM 247 LC-Optimized Mechanical Properties Resulting From Extensive γ' Solutioning," ASME Paper No. 85-GT-107, 1985.

7 Harris, K., Erickson, G. L., and Schwer, R. E., "CMSX Single Crystal, CM DS and Integral Wheel Alloys and Performance," *Proc. High Temperature Alloys for Gas Turbines and Other Applications*, Liège, 1986.

High-Speed Rotor Losses in a Radial Eight-Pole Magnetic Bearing: Part 1—Experimental Measurement

M. E. F. Kasarda

P. E. Allaire

E. H. Maslen

Department of Mechanical, Nuclear, and
Aerospace Engineering,
University of Virginia,
Charlottesville, VA 22903

G. R. Brown

NASA Lewis Research Center,
Cleveland, OH 44135

G. T. Gillies

Department of Mechanical, Nuclear, and
Aerospace Engineering,
University of Virginia,
Charlottesville, VA 22903

The continual increase in the use of magnetic bearings in various capacities, including high-speed aerospace applications such as jet engine prototypes, dictates the need to quantify power losses in this type of bearing. The goal of this study is to present experimentally measured power losses during the high-speed operation of a pair of magnetic bearings. A large-scale test rotor has been designed and built to obtain unambiguous power loss measurements while varying a variety of test parameters. The test apparatus consists of a shaft supported in two radial magnetic bearings and driven by two electric motors also mounted on the shaft. The power losses of the spinning rotor are determined from the time rate of change of the kinetic energy of the rotor as its angular speed decays during free rotation. Measured results for the first set of magnetic bearings, a pair of eight-pole planar radial bearings, are presented here. Data from three different parameter studies including the effect of the bias flux density, the effect of the bearing pole configuration, and the effect of the motor stator on the power loss are presented. Rundown plots of the test with the bearings in the paired pole (NNSS) versus the alternating (NSNS) pole configuration show only small differences, with losses only slightly higher when the poles are in the alternating pole (NSNS) configuration. Loss data were also taken with the motor stators axially removed from the motor rotors for comparison with the case where the motor stators are kept in place. No measurable difference was observed between the two cases, indicating negligible windage and residual magnetic effects. Throughout most of the speed range, the dominant loss mechanism appears to be eddy currents.

Introduction

In studies aimed at characterizing magnetic bearings, some of the least well-known quantities are those related to the rotor losses. In this paper, rotating losses are defined as the losses occurring in the rotor during magnetic bearing operation. They do not include stator losses such as ohmic losses in the stator windings and eddy current losses in the stator due to switching amplifier or controller frequencies. These rotor losses have four components: (1) windage loss, (2) eddy current loss, (3) alternating hysteresis loss, and (4) rotating hysteresis loss. As yet there have been very limited experimental data presented in the open literature on this subject.

Rotating losses are significant in many magnetic bearing applications. In flywheel and aircraft gas turbine applications, a major objective is the minimization of losses of all types, including rotating losses, to maximize the length of time the rotor can operate on a fixed energy/power supply. In large compressors or electric motors, the rotating loss itself may not be so important, but the heating produced by the losses can be a problem if it requires the use of extensive cooling for successful operation of the equipment. In other applications the torque required to rotate the shaft may be adversely increased due to high rotating losses.

While not extensive, some power loss studies have been published in the open literature. Matsumura and Hatake (1992) presented some experimental data. Two pole winding cases were considered: the alternating (NSNS) and paired (NNSS) cases. The experimental results given in the paper and later verified by the present authors indicate that there is little difference in the rotating losses between the alternating and paired pole configurations.

Higuchi et al. (1986) presented some experimental rotating loss data in magnetic bearings. Ueyama and Fujimoto (1990) reported power loss results in an eight-pole radial bearing up to DN = 2.8×10^6. Iron losses were studied for four magnetic materials when the test rig was run in a vacuum. No comparison to theory was performed for the magnetic components of the losses.

Kasarda et al. (1993a, b) conducted loss measurements in a low-speed test rig, operating up to approximately 2800 rpm (DN = 175,000) in air. The loss measurements indicated that bias flux is an important factor but that pole winding sequence and shaft eccentricity were very minor effects. Analytical expressions for the four loss components were developed.

Stephens and Knospe (1995a, b) presented data on power losses in planar radial magnetic bearings for two materials, silicon iron and cobalt iron, at high speeds. They operated the bearing up to 3.1×10^6 DN and at flux densities as high as 1.60 T. Bearing power losses were not measured directly. They employed an iterated, least-squares estimating technique (Stephens and Knospe, 1995a), based upon temperature and other system measurements, to evaluate thermal heating in the bearing and other test rig components. The authors (Stephens and Knospe, 1995b) also showed that paired pole wiring produced somewhat lower losses than the alternating arrangement, and that ratios of core losses for the two wirings are strongly dependent upon flux density and weakly dependent upon rotational speed.

Contributed by the International Gas Turbine Institute and presented at the 41st International Gas Turbine and Aeroengine Congress and Exhibition, Birmingham, United Kingdom, June 10–13, 1996. Manuscript received at ASME Headquarters February 1996. Paper No. 96-GT-470. Associate Technical Editor: J. N. Shinn.

Kasarda et al. (1994) discussed the design of the present high-speed test rig in some detail and gave a sensitivity analysis of the loss modeling based upon the theoretical parameters involved.

This work reports the first power loss results from that test rig. A set of two identical radial magnetic bearings was installed in the test rig and run-down measurements were made. A Hall probe was employed to measure gap fluxes for the bearings.

Power Loss Models

A rotor supported in magnetic bearings is used for taking rundown measurements to determine power loss due to the drag on the rotor from the bearings. The test rig has been designed to measure the power losses in magnetic bearings by accurately measuring the system's dissipation, viz., the conversion of the rotor's kinetic energy into heat. This is done simply by measuring the time it takes for the rotor to run down from one given speed to another. The kinetic energy of the rotor due to rotation is

$$E_k = \tfrac{1}{2} J\omega^2 \tag{1}$$

This kinetic energy is converted to heat in the journal laminations or transferred via viscous coupling to the atmosphere as the rotor decelerates. The power loss is the time derivative of the kinetic energy

$$P_k = \frac{dE_k}{dt} = \frac{d}{dt}\left(\frac{1}{2} J\omega^2\right) = J\omega \frac{d\omega}{dt} + \frac{\omega^2}{2} \frac{dJ}{dt} \tag{2}$$

The second term in Eq. (2) is negligible because the rotor materials do not have large dimensional changes as their temperature increases. The rotor polar moment of inertia, J, is 7.92 $\times 10^{-3}$ N-s^2-m (7.02 $\times 10^{-2}$ lb$_f$-s^2-in.) and $\omega(t)$ is measured so P_k is determined.

The analytical prediction model of the power loss on the rotor (Kasarda 1993a, b, 1994) is made up of four components—alternating hysteresis, rotational hysteresis, eddy currents, and windage effects, respectively—and can be expressed as:

$$P_k = J\omega \frac{d\omega}{dt} = P_{ha} + P_{hr} + P_e + P_w \tag{3}$$

Based on the form of the analytical predictions (Kasarda, 1993a, b, 1994) Eq. (3) can be written in terms of frequency dependence as:

$$P_k = J\omega \frac{d\omega}{dt} = C_h\omega + C_e\omega^2 + C_{se}\omega^4 + C_w\omega^{2.8} \tag{4}$$

where C_h represent a hysteresis coefficient incorporating both the alternating and rotational loss components, C_e represents the eddy current coefficient, C_{se} represents the eddy current skin effect coefficient, and C_w represents the windage coefficient in the respective power loss expressions. These coefficients are expected to be independent of speed and time (Kasarda et al., 1993a, b). Dividing by $J\omega$ results in

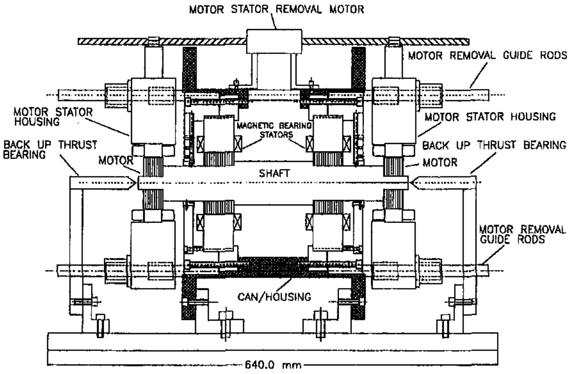

Fig. 1 **Cutaway of experimental apparatus**

$$\frac{d\omega}{dt} = \frac{C_h}{J} + \frac{C_e\omega}{J} + \frac{C_{se}\omega^3}{J} + \frac{C_w\omega^{1.8}}{J} \tag{5}$$

Experimental Arrangement

The apparatus used to measure power loss employs a rotor supported in a pair of magnetic bearings with two induction motors located at the shaft ends. The test rig has been designed so that the only significant loss mechanisms contributing to the deceleration of the rotor are expected to be from the magnetic bearings. To ensure this, no thrust bearing is used that could possibly smear the rundown data and the motor stators are retractable to eliminate any residual magnetic coupling between the motor rotors and stators. A cutaway drawing of the apparatus is shown in Fig. 1.

The test rig is designed to allow for the variation of parameters including magnetic bearing stator geometry, journal material, lamination thickness, and gap length. The main housing is built in a cylindrical or "can" arrangement, which simplifies the substitution of bearing stators while ensuring good alignment. A photograph of the entire apparatus including the controller is shown in Fig. 2.

The two electric motors located on the shaft ends drive the rotor up to top speed, at which point the motors are shut off and the motor stators are mechanically removed from the motor rotors as shown conceptually in Fig. 3. Attached to each of the motor stator housings is a ball screw, which in turn is mounted on a threaded rod. The rods are driven by a DC motor through a 90 deg gearbox and the motor stators are axially removed from the motor rotors while the rotor is suspended and spinning. The motor stator removal system can be seen in the photograph of the apparatus in Fig. 2.

The purpose of removing the motor stators is to eliminate any effects due to possible residual magnetic coupling in the motors. The choice of two motors also aids in balancing any thrust loads might any occur during the retraction operation. There are no thrust bearings, and axial centering is successfully achieved through the reluctance centering effects of the radial magnetic bearings. The entire apparatus shown in Fig. 1 will be placed in a vacuum chamber to eliminate the effect of windage on the rotor power loss measurement in future work.

Nomenclature

a_i = curve fit coefficient
b_i = curve fit coefficient
C_e = eddy current coefficient
C_h = hysteresis coefficient
C_{se} = skin effect coefficient
C_w = windage coefficient
E_k = rotor kinetic energy
J = rotor polar moment of inertia
P_e = eddy current power losses
P_{ha} = hysteresis power loss due to alternating flux
P_{hr} = hysteresis power loss due to rotating flux
P_k = kinetic power loss
t = time
ω = rotor angular velocity

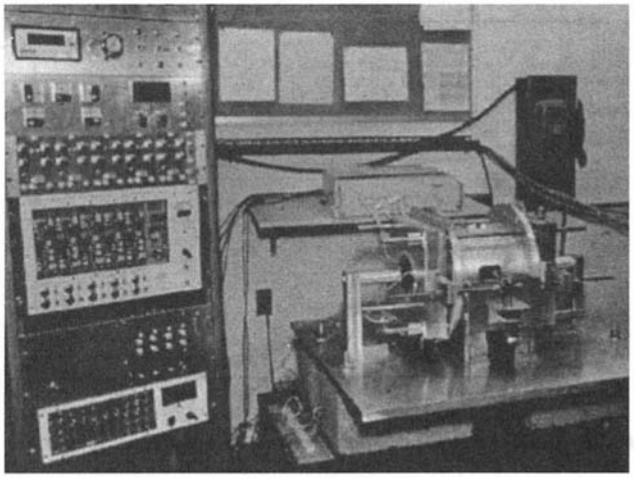

Fig. 2 Test setup

The rotor has been designed to have equal loading on the two magnetic bearings to obtain identical operating characteristics of the bearings. The total length of the rotor is 39.0 cm and the assembled rotor weighs 11.3 kg (25.0 lb). The set of bearings used in the data presented here are an eight-pole radial heteropolar design. The diameter of the bearing journals is 9.1 cm and the axial length is 4.4 cm. The radial bearing clearance, or gap length, is 0.762 mm (0.030 in.). The percentage of the journal surface area covered by the surface area of the stator poles is 53 percent.

This rotor is designed to run up to a maximum DN of 4.5 × 10^6 corresponding to 50,000 rpm or a surface speed of 239 m/s at the bearing. However, the yield strength of the current journal material limits the first set of tests to a top speed of about 32,000 rpm corresponding to a DN of approximately 2.9 × 10^6. Because of its common use in existing magnetic bearings, an M-15 grade 3 percent silicon-iron in a 0.356 mm (0.014 in) lamination thickness has been used to build the set of bearings under analysis. Future bearing journals made from a high-strength cobalt–iron alloy will allow higher speeds.

The speed of the rotor is monitored by a reflective object sensor. A black line has been painted over approximately half the shaft and the resulting signal from the probe passes through a Schmidt trigger, which produces a 5-V peak-to-peak square wave whose frequency matches the rotational frequency of the shaft.

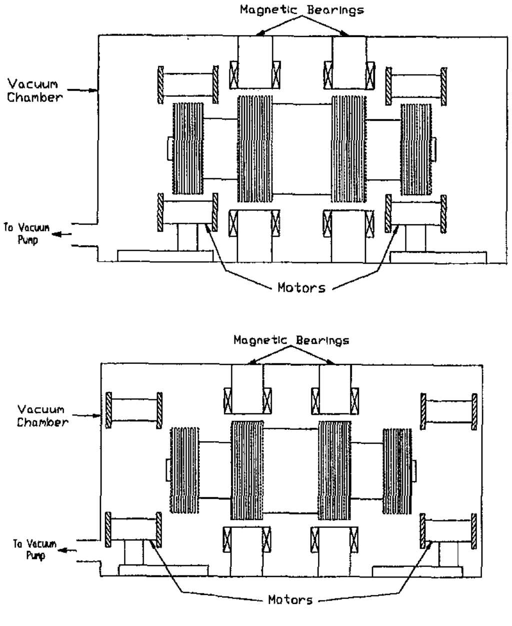

Fig. 3 (*a*) Runup configuration; (*b*) rundown configuration

It is possible that additional control fluxes in the bearings are necessary to control a rotor through highly unbalanced critical speeds, which could result in additional power losses. Since quantifying this effect is not in the scope of the project, every effort was made to eliminate rotor vibrations. The rotor-bearing system has been designed so that all rotor bending modes are located well above the operating speed range. The rotor has also been high-speed balanced to minimize the effect of any residual unbalance on the power losses.

Results

The test rotor operates smoothly with extremely low rundown rotor orbit amplitudes below 0.025 mm (0.001 in.) p–p, well within the back-up bearing diametral clearance of 0.254–0.356 mm. No axial loads are imparted on the rotor during the retraction of the motors and no significant axial motion of the rotor is present. The motor retraction step takes approximately 7 seconds, which is a small fraction of the total rundown test period. The rundown time for an eight-pole planar radial magnetic bearing from 28,000 rpm ranges from approximately 250 seconds to 400 seconds for the cases presented here. Three parameter studies were analyzed with the eight-pole bearing including a study of the effect of motor stator retraction, a variation of pole configuration (NNSS versus NSNS), and a variation of bias flux density.

Data Reduction. Rundown data were evaluated using the model in Eq. (5). For ease of notation in describing the method of data reduction, Eq. (5) is represented as follows

$$\frac{d\omega}{dt} = a_1 + a_2\omega + a_3\omega^3 + a_4\omega^{1.8} \tag{6}$$

where the coefficients are defined as

$$a_1 = \frac{C_h}{J}; \quad a_2 = \frac{C_e}{J}; \quad a_3 = \frac{C_{se}}{J}; \quad a_4 = \frac{C_w}{J}$$

Measured power loss was determined from the rundown curves by first using a minimization routine where the coefficients a_i in the model of the time rate of change of speed (Eq. (6)) were determined for each specific data set.

For every candidate set of coefficients for a specific set of rundown data, a set of values for speed versus time was generated by integrating Eq. (6) and the error between the calculated speed and actual speed was determined. New sets of coefficients are then generated until this error has been minimized using a simplex search method (Press et al., 1989). Once the optimum coefficients have been determined, Eq. (6) is substituted in Eq. (4) and the power loss, P_k, is determined as a function of ω.

Table 1 Model coefficients

	Coefficients Including Skin Effects	Coefficients Without Skin Effects
Hysteresis Coefficient	a_1= -2.0359x10^1 rpm-s^{-1}	b_1 = -2.2071x10^1 rpm-s^{-1}
Eddy Current Coefficient	a_2 = -7.1907x10^{-3} s^{-1}	b_2 = -6.1941x10^{-3} s^{-1}
Skin Effect Coefficient	a_3 = -2.0307x10^{-12} rpm^{-2}-s^{-1}	-------------------
Windage Coefficient	a_4 = -1.3849x10^{-7} $rpm^{-.8}$-s^{-1}	b_3 = -7.8191x10^{-7} $rpm^{-.8}$-s^{-1}

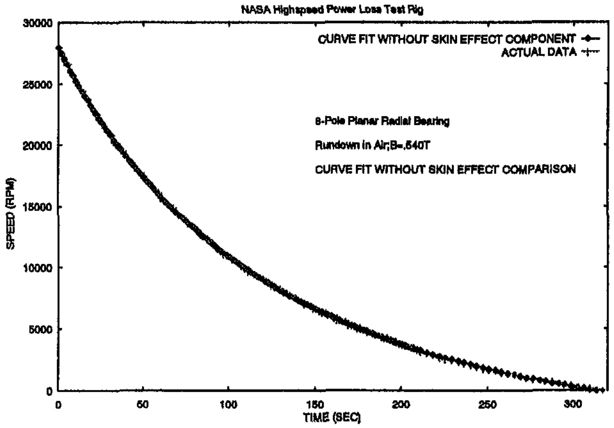

Fig. 4 Experimental curve fit model and actual rundown data

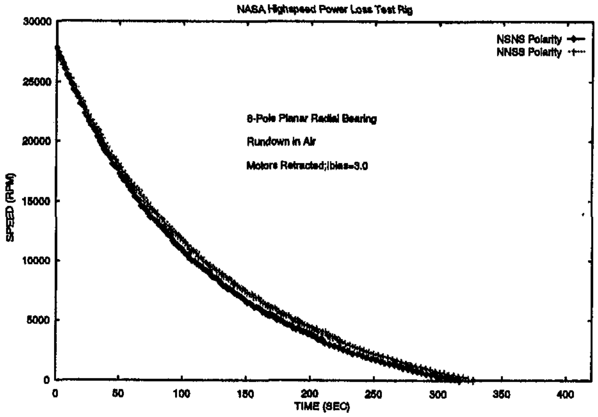

Fig. 6 Effect of stator pole polarity on rotor rundown characteristics

The rms error between the calculated speeds using the optimized coefficients, a_i, and the actual speed for the case when the average bias flux is equal to 0.540 T is only 58 rpm, which is within the estimated measurement uncertainty of ±300 rpm at high speeds. A more detailed uncertainty analysis will be forthcoming. The calculated coefficients are shown in Table 1 to all be negative. However, a_3, which represents the skin effect, is expected to be positive since it begins to decrease the contribution of the eddy currents due to crowding of the currents at the surface of the bearing laminations. To understand this result better, a second attempt at data reduction was run with the following model, which discounts the contribution of the skin effects. This second model is

$$\frac{d\omega}{dt} = b_1 + b_2\omega + b_3\omega^{1.8} \tag{7}$$

The same minimization routine was used and the calculated speeds and actual measured speeds are plotted versus time in Fig. 4. Once again an excellent curve fit is generated with an rms error of 62 rpm and the values of the new coefficients b_i are listed in Table 1.

A calculation of the power loss throughout the speed range using each of the two models (Eq. (6) and (7)) was made. Both models resulted in essentially the same values for the power loss throughout the speed range with only a small variation at the higher speeds.

To examine the sensitivity to the eddy current model, a curve fit was determined for the following model excluding the eddy current component:

$$\frac{d\omega}{dt} = c_1 + c_2\omega^{1.8} \tag{8}$$

A substantially inferior curve fit with an rms error of 400 rpm and particularly poor trends at the ends of the rundown curve was achieved with this model and demonstrates the importance of including the eddy current effects. Similarly, a model excluding the windage contribution was examined and a substantially inferior curve fit with an rms error of 164 rpm was achieved. Apparently it is less damaging to ignore windage than the eddy currents; this supports the conclusion that the eddy current effects are the dominant loss mechanism.

This analysis indicates that the models of the windage and eddy current effects are important components in the data reduction analysis and that skin effects may be present but are not measurable for this set of data. Therefore, the expression without skin effects, Eq. (7), is used to determine the experimental value of power loss, P_k, from the rotor rundown data.

Experimental Data

Effect of Motor Stator Retraction. A single case was run first with the motor stators retracted and then again with the motor stators not retracted. No measurable difference occurs between the two cases, as shown in Fig. 5. This appears to demonstrate that windage is independent of the surrounding annulus. This result would imply that the windage loss can be modeled as flow over a flat plate as presented in Ueyama and Fujimoto (1990) and Kasarda et al. (1993b, b, 1995), as opposed to a model of the Couette flow between a rotating and stationary cylinder. The motor stators have a radial clearance of approximately 0.330 mm (0.013 in.). Since the bearing radial

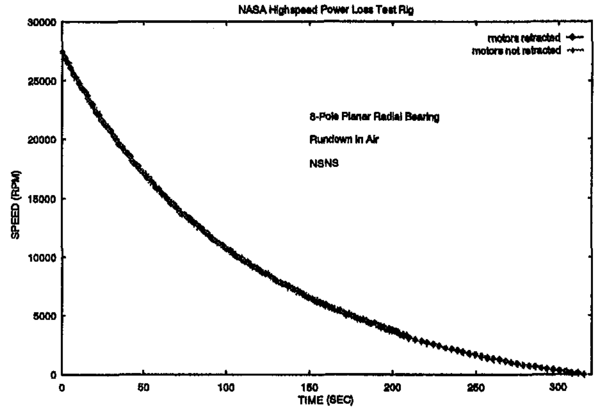

Fig. 5 Effect of motor retraction on rotor rundown characteristics

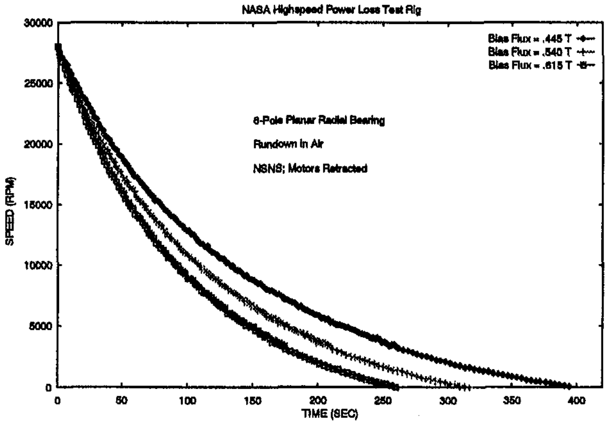

Fig. 7 Effect of bias flux on rotor rundown characteristics

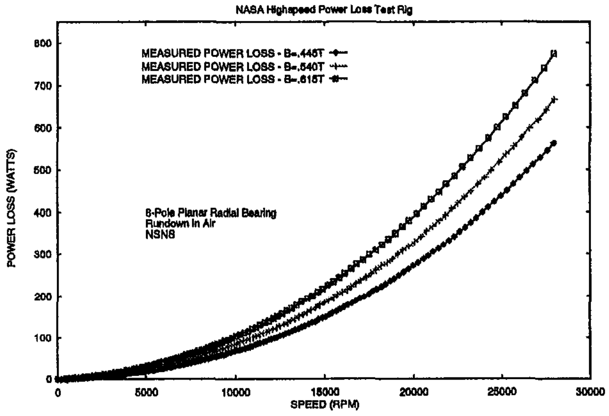

Fig. 8 Effect of bias flux on measured power loss for entire rotor

clearance in this case is 0.762 mm (0.030 in.), and is significantly larger than the motor radial clearance, these results imply that the bearing poles do not protrude significantly into the boundary layer around the bearing journal and their effect can be neglected in the analytical model of the windage loss.

Pole Configuration. As noted above, there has been considerable previous discussion in the literature over the effect of pole configuration on the rotating losses. A case was run with the poles configured in an alternating pattern (NSNS) and compared with the paired-pole configuration (NNSS). The rundown results (speed versus time) are presented in Fig. 6 and demonstrate only a slightly faster rundown (indicating slightly higher rotating losses) for the alternating pole configuration. This is in accordance with the experimental results reported by Stephens et al. (1995b) and Matsumura Hatake (1992).

Variation of Bias Flux. Rundown data was taken for three different bias flux levels. For a given setting of the bias current, a measurement of the flux levels under all of the bearing poles was measured with the rotor stationary using a Hall effect probe and averaged.

The average measured flux densities for the three cases are 0.445 T, 0.540 T, and 0.615 T, respectively. Plots of rundown speed versus time for these three cases are shown in Fig. 7. The case when the bias flux is the smallest shows the longest rundown time, on the order of 400 seconds. The case when the bias flux is at its maximum value shows the shortest rundown time, on the order of 250 seconds.

A power loss, P_k, was determined for each of the three bias flux cases using Eq. (2) neglecting the second term in the expression. A plot of power loss versus speed for these three cases is shown in Fig. 8. At the maximum speed reported, 28,000 rpm, the power loss varies from approximately 563 Watts when $B = 0.445$ T to approximately 774 Watts when $B = 0.615$ T.

Conclusions

Rundown data were taken for a pair of eight-pole heteropolar bearings in air at atmospheric pressure. The effect of the motor stator removal from the rotor was determined to be negligible. The alternating pole configuration (NSNS) was shown to result in only a slightly faster rundown time, demonstrating only a marginally higher power loss than the paired pole configuration (NNSS). The effect of three different levels of bias flux on the losses was examined and significant differences were observed. Measured power losses at the reported top speed of 28,000 rpm for the entire rotor varied between 563 Watts when the bias flux density was 0.445 T to 774 Watts when the bias flux density was 0.615 T. Additional data, including a study that will have a large variation of the experimental parameters including the elimination of the windage effects by use of a vacuum chamber, will be taken. The additional experimental data along with more detailed analytical analysis will result in general power loss expressions for use at the design stage of future magnetic bearings.

Acknowledgments

This research was funded in part by NASA Lewis Research Center and the Commonwealth of Virginia's Center for Innovative Technology. The authors would like to thank Chris Sortore, Dr. Ted Brockett, Michael Baloh, Lance Fujita, and Klaus Brun for the assistance at various points in this project.

References

Higuchi, T., Mizuno, T., and Miyake, S., 1986, "Experimental Study of Rotational Loss in Magnetic Bearings," *Proc. Conf. IPE,* Japan, pp. 53–54.

Kasarda, M. E., Allaire, P. E., Hope, R. W., and Humphris, R. R., 1993a, "Measured and Predicted Losses in Planar Radial Magnetic Bearings," *Proceedings of Mag '93,* Alexandria, VA.

Kasarda, M. E., Allaire, P. E., Hope, R. W., and Humphris, R. R., 1993b, "Comparison of Experimentally Measured and Calculated Losses in Planar Radial Magnetic Bearings," *Proc. Rotating Machinery Conference,* New Jersey Institute of Technology, Vol. 2.

Kasarda, M. E. F., Allaire, P. E., Haslen, E. H., and Gillies, G. T., 1994, "Design of a High Speed Rotating Loss Test Rig for Radial Magnetic Bearings," *Proc. Fourth International Symposium on Magnetic Bearings,* ETH Zurich.

Matsumura, F., and Hatake, K., 1992, "Relation Between Magnetic Pole Arrangement and Magnetic Loss in Magnetic Bearing," *Proc. Third International Conference on Magnetic Bearings,* Alexandria, VA, pp. 274–283.

Press, W. H., Flannery, B. P., Teulolsky, S. A., and Vetterling, W. T., 1989, *Numerical Recipes,* Cambridge University Press.

Stephens, L. S., and Knospe, C. R., 1995a, "Determination of Power Losses in High Speed Magnetic Journal Bearings Using Termperature Measurements," *Experimental Heat Transfer,* No. 8, pp. 35–56.

Stephens, L. S., and Knospe, C. R., 1995b, "Effect of Magnetic Pole Arrangement on Core Loss in Laminated High Speed Magnetic Journal Bearings," submitted to *IEEE Transactions on Magnetics.*

Ueyama, H., and Fujimoto, Y., 1990, "Iron Losses and Windy Losses of Rotational Speed Rotor Suspended by Magnetic Bearings," *Proc. 2nd International Symposium on Magnetic Bearings,* Tokyo, Japan, pp. 237–242.

M. E. F. Kasarda

P. E. Allaire

E. H. Maslen

Department of Mechanical, Nuclear, and
Aerospace Engineering,
University of Virginia,
Charlottesville, VA 22903

G. R. Brown

NASA Lewis Research Center,
Cleveland, OH 44135

G. T. Gillies

Department of Mechanical, Nuclear, and
Aerospace Engineering,
University of Virginia,
Charlottesville, VA 22903

High-Speed Rotor Losses in a Radial Eight-Pole Magnetic Bearing: Part 2—Analytical/Empirical Models and Calculations

The continual increase in the use of magnetic bearings in various capacities, including high-speed aerospace applications such as jet engine prototypes, dictates the need to quantify power losses in this type of bearing. The goal of the present study is to develop and experimentally verify general power loss equations for the high-speed operation of magnetic bearings. Experimental data from a large-scale test rotor have been presented in Part 1 of this study. Analytical/empirical predictions are presented here for the test bearings, a pair of eight-pole planar radial bearings, for comparison to the experimental results from Part 1. Expressions for the four loss components, eddy current, alternating hysteresis, rotating hysteresis, and windage, are also presented. Analytical/empirical predictions for the test bearings at three different bias flux levels demonstrate good correlation with corresponding experimental data. Throughout most of the speed range the dominant loss mechanism appears to be eddy currents.

Introduction

It is common to claim that magnetic bearing losses are "low" compared to those of fluid film and rolling element bearings, but reliable calculations of the losses, or quoted values, are not available in the literature. Not only are these losses difficult to predict, but the variation of the losses with magnetic bearing design parameters such as clearance, rotational speed, flux-path direction, flux level, and lamination thickness is not well understood. The ability to predict rotating losses at the design stage would permit design and optimization for minimal loss.

For example, the two primary flux-path schemes are radial (sometimes called heteropolar because of the different poles, north and south in a plane) and axial/radial (called homopolar because the poles in one radial plane are all of a single type, say north, and the south poles are in another plane located at a different point along the shaft). There are currently no comparable measured values of rotating losses for these two major types of design to allow proper assessment of the relative merits of each scheme. The authors of this paper have not yet tested homopolar bearings and therefore are unable to predict which design has the lower rotating power loss. However, by presenting measured data on a new high-speed loss test rig, this paper will contribute to the eventual quantification of these losses.

While not extensive, some power loss studies have been published in the open literature. Matsumura et al. (1988) discussed magnetic bearing losses, including a partial Fourier analysis of magnetic flux as seen by the rotor as it passes the poles in the bearing. The discussion in the paper indicates that the rate of change of flux at the pole edges is very important and suggests that the sharpness of the rise is the critical factor. Two pole winding cases were considered: the alternating (NSNS) and paired (NNSS) cases. The experimental results given in the paper indicate that there is little difference in the rotating losses between the alternating and paired pole configurations. This result is consistent with the hypothesis that the edge effects dominate the losses.

Ueyama and Fujimoto (1990) reported power loss results in an eight-pole radial bearing. Iron losses were studied for four magnetic materials when the test rig was run in a vacuum. No comparison to theory was performed for the magnetic components of the losses.

Kasarda et al. (1993a, b) conducted loss measurements in a low-speed test rig, operating up to approximately 2800 rpm (DN = 175,000) in air. The loss measurements indicated that bias flux is an important factor but that pole winding sequence and shaft eccentricity were very minor effects. The results were compared to theoretical calculations involving models of the four loss mechanisms indicated above. The theoretical calculations were below the measured values by approximately 24 percent. Kasarda and Allaire (1995) presented data on low-speed power losses and enhancements of the theoretical modeling approach. A dynamic pole-width fraction was introduced to account for the edge effects noted earlier by Matsumura and Hatake (1992). Formulas for effective frequencies and rotor volumes were discussed.

The effect of losses on magnetic bearing controller performance has been addressed by a few researchers. Zmood et al. (1987) developed a transfer function representation that includes a first-order model of the nonrotating eddy current influence for control system analysis. Meeker et al. (1995) address the electromechanical bandwidth limitation introduced by eddy currents induced by control flux variation but also without shaft rotation effects. The effect of the losses on controller performance is beyond the current scope of this work.

Kasarda et al. (1994) discussed the design of the present high-speed test rig in some detail and gave a sensitivity analysis of the loss modeling based upon the theoretical parameters involved. Part 2 of this work reports the analytical/empirical modeling and power loss calculations for comparison to results from that test rig as reported in Part 1 of this paper. A set of two identical radial magnetic bearings was installed in the test rig and run-down measurements were made. A Hall probe was employed to measure gap fluxes for the bearings.

Contributed by the International Gas Turbine Institute and presented at the 41st International Gas Turbine and Aeroengine Congress and Exhibition, Birmingham, United Kingdom, June 10–13, 1996. Manuscript received at ASME Headquarters February 1996. Paper No. 96-GT-471. Associate Technical Editor: J. N. Shinn.

Power Loss Models

Analytical/Empirical Prediction Models. The total power loss exhibited by a rotating shaft supported in magnetic bearings consists of four loss components: alternating hysteresis, rotational hysteresis, eddy currents, and windage. Analytical/empirical models are widely available for each of the four components. The models used in this analysis are slight modifications of the ones presented in detail by Kasarda and Allaire (1995).

Rotational Hysteresis. Rotational hysteresis occurs when the magnitude of the field in a material remains constant but its orientation with respect to the material is changing. The magnitude of the loss is determined based on experimental data presented by Brailsford (1938) that was developed for a generic silicon iron. The authors are currently unaware of any rotational hysteresis loss data supplied by manufacturers for specific materials. The expression presented here has been modified slightly from the earlier form used by Kasarda et al. (1993a, b, 1995) to account for higher flux levels. The expression for rotational hysteresis loss is based on a linear curve fit of the experimental data (Brailsford, 1938) in the region of interest and is expressed as

$$P_{hr} = [3000.0 \times B_{\max} - 500.0][1.0 \times 10^{-7}] \times f_r M_{vr} (\text{Watt/cm}^3) \quad (1)$$

where $B_{\max}$ is the maximum flux density in Tesla, f_r is the effective frequency in Hz, and M_{vr} is the effective volume coefficient for the rotational hysteresis phenomenon. This value for P_{hr} is then multiplied by the total volume of journal laminations (cm^3) to obtain a power loss in Watts. The effective frequency and effective volume coefficient used in this expression will be addressed at the end of this section.

Alternating Hysteresis. The alternating component of the hysteresis loss in a magnetic material is due to the effects of traversing a complete cycle of the BH curve. This occurs in the rotor of a magnetic bearing as it passes the differently polarized pole faces. The loss for one rotor lamination stack is given by the formula from Steinmetz (Knowlton, 1949) as

$$P_{ha} = 10^{-7} \eta f (10000. \times B_{\max})^k M_v (\text{Watts/cm}^3) \quad (2)$$

Steinmetz (Knowlton, 1949) reports that the hysteresis coefficient, η, has a value of approximately 0.00046 for a good grade of silicon iron and that the exponent, k, has an approximate value of 1.6 for flux densities in the range of 0.15 to 1.2 Tesla. The rotational hysteresis loss and the alternating hysteresis loss expressions are added together and used in the calculation of losses as reported at the end of this paper for comparison with the experimentally measured hysteresis loss. The effective frequency f is in Hz, $B_{\max}$ is in Tesla, and M_v is the effective volume coefficient. Equation (2) is then multiplied by the total journal volume (cm^3) to determine the power loss in watts. The effective frequency and effective volume coefficient used in this expression will also be addressed at the end of this section.

Eddy Currents. A formula for the power loss due to eddy currents has been developed by Golding (1961) and others (MIT Electrical Engineering Staff (1943)) by integrating ρI^2 over the volume of the magnetic material, where ρ is the material resistivity and I is the current due to the induced emf from the alternating flux in the rotor laminations. The loss formula, including the first term of the series expansion for the skin effect, is

$$P_e = \frac{\pi^2 d^2 B_{\max}^2 f^2 M_v (10^{-6})}{6\rho} \times \left[1 - \frac{6}{945} \left(\pi d \sqrt{\frac{2(\mu \times 10^{-7}) f}{\rho}} \right)^4 + \cdots \right] \quad (\text{Watts/cm}^3) \quad (3)$$

where, d, the lamination thickness, is 3.56×10^{-4} m, ρ, the nominal iron resistivity, is 4.8×10^{-7} Ω-m, and μ, the relative permeability of the material, is estimated at 6300. These values were obtained from the material manufacturer but can also be found in various texts such as the *Metals Handbook* (Lyman, 1972). The resistivity may vary as the temperature of the laminations increase and is addressed in the results section of this paper.

Other parameters in Eq. (3) include $B_{\max}$, the peak flux density in Tesla, f, the effective eddy current frequency in Hz, and M_v, the effective volume coefficient. This value for P_e is then multiplied by the total journal volume (cm^3) to determine the power loss in Watts. Values used for the effective frequency and volume coefficient used in this expression will also be addressed at the end of this section.

The reduction of data presented in Part 1 shows that minimal skin effects based on this model are present for this set of tests. Therefore, the skin effect term in this equation is neglected and the validity of this term or the choice of series truncation in Eq. (3) cannot be verified at this time.

Windage. The formula to calculate power loss due to windage is based on Von Karman's work for turbulent flow over a flat plate. Ueyama and Fujimoto (1990) achieved good correlation to experimental data of windage loss calculations using a turbulent flow model. While the Reynolds numbers for part of the range of this application are below the transition Reynolds number for turbulent flow over a smooth plate, the surface roughness of the disks justifies the use of the turbulent flow model. Therefore, windage losses on the rotor were calculated based upon the drag force on a turbulent boundary layer as developed by Von Karman and presented by Shames (1982). For a fully turbulent boundary layer on a flat plate of length $2\pi R$ and width L, the drag force is

Nomenclature

b_i = measured coefficients
$B_{\max}$ = maximum magnetic flux density
d = lamination thickness
D = windage drag force on rotor
E_k = rotor kinetic energy
f = effective frequency, Hz
f_r = effective frequency for rotational hysteresis loss
J = rotor polar moment of inertia
k = hysteresis flux exponent
L = rotor axial length
M_v = effective volume coefficient
M_{vr} = effective volume coefficient for rotational hysteresis loss
P_e = eddy current power loss
P_{ha} = hysteresis power loss due to alternating flux
P_{hr} = hysteresis power loss due to rotating flux
P_k = kinetic power loss
P_w = power loss due to windage
R = rotor radius
t = time
T = temperature
U = surface velocity of rotor
α = temperature coefficient
η = hysteresis coefficient
ρ = material resistivity
ρ_g = gas density
ν = gas viscosity
ω = rotor angular velocity

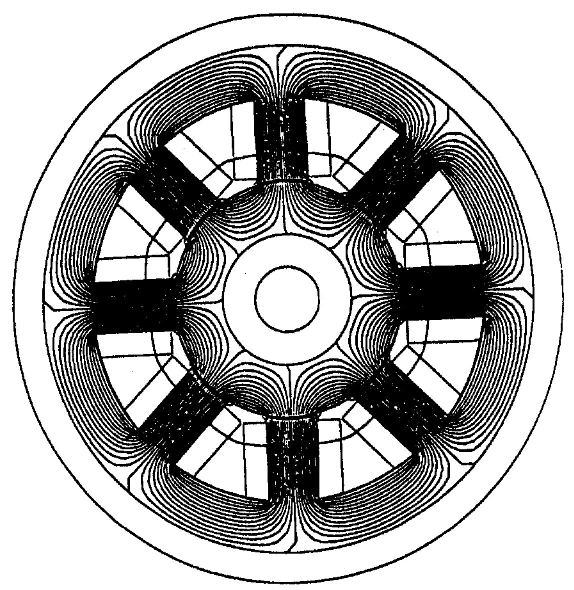

Fig. 1 Finite element plot of lines of magnetic flux for static case (zero shaft rotational speed)

$$D = 0.074\left(\frac{1}{2}\,\rho_g 2\pi R U^2 L\right)\left(\frac{\nu}{2\pi R U}\right)^{0.2} \qquad (4)$$

The surface speed, U, is given as $R\omega$, so this expression becomes

$$D = 0.074\pi\rho_g R^3 L(\omega^2)\left(\frac{\nu}{2\pi R^2\omega}\right)^{0.2} \qquad (5)$$

The windage power loss for each rotor component is

$$P_{w_i} = DU = 0.074\rho_g L\pi R^4\omega^3\left(\frac{\nu}{2\pi R^2\omega}\right)^{0.2} \qquad (6)$$

where ρ_g, the density of air, is 1.2 kg/m^3 and ν, the viscosity of air, is 1.501×10^{-5} m^2/s from Shames (1982) and ω is the shaft rotational frequency in rad/s. The radius, R, of the motor rotors, exposed shaft up to bearings, midspan shaft section, and bearing journals are 0.038 m, 0.025 m, 0.032 m, and 0.045 m, respectively. The associated total lengths, L, of these four areas are 0.057 m, 0.119 m, 0.114 m, and 0.087 m, respectively. The total windage power loss is the sum of the losses on these components.

Effective Frequency and Volume. Effective frequencies and effective volumes are used in Eqs. (1)–(3). All effective frequencies for use in the calculation of the various loss components are expected to be related to the geometry of the bearing stator. The effective frequency for use in the calculation of eddy current and alternating hysteresis effects (Eqs. (2)–(3)), which are dictated by edge effects, has been estimated at 16 times the rotational frequency of the rotor. This value corresponds to the number of edges a portion of the rotor volume must pass during one revolution of the rotor. Fourier analysis suggests 16 times the rotational frequency. This has been examined by Matsumura et al. (1988). This effective frequency is also consistent with the range of possible values determined using the geometric-based estimation technique by Kasarda and Allaire (1995).

The effective frequency coefficient for use in the rotational hysteresis expression, Eq. (1), is determined based on different criteria. Shown in Fig. 1 is a nonrotating two-dimensional finite element analysis (FEM) of the test bearing. The dominant frequency for the rotating hysteresis phenomenon is based upon the number of magnetic field rotations experienced by the rotor per second at a location below the surface of the rotor laminations. The effective frequency used for the evaluation of Eq. (1) is four times the rotational frequency for an eight-pole bearing with a NSNS pole configuration, which is equal to the number of pairs of magnetic flux "loops" experienced during one rotation of the rotor in the FEM analysis in Fig. 1. Each pair represents a complete directional flux reversal.

The effective volume coefficient is another parameter that needs to be determined for each of the loss phenomena. As shown in Fig. 1, the entire volume of journal magnetic material is not filled with magnetic flux at the peak value, unlike the transformer laminations some of these formulas were originally developed for. Therefore, some effective volume, which is less than the total volume, should be used in determining the power losses in Eqs. (1)–(3). Discussion of values used for this analysis is presented in the results section of this paper.

The proper determination of effective frequency and effective volume for the general case will be evaluated after more data are taken on different bearing designs along with the evaluation of corresponding detailed finite element analyses (FEM) and more detailed evaluation of field equations similar to the analyses by Allaire (1995). A FEM code is currently under development at the University of Virginia to allow for a more representative analysis of the experimental case under analysis.

Results

Variation of Bias Flux. Power loss measurements for the test rotor were determined from rundown data for three different bearing bias flux cases as described in detail in Part 1 and are shown in Fig. 2. For a given setting of the bias current, a measurement of the flux levels under all of the bearing poles was made with the rotor stationary using a Hall effect probe and averaged for use in the analytical/empirical prediction models of the bearing losses (Eqs. (1)–(3)). The average measured flux densities for the three cases are 0.445 T, 0.540 T, and 0.615 T, respectively.

A prediction of power loss as described in the analytical/empirical prediction models section, including values listed there for various parameters, was made for each of the three bias flux cases. However, the skin effect term in Eq. (3) was neglected based on the conclusion from the data reduction analysis in Part 1 that the skin effects are negligible for this set of tests. Most parameters such as lamination thickness, journal diameter, etc., are fairly well known. However, some uncertainty is presented in the values used for effective frequency, effective volume, and resistivity.

As discussed earlier, the effective frequency for use in the calculation of eddy current and alternating hysteresis effects

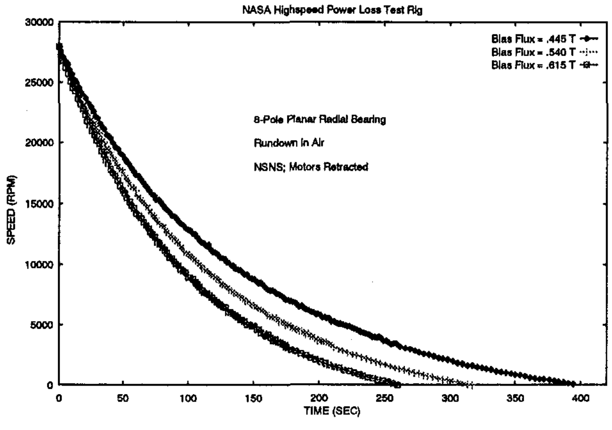

Fig. 2 Effect of bias flux on rotor rundown characteristics

Table 1 Measured coefficients

	Measured Coefficients B = .540 T
Hysteresis Coefficient	$b_1 = -2.2071\text{x}10^1$ rpm-s^{-1}
Eddy Current Coefficient	$b_2 = -6.1941\text{x}10^{-3}$ s^{-1}
Windage Coefficient	$b_3 = -7.8191\text{x}10^{-7}$ rpm$^{-.8}$-s^{-1}

(Eqs. (2)–(3)), which are dictated by edge effects, has been estimated at 16 times the rotational frequency of the rotor. Recall also, that the effective frequency for calculation of the rotating hysteresis loss (Eq. (1)) is estimated at four times the rotational frequency of the rotor based on the number of pairs of magnetic loops traversed by the journal during one revolution of the rotor.

If the respective effective frequencies listed above are assumed to be correct for use in Eqs. (1)–(3), an effective volume for each phenomena can be backed out of the experimental data. The form of the experimental curve fit from Part 1 is

$$\frac{d\omega}{dt} = b_1 + b_2\omega + b_3\omega^{1.8} \tag{13}$$

where b_1 is the hysteresis coefficient, b_2 is the eddy current coefficient, and b_3 is the windage coefficient for the experimental data. The coefficients for the case when the bias flux is equal to 0.540 T are listed in Table 1.

By substituting all parameters except for the coefficient of effective volume, M_v, and rotor speed into the eddy current power loss equation, Eq. (3), and dividing by the rotor polar moment of inertia, J, which is equal to $7.92 \times {}^{10-}3$ N-s^2-m (7.02×10^{-2} lb$_f$-s^2-in.), and the appropriate conversion factor, the resulting calculated coefficient for comparison to the experimental coefficient, b_2, is

$$b_{calc2} = 4.1 \times 10^{-3} M_v \text{ s}^{-1} \tag{14}$$

Setting this value equal to the corresponding measured b_2 from Table 1 and solving for M_v results in

$$M_v \approx 0.15 \tag{15}$$

This value represents the effective fraction of total journal volume where losses are occurring. Note that this number makes physical sense because it is greater than 0.0 and less than 1.0 times the total volume. This effective volume coefficient is consistent with FEM results, which demonstrate that the peak flux occupies much less than the entire volume at a maximum flux level as shown in Fig. 1.

The effective volume coefficient may be different for each loss component. Based on similarities between the eddy current and the alternating hysteresis phenomena, it is assumed that this effective volume coefficient is valid for use in both Eqs. (2) and (3) in determining the calculated power losses. The effective volume coefficient, M_{vr}, for use in the calculation of rotating hysteresis losses has also been determined from a similar comparison of the calculated hysteresis coefficients (added together) from Eqs. (1)–(2) to the appropriate measured hysteresis coefficient, b_1, from Table 1 and results in

$$M_{vr} = 0.42 \tag{16}$$

for use in the rotational hysteresis loss expression (Eq. (1)).

Currently, this is the best method for estimating the values of effective volume. Future tests involving more experimental data and additional FEM analyses will result in a methodology for determining effective volumes and frequencies *a priori*, during the design stage of a bearing.

The resistivity of the silicon iron material will vary with temperature. Since losses in the rotor will result in heat generation, the actual resistivity of the material could vary during the rundown tests. Temperature measurements will be made on future tests but are unavailable for the data presented here. However, the maximum expected temperature rise in the bearings is estimated to be 21°C (based on an estimated maximum temp of ≈ 43°C (110°F) from physically touching the rotor lamination immediately after a test run is completed with the maximum flux density), which results in an 11 percent increase in the resistivity based on the temperature coefficient, α, of iron of 0.005 1/°C in the following equation from Harnwell (1949):

$$\rho = \rho_1[1 + \alpha(T - T_1)] \tag{17}$$

where ρ is the resistivity at T (the temperature after heat generation due to losses) and ρ_1 is the resistivity at ambient conditions ($T_1 = 21°\text{C}$) which is 4.8×10^{-7} Ω-m. The uncertainty of the resistivity is small considering the estimations of effective volumes and frequencies that were made.

Calculated loss values were made using Eqs. (1)–(4) with the assumed values for effective frequencies and volumes as discussed above. A comparison of the measured and calculated losses is shown in Fig. 3 for the cases when the bias flux ($B_{\max}$ in Eqs. (1)–(3)) is set equal to 0.445 T, 0.540 T, and 0.615 T, respectively. There is good correlation between the measured and predicted power loss as shown in Fig. 3. A set of coefficients, b_{calc}, has been determined from the analytical/empirical prediction models and are listed in Table 2 along with the corresponding experimental coefficients, b_i, for the three bias flux cases. As expected, the analytical/empirical coefficients and measured coefficients for the hysteresis and eddy currents are identical for the case when $B = 0.540$ T since this is the case that was used to determine the effective volume as discussed above. A comparison of measured and analytical/empirical coefficients for the other flux cases shows relatively good agreement demonstrating the validity of the choice of effective frequency and effective volume coefficients.

Theory predicts a trend in the eddy current component of the power loss with the square of the bias flux (Eq. (2)). As a verification, the measured eddy current coefficients, b_2, listed in Table 2 have been divided by the square of their respective bias flux values and are listed in Table 3. As shown in Table 3, the new eddy current coefficient values are very close to each other, indicating that the experimentally derived eddy current coefficients conform well to the B^2 dependence model. This is important because it implies that losses actually due to windage are not improperly imputed to eddy currents in the model.

Conclusions

Combined analytical and empirical loss expressions have been developed to model losses in magnetic bearings. Calcu-

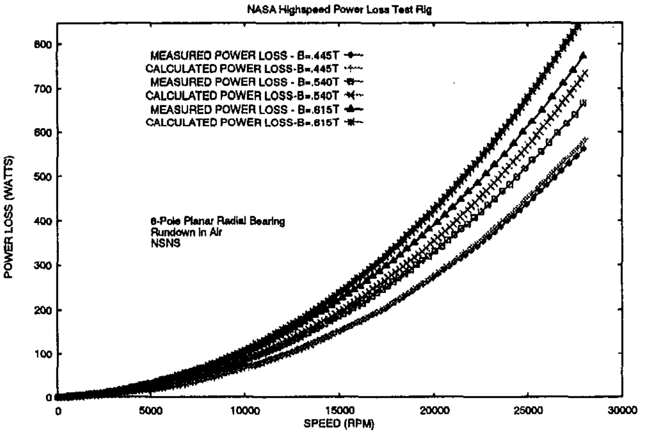

Fig. 3 Comparison of measured power losses and calculated power losses

Table 2 Comparison of experimentally measured model coefficients and predicted analytical/empirical coefficients

	B = .445 T		B = .540 T		B=.615 T	
	Measured Coeff	Analytical/ Empirical Coeff	Measured Coeff	Analytical/ Empirical Coeff	Measured Coeff	Analytical/ Empirical Coeff
Hysteresis ($rpm\text{-}s^{-1}$)	b_1= -17.6	b_{calc1}= -16.4	b_1= -22.1	b_{calc1}= -22.1	b_1= -26.8	b_{calc1}= -26.8
Eddy Current (s^{-1})	b_2= $-4.6\text{x}10^{-3}$	b_{calc2}= $-4.2\text{x}10^{-3}$	b_2= $-6.2\text{x}10^{-3}$	b_{calc2}= $-6.2\text{x}10^{-3}$	b_2= $-7.9\text{x}10^{-3}$	b_{calc2}= $-8.0\text{x}10^{-3}$
Windage ($rpm^{-.8}\text{-}s^{-1}$)	b_3= $-8.6\text{x}10^{-7}$	b_{calc3}= $-1.0\text{x}10^{-6}$	b_3= $-7.8\text{x}10^{-7}$	b_{calc3}= $-1.0\text{x}10^{-6}$	b_3= $-7.1\text{x}10^{-7}$	b_{calc3}= $-1.0\text{x}10^{-6}$

Table 3 Dependence of measured eddy current coefficient on bias flux

	B = .445 T	B = .540 T	B = .615 T
Measured Coeff (b_2) (s^{-1})	$-4.6\text{x}10^{-3}$	$-6.2\text{x}10^{-3}$	$-7.9\text{x}10^{-3}$
Measured Coeff $\div B^2$ (b_2/B^2)($s^{-1}\text{-}T^{-2}$)	$-2.3\text{x}10^{-2}$	$-2.1\text{x}10^{-2}$	$-2.1\text{x}10^{-2}$

lated losses were determined for a test rotor supported in a pair of eight-pole heteropolar bearings from the analytical/empirical models of the four loss components: (1) windage loss, (2) eddy current loss, (3) alternating hysteresis loss, and (4) rotating hysteresis loss. These values were determined for comparison to the measured losses from the experimental data detailed in Part 1 of this study. The effect of three different levels of bias flux on the losses was examined and significant differences were observed. Measured power losses at the reported top speed of 28,000 rpm for the entire rotor varied between 563 Watts when the bias flux density was 0.445 T to 774 Watts when the bias flux density was 0.615 T. A dependence on the square of the bias flux of the eddy current component was demonstrated. Analytical/empirical models including parameter values based on a cursory FEM analysis and empirical values for effective volumes showed reasonable correlation with experimental data. Additional data, including a study that will have a large variation of the experimental parameters including the elimination of the windage effects by use of a vacuum chamber, are planned. The additional experimental data along with more detailed analytical analysis will be used to develop predictive expressions for power loss to be used at the design stage of future magnetic bearings.

Acknowledgments

This research was funded in part by NASA Lewis Research Center and the Commonwealth of Virginia's Center for Innovative Technology. The authors would like to thank Chris Sortore, Dr. Ted Brockett, Michael Baloh, Lance Fujita, and Klaus Brun for the assistance at various points in this project.

References

Allaire, P. E., 1995, "Magnetic and Electric Field Equations for Magnetic Bearing Applications," *Proc. of Mag '95,* Alexandria, VA.

Brailsford, F., 1938, "Rotational Hysteresis Loss in Electrical Shaft Steels," *IEEJ,* pp. 566–575.

Golding, E. W., 1961, *Electric Measurements and Measuring Instrumentation,* 4th ed., Pitman Publishers.

Harnwell, G. P., 1949, *Principles of Electricity and Electromagnetism,* McGraw-Hill, New York.

Kasarda, M. E., Allaire, P. E., Hope, R. W., and Humphris, R. R., 1993a, "Measured and Predicted Losses in Planar Radial Magnetic Bearings," *Proc. Mag '93,* Alexandria, VA.

Kasarda, M. E., Allaire, P. E., Hope, R. W., and Humphris, R. R., 1993b, "Comparison of Experimentally Measured and Calculated Losses in Planar Radial Magnetic Bearings," *Proc. Rotating Machinery Conference,* New Jersey Institute of Technology, Vol. 2.

Kasarda, M. E. F., Allaire, P. E., Maslen, E. H., and Gillies, G. T., 1994, "Design of a High Speed Rotating Loss Test Rig for Radial Magnetic Bearings," *Proc. Fourth International Symposium on Magnetic Bearings,* ETH Zurich.

Kasarda, M. E., and Allaire, P. E., 1995, "Experimentally Measured and Improved Calculated Losses in Planar Radial Magnetic Bearings," STLE Paper No. 96-TC-7B-2.

Knowlton, A. E., editor-in-chief, 1949, *Standard Handbook for Electrical Engineers,* McGraw-Hill, New York.

Lyman, T., ed., 1972, *Metals Handbook,* Addison Wesley, MA.

Matsumura, F., Fujita, M., and Ozaki, Y., 1988, "Characteristics of Friction on Magnetic Bearings," *Trans. IEE of Japan,* Vol. 108-D, No. 5, pp 462–468.

Matsumura, F., and Hatake, K., 1992, "Relation Between Magnetic Pole Arrangement and Magnetic Loss in Magnetic Bearing," *Proc. Third International Conference on Magnetic Bearings,* Alexandria, VA, pp. 274–283.

Meeker, D. C., Maslen, E. H., and Noh, M. D., 1995, "A Wide Bandwidth Model for the Electrical Impedance of Magnetic Bearings," *Proc. Third International Symposium on Magnetic Suspension Technology,* Tallahassee, FL, Dec. 13–15.

MIT Electrical Engineering Staff, 1943, *Magnetic Circuits and Transformers,* Wiley Press.

Press, W. H., Flannery, B. P., Teulolsky, S. A., and Vetterling, W. T., 1989, *Numerical Recipes,* Cambridge University Press.

Shames, I. H., 1982, *Mechanics of Fluids,* McGraw-Hill, New York.

Stephens, L. S., and Knospe, C. R., 1995a, "Determination of Power Losses in High Speed Magnetic Journal Bearings Using Temperature Measurements," *Experimental Heat Transfer,* No. 8, pp. 35–56.

Stephens, L. S., and Knospe, C. R., 1995b, "Effect of Magnetic Pole Arrangement on Core Loss in Laminated High Speed Magnetic Journal Bearings," submitted to *IEEE Transactions on Magnetics.*

Ueyama, H., and Fujimoto, Y., 1990, "Iron Losses and Windy Losses of Rotational Speed Rotor Suspended by Magnetic Bearings," *Proc. 2nd International Symposium on Magnetic Bearings,* Tokyo, Japan, pp. 237–242.

Zmood, R. B., Anand, D. K., and Kirk, J. A., 1987, "The Influence of Eddy Currents on Magnetic Actuator Performance," *Proc. IEEE,* Vol. 75, No. 2.

The Maximum Factor by Which Forced Vibration of Blades Can Increase Due to Mistuning

D. S. Whitehead
Mechanical Engineering Department,
Imperial College,
London, United Kingdom

In 1966 it was shown that the maximum factor by which the amplitude of forced vibration of blades can increase due to mistuning is, with certain assumptions, $\frac{1}{2}(1 + \sqrt{N})$*, where N is the number of blades in the row. This report gives a further investigation of the circumstances when this factor can be obtained. These are small damping, and a relationship must hold between the mistuning distribution* $\gamma(s)$ *and the interblade coupling function* $c(r)$*, where r is the mode number. The mistuning distribution must be symmetric about the blade on which maximum amplitude is to occur,* $s = 0$*. The coupling function must be symmetric about* $r = R$*, where R is the mode number of the excitation. If the coupling is purely mechanical, additional conditions apply. The coupling function* $c(r)$ *must consist of a number of identical symmetric substrips. A 1976 result for mechanical coupling is amended.*

Introduction

Whitehead (1966) gave an analysis that derived the maximum factor by which the vibration amplitude of compressor or turbine blades could be increased due to mistuning of the blades, when the vibration is excited by wakes. This analysis considered rather general coupling between the blades, which could be either aerodynamic or mechanical. If all blades are equally damped, the maximum factor is $\frac{1}{2}(1 + \sqrt{N})$, where N is the number of blades in the disk. It was also shown that this maximum factor can be achieved by an assembly in which just one blade is mistuned. This paper is believed to be entirely correct.

Whitehead (1976) gave a further analysis for the case when the coupling between the blades is purely mechanical. It was alleged that, with this restriction, the greatest factor by which the amplitude could increase is $\frac{1}{2}(1 + \sqrt{(N/2)})$. This will be referred to as "the lower factor." It has been found that the proof leading to the lower factor is invalid, as it was assumed that the responses in traveling wave mode R, where R is the mode number of the excitation, and in traveling wave mode $(N - R)$ were equal. This is not in general true. It was also shown in this paper that the lower factor can be achieved when just one blade is mistuned, and the coupling is purely mechanical, and this analysis is believed to be correct.

The purposes of the present paper are to examine the circumstances under which the maximum factor can be obtained, with general coupling, to correct the 1976 paper, and show how the maximum factor can be achieved in many cases with mechanical coupling.

There is a substantial literature on the effects of mistuning. This has been reviewed by Yiu (1991), who quotes 102 references.

Basic Theory

Consider an assembly of N blades in an axisymmetric disk. It is supposed that the natural frequencies of a single blade are well separated, so that only a single degree of freedom per blade is relevant. Then all blades have mass m. The deflection of blade s is given by $x_s e^{i\omega t}$, where ω is the angular frequency of the excitation and the resulting vibration. The stiffness of the spring supporting the mass on blade s is $k(1 + \gamma_s)$, where γ_s gives the mistuning of blade s. A blade reference angular frequency ω_0 is defined, where $\omega_0^2 = k/m$.

The coupling between blades is such that the force on blade s due to deflection x_u on blade u is $kk_{su}x_u e^{i\omega t}$. k is included here in order to make k_{su} nondimensional. For mechanical coupling the reciprocal theorem applies, $k_{su} = k_{us}$, but this is not in general true for aerodynamic coupling, and will not initially be assumed. Due to the axial symmetry, k_{su} is a function of $(s - u)$ only, and will be written k_{s-u}.

Due to the excitation by rotating wakes passing into the blades, the exciting force on blade s is $kf_s e^{i\omega t}$. k is included here so that f_s has the same dimensions as blade deflection. The case when there is excitation in just one traveling wave mode, with R nodal diameters, is considered, so that

$$f_s = g_R e^{2\pi iRs/N} \tag{1}$$

To fix the phase reference, g_R is taken real and positive.

It will be supposed that all blades have the same damping. Damping is provided by hysteretic dampers with constant $k\delta/\pi$ between blade and ground. If the damping is aerodynamic, this is equivalent to assuming that all traveling wave modes are equally damped. (The case when the traveling wave modes have different damping factors was considered in Whitehead (1966).) Since the main interest is when damping and mistuning effects are both small, the details of how these effects are introduced into the model are of little importance, and this choice has been made on grounds of algebraic simplicity. It is then not necessary to assume in the theory that the damping and mistuning effects are small. For small damping, no coupling, and no mistuning, δ is the logarithmic decrement of free blade vibration.

The motion can be expressed in terms of traveling wave modes. If the complex amplitude in mode r is y_r, then the amplitude of blade s is given by

$$x_s = \sum_{r=0}^{N-1} y_r e^{2\pi irs/N} \tag{2}$$

Equations (1) and (2) can be expressed in matrix form

$$F = EG \tag{3}$$

$$X = EY \tag{4}$$

where the complex matrices are

Contributed by the International Gas Turbine Institute and presented at the 41st International Gas Turbine and Aeroengine Congress and Exhibition, Birmingham, United Kingdom, June 10–13, 1996. Manuscript received at ASME Headquarters February 1996. Paper No. 96-GT-125. Associate Technical Editor: J. N. Shinn.

X column, elements x_s
Y column, elements y_r
E square, symmetric, elements $e^{2\pi irs/N}$
F column, elements f_s
G column, one nonzero real element g_R in row R.

The inverse of E is given by

$$E^{-1} = (1/N)E^{*\prime} \tag{5}$$

where * indicates a transposed matrix, and ′ indicates a complex conjugate. (* makes no difference in this case, since E is symmetric.)

The equation of motion for blade s is then

$$-m\omega^2 x_s = -k(1 + \gamma_s)x_s + kk_{su}x_u - i(k\delta/\pi)x_s + kf_s$$

Writing $p = \omega^2/\omega_0^2 - 1$, a measure of the deviation of the excitation frequency from the reference frequency, this can be written in matrix form

$$(\Gamma + i\delta/\pi I - pI - K)X = F \tag{6}$$

where the matrices are

Γ diagonal with real elements γ_s
I unit matrix
K square with elements k_{su}.

There is a double redundancy implied here, since adding a real constant to the diagonal elements of Γ, and also adding a real constant to the diagonal elements of K, are both equivalent to altering the value of p.

Putting Eqs. (3) and (4) into Eq. (6) and rearranging gives the basic equation in terms of traveling wave modes:

$$(E^{-1}\Gamma E + i\delta/\pi I - pI - E^{-1}KE)Y = G \tag{7}$$

It is convenient to write

$$C = E^{-1}KE = (1/N)E^{*\prime}KE \tag{8}$$

where C is a measure of the coupling effect on the traveling wave modes. The elements of C are given by

$$c_{rv} = \frac{1}{N}\sum_{u=0}^{N-1}\sum_{s=0}^{N-1} k_{s-u}e^{2\pi i(rs-uv)/N}$$

s may be replaced by the variable $w = s - u$. Note that all arithmetic on blade integers, s, u, and w, and on mode integers, r, v, is done modulo N. Then

$$\mathbf{c}_{\mathbf{rv}} = \frac{\mathbf{1}}{\mathbf{N}}\sum_{\mathbf{w=0}}^{\mathbf{N-1}} \mathbf{k}_{\mathbf{w}}\mathbf{e}^{\mathbf{2\pi irw/N}}\sum_{\mathbf{u=0}}^{\mathbf{N-1}} \mathbf{e}^{\mathbf{2\pi iu(r-v)/N}}$$

The second sum is zero unless $r = v$, when it is N. Hence

$$c_{rv} = 0, \quad r \neq v, \quad c_{rr} = \sum_{w=0}^{N-1} k_w e^{2\pi irw/N} \tag{9}$$

The matrix C is therefore diagonal. The elements are the Fourier transform of the k_w coefficients. The real part of C can be interpreted as giving the change of natural frequency of the traveling wave mode r due to coupling effects, when there is no mistuning, and can be due to either mechanical or aerodynamic effects. The imaginary part of C gives the corresponding damping of traveling wave mode r, and since all traveling wave modes are assumed to be equally damped, and that this damping is accounted for by δ, C is real and diagonal.

Perfectly Tuned Blades

If $\gamma_s = 0$ for all s, $\Gamma = 0$, and from Eq. (7)

$$(i\delta/\pi I - pI - C)Y = G$$

so

$$y_r = 0 \quad r \neq R$$

and

$$y_R = g_R/(i\delta/\pi - p - c_{RR})$$

Resonance occurs when $p + c_{RR} = 0$. The ideal complex amplitude in mode R is

$$y_{id} = \pi g_R/i\delta \tag{10}$$

and

$$|y_{id}| = \pi g_R/\delta \tag{11}$$

This is the amplitude on every blade.

Work Equation

Premultiplying Eq. (7) by $Y^{*\prime}$ and taking the imaginary part gives

$$\frac{\delta}{\pi}Y^{*\prime}Y = -\text{Im}(y_R)g_R = \frac{\delta}{\pi}\sum_{r=0}^{N-1}|y_r|^2$$

where Im indicates the imaginary part.

This equation shows that the work dissipated in the dampers is equal to the work done by the excitation. It can be written

$$\sum_{r=0}^{N-1}\frac{|y_r|^2}{|y_{id}|^2} = -\frac{\text{Im}(y_R)}{|y_{id}|} \tag{12}$$

Maximum Possible Amplitude

This section is the same as the Whitehead (1966) paper, but simplified to have the same damping in all traveling wave modes. We write

$$z_r = |y_r|/|y_{id}|$$

From Eq. (12)

$$\sum_{r=0}^{N-1} z_r^2 \leq z_R \tag{13}$$

Suppose that there is one blade, which may be chosen without loss of generality to be blade 0, at which all the traveling wave modes are in phase. This gives the greatest possible amplitude as

$$\frac{\mathbf{x}_{\mathbf{max}}}{|\mathbf{y}_{\mathbf{id}}|} = \sum_{\mathbf{r=0}}^{\mathbf{N-1}} \mathbf{z}_{\mathbf{r}} \tag{14}$$

The left-hand side of Eq. (14), is now optimized subject to condition (13) written as an equality, since the amount of work into the system for a given set of z_r values must be maximized, by adjusting the phase of y_R so that it is pure imaginary and negative. The result is

$$z_R = \tfrac{1}{2}(1 + 1/\sqrt{N}) \tag{15}$$

and

$$z_r = \tfrac{1}{2}(1/\sqrt{N}) \quad r \neq R \tag{16}$$

From Eq. (14) the maximum possible amplification factor is given by

$$x_{\max}/|y_{id}| = \tfrac{1}{2}(1 + \sqrt{N}) \tag{17}$$

Realization of Maximum Amplification Factor

In order to obtain the maximum possible amplification factor, all the y_r components must be in phase on blade 0. Hence, from Eqs. (15) and (16)

$$y_R/y_{id} = \tfrac{1}{2}(1 + 1/\sqrt{N}) \tag{18}$$

and

$$y_r/y_{id} = \tfrac{1}{2}(1/\sqrt{N}) \quad r \neq R \tag{19}$$

It may be noted that y_r, y_R and y_{id} are all pure imaginary. From Eq. (2) the blade amplitudes are

$$x_s/y_{id} = \tfrac{1}{2}e^{2\pi i R s/N} \quad s \neq 0 \tag{20}$$

$$x_0/y_{id} = \tfrac{1}{2}(\sqrt{N} + 1) \tag{21}$$

From Eq. (6), and using Eqs. (3), (4), and (8):

$$(\Gamma + i\delta/\pi I - pI)X - ECY = EG \tag{22}$$

In the following, since C is diagonal, it will be more convenient to write $c(r)$ instead of c_{rr}. Also γ_s will be written $\gamma(s)$. Expanding Eq. (22) for $s = 0$ gives

$$[\gamma(0) + i\delta/\pi - p]\frac{\sqrt{N}+1}{2} - \frac{1}{2\sqrt{N}}\sum_{R=0}^{N-1} c(r) - \frac{c(R)}{2} = i\frac{\delta}{\pi}$$

where the sum is over all values of r, including $r = R$. The real and imaginary parts of this give

$$\gamma(0) - p = \frac{1}{\sqrt{N}+1}\left[\frac{1}{\sqrt{N}}\sum_{R=0}^{N-1} c(r) + c(R)\right] \tag{23}$$

$$\tfrac{1}{2}\delta/\pi(\sqrt{N} + 1) = \delta/\pi \tag{24}$$

Expanding Eq. (22) for $s \neq 0$ gives

$$\left[\gamma(s) + i\frac{\delta}{\pi} - p\right] - \frac{1}{\sqrt{N}}\sum_{r=0}^{N-1} c(r)e^{2\pi i(r-R)s/N} - c(R) = i\frac{2\delta}{\pi}$$

where again the sum is over all values of r, including $r = R$. The real and imaginary parts of this give

$$\gamma(s) - p = \frac{1}{\sqrt{N}}\sum_{r=0}^{N-1} c(r)\cos[2\pi(r-R)s/N] + c(R) \tag{25}$$

$$\frac{\delta}{2\pi} - \frac{1}{2\sqrt{N}}\sum_{r=0}^{N-1} c(r)\sin[2\pi(r-R)s/N] = \frac{\delta}{\pi} \tag{26}$$

Equation (24) implies that δ tends to zero. It is not possible to actually put $\delta = 0$, since this would imply infinite y_{id}. Then Eq. (26) gives

$$\sum_{r=0}^{N-1} c(r)\sin[2\pi(r-R)s/N] = 0$$

where the sum is taken over all values of r, including $r = R$, and the equation is true for all values of s. Neglecting δ in Eq. (26) implies that the damping is much less than either the coupling effects or the mistuning effects.

This shows that all the odd harmonics of $c(r)$ plotted as a function of $(r - R)$ are zero, so that $c(r)$ must be an even function of $(r - R)$. Any even function will do, except a uniform c distribution, since that would mean that the coupling and mistuning effects would be zero, and the damping cannot be made small compared to that.

The required mistuning is then given by Eqs. (23) and (25). It will be noted from Eqs. (23) and (25) that $\gamma(s)$ is an even function of s.

The relationship between $\gamma(s)$ and $c(r)$ may be inverted. The result is

$$c(r) = \frac{1}{\sqrt{N}}\sum_{s=0}^{N-1}[\gamma(s) - p]\cos[2\pi(r-R)s/N] + [\gamma(0) - p] \tag{27}$$

for r not equal to R, and

$$c(R) = \frac{1}{\sqrt{N}(\sqrt{N}+1)}\sum_{s=0}^{N-1}[\gamma(s) - p] + \frac{1}{\sqrt{N}+1}[\gamma(0) - p] \tag{28}$$

The maximum amplification factor can therefore be obtained by arbitrarily specifying either $c(r)$ or $\gamma(s)$ subject to the required symmetry, and the other function is then determined.

These equations show how $\gamma(s)$ and $c(r)$ are almost the Fourier transforms of each other, but that there are special terms for $\gamma(0)$ and $c(R)$. Since a change of excitation frequency, or p, has the same effect as a uniform change to all the $\gamma(s)$ values, p can be set to 0 without loss of generality.

The principal modes and natural frequencies of the undamped but mistuned assembly may be obtained by putting $\delta = 0$ and $G = 0$ in Eq. (22), and p then becomes the eigenvalue. Using Eqs. (18) to (21) for the mode shape then gives exactly Eqs. (23) and (25). This proves that with a combination of coupling distribution and mistuning distribution, which gives the maximum amplification factor, then at the maximum the response is in one principal mode of the undamped system, and occurs at the resonant frequency of that mode.

Example 1
If

$$c(r) = A \quad r \neq R$$

and

$$c(R) = B$$

then Eqs. (23) and (25) reduce to

$$\gamma(o) = A + (1/\sqrt{N})(B - A)$$

and

$$\gamma(s) = B + (1/\sqrt{N})(B - A) \quad s \neq 0$$

so that all blades are mistuned by the same amount except for blade zero. This is the one-blade mistuned case, as in the paper Whitehead (1966), apart from frequency shifts and uniform damping.

Example 2
Suppose that

$$c(r) = A\cos\{2\pi(r - R)/N\} \quad r \neq R$$

$$c(R) = B$$

Then Eqs. (23) and (25) reduce to

$$\gamma(0) = -A/\{(\sqrt{N})(\sqrt{N} + 1)\} + B/(\sqrt{N})$$

$$\gamma(1) = \gamma(-1) = A(N - 2)/(2\sqrt{N}) + B(\sqrt{N} + 1)/(\sqrt{N})$$

and

$$\gamma(s) = -A/(\sqrt{N}) + B(\sqrt{N} + 1)/(\sqrt{N})$$

if s is not 0, 1, or −1.

This is therefore a case of three adjacent blades mistuned. Figure 1 shows the coupling and mistuning distributions for the case $N = 36$, $R = 6$, $A = 0.5$, and $B = 1$.

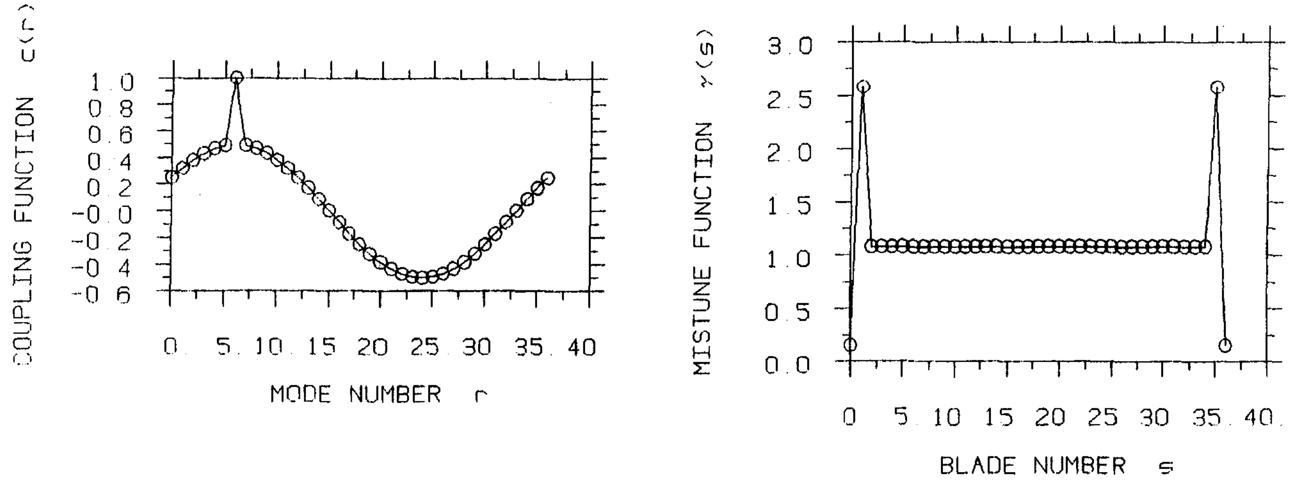

Fig. 1 Example 2: three blades mistuned, $N = 36$, $R = 6$

Taking the second harmonic for the $c(r)$ distribution instead of the first would require blades 2 and -2 to be mistuned as well as blade 0.

Mechanical Coupling Limitation

If the coupling between the blades is purely a spring coupling, then k_w is real and the reciprocal theorem applies, $k_w = k_{-w}$. It follows that c is symmetric about the $r = 0$ point as well as the $r = R$ point.

Suppose that the c function has been specified over the range $0 \le r \le R$. Symmetry about the $r = R$ point then determines c over the range $R \le r \le 2R$, giving a symmetric distribution over $0 \le r \le 2R$. Using the two symmetry conditions, this may be extended to give an infinite array of symmetrical strips of width $2R$.

The c distribution also has to repeat with period N. This is only possible if each strip consists of Q identical symmetric substrips of width $S = 2R/Q$. Then P substrips must just fill the total range $0 \le r \le N$, so that $PS = 2PR/Q = N$.

The procedure for finding for what values of R a maximum solution can be found for a given N is therefore as follows:

Choose S as a factor of N, $2 \le S \le N$.
$P = N/S$.
If S is even, choose any integer Q, $1 \le Q \le 2P$.
If S is odd, choose any even integer Q, $2 \le Q \le 2P$.
The possible values of R are then $QS/2$.

As S increases there are fewer possible values of R, but more freedom in the choice of the c distribution.

Example 3

N even, $S = 2$, $P = N/2$, $R = Q$ can be any integer up to N.

This shows that, at least when N is even, it is always possible to find a coupling distribution and a mistuning distribution that give the maximum possible magnification factor. The coupling distribution is a succession of alternating values, as shown in Fig. 2 for $N = 36$. The mistuning distribution shows just blades 0 and $N/2$ mistuned.

It follows that any attempt to prove the assertion in Whitehead (1976) that the lower factor of $\frac{1}{2}(1 + \sqrt{(N/2)})$ is the maximum with mechanical coupling ($R = 0$ and $R = N/2$ excepted) must fail.

Conclusions

1 The maximum factor by which the amplitude of vibration of any blade can increase due to mistuning is $\frac{1}{2}(1 + \sqrt{N})$.

2 In order to obtain this maximum factor, the first condition is that the damping must be much less than the mistuning and coupling effects.

3 In order to obtain this maximum factor, the second condition is that the coupling distribution $c(r)$ must be symmetric about the point $r = R$, where R is the excitation order, and the corresponding mistuning distribution $\gamma(s)$ must be symmetric about $s = 0$. Subject to these symmetry

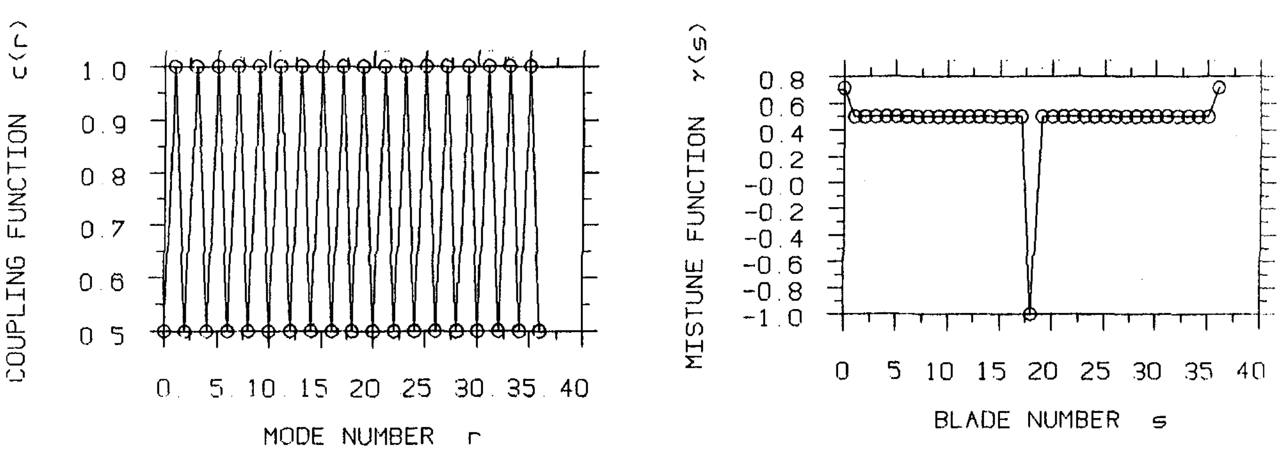

Fig. 2 Example 3: alternating coupling, $N = 36$, any R

conditions, either the coupling distribution or the mistuning distribution can be arbitrarily specified (except for a uniform distribution in either case), and the other is then determined.

4 The vibration at this maximum is then in one principal mode of the mistuned system, and occurs at the natural frequency of that mode.

5 If the coupling is purely mechanical, then an additional condition on $c(r)$ is that it must also be symmetric about $r = 0$. This can only happen if the $c(r)$ distribution consists of P identical symmetric substrips of width S. Particular conclusions about when the maximum factor can be obtained with mechanical coupling are then as follows:

5(*a*) $R = 0$ always gives a solution.

5(*b*) $R = N/2$ always gives a solution if N is even.

5(*c*) If N is even, $S = 2$ gives solutions for all R.

5(*d*) If N is prime, there is no solution except $R = 0$.

6 A statement made in an earlier paper about a lower factor when the coupling is purely mechanical is invalid.

7 As a practical safe upper limit, the factor $\frac{1}{2}(1 + \sqrt{N})$ can be used as the maximum factor by which mistuning can increase the stress in forced vibration.

8 There is a slight advantage in using prime integers for the number of blades in a row, as with purely mechanical coupling the maximum factor cannot then be reached, except for the case $R = 0$, in which case there is usually no significant excitation.

References

Whitehead, D. S., 1966, "Effect of Mistuning on the Vibration of Turbomachine Blades Induced by Wakes," *Jour. Mech. Eng. Sci.*, Vol. 8, pp. 15–21.

Whitehead, D. S., 1976, "Effect of Mistuning on Forced Vibration of Blades With Mechanical Coupling," *Jour. Mech. Eng. Sci.*, Vol. 18, pp. 306–307.

Yiu, H., 1991, "A Review of the Literature on Mistuning Effects in Bladed Disc Vibration," Report No: VUTC/E/92001, Imperial College, London.

J. H. Griffin

W.-T. Wu

Department of Mechanical Engineering,
Carnegie Mellon University,
Pittsburgh, PA 15213

Y. EL-Aini

Chief Engineering Department,
Pratt & Whitney,
West Palm Beach, FL 33410

Friction Damping of Hollow Airfoils: Part I—Theoretical Development

The quest for higher performance engines in conjunction with the requirement for lower life cycle costs has resulted in stage configurations that are more susceptible to high cycle fatigue. One solution is the use of innovative approaches that introduce additional mechanical damping. The present paper describes an approach that may be used to assess the benefits of friction dampers located within internal cavities of a hollow structure. The friction dampers used in this application are often relatively thin devices that, if unconstrained, have natural frequencies in the same range as the natural frequencies of the hollow airfoil. Consequently, the analytical approach that is developed is distinct in that it has to take into account the dynamic response of the damper and how it changes as the amplitude of the vibration increases. In this paper, results from the analytical model are compared with independently generated results from a time integration solution of a three mass test problem. Results from the analytical model are compared with experimental data in a companion paper.

1 Introduction

Modern turbines often have a greater need for increased damping than do older designs, yet their geometry may not lend itself easily to adding traditional damping devices. Many modern turbines have higher specific performance because they have eliminated blade attachments through the use of integrally bladed disks or integrally bladed rings. However, they have also eliminated the friction damping associated with the dovetails and firtrees. As a result, the dynamic magnification factor in stages with modern integrated airfoils is often a factor of two to five times higher than those found in older engines. This is especially a problem because the traditional method of introducing additional damping by using underplatform dampers (Cameron et al., 1990) no longer works, since in the new designs the blades do not have platforms. In response to this need, engine designers have developed *insert* dampers that can be placed inside the airfoil and produce the damping needed in order to insure robust blade designs.

Insert dampers are devices that fit inside blade cavities and produce friction damping by rubbing against the inner wall of the airfoil as it vibrates; Fig. 1. Modern, low-aspect-ratio blades often vibrate in high-frequency chordwise modes that are excited by pressure defects from nearby vanes (Balaji and Griffin, 1995). Insert dampers can be placed relatively near the tips of the blades and could provide effective sources of energy dissipation in these critical modes. However, chordwise modes are complex and a design tool was required for optimizing the damper's geometry and location. This paper discusses the development of such a design tool. BLDAMP, a computer code that can be used to calculate the damped response of blades containing insert dampers.

A review of the literature through 1990 on research associated with modeling friction constraints in turbine blades is given in the paper by Griffin (1990). Of particular relevance to the work presented here are a series of papers involving C.-H. Menq and J. H. Griffin in which they developed the general concepts required for modeling friction constraints in harmonically excited structures. In the current paper the idea of using the harmonic balance method along with receptances to represent linear substructures will be used (Menq and Griffin, 1985). In addition, the equations for the Fourier components of the force developed when the nodes across the friction interface undergo elliptical motion are also needed (Menq et al., 1991). In their 1986 papers with Bielak, Menq and Griffin used a continuous interface model to investigate the importance of microslip qualitatively. In this paper a quantitative microslip model is developed based on contact at discrete nodes.

This paper is organized as follows: In section 2, the basic theory is given. A simplified model of the blade/damper system is developed and the governing equations of the blade, the damper, and the friction interface are given. The solution method is summarized. In section 3, the solution to a numerical test problem is discussed. The last section presents a summary of the results and discusses some of their implications. Predictions based on the theory are compared with experimental data in a companion paper by El-Aini et al. (1996).

2 Theory

2.1 Modeling Simplifications. An exact analysis of the dynamic response of the blade/insert damper system would be extremely complex. For example, the blade's mode shape would be affected by slippage at the blade/damper interface, the higher harmonics generated by the nonlinear friction force would affect the system's response, and the damper could lose contact and ''bounce around'' inside the cavity—which could lead to chaotic response. It would be possible to model these types of behavior analytically if a transient time integration solution method were used to compute the response. However, because these are lightly damped systems, the computational times for each frequency and amplitude condition would be extremely long and it would not be practical to use this approach for parametric studies and design optimization. The goals of this research are more modest. They are to develop a simplified representation of the problem so that it may be solved in a computationally efficient manner, and, yet, still provide a reasonably accurate model of the system's dynamic response.

Which attributes of the system must be retained and which can be simplified? The blade is far stiffer than the damper. As a result, it will be assumed that the blade's mode shape is not affected by the damper, although the change in its resonant

---

Contributed by the International Gas Turbine Institute and presented at the 41st International Gas Turbine and Aeroengine Congress and Exhibition, Birmingham, United Kingdom, June 10–13, 1996. Manuscript received at ASME Headquarters February 1996. Paper No. 96-GT-109. Associate Technical Editor: J. N. Shinn.

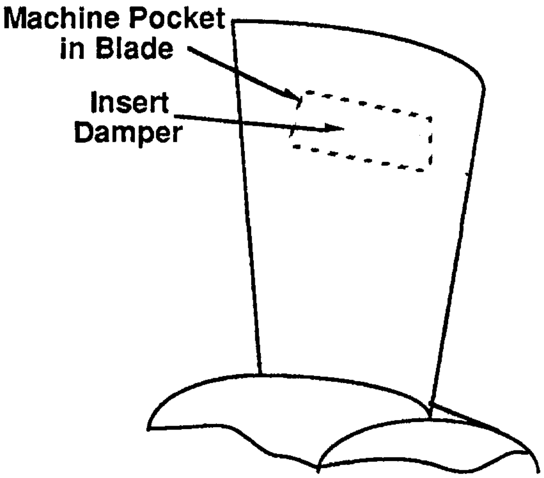

Fig. 1 Schematic of an insert damper

frequency will be computed. The damper, however, may have resonant frequencies near the operating point of interest and must be modeled as a dynamic subsystem. The harmonic balance method will be used to approximate the nonlinear friction forces with only their first harmonic component. The procedure will be used to analyze the blade's response at or very near its resonant frequencies. The higher harmonics of the nonlinear force have smaller amplitudes and higher frequencies. Typically, they are relatively unimportant unless they excite another resonant frequency of either the blade or insert damper. This may happen occasionally, but is not common enough to warrant the development of a more complex multi-harmonic balance analysis. An additional simplification will be the assumption that the blade and damper do not loose contact, and, further, that dynamic variations in the normal load across friction contact nodes will not affect the energy dissipated at the interface nodes. This is a reasonable approximation provided the dynamic variations in the normal loads are relatively small—an assumption that can be checked by the computer code as part of the post-processing of the data.

Two other modeling issues are microslip and geometry. Microslip refers to the concept that only part of the friction interface may actually slip during a cycle and that the amount and location of the slip can depend on the amplitude and frequency of the system. Microslip will be modeled by representing the friction contact as taking place at multiple pairs of points (nodes) that lie across the friction interface. Thus, only some of the nodes may slip, while others remain stuck. The relative motion of the contact nodes must lie in the plane of the friction interface, but can be two dimensional, i.e., elliptical. The orientation of the friction interface between contact nodes has to be able to lie in any direction so that a wide variety of friction damper geometries can be analyzed. A Coulomb friction model is used to represent contact at each pair of nodes on the friction interface.

2.2 Equations Governing Blade Response. If a finite element formulation of the blade is used, the dynamic response of the blade is governed by an equation of the form

$$\mathbf{M}\ddot{\mathbf{x}} + \mathbf{C}\dot{\mathbf{x}} + \mathbf{K}\mathbf{x} - \mathbf{f}_d = \mathbf{f}_e \qquad (1)$$

where $\mathbf{M}$ is the mass matrix, $\mathbf{C}$ the damping matrix, $\mathbf{K}$ the stiffness matrix, $\mathbf{x}$ a nodal displacement vector, $\mathbf{f}_d$ a vector representing the nonlinear reaction forces from the damper, and $\mathbf{f}_e$ a vector representing the external aerodynamic forces. When there is no damper the blade will have natural frequencies equal to ω_j with associated mode shapes, $\mathbf{b}_j$.

Normally, the nonlinear equations implicitly defined in Eq. (1) would be solved iteratively. Here, a more efficient, inverse method is developed by assuming $\mathbf{x}$, determining $\mathbf{f}_d(\mathbf{x})$, and then calculating $\mathbf{f}_e$. To accomplish this assume that the damper is relatively light and flexible and does not significantly affect the mode shape of the blade and that it changes the resonant frequency of the blade by only a small amount. Then, the blade's motion at resonance, with the damper inserted, is given by

$$\mathbf{x} = A\mathbf{b}_j \cos(\omega t) \quad \text{and} \quad |\omega - \omega_j| < \Delta\omega \qquad (2)$$

A procedure for calculating $\mathbf{f}_d(\mathbf{x})$ will be given in section 2.4. Assume now that it can be decomposed into sine and cosine terms with the same frequency, i.e.,

$$\mathbf{f}_d = \mathbf{f}_{dc}\cos(\omega t) + \mathbf{f}_{ds}\sin(\omega t) \qquad (3)$$

Substitution of Eqs. (2) and (3) into (1) yields

$$[A(\mathbf{K} - \mathbf{M}\omega^2)\mathbf{b}_j - \mathbf{f}_{dc}]\cos(\omega t) + [-\mathbf{f}_{ds} - A\omega\mathbf{C}\mathbf{b}_j]\sin(\omega t) = \mathbf{f}_{ec}\cos(\omega t) + \mathbf{f}_{es}\sin(\omega t) \qquad (4)$$

where $\mathbf{f}_{ec}$ and $\mathbf{f}_{es}$ are the cosine and sine components of $\mathbf{f}_e$.

Because of the assumption that the blade's mode shape does not change, Eq. (4) can be multiplied by $\mathbf{b}_j^T$ to give the modal equation for the system's response

$$[(k_j - m_j\omega^2)A - F_c(A, \omega)]\cos(\omega t) - [A\omega c_j + F_s(A, \omega)]\sin(\omega t) = \mathbf{f}_{jc}\cos(\omega t) + \mathbf{f}_{js}\sin(\omega t) \qquad (5)$$

where k_j, c_j, and m_j are the blade's modal stiffness, modal damping, and modal mass, respectively, and where $F_c = \mathbf{b}_j^T\mathbf{f}_{dc}$, $F_s = \mathbf{b}_j^T\mathbf{f}_{ds}$, $f_{jc} = \mathbf{b}_j^T\mathbf{f}_{ec}$, $f_{js} = \mathbf{b}_j^T\mathbf{f}_{es}$.

The magnitude of the external, modal force f_j is given by

$$f_j = \sqrt{f_{jc}^2 + f_{js}^2} \qquad (6)$$

In this nonlinear problem, the resonant frequency, ω_r, of the blade/damper system is a function of the blade's modal amplitude, i.e., for a fixed modal amplitude, A, ω_r corresponds to the value of frequency at which the magnitude of the external force, f_j is a minimum. From Eq. (5), the effective damping in the jth mode at resonance is $F_s/(A\omega_r) + c_j$.

2.3 Equations Governing Damper Response. Assume that the damper contacts the blade at n nodes. Using receptance concepts (Menq and Griffin, 1985) the dynamic response of contact nodes of the damper is governed by an equation of the form

$$\hat{\mathbf{S}}\hat{\mathbf{u}} = \hat{\mathbf{f}} \qquad (7)$$

where $\hat{\mathbf{u}}$, a $3n$ vector, is the displacement vector, $\hat{\mathbf{f}}$ is the force vector from the blade that acts on the damper, and $\hat{\mathbf{S}}$ is a dynamic stiffness matrix that is a function of frequency. The dynamic stiffness or impedance matrix is the inverse of the receptance matrix for the damper nodes and can be calculated from its modes. Here the elements of $\hat{\mathbf{f}}$ are equal in magnitude but opposite in sign to the nonzero elements of $\mathbf{f}_d$.

For purposes of simplifying the presentation, assume that n components are normal to the contact surface and that $2n$ lie in the plane of contact. If there is no slip, then all $3n$ components of $\hat{\mathbf{u}}$ are prescribed as equal to the corresponding ones in $\mathbf{x}$. If there are m nodes that slip, then all n normal components and $(2n - 2m)$ tangential components of $\hat{\mathbf{u}}$ are prescribed. In order to solve for $\hat{\mathbf{f}}$ another $2m$ nonlinear constraints are required. To structure this requirement, partition Eq. (7) into two parts:

$$\begin{bmatrix} S_{11} & S_{12} \\ S_{21} & S_{22} \end{bmatrix} \begin{bmatrix} \mathbf{u}_1 \\ \mathbf{u}_2 \end{bmatrix} = \begin{bmatrix} \mathbf{f}_1 \\ \mathbf{f}_2 \end{bmatrix} \qquad (8)$$

where $\mathbf{u}_1$ are the displacements that are constrained to be the same as those of the blade (dimension $3n - 2m$) and $\mathbf{u}_2$ are the displacements that are different from those in the blade (dimension $2m$). Similarly, partition the blade's motion into two parts, $[\mathbf{u}_{b1}, \mathbf{u}_{b2}]^T$. Then, in Eq. (8) $\mathbf{u}_1$ is prescribed equal to $\mathbf{u}_{b1}$ and $\mathbf{f}_2$ is a function of $(\mathbf{u}_2 - \mathbf{u}_{b2})$ as described in the next section. Then, conceptually the solution is determined as follows. Since $\mathbf{u}_1$ is known, first, solve the second set of equations in Eq. (8) for the $\mathbf{u}_2$ and $\mathbf{f}_2$, i.e., solve

$$\mathbf{S}_{21}\mathbf{u}_1 + \mathbf{S}_{22}\mathbf{u}_2 = \mathbf{f}_2(\mathbf{u}_2, \mathbf{u}_{b2}) \tag{9}$$

Then substitute $\mathbf{u}_2$ in the first set of equations in Eq. (8) to determine $\mathbf{f}_1$. Once the nonlinear forces are determined the blade's response can be calculated from the formulation presented in section 2.2.

2.4 Model of the Friction Force. The goal of this section is to present an approximate method for estimating the friction interface forces $\mathbf{f}_2$. Since for a Coulomb model of friction the magnitude of the friction force is known, the issue is to determine the direction of the nodal friction forces. The approximate method will be based on a procedure that interpolates between the *stuck* and *fully slipping* friction forces.

First, consider the process for calculating the *stuck* friction forces in a node, i.e., the forces just prior to the node starting to slip. For purposes of this discussion, the nodes will be numbered in the order that they slip. The computer algorithm starts with the assumption that all of the nodes are stuck. This is a linear problem and the solution can be scaled to determine the amplitude of the blade that causes the first node to slip, A_s^1. In addition, it is also easy to record the friction force in the first node, $\mathbf{f}_{\text{stuck}}^1$ when it first starts to slip. Then, the amplitude of the blade is gradually increased until the next node starts to slip and A_s^2 and $\mathbf{f}_{\text{stuck}}^2$ are recorded. This process can be repeated for all of the nodes on the friction interface.

When slip occurs, the friction force in the ith node is assumed to be given by Coulomb's law, i.e.,

$$\mathbf{f}_2^i = \mu N_i \,\mathbf{direc}\,(\dot{\mathbf{u}}_{b2}^i - \dot{\mathbf{u}}_2^i) \tag{10}$$

where $\mathbf{f}_2^i$ is a two-dimension friction force vector, μ is the coefficient of friction, N_i is the associated normal force, direc is the direction function, $\dot{\mathbf{u}}_{b2}^i$ is the velocity of the blade node, and $\dot{\mathbf{u}}_2^i$ is the velocity of the damper node. If the blade's frequency ω is not close to one of the damper's natural frequencies and if the amplitude of the blade is large, then the tangential displacement of the damper node is small compared with the tangential displacement of the blade node. Under these conditions, the direction of the friction force that acts on the damper can be approximated as being in the direction of the blade's velocity, that is

$$\mathbf{f}_2^i \approx \mathbf{f}_2^{i*} = \mu N_i \,\mathbf{direc}\,(\dot{\mathbf{u}}_{b2}^i) \tag{11}$$

where $\mathbf{f}_2^{i*}$ is defined as the *fully slipping* friction force associated with the ith node. The specific equations that were used for calculating $\mathbf{f}_2^{i*}$ for two-dimensional, elliptical motion across nodes are Eqs. (23) and (24) of Menq et al. (1991).

The effective friction force at the ith node is determined by interpolating between the stuck and fully slipping values using the equation

$$\mathbf{f}_2^i = \mathbf{f}_2^{i*} D\left(\frac{A}{A_s^i}\right) + \mathbf{f}_{\text{stuck}}^i S\left(\frac{A}{A_s^i}\right) \tag{12}$$

The interpolation functions S and D are taken from the solution to the single point, friction contact problem (Griffin, 1980). Note that S is a "stiffness" interpolation function and that D is a "damping" interpolation function. When a friction contact first starts to slip, it acts primarily as a spring-type constraint, whereas, for large motions, the force it generates is out of phase with the motion and it acts as a damping element. D and S reflect this behavior. For example, when their argument is less than or equal to one, S equals one and D equals zero, i.e., the node is stuck. When their argument is greater than one, then S and D are given by

$$S(\rho) = \frac{\rho}{\pi}[1 - 0.5 \sin(2\theta)] \quad \text{and} \quad D(\rho) = 1 - \frac{1}{\rho}$$

where

$$\theta = \cos^{-1}\left(1 - \frac{2}{\rho}\right) \tag{13}$$

and the node acts progressively more like a fully slipping constraint as the blade's amplitude increases.

2.5 Solution Method

2.5.1 Normalized Results and Optimization. The normal force on the friction interface is developed because the damper is compressed by the walls of the cavity, a spring effect, or because of centrifugal force. In the first case the normal load can be changed by altering the size of the cavity and the amount the damper is compressed. In the latter case, the centrifugal force may be changed by altering the angle of inclination of the friction interface with respect to a radial line. Thus, the designer has control of the total normal load acting on the damper/blade interface. A parameter that may be used to optimize the damper's performance is the sum of the normal forces, N, that act on the interface, i.e.,

$$N = \sum_{i=1}^{n} N_i$$

An interesting aspect of the governing equations of systems that incorporate Coulomb friction models is that they may be normalized with respect to the variable N (assuming that the distribution of normal loads, N_i/N, remain constant) (Cameron et al., 1990). The key result is that the amplitude of the blade divided by N is a unique function of the amplitude of the excitation force divided by N, i.e.,

$$\frac{A}{N} = g\left(\frac{f_i}{N}, \omega\right) \tag{14}$$

Thus, the response of the system needs to be determined as a function of the magnitude of the excitation for only one value of N. The effect of varying N can then be determined through the use of Eq. (14).

Typically, engineers do not know the magnitude of the generalized force that acts on the blade. Since the system is nonlinear and the generalized force is not known, the procedure for optimizing the damper's performance is not obvious. Two methods of viewing the data are frequently used to help optimize the damper's design (Cameron et al., 1990). These are *force performance curves* and *displacement performance curves*. In force performance curves the amplitude of peak response (divided by N) is plotted as a function of the amplitude of the generalized force (divided by N). The effect of varying N can be seen by scaling both axes. Alternatively, the normalized amplitude of peak response can be plotted as a function of "undamped peak response amplitude," i.e., the amplitude that the blade would have if the damper were not present. This is a simple transformation of the force performance curve since the undamped peak response amplitude is directly proportional to the generalized force. However, the displacement performance curve has the advantage that the improvement in blade performance can be seen more directly.

2.5.2 Algorithm. The implementation of the theory resulted in a computer program BLDAMP. BLDAMP uses the following strategies:

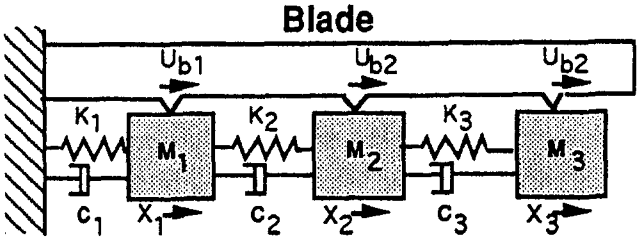

Fig. 2 Test problem

Table 2 Properties of blade

Natural Frequency	100
Modal Mass	1
Modal Stiffness	10000
Modal Damping Ratio	0.003
Displacement, **b**	[1, -0.5, 0.5]

1 *Frequency Range.* Select a blade mode to be analyzed. Under the assumption that the nodes are not slipping the algorithm calculates the contribution of the damper's stiffness to the systems stiffness as F_c/A, refer to (6). This determines the system's peak response frequency when its amplitude is small. The system's response is then calculated over a range of frequencies centered about this stuck frequency.

2 *Amplitude Range.* Select an amplitude range over which the damper's performance will be calculated. Typically, the amplitude is varied from zero to some maximum value that would cause the blade to crack in high cycle fatigue. Specify the number of amplitude increments.

3 *Calculate the Generalized Force.* Start at a low value of A for which the damper does not slip and calculate the generalized force. Increment the amplitude, keep track of which nodes slip, and calculate the generalized force over the entire range of A. Repeat over the entire frequency range and develop a data base of f_i as a function of frequency and amplitude.

4 *Amplitude and Frequency of Peak Response.* For a fixed value of A, search over the range of frequencies to determine the minimum value of the generalized force, $f_{i(\min)}$ and the frequency at which it occurs, ω_r. Then the specified value of A is equal to the amplitude of peak response and ω_r is the frequency of peak response when f_i equals $f_{i(\min)}$ (refer to section 2.2).

3 Example

Consider the test problem indicated in Fig. 2. The "insert damper" is represented by the three degree of freedom system. Its motions are given in terms of the displacements x_1, x_2, and x_3. Its properties are given in terms of consistent units in Table 1. Each damper mass is constrained through friction contact with the "blade." The magnitude of the friction force required for slip to occur across a node is 1000. The blade is assumed to vibrate in a mode with a specified amplitude, i.e., the motions of the blade at the contact points are U_{b1}, U_{b2}, and U_{b3}, where $U_{bi} = Ab_i \cos(\omega t)$, A is the amplitude of the blade's motion, and b_i is the ith component of the blade's modal displacement. The properties of the blade are given in Table 2. Note that the natural frequency of the blade mode of interest is 100 radians per second, whereas the natural frequencies of the unconstrained damper system are 11.6, 46.8, and 71.3. Thus, the test problem represents the case of interest, that of a "flexible" damper in contact with a relatively stiff blade.

Solutions to the test problem were generated by two methods: the approximate method discussed in this paper, and a more exact time integration method. In the time integration method the transient response of the system was determined using a fourth-order Runge–Kutta program for specific values of blade amplitude, A, and frequency ω. The transient response was calculated until it achieved a "steady state," i.e., the response repeated itself to within 1 percent from one cycle to the next.[1] The steady-state modal friction force was calculated over a period, $f_d(t) = \mathbf{b}^T\mathbf{f}_d(t)$, and decomposed into its Fourier components using a Fast Fourier Transform subroutine in order to determine its fundamental harmonic component. The modal force acting on the blade was then calculated using Eqs. (5) and (6). Typical results from the time integration solution are shown in Fig. 3 in which the ratio of the blade's amplitude to the magnitude of the generalized force is plotted as a function of frequency for a series of different blade amplitudes. The amount of slip in the system increases as A, the amplitude of the blade, increases. The curves illustrate several interesting trends. The damping is clearly a nonlinear function of the amplitude of the blade's motion, A. In addition in this example, the frequency of peak response, ω_r, increases as the amount of slip increases. This is because the damper provides additional mass as well as stiffness and both are effectively reduced as the amount of slip increases. In this case, the decrease in effective mass has a greater effect on ω_r than the decrease in stiffness and, consequently, ω_r increases with A.

Table 1 Properties of damper system

Node #	M	C	K
#1	0.250	0.5	200
#2	0.375	0.5	500
#3	0.500	0.5	700

The agreement between the time integration results and the results from BLDAMP is indicated by the results for A equal to three and four shown in Fig. 4 and for A equal to one and two in Fig. 5. In general, the frequency shifts and amplitude trends were reasonably well predicted. The largest discrepancy occurred for A equal to two, Fig. 5. The response is difficult to predict in this range of amplitude because the damping changes

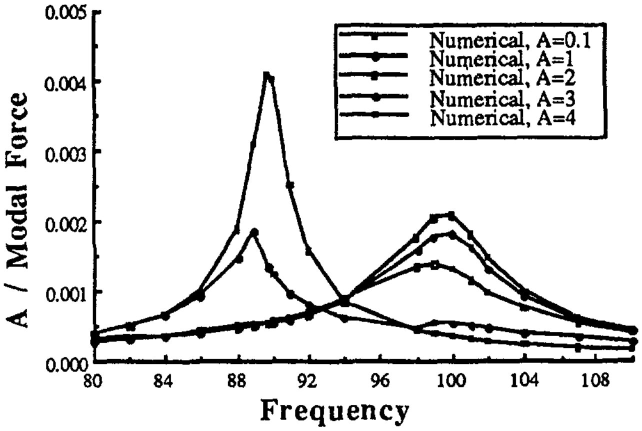

Fig. 3 Response plots generated by time integration

---

[1] The results were also checked for numerical convergence by taking smaller and smaller time steps. The results depicted in the figures corresponded to 512 time steps per cycle of excitation.

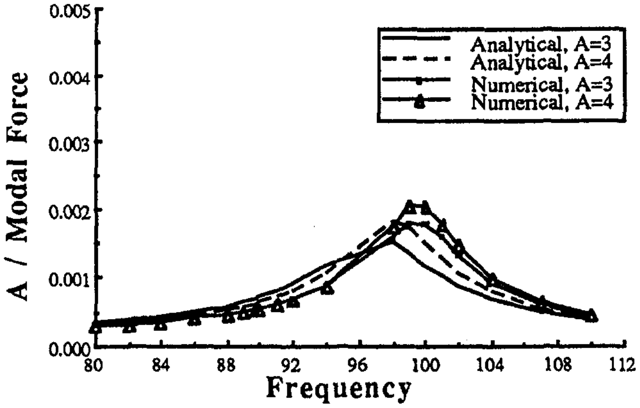

Fig. 4 Comparison on time integration results and theory for blade motions of 3 and 4

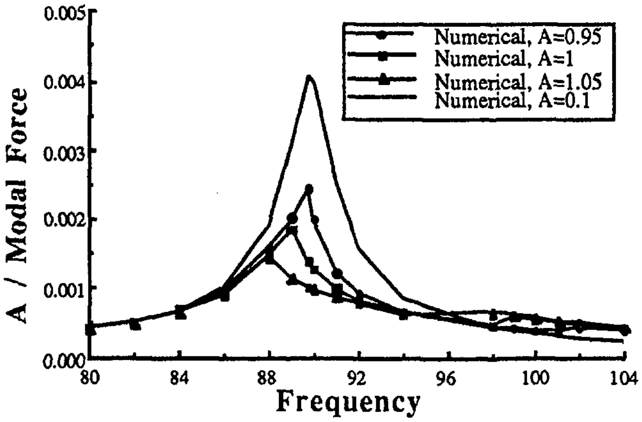

Fig. 6 Sensitivity of response

so quickly. For example, see the high sensitivity of the response to small changes in the input when *A* changes from 0.95 to 1.0 to 1.05; Fig. 6.

The goal of the designer is to predict overall damper performance trends as embodied, for example, by the damper force performance curve of Fig. 7. In Fig. 7 the amplitude of peak response is plotted as a function of the generalized force acting on the blade (refer to section 2.5.1 for a discussion of using performance curves for design). It is interesting to note that the high-sensitivity region in the amplitude plots corresponds to the flat portion of the performance curve. As a consequence, the difficulty associated with accurately predicting the amplitude is not of practical importance from the design point of view. It is clear that BLDAMP provides a reasonably accurate method for estimating the performance curve for this test problem.

4 Summary and Discussion

An approach has been developed for calculating the effect of insert dampers on the dynamic response of blade/damper systems. The problem is difficult to model and analyze because of a number of complicating factors: the friction provides a nonlinear constraint, the damper is relatively flexible and can respond dynamically, only part of the friction interface may slip, and the blade/damper interface is typically a complex shape defined in three dimensions.

A number of simplifications were made to make the problem tractable. The mode shape of the blade was assumed constant, the variations in the normal loads were assumed not to affect the friction calculation, contact is assumed to occur only at a discrete set of points, a simplified friction relationship was used, and the harmonic balance method approximation applied. The resulting algorithm, BLDAMP, was computationally efficient and fairly robust.

A simple test problem was developed in order to provide a bench mark for testing BLDAMP. The damper in the test problem had multiple natural frequencies and, consequently, could respond dynamically. The long time response was calculated using time integration so no assumptions were made about the importance of higher harmonics and the Coulomb friction law was fully implemented on a time step by time step basis. Thus, the test problem provided a reasonable assessment of the veracity of the harmonic balance assumption, the procedure to account for damper flexibility, and the simplified friction. In general, the agreement between the solutions to the test problem generated by time integration and BLDAMP was reasonably good. A more realistic experimental verification of BLDAMP is discussed in the companion paper by El-Aini et al. (1996).

The BLDAMP computer code was developed over a four year period and required a number of improvements to increase its computational efficiency, robustness, and accuracy.[2] An additional feature of the latest version is that it has an option

---

[2] A number of practical problems were encountered in developing the code. For example, for a certain number of contact nodes, how many modes of the damper were needed in order to have a complete basis, and how to smooth the input displacements from the blade's motion so as not unrealistically to excite the high-frequency damper modes?

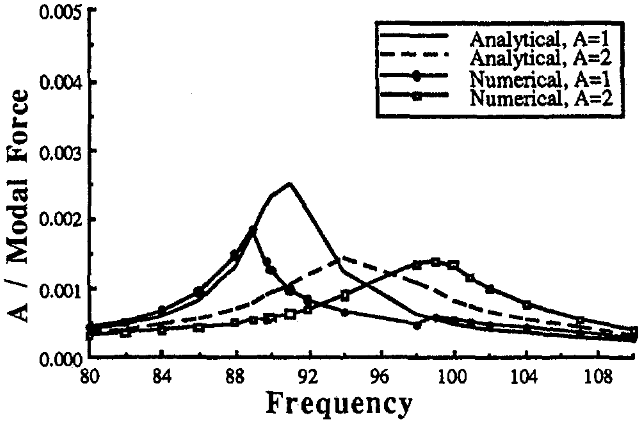

Fig. 5 Comparison of time integration results and theory for blade motions of 1 and 2

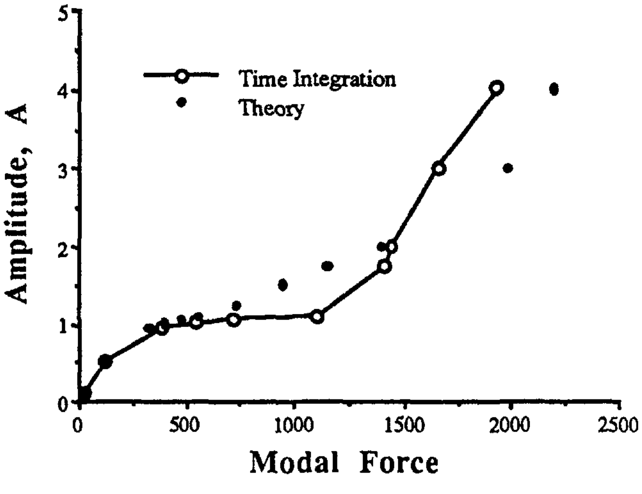

Fig. 7 Comparison of damper performance curves

where it will iteratively solve the full nonlinear friction law as given in Eq. (10). Typically, the computations are an order of magnitude slower and not nearly as robust since they involve solving a set of simultaneous nonlinear equations at each amplitude increment. In addition, the full nonlinear friction version usually predicts very similar results. As a consequence, design studies tend to be carried out with the simplified friction law option and the full nonlinear option used only as verification for few critical cases.

As posed, the problem of solving for the dynamic response of an insert damper is similar to the earthquake problem in which one determines the dynamic response of a structure resting on a vibrating foundation. The insert damper problem is more difficult because the friction interface is large and slip more strongly influences the damper's dynamic response. The reason for this is that for small amplitudes, the damper is constrained and has high natural frequencies, whereas, for large amplitudes, it is much less constrained and has significantly lower natural frequencies. As a result, one finds that for a fixed excitation frequency the damper tends to experience a nonlinear resonance over a very limited range of blade amplitudes where its nonlinear "natural frequency" corresponds to the excitation frequency provided by the blade.

The computer code BLDAMP discussed in this paper and the code developed by Professor Menq at Ohio State (Yang and Menq, 1996) are a new generation of algorithms based on recent developments in representing friction constraints. They are highly efficient and, because they utilize finite element analyses to describe the linear substructures, can represent complex structures with a high degree of structural fidelity. As a result, engineers now have computational tools that can help them understand and optimize the design of two fairly broad classes of frictionally constrained systems using a standard methodology. It is likely that the same methods will be employed to develop codes that represent other types of frictionally constrained systems. Consequently, it is conceivable that in the future these tools not only will allow designers to optimize damping in the engine, but also to control variability and wear.

Acknowledgments

The work reported in this paper was supported by Pratt & Whitney. The authors would like to acknowledge the contribution of Ms. J. Bernhardt, who helped develop the original version of BLDAMP.

References

Balaji, G., and Griffin, J. H., 1995, "The Resonant Response of a Tapered Beam and Its Implications to Blade Vibration," ASME Paper No. 95-GT-453; ASME JOURNAL OF ENGINEERING FOR GAS TURBINES AND POWER, Vol. 119, 1997, pp. 147–152.

Cameron, T. M., Griffin, J. H., Kielb, R. E., and Hoosac, T. M., 1990, "An Integrated Approach for Friction Damper Design," ASME *Journal of Vibration, Acoustics, Stress and Reliability in Design,* Vol. 112, pp. 175–182.

El-Aini, Y. M., Benedict, B. K., and Wu, W. T., 1996, "Friction Damping of Hollow Airfoils: Part II—Experimental Verification," ASME Paper No. 96-GT-110; ASME JOURNAL OF ENGINEERING FOR GAS TURBINES AND POWER, Vol. 120, 1998, this issue, pp. 126–130.

Griffin, J. H., 1980, "Friction Damping of Resonant Stresses in Gas Turbine Engine Airfoils," ASME JOURNAL OF ENGINEERING FOR POWER, Vol. 102, pp. 329–333.

Griffin, J. H., 1990, "A Review of Friction Damping of Turbine Blade Vibration," *International Journal of Turbo and Jet Engines,* Vol. 7, pp. 297–307.

Menq, C-H., and Griffin, J. H., 1985, "A Comparison of Transient and Steady State Finite Element Analyses of the Forced Response of a Frictionally Damped Beam," ASME *Journal of Vibration, Acoustics, Stress, and Reliability in Design,* Vol. 107, pp. 19–25.

Menq, C-H., Chidamparam, P., and Griffin, J. H., 1991, "Friction Damping of Two-Dimensional Motion and Its Application in Vibration Control," *Journal of Sound and Vibration,* Vol. 144, pp. 427–447.

Menq, C-H., Bielak, J., and Griffin, J. H., 1986a, "The Influence of Microslip on Vibratory Response; Part 1: A New Microslip Model," *Journal of Sound and Vibration,* Vol. 107, pp. 279–293.

Menq, C-H., Griffin, J. H., and Bielak, J., 1986b, "The Influence of Microslip on Vibratory Response; Part 2: A Comparison With Experimental Results," *Journal of Sound and Vibration,* Vol. 107, pp. 295–307.

Yang, B. D., and Menq, C.-H., 1996, "Modeling of Friction Contact and Its Application of the Design of Shroud Contact," ASME Paper No. 96-GT-472; ASME JOURNAL OF ENGINEERING FOR GAS TURBINES AND POWER, Vol. 119, 1997, pp. 958–963.

Friction Damping of Hollow Airfoils: Part II—Experimental Verification

Y. M. EL-Aini
Fellow, Aeromechanics,
Structures & Dynamics.

B. K. Benedict
Project Engineer.

W.-T. Wu
Contract Engineer.

Pratt & Whitney,
West Palm Beach, FL 33410-9600

The use of hollow airfoils in turbomachinery applications, in particular fans and turbines, is an essential element in reducing the overall engine weight. However, state-of-the-art airfoil geometries are of low aspect ratio and exhibit unique characteristics associated with platelike modes. These modes are characterized by a chordwise form of bending and high modal density within the engine operating speed range. These features combined with the mistuning effects resulting from manufacturing tolerances make accurate frequency and forced response predictions difficult and increase the potential for High Cycle Fatigue (HCF) durability problems. The present paper summarizes the results of an experimental test program on internal damping of hollow bladelike specimens. Friction damping is provided via sheet metal devices configured to fit within a hollow cavity with various levels of preload. The results of the investigation indicate that such devices can provide significant levels of damping, provided the damper location and preload is optimized for the modes of concern. The transition of this concept to actual engine hardware would require further optimization with regard to wear effects and loss of preload particularly in applications where the preload is independent of rotational speed. Excellent agreement was achieved between the experimental results and the analytical predictions using a microslip friction damping model.

1 Introduction

Turbomachinery designers have always resorted to the use of passive damping concepts to reduce destructive vibratory responses of engine flowpath components to acceptable limits. The most commonly known approaches are: (1) dry friction dampers, (2) viscoelastic dampers, and (3) impact dampers. Dry friction dampers are widely used in jet engine applications, particularly in the form of part-span shrouds on fan blades, tip shrouds on low-pressure turbine (LPT) blades, and platform dampers on high-pressure turbine (HPT) blades. Dry friction dampers are also applied to labyrinth seals and gears in the form of centrifugally loaded split rings. While design criteria for such dampers have been primarily empirical, recent analysis techniques by Griffin (1980) and Griffin and Menq (1991) have been developed and continue to be the focus of many researchers.

Viscoelastic dampers, although easier to analyze, have infrequently been used by turbomachinery designers in the form of constrained-layer treatment to nonrotating structural members. An example of a successful application of this technique is its use on a Pratt and Whitney TF30 fan inlet guide vane. However, sensitivity to temperature and creep has limited the use of viscoelastic treatments on rotating engine components.

Impact dampers are the least used in engine applications. Analytical design methodologies are nearly nonexistent due to the nonlinear nature of the problem. Trial and error experiments by Panossian (1989) have demonstrated the benefit of using loose particles in the liquid oxygen (LOX) inlet splitter vane of the Space Shuttle Main Engine (SSME) to reduce the vibratory response to acceptable levels. Validation of this concept on rotating components is yet to be demonstrated.

The continued pursuit of high thrust-to-weight ratio of both military and commercial engine designs has resulted in airfoil designs that are low-aspect-ratio, hollow, and integrally bladed to the disk. The elimination of part-span shrouds and slotted attachments has resulted in lightly damped stages that are susceptible to HCF durability problems. In addition, the use of low-aspect-ratio airfoils has resulted in responses characterized by high modal density of platelike modes within the engine operating speed range. Therefore, damping augmentation of these new designs has been identified as a critical need.

In this paper, approaches to introduce damping into hollow air-foil-like specimens are examined with emphasis on damping of chordwise flexural modes. Experimental results are summarized and correlated to analytical predictions of a microslip friction damping model by Griffin et al. (Part I of this paper).

2 Experimental Program

2.1 Hollow Specimens. Three hollow specimens (PW10, PW11, and PW12) were used in this investigation with the main differences being in the thickness of the ribs separating the different hollow regions. The specimens are made of Ti-6-4. Two separately machined halves, with the selected rib pattern shown in Fig. 1, are then diffusion bonded together to form the hollow specimen. The cavities at the tip are intentionally left exposed to accept a variety of damper inserts. The specimens are roughly 0.32 in. thick with a skin thickness of 0.062 in. in the airfoil section. The specimens are firmly attached to a fixture using five bolts through the 0.50-in.-thick section at the root. To characterize the modal responses of the hollow specimens, both NASTRAN finite element modal analyses and laboratory techniques, including holography, impact testing, and Stress Pattern Analysis by Thermal Emission (SPATE) were used to quantify the modes of interest as well as to define the appropriate strain gage locations. Figure 2 is a coarse finite element model used to assess the modal characteristics of the specimens. The model is constructed using plate elements to represent the airfoil skins and ribs (shown as dark shaded elements).

A comparison between the NASTRAN and holography mode shapes is shown in Fig. 3. The effect of placing an insert damper

---

Contributed by the International Gas Turbine Institute and presented at the 41st International Gas Turbine and Aeroengine Congress and Exhibition, Birmingham, United Kingdom, June 10–13, 1996. Manuscript received at ASME Headquarters February 1996. Paper No. 96-GT-110. Associate Technical Editor: J. N. Shinn.

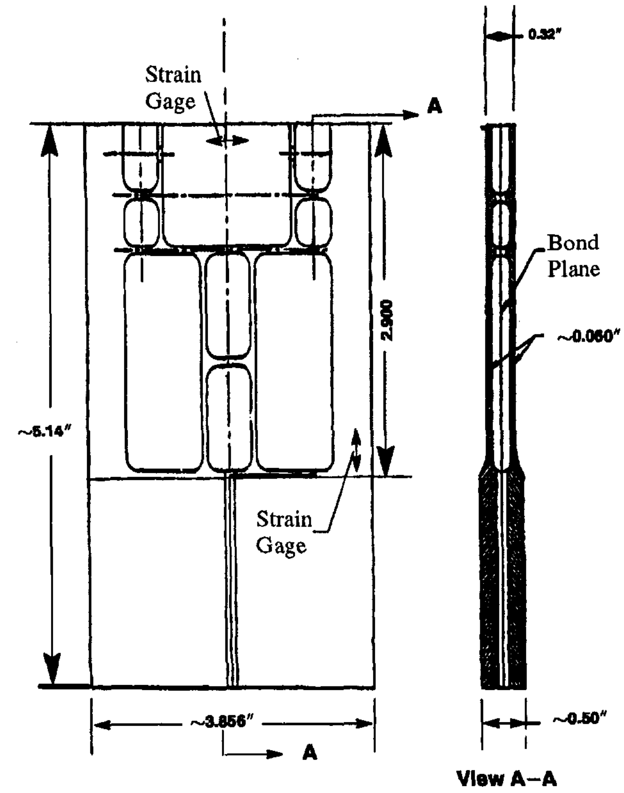

Fig. 1 Hollow specimen with strain gage locations identified

in the tip center cavity is studied extensively for the chordwise mode and to a limited extent on the first torsion mode.

2.2 Damper Design. Four damper configurations, shown in Fig. 4, were designed to fit in the top center cavity, designated in the figure by the rectangular outline. In an ideal situation, validation of such a concept is accomplished in a spin rig environment. However, the limited scope of the program dictated that the damping investigation be conducted on a shaker table. This requirement has further limited the choices of how the damper is loaded against the hollow specimen. To compensate for the lack of the centrifugal loading, the dampers had to be spring-loaded inside the hollow cavity with varying degrees of preload representative of realistic blade running conditions. Furthermore, the damper configurations were selected to provide a range of contact locations to assess its effect on damping effectiveness for the different modes of interest.

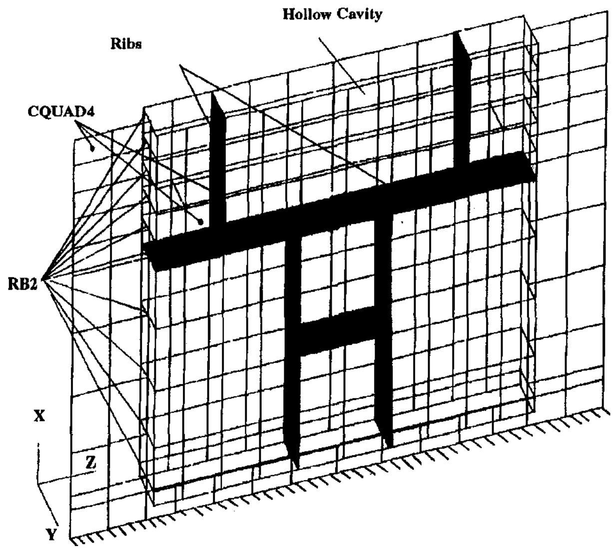

Fig. 2 Finite element model for hollow specimens

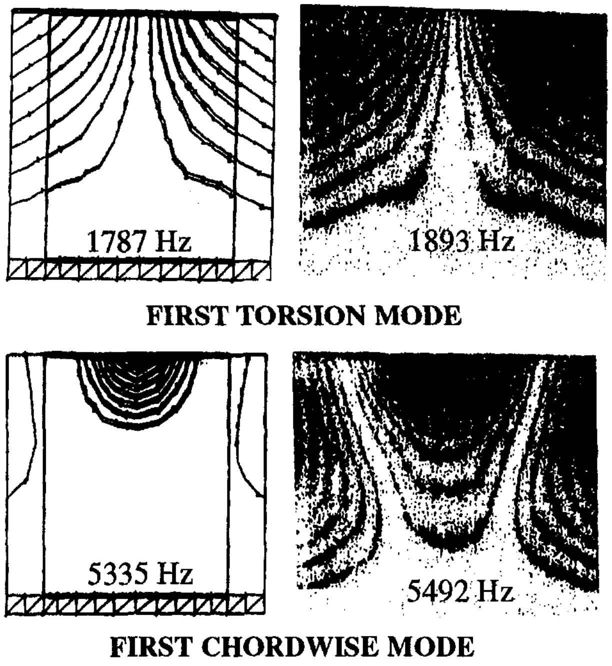

Fig. 3 Comparison between NASTRAN and holographic mode shapes for specimen PW12

2.3 Damper Configurations and Preloads. The selected damper configurations are intended to provide different normal load distribution between the dampers and the interior walls of the cavity to study its effect on damping effectiveness. Each damper was hand formed and then heat treated to restore its

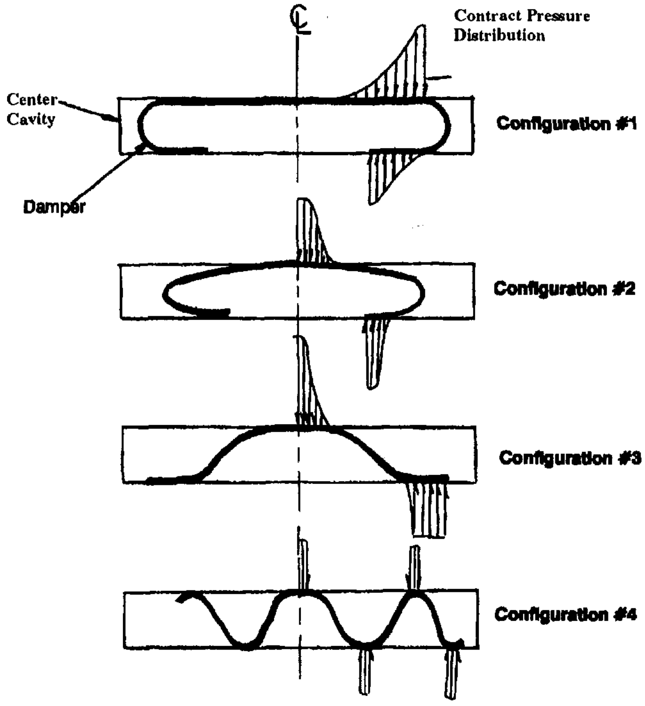

Fig. 4 Damper configurations

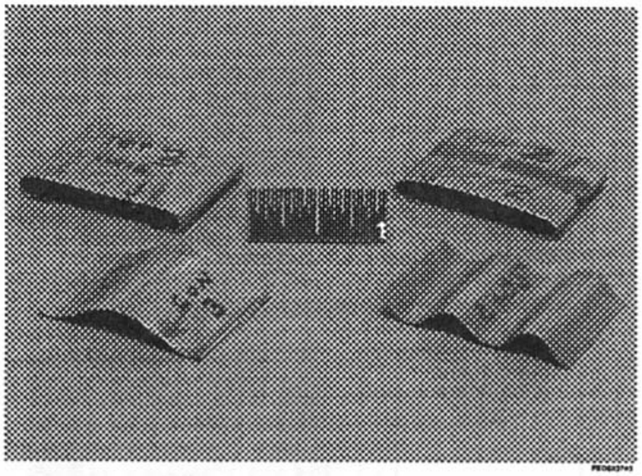

Fig. 5 Photograph of the four damper configurations

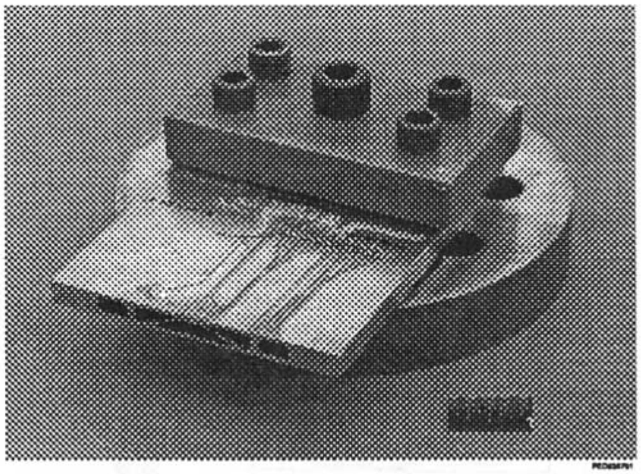

Fig. 6 Specimen PW10 instrumented and mounted between fixture plates

elastic characteristics. Figure 5 is a photograph of the four damper configurations. Three sets of dampers were made for each configuration to provide a matrix of preloads. Later in the program, an additional stiffer damper was made for configuration 3 to expand its database. All dampers were made of 0.020 in. Waspaloy (AMS 5544) sheet stock, except for the fourth damper of configuration 3, which was made of 0.027 in. sheet.

The damper preload for each configuration was determined by a static load test. Each damper is compressed from its initial undeformed height to the height corresponding to the inside dimension of the center cavity of 0.195 in. A summary of the damper matrix preloads is shown in Table 1.

2.4 Test Procedure. The damping characterization tests were accomplished using an electrodynamic shaker to provide the input excitation. The hollow specimen is secured between two fixture plates using the five-bolt pattern illustrated in Fig. 6. A block diagram showing the control loop and data acquisition system is presented in Fig. 7. The strategy for determining the damper effectiveness was to measure the maximum dynamic stress on the hollow specimen in response to a servo-controlled input acceleration measured on the shaker plate. The frequency range of the input was chosen to include the specimen resonance of interest and was swept from low to high at a constant rate of 5 Hz/second. Different sweeps were made at input levels from 10 g to 60 g (single amplitude). The strain gages were conditioned using standard amplifiers and the measurements were made using the computer-controlled acquisition system.

Table 1 Damper matrix and preloads

Damper Configuration	Set	Unloaded Dimension (Inch)	Loaded to 0.195" Dimension (lbs)
1	1	0.223 to 0.228	168
	2	0.210 to 0.215	90
	3	0.200 to 0.2.05	31
2	1	0.224 to 0.250	94
	2	0.232	56
	3	0.210 to 0.215	29
3	1	0.247 to .250	26
	2	0.230 to .235	19
	3	0.210 to .215	9
	4	0.250 (.027" thick)	50
4	1	0.202 to 0.209	177
	2	0.212	100
	3	0.219	50

2.5 Damping Test Matrix. A test matrix of 211 cases were completed using three hollow specimens (PW10, PW11, and PW12) in conjunction with 13 dampers and 6 levels of input excitation. Repeatability tests were not included as part of the test matrix. Major emphasis was directed to the characterization of the chordwise bending mode. Nearly 80 percent of the effort was spent on the chordwise mode and 20 percent on the torsion mode. The damping test matrix for specimen PW10, for the chordwise mode, is shown in Table 2 as an example.

With the exception of one damper (configuration 4, set 1) all dampers were tested in all three hollow specimens. However, configuration 3 was singled out to be the most effective and, therefore, received the largest coverage.

2.6 Damping Test Results. Damping test data were digitized and recorded on permanent electronic files. Each file contains frequency response spectrum data for all strain gages covering the mode of interest. Peak response amplitudes are determined from these response spectrum plots.

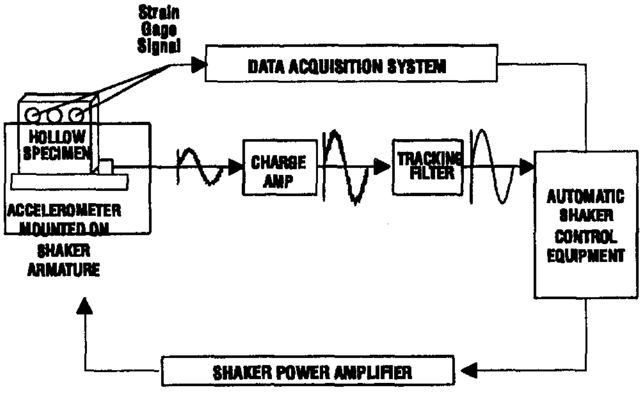

Fig. 7 Block diagram of shaker table control loop and data acquisition system

Table 2 Test matrix for specimen PW10

Specimen	Input G's	Configuration 1			Configuration 2			Configuration 3				Configuration 4			Baseline (undamped)	Mode
		Set 1	Set 2	Set 3	Set 1	Set 2	Set 3	Set 1	Set 2	Set 3	Set 4	Set 1	Set 2	Set 3		
PW10	10							✓	✓	✓	✓				✓	Chordwise
	20							✓	✓	✓	✓				✓	
	30	✓	✓	✓	✓	✓	✓	✓	✓	✓	✓	X	✓	✓	✓	
	40							✓	✓	✓	✓				✓	
	50							✓	✓	✓	✓				✓	
	60							✓	✓	✓	✓				✓	

A typical response spectrum plot for the chordwise mode of specimen PW10, with and without internal dampers, subjected to 30 g input is shown in Fig. 8. Comparisons of the damped and undamped responses indicate significant reduction in the peak amplitude response by an order of magnitude. The resonant frequency of the damped specimen has dropped from 5320 Hz to a range of 5075 to 5200 Hz. This 2 to 5 percent drop in frequency is attributed to the added damping and the additional damper mass.

All damper configurations were extremely effective in suppressing the vibratory response of the chordwise mode. Figure 9 compares the normalized response amplitudes for the different configurations. Configurations 2 and 3 provided the highest reduction in response. This may be attributed to the fact that both dampers have a large contact region in the area corresponding to the maximum vibratory amplitude. The effect of normal load on peak response exhibits the traditional characteristics of friction dampers, namely; the presence of an optimum normal load value that corresponds to the lowest peak response, as shown in Fig. 10.

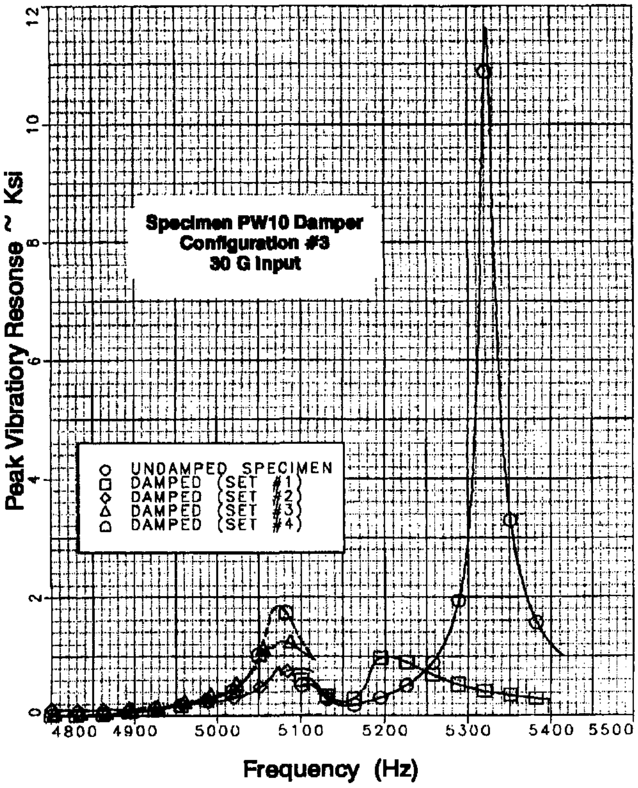

Fig. 8 Frequency response spectra for undamped and damped specimen PW10: chordwise mode

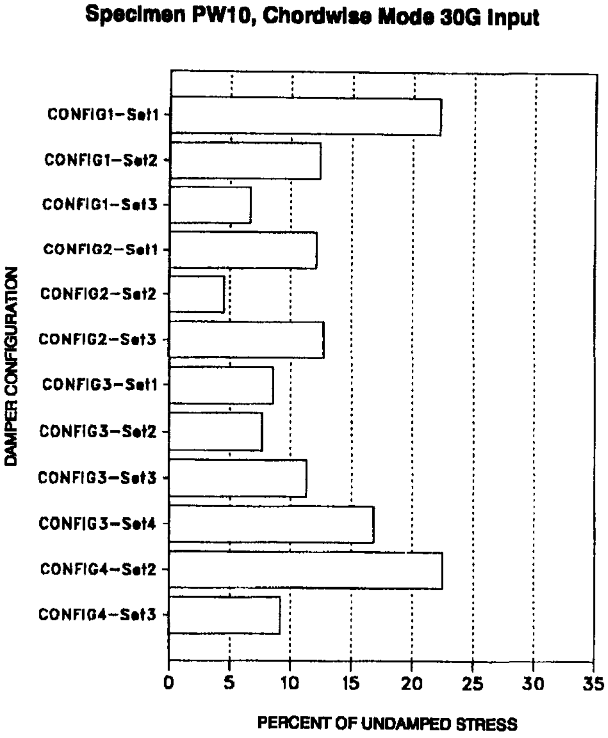

Fig. 9 PW10 damped vibratory responses as percent of undamped stress due to 30 g input: chordwise mode

2.7 Correlations to Analytical Predictions. A microslip friction damping code based on the formulation described in Part I of this paper has been used to predict the damping effectiveness for selected damper configurations. The results of hollow specimen PW10 with damper configuration 3 were selected

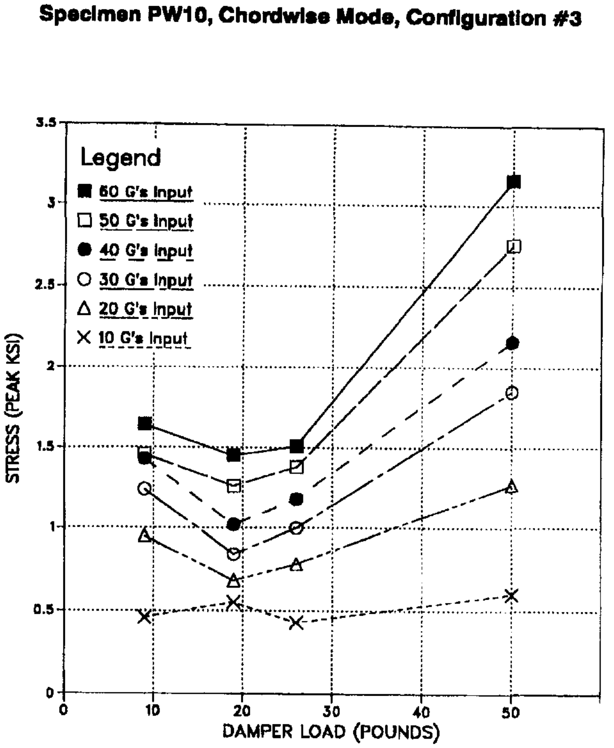

Fig. 10 Effect of damper preload on vibratory stress amplitudes for specimen PW10: chordwise mode

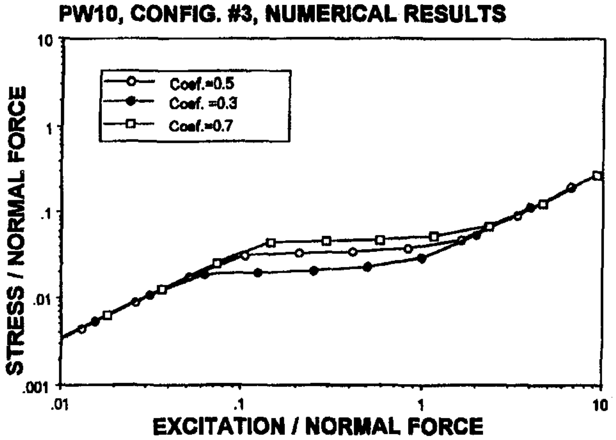

Fig. 11 Predicted damper performance using microslip model

for the correlation. Figure 11 shows the predicted damper performance characteristics for three different coefficients of friction, 0.3, 0.5, and 0.7. Superposition of the test data, normalized by the normal load, on the predicted damper performance curve for a coefficient of friction of 0.3 is shown in Fig. 12. Excellent correlations were achieved in the range where the data were collected. The collapse of the data in the region corresponding to slip on the damper performance curve indicate that the assumptions of Coulomb friction principles are valid under these test conditions.

3 Conclusions

An experimental test program to investigate the effectiveness and viability of using internal friction dampers inside hollow airfoil-like specimens was conducted. In practice, the use of such approaches would rely on the component of the centrifugal load to provide positive contact at all times and, therefore, avoid the potential loss of normal load due to wear or creep. The component of the centrifugal load required to provide the normal load between the damper and the airfoil inside surface is directly proportional to the sine of the airfoil tilt angle measured from a radial plane perpendicular to the engine centerline. Due to the limited scope of the program, however, validation testing was conducted in a nonrotating environment with the intent of simulating the effect of normal loading via spring-loaded dampers. The resulting conclusions should, however, hold true for actual airfoil designs. The results of the test program indicate that internal dampers can provide an order of magnitude reduction in response when customized for the modes of interest. Positioning the damper in a location that corresponds to maximum relative motion is required to maximize performance. While damper performance is generally optimized for a given mode, other modes that exhibit sufficient modal deflections in the vicinity of the damper can also benefit but to a lesser extent. For example, while damper configuration 3 has provided a 92 percent stress reduction for the chordwise bending mode the corresponding stress reduction for the torsion mode is in the range of 75 percent. The sensitivity of the response to the normal load was consistent with the classical characteristics of friction dampers. Optimum normal loads on the order of 20 lb provided the lowest vibratory responses. However, because of the overwhelming effectiveness of the damper, all configurations have demonstrated significant response reductions for all preloads tested. As may be expected with all friction damper applications, damper and/or specimen contact surfaces will experience wear. Provisions to minimize wear, through application of selected coatings or increases in thicknesses in local areas, must be addressed in the design phase.

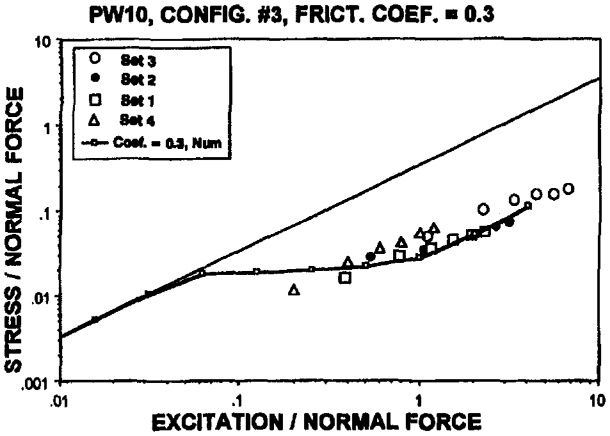

Fig. 12 Correlation of microslip model predictions with test data

Finally, excellent agreement between the experimental test results and the analytical predictions of a microslip friction damping model has been illustrated. Both the trends of the normalized data and the correlation with the analytical model indicate that the use of the Coulomb friction principles is appropriate for the range of excitation levels and normal loads used in this investigation.

Acknowledgments

The investigation in this paper was funded by the Naval Air Warfare Center (NAWC) under Contract #N00140-91-C-2676 with Mr. Peter DiMarco as the contracting officer technical representative. The authors would like to thank W. Thomson, K. Nelson, and H. Powell of the Materials & Mechanics Engineering at Pratt and Whitney for assisting with the experimental test program.

References

Griffin, J. H., 1980, "Friction Damping of Resonant Stresses in Gas Turbine Airfoils," ASME JOURNAL OF ENGINEERING FOR POWER, Vol. 102, pp. 329–333.

Griffin, J. H., and Menq, C.-H., 1991, "Friction Damping of Circular Motion and Its Implication to Vibration Control," ASME *Journal of Vibration and Acoustics*, Vol. 113, pp. 225–229.

Panossian, H. V., 1989, "Nonobstructive Impact Damping Applications for Cryogenic Environments," *Proc. Damping '89*, sponsored by The Flight Dynamics Directorate at Wright Laboratory, WRDC-TR-89-3116, West Palm Beach, FL.

T. N. Shiau

J. S. Rao

Department of Mechanical Engineering,
National Chung Cheng University,
Chia Yi, Taiwan

Y. D. Yu

S. T. Choi

Institute of Aeronautics and Astronautics,
National Cheng Kung University,
Tainan, Taiwan

Steady-State Response and Stability of Rotating Composite Blades With Frictional Damping

Friction dampers are widely used to improve the performance of rotating blades. This paper is concerned with the steady state response and stability analysis of rotating composite plates in the presence of non linear friction damping. Direct Integration Method (DIM) and Harmonic Balance Method (HBM) are used to determine the steady state response due to periodic lateral external forces. In addition, an alternate procedure, Hybrid Method (HM) is proposed for this analysis to substantiate the results from DIM and HBM. The analysis shows that the steady state response is a function of friction damping magnitude as well as its location besides the excitation frequency and the rotational speed. A stability analysis of the composite blades is also made by including periodic in-plane excitation using Floquet-Liapunov theory.

Introduction

In the design of high-speed turbo-engines, it is essential to minimize large vibration amplitudes of the blade to improve the system performance. Although this can be achieved by different ways, such as reduction of the excitation force, or keeping the resonance frequencies off the operation speed, the most effective method is to use friction damping in the structural system. Therefore, the studies of friction damping effect are widely applied to reduce the vibration amplitude of blades.

Damping is a complex phenomenon in turbine blades. The principal sources of damping are friction (interfacial slip), material, and aerodynamic damping (Rao, 1991). It was shown that interfacial slip due to Coulomb damping is the predominant damping compared with interfacial and aerodynamic damping of much lower order. Therefore, a variety of models about friction damping analysis have been successfully developed in the past. These models can be divided into two major categories: (1) macroslip models (Griffin, 1980; Sinha and Griffin, 1984; Srinivasan and Cassenti, 1986; Wang and Chen, 1993), and (2) microslip model (Menq et al., 1986a, b). Moreover, Griffin (1980) and Menq and Griffin (1985), applied the harmonic balance method (HBM) with one-term harmonic to analyze the stress distribution and vibration amplitude. A technique of multi-term HBM was recently presented by Wang and Chen (1993). These studies have been successful in the analysis of the dynamic characteristics of stiffer and shorter blades for the first mode.

In the presence of large amplitudes of rotor whirl, rubbing may take place between the blades and the turbine casing, e.g., see Rao (1995). Due to this rubbing, time-dependent in-plane loads are generated that may cause instability problem.

In this paper, the Direct Integration Method (DIM) and the Harmonic Balance Method (HBM) are used to determine the steady-state response of a rotating composite plate in the presence of nonlinear friction damping. In addition, an alternate procedure, the Hybrid Method (HM), which combines the merits of HBM and the trigonometric collocation method, is proposed to substantiate the results from HBM and DIM.

Further, by using Floquet–Liapunov theory, the stability of the composite blades in the presence of in-plane periodic force is determined. The effects of system parameters on stability, such as the amplitude and frequency of in-plane and lateral forces, and friction damping, are investigated.

Theoretical Analysis

A straight uniform composite laminated blade is shown in the fixed axis system XYZ, rotating at a constant angular velocity $\vec{\Omega}$ about the Z axis. xyz is a rotating coordinate system in which the blade is fixed at a setting angle φ on a rigid disk of radius r, as shown in Fig. 1.

An eight-noded isoparametric element using Mindlin plate theory is adopted. The composite laminate is assumed to be free from delamination and sliding between the layers.

Kinetic Energy. The position vector of a typical point P on the blade (shown in Fig. 1) after deformation can be expressed as:

$$\vec{OP'} = \{\bar{x}\} + \{d\} \tag{1}$$

where $\{\bar{x}\}^T = \{x, y, z\}$, $\{d\}^T = \{u, v, w\}$, and u, v, w are the displacement components in xyz system at point P. The angular velocity of P is $\vec{\Omega} = \{\Omega_x, \Omega_y, \Omega_z\}^T$. The velocity of point P is

$$\begin{aligned}\vec{v} &= \frac{d}{dt}(\vec{OP'}) + \vec{\Omega} \times \vec{OP'} \\ &= \{\dot{d}\} + [A](\{\bar{x}\} + \{d\})\end{aligned} \tag{2}$$

where

$$[A] = \begin{bmatrix} 0 & -\Omega_z & \Omega_y \\ \Omega_z & 0 & -\Omega_x \\ -\Omega_y & \Omega_x & 0 \end{bmatrix}$$

The kinetic energy T of the composite plate is:

$$T = \frac{1}{2}\int\int_V\int \rho\vec{v}\cdot\vec{v}\,dV \tag{3}$$

Substituting Eq. (2) into Eq. (3), the kinetic energy can be obtained as

$$T = T_2 + T_1 + T_0 \tag{4}$$

$$T_2 = \frac{1}{2}\int\int_V\int \rho\{\dot{d}\}^T\{\dot{d}\}\,dV$$

Contributed by the International Gas Turbine Institute and presented at the 41st International Gas Turbine and Aeroengine Congress and Exhibition, Birmingham, United Kingdom, June 10–13, 1996. Manuscript received at ASME Headquarters February 1996. Paper No. 96-GT-469. Associate Technical Editor: J. N. Shinn.

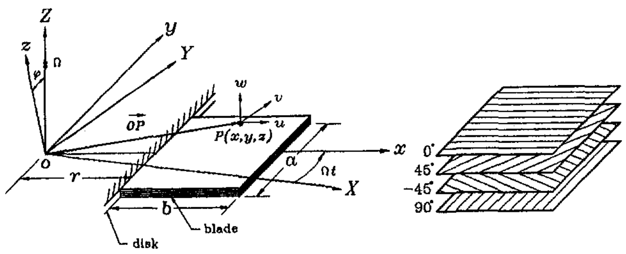

Fig. 1 Configuration of the composite laminate blade

$$T_1 = \int\int_V\int \rho\{\dot{d}\}^T[A]\{d\}dV + \int\int_V\int \rho\{\dot{d}\}^T[A]\{\bar{x}\}dV$$

$$T_0 = \tfrac{1}{2}\int\int_V\int \rho\{d\}^T[A]^T[A]\{d\}dV$$

$$+ \tfrac{1}{2}\int\int_V\int \rho\{\bar{x}\}^T[A]^T[A]\{\bar{x}\}dV$$

$$+ \int\int_V\int \rho\{d\}^T[A]^T[A]\{\bar{x}\}dV \qquad (5)$$

Potential Energy. The total potential energy (U) of the composite plate is the sum of strain energy due to plate bending (U_b) and that due to in-plane initial force (U_p) (Timoshenko and Woinowsky-Krieger, 1959):

$$U = U_b + U_p \qquad (6)$$

$$U_b = \tfrac{1}{2}\int\int_V\int \{\sigma\}^T\{\epsilon\}dV$$

$$U_p = \tfrac{1}{2}\int\int_V\int \{\epsilon_g\}^T[\sigma^o]\{\epsilon_g\}dV \qquad (7)$$

with $\{\sigma\}^T = \{\sigma_x, \sigma_y, \sigma_{xy}, \sigma_{yz}, \sigma_{zx}\}$, $[\sigma^o] = \begin{bmatrix} \sigma_x^o & \sigma_{xy}^o \\ \sigma_{xy}^o & \sigma_y^o \end{bmatrix}$, $\{\epsilon_g\} = \{w_{,x}, w_{,y}\}$ and σ_x^o. σ_y^o, σ_{xy}^o are initial stresses of the blade due to the effect of centrifugal force of the rotating system. For an orthotropic material, the stress–strain relationship is:

$$\{\sigma\} = [\bar{Q}]\{\epsilon\} \qquad (8)$$

where $[\bar{Q}]$ is the transformed reduced stiffness matrix; see Ashton and Whitney (1970). Substituting Eq. (8) into Eq. (6), the strain energy due to bending is

$$U_b = \tfrac{1}{2}\int\int_V\int \{\epsilon\}^T[\bar{Q}]\{\epsilon\}dV \qquad (9)$$

Finite Element. For the eight-noded isoparametric element, the coordinates at any point in the element are expressed as the function of nodal coordinates (see Yang, 1986)

$$x = \sum_{i=1}^{8} \phi_i x_i \quad y = \sum_{i=1}^{8} \phi_i y_i \quad z = \sum_{i=1}^{8} \phi_i z_i$$

which in matrix form are:

$$\{\bar{x}\} = [N_1]\{\underline{x}_n^{(i)}\} \qquad (10)$$

where x_i, y_i, z_i denote the ith nodal coordinate in the global coordinate system, and $[N_1]$ is given in the appendix, $\{\underline{x}_n^{(i)}\}^T = \{x_1, y_1, z_1, x_2, y_2, z_2, \ldots, x_8, y_8, z_8\}$.

According to Mindlin's theory (1951), the displacement components along x, y, z axes can be expressed as

$$u(x, y, t) = u_0(x, y, t) + z\psi_x(x, y, t)$$

$$v(x, y, t) = v_0(x, y, t) + z\psi_y(x, y, t)$$

$$w(x, y, t) = w_0(x, y, t) \qquad (11)$$

where u_0, v_0, and w_0 are the displacement components along x, y, z axes of the corresponding point in the middle plane, and ψ_x, ψ_y are the slopes due to bending about y and x axes. The degrees of freedom u_0, v_0, w_0, ψ_x, ψ_y are expressed in a similar manner as the combination of the nodal degrees of freedom

$$u = \sum_{i=1}^{8} \phi_i u_i + z \sum_{i=1}^{8} \phi_i \psi_{x_i}$$

$$v = \sum_{i=1}^{8} \phi_i v_i + z \sum_{i=1}^{8} \phi_i \psi_{y_i}$$

$$w = \sum_{i=1}^{8} \phi_i w_i$$

$$\{d\} = [N_2]\{q\} \qquad (12)$$

where $\{d\} = \{u, v, w\}^T$, $\{q\} = \{u_1, v_1, w_1, \phi_{x1}, \phi_{y1}, \ldots u_8, v_8, w_8, \phi_{x8}, \phi_{y8}\}^T$ and $[N_2]$ is given in the appendix. Substituting Eq. (11) into the strain-displacement relations (Timoshenko and Woinowsky-Krieger, 1959), we get

$$\epsilon_x = u_{,x} = u_{0,x} + z\psi_{x,x}$$

$$\epsilon_y = v_{,y} = v_{0,y} + z\psi_{y,y}$$

Nomenclature

A = tip center response of the blade
A_0 = static excitation maximum response of the blade
A_i = ith component of the displacement vector amplitude
a = length of the blade
b = width of the blade
$\{F\}$, $\{F_n\}$ = excitation force vector and friction force vector, respectively
f_0 = static lift excitation force
$[M]$, $[C]$, $[K]$ = mass, damping, and stiffness matrix of global nodal D.O.F., respectively
K_G = stiffness of the friction damper
$\{P\}$ = excitation force vector
P_0 = in-plane force amplitude
P_{cr} = buckling force due to static excitation
$[\bar{Q}]$ = transformed reduced stiffness matrix
$\{q\}$ = nodal displacement vector
R = normal per load
r = radius of rotating disk
$[S]$ = transition matrix of FTM
T = kinetic energy
U = potential energy
u, v, w = displacement components in x, y, z directions
z_i = displacement of friction damper
α = in-plane force frequency
$\{\delta\}$ = displacement vector of nodal D.O.F.
μ = coefficient of the friction damper
ρ = density of the layer
ϕ_i = eight-noded element shape function
φ = setting angle of the blade
$\{\epsilon(t)\}$ = small disturbance vector
Ω_f = fundamental frequency
Ω_p = frequency of lateral excitation force
$\vec{\Omega}$ = angular velocity of disk
ω_{n1} = nonrotating blade first natural frequency
ξ^c, ξ^s = harmonic amplitudes of displacement

$$\gamma_{xy} = u_{,y} + v_{,x} = u_{0,y} + v_{0,x} + z(\psi_{x,y} + \psi_{y,x})$$
$$\gamma_{yz} = v_{,z} + w_{,y} = w_{0,y} + \psi_y$$
$$\gamma_{zx} = u_{,z} + w_{,x} = w_{0,x} + \psi_x \qquad (13)$$

$\{\epsilon\}$ and $\{\epsilon_g\}$ are now expressed as:

$$\{\epsilon\} = [N_3]\{q\} \qquad (14)$$

$$\{\epsilon_g\} = [N_4]\{q\} \qquad (15)$$

where $[N_3]$ and $[N_4]$ are given in the appendix. Substituting Eqs. (10) to (15) into Eqs. (4), (7), and (9) and using Jacobian transformation, we get

$$T_2 = \frac{1}{2}\int\int_V\int \rho\{\dot{q}\}^T[N_2]^T[N_2]\{\dot{q}\}dV \qquad (16)$$

$$T_1 = \int\int_V\int \rho\{\dot{q}\}^T[N_2]^T[A][N_2]\{q\}dV + \int\int_V\int \rho\{\dot{q}\}^T[N_2]^T[A][N_1]\{\underline{x}_n^{(l)}\}dV \qquad (17)$$

$$T_0 = \frac{1}{2}\int\int_V\int \rho\{q\}^T[N_2]^T[A]^T[A][N_2]\{q\}dV + \frac{1}{2}\int\int_V\int \rho\{\underline{x}_n^{(l)}\}^T[N_1]^T[A]^T[A][N_1]\{\underline{x}_n^{(l)}\}dV + \int\int_V\int \rho\{q\}^T[N_2]^T[A]^T[A][N_1]\{\underline{x}_n^{(l)}\}dV \qquad (18)$$

$$U_b = \frac{1}{2}\int\int_V\int \{q\}^T[N_3]^T[\bar{Q}][N_3]\{q\}dV \qquad (19)$$

$$U_p = \frac{1}{2}\int\int_V\int \{q\}^T[N_4]^T[\sigma^o][N_4]\{q\}dV \qquad (20)$$

The excitation force is considered to consist of three components: (1) nozzle passing harmonic force, (2) nonlinear dry friction force, and (3) in-plane periodic force (for stability analysis). The nozzle passing force is

$$\vec{F}_e = \begin{Bmatrix} F_1 \\ F_2 \\ F_3 \end{Bmatrix} \cos \Omega_p t \qquad (21)$$

with the equivalent nodal force given by

$$\{F\}_e = \left(\int_A\int [N_2]\begin{Bmatrix} F_1 \\ F_2 \\ F_3 \end{Bmatrix}_n dA\right) \cos \Omega_p t$$

$$= \{F\}_{en} \cos \Omega_p t \qquad (22)$$

Using the Lagrangian approach, we now can obtain,

$$[M]_e\{\ddot{q}\} + [G]_e\{\dot{q}\} + [K]_e\{q\} + \{f_c\}_e = \{F\}_e \qquad (23)$$

$$[M]_e = \int\int_V\int \rho[N_2]^T[N_2]dV$$

$$[G]_e = 2\int\int_V\int \rho[N_2]^T[A][N_2]dV$$

$$[K]_e = -\int\int_V\int \rho[N_2]^T[A]^T[A][N_2]dV + \int\int_V\int \rho[N_3]^T[\bar{Q}][N_3]dV + \int\int_V\int \rho[N_4]^T[\sigma^0][N_4]dV$$
$$= [K_r]_e + [K_e]_e + [K_g]_e$$

$$\{f_c\}_e = -\int\int_V\int \rho[N_2]^T[A]^T[A][N_1]dV\{\underline{x}_n^{(l)}\}$$

where the matrix $[G]_e$ is due to the Coriolis effect, $[K_r]_e$ is the rotary stiffness matrix, $[K_e]_e$ is the elastic stiffness matrix, and $[K_g]_e$ is the geometric stiffness matrix. $[\sigma^0]$ is the in-plane stress matrix of the blade due to the centrifugal force as well as the external periodic in-plane force mentioned above, $\{f_c\}_e$ is the centrifugal force, and $\{F\}_e$ is the equivalent nodal force. When the in-plane periodic force is considered for the stability analysis, $[K_g]_e$ is a function of time.

Assembling the elemental matrices, the system equations of motion for the rotating blade in global coordinates can be obtained as:

$$[M]\{\ddot{\delta}\} + [C]\{\dot{\delta}\} + [K]\{\delta\} = \{F\} \qquad (24)$$

where $\{\delta\}$ denotes the displacement vector including all the degrees of freedom of the system and $\{F\}$ is excitation force vector. The damping matrix in the equation above consists of the gyroscopic matrix $[G]$ and structural damping is added into this by including $\eta[K]$, so that $[C] = \eta[K] + [G]$.

Steady-State Response

To determine the steady-state response in the presence of nonlinear dry friction damping, the system equation, Eq. (24), is written as

$$[M]\{\ddot{\delta}\} + [C]\{\dot{\delta}\} + [K]\{\delta\} = \{F\} + \{F_n\} \qquad (25)$$

where $\{F_n\}$ is the nonlinear friction force vector. This vector is determined as follows.

(i) HBM Approximation. The steady-state solution of Eq. (25) with a one-term approximation is taken as

$$\{\delta\} = \{a\}_1 \cos(\Omega_p t) + \{b\}_1 \sin(\Omega_p t) \qquad (26)$$

For the purpose of obtaining the friction force in Eq. (25), the system model in Fig. 2 is used where R, μ, and K_G represent the normal preload, the friction coefficient of the damper, and its stiffness in the direction of relative motion, respectively. The friction damper is applied at one or several nodal locations of the composite plate. Following Griffin (1980) the component f_{ni} at the ith node of the nonlinear friction force vector $\{F_n\}$ is expressed as

$$f_{ni} = \begin{cases} K_G(\delta_i - z_i) & \text{when } K_G|\delta_i - z_i| \le \mu R \\ \mu R \text{ sign } (\dot{z}_i) & \text{when } K_G|\delta_i - z_i| \ge \mu R \end{cases} \qquad (27)$$

where z_i is the displacement of the friction damper, as shown in Fig. 2, and δ_i is the ith nodal component of the displacement vector in Eq. (26). The nodal displacement can be written as $\delta_i = A_i \cos\theta_i$, where $\theta_i = \Omega_p t - \phi_i$ and the angle ϕ_i is the phase difference between the external excitation force and the response.

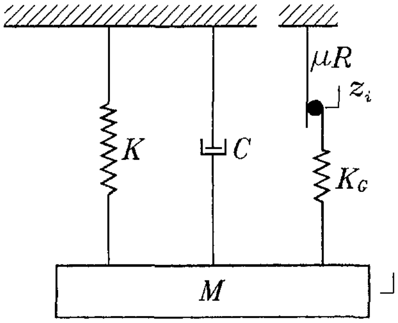

Fig. 2 Model of frictional damping system

A typical relationship between the response and the friction force is shown in Fig. 3; see Griffin (1980). The damper is in stick and slip conditions during the *EF* and *FG* sections, respectively. Then the displacement of the friction damper, z_i, is

$$\begin{cases} EF: z_i = A_i - \dfrac{\mu R}{K_G} & 0 \le \theta_i \le \theta_{fi} \\[2ex] FG: z_i = \dfrac{\mu R}{K_G} + \delta_i & \theta_{fi} \le \theta_i \le \pi \end{cases} \tag{28}$$

$$z_i(\theta) = -z_i(\theta + \pi) \tag{29}$$

$$\theta_{fi} = \cos^{-1}\left(1 - \frac{2\mu R}{K_G A_i}\right) \tag{30}$$

z_i can be expressed as

$$z_i = a_i^* \cos \theta_i + b_i^* \sin \theta_i \tag{31}$$

$$a_i^* = \frac{1}{\pi}\int_0^{2\pi} z_i \cos \theta_i \, d\theta_i = \frac{A_i}{\pi}\left[\frac{1}{2}\sin(2\theta_{fi}) + (\pi - \theta_{fi})\right]$$

$$b_i^* = \frac{1}{\pi}\int_0^{2\pi} z_i \sin \theta_i \, d\theta_i = \frac{A_i}{\pi}\sin^2(\theta_{fi})$$

$$\begin{aligned} f_{ni} &= K_G(\delta_i - z_i) = K_G(A_i - a_i^*)\cos\theta_i - K_G b_i^* \sin\theta_i \\ &= [K_G(A_i - a_i^*)\cos\phi_i + K_G b_i^* \sin\theta_i]\cos\Omega_p t \\ &\quad + [K_G(A_i - a_i^*)\sin\phi_i - K_G b_i^* \cos\theta_i]\sin\Omega_p t \\ &= f^{\,i}_{N1}\cos\Omega_p t + f^{\,i}_{N2}\sin\Omega_p t \end{aligned} \tag{32}$$

We write the nonlinear friction force vector $\{F_n\}$ as

$$\{F_n\} = \{f_{N1}\}\cos\Omega_p t + \{f_{N2}\}\sin\Omega_p t \tag{33}$$

The lateral excitation force vector $\{F\}$ is expressed as

$$\{F\} = \{f_{L1}\}\cos\Omega_p t + \{f_{L2}\}\sin\Omega_p t \tag{34}$$

With the help of Eqs. (26), (33), (34), Eq. (25) becomes

$$\begin{bmatrix} [K] - \Omega_p^2[M] & \Omega_p[C] \\ -\Omega_p[C] & [K] - \Omega_p^2[M] \end{bmatrix}\begin{Bmatrix} \{a\}_1 \\ \{b\}_1 \end{Bmatrix} = \begin{Bmatrix} \{F_1\}_1 \\ \{F_2\}_1 \end{Bmatrix} \tag{35}$$

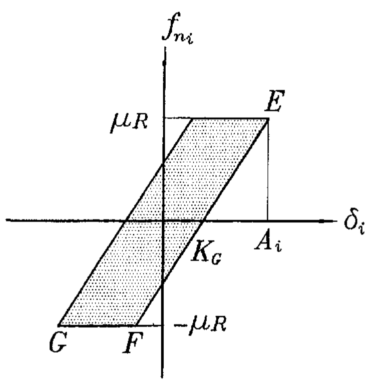

Fig. 3 Loop friction force versus response

where $\{F_1\} = \{f_{L1}\} + \{f_{N1}\}$ and $\{F_2\} = \{f_{L2}\} + \{f_{N2}\}$. Let

$$[T] = \begin{bmatrix} [K] - \Omega_p^2[M] & \Omega_p[C] \\ -\Omega_p[C] & [K] - \Omega_p^2[M] \end{bmatrix}$$

$$\{D\} = \begin{Bmatrix} \{a\}_1 \\ \{b\}_1 \end{Bmatrix} \quad \{R_f\} = \begin{Bmatrix} \{F_1\}_1 \\ \{F_2\}_1 \end{Bmatrix}$$

Equation (35) can then be rearranged as

$$\begin{bmatrix} [T_{11}] & [T_{12}] \\ [T_{21}] & [T_{22}] \end{bmatrix}\begin{Bmatrix} \{D_1\} \\ \{D_2\} \end{Bmatrix} = \begin{Bmatrix} \{R_{f1}\} \\ \{R_{f2}\} \end{Bmatrix} \tag{36}$$

where the subscripts 1 and 2 represent coordinates associated with the linear and nonlinear components, respectively. From Eq. (36) we can obtain

$$\{D_1\} = [T_{11}]^{-1}(\{R_{f1}\} - [T_{12}]\{D_2\}) \tag{37}$$

$$\begin{aligned} \{D_2\} &= ([T_{21}][T_{11}]^{-1}[T_{12}])^{-1} \\ &\quad \times ([T_{21}][T_{11}]^{-1}\{R_{f1}\} - \{R_{f2}\}) \end{aligned} \tag{38}$$

Starting with linear steady-state solution for A_i, the Newton–Raphson iteration method is used to solve Eq. (38) and determine the solution for $\{D_2\}$. Substituting the same in Eq. (37), $\{D_1\}$ is determined.

(ii) HM Approximation An alternate algorithm proposed is a hybrid method (HM), which combines the merits of HBM and the trigonometric collocation method with condensation techniques. Equation (25) is rearranged as

$$\begin{aligned} &\begin{bmatrix} [M_{11}] & [M_{12}] \\ [M_{21}] & [M_{22}] \end{bmatrix}\begin{Bmatrix} \{\ddot{\delta}_1\} \\ \{\ddot{\delta}_2\} \end{Bmatrix} + \begin{bmatrix} [C_{11}] & [C_{12}] \\ [C_{21}] & [C_{22}] \end{bmatrix}\begin{Bmatrix} \{\dot{\delta}_1\} \\ \{\dot{\delta}_2\} \end{Bmatrix} \\ &\quad + \begin{bmatrix} [K_{11}] & [K_{12}] \\ [K_{21}] & [K_{22}] \end{bmatrix}\begin{Bmatrix} \{\delta_1\} \\ \{\delta_2\} \end{Bmatrix} = \begin{Bmatrix} \{F_1^c\} \\ \{F_2^c\} \end{Bmatrix}\cos\Omega_p t \\ &\qquad + \begin{Bmatrix} \{F_1^s\} \\ \{F_2^s\} \end{Bmatrix}\sin\Omega_p t + \begin{Bmatrix} \{0\} \\ \{f_N\} \end{Bmatrix} \end{aligned} \tag{39}$$

where the subscripts 1 and 2 represent coordinates associated with the linear and nonlinear components, respectively. It assumes that the periodic response of the system can be approximately expressed as a finite Fourier series in real form as follows:

$$\begin{Bmatrix} \delta_1 \\ \delta_2 \end{Bmatrix} = \sum_{j=1}^{N_w}\left(\begin{Bmatrix} \{\xi_{Lj}^c\} \\ \{\xi_{Nj}^c\} \end{Bmatrix}\cos\omega_j t + \begin{Bmatrix} \{\xi_{Lj}^s\} \\ \{\xi_{Nj}^s\} \end{Bmatrix}\sin\omega_j t\right) \tag{40}$$

where $\omega_j = j\Omega_f$, $\Omega_f = (p/q)\Omega_p$ with p and q nonzero positive integers such that p/q is an irreducible fraction, and N_w is the number of Fourier series terms retained. p and q can be suitably chosen, depending on whether super or subharmonic solutions are sought. In this paper Ω_f is taken as Ω_p. Substitution of Eq. (40) into Eq. (39), with decomposition of those equations into the corresponding nonlinear and linear components, yields

$$\sum_{j=1}^{N_w}([K_{11}|K_{12}] - \omega_j^2[M_{11}|M_{12}]) \times \left(\begin{Bmatrix} \{\xi_{Lj}^c\} \\ \{\xi_{Nj}^c\} \end{Bmatrix}\cos\omega_j t + \begin{Bmatrix} \{\xi_{Lj}^s\} \\ \{\xi_{Nj}^s\} \end{Bmatrix}\sin\omega_j t\right)$$

$$+ \sum_{j=1}^{N_w} [C_{11}|C_{12}]\left(-\omega_j \begin{Bmatrix} \{\xi_{Lj}^c\} \\ \{\xi_{Nj}^c\} \end{Bmatrix} \sin \omega_j t + \omega_j \begin{Bmatrix} \{\xi_{Lj}^s\} \\ \{\xi_{Nj}^s\} \end{Bmatrix} \cos \omega_j t \right) = \{F_1^c\} \cos \Omega_p t + \{F_1^s\} \sin \Omega_p t \quad (41)$$

$$\sum_{j=1}^{N_w} ([K_{21}|K_{22}] - \omega_j^2 [M_{21}|M_{22}]) \times \left(\begin{Bmatrix} \{\xi_{Lj}^c\} \\ \{\xi_{Nj}^c\} \end{Bmatrix} \cos \omega_j t + \begin{Bmatrix} \{\xi_{Lj}^s\} \\ \{\xi_{Nj}^s\} \end{Bmatrix} \sin \omega_j t \right)$$

$$+ \sum_{j=1}^{N_w} [C_{21}|C_{22}]\left(-\omega_j \begin{Bmatrix} \{\xi_{Lj}^c\} \\ \{\xi_{Nj}^c\} \end{Bmatrix} \sin \omega_j t + \omega_j \begin{Bmatrix} \{\xi_{Lj}^s\} \\ \{\xi_{Nj}^s\} \end{Bmatrix} \cos \omega_j t \right)$$

$$= \{F_2^c\} \cos \Omega_p t + \{F_2^s\} \sin \Omega_p t + \{f_N\} \quad (42)$$

Using the harmonic balance technique, the following equations can be obtained from Eq. (41):

$$\begin{Bmatrix} \{\xi_{Lj}^c\} \\ \{\xi_{Lj}^s\} \end{Bmatrix} = \begin{bmatrix} [K_{11}] - \omega_j^2 [M_{11}] & \omega_j [C_{11}] \\ -\omega_j [C_{11}] & [K_{11}] - \omega_j^2 [M_{11}] \end{bmatrix}^{-1} \times \left(\begin{Bmatrix} \{\bar{F}_1^c\} \\ \{\bar{F}_1^s\} \end{Bmatrix} - \begin{bmatrix} [K_{12}] - \omega_j^2 [M_{12}] & \omega_j [C_{12}] \\ -\omega_j [C_{12}] & [K_{12}] - \omega_j^2 [M_{12}] \end{bmatrix} \times \begin{Bmatrix} \{\xi_{Nj}^c\} \\ \{\xi_{Nj}^s\} \end{Bmatrix} \right) \quad (43)$$

where the forcing vectors $\{\bar{F}_1^c\}$ and $\{\bar{F}_1^s\}$ are defined as

$$\begin{Bmatrix} \{\bar{F}_1^c\} \\ \{\bar{F}_1^s\} \end{Bmatrix} = \begin{cases} \begin{Bmatrix} \{F_1^c\} \\ \{F_1^s\} \end{Bmatrix} & \text{if } \omega_j = \Omega_p \\ \begin{Bmatrix} \{0\} \\ \{0\} \end{Bmatrix} & \text{if } \omega_j \neq \Omega_p \end{cases}$$

It is more convenient to rewrite Eq. (43) in the following form and expand:

$$\begin{Bmatrix} \{\xi_{Lj}^c\} \\ \{\xi_{Lj}^s\} \end{Bmatrix} = \begin{bmatrix} [T_j^c] \\ [T_j^s] \end{bmatrix} \begin{Bmatrix} \{\bar{F}_1^c\} \\ \{\bar{F}_1^s\} \end{Bmatrix} - \begin{bmatrix} [R_j^c] \\ [R_j^s] \end{bmatrix} \begin{Bmatrix} \{\xi_{Nj}^c\} \\ \{\xi_{Nj}^s\} \end{Bmatrix} \quad (44)$$

$$\begin{Bmatrix} \{\xi_{Lj}^c\} \\ \{\xi_{Nj}^c\} \end{Bmatrix} = \begin{bmatrix} & -[R_j^c] & \\ [I] & & [0] \end{bmatrix} \begin{Bmatrix} \{\xi_{Nj}^c\} \\ \{\xi_{Nj}^s\} \end{Bmatrix} + \begin{bmatrix} [T_j^c] \\ [0] \end{bmatrix} \begin{Bmatrix} \{\bar{F}_1^c\} \\ \{\bar{F}_1^s\} \end{Bmatrix} \quad (45)$$

$$\begin{Bmatrix} \{\xi_{Lj}^s\} \\ \{\xi_{Nj}^s\} \end{Bmatrix} = \begin{bmatrix} & -[R_j^s] & \\ [0] & & [I] \end{bmatrix} \begin{Bmatrix} \{\xi_{Nj}^c\} \\ \{\xi_{Nj}^s\} \end{Bmatrix} + \begin{bmatrix} [T_j^s] \\ [0] \end{bmatrix} \begin{Bmatrix} \{\bar{F}_1^c\} \\ \{\bar{F}_1^s\} \end{Bmatrix} \quad (46)$$

Substitution of Eqs. (45) and (46) into Eq. (42) yields

$$\sum_{j=1}^{Nw} ([E_j^c] \cos \omega_j t + [E_j^s] \sin \omega_j t) \begin{Bmatrix} \{\xi_{Nj}^c\} \\ \{\xi_{Nj}^s\} \end{Bmatrix} = \{H_c\} \cos \Omega_p t + \{H_s\} \sin \Omega_p t + \{f_N\} \quad (47)$$

$$[E_j^c] = ([K_{21}|K_{22}] - \omega_j^2 [M_{21}|M_{22}]) \begin{bmatrix} & -[R_j^c] & \\ [I] & & [0] \end{bmatrix} + \omega_j [C_{21}|C_{22}] \begin{bmatrix} & -[R_j^s] & \\ [0] & & [I] \end{bmatrix} \quad (48)$$

$$[E_j^s] = ([K_{21}|K_{22}] - \omega_j^2 [M_{21}|M_{22}]) \begin{bmatrix} & -[R_j^s] & \\ [0] & & [I] \end{bmatrix} + \omega_j [C_{21}|C_{22}] \begin{bmatrix} & -[R_j^c] & \\ [I] & & [0] \end{bmatrix} \quad (49)$$

$$\{H_s\} = \{F_2^c\} - ([[K_{21}] - \omega_l [M_{21}]][T_l^c] + \omega_l [C_{21}][T_l^s]) \begin{Bmatrix} \{F_1^c\} \\ \{F_1^s\} \end{Bmatrix} \quad (50)$$

$$\{H_c\} = \{F_2^s\} - ([[K_{21}] - \omega_l [M_{21}]][T_l^s] - \omega_l [C_{21}][T_l^c]) \begin{Bmatrix} \{F_1^c\} \\ \{F_1^s\} \end{Bmatrix} \quad (51)$$

It may be noted that the subscript l shown in Eqs. (50) and (51) is specified for that harmonic frequency with $\omega_l = \Omega_p$. In general, the components f_{ni} of the nonlinear forcing vector $\{f_N\}$ can be

$$f_{ni} = \begin{cases} K_G(\delta_i + A_i) - \mu R & -A_i < \delta_i < x_i \quad \text{and} \quad \dot{\delta}_i > 0 \\ \mu R & x_i < \delta_i < A_i \quad \text{and} \quad \dot{\delta}_i > 0 \\ K_G(\delta_i - A_i) + \mu R & x_i < \delta_i < A_i \quad \text{and} \quad \dot{\delta}_i < 0 \\ -\mu R & -A_i < \delta_i < x_i \quad \text{and} \quad \dot{\delta}_i < 0 \end{cases}$$

where $x_i = 2K_G \cdot \mu R - A_i$; see Fig. 3.

The final step in the solution is the application of the collocation technique to determine the unknown Fourier coefficients in Eq. (47). It is easy to show that if the order of vector $\{f_N\}$ is N, then the total number of unknown Fourier coefficients in Eq. (47) is $N \times (2 \times N_w)$, and the collocation points, N_T, have to be greater than or equal to $2N_w$. Here, N_T is taken as $2N_w$. The corresponding time interval Δt chosen in this study is

$$\Delta t = \frac{2\pi}{\Omega} \frac{1}{N_T}$$

Hence, the time at the nth collocation point can be written

$$t_n = (n - 1) \cdot \Delta t; \quad n = 1, 2, \ldots N_T$$

Then, the final nonlinear algebraic equations for the nth time collocation point are given by

$$\sum_{j=1}^{Nw} ([E_j^c] \cos \omega_j t_n + [E_j^s] \sin \omega_j t_n) \begin{Bmatrix} \{\xi_{Nj}^c\} \\ \{\xi_{Nj}^s\} \end{Bmatrix} = \{H_c\} \cos \Omega_p t_n + \{H_s\} \sin \Omega_p t_n + \{f_N\}$$

$$n = 1, 2, \ldots, N_T \quad (52)$$

The Fourier coefficients, $\{\xi_{Ni}^c\}$ and $\{\xi_{Ni}^s\}$, can be obtained by solving Eq. (52) using the Newton–Raphson iteration method. Substituting these coefficients back into Eq. (43), one can obtain the rest of the Fourier coefficients $\{\xi^c_{Li}\}$ and $\{\xi^s_{Li}\}$.

Stability Analysis

Consider the steady-state periodic solution of Eq. (25) to be $\{\delta_0(t)\}$. With a small disturbance $\{\epsilon(t)\}$, the system steady-state response can be expressed as

$$\{\delta(t)\} = \{\delta_0(t)\} + \{\epsilon(t)\} \tag{53}$$

Substitution of Eq. (53) into Eq. (25) yields

$$[M]\{\ddot{\epsilon}(t)\} + [C]\{\dot{\epsilon}(t)\} + [K(t)]\{\epsilon(t)\} = \{F_n(t, \{\delta\})\} - \{F_n(t, \{\delta_0\})\} \tag{54}$$

The system stability is governed by solution of Eq. (54). By using the first-order Taylor series expansion, Eq. (54) can be approximated by

$$[M]\{\ddot{\epsilon}(t)\} + [C]\{\dot{\epsilon}(t)\} + [K]\{\epsilon(t)\} = [Q_1(t)]\{\epsilon\} + [Q_2(t)]\{\dot{\epsilon}\} \tag{55}$$

$$[Q_1(t)] = \left.\frac{\partial\{F_n\}}{\partial\{\delta\}}\right|_{\{\delta\}=\{\delta_0\}}$$

$$[Q_2(t)] = \left.\frac{\partial\{F_n\}}{\partial\{\dot{\delta}\}}\right|_{\{\delta\}=\{\delta_0\}}$$

The linearized periodic system, Eq. (55), is rearranged as

$$[M^*]\{\ddot{\epsilon}\} + [C^*]\{\dot{\epsilon}\} + [K^*]\{\epsilon\} = \{0\} \tag{56}$$

$$[C^*] = [C] - [Q_2(t)]$$

$$[K^*] = [K] - [Q_1(t)]$$

The stability can be examined by solving the eigenvalues of the Floquet transition matrix (FTM) of Eq. (56). From the Floquet–Liapunov theory, the steady-state periodic response is stable only when the maximum absolute value of the eigenvalues of FTM is less than one, i.e.,

$$|\Lambda|_{\max} < 1.0 : \text{Stable}$$

$$|\Lambda|_{\max} \geq 1.0 : \text{Unstable}$$

For convenience, Eq. (56) is cast into first-order form

$$\{\dot{q}\} = [S]\{q\} \tag{57}$$

$$\{q\} = \{\dot{\epsilon}, \epsilon\}^T$$

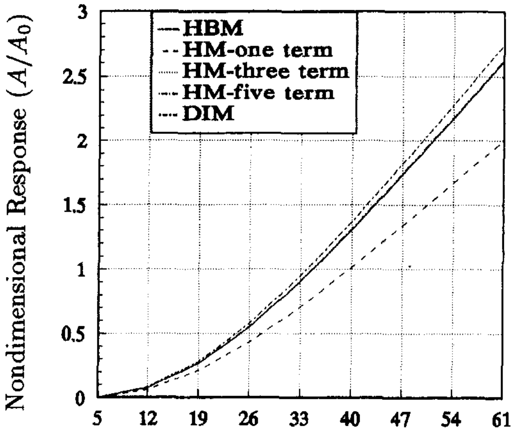

Fig. 5 Comparison of HBM, HM, DIM

$$[S] = [M^*]^{-1}\begin{bmatrix} -[C^*] & -[K^*] \\ [M^*] & [0] \end{bmatrix}$$

Assuming that $[L(t)]$ is a solution matrix of Eq. (57) with initial condition $[L(0)] = [I]$, then the transition matrix is $[L(T)]$ with $T = 2\pi/\alpha$. The stability of the system motion can be determined by solving corresponding eigenvalues of FTM; see Jean (1990).

Numerical Examples and Results

Example 1. A $[0/\pm45/90]_{\text{sym}}$ composite midplane symmetric laminate blade with $a = 0.1524$ m, $b = 0.0381$ m, $t = 0.000528$ m mounted on a 0.0381 m radius disk is considered. The aspect ratio of the blade is 4. The material properties are $E_1 = 128$ GPa, $E_2 = 11$ GPa, G_{12}, $G_{13} = 4.48$ GPa, $G_{23} = 1.53$ GPa, Poisson's ratio $\nu_{12} = 0.25$, density $\rho = 1.5 \times 10^3$ kg/m^3. The stiffness of the friction damper in the direction of relative motion K_G is taken as 3500 N/m. The lateral excitation force is taken to be aerodynamic in nature, which is normal to the upstream flow. Such a force can be determined by a flow path analysis in a stage (Rao, 1993). Here for simplicity, the components of such a force in the transverse and chordwise directions are taken as Transverse force $= 1.0 \times 10^4 e^{i\Omega_p t}$ N/m^2, Chordwise force $= 5 \times 10^3 e^{i\Omega_p t}$ N/m^2. Sixteen elements are used as shown in Fig. 4 for the analysis with setting angle of the blade $\varphi = 0$ deg and rotational speed $\vec{\Omega} = 0.1\omega_{n1}$. The response is determined by HBM, HM, and DIM using the Newmark method with

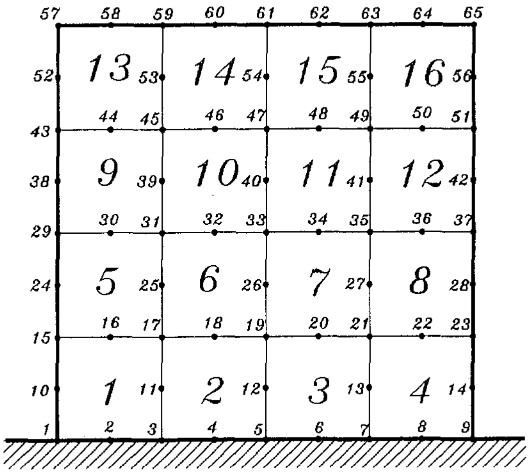

Fig. 4 Sixteen-element mesh of the composite blade

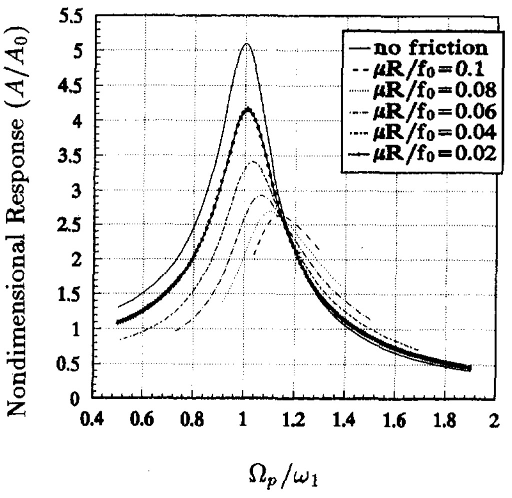

Fig. 6 Effect of excitation frequency with friction at nodes 60, 61, 62

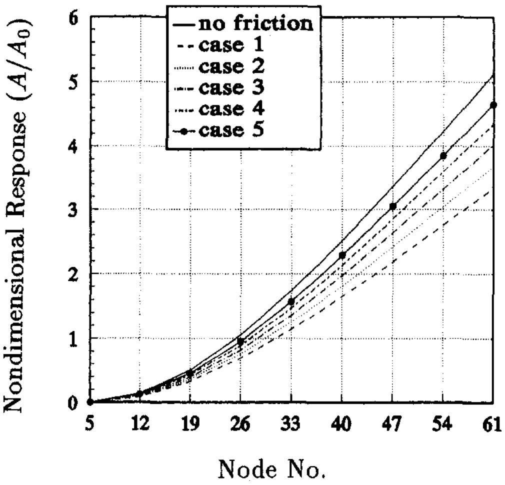

Fig. 7 Effect of friction force applied location with $\Omega_p/\omega_1 = 1.0$

friction forces at different nodal locations and nondimensional excitation frequencies. The results obtained are shown in Figs. 6 to 8. In these figures, A_0 is the static excitation maximum response and f_0 is the static lift force in the transverse direction of the blade.

Figure 5 shows the nondimensional response A/A_0 at different nodes by different methods with the friction force applied at nodes 60, 61, and 62 for lateral excitation frequency Ω_p equal to the first nonrotating blade natural frequency ω_{n1} and $\mu R/f_0 = 0.06$. The HM one-term approximation predicted lower results; a three-term approximation result rapidly converged with HBM as seen in the figure. The results obtained by DIM are upper bounded, predicting slightly higher values over HBM.

The response of the blade tip center with friction force applied on nodes 60, 61, and 62 is shown in Fig. 6 as a function of nondimensional excitation frequency Ω_p/ω_{n1}. The results show that the peak response occurs at $\Omega_p > \omega_{n1}$ and as the friction is increased, the peak shifts to the right. Moreover, there is a crossover frequency around $\Omega_p = 1.175\omega_{n1}$ beyond which friction increases response.

Figures 7 and 8 show the response with nondimensional excitation frequencies $\Omega_p/\omega_{n1} = 1$ and 1.2, respectively. Five different cases with $\mu R/f_0 = 0.04$ are considered and listed as follows:

- Case 1—friction on tip nodes 60, 61, and 62.
- Case 2—friction on nodes 53, 54, and 55 located in the middle of the top row of elements.

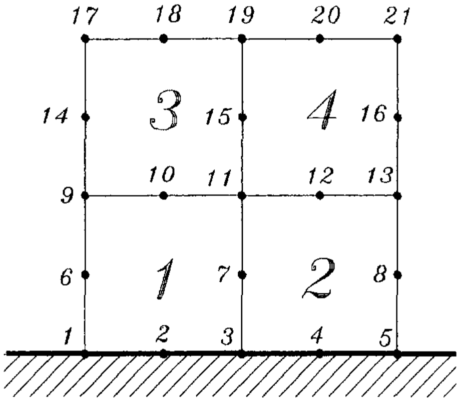

Fig. 9 Four-element mesh of the composite blade

- Case 3—friction on nodes 46, 47, and 48 located below the nodes of case 2.
- Case 4—friction on nodes 39, 40, and 41 located in the middle of the second row of elements from the top row.
- Case 5—friction on nodes 32, 33, and 34 located below the nodes of case 4.

Note that all the nodes in these cases are located adjacent to the central axis of the blade. The results from Fig. 7 show that for $\Omega_p/\omega_{n1} = 1$, the friction force is helpful in suppressing the amplitude of vibration. It is also noted that damping is more effective when it is applied at nodes closer to the tip of the blade. Figure 8 indicates that friction is undesirable after the crossover point $\Omega_p = 1.175\omega_{n1}$ in the sense that friction increases the response of the blade. Also friction away from the tip is less effective in suppressing the amplitude of vibration.

Example 2. An external periodic in-plane force with amplitude P_0 and frequency α is applied at the tip center of the blade considered in example 1 above. The blade is discretized into four elements as shown in Fig. 9 and K_G is taken as 4000 N/m. The buckling load of the blade under stationary condition P_{cr} is estimated from $\alpha = 0$ and $\Omega_p = 0$ to be equal to 6570 N.

The nondimensional steady-state response obtained by Newmark direct integration method for $\alpha/\omega_{n1} = 0.1$ and $\mu R/f_0 = 0.04$ for three different values of lateral excitation frequency is given in Fig. 10 as a function of the distance from the root of the blade. The friction is applied on the nodes 18, 19, and 20 and two different cases, one with no in-plane load and the other with 0.05 critical load are considered. It is seen

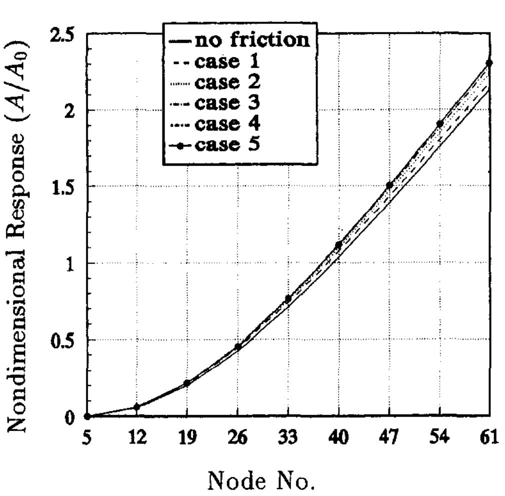

Fig. 8 Effect of friction force applied location with $\Omega_p/\omega_1 = 1.2$

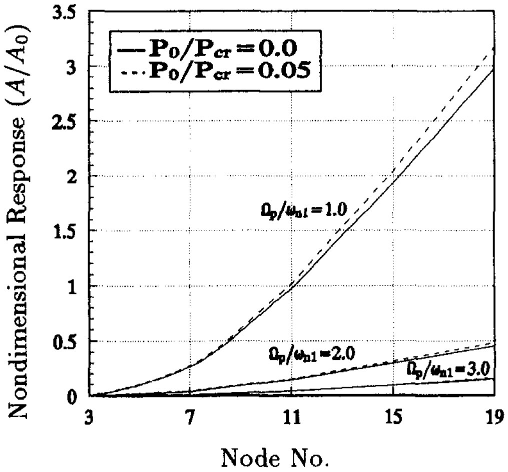

Fig. 10 Steady-state response for $\alpha/\omega_{n1} = 0.1$ friction at nodes 18–20 and $\mu R/f_0 = 0.04$

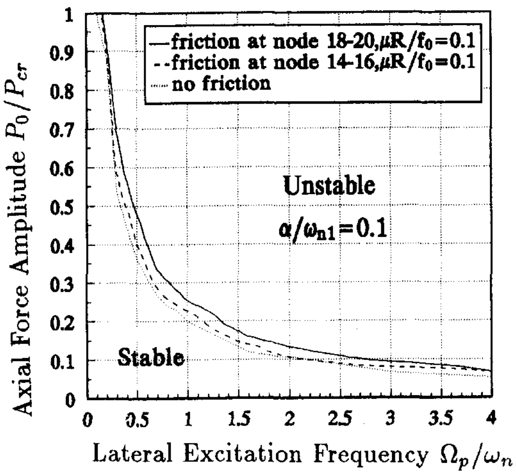

Fig. 11 Stability with respect to different P_0/P_{cr} and Ω_p/ω_{n1}

that the steady-state response increases in the presence of in-plane force. Also, the response near the stationary blade natural frequency is much higher and it decreases with further increasing lateral excitation frequency.

The stability results obtained in accordance with the analytical procedure given earlier are given in Figs. 11–13. Figure 11 gives a map of the stability as a function of the lateral excitation frequency and the in-plane force amplitude for in-plane excitation frequency $\alpha = 0.1$ times the stationary blade natural frequency. Also, three cases of friction are considered as indicated in the figure. From this figure it can be deduced that:

1 The blade remains stable for very low lateral excitation frequencies even when the in-plane force is close to the buckling load, because of the centrifugal in-plane force acting on the blade.
2 When the excitation frequency is increased, the magnitude of the in-plane force is considerably reduced to keep the blade under stable condition. Near the resonance condition, the blade under stable condition can sustain magnitudes of the in-plane force only of the order of a fifth of the buckling load. With increased lateral excitation frequency, the in-plane load the blade can carry for stable condition decreases further, though at a lower rate.
3 For very low lateral excitation frequencies, friction seems to be undesirable.

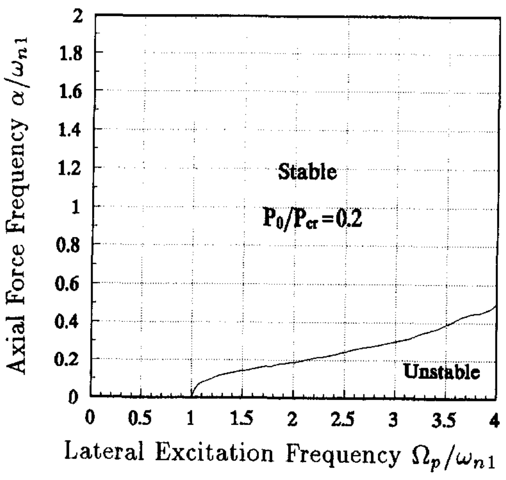

Fig. 12 Stability with respect to different α/ω_{n1} and Ω_p/ω_{n1} with friction force $\mu R/f_0 = 0.1$ on nodes 14–16

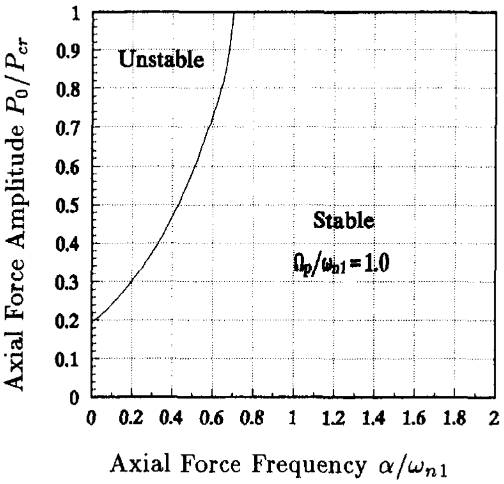

Fig. 13 Stability with respect to different P_0/P_{cr} and α/ω_{n1} with friction force $\mu R/f_0 = 0.1$ on nodes 14–16

Figure 12 shows the stability map as a function of lateral and in-plane excitation frequencies for $P_0/P_{cr} = 0.2$. It may be deduced from the figure that:

1 When the in-plane excitation frequency is zero, i.e., under steady in-plane load, the blade is stable for frequencies of lateral excitation below the blade natural frequency.
2 As the in-plane forcing frequency is increased, the lateral excitation frequency becomes higher for unstable conditions of the blade. Instability exists for low in-plane force excitation frequencies and high lateral force excitation frequencies.
3 The stability condition is improved with higher in-plane force frequencies.

The stability map of the blade as a function of in-plane force magnitude and frequency is given in Fig. 13 for $\Omega_p/\omega_{n1} = 1.0$. It can be seen that for a given frequency of excitation, the blade becomes unstable as the magnitude of excitation is increased. As long as the in-plane force magnitude is less than the buckling load, the system remains stable for the frequency of in-plane excitation force is more than 0.7 times the natural frequency of the blade.

Conclusion

A three-term approximation hybrid method gives good convergency with harmonic balance method. The results obtained by DIM are upper bounded, predicting slightly higher values over HBM.

Under lateral excitation in the presence of friction, the peak response occurs at a frequency greater than the natural frequency of the blade. As the friction is increased, the peak shifts further to the right of the natural frequency. There is a crossover frequency around 1.175 times the natural frequency, beyond which friction increases response and is undesirable in this range. Damping is more effective when it is applied at nodes closer to the tip of the blade for frequencies of excitation lower than the crossover frequency and that friction away from the tip is less effective to suppress the amplitude of vibration for frequencies beyond the crossover point.

The magnitude of the in-plane force is considerably reduced for larger lateral excitation frequencies to keep the blade under stable condition. Near the resonance condition, the blade under stable condition can sustain very small in-plane forces. Under steady in-plane load, the blade is stable for frequencies of lateral excitation below the blade natural frequency. Instability exists for low in-plane force excitation frequencies and high lateral force frequencies. The stability condition is improved with higher in-plane force frequencies. As long as the in-plane force magnitude is less than the buckling load, the system remains stable for the frequency of in-plane excitation force more than 0.7 times the natural frequency of the blade.

References

Ashton, J. E., and Whitney, J. M., 1970, *Theory of Laminated Plates*, Technomic Publishing Co., Stamford, CT.

Griffin, J. H., 1980, "Friction Damping of Resonant Stresses in Gas Turbine Engine Airfoils," ASME JOURNAL OF ENGINEERING FOR POWER, Vol. 102, pp. 329–333.

Jean, A. N., 1990, "Application of Condensation Technique to Nonlinear Rotordynamic Systems," Ph.D Thesis, National Cheng Kung University, Tainan, Taiwan.

Menq, C. M., Bielak, J., and Griffin, J. H., 1986a, "The Influence of Microslip on Vibration Response," *Journal of Sound and Vibration*, Vol. 107, pp. 279–293.

Menq, C. M., Griffin, J. H., and Bielak, J., 1986b, "The Forced Response of Shrouded Fan Stage," ASME *Journal of Vibration, Acoustics, Stress, and Reliability in Design*, Vol. 108, pp. 50–55.

Menq, C. M., and Griffin, J. H., 1985, "A Comparison of Transient and Steady State Finite Element of Forced Response of a Frictionally Damped Beam," ASME *Journal of Vibration, Acoustics, Stress, and Reliability in Design*, Vol. 107, pp. 19–25.

Mindlin, R. D., 1951, "Influence of Rotatory Inertia and Shear on Flexural Motions of Isotropic, Elastic Plates," ASME *Journal of Applied Mechanics*, Vol. 18, pp. 31–38.

Rao, J. S., 1991, *Turbomachine Blade Vibration*, Wiley, New York.

Rao, J. S., 1993, *Turbomachine Unsteady Aerodynamics*, Wiley Eastern Ltd., New Delhi.

Rao, J. S., 1995, "Fracture Mechanics Analysis of a Last Stage Steam Turbine Blade Failure," ASME DE-Vol. 84-2, Vol. 3–Part B, pp. 1173–1180.

Sinha, A., and Griffin, J. H., 1984, "Effects of Static Friction on the Forced Response of Frictionally Damped Turbine Blades," ASME JOURNAL OF ENGINEERING FOR GAS TURBINES AND POWER, Vol. 106, pp. 65–69.

Srinivasan, A. V., and Cassenti B. N., 1986, "A Nonlinear Theory of Dynamic Systems With Dry Friction Forces," ASME JOURNAL OF ENGINEERING FOR GAS TURBINES AND POWER, Vol. 108, pp. 525–530.

Timoshenko, S., and Woinowsky-Krieger, S., 1959, *Theory of Plates and Shells*.

Wang, J. N., and Chen, W. K., 1993, "Investigation of the Vibration of a Blade With Friction Damper by HBM," ASME JOURNAL OF ENGINEERING FOR GAS TURBINES AND POWER, Vol. 115, pp. 294–299.

Yang, T. Y., 1986, *Finite Element Structural Analysis*, Prentice-Hall.

APPENDIX

$$[N_1] = \begin{bmatrix} \phi_1 & 0 & 0 & 0 & 0 & \cdots & \phi_8 & 0 & 0 & 0 & 0 \\ 0 & \phi_1 & 0 & 0 & 0 & \cdots & 0 & \phi_8 & 0 & 0 & 0 \\ 0 & 0 & \phi_1 & 0 & 0 & \cdots & 0 & 0 & \phi_8 & 0 & 0 \end{bmatrix}$$

$$[N_2] = \begin{bmatrix} \phi_1 & 0 & 0 & z\phi_1 & 0 & \cdots & \cdots & \phi_8 & 0 & 0 & z\phi_8 & 0 \\ 0 & \phi_1 & 0 & 0 & z\phi_1 & \cdots & \cdots & \phi_8 & 0 & 0 & z\phi_8 & \\ 0 & 0 & \phi_1 & 0 & 0 & \cdots & \cdots & 0 & 0 & \phi_8 & 0 & 0 \end{bmatrix}$$

$$[N_3] = \begin{bmatrix} \phi_{1,x} & 0 & 0 & z\phi_{1,x} & 0 & \cdots & \cdots & \phi_{8,x} & 0 & 0 & z\phi_{8,x} & 0 \\ 0 & \phi_{1,y} & 0 & 0 & z\phi_{1,y} & \cdots & \cdots & 0 & \phi_{8,y} & 0 & 0 & z\phi_{8,y} \\ \phi_{1,y} & \phi_{1,x} & 0 & z\phi_{1,y} & z\phi_{1,x} & \cdots & \cdots & \phi_{8,y} & \phi_{8,x} & 0 & z\phi_{8,y} & z\phi_{8,x} \\ 0 & 0 & \phi_{1,y} & 0 & \phi_1 & \cdots & \cdots & 0 & 0 & \phi_{8,y} & 0 & \phi_8 \\ 0 & 0 & \phi_{1,x} & \phi_1 & 0 & \cdots & \cdots & 0 & 0 & \phi_{8,x} & \phi_8 & 0 \end{bmatrix}$$

$$[N_4] = \begin{bmatrix} 0 & 0 & \phi_{1,x} & 0 & 0 & \cdots & 0 & 0 & \phi_{8,x} & 0 & 0 \\ 0 & 0 & \phi_{1,y} & 0 & 0 & \cdots & 0 & 0 & \phi_{8,y} & 0 & 0 \end{bmatrix}$$

where $\phi_1, \phi_2, \ldots, \phi_8$ denote shape functions.

F. Chu[1]
Department of Precision Instruments,
Tsinghua University,
Beijing 100084, China

R. Holmes
Department of Mechanical Engineering,
University of Southampton,
Southampton, SO17 1BJ, United Kingdom

The Effect of Squeeze Film Damper Parameters on the Unbalance Response and Stability of a Flexible Rotor

There has been much research work carried out on various aspects of individual squeeze-film dampers (SFDs) but very little on the interplay between a damper and the rotating assembly of which it forms a part. In this paper, a flexible rotor-bearing assembly in a configuration, typical of a small centrifugal pump and incorporating an SFD, is investigated theoretically and experimentally from the points of view of forced vibration control and stability control. It is found that change in rotor unbalance, SFD static eccentricity ratio, and SFD supply pressure can cause significant movement of system resonances and vibration resulting from excessive damping. The provision of an SFD also delays the onset of instability and because of its nonlinearity, the SFD contributes more damping than can a linear damper when the vibration amplitude becomes large as instability develops. It is shown that this instability is curbed at some limit cycle, whose frequency is a system natural frequency.

Introduction

The squeeze-film damper (SFD) has for some years been widely used in rotating machinery assemblies. It has the ability of attenuating vibration and stabilizing the system by providing multidirectional damping. Broadly speaking, there are two different configurations of the squeeze-film damper. One is the arrangement where a centralizing "retainer" spring, in the form of a squirrel cage, is connected to the outer race of its rolling-element bearing and acts as a parallel element within the squeeze-film annulus. The second is a structure without a retainer spring, where, for a horizontal machine say, the outer race of the rolling-element bearing is assumed to remain at the bottom of the SFD clearance circle until the unbalance forces become large enough to create lift.

One of the advantages of the configuration with a retainer spring is the ability to tune the critical speeds of the system away from the operating range to ensure smooth running. However, when different unbalances, different SFD static eccentricity ratios, and different SFD supply pressures are applied, the system resonances will often migrate from their expected positions. In particular, if SFD damping is excessive, which can sometimes occur with increase in the SFD supply pressure or in the static SFD eccentricity ratio, resonant frequencies of the assembly may approach the corresponding frequencies for the model without retainer spring. This is because the SFD "locks out" the retainer spring, thus rendering it inoperative. Previous research work, e.g., [1] has examined the vibration performance of the squeeze-film damper with retainer spring while Holmes and Dogan [2] investigated some features of the squeeze-film damper without retainer spring. This paper is aimed at a direct comparison of the vibration performance of each of the two different configurations. A flexible rotor-bearing assembly in a configuration, typical of a small centrifugal pump and incorporating an SFD, is investigated from the points of view of forced vibration control and stability control. The schematic diagram of the assembly is shown in Fig. 1. It consists of a flexible stepped shaft supported in two ball bearings, one of which is self-aligning; the other is flexibly mounted on four supporting bars, constituting a centralizing spring. An SFD annulus is placed around the outer race of the latter ball bearing to attenuate rotor vibration.

Test Rig Description

The experimental rig used for the investigation of the performance of the squeeze-film damper replicates the assembly shown in Fig. 1(*a*). Oil is pumped via three holes and a central groove into the annular clearance space of the SFD (Fig. 1(*b*)). The shaft carries an overhung disk held by a taperlock bush. The drive shaft is connected to the main shaft by a flexible rubber coupling to isolate the test shaft from any vibration influence from the motor (Fig. 1(*c*)).

The squeeze-film damper has a two-land geometry and is unsealed. Its parameters are as follows:

Journal radius = 50 mm

Radial clearance = 0.1 mm

Land length = 10 mm

Oil viscosity = 0.00375 Ns/m^2

The rig was first impulse tested to obtain its undamped natural frequencies. For the configuration with a retainer spring, in order to eliminate the influence of oil damping, the damper ring was temporarily detached from the rig. The test result at the SFD ball bearing is shown in Fig. 2(*a*) and gives a first undamped natural frequency of 14 Hz and a second of 41 Hz. The retainer spring was then made inoperative by shimming the SFD annulus within the damper ring. The corresponding impulse test result is shown in Fig. 2(*b*) and indicates a first undamped natural frequency of 31.2 Hz and a second of 88.0 Hz.

Before running, the shaft was first balanced, then the overhung disk, and finally the two together. One of several unbalance masses could be screwed into the overhung disk for investigation purposes. In order to observe the effects of different levels of unbalance, this was chosen such that the nondimensional eccentricity of mass unbalance Q_c at the position of the

---

[1] Former address: Department of Mechanical Engineering, University of Southampton, Southampton, SO17 1BJ, UK.

Contributed by the International Gas Turbine Institute and presented at the 41st International Gas Turbine and Aeroengine Congress and Exhibition, Birmingham, United Kingdom, June 10–13, 1996. Manuscript received at ASME Headquarters February 1996. Paper No. 96-GT-377. Associate Technical Editor: J. N. Shinn.

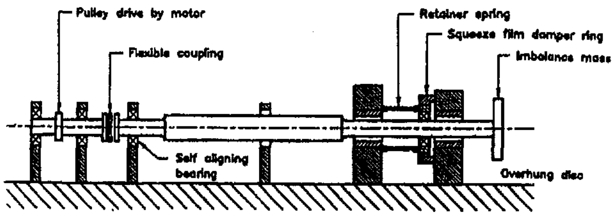

Fig. 1(*a*) Schematic diagram of experimental rig

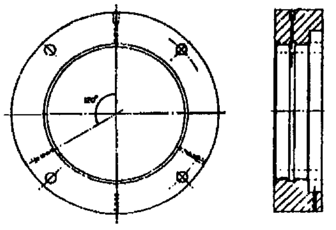

Fig. 1(*b*) Detail of squeeze film damper

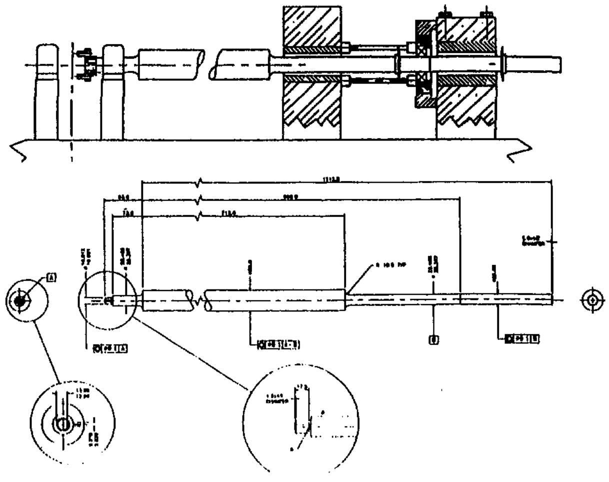

Fig. 1(*c*) Detail of main shaft assembly

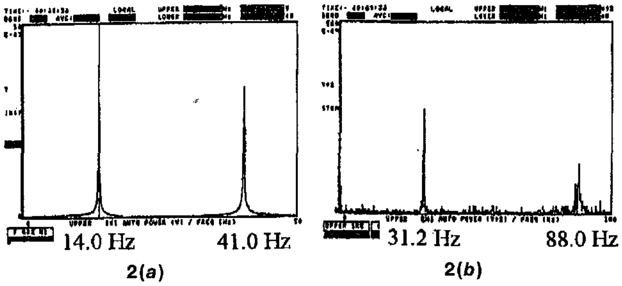

2(*a*) 2(*b*)

Fig. 2 (*a*) Undamped natural frequencies of the configuration with retainer spring; (*b*) undamped natural frequencies of the configuration without retainer spring

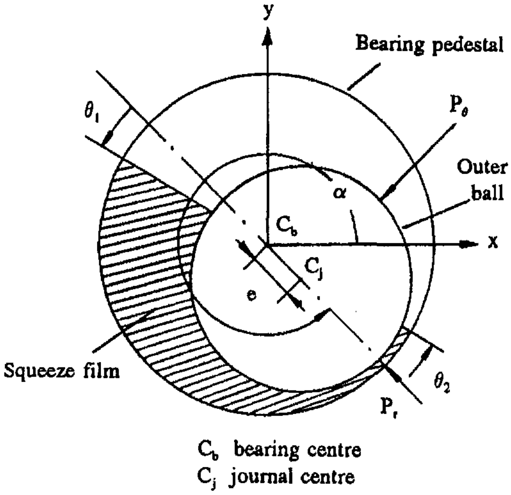

Fig. 3 Squeeze film damper

overhung disk had values of 1.12, 0.649, and 0.148. Q_c is defined as the quotient, eccentricity of mass unbalance at the overhung disk divided by SFD clearance.

Squeeze Film Forces

With reference to Fig. 3, P_r and P_θ are the radial and transverse squeeze-film forces obtained by integrating the dynamic pressure distributions within the squeeze-film annulus, taking due account of film rupture, and α is the attitude angle of the shaft in the SFD annulus. This squeeze-film can be rather difficult to specify, particularly with respect to its extent around the circumference of the rolling element bearing. This is largely due to cavitation in the oil, which arises when negative pressures are produced between rapidly separating surfaces during vibration and which cannot be compensated by sufficient supply pressure. To achieve an understanding of the way in which this oil-film extent governs the vibration performance we shall

Nomenclature

c = squeeze-film damper radial clearance
c_o = damping coefficient of linear damper
c_{xx}, c_{yy} = damping coefficients of the annular seal in horizontal and vertical directions
c_{xy}, c_{yx} = cross-coupled damping coefficients of the annular seal
e = eccentricity in SFD
F_x, F_y = annular seal forces in horizontal and vertical directions
j = imaginary unit
k_{xx}, k_{yy} = stiffness coefficients of the annular seal in horizontal and vertical directions
k_{xy}, k_{yx} = cross-coupled stiffness coefficients of the annular seal
L = damper-land length
m = effective mass
m_{xx}, m_{yy} = inertia coefficients of the annular seal in horizontal and vertical directions
P_x, P_y = squeeze-film forces in horizontal and vertical directions
P_r, P_θ = squeeze-film forces in radial and transverse directions
P_{sup} = supply pressure
Q_c = u/c
R = damper radius
u = eccentricity of mass unbalance at overhung disk
x, y = displacements in horizontal and vertical directions divided by SFD radial clearance
X, Y = amplitudes of displacements x, y
x_1 = vibration at overhung disk
α = attitude angle in squeeze-film damper
ϵ = eccentricity ratio in squeeze-film damper = e/c
ϵ_o = static eccentricity ratio
η = oil viscosity
θ = circumferential coordinate
λ = eigenvalue
ω = imaginary part of eigenvalue λ
Ω = angular velocity of rotor
$'$ = d/dt

consider the two classical extremes—the full (2π) film and the half (π) film.

The forces P_r and P_θ are then given [3] for the short π film by

$$P_r = \frac{\eta R L^3 \pi}{c^3} \frac{1 + 2\epsilon^2}{(1 - \epsilon^2)^{5/2}} \epsilon'$$

$$P_\theta = \frac{\eta R L^3 \pi}{c^3} \frac{\epsilon \alpha'}{(1 - \epsilon^2)^{3/2}} \qquad (1)$$

and for the π film [3] by

$$P_r = \frac{\eta R L^3 \Omega}{c^2} [\alpha' \epsilon g_1 + \epsilon' g_2]$$

$$P_\theta = \frac{\eta R L^3 \Omega}{c^2} [\alpha' \epsilon g_3 + \epsilon' g_1] \qquad (2)$$

where

$$g_1 = -2\epsilon \cos^3 \theta_1 (1 - \epsilon^2 \cos^2 \theta_1)^{-2}$$

$$g_2 = \epsilon \sin \theta_1 [3 + (2 - 5\epsilon^2) \cos^2 \theta_1](1 - \epsilon^2)^{-2} \times (1 - \epsilon^2 \cos^2 \theta_1)^{-2} + \psi(1 + 2\epsilon^2)(1 - \epsilon^2)^{-5/2}$$

$$g_3 = \epsilon \sin \theta_1 (1 - 2\cos^2 \theta_1 + \epsilon^2 \cos^2 \theta_1)(1 - \epsilon^2)^{-1} \times (1 - \epsilon^2 \cos^2 \theta_1)^{-2} + \psi(1 - \epsilon^2)^{-3/2}$$

$$\tan \theta_1 = -\epsilon'/\epsilon\alpha'$$

$$\psi = \frac{\pi}{2} + \tan^{-1} [\epsilon \sin \theta_1 (1 - \epsilon^2)^{-1/2}]$$

For circular orbits concentric about the centre of the SFD, the forces P_r and P_θ for the short π film reduce to

$$P_r = 0$$

$$P_\theta = \frac{\eta R L^3 \pi \epsilon \Omega}{c^3 (1 - \epsilon^2)^{3/2}} \qquad (3)$$

and for the π film to

$$P_r = \frac{2\eta R L^3 \epsilon \Omega e}{c^3 (1 - \epsilon^2)^2}$$

$$P_\theta = \frac{\eta R L^3 \pi e \Omega}{2c^3 (1 - \epsilon^2)^{3/2}} \qquad (4)$$

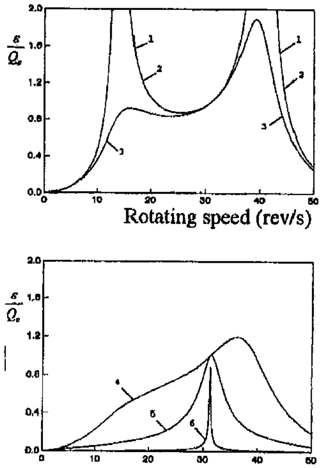

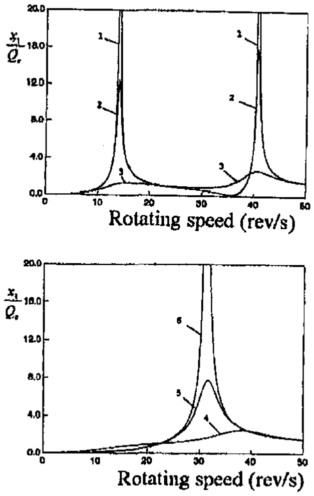

1. $c_0 = 10$ Ns/m, 2. $c_0 = 100$ Ns/m, 3. $c_0 = 1{,}000$ Ns/m

4. $c_0 = 2 \times 10^3$ Ns/m, 5. $c_0 = 10 \times 10^3$ Ns/m, 6. $c_0 = 200 \times 10^3$ Ns/m

Fig. 4 Fig. 5

Fig. 4 Linear responses ϵ/Q_c for different values of damping coefficient c_o

Fig. 5 Linear responses x_1/Q_c for different values of damping coefficient c_o

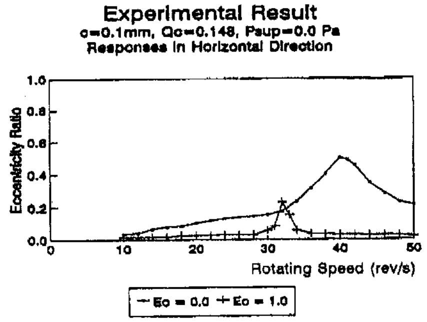

Fig. 6 Vibration responses for the configuration with retainer spring

The SFD parameters used here give for the 2π film an effective linear damping from the two lands as

$$c_o = 2\pi\eta R(L/c)^3 = 1.178 \times 10^3 \text{ Ns/m}$$

For the π film, the corresponding value is

$$c_o = \pi\eta R(L/c)^3 = 0.589 \times 10^3 \text{ Ns/m}$$

These linear dampings relate only to small vibrations ($\epsilon \rightarrow 0$).

Theoretical Predictions of Responses Due to Linear Damping Assumed at the SFD

A great deal of intuitive experience can be gleaned from a linear approach to this problem. If we assume linear damping at the SFD position for the configuration with retainer spring, then a theoretical vibration analysis of the assembly using a transfer matrix method with ten shaft stations provides the SFD response curves of Fig. 4. It can be seen that as damping is increased, the resonant peaks change from values of 14 and 41 rev/s, appropriate to the configuration with retainer spring to a value of 31.2 rev/s, appropriate to the configuration without retainer spring.

Figure 5 shows the corresponding responses at the overhung disk position and again these changes can be seen. This time, however, there is a reverse sequence for curves 4, 5, and 6 in the lower graph, compared with these in the lower graph of Fig. 4.

Experimental Results

The Effect of the SFD Static Eccentricity Ratio. First the vibration for the configuration with retainer spring was examined by employing different SFD static eccentricity ratios. A small unbalance with $Q_c = 0.148$ was applied on the overhung disk. Oil was supplied to fill the SFD clearance, after which the supply pump was shut off to reduce the SFD damping to an absolute minimum. Figure 6 shows two response curves taken at the SFD position. With an SFD static eccentricity ratio ϵ_o at zero, the squeeze film damper has concentric orbits of varying dynamic eccentricity ratio depending on rotor speed. In this case, the response shows a resonance at about 40 rev/s (the higher undamped natural frequency) but no peak at 14 rev/s (the lower undamped natural frequency). By comparing with Fig. 2(*a*), it is apparent that SFD damping has completely suppressed the first resonance and has little effect on the position of the second resonance.

When the static SFD eccentricity ratio is made unity, that is the retainer spring support is raised so that the SFD touches its

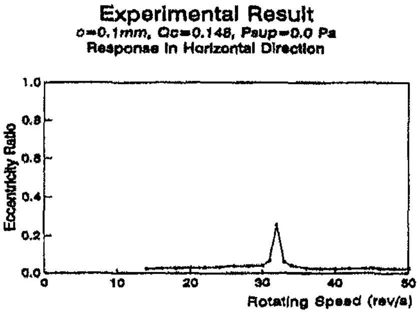

Fig. 7 Vibration response for the configuration without retainer spring

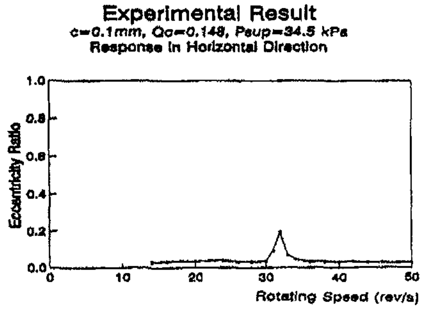

Fig. 9 Vibration response for the configuration without retainer spring

journal when stationary, then the resonance is observed to move to a new value of 31.8 rev/s (Fig. 6), which is very close to the *first undamped natural frequency of the configuration without* a retainer spring (Fig. 2(*b*)). This is due to the increased SFD damping partially locking out the retainer spring. In the process it is also seen to generally reduce the response. A comparison of Figs. 4 (lower) and 6 shows a very similar trend and confirms that increased damping arises due to the increased static eccentricity.

Consider now the response for the configuration without retainer spring. Figure 7 was obtained under the same conditions of oil supply and unbalance as used in Fig. 6. It is apparent that the position of the resonance is the same as for the configuration with retainer spring where the static SFD eccentricity ratio is unity (Fig. 6). Indeed the peak amplitude is almost identical and the only difference is in the breadth of the response at resonance.

We now consider another case by providing an oil supply to the SFD at 34.5 kPa. The corresponding responses are shown in Fig. 8, where, for zero static eccentricity, the only resonance occurs at about 34 rev/s. When the static SFD eccentricity ratio is increased to unity, this resonance moves to a new position at a speed of about 31.8 rev/s. This is again the same as the position for the configuration without retainer spring, as shown in Fig. 9. Again the peak amplitude is the same and again any difference lies in the breadth of the response at resonance.

From Figs. 6 to 9 there is a clear indication that the higher static SFD eccentricity ratio produces higher system damping, with a change in the position of resonance. For a static eccentricity ratio of unity, the presence of the retainer spring has little effect and the two configurations (with and without retainer spring) show similar vibration response curves and have virtually the same dynamic performances, irrespective of supply pressure. This is shown by comparison of Figs. 6 and 7 and of Figs. 8 and 9.

The Effect of Supply Pressure. For a static eccentricity ratio of zero, Figs. 6 and 8 indicate that the higher supply pressure produces higher system damping and that such damping suppresses vibration. This is almost certainly due to maintaining the SFD clearance full of oil. There is also a shift in the resonance of the configuration with retainer spring to a new frequency. This is thus akin to the effect of increasing the static eccentricity ratio in both Figs. 6 and 8.

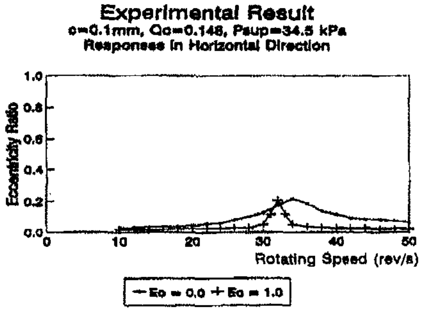

Fig. 8 Vibration responses for the configuration with retainer spring

For concentric vibration ($\epsilon_o = 0$), as the supply pressure is increased from 0.0 Pa to 34.5 kPa, there is a shift in resonance position from 40.0 rev/s to around 34.0 rev/s (Figs. 6 and 8). It is expected that if the supply pressure is further increased, the resonance will finally reach a value of 31.8 rev/s, the value *without retainer spring* (Figs. 7 and 9). For eccentric vibration with a static SFD eccentricity ratio of unity, increasing the supply pressure leads to no change in the position of the resonance, which remains at around 31.8 rev/s (Figs. 6 and 8). The reason for this is that the system damping is always high and is caused by the high static eccentricity ratio. As supply pressure and hence damping is increased, it can only reduce the peak value of the vibration and make no further shift in the resonant frequency. If we compare Fig. 7 with Fig. 9 for the configuration without retainer spring, a similar situation can be observed as in the eccentric case for the configuration with retainer spring.

It can be concluded that, for the configuration with retainer spring, for the static SFD eccentricity ratio of unity, in the supply pressure range discussed (zero to 34.5 kPa), increasing the supply pressure can only suppress the vibration amplitudes but make no change in the positions of the resonance. For the configuration with retainer spring for the concentric case, any increase in the supply pressure will cause a shift in the position of the resonance down to a lower value, as long as it has not yet reached the extreme of 31.8 rev/s.

The Effect of Unbalance. For a high-speed rotating assembly, it is very important to ensure that the shaft is well balanced and runs in a quiet regime. Unfortunately, there will always be some residual unbalance, which, if large enough, will cause severe vibration. This can sometimes lead to fracture of the shaft and damage to the foundation. Also it may change the position of the resonance for the configuration with retainer spring and make it unpredictable at the design stage.

Figure 10 shows three response curves for concentric vibration ($\epsilon_o = 0$) for the configuration with retainer spring. For low unbalance, say $Q_c = 0.148$, as shown by the lowest curve, the position of the resonance is at about 34 rev/s. If unbalance is increased, $Q_c = 0.649$, a resonance is observed at around 33 rev/s and if unbalance is $Q_c = 1.12$, the position is at 32 rev/s. This trend can be clearly seen in Fig. 10.

Now let us compare these curves with corresponding curves for the configuration without retainer spring, as shown in Fig. 11. In the latter case, despite the increase in unbalance, the positions of the resonance remain the same at around 32 rev/s. Thus it is concluded that for the configuration without retainer spring, unbalance has no effect on the position of the resonance, while for the configuration with retainer spring, higher unbalance gives rise to a resonance at a lower frequency.

It is well known that a rotor-bearing system incorporating a squeeze-film damper is a nonlinear system and that the oil film

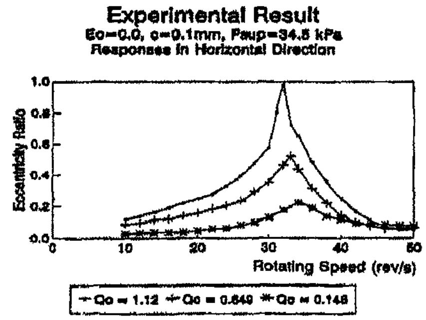

Fig. 10 Vibration responses for the configuration with retainer spring

forces are nonlinear functions of journal displacement and velocity. As the SFD eccentricity ratio increases, the transverse oil-film force, which embodies the damping of the oil film, increases in a strongly nonlinear fashion. This increase causes higher damping and consequently a change in the position of the resonance. This is consistent with the theoretical findings of Fig. 4.

Vibration in the Overhung Disk Position. A probe was placed at the position of the overhung disk to measure vibration there. For this purpose, we only take the simple case of concentric vibration for the system with retainer spring and the effect of supply pressure alone is examined. Because increasing the supply pressure or unbalance or the SFD static eccentricity has the same effect as increasing the damping, the effects of changing the other two parameters can be concluded accordingly. Figure 12 shows two vibration wave forms recorded from the overhung disk position, for a rotational speed of 29 rev/s. When the supply pressure is zero, moderate vibration as shown in Fig. 12(*a*) is obtained. If the supply pressure is increased to 34.5 kPa, severe vibration is observed as in Fig. 12(*b*). In the latter case the vibration amplitude is nearly twice that of the former. This is in accord with the theoretical results of Fig. 5 (lower), which shows that once the damping has resulted in a fairly flat response (e.g., 4) then increased damping increases the height of the peak response (e.g., 5).

As discussed earlier, for the configuration with retainer spring, if damping in the system is high enough, the spring may be locked up and thus behave like the configuration without retainer spring. As damping is being increased, the vibration mode of the system thus changes from one form to another. This is the reason for the severe vibration at the position of the overhung disk resulting from increase in supply pressure and hence damping.

It can thus be concluded that for the configuration with retainer spring, the SFD parameters have to be chosen carefully to make the damping level in the system neither too high nor too low, to avoid severe vibrations at the position of the squeeze film damper or the position of the overhung disk.

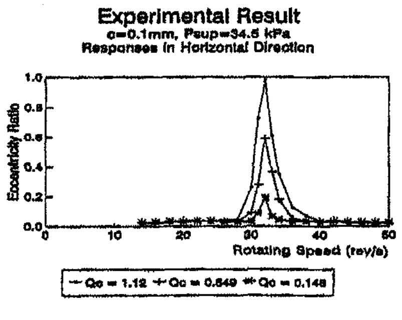

Fig. 11 Vibration responses for the configuration without retainer spring

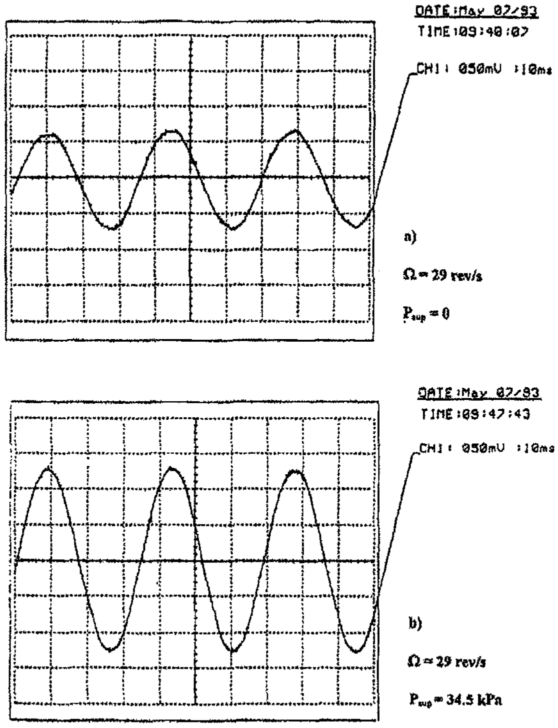

Fig. 12 Vibration at the overhung disk position for the configuration with retainer spring at 29 rev/s, $Q_c = 0.094$

The Seal as a Promoter of Instability

This paper continues with some comments on the role of an SFD in counteracting destabilizing influences in a rotating system. In some rotating assemblies such as centrifugal pumps, annular seals are used around the impellers. Besides their design function of reducing leakage flow, these seals have the potential to produce destabilizing forces and have a significant influence on the vibration and stability of the pump rotor. Generally the dynamic characteristics of a seal are expressed by inertia, damping, and stiffness coefficients. Due to the presence of cross-coupled force terms, some of these motion-dependent forces develop strong destabilizing effects, reducing the overall net positive damping forces acting on the rotor.

Instability occurring in a rotating assembly can be suppressed effectively by increasing the positive damping in the system. In this respect, the squeeze-film damper (SFD) can provide a good solution by delaying the onset of instability. Also because of its nonlinearity, the SFD can contribute more damping than can a linear damper when the vibration amplitude becomes large as instability develops.

According to Massmann and Nordmann's results [4], the annular seal can be modeled by a linear system with stiffness, damping, and inertia coefficients. Equivalent forces can be expressed as

$$\begin{Bmatrix} F_x \\ F_y \end{Bmatrix} = \begin{bmatrix} m_{xx} & 0 \\ 0 & m_{yy} \end{bmatrix} c \begin{Bmatrix} \ddot{x} \\ \ddot{y} \end{Bmatrix} + \begin{bmatrix} c_{xx} & c_{xy} \\ c_{yx} & c_{yy} \end{bmatrix} c \begin{Bmatrix} \dot{x} \\ \dot{y} \end{Bmatrix} + \begin{bmatrix} k_{xx} & k_{xy} \\ k_{yx} & k_{yy} \end{bmatrix} c \begin{Bmatrix} x \\ y \end{Bmatrix} \quad (5)$$

where x, y are displacements in horizontal and vertical directions divided by SFD clearance.

We shall take the inertia (m), damping (c), and stiffness (k) coefficients typically for a small pump as

$$m_{xx} = m_{yy} = 0.8 \text{ (kg)},$$

$$c_{xx} = c_{yy} = 80 \text{ (Ns/m)},$$

$$c_{xy} = -c_{yx} = 0.0071\Omega \text{ (Ns/m)},$$

$$k_{xx} = k_{yy} = 1.605 \times 10^4 - 0.0001165\Omega^2 \text{ (N/m)},$$

$$k_{xy} = -k_{yx} = 4.365\Omega \text{ (N/m)},$$

where Ω is the rotating speed in rpm.

Stability Considerations

In the context of Fig. 1 the seal is placed around the overhung disk, which represents the pump impeller. Let us again consider a system that incorporates a linear damper. In this case, the oil film forces can again be assumed to be

$$P_x = -c_o c\dot{x}, \quad P_y = -c_o c\dot{y} \tag{6}$$

where c_o is the equivalent damping coefficient of a linear damper.

For a given operating condition, the system will be stable if all the eigenvalues λ that enable the eigen-equation $D(\lambda) = 0$ to be satisfied are such that their real parts are negative. Even one root with a positive real part is sufficient to indicate unstable conditions. If the relation between s, the real part of the eigenvalue, and the rotating speed is obtained, stability for the system can be assessed. A numerical search for all the roots of the eigen equation can be very time-consuming, and tends to lead to a loss of physical insight. For the eigen-equation $D(\lambda) = 0$, the Leonhard locus [5] retains a "feel" for the underlying principles.

Consider the complex λ plane and the complex D plane. The function $D(\lambda)$ maps each point in the λ plane to a corresponding point in the D plane. The roots of the eigen-equation can be regarded as those points in the λ plane that map to the origin of the D plane. A point traveling along the imaginary axis in the λ plane, from $\omega = 0$ to $\omega = \infty$, will map to a curved locus in the D plane known as the Leonhard locus. For a stable system all the roots will lie to the left-hand side of the locus in the λ plane. This implies that the Leonhard locus will be such that the origin is always to its left-hand side. Thus, for stability, the Leonhard locus must encircle the origin, in an anti-clockwise direction, as ω increases from zero. At the threshold of stability the Leonhard locus will pass exactly through the origin of the D plane.

Let us take an example to analyze the instability problem for the chosen rotordynamic system. The combined rotor-damper-seal system is assumed to be supported by a linear damper with damping coefficient c_o being 0.589×10^3 Ns/m say, to simulate the linear π model for the SFD. Figure 13 shows the two Leonhard loci for this case. It is seen that as the frequency ω increases the curve for $\Omega = 65.4$ rev/s encircles the origin in an anticlockwise direction and the curve for $\Omega = 65.5$ rev/s does not. Therefore, 65.5 rev/s can be reasonably regarded as the onset speed for instability of the system.

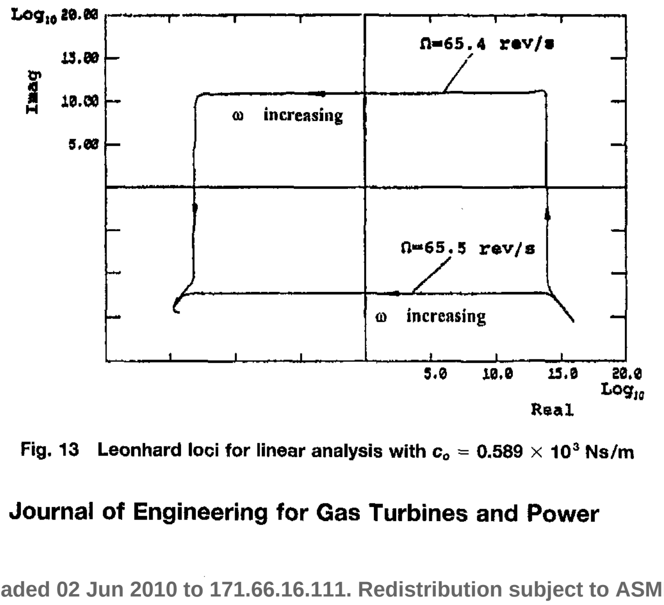

Fig. 13 Leonhard loci for linear analysis with $c_o = 0.589 \times 10^3$ Ns/m

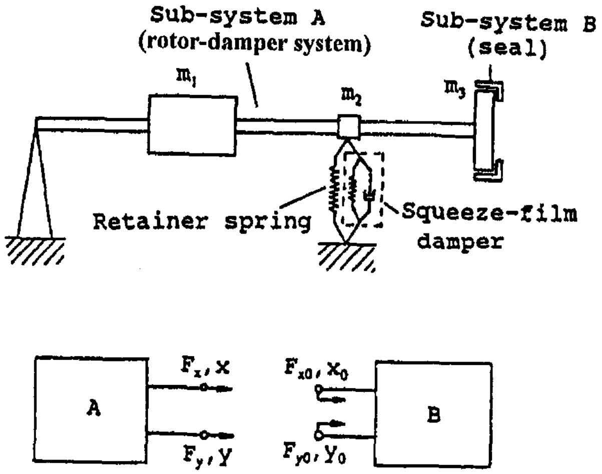

Fig. 14 Schematic of the combined rotor-damper-seal system

The Dynamic Stiffness Method. As an alternative, the Dynamic Stiffness Method may also be used to analyze the stability of the rotordynamic system, incorporating, say, the linear π model of the SFD.

Consider a composite system consisting of two subsystems A and B, where in this case, the subsystem A is the rotating assembly consisting of rotor and linear SFD damper and the subsystem B is the seal, as shown in Fig. 14. Subsystem A is isotropic. Apply forces of amplitudes F_x, and F_y, as shown at the overhung disk. Let the amplitudes of the responses be X and Y also at the disk. Then the dynamic stiffness $\bar{Z}_x$ and $\bar{Z}_y$ for the shaft at the disk may be defined as follows:

$$\bar{Z}_x = \frac{F_x}{X}, \quad \bar{Z}_y = \frac{F_y}{Y} \tag{7}$$

Since the shaft is circular and isotropic and the damper is isotropic, these two dynamic stiffness will be complex and equal. They can be written as:

$$\bar{Z} = \bar{Z}_x = \bar{Z}_y = \frac{F_x}{X} = \frac{F_y}{Y} = a + jb \tag{8}$$

Subsystem B (the seal) has many terms and the force-deflection relationships are of the form:

$$F_{xo} = \bar{Z}_{xx}X_o + \bar{Z}_{xy}Y_o$$

$$F_{yo} = \bar{Z}_{yx}X_o + \bar{Z}_{yy}Y_o \tag{9}$$

where

$$\bar{Z}_{xx} = (k_{xx} - m_{xx}\omega^2) + i\omega c_{xx}$$

$$\bar{Z}_{yy} = (k_{yy} - m_{yy}\omega^2) + i\omega c_{yy}$$

$$\bar{Z}_{xy} = k_{xy} + i\omega c_{xy}$$

$$\bar{Z}_{yx} = k_{yx} + i\omega c_{yx}$$

As explained earlier, some of the terms are functions of rotating speed Ω.

Now connect the two subsystems together at the mass m_3. At the borderline between stability and instability the system will vibrate at a natural frequency and no force will be required. This condition can be expressed as:

$$F_x + F_{xo} = 0, \quad F_y + F_{yo} = 0$$

Also at the connecting point

$$X = X_o, \quad Y = Y_o$$

The following relationships can thus be established

$$\begin{aligned} \bar{Z}X + \bar{Z}_{xx}X + \bar{Z}_{xy}Y &= 0 \\ \bar{Z}Y + \bar{Z}_{yx}X + \bar{Z}_{yy}Y &= 0 \end{aligned} \tag{10}$$

whence

$$\bar{Z} = -\tfrac{1}{2}(\bar{Z}_{xx} + \bar{Z}_{yy}) \pm \tfrac{1}{2}\sqrt{(\bar{Z}_{xx} - \bar{Z}_{yy})^2 + 4\bar{Z}_{xy}\bar{Z}_{yx}} \tag{11}$$

$$= \bar{Z}_1(\omega) \quad \text{and} \quad \bar{Z}_2(\omega) = a_o + jb_o, \text{ say} \tag{12}$$

Equation (12) establishes the condition for the borderline between stability and instability.

The procedure for finding the instability onset speed is thus as follows:

1 Calculate $\bar{Z}(\omega)$ from a linear analysis for the subsystem A (the rotor and its SFD) as $\bar{Z}(\omega) = a(\omega) + jb(\omega)$. Thus, at the stability borderline $a + jb = a_o + jb_o$, i.e., $a = a_o + j(b_o - b)$;

2 Select a rotating speed $\Omega = \Omega_1$ say;

3 Find $\bar{Z}_1(\omega)$ and $\bar{Z}_2(\omega)$ from Eq. (12) as $\bar{Z}_1(\omega)$ or $\bar{Z}_2(\omega) = a_o(\omega) + jb_o(\omega)$. Plot $a_o(\omega)$ and $(b_o - b) = f(\omega)$ for both $\bar{Z}_1$, and $\bar{Z}_2$ (Fig. 15(*a*));

4 Compare $b_o(\omega)$ with $b(\omega)$ to find a value of ω such that $b_o(\omega) - b(\omega) \rightarrow 0$, and record this value of ω as ω_1 and the corresponding a_o as a_1 (Fig. 15(*a*));

5 Select another speed $\Omega = \Omega_2$ and find another frequency ω_1 and the corresponding a_1;

6 Plot a curve for the relation between a_1 and ω_1 (Fig. 15(*b*);

7 Superimpose this curve on the curve of $a(\omega)$ (Fig. 15(*b*));

8 Find the intersection of these two curves and record ω for this intersection as ω_i and the corresponding value of Ω as Ω_i. This value of Ω_i is the instability-onset speed and ω_i is the instability-onset frequency.

A further advantage of this procedure is that one subsystem (say the seal) can be maintained unaltered and the other (say the rotor and SFD) amended as required to provide a requisite instability onset speed.

Stability Analysis. By using this dynamic stiffness method the stability for the whole system can now be assessed. When no oil is supplied, the system will become unstable at the very low rotating speed of 29.4 rev/s, as shown in Fig. 16(*a*). If damping with the coefficient value of $c_o = 0.589 \times 10^3$ Ns/m is applied, the rotating speed for the onset of instability is 65.5 rev/s, shown in Fig. 16(*b*). This is the case of a linear damper using the π model and compares accurately with the value obtained from the Leonhard locus. If the damping is increased to $c_o = 1.178 \times 10^3$ Ns/m, equivalent to a linear damper using the 2π model, the corresponding rotating speed is increased to 85.8 rev/s (Fig. 16(*c*)). It is clear that increase in linear damping is beneficial in delaying the onset of instability.

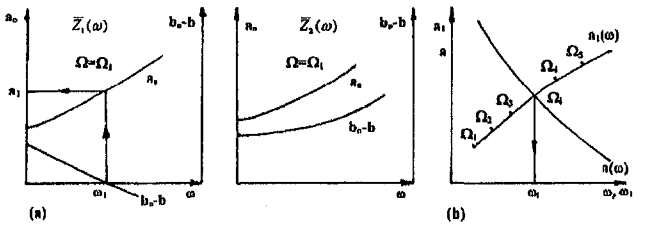

Fig. 15 Dynamic stiffness graphs

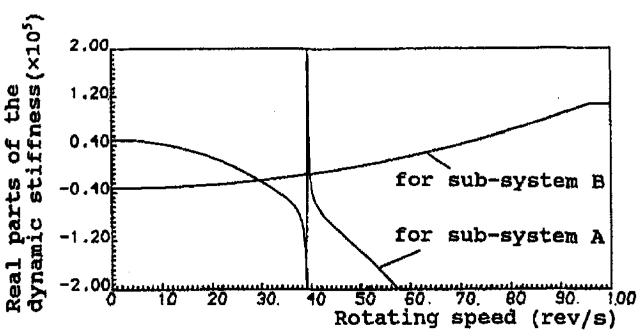

Fig. 16(*a*) Dynamic stiffness diagram for linear analysis with $c_o = 0$

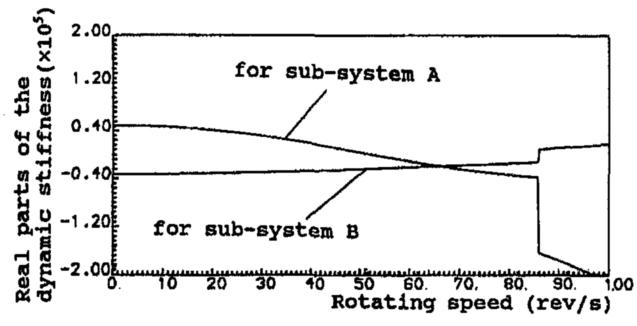

Fig. 16(*b*) Dynamic stiffness diagram for linear analysis with $c_o = 0.589 \times 10^3$ Ns/m

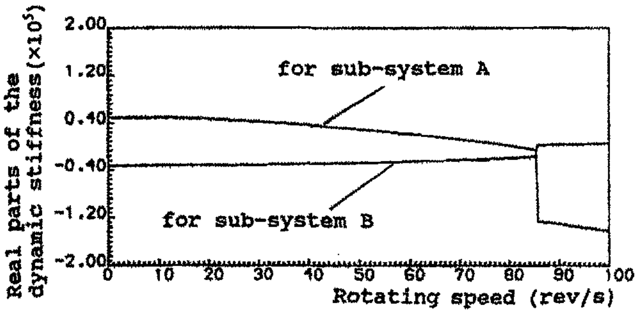

Fig. 16(*c*) Dynamic stiffness diagram for linear analysis with $c_o = 1.178 \times 10^3$ Ns/m

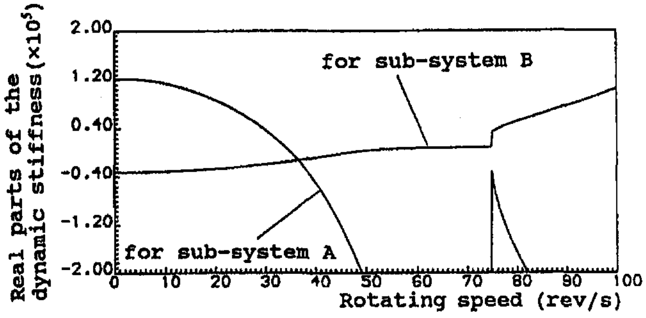

Fig. 16(*d*) Dynamic stiffness diagram for linear analysis with $c_o = 0.589 \times 10^3$ Ns/m

At this stage the effect of the retainer spring stiffness at the position of the squeeze-film damper may be examined. Let us consider another case where all conditions are the same as used in Fig. 16(*b*) except that the retainer spring stiffness is increased to five times the previous value. The result is shown in Fig. 16(*d*) where the instability onset speed is reduced to 36.5 rev/s, well below 65.5 rev/s. The increased stiffness thus gives rise to a lower instability onset speed because the damper is not allowed to exert its original influence.

If with the original value of retainer spring stiffness the seal forces are halved and the SFD clearance is increased to 0.15

mm to reduce the damping offered by the squeeze film damper, the effect of damping can be further examined as the instability progresses to a large dynamic eccentricity. In this case, the effective linear damping coefficients can be calculated as

$$c_o = \pi\eta R(L/c)^3 = 0.1745 \times 10^3 \text{ N.s/m} \quad \text{for the } \pi \text{ film}$$

$$c_o = 2\pi\eta R(L/c)^3 = 0.349 \times 10^3 \text{ N.s/m} \quad \text{for the } 2\pi \text{ film}$$

Without oil supplied the instability onset speed is 27.5 rev/s. For the π model the onset speed is 46.3 rev/s, and for the 2π model 65.0 rev/s.

Let us now examine the nonlinear effect of the squeeze-film damper, as the instability progresses. For this we need to establish a more comprehensive numerical method since much greater problems are posed in calculating a rotor response. A linear program can no longer be used even in an iterative fashion since, although the final orbit may be circular and concentric, its frequency will in general be unknown. Also the transient in reaching any final orbit will be of interest.

In this paper a method previously described in [6] is adapted to the multi-degree-of-freedom assembly. For horizontal x and vertical y directions at stations along the shaft, denoted by a suffix to x, y, we write

$$s_1 = \tau, \quad s_2 = x_1, \quad s_3 = x_1', \quad s_4 = y_1, \quad s_5 = y_1',$$
$$s_6 = x_2, \quad s_7 = x_2', \quad s_8 = y_2, \quad s_9 = y_2', \ldots \quad (13)$$

etc., for all stations.

These equations of motion can be represented as a set of first-order differential equations

$$S' = F(S)$$

and a set of iteration formulae is obtained as

$$s_1^{n+1} = s_1^n + h$$
$$s_2^{n+1} = s_2^n + (s_3^n + s_3^{n+1})h/2$$
$$s_4^{n+1} = s_4^n + (s_5^n + s_5^{n+1})h/2$$
$$s_6^{n+1} = s_6^n + (s_7^n + s_7^{n+1})h/2$$
$$s_8^{n+1} = s_8^n + (s_9^n + s_9^{n+1})h/2, \text{ etc} \quad (14)$$

The other variables can be obtained from the following iteration formula:

$$\cdot_{m+1}\bar{s}^{n+1} = \cdot_m\bar{s}^{n+1} + \left\{ I - \frac{h}{2}\,\cdot_m\bar{J}^{n+1} \right\}^{-1}$$
$$\times \left\{ \bar{s}^n - {}_m\bar{s}^{n+1} + \frac{h}{2}(\bar{f}^{\,n} + {}_m\bar{f}^{\,n+1}) \right\} \quad (15)$$

where

$$\bar{s} = (s_3, s_5, s_7, s_9, \ldots)^T, \quad \bar{f} = (f_3, f_5, f_7, f_9, \ldots)^T$$

and $\cdot_m\bar{J}^{n+1}$ is a Jacobian matrix

$$\bar{J} = \left\{ \frac{h}{2}\frac{\partial \bar{f}}{\partial s_2} + \frac{\partial \bar{f}}{\partial s_3}, \frac{h}{2}\frac{\partial \bar{f}}{\partial s_4} + \frac{\partial \bar{f}}{\partial s_5}, \frac{h}{2}\frac{\partial \bar{f}}{\partial s_6} + \frac{\partial \bar{f}}{\partial s_7}, \right.$$
$$\left. \frac{h}{2}\frac{\partial \bar{f}}{\partial s_8} + \frac{\partial \bar{f}}{\partial s_9}, \ldots \right\} \quad (16)$$

evaluated at $\cdot_m\bar{f}^{\,n+1}$.

Let us choose a rotating speed of say 50 rev/s. If a nonlinear π model (Eq. (2)) is considered, the system is unstable at this rotating speed under the linear analysis because the instability onset speed is 46.3 rev/s. Numerical integration of the differential equations of the whole system incorporating the seal indicates the full picture of the re-stabilizing ability of the squeeze-film damper. When the vibration amplitudes are small, the linear effect dominates and the system is unstable. This trend continues until about $\Omega t/2\pi = 270$ (Fig. 17(*a*)). After that the system limit-cycles and the vibration amplitudes remain unchanged. This is due to the nonlinearity of the squeeze-film damper. When the vibration amplitudes become large, the squeeze-film damper provides much more damping than its linear equivalent; this damping limits the instability and the vibration response stabilizes. It can also be seen that the limit-cycling frequency is about 17 Hz, which is the lowest natural frequency of the assembly, including the seal.

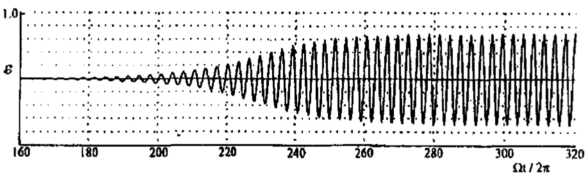

Fig. 17(*a*) Vibration response of the squeeze-film damper for the π film model at 50 rev/s

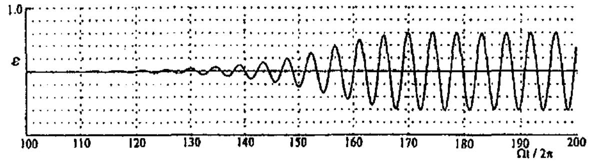

Fig. 17(*b*) Vibration response of the squeeze-film damper for the 2π film model at 70 rev/s

For the 2π film model (Eq. (1)) a rotating speed of 70 rev/s is chosen for the comparison. At this rotating speed the system is again unstable under the linear analysis, the instability onset speed being 65.0 rev/s. Figure 17(*b*) shows that the vibration amplitude increases until $\Omega t/2\pi = 170$, after which point the eccentricity ratio stays at around 0.6 and the system becomes dynamically stable. In this case the limit-cycling frequency is 16 Hz.

The stability of the system is thus affected by many elements, including seal forces, SFD damping, and the retainer spring stiffness. As an equivalent linear element, the squeeze film damper can effectively increase the instability onset speed of the system and as a nonlinear element has a strong restabilizing ability by providing extra damping when the instability develops.

Conclusions

This paper has dealt with the use of a squeeze film damper with a flexible rotor to control unbalance vibration, delay the onset of rotational instability and restabilize the system after initial instability has commenced. In the process the so-called Leonhard locus and the Dynamic Stiffness Method have been used to gain insight into the linear stability of the system and a fast numerical integration method has been used to speed up the time-marching computation when investigating the nonlinear performance.

It is found from the experimental rig that for the configuration without the retainer spring, any increase in the supply pressure and in unbalance make no change in the speed at which resonance occurs. For the configuration with retainer spring, increase in the static SFD eccentricity ratio and/or the supply pressure and/or unbalance moves the position of resonance to a lower speed. Provided the resonance has moved to its extreme position corresponding to the resonance without retainer spring, any further increase in any of these three parameters makes no further change in the position of resonance.

Consideration should thus be given at the design stage to such shifts of the resonance position to ensure smooth running for the rotating assembly. High damping may "lock up" any retainer spring at the position of the squeeze-film damper and cause severe vibration at the position of any overhung disk. This can often lead to the rotor–stator friction and consequent damage. If there is a high level of squeeze film damping in the system, the retainer spring may thus lose its function such that the two configurations show similar dynamic performances and give similar response curves.

References

1 Holmes, R., and Box, S., "On the Use of Squeeze-Film Dampers in Rotor Support Structures," *Machine Vibration,* Vol. 1, 1992, pp. 71–79.

2 Holmes, R., and Dogan, M., "Investigation of a Rotor Bearing Assembly Incorporating a Squeeze-Film Damper Bearing," *Journal of Mechanical Engineering Science,* Vol. 24, No. 3, 1982, pp. 129–137.

3 Humes, B., and Holmes, R., "The Role of Subatmospheric Film Pressure on the Vibration Performance of Squeeze Film Bearings," *Journal of Mechanical Engineering Science,* Vol. 20, No. 5, 1978, pp. 283–289.

4 Massmann, H., and Nordmann, R., "Some New Results Concerning the Dynamic Behaviour of Annular Turbulent Seals," *Proc. NASA Conference on Instability in Rotating Machinery,* Nevada, USA, June 1985, pp. 179–194.

5 Naslin, P., *The Dynamics of Linear and Non-Linear Systems,* Blackie, 1965.

6 Craven, A. H., and Holmes, R., "The Vibration of Engine Crankshafts—a Fast Numerical Solution," *International Journal for Numerical Methods in Engineering,* Vol. 5, 1972, pp. 17–24.

G. T. Zheng
P.O. Box 137,
Dept. of Astronautics and
Applied Mechanics,
Harbin Institute of Technology,
Harbin, China

Vibration of a Rotor System With a Switching Crack and Detection of the Crack

The existence of a "breathing" crack can not only cause variations in harmonic components but also produce extra transient components into vibration signals of a rotor system. In the present paper, the composition of cracked rotor vibration signals is studied first by some analytical methods. Based on this study, an approach of signal processing is suggested to detect transient components of the vibration signals and thereby the crack.

1 Introduction

A fatigue crack in the shaft of a rotor system may lead to catastrophic failure of the system (Schöllhorn et al., 1993). Early detection of cracks in rotors is of significant importance to the reliability and the durability of many rotating machines. Because of the high complexity of the problem, over the past twenty years, much effort has been devoted to the research on understanding dynamic properties and developing mathematical models for rotating machinery with cracked shafts (Dimarogonas and Paipetis, 1983; Gasch, 1976, 1988; Huang et al., 1993; Lee et al., 1992; Wauer, 1990). To find effective monitoring procedures using vibration signals is a major aim of this research (Gasch, 1993; Lee et al., 1992; Collins et al., 1991; Mayes and Davies, 1984; Nelson and Nataraj, 1986).

The vibration of a cracked rotor may have many features. An important one is that the amplitude of the second harmonic component of the vibration signal is greatly increased comparing with the case in which the rotor does not have any cracks (Davies and Mayes, 1984; Gasch, 1988). However, other failures, such as misalignment, may also cause an increase in the amplitude of the second harmonic component (Lyon, 1988; Imam et al., 1989; Rao, 1991). By applying periodic axial impulses to a rotating cracked shaft model, Collins et al. (1991) suggested that extra peaks in the spectrum are a dynamic property of the cracked shaft. The dynamic properties of a cracked rotor passing through critical speed can also be used to detect the crack (Plaut and Andruet, 1994). The rotating speed is an important factor for the detectability of the crack. If the speed is near $k\omega/n$ ($n = 1, 2, 3, \ldots, k = 1, 2$ and ω is the critical speed), subharmonic resonance may become a primary source of information about the crack (Dimarogonas and Papadopoulos, 1983; Huang et al., 1993; Krämer, 1993). The critical speed in the case of small crack depth is not sensitive to the crack (Lee et al., 1992). For a relatively large crack, the changes in the natural frequencies can be used to detect the crack because of the fact that a fatigue crack can produce transient vibrations (Sekhar and Prabhu, 1992).

A crack influences the local stiffness and damping of the rotor and changes the dynamic behavior of the rotating system. It behaves like an external exciting force to the system. Söffker et al. (1993) developed an observer-based method by which external disturbance forces produced by a crack can be reconstructed. It is shown by a numerical simulation result that a crack with depth of 5 percent of the radius of the rotor can be detected. This method requires mathematical models of both the rotor system and the crack. When the mathematical model of a rotor system is given, the position of a crack can also be located (Ratan et al., 1996). In practical situations, there is difficulty in obtaining accurate mathematical model of a complicated rotor system. Owing to insufficient knowledge about the nature of the true stiffness variation due to the crack, it is also difficult to obtain an accurate mathematical model for the crack.

In the present paper, the composition of cracked rotor vibration signals is studied with some analytical methods. Based on this study, an approach of signal processing is suggested for the detection of cracks.

2 Composition of Cracked Rotor Vibration Signals

The composition of the vibration signal measured from a cracked rotor system is mainly defined by the dynamic properties of the system itself. To investigate the vibration behavior of cracked rotor systems, many crack models have been proposed (Gasch, 1993; Wauer, 1990). A common feature of these models is that there exists a "switching condition" to decide whether the additional stiffness and damping matrix should be added to the dynamic equation of the system. The additional stiffness and damping matrix represent the influence of a fatigue crack on the dynamic properties of the rotor system. It is a function of time and the rotating speed. In general, the system equation of motion can be written as

$$\begin{aligned} M\ddot{V}(t) + C\dot{V}(t) + KV(t) \\ = \delta(\Omega t)(\Delta K(\Omega t)V(t) + \Delta C(\Omega t)\dot{V}(t)) + f(t, \Omega) \quad (1) \end{aligned}$$

where M, C, and K are mass, damping, and stiffness matrix, respectively; ΔK and ΔC are additional stiffness matrix and damping matrix produced by the crack, respectively; t represents time, Ω is the rotating speed of the shaft, f represents unbalance forces and gravity, for the hinge model (Gasch, 1976)

$$\delta(\Omega t) = \begin{cases} 0 & \text{When the crack closes} \\ 1 & \text{When the crack opens} \end{cases}$$

In the stationary coordinates, if a lumped-mass model is used, the variation in the stiffness and the damping matrix can be expressed as (Gasch, 1993)

$$H\left(\begin{bmatrix} \cos^2 \Omega t & 0.5 \sin 2\Omega t \\ 0.5 \sin 2\Omega t & \sin^2 2\Omega t \end{bmatrix}\right) \Delta P\delta, \; P = K \text{ or } C \quad (2)$$

Contributed by the International Gas Turbine Institute for publication in the JOURNAL OF ENGINEERING FOR GAS TURBINES AND POWER. Manuscript received at ASME Headquarters October 1997. Associate Technical Editor: H. Nelson.

where H is a matrix function for defining the position of the crack.

If a rotor system is linear, Eq. (1) can be recast into the state space equation:

$$\dot{S}(t) + (A + \delta\Delta A(\Omega t))S(t) = F(t) \qquad (3)$$

where

$$S(t) = \begin{Bmatrix} V(t) \\ \dot{V}(t) \end{Bmatrix}, \quad A + \delta\Delta A(\Omega t) = \begin{bmatrix} 0 & I \\ M^{-1}(K - \delta(\Omega t)H\Delta K(\Omega t)) & M^{-1}(C - \delta(\Omega t)H\Delta C(\Omega t)) \end{bmatrix}, \quad F(t) = \begin{Bmatrix} 0 \\ M^{-1}f \end{Bmatrix}$$

For a "breathing" crack, the equation is linear with respect to each state of the crack, i.e., the equation is piecewise linear. For each state of the crack, solving Eq. (3) yields (Reid, 1983)

$$S(t) = \Phi(t, t_0, \delta)S(t_0) + \int_{t_0}^{t} \Phi(t, \tau, \delta)F(\tau)d\tau \qquad (4)$$

where $t \in (t_0, T]$ during which the crack stays in one state, $\Phi(t, t_0, \delta)$ is the state transition matrix.

If the crack closes during $(t_0, T]$, the vibration signal can be expressed as

$$S(t) = \sum_{i=1} U_i e^{\lambda_i(t-t_0)} + \sum_{i=1} V_i/(\lambda_i - j\Omega)e^{j\Omega t} + E \qquad (5)$$

where $\lambda_i = \zeta_i + j\omega_i$, ζ_i and ω_i are damping coefficient and natural frequency of the system, respectively; E represents complex conjugate part of the solution, $t \in (t_0, T]$.

If the crack keeps opening in the time interval $(t_0, T]$, Eq. (3) is time varying. In general, there is no analytical solution for the equation. If the crack is small, with the method of multiple scales (Nayfeh and Mook, 1979), the vibration can be approximately expressed as

$$X(t) = \sum_{i=1} U_i e^{\lambda_i t} + \sum_{k=1}\sum_{i=1} V_{ik}/(\lambda_i - jk\Omega)e^{jk\Omega t}$$

$$+ \sum_{\substack{m=1,n=1 \\ m\neq n}} \sum_{k=1} W_{mnk}/(\lambda_m + \lambda_n - jk\Omega)e^{jk\Omega t} + E \qquad (6)$$

where λ_i are the eigenvalues of matrix A, E represents the complex conjugate part of the solution, U_i, V_{ik}, and W_{mnk} are coefficients determined by the system parameters and the initial conditions at the instant that the crack begins to open; $i, k, m, n = 1, 2, 3, \ldots$.

Equation (6) is not valid for the case of large cracks. For a big crack, with the rule of composition for the state transition matrix, by dividing the time interval $(t_0, t]$ into a sequence of small time interval $t_0 < t_1 < t_2 \ldots < t_n = t$, and letting matrix $A + \Delta A(\Omega t)$ be constant in each such small time interval, the state transition matrix can be approximately expressed as (Reid, 1983)

$$\Phi(t, t_0) = \prod_{k=1}^{n} \Phi(t_{k-1}, t_k) = \prod_{k=1}^{n} U_k e^{\Lambda_k(t_k - t_{k-1})} V_k^T \qquad (7)$$

where $A + \Delta A(\Omega t) = A_k = U_k\Lambda_k V_k^T$, $t \in (t_{k-1}, t_k]$. Substituting Eq. (7) into Eq. (4) yields

$$S(t) = \prod_{k=1}^{n} U_k e^{\Lambda_k(t_k - t_{k-1})} V_k^T Y(t_0) + Q(\Omega, \theta)$$

$$+ Q(-\Omega, -\theta) + R(\Omega) + R(-\Omega) \qquad (8)$$

$$Q(\Omega, \theta) = 0.5[\sum_{k=1}^{n} e^{j\Omega t_k + j\theta} \Phi(t, t_k)U_k(\Lambda_k - j\Omega)^{-1}$$

$$\times (1 - e^{(-j\Omega+\Lambda_k)(t_k - t_{k-1})}) V_k^T]\{(M^{-1}F)^T, 0^T\}^T$$

$$R(\Omega) = \sum_{k=1}^{n} \Phi(t, t_k)U_k(\Lambda_k - j\Omega)^{-1}$$

$$\times (1 - e^{\Lambda_k(t_k - t_{k-1})}) V_k^T \{(M^{-1}G)^T, 0^T\}^T$$

where $\Lambda = \text{diag}\{\lambda_1, \lambda_2, \lambda_3, \ldots, \lambda_N\}$, G represents the gravity, and the unbalance force is $F \cos(\Omega t + \theta)$. It can be seen from Eq. (8) that the natural frequencies of the system vary with time.

From this analysis, for a linear system, even though the system is at steady state, the cracked rotor vibration signal is composed of transient components and harmonic components. The transient vibration is determined by vibrations of those instants at which the crack opens or closes. This means that the initial condition of the transient vibration corresponding to different "breathing" of the crack may be different. If the system is sensitive to changes in initial conditions, the vibration generated by the crack may be chaotic (Moon, 1987; Müller et al., 1994).

It is known from Eq. (2) that a crack will destroy the symmetry of a rotor. With reference to the stationary coordinates, the crack will cause the coupling of vibrations in two orthogonal directions to be time varying. Different from asymmetric rotor systems, with the "breathing" of the crack, the rotor system behaves as though it is periodically excited by impulsive forces and the corresponding vibration signal contains transient components. With the properties of vibration signals, a "breathing" crack can also be distinguished from local rubbings between rotors and stators in a rotor system. In the case of the rubbing, the vibration signal may only record one impulse-like excitation in each cycle, but for the crack the signal will record at least two such excitations.

Along with the continuous opening and closing, the crack brings energy to the system. As a result, the amplitude of the cracked vibration increases. Because of the material damping, the oil-film damping, and other kinds of damping, the energy of the vibration is in the same time also be dissipated. As a result, the initial condition will be different for each time of opening and closing. If the input and the dissipation of the energy are in a state of balance, the amplitude of the vibration will possibly be kept at a certain level. However, if the size of the crack is large enough, this balance will be destroyed and the level of the vibration will be increased greatly, such as the accident that happened in a 963-MW turbogenerator (Schöllhorn et al., 1993).

3 Crack Detection

With this study on the composition of the cracked rotor vibration signal, besides the variation in the second harmonic component, the vibration signal generated by a fatigue crack can possibly be distinguished from other kinds of vibration signals by three features: extra transient vibration components, no fewer than two times of impulse-like excitations per rotation and chaotic vibrations. Since the unbalance response of a rotor system with journal bearings may also be chaotic (Brown et al., 1994), a practical approach is to detect those transient vibrations generated by the crack with a method of signal processing. In this paper, the Gabor transform is suggested to calculate the envelope of some frequency components. From the aspect of system theory, the response of a system to an impulsive force is the combination of a set of modulated signals; each carrier frequency is the natural frequency of the system. On the other hand, for a given carrier frequency, the envelope analysis is a process of demodulation. The peak on the envelope corresponds to the impulsive force. Hence the envelope can reveal the pattern of transient vibration components.

Methods of vibration signal processing are important tools of many machinery condition monitoring and fault diagnosis (MCMFD) systems, especially for turbine machines (Lyon, 1988; Ericsson, 1985). The vibration signal processing can use the facilities of existing MCMFD systems and reduce the cost for equipping extra instruments. Although vibration signal processing has obtained wide application in mechanical engineering areas for identifying damage (Lyon, 1988; McFadden and Zheng, 1993), it is relatively new for the purpose of detecting cracks in rotors.

There are many methods of signal processing available for detecting transient components. Among them are the short-time Fourier transform, the Gabor transform, and the wavelet transform. These transforms can all be considered as a class of windowed Fourier transform because their kernels are composed of a time domain window function and a frequency function. An interpretation of these methods is the envelope analysis (Zheng and McFadden, 1994). A common problem of these methods is that they do not have simultaneous high time and frequency resolution (Chui, 1992). The vibration signal of a rotor system, especially turbo-machinery, is generally dominated by harmonics of rotating speed and sub- or superharmonics produced by nonlinearities of journal bearings. If these harmonics are not removed from the signal, because of the problem in the resolution, the transient components may be masked and cannot be resolved.

Harmonic components can be removed with the aid of the Fourier transform and the inverse Fourier transform. Any finite duration discrete signal $s(n)(n = 1, 2, 3, \ldots, N)$ can be represented by a discrete Fourier transform as (Oppenheim and Willsky, 1983)

$$s(n) = \sum_{k=1}^{N} a_k e^{jk(2\pi/N)n} \qquad (9.a)$$

where

$$a_k = \frac{1}{N} \sum_{n=1}^{N} s(n) e^{-jk(2\pi/N)n} \qquad (9.b)$$

After obtaining $a_k (k = 1, 2, 3, \ldots N)$ with Eq. (9.b) or a N point discrete Fourier transform, let those Fourier transform coefficients whose subscripts k satisfy the following equation:

$$\frac{kN_0}{N} = m \qquad (10)$$

be zero. In Eq. (10), N_0 is the number of samples per rotation, $m = 1, 2, 3, \ldots M$ represents the order of harmonics. Reconstructing the signal with Eq. (9.a) or an N-point inverse Fourier transform, the harmonics are removed from the signal and the residual signal will not contain harmonics. As a result, only the transient components are kept. The residue is a reconstruction of the transient components produced by the crack.

At steady state, if there are no other forces that can excite transient vibrations to the system, the residual signal is the collection of all transient components produced by the crack. In practical situations, the signal may be contaminated by noises. Because the crack may open and close in a random way, the time domain average method, a widely used method in most machinery condition monitoring and fault diagnosis systems, may be not suited to removing noises. An effective approach is to let the residual signal pass through a bandpass filter or a lowpass filter with the consideration that most of the energy of the noises is distributed in a high-frequency range. Since the Gabor transform has the function of bandpass filter (Zheng and McFadden, 1994), this can be done along with the Gabor transform.

The definition of the discrete Gabor transform is

$$A(m, f_k) = [\sum_n (s(n) e^{-\alpha(m-n)^2}) e^{-j2\pi f_k/Nn}] \, e^{j2\pi f_k/Nm} \qquad (11)$$

where f_k is a central analysis frequency, m is the central analysis time, $s(n)$ is vibration signal, N is the number of samples used in the Fourier transform for calculating f_k from the measured signal, the parameter α determines the width of the time domain window (Chui, 1992). In Eq. (11), m and n are positive integers corresponding to the sampling number of the signal. Basically, the Gabor transform provides a bank of band-pass filters, whose central frequencies are the central analysis frequencies and widths are the width of the window function in the frequency domain. The envelope of the signal is

$$E(m, f_k) = |A(m, f_k)| \qquad (12)$$

We substitute the vibration signal studied in section 2 into Eq. (12). If it is supposed that the length of the signal covered by the time domain window is short enough that the signal can be taken as stationary, then the vibration signal can be rewritten as

$$s(n) = \sum_{i=1} S_i \cos(\omega_i n \Delta t + \alpha_i) \qquad (13)$$

where Δt is the sampling interval and ω_i represents frequency. If the width of the frequency domain window is also narrow enough, the result of the transform will have the form

$$|A(m, f_k)| = |C_i S_i[\cos(\omega_i t + \alpha_i) + j \sin(\omega_i t + \alpha_i)]| = |C_i S_i| \qquad (14)$$

where C_i is a function of the parameters of the window function. In this way, for a given central analysis frequency, by moving the time domain window along the time axis, the envelope of the corresponding frequency component can be obtained. If this frequency component is a transient component produced by the crack, for each rotation of the rotor, there will be at least two high peaks on the envelope.

A difficulty in the Gabor transform is the choice of parameter α. It is known from the results of section 2 that the cracked rotor vibration signal contains transient components of the form $u(t - t_s) \exp(-\xi_i t) \cos(\omega_i t)$, where $u(t - t_s)$ is a step function and t_s is the instant at which the crack changes its state. The spectrum of such a component will consist of a broad peak reaching its maximum value around ω_i, but extending over the whole frequency domain. The vibration signal of a rotor system is certain to contain a great number of such components. Due to the width of the frequency domain window, other transient components may interfere, so the choice of parameter α should also take the requirement on the frequency domain window into consideration. When a rotor system is at steady state, it is recommended that

$$\alpha = -4 \ln \epsilon / T^2 \qquad (13)$$

where ϵ is a very small positive value, usually chosen as 0.001; T is the number of samples for each rotation.

If the natural frequencies of a rotor system are given and they can be identified from the spectrum of the vibration signal, these natural frequencies should be chosen as the central analysis frequencies. In other situations, high peaks in the spectrum

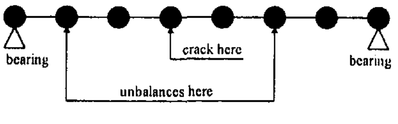

Fig. 1 Rotor model

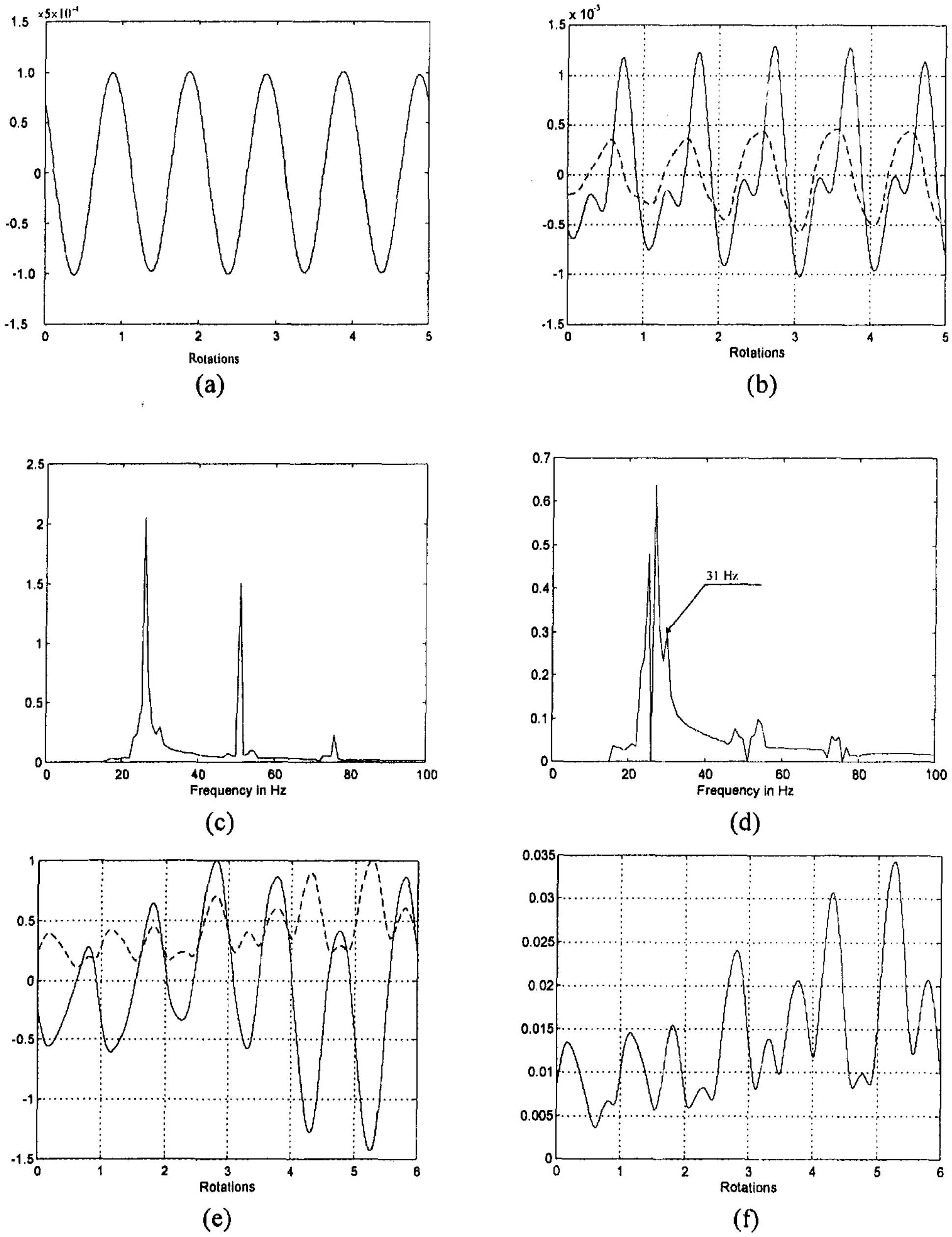

Fig. 2 Numerical example: (*a*) vibration without crack; (*b*) vibration with crack (solid line: signal; dashed line: residual signal); (*c*) spectrum of cracked vibration; (*d*) spectrum of the residual signal; (*e*) 31 Hz frequency component and its envelope of vibration signal (solid line: frequency component; dashed line: envelope); (*f*) envelope of 30 Hz frequency component

can be chosen as the central analysis frequencies. The central analysis time should be the same as those time instants at which the signal is sampled.

4 Applications of the Signal Processing Method

The first application is a numerical example. Since the present work is not for discussing crack models, although there are many crack models (Wauer, 1990), a simple model suggested by Gasch (1976) is chosen. It is a "switching" model. The "switching function" in stationary coordinates is given in an explicit form by Söffker et al. (1993). The shaft model of Söffker et al. is used. A difference is that the bearings have different dynamic coefficients. This model is a lumped-mass model, as shown in Fig. 1; the details are listed in the appendix. A crack is located at the fourth lumped mass counted from the left. Two unbalances are located at the second and sixth lumped mass, counted from the left. The shaft is supported by two identical bearings, which have cross-coupled stiffness and damping. The dynamic coefficients of the bearings are listed in the appendix. The natural frequencies of the uncracked system are:

4.16 Hz, 4.23 Hz, 16.68 Hz, 16.75 Hz, 30.98 Hz, 31.05 Hz, 44.09 Hz, 44.15 Hz, 55.09 Hz, 55.16 Hz, 63.40 Hz, 63.47 Hz, 68.56 Hz, 68.63 Hz, 70.20 Hz, 70.23 Hz

Considering the fact that most turbomachines rotate at a constant speed during most of their operating time, let the shaft rotate at a constant speed 1500 rpm.

The crack is a transverse one with a depth of 10 percent of the shaft radius. The vibration is simulated with a Runge–Kutta algorithm provided by MATLAB. The lateral vibration in the vertical direction at the left bearing is measured. Figures 2(*a*)

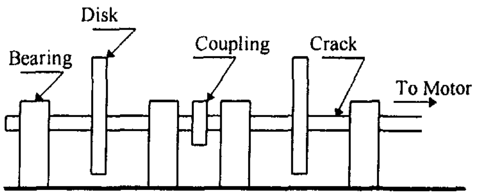

Fig. 3 Test rig for cracked rotor-bearing system vibration

and 2(*b*) are the time history before and after the crack occurred. It can be seen by comparing Fig. 2(*a*) with Fig. 2(*b*) that after the crack occurred, the amplitude of the vibration is increase greatly.

The spectrum of the cracked vibration signal is depicted in Fig. 2(*c*). It can seen from this diagram that the signal is dominated by harmonics. Figure 2(*d*) is the spectrum of the signal after harmonic components are removed. Some frequencies of the residual signals are approximately the natural frequencies of the system, but some others are not. Figure 2(*b*) also contains the residual signal. An envelope of the residual signal is shown in Figs. 2(*e*) and 2(*f*) (the central analysis frequency is 31 Hz). The envelope is composed of a train of regular spaced peaks, approximately two peaks for each rotation. These peaks have different height. This is a feature of cracked rotor vibration.

The second application is an experiment made on a rotor-bearing system test rig. The diameter of the rotor is 80 mm. A transverse fatigue crack was produced on a fatigue test machine after about 50 hours of continuous operation. The depth of the crack is about 0.25 of the diameter. The position of the crack is shown in Fig. 3. After the crack was produced, the shaft was dynamically balanced to remove unbalances. Figure 4(*a*) shows the vibration signal measured at the far right bearing in the vertical direction. The residual signal is also shown in Fig. 4(*a*). Obviously, besides harmonic components, the signal also contains some transient components. Figure 4(*b*) shows the spectrum of the signal. During the measurement, the system was at steady state and the rotating speed was 1800 rpm.

Figures 4(*c*) and 4(*d*) are 73 Hz frequency component and its envelope. Obviously, in each cycle, there are approximately two peaks on the envelope.

5 Discussions

Removing harmonics of the rotating speed from vibration signals is necessary for the detection of cracks. Although a crack may cause a variation in the amplitude of some harmonics, considering the fact that vibration signals of a practical rotor-bearing system may generally be dominated by harmonics produced by nonlinearity of bearings and some other failures may also cause an increase in the amplitude of the harmonics, it is not proper to choose the variation in the harmonics as a major symptom for the crack detection.

The ''breathing'' of a crack excites transient vibration to the system. Although the time-varying properties of the stiffness and damping parameters caused by the crack will change the natural frequencies of the system, in an early stage of the crack, this change may be so small that can be neglected. Thus these transient components may still be distributed at the location of natural frequencies of the system on a joint time-frequency plane. To detect a fatigue crack from the changes in the natural frequencies may be not suited to the early detection.

The problem of the Gabor transform is that it does not have simultaneous high resolution in both the time domain and the frequency domain. As a result, an interpretation of the transform will be to approximate all transient components in a given frequency band with one transient component $A(t)$ exp $(j\omega t)$ (ω is the central analysis frequency and $A(t)$ is the envelope). The

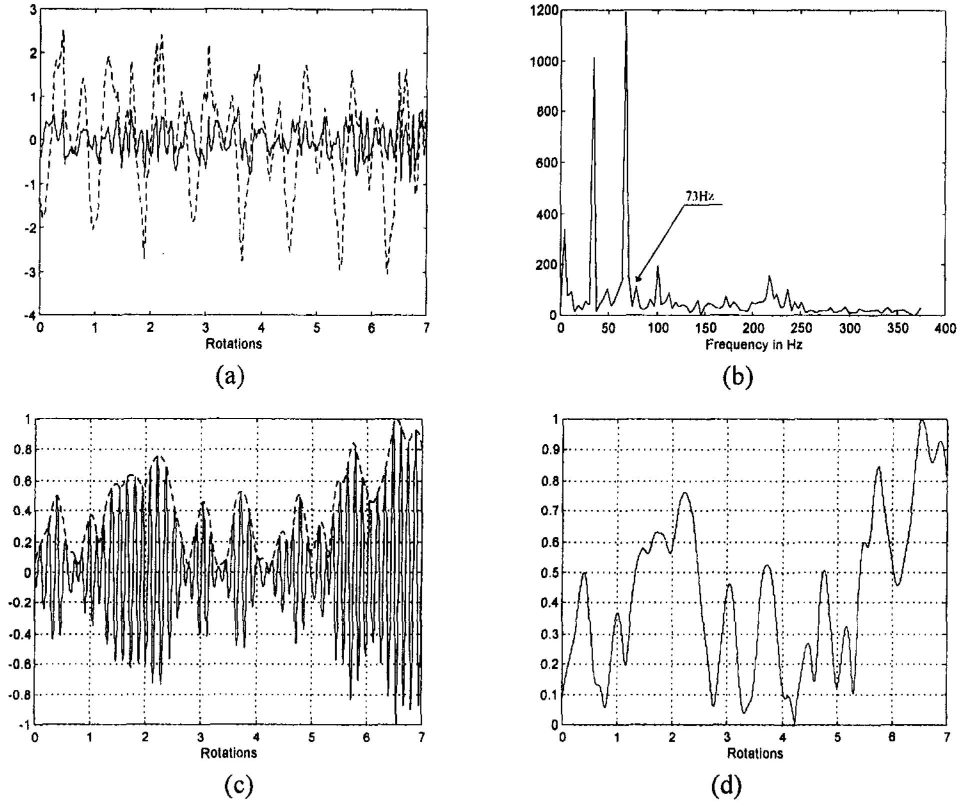

(a) (b)

(c) (d)

Fig. 4 Experimental example: (*a*) vibration with crack (solid line: residual signal; dashed line: signal); (*b*) spectrum of cracked vibration; (*c*) 73 Hz frequency component and its envelope of vibration signal (solid line: frequency component; dashed line: envelope); (*d*) envelope of 73 Hz frequency component

pattern of the envelope is important to the correct detection of a fatigue crack. Having at least two peaks for nearly every rotation on the envelope of a transient component is an important feature of the cracked rotor vibration signal. This feature enables it to be distinguished from other vibrations, such as those produced by asymmetric shafts or rubbings between rotors and stators.

6 Conclusion

An advantage of the signal processing method in the detection of fatigue crack is that it does not require much knowledge about a machinery system, such as mathematical model and natural frequencies. The method proposed in the present paper only requires the knowledge on the pattern of the envelope of the transient components. With the Gabor transform, the envelope of the transient component is obtained.

The vibration of a cracked rotor system is excited both by unbalance forces and by variations in the parameters. The vibration is composed of transient components and harmonic components. In practical situations, a procedure of preprocessing signal, such as removing harmonics from the signal, is necessary, especially for those systems with nonlinearities and some other kinds of failures. With this procedure, the transient components produced by the crack can be revealed.

The presented method can also be used as an auxiliary tool in the conventional spectral analysis method for the detection of other kinds of failures, which can produce transient components to vibration signals, in a rotating machinery system.

Acknowledgments

This work is sponsored by the Aerospace Research Foundation of China.

References

Brown, R. D., Addison, P., and Chan, A. H. C., 1994, "Chaos in the Unbalance Response of Journal Bearings," *Nonlinear Dynamics*, Vol. 5, pp. 421–432.

Chui, C. K., 1992, *An Introduction to Wavelets. Volume 1: Wavelet Analysis and Its Applications*, Academic Press, New York.

Collins, K. R., Plaut, R. H., and Wauer, J., 1991, "Detection of Cracks in Rotating Timoshenko Shafts Using Axial Impulses," ASME *Journal of Vibration and Acoustics*, Vol. 113, pp. 74–78.

Davies, W. G. R., and Mayes, I. W., 1984, "The Vibrational Behaviour of a Multi-Shaft Multi-Bearing System in the Presence of a Propagating Traverse Crack," ASME *Journal of Vibration, Acoustics, Stress, and Reliability in Design*, Vol. 106, pp. 146–153.

Dimarogonas, A. D., and Paipetis, S. A., 1983, *Analytical Methods in Rotor Dynamics*, Applied Science Publishers, London.

Dimarogonas, A. D., and Papadopoulos, C. A., 1983, "Vibration of Cracked Shafts in Bending," *Journal of Sound and Vibration*, Vol. 91, No. 4, pp. 583–593.

Ericsson, U., 1985, "Vibration Monitoring—The State of the Art—With Case Studies," VDI-Berichte 568, VDI-Verlag, Düsseldorf, pp. 289–303.

Friedlander, B., and Porat, B., 1989, "Detection of Transient Signals by the Gabor Representation," *IEEE Transaction, Acoustics, Speech, Signal Processing*, Vol. 37, No. 2, pp. 169–180.

Gasch, R., 1976, "Dynamic Behaviour of a Simple Rotor With a Cross-Sectional Crack," *Vibration in Rotating Machinery*, Institution of Mechanical Engineers, London, pp. 123–128.

Gasch, R., 1988, "Dynamics Behaviour of the Laval Rotor With a Cracked Hollow Shaft—a Comparison of Crack Models," *Vibration in Rotating Machinery*, Institute of Mechanical Engineers, Edinburgh, pp. 463–472.

Gasch, R., 1993, "A Survey of the Dynamic Behaviour of a Simple Rotating Shaft With a Transverse Crack," *Journal of Sound and Vibration*, Vol. 160, No. 2, pp. 313–332.

Huang, S. C., Huang, Y. M., and Shieh, X. X., 1993, "Vibration and Stability of Rotating Shaft Containing a Transverse Crack," *Journal of Sound and Vibration*, Vol. 163, No. 3, pp. 387–401.

Imam, I., Azzaro, S. H., Bankert, R. J., and Scheibel, J., 1989, "Development of an On-Line Rotor Crack Detection and Monitoring System," ASME *Journal of Vibration, Acoustics, Stress, and Reliability in Design*, Vol. 111, pp. 241–250.

Krämer, E., 1993, *Dynamics of Rotors and Foundations*, Springer-Verlag.

Lee, C. W., Yun, J. S., and Jun, O. S., 1992, "Modelling of a Simple Rotor With a Switching Crack and Its Experimental Verification," ASME *Journal of Vibration and Acoustics*, Vol. 114, pp. 217–225.

Lyon, R. H., 1988, "Vibration Based Diagnostics of Machine Transients," *Sound and Vibration*, Sept. (1988), pp. 18–22.

Mayes, I. W., and Davies, W. G. R., 1984, "Analysis of the Response of a Multi-Rotor-Bearing System Containing a Transverse Crack in a Rotor," ASME *Journal of Vibration, Acoustics, Stress, and Reliability in Design*, Vol. 106, pp. 139–145.

McFadden, P. D., and Zheng, G. T., 1993, "Application of the Wavelet Transform to the Early Detection of Gear Failure by Vibration Analysis," Department of Engineering Science, Oxford University, Report OUEL 1999/93.

Moon, F. C., 1987, *Chaotic Vibration, An Introduction for Applied Scientists and Engineers*, Wiley, New York.

Müller, P. C., Bajkowski, J., and Söffker, D., 1994, "Chaotic Motions and Fault Detection in a Cracked Rotor," *Nonlinear Dynamics*, Vol. 5, pp. 233–254.

Nayfeh, A. H., and Mook, D. T., 1979, *Nonlinear Oscillations*, Wiley, New York.

Nelson, H. D., and Nataraj, C., 1986, "The Dynamics of a Rotor System With a Cracked Shaft," ASME *Journal of Vibration, Acoustics, Stress, and Reliability in Design*, Vol. 108, pp. 189–196.

Oppenheim, A. V., and Willsky, A. S., 1983, *Signals and Systems*, Prentice-Hall International, Inc., pp. 306–309.

Plaut, R. H., and Andruet, R. H., 1994, "Behaviour of a Cracked Rotating Shaft During Passage Through a Critical Speed," *Journal of Sound and Vibration*, Vol. 173, No. 5, pp. 577–589.

Rao, J. S., 1991, *Rotor Dynamics*, Wiley Eastern Ltd.

Ratan, S., Baruh, H., and Rodriguez, J., 1996, "On-Line Identification and Location of Rotor Cracks," *Journal of Sound and Vibration*, Vol. 194, No. 1, pp. 64–78.

Reid, J. G., 1983, *Linear System Fundamentals: Continuous and Discrete, Classic and Modern*, McGraw-Hill, New York.

Schöllhorn, V. K., Ebi, G., and Steigleder, K., 1993, "Frettinganrisse in einem 936-MW-Turbogeneratorrotor," *VGB Kraftwerkstechnik*, Vol. 73, No. 4, pp. 340–344.

Sekhar, A. S., and Prabhu, B. S., 1992, "Crack Detection and Vibration Characteristics of Cracked Shafts," *Journal of Sound and Vibration*, Vol. 157, No. 2, pp. 375–381.

Söffker, D., Bajkowski, J., and Müller, P. C., 1993, "Detection of Cracks in Turborotors—A New Observer Based Method," ASME *Journal of Dynamic Systems, Measurement, and Control*, Vol. 115, pp. 518–524.

Wauer, J., 1990, "On the Dynamics of Cracked Rotors: A Literature Survey," *Applied Mechanics Review*, Vol. 43, No. 1, pp. 13–17.

Zheng, G. T., and McFadden, P. D., 1994, "Windowed Fourier Transform of Mechanical Vibration Signals," Department of Engineering Science, Oxford University, Report OUEL 2036/9417.

APPENDIX

The shaft model used here is from Söffker et al. (1993). It is a lumped-mass model with seven beam elements. Length $l = 600$ mm; radius $r = 140$ mm; Young's modulus $E = 2.1 \times 10^5$ N/mm^2; specific gravity $\rho = 7860$ kg/m^3; rotative speed $n = 1500$ rpm, damping matrix $C = 0.0001$ K (K stiffness matrix), eccentricity $e = 0.02$ mm. Two unbalances are at the position of the second and the sixth lumped-mass counted from the left:

$$f_3 = -mg + me(n\pi/30)^2 \sin(n\pi t/30),$$

$$f_4 = me(n\pi/30)^2 \cos(n\pi t/30),$$

$$f_{11} = -mg + me(n\pi/30)^2 \sin(n\pi t/30 + 0.25\,\pi),$$

$$f_{12} = me(n\pi/30)^2 \cos(n\pi t/30 + 0.25\,\pi).$$

The condition for crack opening is

$$y_7 \cos(\Omega t) + y_8 \sin(\Omega t) > 0.5\,[(y_7 + y_9)\cos(\Omega t) + (y_6 + y_{10})\sin(\Omega t)] \qquad (A.1)$$

where y_i is displacement in the state vector. The variation in the stiffness is

$$\Delta K = 0.038 \times 24\, EJ/l^3 \qquad (A.2)$$

The dynamic coefficients of the bearings are

$k_{yy} = 750{,}000$ N/mm $\quad c_{yy} = 640$ N-s/mm

$k_{yz} = 26{,}000$ N/mm $\quad c_{yz} = 420$ N-s/mm

$k_{zy} = 6800$ N/mm $\quad c_{zy} = -120$ N-s/mm

$k_{zz} = 750{,}000$ N/mm $\quad c_{zz} = 440$ N-s/mm

where y denotes the vertical direction and z denotes the horizontal direction of the stationary coordinates.

A Viscoplastic Constitutive Theory for Monolithic Ceramics—I

L. A. Janosik
NASA Lewis Research Center,
Cleveland, OH 44135

S. F. Duffy
Cleveland State University,
Cleveland, OH 44115

This paper, which is the first of two in a series, provides an overview of a viscoplastic constitutive model that accounts for time-dependent material deformation (e.g., creep, stress relaxation, etc.) in monolithic ceramics. Using continuum principles of engineering mechanics, the complete theory is derived from a scalar dissipative potential function first proposed by Robinson (1978), and later utilized by Duffy (1988). Derivations based on a flow potential function provide an assurance that the inelastic boundary value problem is well posed, and solutions obtained are unique. The specific formulation used here for the threshold function (a component of the flow potential function) was originally proposed by Willam and Warnke (1975) in order to formulate constitutive equations for time-independent classical plasticity behavior observed in cement and unreinforced concrete. Here constitutive equations formulated for the flow law (strain rate) and evolutionary law employ stress invariants to define the functional dependence on the Cauchy stress and a tensorial state variable. This particular formulation of the viscoplastic model exhibits a sensitivity to hydrostatic stress, and allows different behavior in tension and compression.

Introduction

With increasing use of ceramic materials in high-temperature applications, the need arises to predict thermomechanical behavior accurately. This paper will focus on inelastic deformation behavior associated with these service conditions. A number of constitutive theories for materials that exhibit sensitivity to the hydrostatic component of stress have been proposed that characterize deformation using time-independent classical plasticity as a foundation. Corapcioglu and Uz (1978) reviewed several of these theories by focusing on the proposed form of the individual yield function. The review includes the works of Kuhn and Downey (1971), Shima and Oyane (1976) and Green (1972). Not included is the work by Gurson (1977) who not only developed yield criteria and a flow rule, but also discussed the role of void nucleation. Subsequent work by Mear and Hutchinson (1985) extended Gurson's work to include kinematic hardening of the yield surfaces. Although the previously mentioned theories admit a dependence on the hydrostatic component of stress, none of these theories allow different behavior in tension and compression. Willam and Warnke (1975) proposed a yield criterion for concrete that admits a dependence on the hydrostatic component of stress and explicitly allows different material responses in tension and compression. Several formulations of their model exist, i.e., a three-parameter formulation and a five-parameter formulation. For simplicity the work presented here builds on the three-parameter formulation.

The aforementioned theories are somewhat lacking in that they are unable to capture creep, relaxation, and rate-sensitive phenomena exhibited by ceramic materials at high temperature. A noted exception is the recent work by Ding et al. (1994), as well as the work by White and Hazime (1995). Another exception is a paper by Liu et al. (1997), which is an extension of the work presented by Ding and co-workers. As these authors point out, when subjected to elevated service temperatures, ceramic materials exhibit complex thermomechanical behavior that is inherently time dependent, and hereditary in the sense that current behavior depends not only on current conditions, but also on thermomechanical history. This paper presents the formulation of a macroscopic continuum theory that captures these time-dependent phenomena. Specifically, the overview contained in this paper focuses on the complete multiaxial derivation of the constitutive model, and examines the attending geometric implications when the Willam–Warnke (1975) yield function is utilized as a scalar threshold function. A second paper, which will appear shortly, examines specific time-dependent stress–strain behavior that can be modeled with the constitutive relationship presented in this article. No attempt is made here to assess the accuracy of the model in comparison to experiment. A quantitative assessment is reserved for a later date, after the material constants have been suitably characterized for a specific ceramic material. The quantitative assessment could easily dovetail with the nascent efforts of White and co-workers.

Flow Potential

Early work in the field of metal plasticity indicated that inelastic deformations are essentially unaffected by hydrostatic stress. This is not the case for ceramic-based material systems, unless the ceramic is fully dense. The theory presented here allows for fully dense material behavior as a limiting case. In addition, as Chuang and Duffy (1994) point out, ceramic materials exhibit different time-dependent behavior in tension and compression. Thus inelastic deformation models for ceramics must be constructed in a fashion that admits sensitivity to hydrostatic stress and differing behavior in tension and compression. This will be accomplished here by developing an extension of a J_2 model first proposed by Robinson (1978) and later extended to sintered powder metals by Duffy (1988). Although the viscoplastic model presented by Duffy (1988) admitted a sensitivity to hydrostatic stress, it did not allow for different material behavior in tension and compression.

The complete theory is derivable from a scalar dissipative potential function identified here as Ω. Under isothermal conditions this function is dependent upon the applied stress (σ_{ij}) and internal state variable (α_{ij}), i.e.,

$$\Omega = \Omega(\sigma_{ij}, \alpha_{ij}) \tag{1}$$

Contributed by the International Gas Turbine Institute and presented at the 41st International Gas Turbine and Aeroengine Congress and Exhibition, Birmingham, United Kingdom, June 10–13, 1996. Manuscript received at ASME Headquarters February 1996. Paper No. 96-GT-368. Associate Technical Editor: J. N. Shinn.

The stress dependence for a J_2 plasticity model or a J_2 viscoplasticity model is usually stipulated in terms of the deviatoric components of the applied stress, i.e.,

$$S_{ij} = \sigma_{ij} - (1/3)\sigma_{kk}\delta_{ij} \tag{2}$$

and a deviatoric state variable

$$a_{ij} = \alpha_{ij} - (1/3)\alpha_{kk}\delta_{ij} \tag{3}$$

For the viscoplasticity model presented here these deviatoric tensors are incorporated, along with the effective stress

$$\eta_{ij} = \sigma_{ij} - \alpha_{ij} \tag{4}$$

and an effective deviatoric stress, identified as

$$\Sigma_{ij} = S_{ij} - a_{ij} \tag{5}$$

Both tensors, i.e., η_{ij} and Σ_{ij}, are utilized for notational convenience.

The potential nature of Ω is exhibited by the manner in which the flow and evolutionary laws are derived. The flow law is derived from Ω by taking the partial derivative with respect to the applied stress, i.e.,

$$\dot{\epsilon}_{ij} = \frac{\partial \Omega}{\partial \sigma_{ij}} \tag{6}$$

The adoption of a flow potential and the concept of normality, as expressed in Eq. (6), were introduced by Rice (1970). In his work the relationship above was established using thermodynamic arguments. The authors wish to point out that Eq. (6) holds for each individual inelastic state.

The evolutionary law is similarly derived from the flow potential. The rate of change of the internal stress is expressed as

$$\dot{\alpha}_{ij} = -h\,\frac{\partial \Omega}{\partial \alpha_{ij}} \tag{7}$$

where h is a scalar function of the inelastic state variable (i.e., the internal stress) only. Using arguments similar to Rice's, Ponter and Leckie (1976) have demonstrated the appropriateness of this type of evolutionary law.

To give the flow potential a specific form, the following integral format proposed by Robinson (1978) is adopted:

$$\Omega = K^2\left[\left(\frac{1}{2\mu}\right)\int F^n dF + \left(\frac{R}{H}\right)\int G^m dG\right] \tag{8}$$

where μ, R, H, and K are material constants. In this formulation μ is a viscosity constant, H is a hardening constant, n and m are unitless exponents, and R is associated with recovery. The octahedral threshold shear stress K appearing in Eq. (8) is generally considered a scalar state variable that accounts for isotropic hardening (or softening). However, since isotropic hardening is often negligible at high homologous temperatures (≥ 0.5), to a first approximation K is taken to be a constant for metals. This assumption will be adopted in the present work regarding ceramic materials. The reader is directed to the work by Janosik (1998) for specific details regarding the experimental test matrix needed to characterize these parameters.

Several of the quantities identified as material constants in the theory are strongly temperature dependent in a nonisothermal environment. However, for simplicity, the present work is restricted to isothermal conditions. A paper by Robinson and Swindeman (1982) provides the approach by which an extension can be made to nonisothermal conditions. The present article concentrates on representing the complexities associated with establishing an inelastic constitutive model that will satisfy the assumptions stipulated herein for ceramic materials.

The dependence upon the effective stress Σ_{ij} and the deviatoric internal stress a_{ij} are introduced through the scalar functions

$$F = F(\Sigma_{ij}, \eta_{ij}) \tag{9}$$

and

$$G = G(a_{ij}, \alpha_{ij}) \tag{10}$$

Inclusion of η_{ij} and α_{ij} will account for sensitivity to hydrostatic stress. The concept of a threshold function was introduced by Bingham (1922) and later generalized by Hohenemsser and Prager (1932). Correspondingly, F will be referred to as a

Nomenclature

a_{ij} = deviatoric component of the state variable tensor

B = constant (in general polynomial form of F)

C = coefficient used to simplify expressions for flow and evolutionary laws

F = Bingham–Prager threshold function

G = scalar state function

H = hardening constant

h = scalar hardening function dependent on the inelastic state variable

I_1, J_2, J_3 = invariants associated with the Willam–Warnke threshold function F

$\mathcal{J}_1, \mathcal{J}_2, \mathcal{J}_3$ = invariants associated with the scalar function G

K = octahedral threshold shear stress

m, n = unitless exponents

R = recovery constant

r = position vector in Π-plane representing deviatoric component of a stress state

S_{ij} = deviatoric component of applied stress tensor

u, v = component of position vector r

Y = normalized threshold stress

α_{ij} = internal state variable tensor

$\dot{\alpha}_{ij}$ = state variable evolutionary law

δ_{ij} = Kronecker delta

ϵ_{ij} = flow law (inelastic strain rate)

η_{ij} = effective stress tensor

θ = angle of similitude measured in the Π-plane

λ = scalar function in general polynomial form of F; dependent on J_3 through the angle of similitude θ

μ = viscosity constant

Π = plane perpendicular to the hydrostatic stress line in the Haigh–Westergaard stress space (i.e., the Π-plane)

π = 3.14159 . . .

ρ = Willam–Warnke hydrostatic threshold parameter

Σ_{ij} = effective deviatoric stress tensor

σ = threshold stress

σ_{ij} = applied Cauchy stress tensor

Ω = scalar dissipative potential function

$\tilde{\ }$ = denotes parameters associated with scalar function F

$\hat{\ }$ = denotes parameters associated with scalar function G

$\dot{\ }$ = rate

Subscripts

bc = equal biaxial compressive

c = compressive

i, j, k = tensorial components

m, n = tensorial components

q, u, v = tensorial components

t = tensile

Bingham–Prager threshold function. Inelastic deformation occurs only for those stress states where

$$F(\Sigma_{ij}, \eta_{ij}) > 0 \tag{11}$$

For frame indifference, the scalar functions F and G (and hence Ω) must be form invariant under all proper orthogonal transformations. This condition is ensured if the functions depend only on the principal invariants of Σ_{ij}, a_{ij}, η_{ij}, and α_{ij}, that is

$$F = F(\tilde{I}_1, \tilde{J}_2, \tilde{J}_3) \tag{12}$$

and

$$G = G(\mathcal{I}_1, \mathcal{J}_2, \mathcal{J}_3) \tag{13}$$

where

$$\tilde{I}_1 = \eta_{ii} \tag{14}$$

$$\tilde{J}_2 = (\tfrac{1}{2})\Sigma_{ij}\Sigma_{ij} \tag{15}$$

$$\tilde{J}_3 = (\tfrac{1}{3})\Sigma_{ij}\Sigma_{jk}\Sigma_{ki} \tag{16}$$

and

$$\mathcal{I}_1 = \alpha_{ii} \tag{17}$$

$$\mathcal{J}_2 = (\tfrac{1}{2})a_{ij}a_{ij} \tag{18}$$

$$\mathcal{J}_3 = (\tfrac{1}{3})a_{ij}a_{jk}a_{ki} \tag{19}$$

These scalar quantities are elements of what is known in invariant theory as an integrity basis for the functions F and G.

A three parameter flow criterion proposed by Willam and Warnke (1975) will serve as the Bingham–Prager threshold function, F. The Willam–Warnke criterion uses the previously mentioned stress invariants to define the functional dependence on the Cauchy stress (σ_{ij}) and internal state variable (α_{ij}). In general, this flow criterion can be constructed from the following general polynomial:

$$F = \lambda\left(\frac{\sqrt{\tilde{J}_2}}{\sigma_c}\right) + B\left(\frac{\tilde{I}_1}{\sigma_c}\right) - 1 \tag{20}$$

where σ_c is the uniaxial threshold flow stress in compression and B is a constant determined by considering homogeneously stressed elements in the virgin inelastic state, i.e.,

$$\alpha_{ij} = 0 \tag{21}$$

Note that a threshold flow stress is similar in nature to a yield stress in classical plasticity. In addition, λ is a function dependent on the invariant $\tilde{J}_3$ and other threshold stress parameters that are defined momentarily. The specific details in deriving the final form of the function F can be found from Willam and Warnke (1975), and this final formulation is stated here as

$$F(\tilde{I}_1, \tilde{J}_2, \tilde{J}_3) = \frac{1}{\sigma_c}\left[\frac{1}{r(\tilde{\theta})}\right]\left[\frac{2\tilde{J}_2}{5}\right]^{1/2} + \frac{\tilde{I}_1}{3\rho\sigma_c} - 1 \tag{22}$$

for brevity. The function F is implicitly dependent on $\tilde{J}_3$ through the function r, which is characterized in the next section. This function is dependent on the angle of similitude $\tilde{\theta}$, which is defined by the expression

$$\cos(3\tilde{\theta}) = \frac{(3\sqrt{3})\tilde{J}_3}{2(\tilde{J}_2)^{3/2}} \tag{23}$$

The invariant $\tilde{I}_1$ in Eq. (22) admits a sensitivity to hydrostatic stress. The invariant $\tilde{J}_3$ in Eq. (23) accounts for different behavior in tension and compression, since this invariant changes sign when the direction of a stress component is reversed. The parameter ρ characterizes the tensile hydrostatic threshold flow stress. This parameter will also be considered in more detail in the next section.

A similar functional form is adopted for the scalar state function G, i.e.,

$$G(\mathcal{I}_1, \mathcal{J}_2, \mathcal{J}_3) = \frac{1}{\sigma_c}\frac{1}{r(\hat{\theta})}\left[\frac{2\mathcal{J}_2}{5}\right]^{1/2} + \frac{\mathcal{I}_1}{3\rho\sigma_c} \tag{24}$$

The function G stipulated in the expression above is implicitly dependent on $\mathcal{J}_3$ through a second angle of similitude, $\hat{\theta}$, which is defined by the expression

$$\cos(3\hat{\theta}) = \frac{(3\sqrt{3})\mathcal{J}_3}{2(\mathcal{J}_2)^{3/2}} \tag{25}$$

This formulation assumes a threshold does not exist for the scalar function G, and follows the framework of previously proposed constitutive models based on Robinson's (1978) viscoplastic law.

Threshold Parameters

For the Willam–Warnke three-parameter formulation, the model parameters include σ_t, the tensile uniaxial threshold stress, σ_c, the compressive uniaxial threshold stress, and σ_{bc}, the equal biaxial compressive threshold stress. The function $r(\tilde{\theta})$ appearing in Eq. (22) and the function $r(\hat{\theta})$ appearing in Eq. (24) depend implicitly on these parameters. This is demonstrated later in this section.

To explore the nature of the potential function, level surfaces of Ω are projected onto various stress subspaces for the virgin inelastic state. Restricting our view to the virgin inelastic state implies surfaces of Ω = const are also surfaces of F = const. As noted previously, F plays the role of a Bingham–Prager threshold function. Since there are an infinite family of surfaces F = const, each associated with a particular magnitude of the inelastic strain rate, we restrict the scope of this discussion to threshold surfaces to gain an understanding of the physical nature of the current model.

The parameters σ_t and σ_c are depicted in Fig. 1 where a threshold surface ($F = 0$) has been projected onto the $\sigma_{11}-\sigma_{22}$ stress subspace. For illustration, a set of threshold flow stress

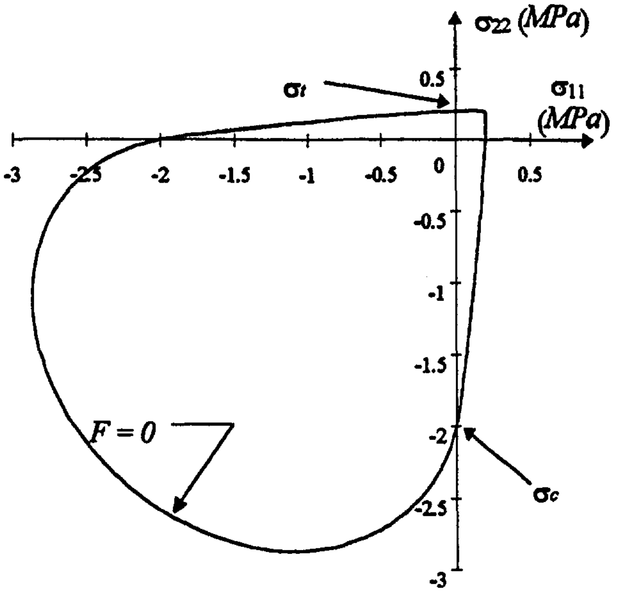

Fig. 1 Threshold function projected onto the $\sigma_{11}-\sigma_{22}$ stress plane

values has been adopted that roughly corresponds to values anticipated for isotropic monolithic ceramics. Specifically, the compressive uniaxial threshold stress value is $\sigma_c = 2.00$ MPa. The tensile uniaxial threshold stress value is $\sigma_t = 0.20$ MPa, and the equal biaxial compressive threshold stress value is $\sigma_{bc} = 2.32$ MPa. Using these stress threshold values, the flow function in Fig. 1 defines a smooth flow surface for any combination of stresses. States of stress lying within the flow surface depicted in this figure represent elastic states of stress. Inelastic flow occurs when any load path reaches this surface, or other surfaces beyond (i.e., surfaces where $F > 0$). It is readily discerned from this figure that the constitutive model allows different flow behavior in tension and compression.

The threshold parameter σ_{bc} can be seen when a cutting plane is passed through the flow surface ($F = 0$) in the Haigh–Westergaard stress space. Specifically the cutting plane contains the hydrostatic stress line and it intersects the conic surface ($F = 0$) along two lines (see Fig. 2). By convention, these lines of intersection are termed meridians. The relative position of each meridian is defined by the angle of similitude $\tilde{\theta}$ (which is depicted in Fig. 3). For the tensile meridian $\tilde{\theta} = 0$, and for the compressive meridian $\tilde{\theta} = \pi$. The tensile and compressive meridians, depicted in Fig. 2, are linear for the three-parameter Willam–Warnke criterion. Meridians are nonlinear for the five-parameter formulation. In Fig. 2 all three parameters, i.e., σ_t, σ_c, and σ_{bc} are visible. These parameters are defined by the intersection of load paths with the flow surface. This characterization of the threshold flow stresses is described in detail by Palko (1992). Also note that this formulation of the Bingham–Prager flow function introduces a dependence on the hydrostatic component of the stress state. Combining views from Figs. 2 and 3 in the Haigh–Westergaard stress space yields a flow surface in the shape of a pyramid with a triangular base. As a reference, typical J_2 plasticity models have yield surfaces that are right circular cylinders in the Haigh–Westergaard stress space.

In lieu of the previously mentioned three threshold stress parameters, the threshold parameters

$$\rho = \frac{Y_{bc}Y_t}{Y_{bc} - Y_t} \tag{26}$$

$$r_t = \left(\frac{6}{5}\right)^{1/2} \frac{Y_{bc}Y_t}{2Y_{bc} + Y_t} \tag{27}$$

and

$$r_c = \left(\frac{6}{5}\right)^{1/2} \left[\frac{Y_{bc}Y_t}{3Y_{bc}Y_t + Y_{bc} - Y_t}\right] \tag{28}$$

are utilized in order to simplify the expression presented later for the function r. These alternative threshold stress parameters are dependent on the parameters σ_t, σ_c, and σ_{bc}. Specifically, the normalized threshold stresses

$$Y_t = \frac{\sigma_t}{\sigma_c} \tag{29}$$

and

$$Y_{bc} = \frac{\sigma_{bc}}{\sigma_c} \tag{30}$$

are introduced to simplify Eqs. (26)–(28). Details of the derivations for the parameters appearing in Eqs. (26)–(28) can be found from either Palko (1992) or Chen (1982).

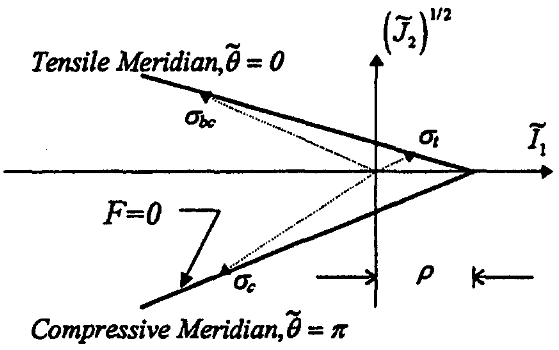

Fig. 2 Threshold flow stresses defined by the tensile and compressive meridians

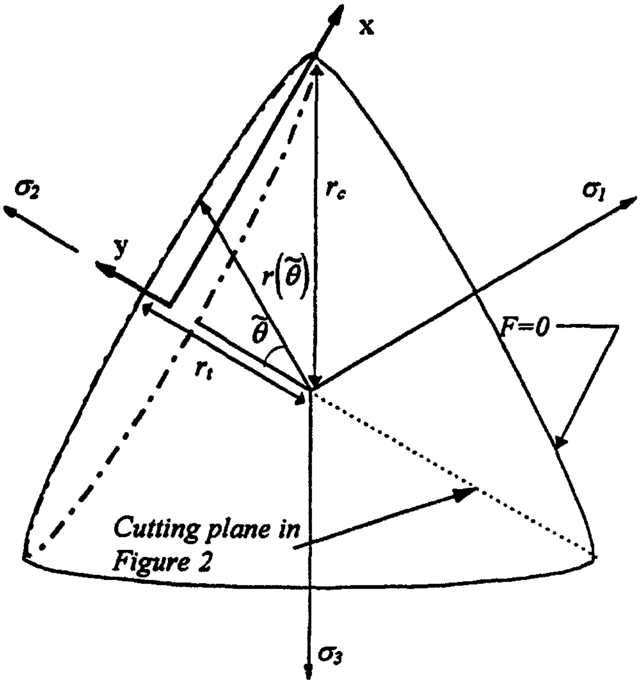

Fig. 3 Flow surface projected onto the Π-plane in the Haigh–Westergaard stress space

The parameter ρ is depicted graphically in Fig. 2. As noted earlier, this parameter is the tensile threshold hydrostatic flow stress. Willam and Warnke postulated that a single sector ($-\pi/3 \leq \theta \leq \pi/3$) of the flow surface in the Π-plane could be represented as a segment of an ellipse. The major and minor axes of the ellipse are formulated as functions of the intercepts r_c and r_t (see Fig. 3). The minor axis of the ellipse is assumed to coincide with a tensile axis. However, the center of the ellipse does not necessarily coincide with the hydrostatic axis, either for a material in the virgin state, or for a material that has been subjected to a service history. The reader should consult Palko (1992) for the complete derivation. With the function $r(\tilde{\theta})$ defined flow surface can be completely mapped in a Π-plane, as depicted in Fig. 3.

For either $\tilde{\theta}$ or θ the function $r(\theta)$ is defined as

$$r(\theta) = \frac{u(\theta)}{v(\theta)} \tag{31}$$

where

$$u(\theta) = 2r_c(r_c^2 - r_t^2)\cos(\theta) + r_c(2r_t - r_c)[4(r_c^2 - r_t^2) \times \cos^2(\theta) + 5r_t^2 - 4r_tr_c]^{1/2} \tag{32}$$

and

$$v(\theta) = 4(r_c^2 - r_t^2)\cos^2(\theta) + (r_c - 2r_t)^2 \qquad (33)$$

For the definitions expressed in Eqs. (31)–(33)

$$-\frac{\pi}{3} \le \theta \le \frac{\pi}{3} \qquad (34)$$

Physically, $r(\tilde{\theta})$ represents the deviatoric component of a stress state, since this vector lies in the Π-plane. Note that Eq. (31) yields $r(\tilde{\theta}) = r_t$ for the special case of $\tilde{\theta} = 0$. Similarly, $r(\tilde{\theta}) = r_c$ for $\tilde{\theta} = \pi/3$.

Flow Surfaces: Interpretation

As in Robinson's original theory, the current model is closely tied to the concepts of a potential function and normality. It is this potential-normality structure that provides a consistent framework. According to the stability postulate of Drucker (1959), the concepts of normality and convexity are important requirements, which must be imposed on the development of a flow or yield surface. Constitutive relationships developed on the basis of these requirements assure that the inelastic boundary-value problem is well posed, and solutions obtained are unique. Experimental work by Robinson and Ellis (1985) has demonstrated the validity of the potential-normality structure relative to an isotropic J_2 alloy (i.e., type 316 stainless steel). With this structure, the direction of the inelastic strain rate vector for each stress point on a given surface is directed normal to the flow surface F = const (see Fig. 4). Without experimental evidence to the contrary, it is postulated that this structure is similarly valid for isotropic monolithic ceramic materials.

For constitutive models based on Robinson's (1978) original framework flow surfaces generated by nonzero values of F are associated with different inelastic strain rates. Figure 4 illustrates a typical family of level surfaces generated by monotonically increasing the magnitude of F ($\alpha_{ij} = 0$). The family is projected onto the σ_{11}–σ_{22} stress plane. Large values of F = const correspond to flow surfaces that eventually cluster, forming a limiting surface. This implies large changes in inelastic strain rate for only small stress changes, analogous to the yield condition of classical plasticity. This feature was pointed out originally by Rice (1970) for constitutive models based on Eq. (6).

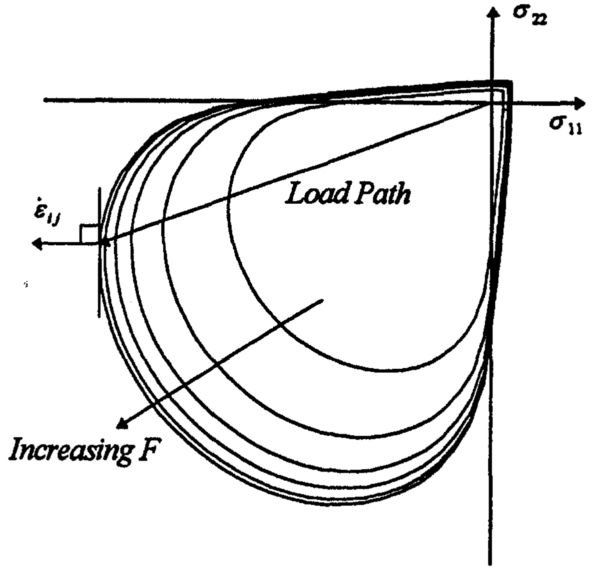

Fig. 4 Flow surfaces associated with a monotonically increasing value of the flow function F

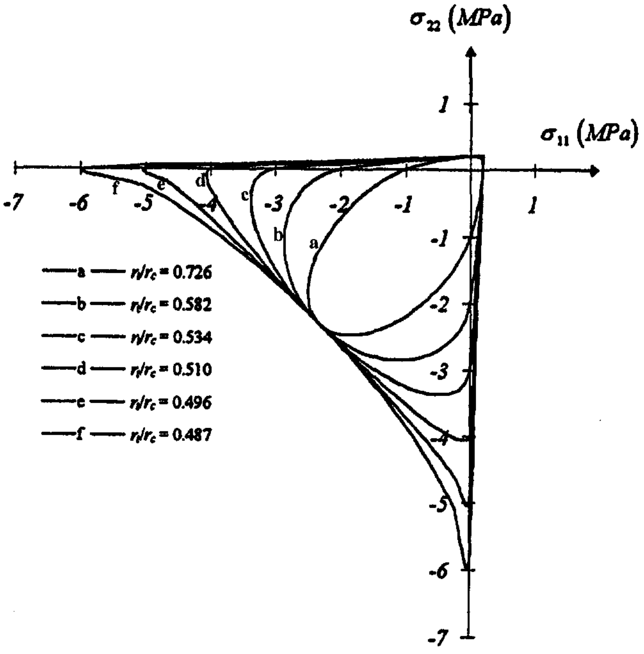

Fig. 5 Flow surfaces as a function of the ratio r_t/r_c

The convexity of the proposed flow surface assures stable material behavior, i.e., positive dissipation of inelastic work, which is based on thermodynamic principles. The convexity requirement also implies that level surfaces of a function are closed surfaces, since an open region of the flow surface allows the existence of a load path along which failure will never occur. For the Willam–Warnke model, convexity is assured if the ratio of the intercepts in the Π-plane satisfies the condition $1.0 \ge r_t/r_c > 0.5$. The family of surfaces shown in Fig. 5 illustrates the concept of convexity for surfaces having various r_t/r_c ratios. Here the values of the ratio vary from 0.726 to 0.487. Notice the surfaces identified as "e" and "f" violate the convexity condition.

Finally, the Willam–Warnke flow criterion (and the constitutive theory presented herein) degenerates to simpler models under special limiting conditions. For the case of $r_c = r_t = r_o$, where r_o is the same for any angle $\tilde{\theta}$, the model degenerates to a two-parameter formulation, i.e., the Drucker–Prager flow criterion. When projected onto the σ_{11}–σ_{22} stress plane under these conditions, the flow surface depicted in Fig. 1 degenerates to an ellipse (see Fig. 6). Note that the major axis of this ellipse

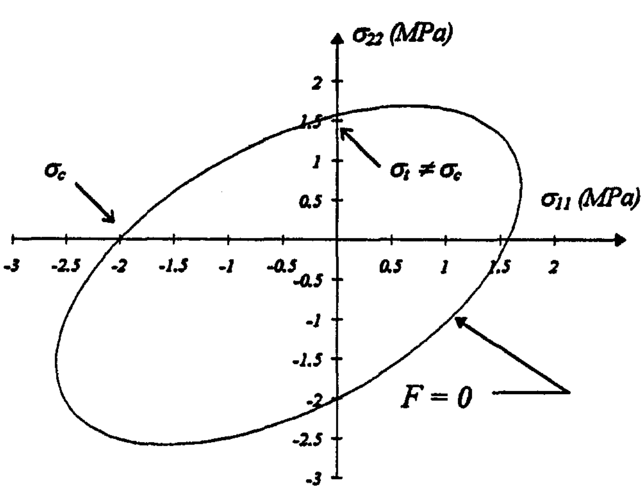

Fig. 6 Flow surface for the Drucker–Prager formulation

is aligned with the bisector of the first and third quadrants, and the intercepts along the σ_{11} and σ_{22} axes represent uniaxial tensile and compressive threshold stresses that are not equal in magnitude, even though the flow surface degenerates to a circle in the Π-plane. The Drucker–Prager formulation yields different tensile and compressive threshold stresses because the formulation produces a right circular cone in the three-dimensional Haigh–Westergaard stress space. For the special case where $r_c = r_t = r_o$ and $\rho = \infty$, the Willam–Warnke model reduces to the single-parameter Von Mises criterion. For this case, the flow surface degenerates to a circle in the Π-plane (a right circular cylinder in the three-dimensional Haigh–Westergaard stress space) and an ellipse in $\sigma_{11}-\sigma_{22}$ stress space, which is depicted in Fig. 7.

Stress–Strain Relationship

Employing the chain rule for differentiation and taking the partial derivative of Ω with respect to σ_{ij}, as indicated in Eq. (6), yields

$$\dot{\epsilon}_{ij} = \left(\frac{\partial\Omega}{\partial F}\right)\left[\frac{\partial F}{\partial \tilde{I}_1}\frac{\partial \tilde{I}_1}{\partial \eta_{kl}}\frac{\partial \eta_{kl}}{\partial \sigma_{ij}} + \frac{\partial F}{\partial \tilde{J}_2}\frac{\partial \tilde{J}_2}{\partial \Sigma_{uv}}\frac{\partial \Sigma_{uv}}{\partial S_{mn}}\frac{\partial S_{mn}}{\partial \sigma_{ij}} + \frac{\partial F}{\partial \tilde{J}_3}\frac{\partial \tilde{J}_3}{\partial \Sigma_{uv}}\frac{\partial \Sigma_{uv}}{\partial S_{mn}}\frac{\partial S_{mn}}{\partial \sigma_{ij}}\right] \quad (35)$$

where Eq. (8) has been utilized to define Ω.

Evaluating the partial derivative terms in Eq. (35) yields the following expression for the flow law

$$\dot{\epsilon}_{ij} = C_0\left[C_1\delta_{ij} + C_2\Sigma_{ij} + C_3\left(\Sigma_{jq}\Sigma_{qi} - \frac{2\tilde{J}_2\delta_{ij}}{3}\right)\right] \quad (36)$$

where the magnitudes of the coefficients C_0, C_1, C_2, and C_3 are dependent on the invariants defined in Eqs. (14)–(16) (i.e., $\tilde{I}_1$, $\tilde{J}_2$, and $\tilde{J}_3$), the three threshold parameters (i.e., σ_t, σ_c, and σ_{bc}), and the flow potential parameters utilized in Eq. (8) (i.e., μ, K, and n). The first coefficient is defined by the expression

$$C_0 = \frac{K^2F^n}{2\mu} \quad (37)$$

The remaining three coefficients are defined as

$$C_1 = \frac{1}{3\rho\sigma_c} \quad (38)$$

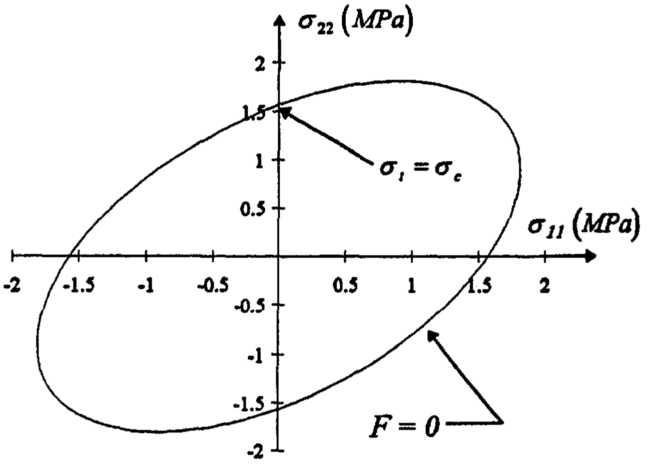

Fig. 7 Flow surface for the Von Mises formulation

$$C_2 = \left[\frac{1}{2r(\tilde{\theta})\sigma_c}\right]\left[\frac{2}{5\tilde{J}_2}\right]^{1/2} - \frac{1}{\sigma_c}\left[\frac{1}{r(\tilde{\theta})}\right]^2\left[\frac{2\tilde{J}_2}{5}\right]^{1/2}\left[\frac{\partial r(\tilde{\theta})}{\partial \tilde{J}_2}\right] \quad (39)$$

and

$$C_3 = -\frac{1}{\sigma_c}\left[\frac{2\tilde{J}_2}{5}\right]^{1/2}\left[\frac{\partial r(\tilde{\theta})}{\partial \tilde{J}_3}\right]\left[\frac{1}{r(\tilde{\theta})}\right]^2 \quad (40)$$

Note that the partial derivatives of $r(\tilde{\theta})$ appearing in Eqs. (39) and (40) are defined as

$$\frac{\partial r(\tilde{\theta})}{\partial \tilde{J}_2} = \left\{\frac{1}{v(\tilde{\theta})}\left[\frac{du(\tilde{\theta})}{d\tilde{\theta}}\right] - \frac{u(\tilde{\theta})}{v^2(\tilde{\theta})}\left[\frac{dv(\tilde{\theta})}{d\tilde{\theta}}\right]\right\} \times \left\{\frac{3\sqrt{3}\tilde{J}_3}{2\tilde{J}_2[4(\tilde{J}_2)^3 - 27(\tilde{J}_3)^2]^{1/2}}\right\} \quad (41)$$

and

$$\frac{\partial r(\tilde{\theta})}{\partial \tilde{J}_3} = -\left\{\frac{1}{v(\tilde{\theta})}\left[\frac{du(\tilde{\theta})}{d\tilde{\theta}}\right] - \frac{u(\tilde{\theta})}{v^2(\tilde{\theta})}\left[\frac{dv(\tilde{\theta})}{d\tilde{\theta}}\right]\right\} \times \left\{\frac{\sqrt{3}}{[4(\tilde{J}_2)^3 - 27(\tilde{J}_3)^2]^{1/2}}\right\} \quad (42)$$

where

$$\frac{du(\tilde{\theta})}{d\tilde{\theta}} = 2r_c(r_t^2 - r_c^2)\sin(\tilde{\theta}) + \frac{4r_c(2r_t - r_c)(r_t^2 - r_c^2)\sin(\tilde{\theta})\cos(\tilde{\theta})}{[4(r_c^2 - r_t^2)\cos^2(\tilde{\theta}) + 5r_t^2 - 4r_tr_c]^{1/2}} \quad (43)$$

and

$$\frac{dv(\tilde{\theta})}{d\tilde{\theta}} = 8(r_t^2 - r_c^2)\sin(\tilde{\theta})\cos(\tilde{\theta}) \quad (44)$$

Similarly, utilizing the chain rule for differentiation and taking the partial derivative of Ω with respect to the internal stress α_{ij} as indicated in Eq. (7) yields

$$\begin{aligned}\dot{\alpha}_{ij} &= -h\left(\frac{\partial\Omega}{\partial F}\frac{\partial F}{\partial \alpha_{ij}} + \frac{\partial\Omega}{\partial G}\frac{\partial G}{\partial \alpha_{ij}}\right)\\ &= -h\left\{\left(\frac{\partial\Omega}{\partial F}\right)\left[\frac{\partial F}{\partial \tilde{I}_1}\frac{\partial \tilde{I}_1}{\partial \eta_{kl}}\frac{\partial \eta_{kl}}{\partial \alpha_{ij}} + \frac{\partial F}{\partial \tilde{J}_2}\frac{\partial \tilde{J}_2}{\partial \Sigma_{uv}}\frac{\partial \Sigma_{uv}}{\partial a_{mn}}\frac{\partial a_{mn}}{\partial \alpha_{ij}} + \frac{\partial F}{\partial \tilde{J}_3}\frac{\partial \tilde{J}_3}{\partial \Sigma_{uv}}\frac{\partial \Sigma_{uv}}{\partial a_{mn}}\frac{\partial a_{mn}}{\partial \alpha_{ij}}\right] + \left(\frac{\partial\Omega}{\partial G}\right)\left[\frac{\partial G}{\partial \mathcal{I}_1}\frac{\partial \mathcal{I}_1}{\partial \alpha_{ij}} + \frac{\partial G}{\partial \mathcal{J}_2}\frac{\partial \mathcal{J}_2}{\partial a_{uv}}\frac{\partial a_{uv}}{\partial \alpha_{ij}} + \frac{\partial G}{\partial \mathcal{J}_3}\frac{\partial \mathcal{J}_3}{\partial a_{uv}}\frac{\partial a_{uv}}{\partial \alpha_{ij}}\right]\right\}\end{aligned} \quad (45)$$

Evaluating the partial derivative terms in Eq. (43) yields the following expression for the evolutionary law:

$$\dot{\alpha}_{ij} = h\left\{\dot{\epsilon}_{ij} - C_4\left[C_1\delta_{ij} +.C_5a_{ij} + C_6\left(a_{jq}a_{qi} - \frac{2\mathcal{J}_2\delta_{ij}}{3}\right)\right]\right\} \quad (46)$$

where $\dot{\epsilon}_{ij}$ is given in Eq. (36). The magnitudes of the coefficients C_4, C_5, and C_6 are dependent on the invariants defined in Eqs. (17)–(19) (i.e., $\mathcal{I}_1$, $\mathcal{J}_2$, and $\mathcal{J}_3$), the three threshold parameters (i.e., σ_t, σ_c, and σ_{bc}), and the flow potential parameters utilized in equation (8) (i.e., R, H, K, and m). The first coefficient is defined by the expression

$$C_4 = \frac{K^2 R G^m}{H} \tag{47}$$

The remaining two coefficients are defined as

$$C_5 = \left[\frac{1}{2r(\hat{\theta})\sigma_c}\right]\left[\frac{2}{5\mathcal{J}_2}\right]^{1/2} - \frac{1}{\sigma_c}\left[\frac{1}{r(\hat{\theta})}\right]^2\left[\frac{2\mathcal{J}_2}{5}\right]^{1/2}\left[\frac{\partial r(\hat{\theta})}{\partial \mathcal{J}_2}\right] \tag{48}$$

and

$$C_6 = -\frac{1}{\sigma_c}\left[\frac{2\mathcal{J}_2}{5}\right]^{1/2}\left[\frac{\partial r(\hat{\theta})}{\partial \mathcal{J}_3}\right]\left[\frac{1}{r(\hat{\theta})}\right]^2 \tag{49}$$

Note that the partial derivatives of $r(\hat{\theta})$ appearing in Eqs. (48) and (49) are defined as

$$\frac{\partial r(\hat{\theta})}{\partial \mathcal{J}_2} = \left\{\frac{1}{v(\hat{\theta})}\left[\frac{du(\hat{\theta})}{d\hat{\theta}}\right] - \frac{u(\hat{\theta})}{v^2(\hat{\theta})}\left[\frac{dv(\hat{\theta})}{d\hat{\theta}}\right]\right\} \times \left\{\frac{3\sqrt{3}\,\mathcal{J}_3}{2\,\mathcal{J}_2[4(\mathcal{J}_2)^3 - 27(\mathcal{J}_3)^2]^{1/2}}\right\} \tag{50}$$

and

$$\frac{\partial r(\hat{\theta})}{\partial \mathcal{J}_3} = -\left\{\frac{1}{v(\hat{\theta})}\left[\frac{du(\hat{\theta})}{d\hat{\theta}}\right] - \frac{u(\hat{\theta})}{v^2(\hat{\theta})}\left[\frac{dv(\hat{\theta})}{d\hat{\theta}}\right]\right\} \times \left\{\frac{\sqrt{3}}{[4(\mathcal{J}_2)^3 - 27(\mathcal{J}_3)^2]^{1/2}}\right\} \tag{51}$$

Equations (36) and (46) constitute a multiaxial statement of a constitutive theory for isotropic materials. In the present and subsequent developments, it will serve as an inelastic deformation model for ceramic materials.

Summary and Conclusions

A multiaxial continuum theory was presented for predicting the inelastic response of isotropic monolithic ceramic materials. The viscoplastic constitutive model was derived from a single scalar dissipative function, which has similar geometric interpretations (e.g., convexity and normality) to the yield function encountered in classical plasticity. By adopting a flow potential to derive the theory, certain required continuum properties can be demonstrated, thereby ensuring that the resulting inelastic boundary value problem is well-posed, and solutions obtained are unique.

Constitutive equations for the flow law (strain rate) and evolutionary law are formulated based on a threshold function, which exhibits a sensitivity to hydrostatic stress and allows different behavior in tension and compression. Further, inelastic deformation is treated as inherently time dependent. A rate of inelastic strain is associated with every state of stress. As a result, creep, stress relaxation, and rate sensitivity are phenomena resulting from applied boundary conditions and are not treated separately in an ad hoc fashion.

The overview presented in this paper has provided a qualitative assessment of the capabilities of this viscoplastic model in capturing the complex thermomechanical behavior exhibited by ceramic materials at elevated service temperatures. Incorporating this model into a nonlinear finite element code would provide industry the means to numerically simulate the inherently time-dependent and hereditary phenomena exhibited by these materials in service.

References

Bingham, E. C., 1922, *Fluidity and Plasticity,* McGraw-Hill, New York.

Chen, W. F., 1982, *Plasticity in Reinforced Concrete,* McGraw-Hill, New York.

Chuang, T.-J., and Duffy, S. F., 1994, "A Methodology to Predict Creep Life for Advanced Ceramics Using Continuum Damage Mechanics," *Life Prediction Methodologies and Data for Ceramic Materials,* ASTM STP 1201, C. R. Brinkman and S. F. Duffy, eds., American Society for Testing and Materials, Philadelphia, pp. 207–227.

Corapcioglu, Y., and Uz, T., 1978, "Constitutive Equations for Plastic Deformation of Porous Materials," *Powder Technology,* Vol. 21, pp. 269–274.

Ding, J.-L., Liu, K. C., and Brinkman, C. R., 1994, "A Comparative Study of Existing and Newly Proposed Models for Creep Deformation and Life Prediction of Si3N4," in: *Life Prediction Methodologies and Data for Ceramic Materials,* ASTM STP 1201, C. R. Brinkman and S. F. Duffy, eds., American Society for Testing and Materials, Philadelphia, pp. 62–83.

Drucker, D. C., 1959, "A Definition of Stable Inelastic Material," ASME *Journal of Applied Mechanics,* Vol. 26, pp. 101–106.

Duffy, S. F., 1988, "A Unified Inelastic Constitutive Theory for Sintered Powder Metals," *Mechanics of Materials,* Vol. 7, pp. 245–254.

Green, R. J., 1972, "A Plasticity Theory for Porous Solids," *International Journal for Mechanical Sciences,* Vol. 14, pp. 215.

Gurson, A. L., 1977, "Continuum Theory of Ductile Rupture by Void Nucleation and Growth: Part I—Yield Criteria and Flow Rules for Porous Ductile Media," ASME *Journal of Engineering Materials and Technology,* Vol. 99, pp. 2–15.

Hohenemser, K., and Prager, W., 1932, "Ueber die Ansaetze der Mechanik Isotroper Kontinua," *Zeit fuer angewandte Mathematik und Mechanik,* Vol. 12.

Janosik, L. A., 1998, "A Unified Viscoplastic Constitutive Theory for Monolithic Ceramics," Master's Thesis, Cleveland State University, Cleveland, OH.

Kuhn, H. A., and Downey, C. L., 1971, "Deformation Characteristics and Plasticity Theory of Sintered Powder Metals," *International Journal of Powder Metallurgy,* Vol. 7, pp. 15–25.

Liu, K. C., Brinkman, C. R., Ding, J.-L., and Liu, S., 1997, "Predictions of Tensile Behavior and Strengths of Si_3N_4 Ceramic at High Temperatures Based on a Viscoplastic Model," ASME JOURNAL OF ENGINEERING FOR GAS TURBINES AND POWER, Vol. 119, pp. 200–204.

Mear, M. E., and Hutchinson, J. W., 1985, "Influence of Yield Surface Curvature on Flow Localization in Dilatant Plasticity," *Mechanics of Materials,* Vol. 4, pp. 395–407.

Palko, J. L., 1992, "Interactive Reliability Model for Whisker-Toughened Ceramics," Master's Thesis, Cleveland State University, Cleveland, OH.

Ponter, A. R. S., and Leckie, F. A., 1976, "Constitutive Relationships for Time-Dependent Deformation of Metals," ASME *Journal of Engineering Materials and Technology,* Vol. 98.

Rice, J. R., 1970, "On the Structure of Stress-Strain Relations for Time-Dependent Plastic Deformation in Metals," ASME *Journal of Applied Mechanics,* Vol. 37, p. 728.

Robinson, D. N., 1978, "A Unified Creep-Plasticity Model for Structural Metals at High Temperature," ORNL/TM 5969.

Robinson, D. N., and Swindeman, R. W., 1982, "Unified Creep-Plasticity Constitutive Equations for 2-1/4 CR-1 Mo Steel at Elevated Temperature," ORNL/TM 8444.

Robinson, D. N., and Ellis, J. R., 1985, "Experimental Determination of Flow Potential Surfaces Supporting a Multiaxial Formulation of Viscoplasticity," *Proc. 5th International Seminar on Inelastic Analysis and Life Prediction in High Temperature Environments,* Paris, France.

Shima, S., and Oyane, M., 1976, "Plasticity Theory for Porous Metals," *International Journal of Mechanical Sciences,* Vol. 18, p. 285.

White, C. S., and Hazime, R. M., 1995, "Internal Variable Modeling of the Creep of Monolithic Ceramics," *Proc. 11th Biennial Conference on Reliability, Stress Analysis, and Failure Prevention,* O. Jadaan, ed., The American Society of Mechanical Engineers, Philadelphia, PA.

Willam, K. J., and Warnke, E. P., 1975, "Constitutive Model for the Triaxial Behaviour of Concrete," *Int. Assoc. Bridge Struct. Eng. Proc.,* Vol. 19, pp. 1–30.

Creep Life of Ceramic Components Using a Finite-Element-Based Integrated Design Program (CARES/CREEP)

L. M. Powers
Cleveland State University,
Cleveland, OH 44115

O. M. Jadaan
University of Wisconsin—Platteville,
Platteville, WI 53818

J. P. Gyekenyesi
NASA-Lewis Research Center,
Cleveland, OH 44135

The desirable properties of ceramics at high temperatures have generated interest in their use for structural applications such as in advanced turbine systems. Design lives for such systems can exceed 10,000 hours. The long life requirement necessitates subjecting the components to relatively low stresses. The combination of high temperatures and low stresses typically places failure for monolithic ceramics in the creep regime. The objective of this paper is to present a design methodology for predicting the lifetimes of structural components subjected to creep rupture conditions. This methodology utilizes commercially available finite element packages and takes into account the time-varying creep strain distributions (stress relaxation). The creep life of a component is discretized into short time steps, during which the stress and strain distributions are assumed constant. The damage is calculated for each time step based on a modified Monkman–Grant creep rupture criterion. Failure is assumed to occur when the normalized accumulated damage at any point in the component is greater than or equal to unity. The corresponding time will be the creep rupture life for that component. Examples are chosen to demonstrate the CARES/CREEP (Ceramics Analysis and Reliability Evaluation of Structures/CREEP) integrated design program, which is written for the ANSYS finite element package. Depending on the component size and loading conditions, it was found that in real structures one of two competing failure modes (creep or slow crack growth) will dominate. Applications to benchmark problems and engine components are included.

Introduction

Advanced structural ceramics are becoming viable materials for many high-temperature applications including gasoline, diesel, and gas turbine engine components. Attractive properties such as low density, high strength, high stiffness, and corrosion resistance are allowing ceramics to supplant alloys in these demanding applications. The result is lower engine emissions, higher fuel efficiency, and more optimum design.

As design protocols emerge for these material systems, designers must be aware of several innate characteristics of ceramics. These include the degrading ability of ceramics to carry sustained loading. Generally, time-dependent failure in ceramics occurs because of two different delayed failure mechanisms, slow crack growth (SCG) and creep rupture. SCG usually initiates at a pre-existing flaw and continues until a critical crack length is reached, causing catastrophic failure (Wiederhorn, 1974). Creep rupture, on the other hand, occurs because of bulk damage in the material in the form of void nucleation and coalescence that eventually leads to macrocracks, which then propagate to failure (Grathwohl, 1984).

Based on the two different delayed failure mechanisms presented above, probabilistic analysis and design methodologies are utilized to predict the lifetime of ceramic components subjected to sustained loading conditions leading to failure in SCG mode. Several integrated design codes such as CARES (Nemeth et al., 1990), CARES/LIFE (Nemeth et al., 1993), and SPSLIFE (Saith et al., 1994) are available and have been demonstrated to be successful in predicting the failure probability for ceramic components subjected to fast fracture and SCG failure modes.

However, no such integrated design codes exist currently for predicting the nonlinear behavior and lifetime of ceramic components subjected to creep rupture conditions. One reason for this is the type of ceramics that existed until recently. These ceramics were processed using relatively large amounts of sintering aids that resulted in glassy intergranular phases, which become viscous at high temperatures, thus limiting their creep resistance in the temperature range where ceramics are needed most.

The advent of new techniques in ceramic processing technology has yielded a new class of ceramics that are highly resistant to creep at high temperatures (Ferber et al., 1994; Ding et al., 1994; Menon et al., 1994a). Such desirable properties have generated interest in using ceramics for turbine engine component applications where the design lives for such systems are on the order of 10,000 to 30,000 hours. These long life requirements necessitate subjecting the components to relatively low stresses. The combination of high temperatures and low stresses typically places failure for monolithic ceramics in the creep and creep rupture region of a time–temperature–failure mechanism map (Wiederhorn et al., 1994; Quinn, 1990).

The objective of this paper is to describe an analytical methodology and an integrated design program named CARES/CREEP (Ceramics Analysis and Reliability Evaluation of Structures/CREEP) to be used for predicting the lifetimes of ceramic structural components subjected to creep rupture conditions. This methodology utilizes commercially available finite element packages and takes into account the transient state of stress and creep strain distributions (stress relaxation). The creep life of a component is discretized into short time steps, during which the stress distribution is assumed constant. The

---

Contributed by the International Gas Turbine Institute and presented at the 41st International Gas Turbine and Aeroengine Congress and Exhibition, Birmingham, United Kingdom, June 10–13, 1996. Manuscript received at ASME Headquarters February 1996. Paper No. 96-GT-369. Associate Technical Editor: J. N. Shinn.

damage is calculated for each time step based on a modified Monkman–Grant (MMG) creep rupture criterion (Menon et al., 1994b). The cumulative damage is subsequently calculated as time elapses in a manner similar to Miner's rule for cyclic fatigue loading. Failure is assumed to occur when the normalized cumulative damage at any point in the component reaches unity. The corresponding time will be the creep rupture life for that component.

The CARES/CREEP program is made up of two modules, and is currently customized to run as a postprocessor to the ANSYS finite element code. The first module is a parameter estimation program used to compute the primary creep parameters based on the time hardening rule, the steady-state parameters based on the Norton equation, and the creep rupture parameters based on the MMG criterion. The second module contains the coding for calculating the cumulative damage, and thus the creep rupture life for the component in question.

Background

Engineers involved in designing components against creep failure are generally interested in calculating the creep deformation and predicting the lifetime for these components when subjected to sustained multi-axial thermomechanical loading. Both endeavors include modeling the material's creep behavior using appropriate constitutive equations, and subsequently choosing a rupture criterion suitable to that material. This section contains a brief literature review on creep covering these two perspectives.

Creep Constitutive Relations. The creep strain curve resulting from a constant load test is a function of stress, temperature, and time. Many uniaxial constitutive laws have been proposed to describe such standard creep curves. Currently, there exist two general formulations for creep modeling. The first is referred to as the equation of state formulation and assumes that the material behavior depends on the present state only. The second approach, named memory theory (Krempl, 1974), takes into account that the material remembers the loading and temperature history and thus responds accordingly. At this point, most of the material modeling discussed in the literature is based on the equation of state formulation because of its proven success and relative ease of use with computer programs. Thus, only models based on the equation of state formulation will be reviewed.

Several proposed constitutive relations are capable of simulating the entire creep curve (primary, secondary, and tertiary). These laws include the theta projection method (Evans and Wilshire, 1985; Evans et al., 1987; Foley et al., 1992; Maruyama and Oikawa, 1987), the continuum damage mechanics approach (Kachanov, 1960; Dunne et al., 1990; Hayhurst et al., 1975; Othman and Hayhurst, 1990), and the internal (back) stress model (White and Hazime, 1995; Brown et al., 1989; Kraus, 1980; LeGac and Duval, 1980).

Many types of ceramics, however, do not display tertiary creep behavior (Sundberg et al., 1994; Cuccio et al., 1995; Ohji and Yamauchi, 1993; Lewis and Ostvoll, 1992; Sankar et al., 1994). Therefore, it is appropriate for creep analysis of ceramics to use constitutive equations describing only the primary and secondary creep regions. Many formulas, and combinations of these formulas, exist for such formulation. One of these constitutive laws is known as the Bailey–Norton time hardening rule (Kraus, 1980; Norton, 1929; Boyle and Spence, 1983) and is given by the following equation:

$$\dot{\epsilon} = a_1 \sigma^{a_2} t^{a_3} \exp\left[-\frac{Q}{RT} \right] \tag{1}$$

where $\dot{\epsilon}$ is the creep strain rate; σ, t, and T are the stress, time, and absolute temperature. The material constants a_1, a_2, a_3, and Q are determined from experiments and R is the universal gas constant. The Baily–Norton constitutive law was selected to describe the creep behavior of ceramics in the CARES/CREEP code, because of its widespread use, and success in fitting the creep data as a function of stress, temperature, and time. Furthermore, this relationship, in association with Prandlt–Reuss plasticity flow rule, satisfies four basic requirements for multi-axial creep analysis (Kraus, 1980). These requirements are: (1) The multiaxial formulation must reduce to the uniaxial formulation when appropriate, (2) the model contains constancy of volume for creep conditions, (3) the model reflects lack of influence of hydrostatic stress, and (4) principal directions of stress and strain coincide. The constancy of volume requirement is a result of the original development of this theory for metals. Ceramics contain voids, which expand under creep conditions. A theory incorporating this phenomenon is not available for finite element calculations.

Creep Rupture. The majority of current engineering design methodologies against creep fit into four major categories. The first is graphic, where the time to reach a given strain, or fracture, at a given stress or temperature is obtained from a creep life diagram. Some of the techniques that belong to this group are the Larson–Miller (Larson and Miller, 1952), Sherby–Dorn (Orr et al., 1954), minimum commitment (Manson and Ensign, 1971), Manson–Halferd (Manson and Halferd, 1953), Manson–Succop (Conway, 1968), Quinn (1986), and Jones (1986) methods. These approaches utilize parameters that when plotted against stress would yield unique curves that can be used to predict the life of components subjected to creep rupture loading.

The second category includes analytical methods to predict the creep life for structural components. The Monkman–Grant (MG) method (Monkman and Grant, 1956) is one of the most utilized approaches for ceramics and is based on a power relation between time to failure and steady-state creep rate given by the following equation:

$$\dot{\epsilon}^{b_2} t_f = b_1 \tag{2}$$

where t_f is the time to failure and b_1 and b_2 are constants. This equation assumes that a unique curve can describe failure for a given material independent of temperature. This assumption was found to be invalid for some ceramic materials (Ferber and Jenkins, 1992; Luecke et al., 1993; Menon et al., 1994a), which displayed stratification of the MG curve depending on the temperature level. Thus, a modified Monkman–Grant equation was introduced (Menon et al., 1994b) to take the temperature into account and is given by the following formula:

$$\ln t_f = d_1 - d_2 \ln \dot{\epsilon} + \frac{d_3}{T} \tag{3}$$

where d_1, d_2, and d_3 are constants. The MG and the MMG criteria were found to be very successful in describing the creep rupture behavior for ceramics, and thus are used heavily in the ceramics literature. For this reason, these criteria were selected as the basis for predicting the creep life of ceramic components in the CARES/CREEP code. Note that the MMG criterion collapses to the MG criterion when d_3 is set equal to zero.

Differential formulations constitute the models making up the third category of approaches for creep rupture prediction. Continuum damage mechanics (Kachanov, 1960; Dunne et al., 1990; Hayhurst et al., 1975; Othman and Hayhurst, 1990), and internal (back) stress concepts (White and Hazime, 1995; Brown et al., 1989; Kraus, 1980; LeGac and Duval, 1980) belong to this category.

Probabilistic formulations make up the fourth category for creep rupture life prediction. Currently, most ceramic researchers utilize deterministic approaches to describe creep deformation (hence, creep parameters), and to even predict creep rupture lives. Ceramic creep deformation, and thus creep parameters, display less stochastic and more deterministic behavior compared to fast fracture and slow crack growth failure data. An indication of that is the absence of the so-called "size effect" (Wiederhorn, et al., 1993), which is a characteristic for the probabilistic behavior of brittle fracture in ceramics.

However, some ceramics tend to display significant scatter in the creep rupture data (Khandelwal et al., 1995). The advent of new ceramic fabrication techniques, such as HIP with low levels of sintering phases, have resulted in materials that are highly resistant to creep. These improved fabrication methods yield thinner amorphous grain boundary phases, which are subsequently crystallized using heat treatment. For such materials (Ferber et al., 1994; Menon et al., 1994a) cavitation was found to control the creep deformation, while SCG controlled failure. This type of failure mechanism could be one of the reasons contributing to the significant scatter in the creep rupture data, and thus fuels the argument for utilizing probabilistic rather than deterministic procedures for predicting the creep life of ceramic components.

The theoretical development for stochastically predicting the creep life of ceramic structures is not well developed and still is in its infancy. One theory is based on the premise that both SCG and creep failure modes are acting simultaneously (Lange, 1976). Another combines continuum damage mechanics and the Weibull distribution, assuming that the failure processes for SCG and creep are separable (Duffy and Gyekenyesi, 1989).

A probabilistic creep theory is not well developed at this point. Also, data to support the probabilistic treatment are not available. The CARES/CREEP code (at this time) utilizes a deterministic approach to predict creep life. Incorporating probabilistic creep life prediction is, however, planned for future enhancements of the code.

Theory

The creep response of a ceramic component must be evaluated in order to determine its service life. Monolithic ceramics usually exhibit primary and secondary creep behavior, while failure occurs without warning. The life of a component is determined by calculating the damage over time. Creep of ceramic components is divided into two phases: evaluating the nonlinear stress response and assessing the damage of the component.

Nonlinear Stress Response. The creep curve is broken up into three stages: primary, secondary, and tertiary. The models for this response were built to match the experimental data with the ANSYS creep equations. The three regions of the creep curve are considered separately. Primary and secondary creep may be modeled within the finite element software where tertiary creep is not taken into account. The tertiary stage is usually not modeled since it implies impending failure. ANSYS contains a library of strain rate equations characteristic of materials being used in creep design applications. The creep strain rates for primary and secondary creep are a function of stress, time, and temperature.

ANSYS does not divide creep into unique stages as is done in conventional creep physics. Both primary and secondary creep are assumed to be in effect simultaneously. Thus, the material constants for these relations must be computed to account for this effect. The total creep strain is given by

$$\epsilon_{cr} = \epsilon_p + \epsilon_s \tag{4}$$

where ϵ_p is the primary and ϵ_s is the secondary components of creep strain. The primary creep strain rate is given as

$$\dot{\epsilon}_p = C_1 \sigma^{C_2} t^{C_3} \exp\left[-\frac{C_4}{T}\right] \tag{5}$$

The secondary creep strain rate is given by

$$\dot{\epsilon}_s = C_7 \sigma^{C_8} \exp\left[-\frac{C_{10}}{T}\right] \tag{6}$$

where C_i are constants and parameters determined from creep experiments. These constants are not numbered sequentially since i is the location of the value in the ANSYS data table.

Typically, data available from creep experiments will be in the form of a creep response curve, where the strain is recorded as a function of time when a constant load is applied. In order to evaluate material properties, several of these tests should be conducted at varying stress levels and temperatures. After subtracting the elastic strain from the total strain, the first step in parameter estimation is to determine the parameters for secondary creep. To evaluate the material parameters for Eq. (6), the minimum creep rate, $d\epsilon/dt$, is evaluated for each specimen. This value may be obtained graphically or by assuming the creep response curve is linear over a fixed time and performing a least-squares best-fit analysis on the data. The second method is preferable for computer algorithms where large amounts of data are processed numerically. The time where linearity begins varies for each specimen. This value is defined as the primary to secondary transition time, t_{ps}.

Once the minimum creep rates for all of the specimens are known, the parameters C_7, C_8, and C_{10} may be determined. An iterative procedure (Sundberg et al., 1994), is used to find these values as a function of $\dot{\epsilon}_s$, σ, and T. Equation (6) is rearranged twice to isolate two of the variables for a least squares analysis. These relationships are

$$\ln\,[\dot{\epsilon}_s \sigma^{-C_8}] = \ln\,(C_7) - \frac{C_{10}}{T} \tag{7}$$

and

$$\ln\left[\dot{\epsilon}_s \exp\left(\frac{C_{10}}{T}\right)\right] = \ln\,(C_7) + C_8 \ln \sigma \tag{8}$$

Initially, C_8 is assigned a default or user-supplied value, and then a least-squares best-fit analysis is done to find C_7 and C_{10}. Using the improved estimation on C_{10}, Eq. (8) is evaluated for estimates on the other parameters. This process continues until the solution converges.

The primary creep parameters, C_i, $i = 1, 4$, may be evaluated at this point. Since ANSYS divides the creep response as given by Eq. (4), the primary component of creep strain is evaluated by subtracting the secondary creep strain from the total creep strain. The secondary creep strain is calculated using the secondary creep parameters estimated for the material. The primary creep strain component is evaluated over the entire duration of the test. The primary creep parameters are evaluated by integrating Eq. (5):

$$\epsilon_p = \frac{C_1}{C_3 + 1} \sigma^{C_2} t^{C_3 + 1} \exp\left[-\frac{C_4}{T}\right] \tag{9}$$

The constants C_1, C_2, C_3, and C_4 are determined from multiple regression using least squares analysis. All constants from Eqs. (5) and (6) are now known. These values are entered into the ANSYS data table, and the nonlinear creep finite element analysis can now be performed for a component.

Damage Assessment. Due to stress redistribution during creep loading conditions, the steady-state (secondary) creep rate, $\dot{\epsilon}$, also varies with time. Therefore, the Monkman–Grant failure criterion may not be used in the form in Eqs. (2) and (3) to predict lifetime. The following concept, based on damage accumulation, can be used to predict service life with the Monkman–Grant criterion.

The component's predicted life is determined based on a damage function, D. The damage function is generally defined as

$$0 \leq D \leq 1$$

where $D = 0$ for an undamaged component and $D = 1$ for a failed component. If failure is assumed to occur at time $t = t_f$, then the damage, D, is equal to unity at that time. A nonlinear analysis divides the time into steps, over which the stress and strain rates are assumed to be constant. The cumulative damage is subsequently calculated as time elapses in a manner similar to Miner's rule for fatigue loading. The damage is expressed

$$D = \frac{\Delta t_1}{t_{f1}} + \frac{\Delta t_2}{t_{f2}} + \ldots + \frac{\Delta t_n}{t_{fn}} = \sum_{i=1}^{n} \frac{\Delta t_i}{t_{fi}} \qquad (10)$$

where t_{fi} is the creep rupture time based on the loading conditions during the ith time step, Δt_i is the duration of the ith time step, and n is the number of time steps to failure.

The creep rupture time for the ith time step, t_{fi}, is determined using an appropriate failure criterion. For the Monkman–Grant criterion given in Eq. (2), this time is

$$t_{fi} = \frac{b_1}{\dot{\epsilon}_i^{b_2}} \qquad (11)$$

where $\dot{\epsilon}_i$ is the creep strain rate for the ith time step. Substituting the secondary creep strain rate into Eq. (11) yields

$$t_{fi} = \frac{b_1}{\left(C_7 \sigma_i^{C_8} \exp\left[-\frac{C_{10}}{T_i}\right]\right)^{b_2}} \qquad (12)$$

where σ_i and T_i are the stress and temperature of the ith time step. Substituting Eq. (12) into Eq. (10) gives an expression for the damage

$$D = \frac{C_7^{b_2}}{b_1} \sum_{i=1}^{n} \sigma_i^{b_2 C_8} \exp\left[-\frac{b_2 C_{10}}{T_i}\right] \Delta t_i \qquad (13)$$

Failure is assumed to occur when the normalized cumulative damage at any point in the component reaches unity. The corresponding time will be the creep rupture life for that component.

The modified Monkman–Grant (MMG) criterion may also be applied to compute the damage. Substituting the secondary creep strain rate into Eq. (3) yields

$$t_{fi} = C_7^{-b_2} \sigma_i^{-C_8 b_2} \exp\left[d_1 + \frac{C_{10} d_2}{T_i} + \frac{d_3}{T_i}\right] \qquad (14)$$

where σ_i and T_i are the stress and temperature of the ith time step. Substituting Eq. (14) into Eq. (10) gives an expression for the damage

$$D = C_7^{d_2} \sum_{i=1}^{n} \exp - \left[d_1 + \frac{d_2 C_{10}}{T_i} + \frac{d_3}{T_i}\right] \sigma_i^{d_2 C_8} \Delta t_i \qquad (15)$$

Failure is assumed to occur when the normalized cumulative damage at any point in the component reaches unity. The corresponding time will be the creep rupture life for that component.

Program Capability

The CARES/CREEP integrated design computer program predicts the service life of a monolithic ceramic component as a function of its geometry and loading conditions. CARES/CREEP couples commercially available finite element programs, with design methodologies to account for material failure from creep rupture. The code is divided into two separately executable modules, CARES/CRPEST and CARES/CREEP, which perform: (1) calculation of parameters from experimental data using laboratory specimens; and (2) damage evaluation of thermomechanically loaded ceramic components, respectively. Finite element heat transfer and nonlinear stress analyses are used to determine the temperature and stress distributions in the component. The creep life of a component is discretized into short time steps, during which the stress and strain distributions are assumed constant. The damage is calculated for each time step based on a modified Monkman–Grant creep rupture criterion. Failure is assumed to occur when the normalized accumulated damage at any point in the component is greater than or equal to unity. The corresponding time will be the creep rupture life for that component. CARES/CREEP produces a cumulative damage plot for graphic rendering of the structure's critical regions.

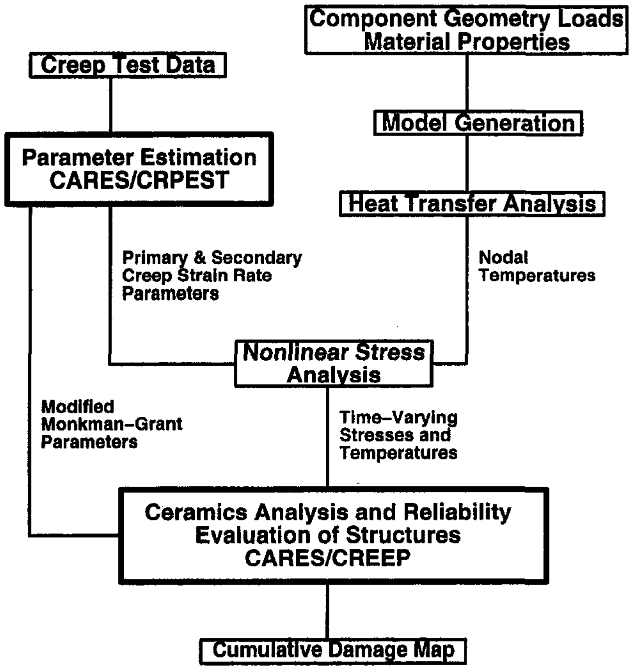

Fig. 1 Block diagram for the creep analysis of a monolithic ceramic component using CARES/CREEP

A schematic representation of the integrated design process is shown in Fig. 1. The CARES/CREEP algorithm makes use of the nonlinear stress analysis capabilities of the ANSYS finite element program. Before building a model in ANSYS, the creep response of the material must be known. An input file containing these parameters is generated by the parameter estimation module of CARES/CRPEST. This module is written in FORTRAN 77 and has as its input data from creep tests. After the parameter estimation and nonlinear analysis has been completed, the second half of the CARES/CREEP program may be run. This module is executed from within the ANSYS program and is written in APDL (Ansys Parametric Design Language). APDL routines usually take the form of an ANSYS macro, which is a sequence of ANSYS commands recorded on a file for repeated use. By recording these commands on a macro, they can be executed with one ANSYS command. When this execution is completed, a damage map of the component is displayed in the graphics window. This map consists of a contour plot of the component's damage at the time when failure has taken place, or at any design life.

The parameter estimation module computes the Norton, Bailey–Norton, and modified Monkman–Grant coefficients from uniaxial creep tests. Experimental data may be in one of two forms. The first is the more complete set of data. A standard creep test involves applying a constant load over a period of

Table 1 ANSYS structural elements with creep capabilities

	Thermal	Structural	Geometry	Nodes
2-D	PLANE35	PLANE2	Triangle	6
	PLANE55	PLANE42	Triangle	3
			Quadrilateral	4
	PLANE77	PLANE82	Triangle	6
			Quadrilateral	8
3-D	SOLID70	SOLID45	Tetrahedron	4
			Prism	6
			Hexahedron	8
	SOLID87	SOLID92	Tetrahedron	10
Shell		SHELL43	Triangle	3
			Quadrilateral	4
		SHELL51	Line	2

time or until the specimen fails. The strain is recorded as a function of time for varying test temperatures and loads. All parameters, primary and secondary creep strains and for the modified Monkman–Grant equation, may be evaluated from this data. After the title and elastic modulus, the input file consists of a header line for each test which contains the test temperature and load, followed by two columns, strain and time. The data set ends with a marker to indicate the start of a new data set. The second available data option yields secondary creep and Monkman–Grant parameters. For this data set the strain versus time curves are not required, but the minimum strain rate (secondary creep strain rate) and time to failure are input. The input consists of four columns of data, with one line of data for each test specimen. The data entries are temperature, stress level, minimum strain rate, and time to failure.

CARES/CREEP is an ANSYS macro, which computes the damage for each element. The damage is evaluated for the modified Monkman–Grant failure criterion as given in Eq. (10). Finite element analysis is an ideal mechanism for obtaining the stress distribution needed to calculate the survival probability of a structure. Each element can be made arbitrarily small, such that the stresses can be taken as constant throughout each element (or subelement). In CARES/CREEP, the damage calculations are performed at the element centroid, or optionally, at the node points. Using the nodal points enables the element to be divided into subelements, where the stresses and temperatures are calculated.

Input Information. The CARES/CREEP analysis is closely coupled to the ANSYS general purpose finite element package. As a result of this integration, the input for CARES/CREEP is centered around ANSYS input and restrictions. The requirements for a CARES/CREEP analysis do not extend beyond those for the appropriate ANSYS analysis. This program runs as a macro, so information from the ANSYS database does not need to be extracted for further manipulation outside the finite element program.

ANSYS contains a vast element library, which includes elements for structural, thermal, magnetic and electronic field, and fluid analysis. A thermomechanical analysis of a ceramic component would involve the thermal and structural elements. ANSYS contains several elements with creep modeling capabilities. A list of the two-dimensional, three-dimensional, and shell elements is given in Table 1. Additional elements with creep capabilities include beam and pipe elements, which are not commonly used to model ceramic components. All two-dimensional structural elements have two degrees of freedom per node and may be used for plane stress, plane strain or axisymmetric analysis. The three-dimensional structural elements, which would be most commonly used for ceramic component analysis, have 3 degrees of freedom per node.

The three-dimensional hexahedron element with midside (20), SOLID95, nodes does not have creep modeling features. If midside nodes are desired for a three-dimensional analysis, the 10-node tetrahedral element, SOLID92, must be used.

The required steps for a CARES/CREEP thermomechanical analysis are:

PREP7—Construct the model with thermal boundary conditions
SOLUTION—Heat transfer solution
ETCHG—Change element type to their corresponding element type, in this case, thermal to structural
/INPUT, CRPEST, ANS—Read CRPEST input from a file generated by CRPEST
SOLUTION—Apply mechanical BC's and loads and solve
POST1—Enter POST1 for postprocessing
CARESCR—Execute CARES/CREEP to calculate accumulated damage

where PREP7, SOLUTION, and POST1 are ANSYS process operations, ETCHG and /INPUT are ANSYS commands, and CARESCR is the CARES/CREEP macro. The ANSYS program is divided into several processors each serving a particular purpose. The general preprocessor (PREP7) is where the model is built. Boundary conditions are applied and the solution is obtained in the SOLUTION phase. The evaluation of the results of a solution takes place in POST1.

A typical input file for the CARES/CRPEST code is given in Fig. 2. The '/' commands are used for program control and general information. Program control includes SCRIT, PSRATIO, DATAOPT, START, STOP, and END. The purpose for each of these is shown in Fig. 2 with two exceptions. The SCRI keyword directs which stress will be used in the creep calculations. The options for this command correspond to input for the ANSYS *vget command. The DATAOP keyword specifies which type of data will be supplied for the creep response of the material. The FULL option, DATAOP = 1, is demon-

```
/TITLE,Example Problem #1
/EMOD,400.E+09                  ! elastic modulus
/MATID,1                        ! material number
/SCRIT,1                        ! stress for damage calculation
                                    1 - equivalent
                                    2 - maximum principal
/PSRAT,0.333                    ! default t_ps/t_f ratio
/DATAOP,1                       ! full time-strain history
/FAILCR,1                       ! failure criteria option
                                    1 - modified Monkman-Grant
                                    2 - Monkman-Grant
/RGAS                           ! universal gas constant
/TOFFST                         ! specifies the offset temperature from
                                    absolute zero to zero
                                ! 1st specimen
/START stress temperature tps
 t,ε                            ! time-strain, paired data
 ...
/STOP
                                ! 2nd specimen
/START stress temperature tps
 t,ε                            ! time-strain, paired data
 ...
/STOP
 .
//END
```

Fig. 2 CRPEST input file

strated in Fig. 2. The SECOND option, DATAOP = 2, indicates secondary creep rates will be input. The data include stress, temperature, secondary creep strain, and time to failure for each specimen tested. Secondary creep strain rate parameters are calculated from these data.

Output Information. Output for this program is divided into two parts depending on which program is executed. The CRPEST output contains a summary of specimen data and the estimated parameters. An echo of the command parameters and their interpretation is also included. For the iterative solutions the values at each step are also given.

The first part of all CARES/CREEP output data contains an echo of ANSYS runtime statistics and CARES/CREEP control input. The damage for each element is output at the time to failure as well as the time history of the elements with the highest accumulated damage. The cumulative damage for each element is stored in an element table within ANSYS so that the cumulative damage map may be constructed. After the CARES/CREEP macro is executed, this map appears in the ANSYS graphics window. The data is stored in the element table for future use.

Examples

Benchmark problems of creep life prediction for ceramic components under multi-axial loading are used to validate the CARES/CREEP program. Two examples of ceramic components under multiaxial loads are presented here. The first example is the spin disk, which was a part of AlliedSignal's program to develop and demonstrate life prediction methods for ceramic components of advanced vehicular engines (Cuccio et al., 1995). The failure mechanisms for this example were found to be a combination of creep and slow crack growth. The second problem was a silicon nitride notched tensile specimen, which was analyzed as a part of Saint-Gobain/Norton advanced heat engines applications program (Sundberg et al., 1994). Both of these efforts were sponsored by the Department of Energy as a part of the Ceramic Technology Project.

Spin Disk. This example demonstrates the use of CARES/CREEP and CARES/LIFE to predict the time-dependent behavior of ceramic components under multiaxial loads. The data for this example are from work done by AlliedSignal Engines on the life prediction methodology for ceramic components (Cuccio et al., 1995). This work included tests on silicon nitride NT154 for a variety of uniaxial and multiaxial specimens. The uniaxial tests were conducted on three- and four-point bend and tensile specimens at temperatures ranging from ambient to 1400°C. Confirmatory tests were designed to simulate the stress, size, and loading conditions that represent actual engine components. Three multiaxial tests were conducted: notched tensile, tension-torsion, and the spin disk.

Life predictions for the spin disk were chosen to validate the CARES/CREEP code. Buttonhead uniaxial test specimens were used to determine the creep parameters and consequently serve as a basis for these predictions. The tension test is the preferred method for characterizing the high-temperature properties of the silicon nitride. The uniaxial test geometry consists of a buttonhead cylindrical specimen with a gage section diameter of 6.35 mm. The highest creep strain rates should be confined to the gage section rather than the pin-loaded holes. The creep characteristics of silicon nitride (NT154) when isothermally loaded in uniaxial tension at temperatures in the 1200–1400°C range have been investigated. The strain as a function of time for each test is known. The total data base consisted of 83 specimens for various temperatures and loads. With this information the primary and secondary creep may be characterized for this material.

Iterating over Eqs. (7) and (8), the secondary creep rate parameters converged after 52 iterations. The parameters, C_7, C_8, and C_{10}, are $2.78 \times 10^{-31}/\mathrm{Pa}^{6.94}$ h, 6.94, and 114,000 K, respectively. These parameters are assumed to be material constants. To determine whether they vary from one specimen to the other, the experimental secondary creep strain rate is plotted as a function of the analytical secondary creep strain rate, Fig. 3. The analytical value is found using Eq. (6) and the constants estimated for the material and the stress and temperature conditions of the individual specimen. If the analytical and experimental creep rates are equal, the data point will lie on the line in Fig. 3. Since all of the points are relatively close to the line, the estimated parameters for this material adequately characterize the secondary creep rate of the individual uniaxial test specimens. The primary creep parameters as given in Eq. (5) were calculated and are $C_1 = 5.14 \times 10^{-6}/\mathrm{Pa}^{1.05}\ \mathrm{h}^{0.21}$, $C_2 = 1.05$, $C_3 = 0.785$, and $C_4 = 25290$ K.

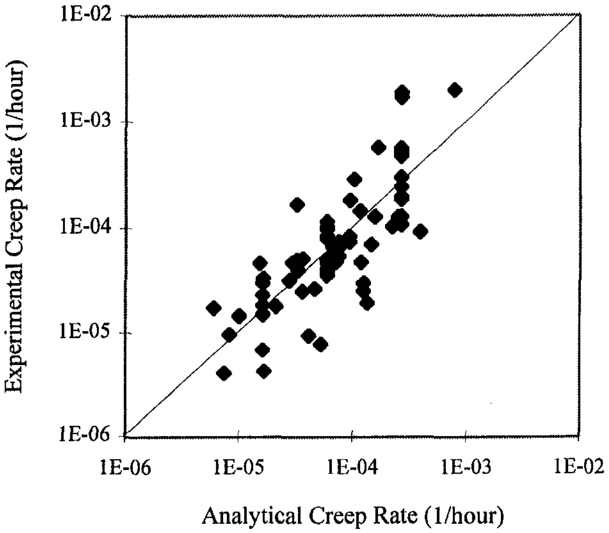

Fig. 3 Experimental versus analytical creep rates for NT154 ceramic from Saint-Gobain/Norton

The strain as a function of time for a uniaxial specimen whose temperature and applied load were 1371°C and 145 MPa, respectively, is shown in Fig. 4. The experimental results (solid line) and the analytical strains (dashed line) are plotted. Both a primary and secondary creep regime are present. The analytical curve was generated using the material constants given above. The analytical curve is the sum of the primary and secondary creep strain in order to be compatible with the creep modeling in ANSYS. The analytical creep response is plotted with its

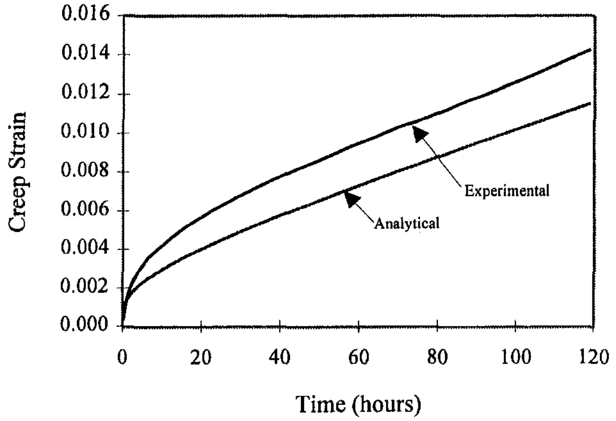

Fig. 4 Creep strain as a function of time for a smooth tensile specimen at 1371°C and 145 MPa

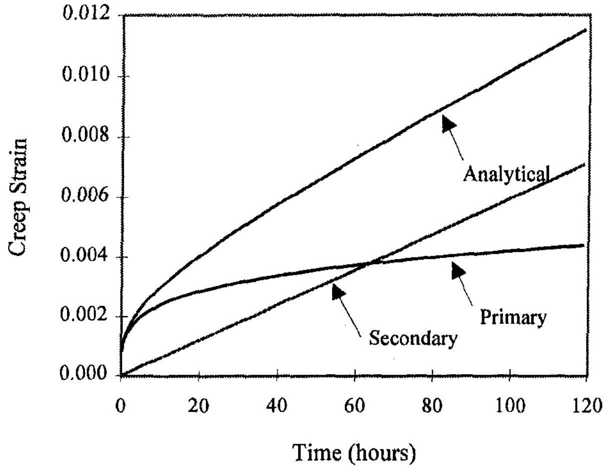

Fig. 5 Components of creep strain as a function of time for a smooth tensile specimen at 1371°C and 145 MPa

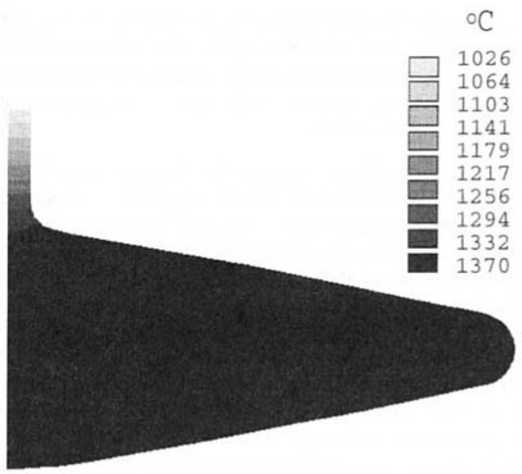

Fig. 7 Temperature distribution in the silicon nitride spin disk

primary and secondary creep components separated in Fig. 5. Both Figs. 4 and 5 are shown to demonstrate the manner in which the creep strain is handled within the ANSYS program. The correlation of the analytical and experimental data is exceptional for this specimen. Typically, experimental creep rates within a factor of two of the analytical creep rate are within acceptable limits for these materials.

The mesh for the spin disk is shown in Fig. 6. The ANSYS model contains 1126 axisymmetric elements (PLANE82). The maximum diameter of the disk is 0.137 m. The height of the disk is 0.0483 m including the shaft. A rotational velocity was applied to the disk. The disk is constrained in the shaft to prevent rigid body translation in the vertical direction. The temperature distribution in the spin disk is not uniform in the shaft region. This distribution is plotted in Fig. 7. The temperature of the body of the disk is 1370°C.

The creep life of the spin disk was estimated at 5500 hours. The life of these components in laboratory experiment was approximately 10 hours. Test results indicated that the disks did not fail in the creep regime. Possible failure mechanisms included slow crack growth and surface (machining) damage. A fast fracture and slow crack growth analysis was conducted on the disks as well. The equivalent stress distribution as well as the maximum principal stress distribution were examined for the disks. The Von Mises (equivalent) and maximum principal stress distributions are plotted as a function of time in Figs. 8 and 9 for a disk at 50,000 rpm. CARES/CREEP predictions were based on the equivalent stress in the disk. At time = 0, Fig. 8(*a*), the equivalent stress is maximum in the center of the disk. The maximum remains in the center for the duration of service, Fig. 8(*b*). The distribution of the maximum principal stress as a function of time is much different. At time = 0, Fig. 9(*a*), the maximum value is at the center of the disk. As time passes, the maximum value resides on the surface, Fig. 9(*b*). At life as low as 100 hours, the surface stress is close to the maximum value in the interior of the disk. Fast fracture and slow crack growth analysis are most closely a function of the maximum principal stress.

The results of a creep and a slow crack growth analysis cannot be compared directly since the evaluated quantities are not the same. The creep life is found in terms of the damage sustained over the service life of a component. Failure due to fast fracture and slow crack growth is quantified by assigning a probability of failure or survival to a component for a given

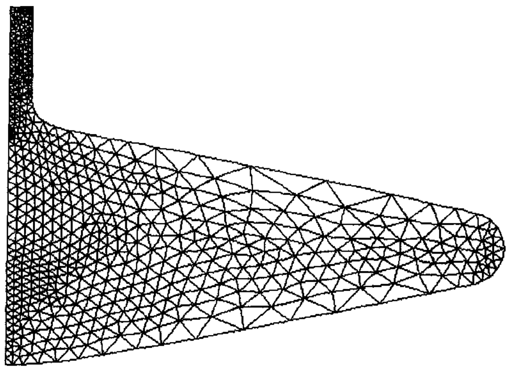

Fig. 6 Axisymmetric finite element mesh for the spin disk

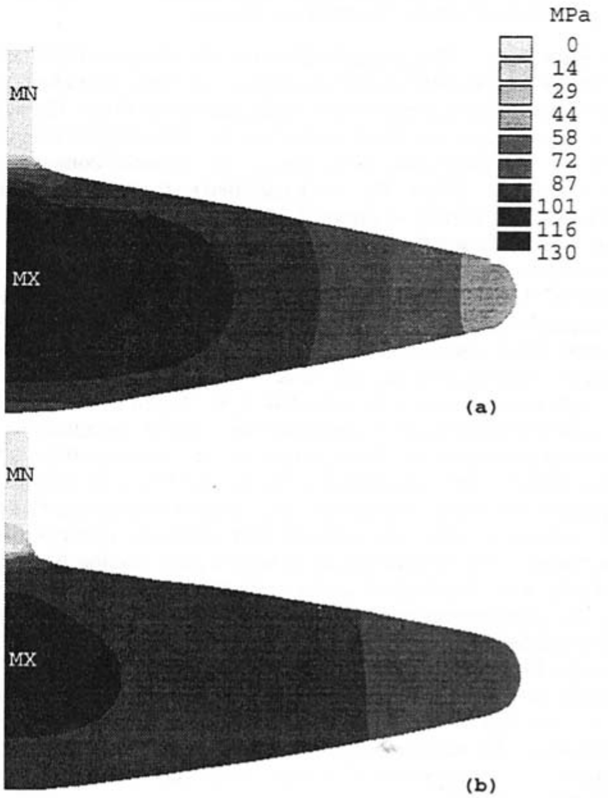

Fig. 8 Von Mises stress distribution in the spin disk at time equal to (*a*) zero and (*b*) 5500 hours

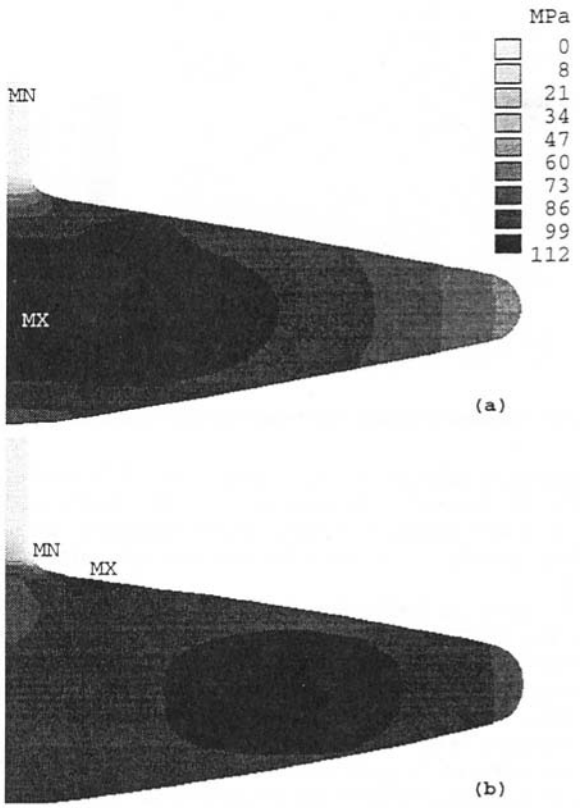

Fig. 9 Maximum principal stress distribution in the spin disk at time equal to (*a*) zero and (*b*) 5500 hours

lifetime. If that probability of failure is less than one that has been established as acceptable for design then the component may be suitable for that application. A general comparison of the two analyses will be made in order to understand the mechanisms behind the failure of these disks.

The cumulative damage for the spin disk after 5500 hours is plotted in Fig. 10. The damage is maximum and equal to one at the center. CARES/CREEP then predicts a lifetime in creep of 5500 hours. The slow crack growth analysis predicts much smaller lifetime. The fast fracture (instantaneous) probability of failure is 0.001. After 100 hours, the probability of failure is 0.05. With probability of failures of this magnitude, the disks would be expected to fail due to slow crack growth. In addition, the spin disks were also found to fail at the surface and the potential for damage due to surface finishing operations most likely contributed to their ultimate failure.

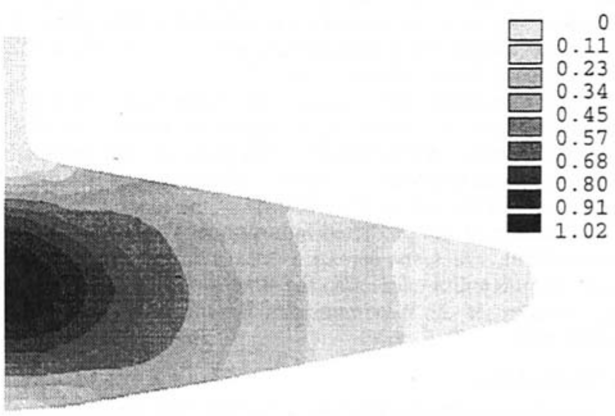

Fig. 10 Cumulative damage in the spin disk after 5500 hours

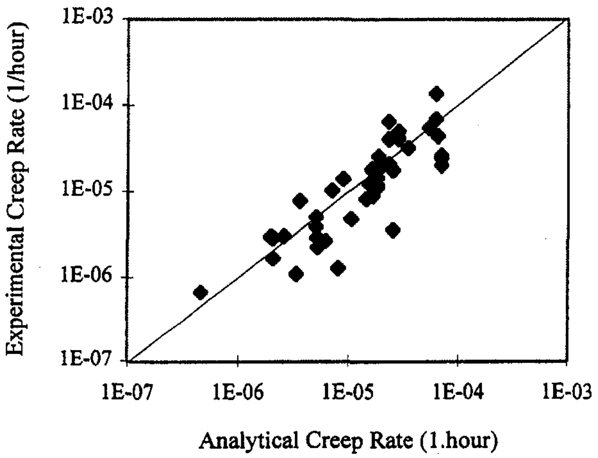

Fig. 11 Experimental versus analytical creep rates for NCX-5100 ceramic from Saint-Gobain/Norton

Notched Tensile Specimen. The aim of this example is to predict the multi-axial creep rupture behavior of silicon nitride, NCX-5100, from data obtained from uniaxial specimens (Sundberg et al., 1994). This effort was a part of a study of the joining of silicon nitride to silicon nitride. Creep experiments were conducted on two types of specimens. First, smooth tensile tests were investigated in order to characterize the creep response of the silicon nitride. Second, experiments on notched tensile bars provided a multiaxial loading condition where the creep life may be predicted from data obtained from the smooth tensile specimens.

The tension test is the preferred method for characterizing the high-temperature properties of the silicon nitride. The uniaxial test geometry consists of a flat dog-bone with tapered holes to account for the relief of out-of-plane alignment. The highest creep strain rates should be confined to the gage section rather than the pin-loaded holes. The creep characteristics of silicon nitride (NCX-5100) when isothermally loaded in uniaxial tension at temperatures in the 1275–1425°C range have been investigated. The minimum creep rate, temperature, stress, and time to failure for each specimen are known. The secondary creep rate and Monkman–Grant parameters were computed from this data set.

Iterating over Eqs. (7) and (8), the secondary creep rate parameters converged after 14 iterations. The parameters C_7, C_8, and C_{10} are $7.858 \times 10^{-26}/\mathrm{Pa}^{6.75}$ h, 6.75, and 127,560 K, respectively. These parameters are assumed to be material

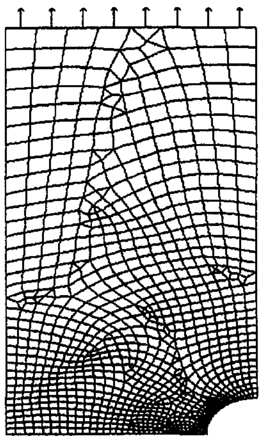

Fig. 12 Axisymmetric finite element mesh for the notched specimen

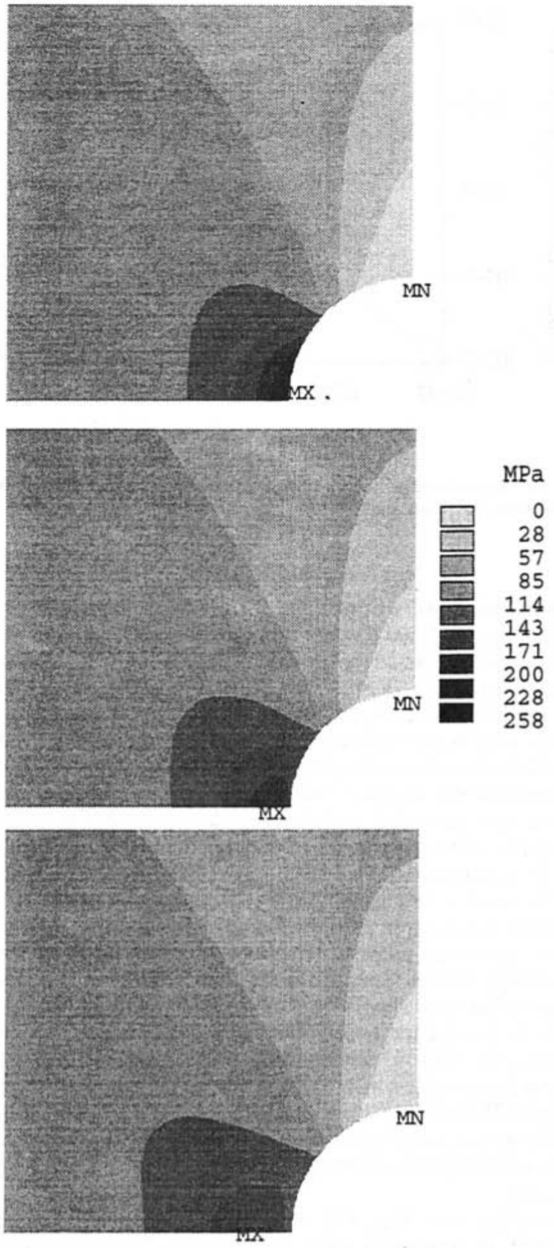

Fig. 13 Maximum principal stress in the notched tensile specimen at time equal to (*a*) zero, (*b*) 10, and (*c*) 100 hours

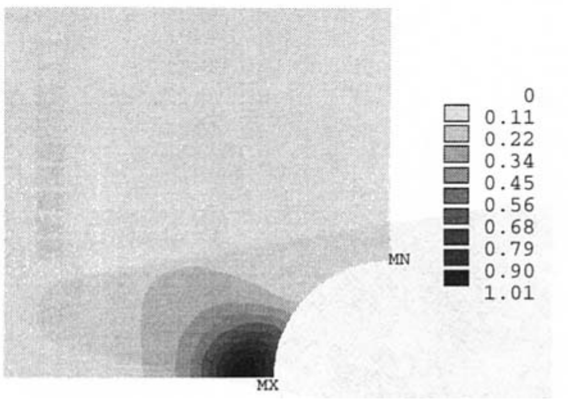

Fig. 14 Cumulative damage distribution in the notched tensile specimen

constants. To determine if they vary from one specimen to the other, the experimental secondary creep strain rate is plotted as a function of the analytical secondary creep strain rate, Fig. 11. The analytical value is found using Eq. (6) and the constants estimated for the material and the stress and temperature conditions of the individual specimen. If the analytical and experimental creep rates are equal, the data point will lie on the line in Fig. 11. Since all of the points are relatively close to the line, the estimated parameters for this material reasonably characterize the secondary creep rate of the individual uniaxial test specimens.

Table 2 Predictions and experimental results for the notched tensile specimens

Reduced Section Stress (MPa)	Predicted Failure Time (hours)	Experimental Failure Time (hours)
105	179.	314.
120	80.	44.
135	42.	39.
150	21.	3.5

The mesh and load applied for this example is shown in Fig. 12. The ANSYS model contains 1047 axisymmetric elements (PLANE-82). In addition to the axisymmetric loading and geometry conditions, the bar is also symmetric in the longitudinal direction. One-half of the bar is meshed as shown in Fig. 12. The notch is on the outside of the bar and its radius is 20 percent of the radius of the gage section of the tensile specimen. The model was long enough in the direction of the load so that the stress distribution in the bar is uniform and equal to the applied load divided by the area. The mesh was refined so that the multiaxial stress state at the notch root will then be characterized.

Four notched bars were tested. The reduced section average stresses were 105, 120, 135, and 150 MPa. The maximum principal stress (120 MPa reduced average section stress) as a function of time for the bar is shown in Fig. 13. Figures 13(*a*), 13(*b*), and 13(*c*) are the maximum principal stresses at 0, 10, and 100 hours. The stress away from the notch is constant and uniaxial. When the load is initially applied, time = 0, the maximum principal stress is at the root of the notch. As time progresses, the stress relaxes and, the local maximum moves into the interior of the notched bar. This will influence the damage calculations and it was found that the location of the maximum cumulative damage moves away from the surface as a function of the predicted failure time.

The Monkman–Grant parameters were determined from the smooth tensile specimens. The NCX-5100 material did not display stratification of the Monkman–Grant curve and therefore the Monkman–Grant criterion was used. The values of b_1 and b_2 from Eq. (2) are $6.87 \times 10^{-3}\ \mathrm{h}^{0.073}$ and 0.927, respectively. Table 2 gives a summary of the failure predictions for the notched bars as a function of their reduced section stress. The predicted life for these specimens matches reasonably well the experimental failure times.

For this example, the damage calculations were based on the maximum principal stress values. Figure 14 shows a cumulative damage map for the 120 MPa bar after 80 hours. The cumulative damage is equal to one and is located near to but not directly at the root of the notch. The location of the maximum damage is a function of the predicted failure time. For higher stresses, lower failure times, the damage is maximum closer to the notch root. As the stress decreases, the time to failure increases and the location of the maximum damage moves away from the notch root.

Conclusions

A general purpose creep life prediction code has been generated, which is integrated with ANSYS finite element software, and can be used to design structural ceramic components. The program includes the Monkman–Grant and modified Monkman–Grant failure criteria to evaluate the damage of a ceramic component. This methodology will be extended for additional creep laws and failure criteria. The methodology will be enhanced to include stochastic effects, and therefore make the results of the program compatible with slow crack growth phenomenon as in CARES/LIFE.

References

Brown, S., Kim, K., and Anand, L., 1989, "An Internal Variable Constitutive Model for Hot Working of Metals," *International Journal of Plasticity,* Vol. 5, pp. 85–130.

Boyle, J., and Spence, J., 1983, *Stress Analysis for Creep,* Butterworth & Co., London.

Conway, J. B., 1968, *Stress-Rupture Parameters: Origin, Calculations, and Use,* Gordon and Breach, Science Publishers, New York.

Cuccio, J., Brehm, P., Fang, H., Hartman, J., Meade, W., Menon, M., Peralta, A., Song, J., Strangman, T., Wade, J., Wimmer, J., and Wu., D., 1995, "Life Prediction Methodology for Ceramic Components of Advanced Heat Engines, Phase I," Oak Ridge National Lab, ORNL-Sub/89-SC674/1/V1.

Ding, J.-L., Liu, K. C., More, K. L., and Brinkman, C. R., 1994, "Creep and Creep Rupture of an Advanced Silicon Nitride Ceramic," *Journal of the American Ceramic Society,* Vol. 77, pp. 867–874.

Duffy, S. F., and Gyekenyesi, J. P., 1989, "Time Dependent Reliability Model Incorporating Continuum Damage Mechanics for High-Temperature Ceramics," NASA TM-102046.

Dunne, F., Othman, A., Hall, F., and Hayhurst, D., 1990, "Representation of Uniaxial Creep Curves Using Continuum Damage Mechanics," *International Journal of Mech. Science,* Vol. 32, No. 11, pp. 945–957.

Evans, R., and Wilshire, B., 1985, "The θ Projection Concept," *Creep of Metals and Alloys,* The Institute of Metals, London, pp. 197–256.

Evans, R., Murakami, T., and Wilshire, B., 1987, "The Generation of Long-Term Creep Data for Silicon Nitride Ceramics," *British Ceramics—Proceedings,* No. 39.

Ferber, M., and Jenkins, M., 1992, "Evaluation of the Strength and Creep-Fatigue Behavior of Hot Isostatically Pressed Silicon Nitride," *Journal of the American Ceramic Society,* Vol. 75, pp. 2453–2462.

Ferber, M., Jenkins, M., Nolan, T., and Yeckley, R., 1994, "Comparison of the Creep and Creep Rupture Performance of Two HIPed Silicon Nitride Ceramics," *Journal of the American Ceramic Society,* Vol. 77, pp. 657–665.

Foley, M., Rossi, G., Sundberg, G., Wade, J., and Wu, F., 1992, "Analytical and Experimental Evaluation of Joining Silicon Carbide to Silicon Carbide and Silicon Nitride to Silicon Nitride for Heat Engine Applications," Final Report, Ceramic Technology for Advanced Heat Engines, Oak Ridge National Lab.

Grathwohl, G., 1984, "Regimes of Creep and Slow Crack Growth in High-Temperature Rupture of Hot-Pressed Silicon Nitride," in: *Deformation of Ceramics II,* Tressler, R. E., and Bradt, R. C., eds., Plenum Press, New York, pp. 573–586.

Hayhurst, D., Dimmer, P., and Chernuka, M., 1975, "Estimates of the Creep Rupture of Lifetime of Structures Using the Finite Element Method," *Journal of Mechanical Physics of Solids,* Vol. 23, pp. 335–355.

Jones, D., 1986, "Phenomenological Analysis of Time–Temperature Mechanical Behavior of Ceramic Materials," *Proc. 10th Annual Conference on Composites and Advanced Ceramic Materials,* Cocoa Beach, FL.

Kachanov, L., 1960, *The Theory of Creep,* English Translation, Kennedy, A., ed., British Library, Wetnerley.

Khandelwal, P. K., Provenzano, N. J., and Schneider, W. E., 1995, "Life Prediction Methodology for Ceramic Components of Advanced Vehicular Heat Engines—Final Report," Ceramic Technology Project, Oak Ridge National Lab.

Krempl, E., 1974, "Cyclic Creep—An Interpretive Literature Survey," *Welding Research Council Bulletin,* No. 195, pp. 63–123.

Kraus, H., 1980, *Creep Analysis,* Wiley, New York.

Lange, F., 1976, "Interrelations Between Creep and Slow Crack Growth for Tensile Loading Conditions," *International Journal of Fracture,* Vol. 12, pp. 739–744.

Larson, F., and Miller, J., 1952, "A Time–Temperature Relationship for Rupture and Creep Stresses," *Transactions ASME,* Vol. 74, pp. 765–771.

Le Gac, H., and Duval, P., 1980, "Constitutive Relations for the Non-elastic Deformation of Polycrystalline Ice," *IUTAM Symposium on the Physics and Mechanics of Ice,* pp. 51–59.

Lewis, G., and Ostvoll, A., 1992, "Constitutive Equations for the Creep of a Silicon Carbide Whisker-Reinforced Polycrystalline Alumina Composite Material," *Journal of the American Ceramic Society,* Vol. 75, No. 12, pp. 3481–3484.

Luecke, W., Wiederhorn, S., Hockey, B., and Long, G., 1993, "Cavity Evolution During Tensile Creep of Si3N4," *Materials Research Society Symposium Proceedings,* Vol. 287, pp. 467–472.

Manson, S., and Ensign, C., 1971, "A Specialized Model for Analysis of Creep-Rupture Data by the Minimum Commitment Method, Station-Function Approach," NASA TM-X-52999.

Manson, S., and Halferd, A., 1953, "A Linear Time–Temperature Relation for Extrapolation of Creep and Stress-Rupture Data," NASA TN-2890.

Maruyama, K., and Oikawa, H., 1987, "On Physical Bases of the Modified Projection Concept," *Proc. 3rd International Conference on Creep and Fracture of Engineering Materials and Structures,* Wilshire and Evans, eds.

Menon, M., Fang, H., Wu, Jenkins, M., Ferber, M., More, K., Hubbard, C., and Nolan, T., 1994a, "Creep and Stress Rupture Behavior of an Advanced Silicon Nitride: Part I, Experimental Observations," *Journal of the American Ceramic Society,* Vol. 77, pp. 1217–1227.

Menon, M., Fang, H., Wu, D., Jenkins, M., and Ferber, M., 1994b, "Creep and Stress Rupture Behavior of an Advanced Silicon Nitride: Part III, Stress Rupture and Monkman-Grant Relationship," *Journal of the American Ceramic Society,* Vol. 77, pp. 1235–1241.

Monkman, F., and Grant, N., 1956, "An Empirical Relationship Between Rupture Life and Minimum Creep Rate in Creep-Rupture Test," *Proc. American Society for Testing and Materials,* Vol. 56, 593–620.

Nemeth, N. N., Manderscheid, J. M., and Gyekenyesi, J. P., 1990, "Ceramics Evaluation and Reliability Analysis of Structures (CARES), Users and Programmers Manual," NASA TP-2916.

Nemeth, N. N., Powers, L. P., Janosik, L. A., and Gyekenyesi, J. P., 1993, "Ceramics Analysis and Reliability Evaluation of Structures Life Prediction Program, Users and Programmers Manual," NASA TM, to be published.

Norton, F., 1929, *The Creep of Steel at High Temperatures,* McGraw-Hill.

Ohji, T., and Yamauchi, Y., 1993, "Tensile Creep and Creep Rupture Behavior of Monolithic and SiC-Whisker-Reinforced Silicon Nitride Ceramics," *Journal of the American Ceramic Society,* Vol. 76, pp. 3105–3112.

Orr, R., Sherby, O., and Dorn, J., 1954, "Correlations of Rupture Data for Metals at Elevated Temperatures," *Transactions American Society for Metals,* Vol. 46, p. 113.

Othman, A., and Hayhurst, D., 1990, "Multi-axial Creep Rupture of a Model Structure Using a Two Parameter Material Model," *International Journal of Mechanical Science,* Vol. 32, pp. 35–48.

Quinn, G. D., 1986, "Static Fatigue Resistance of Hot Pressed Silicon Nitride," *Fracture Mechanics of Ceramics,* Vol. 8, Bradt et al., eds., Plenum Press, pp. 319–332.

Quinn, G. D., 1990, "Fracture Mechanism Maps for Advanced Structural Ceramics, Part 1, Methodology and Hot Pressed Silicon Nitride Results," *Journal of Materials Science,* Vol. 25, pp. 4361–4376.

Saith, A., Norton, P., and Parthasarathy, V., 1994, "SPSLIFE: Application to Preliminary Design Evaluation and Life Assessment of CSGT Components," ASME Paper No. 94-GT-486.

Sankar, J., Krishnaraj, S., Vaidyanathan, X., and Kelkar, A., 1994, "Elevated Temperature Behavior of Sintered Silicon Nitride Under Pure Tension, Creep, and Fatigue," *Life Prediction Data and Methodologies for Ceramic Materials,* ASTM STP 1201, Brinkman, C. R., and Duffy, S. F., eds., American Society for Testing and Materials, Philadelphia, pp. 19–35.

Sundberg, G., Vartabedian, A., Wade, J., and White, C., 1994, "Analytical and Experimental Evaluation of Joining Silicon Carbide to Silicon Carbide and Silicon Nitride to Silicon Nitride for Advanced Heat Engine Applications Phase II," Final Report, Ceramic Technology Project, Oak Ridge National Lab.

Wiederhorn, S. M., 1974, "Subcritical Crack Growth in Ceramics," *Fracture Mechanics of Ceramics,* Vol. 2, Bradt, R. C., et al., eds., Plenum Press, New York, pp. 613–646.

Wiederhorn, S., Quinn, G., and Krause, R., 1993, "Fracture Mechanism Maps: Their Applicability to Silicon Nitride," *Life Prediction Methodologies and Data for Ceramic Materials,* ASTM STP-1201, Brinkman, C. R., and Duffy, S. F., eds., American Society for Testing and Materials, Philadelphia, pp. 36–61.

White, C., and Hazime, R., 1995, "Internal Variable Modeling of the Creep of Monolithic Ceramics," *Proc. 11th Biennial Conference on Reliability, Stress Analysis, and Failure Prevention,* Jadaan, O., ed., Philadelphia, PA, ASME.

Radial Turbine Development for the 100 kW Automotive Ceramic Gas Turbine

N. Nakazawa

H. Ogita

M. Takahashi

T. Yoshizawa

Y. Mori

Japan Automobile Research Institute, Inc.,
Mitsubishi Motors Corp.,
Tsukuba, Ibaraki, Japan

The development of turbine components for the automotive 100 kW ceramic gas turbine has entered the final stage of the seven-year project and is making satisfactory progress toward the goals. We have attained the interim targets of the aerodynamic performances and have been carrying out tests to further improve efficiency. As for ceramic parts, we have changed the material of the turbine rotor to a new one that is excellent in long-sustained and high-temperature strength properties, and have confirmed substantial strength at high temperature through hot-spin tests. After evaluating blade-vibration stress through analyses and experiments, we completed an endurance evaluation at 1200°C (1473 K) TIT (Turbine Inlet Gas Temperature) and a rated speed of 100,000 rpm. We are now carrying out endurance tests at 1350°C (1623 K) TIT. For ceramic stationary parts, we already finished the evaluations at 1200°C TIT and are also conducting an endurance test at 1350°C TIT. Using these parts in a full-assembly test, together with other elements, we confirmed that they cause no functional problem in tests performed at 1200°C TIT level up to the rated speed (100,000 rpm), and are evaluating their performances.

Introduction

The development of the "100 kW automotive ceramic gas turbine (CGT)," which demonstrates excellent properties in terms of being highly efficient and less pollutive, and having multifuel capability, has been in progress since 1990. CGT development was started as a project of the Agency of Natural Resources and Energy, Ministry of International Trade and Industry, and is chiefly conducted by the Petroleum Energy Center (PEC) under the cooperation of related industries, such as the petroleum, automobile, and ceramic industries [1].

Among CGT elements, turbine components are the most important. Ceramics are used for turbines because turbine components are exposed to high-temperature gas and required to attain the target aerodynamic performances after securing strength reliability [2–4]. Figure 1 shows the overall structure of turbine components. At present, the evaluation at 1200°C (TIT) has been completed, and that at 1350°C TIT, the target, is under way. This report will introduce the development of the rotors and nozzles, which are main parts of the turbine components.

Turbine Basic Design Specifications

With regard to the aerodynamic performance of turbines, we have made efforts for optimization of blade design, while making tradeoffs between the performance and strength reliability to match the characteristics of the ceramic materials. In evaluation of the aerodynamic performance, we carried out tests at low temperatures under corrected aerodynamic conditions to ward off possible errors in temperature measurements using metallic model parts. Reviewing the first design, which is based on the initial design specifications, in order to improve efficiency particularly at a low pressure ratio, we increased the degree of reaction and improved the flow velocity distribution. We thereby successfully achieved the interim target performance. In addition, we also conducted performance evaluations of ceramic rotors and nozzles and confirmed their performance to be the same as that of the metallic parts.

On the other hand, target values that had been initially set for the long-term, high-temperature strength properties of rotor materials, as described in the next section, were found to be difficult to attain, so the rated speed was reviewed and changed from 110,000 rpm to 100,000 rpm. Furthermore, in consideration of the indefinite factors of the long-term, high-temperature strength of ceramic material, we designed and manufactured a prototype in which the centrifugal stress was reduced 8 to 10 percent at the same speed to make it a primary requirement to secure strength, by reducing the number of blades from 14 to 12, and the inlet's outer diameter from 127 to 122 mm.

Table 1 shows the specifications for the respective turbines. Figure 2 shows the basic dimensions of the rotors and nozzles. At present, renewed efforts in design and experiment for still higher efficiency are under way to achieve the final target. This paper describes the status of development of ceramic rotors and nozzles (Figs. 3 and 4) manufactured, tested, and evaluated so far.

Rotor Materials

The design targets for the strength and reliability of a rotor are a failure probability of 10^{-5} under the conditions of 300 hours of rated continuous operation and 10,000 cold starts. We set the stress levels under the individual operating conditions on the basis of the material data acquired in the initial stage of development, and determined the basic specifications, including tip-speed, number of blades, hub shape, etc. Figure 5 shows the strength data on the typical materials. From the previously acquired fast fracture flexural strength data, the target values of material strength were estimated and adopted for the design. The material test data and rotor burst test data later obtained, however, revealed that the original data contained evidence of the stress relaxation effects peculiar to the flexural tests at 1200 to 1400°C. It also became clear from the hot spin tests and material test data described later how differences are between fast fractural and static fatigue strengths. In order to reduce the stress level, therefore, we decided to change the rated speed from 110,000 to 100,000 rpm.

We had set the design target values on the basis of the limited material data available at the beginning of the project, and it seems that there was a problem in interpreting the meaning of

---

Contributed by the International Gas Turbine Institute and presented at the 41st International Gas Turbine and Aeroengine Congress and Exhibition, Birmingham, United Kingdom, June 10–13, 1996. Manuscript received at ASME Headquarters February 1996. Paper No. 96-GT-366. Associate Technical Editor: J. N. Shinn.

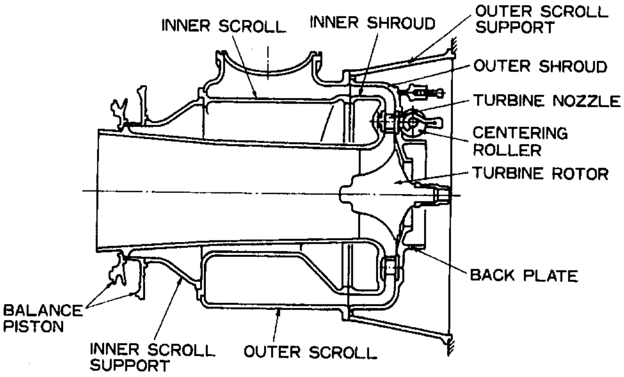

Fig. 1 Structure of turbine components

Table 1 Turbine specification at rated point

	Initial Design	Final Design
Rotor Speed (rpm)	110,000	100,000
Gas Flow (kg/s)	0.421	0.449
Inlet Pressure (MPa)	47.8	46.9
Inlet Temp. (℃/K)	1350/1623	1350/1623
Expansion Ratio	4.25	4.13

the presented data from manufacturers. The fast fracture and the 300-hour static fatigue data with respect to temperature, re-evaluated by material tests performed later, are jointly shown in Fig. 5. The high-temperature strength decline of the SN91 is greater than the SN88M, especially in static fatigue strength.

Since the flexural tests on the high-temperature side involve problems as mentioned above, we decided to evaluate the materials by tensile tests. Figure 6 shows the results of the tests at 1200°C. The fracture mechanism of the SN88M is due to what is known as slow crack growth. The results, if modified on the basis of the volume effect, coincide with those of the flexural tests in Fig. 5. With regard to the SN91, on the other hand, its decline in strength with respect to time is larger than during flexural tests, revealing an unstable region in its use as a material. Since the SN88 series appeared to be technically difficult to manufacture at the beginning of the project, we initially did not adopt it as a rotor material. What we adopted first was the SN91, which provided relatively high values in the cold spin tests. Beginning in the latter half of the evaluation tests at 1200°C TIT, however, we changed the material to the SN88M.

With regard to the mechanism of a radical decline in strength on the high-temperature side, we performed high-temperature

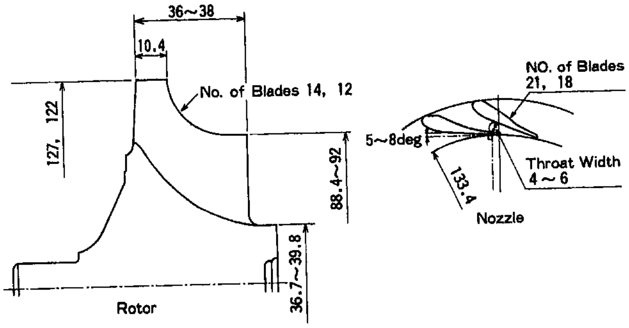

Fig. 2 Basic dimensions (mm) of rotor and nozzle

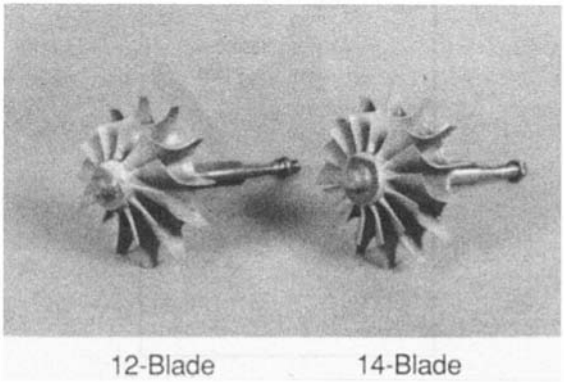

Fig. 3 SN88M turbine rotors

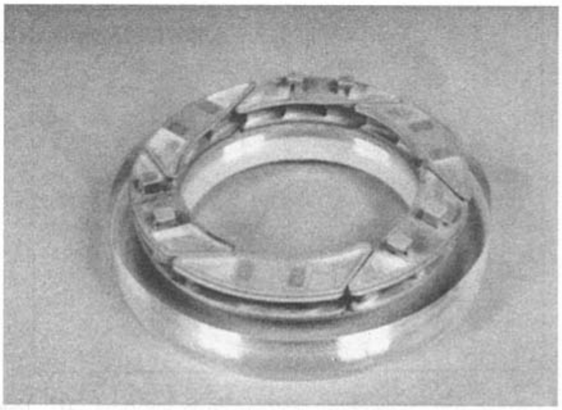

Fig. 4 SN88 turbine nozzle

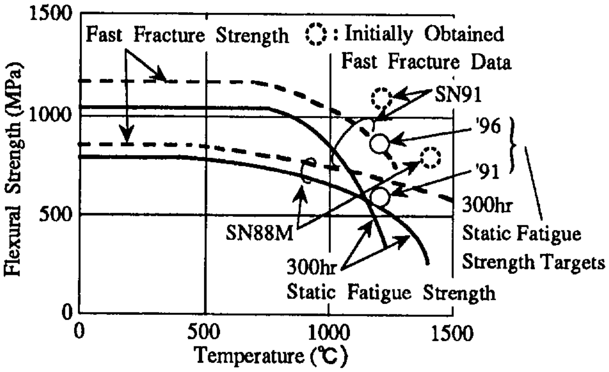

Fig. 5 SN88M, SN91 strength properties

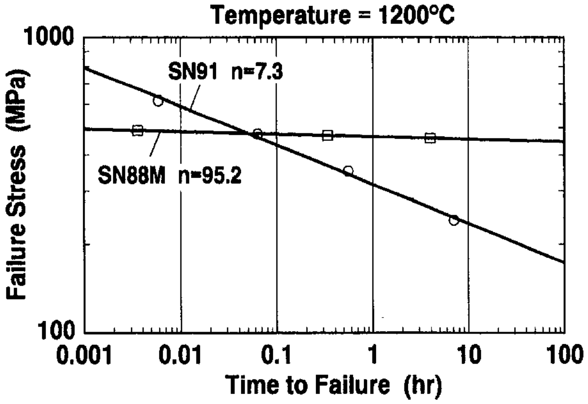

Fig. 6 Static tensile fatigue properties of SN91 & SN88M (n: static fatigue exponent)

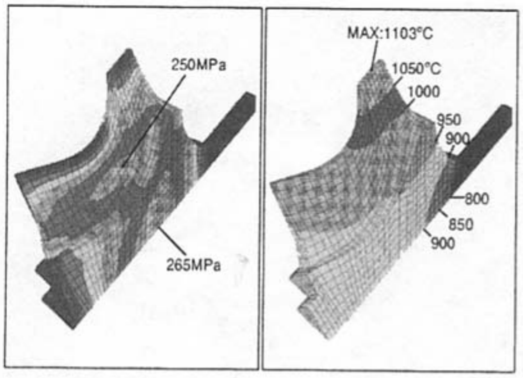

Fig. 7 Stress and temperature distribution in the rotor (TIT; 1350°C, 100,000 rpm rated conditions, SN88M)

exposure tests on the respective materials in the atmosphere and confirmed intergranular voids produced due to the phenomena of the movement of sintering aids in the material microstructure to the surface and their oxidations. These voids are coupled and lead to fracture in the stress field, constituting a widely variable fracture mechanism dependent on the exposed atmosphere and stress conditions. Therefore, use of the materials under high-stress condition at temperatures exceeding their limit temperatures should be avoided.

Centrifugal Strength Design and Evaluation of Rotors

Figure 7 shows the results of analyses of the stress and temperature distributions of the first design rotor made of the SN88M at the rated 100,000 rpm and 1350°C TIT. Because of a relatively high expansion ratio and high tip speed, the maximum temperature in the rotor is approx. 1100°C. The temperature in the high stress region is also below 1050°C. Figure 8 shows the failure probability distribution of fast fracture per unit volume obtained from the strength characteristics of the SN88M in Fig. 5 by assuming that Weibull Modulus $m = 15$, which is necessary to attain rotor strength and reliability target described before [5]. The failure probability peaks exist at the rotor hub center and blade roots on the suction side. These are areas where special considerations must be incorporated to eliminate material defects. The reliability analyses of the rotors were performed by the analytical code based on CARES [6].

For evaluation of materials and manufacturing processes of the rotors, the test pieces cut out from the rotors were subjected to strength tests, and then cold spin tests, hot spin tests, and endurance tests were carried out successively. The evaluation results were fed back to the materials and manufacturing technologies, and the design and analytical procedures were reviewed. For the ultimate goal of supplying a reliable and durable rotors for engine tests, we carried on our developmental activities in two separate stages from 1200°C to 1350°C TIT.

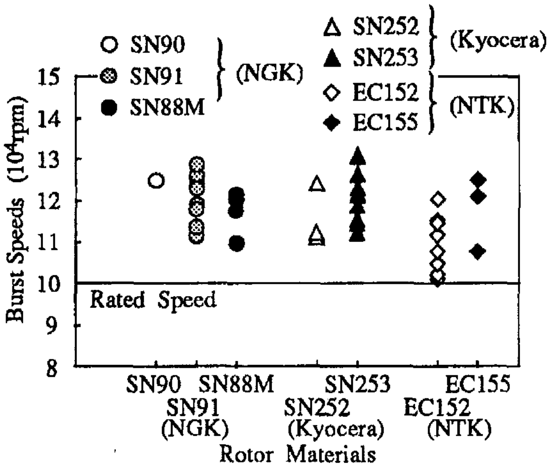

Fig. 9 Hot spin test results (TIT; 1200°C)

Figure 9 shows the burst speeds of the first design rotors made of various materials (SN90, 91, 88M/NGK, SN252, 253/Kyocera, EC152, 155/NTK) in the hot spin tests at 1200°C TIT. A hot spin test is an experiment performed by supplying combustion gas to the subject rotor and increasing its speed in stages under predetermined conditions, while absorbing the load with the compressor, to find the burst speed. Since there are no nozzle vanes upstream of the rotor, and the gas that is not accelerated enough through the scroll-like gas passage flows into the rotor, the relative total temperature is higher than under actual engine conditions.

In the hot spin tests at 1200°C TIT, therefore, as indicated by the analysis results of Fig. 10, the material temperature in the high-stress region of the rotor is a little higher than that in the rated condition of 1350°C TIT. The hot spin tests, therefore, are overspeed burst tests under about 150°C TIT or higher excess condition, as well as evaluation tests that allow for the margins for strength variance on the high temperature side of the materials and the operating temperature variation. The burst speeds of the various materials at 1200°C TIT shown in Fig. 9, with some exceptions, are almost equivalent in their strength level and scattering.

As previously stated, we reviewed the material strength test data. The SN91 declined its strength at more than 900°C and showed a high time dependency. It became clear that these are due to the intrinsic characteristics of the material containing the sintering aids. For this reason, we decided to change the rotor material to the SN88M.

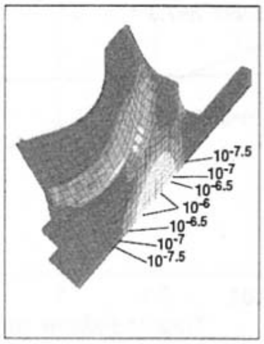

Fig. 8 Failure probability distribution in the rotor (TIT; 1350°C, 100,000 rpm, rated conditions, SN88M)

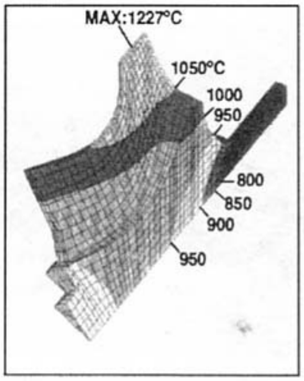

Fig. 10 Temperature distribution in the rotor (TIT; 1200°C, 100,000 rpm, hot spin test conditions)

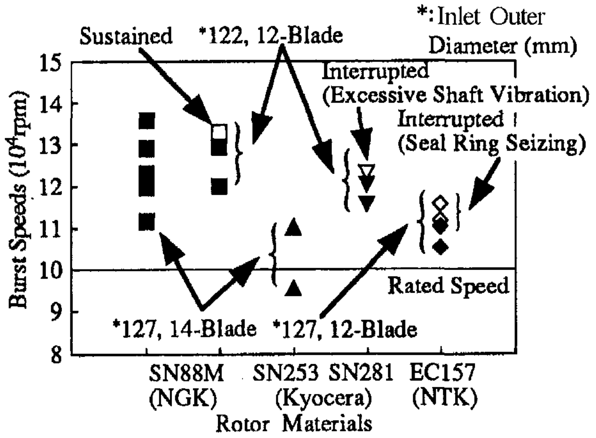

Fig. 11 Hot spin test results (TIT; 1350°C)

Figure 11 shows the results of hot-spin tests at 1350°C TIT on the rotors made of various types of materials (SN88M/NGK, SN253, 281/Kyocera, EC157/NTK). The rotor specifications include the first design, which is a 14-blade rotor with 127 mm in inlet outer diameter, and new designs, which are lower centrifugal stress version rotors associated with the respective materials (12-blade type with 122 mm diameter and 12-blade type with 127 mm diameter) incorporating the steps for improving blade vibration strength as described later. The hot spin test rig is also near its limits in both gas temperature and speed, giving some cases where the tests are intermediately interrupted. The Weibull plots of the SN88M rotors on which many more test data are available and which show a relatively high strength are shown in Fig. 12 in comparison with those of the SN91. The data on the SN88M at 1200°C TIT and 1350°C TIT may be evaluated as almost the same population, showing practically no decline dependent on temperature as indicated by the material data. In addition, the data on the two types of rotors different in stress level may also be evaluated as the same population, indicating that the materials have become more stable in the manufacturing phase as well. Although Weibull Modulus $m = 11$, the experiment values recently acquired among the subject rotors delivered during the period of about two years are at around a rotor tip speed of 900 m/s, creating a tendency to make variance larger. The tendency represents improvements in manufacturing process technology. In the event a manufacturing process is established, the potential of Weibull Modulus $m = 15$ through 20 can be expected.

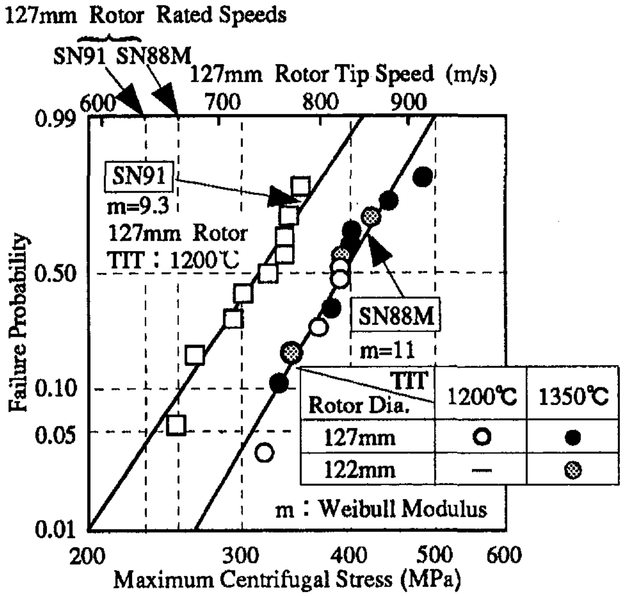

Fig. 12 Weibull plots of hot spin test results

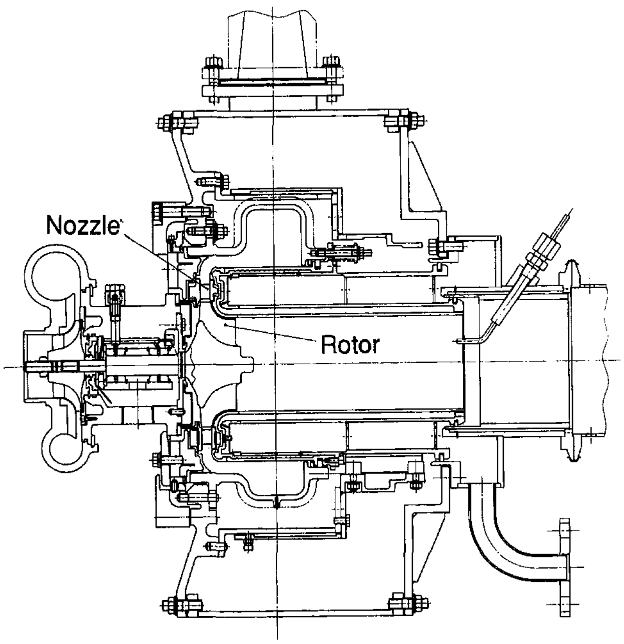

Fig. 13 High-temperature turbine test rig

Following the hot spin tests, both the SN91 and SN88M rotors were subjected to endurance tests by installing them in the test rig of Fig. 13 together with the nozzles. The high-temperature structure portion of the test rig, except the subject nozzle and rotor, is made of super alloys, and air cooling is done to enable it withstand continuous operation at 1350°C TIT. The life prediction of each of the rotors analyzed from the material characteristics of Fig. 5 and the actual results of the hot spin tests and endurance tests are shown in Figs. 14 and 15. While the life prediction values tend to be somewhat lower than the actual data, the SN91 rotors are hard to adopt for many hours of operation at 1200°C TIT. As for the SN88M rotors, it seems that their 100-hour level durability at 1350°C TIT can be assured by applying cold or hot spin screening proof tests to the rotors at the lower side of scattering. The endurance tests at 1350°C TIT are now being carried out.

The SN91 and SN88M coordinated in terms of the Larson–Millar parameters used for evaluation of the creep rupture of super alloys are shown in Fig. 16. Two regions clearly different

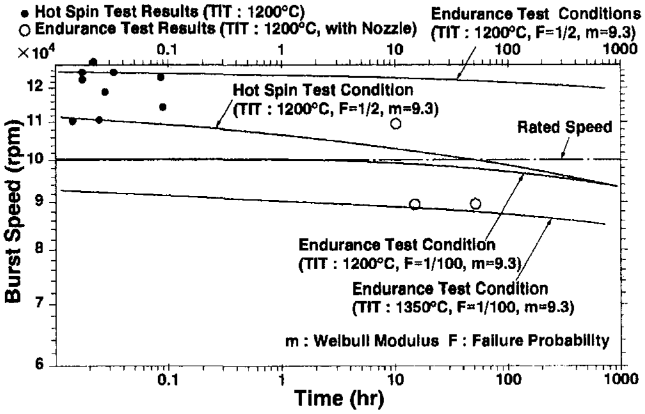

Fig. 14 Life prediction and test results of SN91 rotor

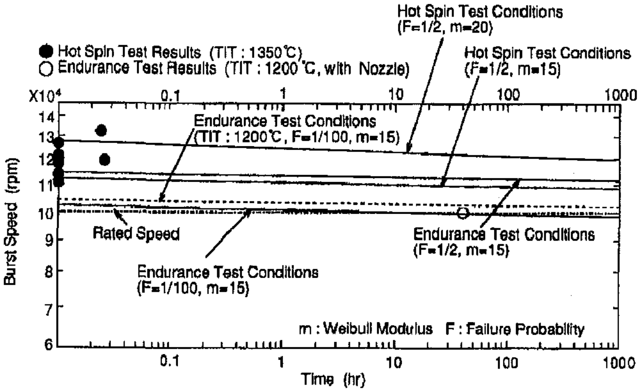

Fig. 15 Life prediction and test results of SN88M rotor (TIT; 1350°C, except ○, -----)

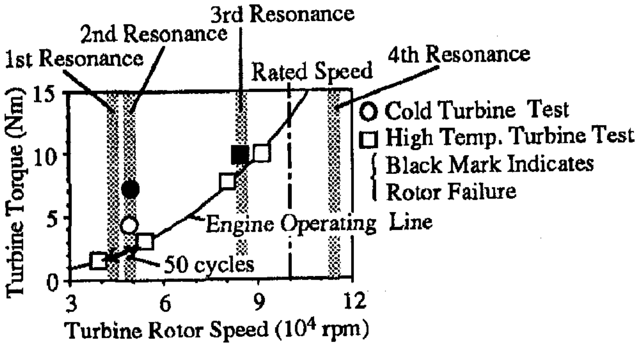

Fig. 17 Extent of damage due to blade-vibration stress (SN91, first design rotor)

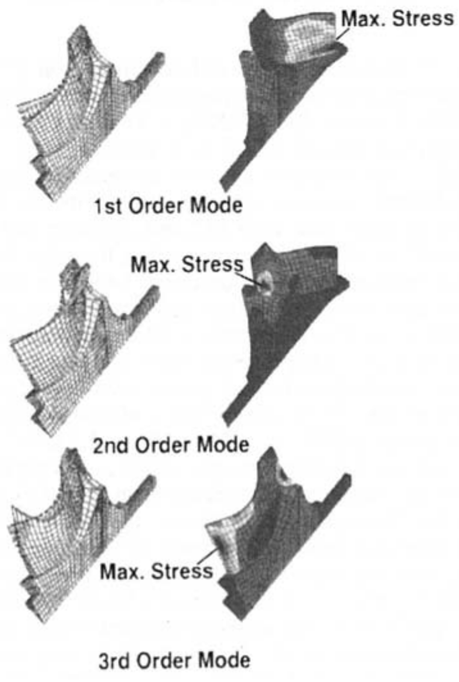

Fig. 18 Blade-vibration modes and stress distributions

in fracture pattern exist. On the high-temperature, long-term side, changes in the quality of the material microstructure occur as mentioned above. The tendency is obvious in the SN91 in which it appears at the low Larson–Millar parameter values, and there is also large scattering. The scallop region, which is relatively high in both stress and temperature levels, is the most likely cause for fracture of the SN91 rotors. On the SN88M rotors, however, both the stress and the Larson–Millar parameter have proper margins.

Rotor Blade Vibration Strength

As the procedures for development of turbines, the data on aerodynamic performance were first acquired and evaluated by low-temperature air through use of metallic model rotors. Blade design was then determined and ceramic rotors were manufactured to proceed with strength experiments and evaluations. To verify the aerodynamic performance of the ceramic rotors, they were placed in low-speed, high-load operation under low-temperature air to simulate aerodynamic conditions, but there happened rotor failures in those tests. The results of subsequent analysis and study revealed that the cause for the failure was the second-order mode blade vibration stress generated by the blades resonating with the nozzle wakes. Figure 17 shows the relation between the blade resonance ranges and turbine loads. At the second-order mode resonance point, about three times of the turbine torque in the engine caused the failures. If it is lowered to a level equivalent to the engine load, no failure occurs. In the high-temperature turbine durability tests, however, the rotor broke down in the third-order mode as well. Therefore, we conducted further experiments for analysis and further study. Figure 18 shows the vibration patterns of the first, second, and third-order modes and the stress distributions that exist in the operating range of the engine. The primary cause seemed to be that the vibration damping factors of the ceramic materials were smaller than those of metals. To measure the vibration damping factors, therefore, we used the equipment shown in Fig. 19. The ceramic materials, compared with heat-resistant metallic materials, have much less internal friction. The internal friction of the SN91 for example was found to be approximately 0.1 of that of the metallic materials, and that of the SN88M was found to be approximately 0.3. On the other

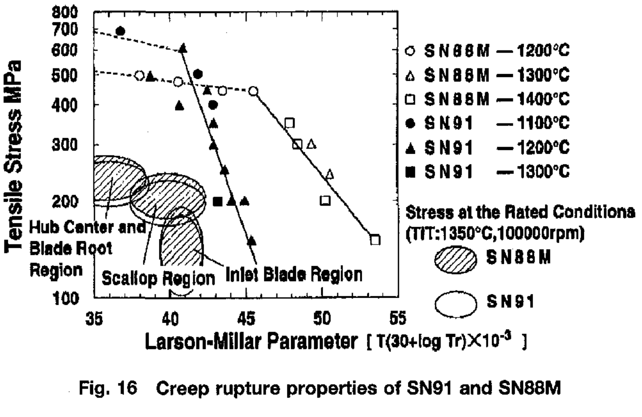

Fig. 16 Creep rupture properties of SN91 and SN88M

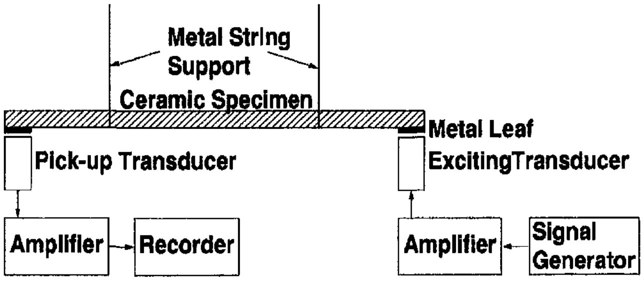

Fig. 19 Measurement equipment of internal friction

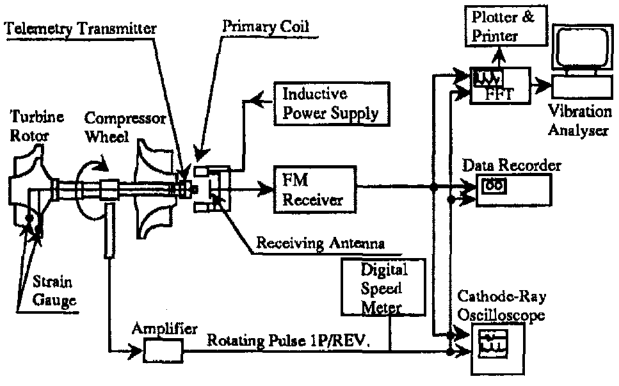

Fig. 20 **Measurement system diagram of blade-vibration stress**

hand, the SN88M is better than the SN91 in the vibration strength aspect as well.

To clarify the blade vibration strength criteria, resonance point vibration stress in the first design metallic model rotors was measured by the strain gages bonded in the vicinity of the stress peak points and a FM telemeter. Low-temperature air was set flowing to see the behavior of vibration stresses under loaded conditions on the blade surface, and to know the total damping factors inclusive of aerodynamic elements and the exciting forces originating from the nozzle wakes. Figure 20 shows the measurement system. Figure 21 shows the measured stress values for the loads, and the peak point stresses estimated from the measuring point stresses. The exciting force proportionally increases with respect to the turbine load. The sensitivity to vibration stress is about equal in the first and third-order modes. In the second-order mode, the sensitivity is about 40 percent higher than in the first and third modes.

The damping characteristics of the ceramic materials and exciting force levels measured by the above-mentioned procedures were applied to the vibration stress analyses of the ceramic rotor blades. Then we calculated the failure probability or safety factor combining the centrifugal stress from static and cyclic fatigue strength of the materials and found the criteria in comparison with the actual fracture conditions. Although it became clear that the fracture probability in the first and second-order modes could be put down low enough by changing the material to SN88M, which has greater internal friction and reviewing blade thickness distribution, we decided to exclude the third resonance points from the operating range of the engine, because the excitative force was large and the centrifugal stress level high. Therefore, we changed the number of nozzle vanes from 21 to 18 and increased the level of the third-order mode vibration frequency. In addition, by use of a scaled-up nozzle model, the pattern of the nozzle wakes were measured by pitot tubes along the flow direction. The results obtained reveal sufficient damping of the wakes over a distance from the nozzle trailing edge to the rotor tip.

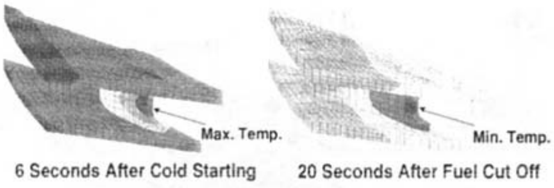

Fig. 22 **Turbine nozzle temperature distribution**

Nozzle Design and Evaluation

From the manufacturing standpoint, the nozzle is split into six segments as shown in Fig. 4 and made from SN88 supplied by NGK. Three of the segments have radial keys provided on both side plates for centering between the rotor and the shroud. The stationary structural portion, as shown in Fig. 1, is stacked up by the spring forces and balance piston forces. For a pressure difference that occurs due to expansion in the nozzle, the gas is sealed by the inner and outer peripheral portions of the side plates. In the first design specification, the number of nozzle

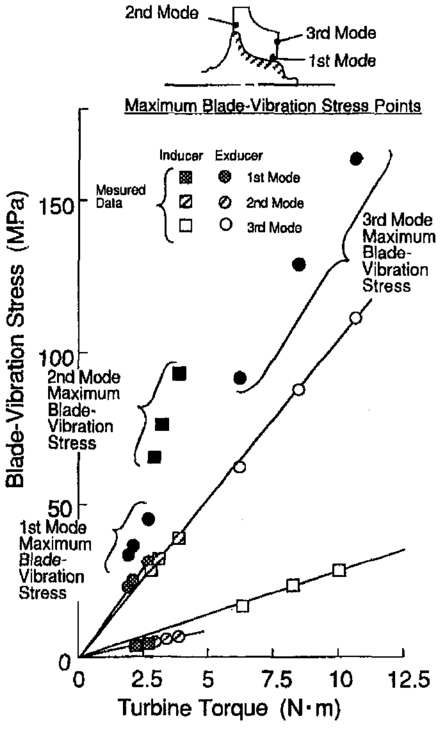

Fig. 21 **Measurement results of blade-vibration stress**

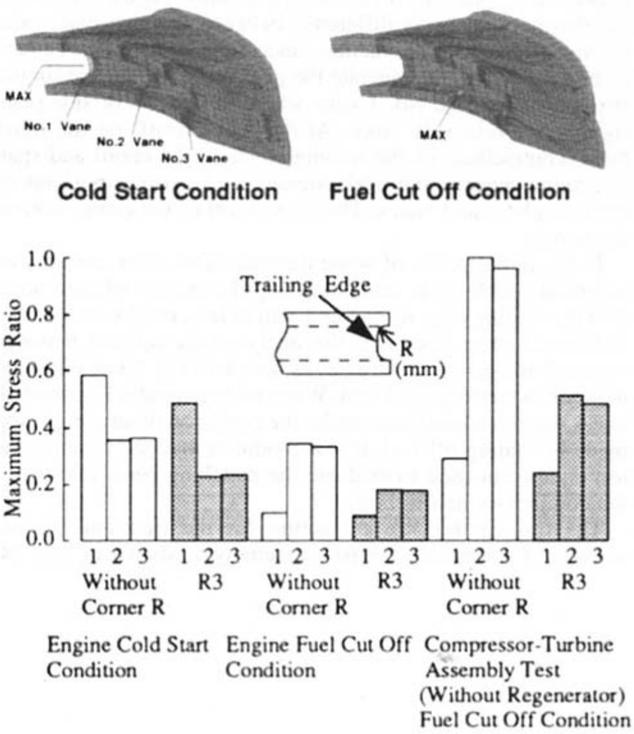

Fig. 23 **Maximum thermal stress of turbine nozzle**

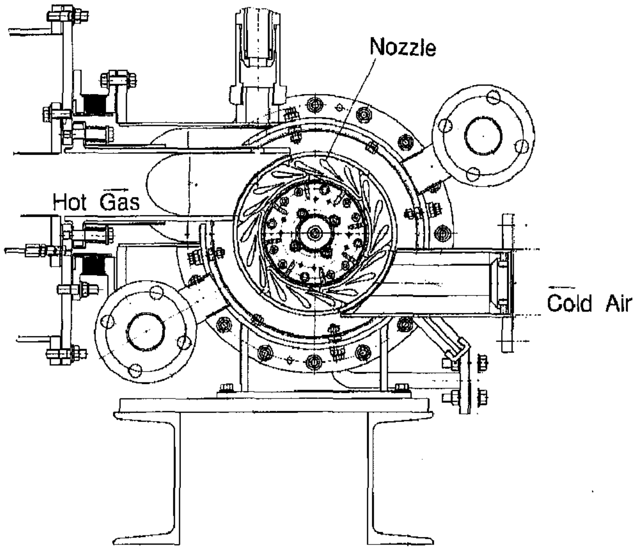

Fig. 24 Nozzle thermal-shock test rig

vanes was set at 21, and the nozzle was configured by three- and four-vane segments. To avoid resonance with the third-order mode of the rotor blades, the 18-vane nozzle was configured by three-vane segments only.

What affects the life of a nozzle is the thermal stresses generated by transient temperature distributions at cold starts and stops. Analyses were made by setting the severest condition of raising the temperature in step to 1350°C when the combuster was ignited at the cold start, and cutting off the fuel from 1350°C. Figure 22 shows the temperature distribution when the maximum temperature gradient is generated at the cold start and fuel cut-off. In all of the cases, a relatively large temperature gradient is produced at the vane trailing edges. The temperature gradient at the fuel cut-off, however, is not so sharp as at the cold start, because the gas temperature fall is slower due to the accumulated heat effect of the regenerators. At the cold start, the thermal expansion difference between the side plates and the vanes in the chord direction concentrate strains at the centers of trailing edges and generate the peak stresses. The maximum stress occurs in the No. 1 vane where the effects of side plate rigidity are relatively large. At the fuel cut-off, on the other hand, contractions of the trailing edges in the chord and span directions generate the peak stresses in the corner portions of the side plates and vanes. The stress level of the center vane is the largest.

In the initial phase of some thermal shock tests, because of technical problems in manufacturing the nozzle whose corner *R* of the trailing edge roots was 1 mm or less, cracks attributable to thermal stress occurred. We analyzed the relation between corner *R* and generated stresses as shown in Fig. 23 and decided to secure a corner *R* of 3 mm. When no regenerator is provided, stress reaches a maximum under the condition of an abrupt stop made by cutting off fuel. It is a condition that can occur in the test equipment used to evaluate the matching performances of the compressor and turbine.

The test rig for life evaluation for the transient thermal stresses of the nozzle segment assembly is shown in Fig. 24. The test rig is designed for cyclic exposures of the nozzle segments to the high-speed streams of TIT level hot gas and cold air to provide transient temperature distributions. Endurance tests were performed by inserting thermocouples in a vane in one of the segments to monitor temperature change patterns and giving temperature gradients 1.2 to 1.4 times the analyzed values of Fig. 23. The endurance tests were performed in two stages of 1200°C and 1350°C TIT. In the respective stages, 250 cycles were completed.

Conclusion

Because of the current circumstances in the long-term strength of the rotor materials, we decided to change the rated speed from 110,000 to 100,000 rpm. At the phase of the evaluation tests at 1200°C TIT, we decided to change the rotor material to one that provided more stable long-term stability on the high temperature side. From the hot spin tests at 1350°C TIT, it became clear that a material with enough durability and reliability for use in engine tests could be made available. At present, 1350°C TIT endurance tests are under way.

Rotor blade failures occurred because of their resonances with the nozzle wakes. The primary cause is that the damping characteristics of the ceramic materials are much smaller than those of metals. We analyzed the material characteristics and measured vibration stress to review the analytical procedures and criteria. We implemented a design in which the third-order mode resonance points were removed from the operating range. For the first and second-order modes, design considerations were incorporated to make sure that the allowable vibration stress limits were not exceeded.

The nozzle configured by six segments has successfully completed 250 cycles of heating and cooling thermal shock tests simulating engine starts and stops at 1350°C TIT maximum.

Both the rotors and nozzles have been subjected to experiments up to 100,000 rpm at 1200°C TIT with all the component elements installed in the full-assembly test rig having the same basic configuration as the engine. Planning is under way to increase TIT to 1350°C step by step in this full assembly test rig.

Acknowledgments

The authors are grateful to the Agency of Natural Resources and Energy of the Ministry of International Trade and Industry for making this research possible, and also grateful to PEC for permitting of publications this paper. The authors would also like to thank members of JARI and other cooperative companies for technical support.

References

1 Nishiyama, T., et al., "Status of the Automotive Ceramic Gas Turbine Development Program—Year Four Progress," ASME Paper 95-GT-447.

2 Nakazawa, N., et al., "The Turbine Components Development for the 100 kW Automotive Ceramic Gas Turbine," ASME Paper 93-GT-64.

3 Watanabe, M., and Ogita, H., "Evaluation of Ceramic Rotor Strength by Cold and Hot Spin Tests," ASME Paper 94-GT-460.

4 Izumi, T., et al., "The Turbine Components Development for the 100 kW Automotive Ceramic Gas Turbine (Stationary Parts)," *Preprints of 9th GTSJ Autumn Meeting*, Oct. 1994, pp. 39–46.

5 Nakazawa, N., et al., "Development of Turbine Components for the 100 kW Ceramic Gas Turbine," *Proc. 1995 Yokohama International Gas Turbine Congress*, 95-YOKOHAMA-IGTC-63, Oct. 1995.

6 Nemeth, N., Mandersheid, J., and Gyekenyesi, J., "Ceramics Analysis and Reliability Evaluation of Structures (CARES)," NASA Technical Paper 2916, 1989.

Progress on the European Gas Turbine Program "AGATA"

R. Gabrielsson
Volvo Aero Corporation,
Trollhättan, Sweden

G. Holmqvist
Volvo Aero Turbines,
Malmö, Sweden

The four-year European Gas Turbine Program "AGATA" was started in January 1993 with the objective of developing three critical components aimed at a 60 kW turbogenerator in an hybrid electric vehicle: a catalytic combustor, a radial turbine wheel and a static heat exchanger. The AGATA partners represent car manufacturers as well as companies and research institutes in the turbine, catalyst, and ceramic material fields in both France and Sweden. This paper outlines the main results of the AGATA project for the first three-year period. Experimental verification of the components started during the third year of the program. A high-pressure/temperature test rig for the combustor and the heat exchanger tests has been built and is now being commissioned. A high-temperature turbine spin rig will be ready late 1995. The turbine wheel design is completed and ceramic Si_3N_4 spin disks have been manufactured by injection molding and Hot Isostatic Pressing (HIP). A straight blade design has been selected and FEM calculations have indicated that stress levels that occur during a cold start are below 300 MPa. The catalytic combustor final design for full-scale testing has been defined. Due to the high operating temperature, 1350°C, catalyst pilot tests have included aging, activity, and strength tests. Based on these tests, substrate and active materials have been selected. Initial full-scale tests including LDV measurements in the premix duct will start late 1995. The heat exchanger design has also been defined. This is based on a high-efficiency plate recuperator design. One critical item is the ceramic thermoplastic extrusion manufacturing method for the extremely thin exchanger plates another is the bonding technique: ceramic to ceramic and ceramic to metal. Significant progress on these two items has been achieved. The manufacturing of quarter scale prototypes is now in process.

Introduction

The European EUREKA Gas Turbine Program "AGATA" [*A*dvanced *G*as *T*urbine for *A*utomobiles] has been running since Jan 1993 with the objective of developing three critical components for a 60 kW turbogenerator in an hybrid electric vehicle: a catalytic combustor, a radial turbine wheel, and a static heat exchanger. The objective is to develop and test the three components individually as a full-scale feasibility study for future automotive applications.

Pollutant emissions and fuel economy are prime and growing concerns in the development of energy converters for automobile applications. For both issues, high-performance objectives will have to be reached regardless of possible changes in the type and quality of available fuels.

Technical specifications for the gas turbine, excluding electric generator, are as follows:

- Mechanical output: 60 kW
- Specific fuel consumption minimum: 200 g/kWh
- Turbine inlet temperature: 1623 K
- Maximum pollution emission: ULEV or similar European standards
- Fuel: Diesel or alternative fuels

The AGATA partners represent car manufacturers as well as companies and research institutes in the turbine, catalyst, and ceramic material fields in both France and Sweden, as listed below:

AC Cerama AB	(S; company)	Ceramics
Aerospatiale	(F, company)	Ceramics
Allied Signal Catal. Environ. (ACE)	(F, company)	Catalyst
Allied Signal Turbo SA	(F, company)	Turbines Ceramics
CEA/Cerem	(F, research lab)	Materials
Ceramiques et Composites	(F, company)	Ceramics
GRETH	(F, resarch lab)	Heat exchangers
Institute Francais du Petrole	(F, research lab)	Combustion Catalyst
ONERA	(F, research lab)	Turbines Combustion Heat exchangers
Peugeot SA	(F, company)	Automobile
Renault	(F, company)	Automobile
Volvo Aero Corporation	(S, company)	Turbines Ceramics

Program Status

During the first two years of the program, design of the components, selection of manufacturing processes, and definition of the test equipment has been completed. A dynamic system model has also been developed for the AGATA engine. The following important component parameters have been analytically defined:

- Turbine wheel efficiency 86 percent.
- Catalytic combustor premixing zone and catalytic section final design including predicted fuel/air profile, degree of vaporization, autoignition risks, and catalyst formulation.

Contributed by the International Gas Turbine Institute and presented at the 41st International Gas Turbine and Aeroengine Congress and Exhibition, Birmingham, United Kingdom, June 10–13, 1996. Manuscript received at ASME Headquarters February 1996. Paper No. 96-GT-362. Associate Technical Editor: J. N. Shinn.

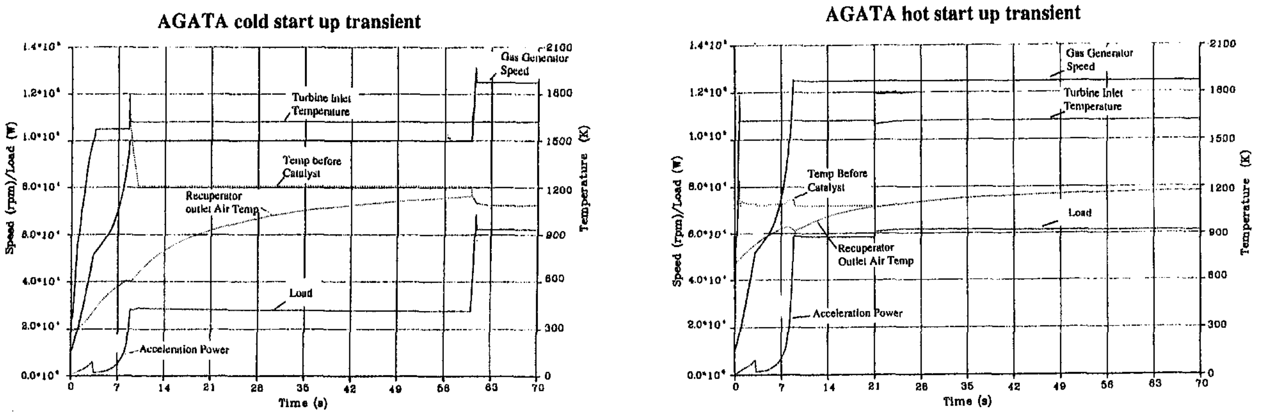

Fig. 1 Cold and hot start transients

- Fixed geometry heat exchanger performance and dimensions. The total volume and weight will be 55 liters and 50 kg (casing included).

Manufacturing of hardware is ongoing. Full-scale hardware for first tests will be ready October 1995.

A high-pressure/temperature test rig for full-scale combustor and heat exchanger tests has been built and is now being comissioned. LDV evaluation tests of flow patterns in the premix duct upstream of the combustor catalyst section will start December 1995. A high-temperature turbine spin rig will be ready late 1995.

During the third year of the program, experimental verification of scaled components was carried out. Ceramic materials and active catalyst materials have been focused on. Active catalyst material screening and performance testing including aging has been performed in a pilot scale test rig. Heat exchanger matrix test samples have been tested at high temperature in order to evaluate thermal fatigue behavior and bonding properties.

System Definition

The AGATA program is dedicated to the development of critical gas turbine components. The engine system is based on a dynamic model developed at Volvo Aero Turbines taking into account thermal storage in heat exchanger and catalytic combustor as well as a thermal model of heat losses in the engine housing. The main activities have been to define and model steady-state transient conditions for hybrid vehicle driving conditions in order to account for their impact on temperature fluctuations and the consequent effects on stress and life.

Steady-state calculations at 298 K and 101.3 kPa inlet conditions give the following values:

Load, percent	SFC, g/kWh	Thermal efficiency, percent	Combustor inlet temperature, K	Turbine inlet temperature, K
100	200	42	1208	1623
50	211	39	1208	1518

The part-load SFC depends on the gas turbine control strategy. Increasing Turbine Inlet Temperature leads to decreasing SFC. At 50 percent load, SFC = 211 g/kWh is obtained at TIT = 1518 K, while SFC = 208 g/kWh can be obtained at TIT = 1623 K. This high TIT at 50 percent load, however, leads to increased combustor air inlet temperature. This can be a limiting parameter depending on the auto-ignition risk in the fuel premix duct upstream of the catalytic section.

Besides the cold start transient, a number of hot start and load transients have also been evaluated. The cold and hot start transients are shown in Fig. 1. The schedule for the cold start, which is the critical condition for the ceramic parts, has been chosen in order to separate thermal and centrifugal mechanical stress. This is achieved by a start procedure as follows. Increase turbine inlet temperature, TIT, to a maximum 1623 K and accelerate the gas generator speed to 80 percent. The gas generator speed is held at 80 percent for 60 s, allowing temperature gradients to even out. During hot start conditions there is, however, no limitation on the start cycle. In practice, the driving cycle for a recuperated gas turbine would normally only include one cold start per day because of heat storage in the recuperator. During the typical hot start, the acceleration to 100 percent speed and maximum power takes 9 s.

Load transients are of importance in automotive applications. This is true also for hybrid applications because battery charging efficiency is improved when the engine power follows the road demand. Calculated acceleration time from 30 percent to full load is 0.9 s and from 50 percent to full load 0.5 s with a gas generator speed increase from 102,000 to 125,000 rpm.

The stop transient evaluation has been performed for a number of possible situations. A stop transient with fuel shut down from full load gives a positive output power for 25 seconds. The total time to shut down is 75 s. A load transient and the stop transient from full load are shown in Fig. 2.

Comparing the AGATA recuperated gas turbine with a regenerated gas turbine shows a slower response at cold start but the leakage problem is less pronounced. The planned component rig tests will include simulations of transient conditions.

Ceramic Turbine Wheel

A radial turbine wheel with a straight blade design has been selected. Based on fluid dynamic calculations, the efficiency has been estimated to be 86 percent with a wheel speed of 125,000 rpm. The following factors were considered in the design:

- Optimization to minimize the blade root stress with a design work factor of 1.15 and a tip speed of 600 m/s.
- The possibility to be manufactured by injection moulding, i.e., mold removability without sacrificing the requirement for high efficiency.
- The blade root thickness has been increased in order to move the maximum stress from the blade root to the centre of the wheel hub. This is a result of the need to avoid high stresses at the as-sintered surface of the blade root due to material limitations.
- The overall stress level is a combination of thermal stress, maximized at the blade root and centrifugal stress maximized at the wheel centre. In order to minimize this combination during cold starts, the previously described start schedule with a two-step speed increase was chosen.

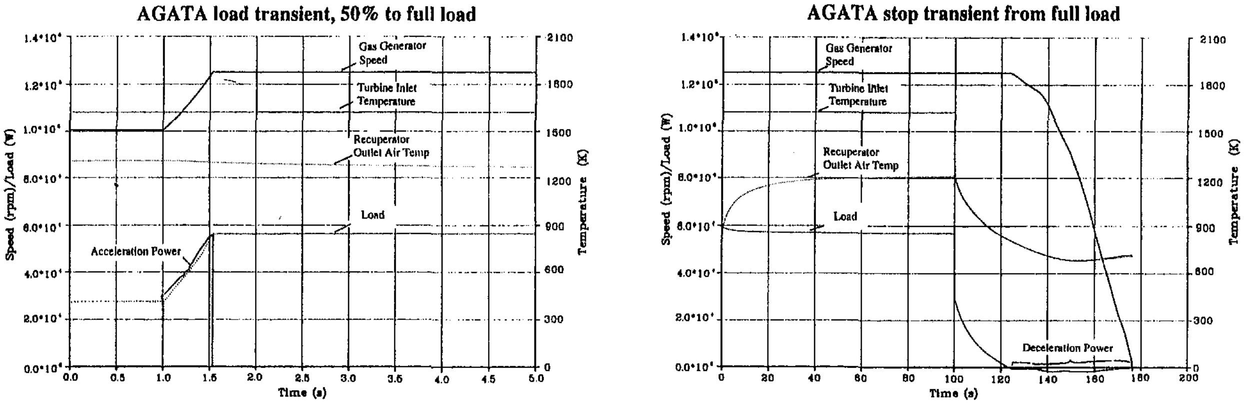

Fig. 2 Load transient from 50 to 100 percent and stop transient

FEM calculations have indicated that the stress level during cold start is below 300 MPa, see Fig. 3. This can be compared with a stress level of 366 MPa if the wheel speed was not restricted to 80 percent during the first 60 seconds.

- The overall failure probability is below 10^{-3}, which is considered acceptable.

Silicon nitride (Si_3N_4) based material compositions with yttrium oxide as sintering aid have been investigated. The mechanical characteristics have shown very promising properties [1–3].

Two manufacturing methods have been evaluated in parallel:

- Volvo-AC Cerama are developing their processing technology for the radial ceramic turbine wheel, combining two green forming techniques with their proprietary glass encapsulation–hot isostatic pressing (HIP) technique. The hub section of the wheel is formed by cold isostatic pressing while the blade-ring is injection molded. After binder burn-out the hub and blade ring are green-joined, glass encapsulated, and HIPed. The advantage of this technique is that the binder burn-out is much easier and quicker for two smaller pieces than for a one-piece injection moulded turbine wheel. The advantage of glass encapsulated HIPing is that virtually all pores and internal cracks are eliminated. The AC Cerama Si_3N_4, designated CSN 101, has been extensively tested. Stress rupture testing as well as tensile creep tests have been performed. These results are presented in a separate ASME paper [4].
- Ceramiques et Composites has continued the investigation of their new processing method. This involves a one-piece wheel design. The wheel is injection molded using a preceramic binder, which can be pyrolyzed into Si_3N_4. The wheel is then sintered by Gas Pressure Sintering (GPS).

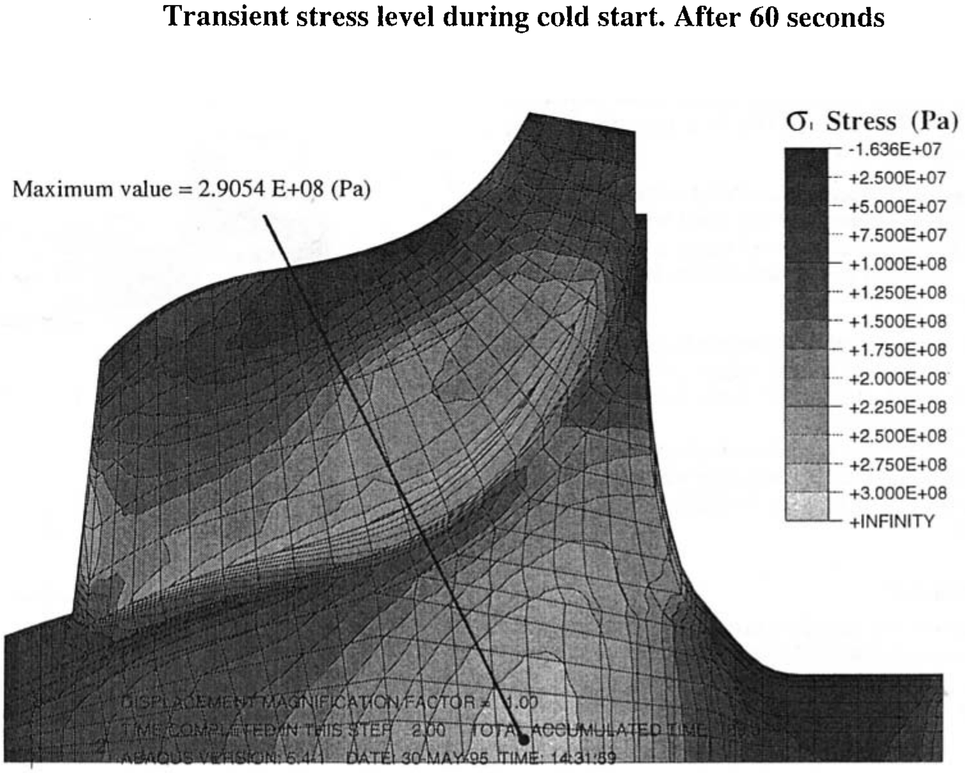

Fig. 3 FEM stress calculation at cold start transient

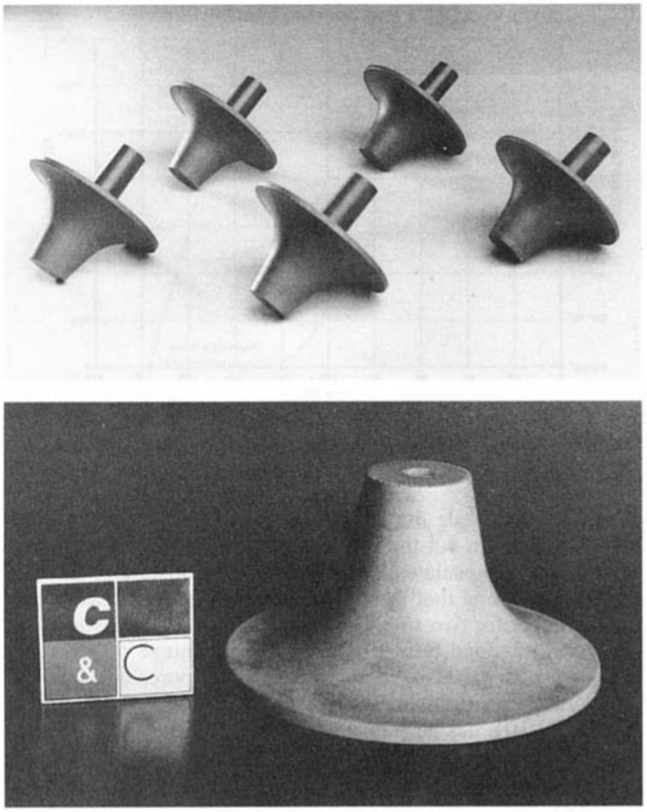

Fig. 4 Dummy wheels: AC Cerama (above) and C & C (below)

These two processing methods have been further developed during the third year of the program and the present status is that full scale disks have been produced by both methods. Examples of the dummy wheels are shown in Fig. 4. These dummy wheels will be cold spin burst tested during December 95. The tooling manufacture for full scale wheels has recently started. More details on Si_3N_4 components and mechanical properties are given elsewhere [1–4].

The wheel shaft joining process has been further developed and investigated by CEA/Cerem. This is a two step brazing process as shown in Fig. 5, where:

- First the ceramic surface is metallized with a braze alloy with low melting temperature but good wettability.
- Finally the brazing is carried out using a higher melting point braze alloy and interlayer between the metallic and ceramic part.

Good torsion test results at high temperature have been obtained for brazed joints. Measured torque values of 10–20 Nm in the temperature interval 400–500°C have been obtained for different joining configurations.

Full-scale ceramic turbine wheel cold spin tests of dummy wheels will start in December 95 and continue with high-temperature/high-pressure spin tests at ONERA during the final year of the project.

Catalytic Combustor

The catalytic combustor technical program is focused on the development of ceramic structural components and on the catalytic combustion. The catalytic combustor section layout, Fig. 6, is a laboratory design having the following components in line:

- Preheater
- Mixing zone including bypass valve
- Premix duct
- Catalytic reactor

The preheater design is based on a diffusion combustor concept and is optimized for low NO_x emissions. It has been sized on the basis of the transient cold start simulations and will be operated only during the start-up period of 60 seconds. It will be bypassed for all other engine conditions.

In the premix duct, fuel is vaporized and mixed with air. The most important parameters for the catalytic combustion are to achieve complete vaporization and fuel/air homogeneity before the fuel enters the catalyst. In order to obtain high hetero/homogeneous combustion efficiency with low emission values, it is also important to create an even velocity profile at the catalytic section inlet. Another critical limitation for the premix duct is auto-ignition because of the high inlet temperature to the combustor in a recuperated gas turbine. This means that the fuel/air mixture can pre-ignite in the duct upstream of the catalyst and result in high NO_x emissions and combustor overheating. A premix duct configuration based on a venturi concept has been chosen. Fuel is injected upstream of the venturi minimum section with injectors angled relative to the air flow. Mixing is achieved with a inlet radial/axial turbulence generator in the venturi inlet, while the turbulence level downstream is kept low in order to minimize the auto-ignition risk. The residence time has also been minimized for the same reason.

Numerical simulations of flow pattern and fuel/air ratio represented as adiabatic temperatures have been performed. These calculations show velocity variations in the venturi outlet from 32.5 m/s in the center to 20 m/s at the periphery and an adiabatic temperature distribution with a maximum of 1660 K in the center. This is higher than the specified catalyst temperature and means that the catalyst substrate material needs to be very carefully verified. The calculated degree of evaporation is 95 percent.

However, the calculated fuel/air profiles and degree of evaporation are highly dependent on the fuel injector geometry and its estimated performance.

A dynamic catalyst code has been developed at Volvo Technological Development in order to simulate the catalytic reactor behavior during transient conditions. The dynamic catalyst code is based on a "tank in series" model with Langmuir-Hinsel-

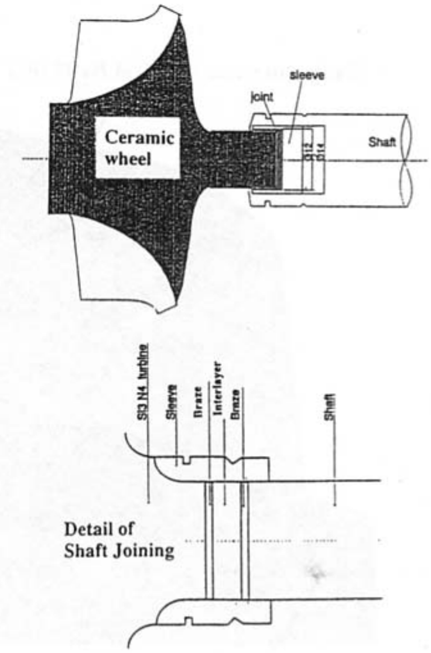

Fig. 5 Wheel shaft joining

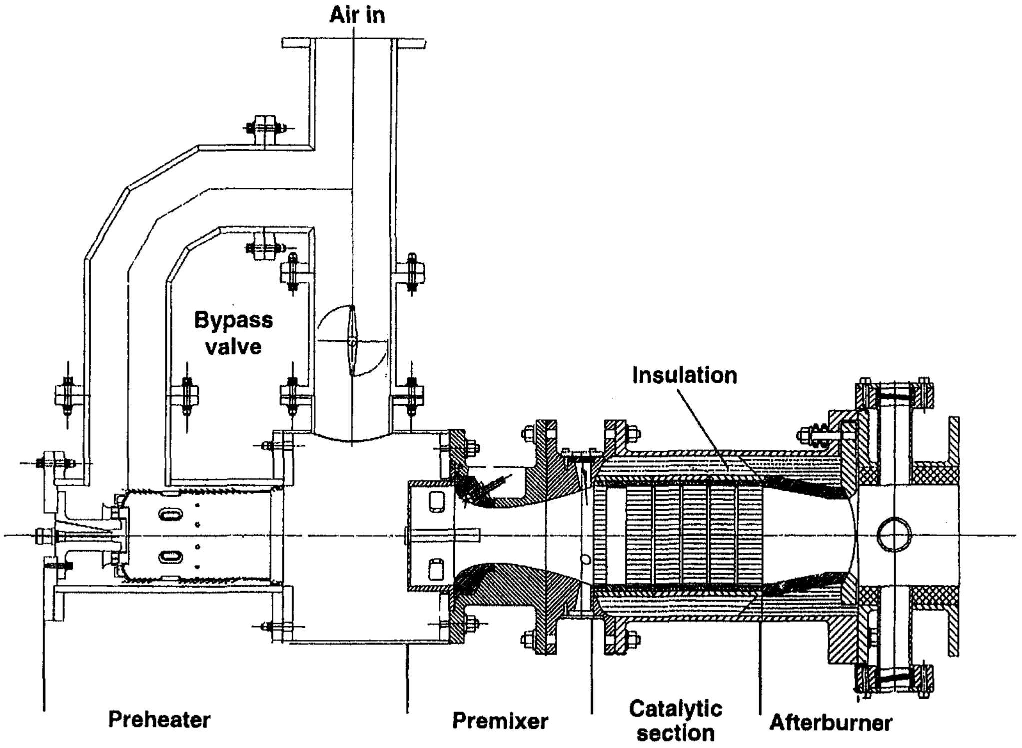

Fig. 6 AGATA catalytic combustor layout

wood surface kinetics and a two-step homogenous reaction mechanism for *n*-octane [5].

Figure 7 shows an example of predicted catalyst inlet and outlet temperatures and CO emissions during load changes from 100 percent load to idle condition. In this calculation, two possible idle conditions have been evaluated. When idling, the gas generator speed and TIT are reduced. Two different TIT conditions were analyzed, 1200 and 620°C. The lower TIT resulted in incomplete homogenous combustion in the reactor due to the compact hetero/homogenous reactor design. This has an extreme impact on CO formation.

As shown in Fig. 8 the dynamic model has also been used to model the light-off behavior of the catalytic reactor. The model shows qualitatively good agreement in light-off temperature, 400°C, compared with test results of 380°C. The test results were obtained by using two consecutive inlet temperature ramps, first and second ramp. As shown both experimentally and theoretically, CO emissions are formed in a limited temperature region before homogenous complete combustion is achieved. It is thus important to minimize the time in this temperature region in order to limit the start-up CO emissions.

The catalyst active material and substrate have been chosen after a screening process involving:

- Pilot tests in the test rig at IFP.
- Accelerated aging at 1350°C in flowing moist air for 3 hours at ACE.

Based on these results, the catalytic section materials for the first full-scale prototype were chosen. Two alternative substrate materials will be tested:

- Cordierite Ex22 (Corning). This material has excellent thermal shock properties, but will not be acceptable at the AGATA specified full load condition due to its overly low melting point.
- Ceramiques et Composites oxide ceramic material. This material exhibit a significant higher melting point although lacking the extremely good thermal shock resistance of cordierite.

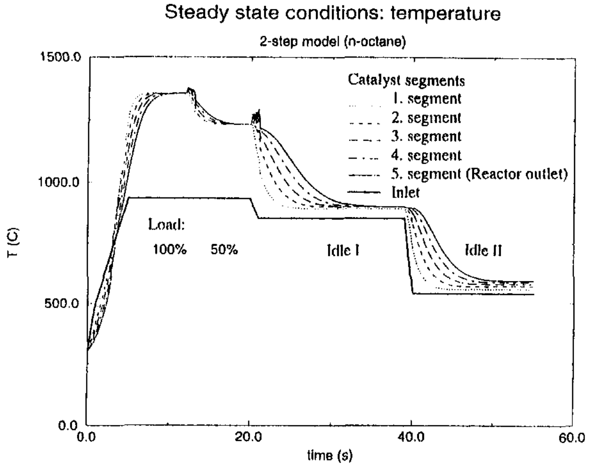

Fig. 7 (*a*) Catalyst segment outlet temperature for four load levels as a function of time

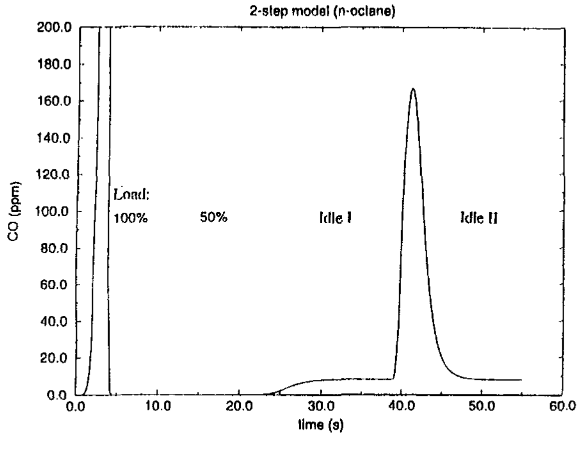

Fig. 7 (*b*) CO emissions at the catalytic reactor outlet for four load levels

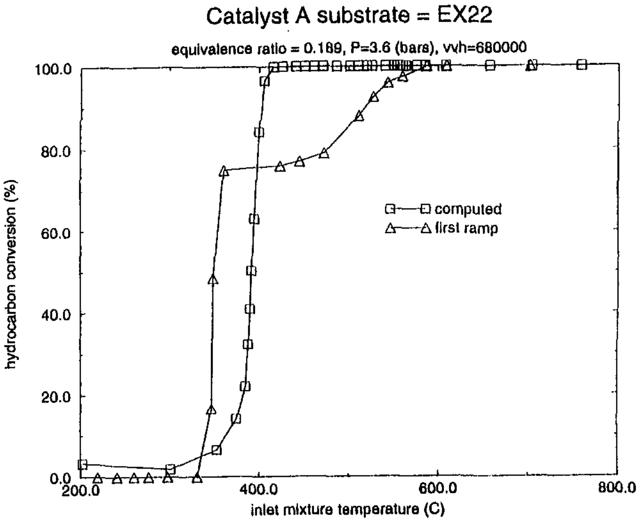

Fig. 8(*a*) Hydrocarbon conversion as a function of catalytic reactor inlet temperature. Calculated light-off temperature: 400°C. Measured light-off temperature (first ramp): 380°C.

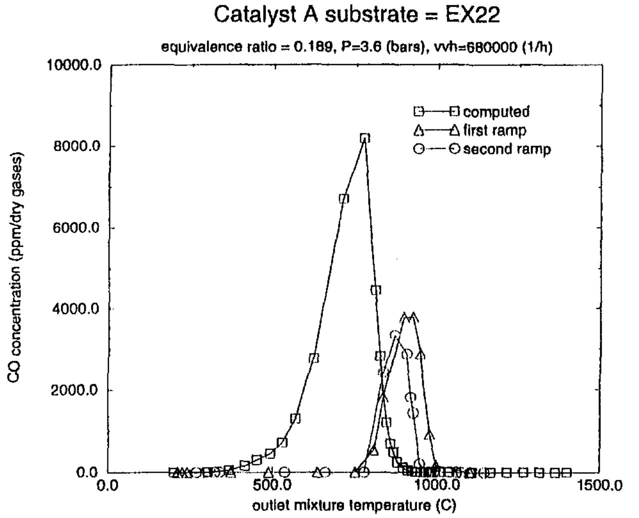

Fig. 8(*b*) CO emissions as a function of catalytic reactor outlet temperature, calculated and measured (first and second ramp)

Conversion tests after the accelerated aging procedure for these material combinations are shown in Fig. 9.

Manufacturing of the full-scale catalytic combustor is under way and will be ready for the first aerodynamic tests during December 1995. The test rig shown in Fig. 10 is now being commissioned. This test rig will simulate the actual AGATA steady-state conditions. Transient simulation will be dependent on the rig heat exchanger heat storage.

Heat Exchanger

The technical program is focused on the development and validation of a ceramic high efficiency (90 percent), fixed-geometry heat exchanger/recuperator. The concept is based on stacking undulated (wavy) layers separated by thin flat sheets. Due to the high thermal efficiency required and the volume constraints, a counterflow design has been adopted. Ceramic extrusion technology has been developed in order to produce extremely thin-walled parts with minimum deformation.

The design of the heat exchanger matrix and the inlet and outlet zones has been completed. A matrix configuration with a gas channel height of 3 mm and an air channel of 2 mm has been chosen. The thickness of the undulating sheets has been chosen as 0.2 mm, while the flat sheet thickness has been set to 0.3 mm in order to ensure a good pressure resistance.

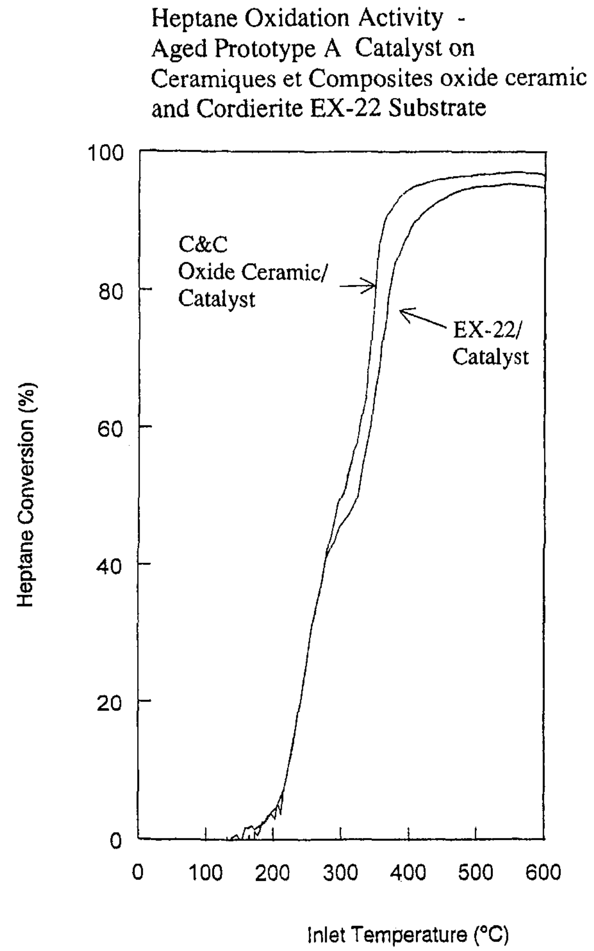

Fig. 9 AGATA catalyst prototype: heptane conversion versus temperature

Thermomechanical calculations were performed using the AGATA transient start-up conditions, which create the highest temperature gradients within the ceramic matrix and therefore induce the highest stresses. Under transient conditions, two types of stress were calculated, periodic stresses created by the temperature gradient existing across the ceramic wall thickness and global stresses induced into the matrix due to the nonlinear temperature field and rigid nature of the matrix. Two ceramic materials have been evaluated, silicon carbide and cordierite. The thermal properties of cordierite lead to lower thermal

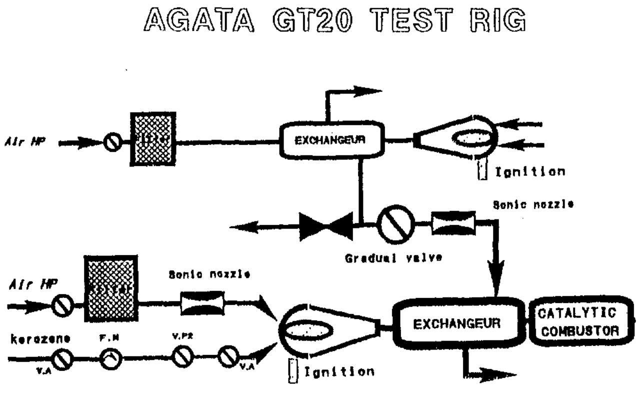

Fig. 10 Catalytic combustor test rig

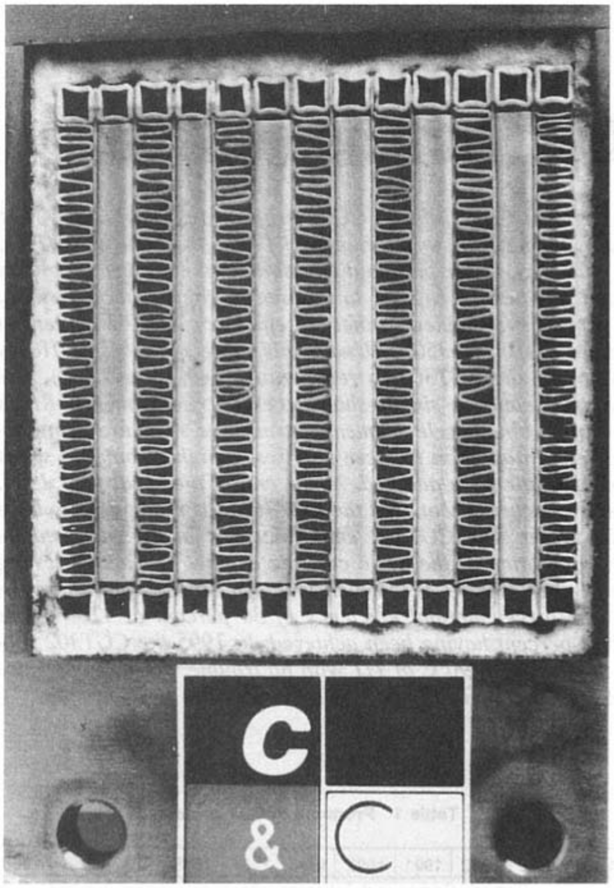

Fig. 11 Heat exchanger test sample after high-temperature cyclic tests

stresses, which makes cordierite the preferred choice despite the higher strength of SiC. Therefore cordierite has been chosen for the prototype heat exchangers.

The cordierite heat exchanger matrix volume and weight is 40 liters and 35 kg. The total volume and weight including inlet/outlet zones and casing would be about 55 liters and 50 kg.

From the ceramic material point of view, the cordierite has shown excellent results with bonding. The thermomechanical resistance of cordierite bonded elements has been evaluated in start and shut-down cycling conditions up to 1100°C. During these tests, the samples were periodically dismantled and inspected for signs of damage. The bonding between the individual elements appeared to be very resistant to transient thermal stresses, while some microcracks were found in air sealing bars at the edges of the samples. A 50 × 50 × 50 mm test sample is shown in Fig. 11.

A complete quarter-scale heat exchanger is now being manufactured. This reduced scale recuperator will be tested under AGATA specified steady-state and transient conditions. The most critical aspect in the design of this component is the connection between the metallic casing and the ceramic inlet and outlet zones. Complete air and gas sealing is required both at room temperature and at 1000°C. The test series with the reduced scale recuperator is planned to start in December 1995.

Conclusions

During the third year of the AGATA program, the design of the three critical components has been finalized and experimental verification of the components has started. The main achievements for the three critical components can be summarized in the following points:

- The turbine wheel design has been defined and ceramic dummy wheels have been manufactured. The Si_3N_4 ceramic exhibits very good mechanical properties.
- The full-scale catalytic combustor is now being manufactured. Based on extensive material screening, both ceramic honeycomb substrate and catalyst active materials have been chosen.
- A complete quarter-scale heat exchanger is being manufactured. Samples have been tested and shown to be very resistant to transient thermal stresses.

Acknowledgments

The authors would like to thank the AGATA partners for their contribution to the technical reports, the French Ministry of Research (MESR), and NUTEK (Sweden), for their sponsorship.

References

1 Larker, H. T., Adlerborn, J. E., and Lundberg, R., ''HIPed Silicon Nitride Wheel Development,'' *Proc. 5th Int. Symp on Ceramic Materials and Components for Engines,* Shanghai, China, 1994.

2 Lundberg, R., ''AGATA—A European Ceramic Gas Turbine for Hybrid Vehicles,'' ASME Paper No. 94-GT-8, 1994.

3 Lundberg, R., Gabrielsson, R., Adlerborn, J., ''Development of Silicon Nitride Components for AGATA—A European Gas Turbine for Hybrid Vehicles,'' *Proc. Int. Gas Turbine Congress,* Yokohama, Japan, Oct. 22–27, 1995.

4 Lundberg, R., and Adlerborn, J. ''Silicon Nitride Components for AGATA—A European Gas Turbine for Hybrid Vehicles,'' ASME Paper No. 96-GT-287, 1996.

5 Westbrook, C. K., and Dryer, F. L., *Combustion Science and Technology,* Vol. 27, 1981, pp. 31–34.

Research and Development of Ceramic Gas Turbine (CGT302)

I. Takehara

I. Inobe

T. Tatsumi

Y. Ichikawa

H. Kobayashi

Engineering Department
Industrial Gas Turbine Division,
Kawasaki Heavy Industries, Ltd.,
Akashi, Japan

The ongoing Japanese Ceramic Gas Turbine (CGT) project, as a part of the New Sunshine Project funded by the Ministry of International Trade and Industry (MITI), aims to achieve higher efficiency, lower pollutant emission, and multifuel capability for small to medium sized gas turbine engines to be used in cogeneration systems. The final target of this project is to achieve a thermal efficiency over 42 percent at a turbine inlet temperature (TIT) of 1350°C. Under this project, Kawasaki Heavy Industries (KHI) is developing the CGT302 (a regenerative twin-spool CGT). The CGT302 has several unique features: simple-shaped ceramic components, KHI's original binding system for turbine nozzle segments, stress-free structure using ceramic springs and rings, etc. In addition to these features, a high turbine tip speed and a metal plate fin recuperator were adopted. At the end of the fiscal year 1994, an intermediate appraisal was carried out, and the CGT302 was recognized to have successfully achieved its target. The CGT302 endurance test at the intermediate stage required 20 hours' operation of the basic ceramic engine. The actual testing accomplished 40 hours at over 1200°C TIT, which included 30 hours of operation without disassembling. The target thermal efficiency of 30 percent at 1200°C has almost been reached, 29.2 percent having been achieved. In 1995 the CGT302 successfully recorded 33.1 percent at 1190°C of TIT with no trouble. We will introduce the current status of R&D of the CGT302 and its unique features in this paper.

Introduction

The Japanese CGT development program is promoted by the Japanese Ministry of International Trade and Industry (MITI), as a part of its "New Sunshine Project" with the aim of saving energy and protecting the environment. The development of the CGT has three stages: (1) 900°C MGT (metal gas turbine), (2) 1200°C Basic CGT, and (3) 1350°C Pilot CGT, as shown in Table 1.

In 1994 this program, which started in 1988, came to an intermediate appraisal. As a result of the intermediate appraisal, MITI decided in 1995 to renew its contract for a two-year extension.

Kawasaki Heavy Industries (KHI) is taking part in this program and has been developing CGT, which is named the CGT302 (300 kW regenerative twin-spool ceramic research gas turbine engine) jointly with Kyocera Corporation (KC) for the ceramic components and Sumitomo Precision Products (SPP) for recuperator.

The specifications of the CGT302 are shown in Table 2. By the end of the fiscal year 1994, KHI successfully achieved the second-stage target and started to develop the final 1350°C CGT. Figure 1 shows the real cut-away model of the CGT302 engine.

In this paper, we describe the current status of the CGT302 development. For more information and details, refer to [1, 2] and others.

Features of CGT302

This engine aims to obtain a thermal efficiency of 42 percent by using ceramic components in, as it were, "the hot section" of a gas turbine engine. About 20 Si_3N_4 ceramic parts are used in the CGT302 and all the ceramic parts, except ceramic coil springs, are made of Kyocera SN-252.

Table 1 Progress of CGT project

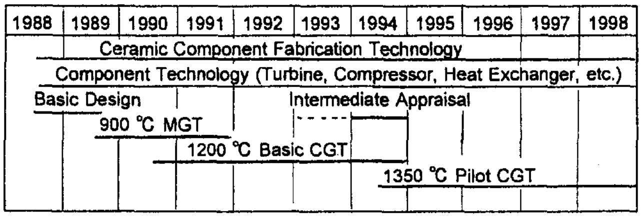

Figure 2 shows the cross section of the CGT302, and all the ceramic components are shown in Fig. 3.

The CGT302 has several unique features:

(*i*) conventional design and metal recuperator,
(*ii*) gas-generator turbine (GGT) and power turbine (PT) nozzles fabricated by unique binding technology, and
(*iii*) stress-free structure using ceramic wave rings and coil springs.

Table 2 Specification of CGT302

Item	Unit	Final Target (Pilot CGT)	Target (Basic CGT)
Mazimum Power	kW(ps)	300 (408)	140 (190)
Thermal Efficiency	%	42	30
Turbine Inlet Temp.	℃	1,350	1,200
Air Flow Rate	kg/s	0.89	0.68
Pressure Rate	–	8	5.9
GGT Speed	rpm	76,000	68,400
PT Speed	rpm	57,000	51,300
Compressor Efficiency	%	82	78
Turbine Efficiency (GGT+PT)	%	85.5	82.2
Heat Exchanger Efficiency	%	80	78

Contributed by the International Gas Turbine Institute and presented at the 41st International Gas Turbine and Aeroengine Congress and Exhibition, Birmingham, United Kingdom, June 10–13, 1996. Manuscript received at ASME Headquarters February 1996. Paper No. 96-GT-477. Associate Technical Editor: J. N. Shinn.

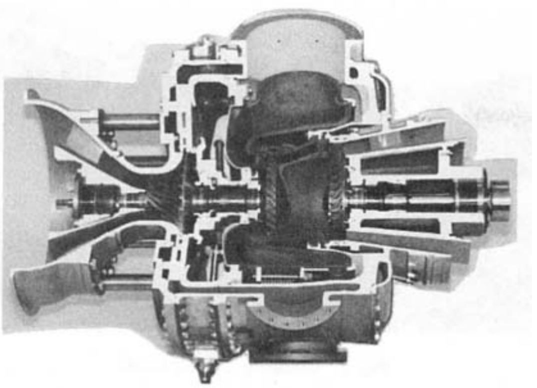

Fig. 1 Real engine cut-away model

1 Conventional Design and Metal Recuperator. For the purpose of applying ceramics to gas turbine components, we adhered to conventional design and structure for avoiding any other difficulties of engine development except ceramics problems themselves. Simple and familiar layout, such as a single can combustor, the scroll, and the metal recuperator for the heat exchanger, represent our concept and design. For the recuperator, as we adopted a higher pressure ratio, the exhaust gas temperature (EGT) has dropped, and it was possible to use the metal recuperator with the proven technology.

2 Gas-Generator (GGT) and Power Turbine (PT) Nozzles Fabricated by Unique Binding Technology. The binding method for turbine nozzles in KHI's original. Usually, the nozzles in gas turbines are divided into segments, which have a complex shape such as a blade airfoil in order to reduce thermal stress on the thin airfoil and massive shroud. We studied a new procedure for nozzle assembly by binding segments together with SiC fibers. The SiC fibers are subsequently converted into fiber-reinforced ceramic (FRC), and finally into a monolithic ceramic ring. The nozzle assembled by this method has advantages as follows: high temperature and thermal stress resistance, ease of handling and installing in the engine system, and so on. The GGT and PT nozzles bound by ceramic fibers are shown in Fig. 4.

3 Stress-Free Structure Using Ceramic Wave Rings and Coil Springs. One of conspicuous features of the CGT302 is the stress-free structure using elastic ceramic components. Stationary ceramic parts of the CGT302 can be divided into three main section: scroll, GGT nozzle, and PT nozzle. These three sections are supported independently of each other, to the metal frame of the engine pushing via ceramic springs. For the purpose of sealing between each section, ceramic piston rings are used for inner and outer seals, and wave rings made of ceramics are used for a symmetric seal. In constructing these system, it is possible to absorb thermal expansion and displacement in the engine system. Figure 5 shows the stress-free supporting system of the CGT302.

R&D of Engine Components

1 Turbine. Turbine component tests for the basic CGT, i.e., cold and hot spin tests, and thermal shock tests, were carried out. These tests were successfully completed by 1994 and now we are evaluating the actual engine.

Through the turbine component tests and engine tests, some turbine parts were improved. The lightweight GGT nozzle assembly and a monolithic outer scroll casing, which was a four-piece composite component originally to reduce thermal stress (the outer casing is the largest part about 320 mm in diameter), were redesigned. For the outer casing, as it was found that a monolithic inner scroll casing having approximately the same size could be used for the rig and engine tests, we tried a monolithic outer casing to simplify and shorten the fabricating process and period. The improved nozzles and outer casing compared with the original are shown in Fig. 6. These parts were evaluated by 30-cycle thermal shock tests (from 150°C to 1200°C) on the rig, and tests were successfully completed.

In the engine testing, particularly in high-speed operation, sometimes a chipping of the GGT blade occurred. Figure 7 shows a typical case of chipping of the GGT blade. Small particles, such as carbon deposition or small chips (metals, ceramics, and other materials) in the engine system or the air, seem to cause foreign object damage (FOD). As one measure against FOD, a massive blade with a blunt leading edge and a trailing edge made twice thicker than before was designed. The number of blades was reduced to 28 from 34. The improved blade and the original blade are shown in Fig. 8.

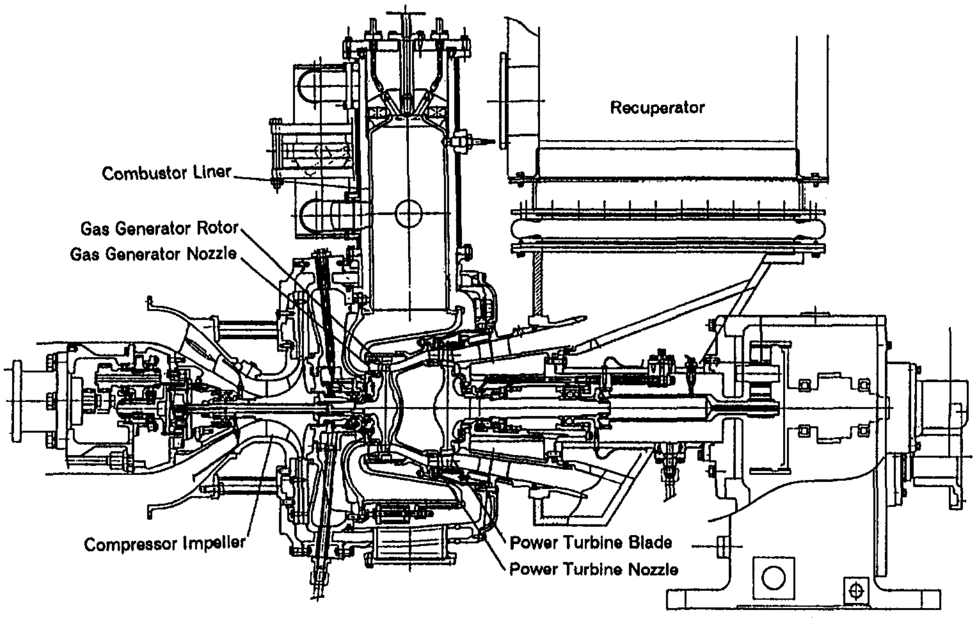

Fig. 2 Cross section of CGT302

Fig. 3 All ceramic components of CGT302

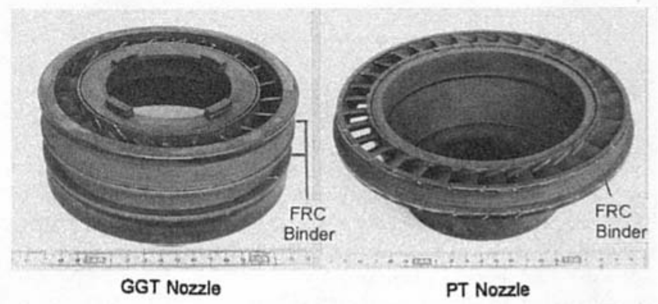

Fig. 4 GGT and PT nozzle

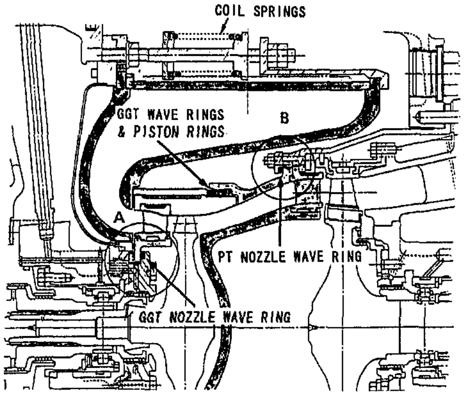

Fig. 5 Stress-free supporting system

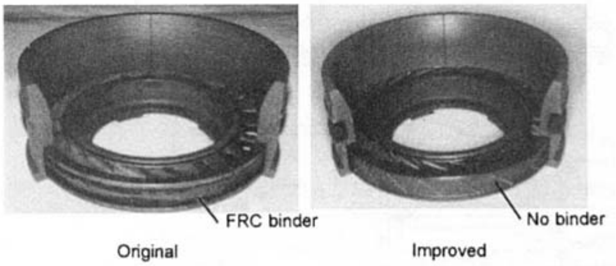

Fig. 6 Improved and original GGT nozzle

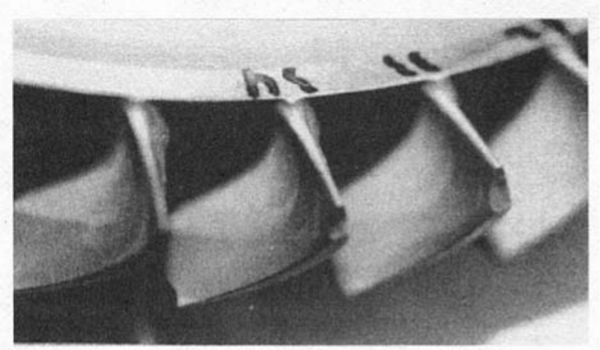

Fig. 7 Chipping of GGT blade

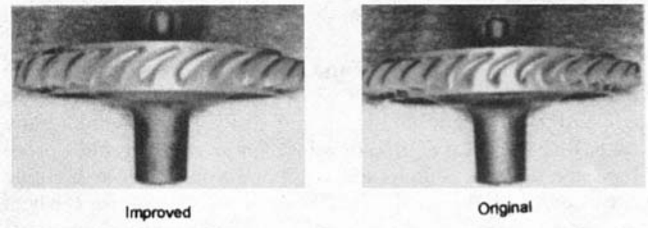

Fig. 8 Improved and original GGT rotor

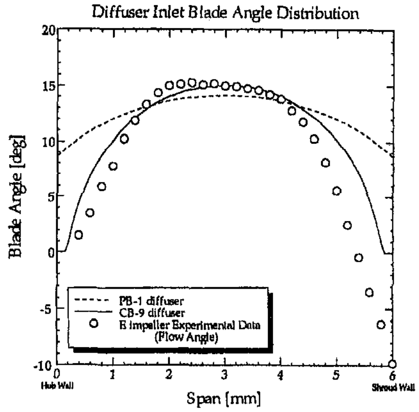

Fig. 9 Measured outlet angle of type *E*

Turbine performance was also measured and evaluated on the actual engine (using the original GGT). Because of difficulties in measuring on the ceramic component, turbine efficiency was measured by joining the GGT and the PT. The measured efficiency was 86.2 percent, greater than the basic CGT target of 82.2 percent and the pilot of 85.5 percent.

2 Compressor. The CGT302 has a single-stage impeller, whose specifications are a 0.89 kg/s air flow rate and a pressure ratio of 8 with an adiabatic efficiency of over 82 percent as the final target. We designed five types of impeller with different airfoils and several angled diffusers. Over the last few years, compressor rig tests have been carried out.

By 1994, it was proved that the type *E* (front loading airfoil type) impeller is the best. In 1995, we achieved the intermediate target (78 percent adiabatic efficiency) using the type *E* with a newly designed channel diffuser (CB-9), in which the diffuser inlet angle distribution is adjusted to the measured impeller air outlet angle distribution. Figure 9 shows the measured air outlet angle distribution of the type *E* impeller and the designed diffuser air inlet angle.

The performance of the type *E* with the CB-9 channel diffuser is shown in Fig. 10, compared with when the originally designed PB-1 pipe diffuser is used. The efficiency of the combination CB-9 gains approximately two points over the PB-1. Matching points of both diffusers tend to lead to a higher flow rate and it comes to a narrower operation range in the high-speed region.

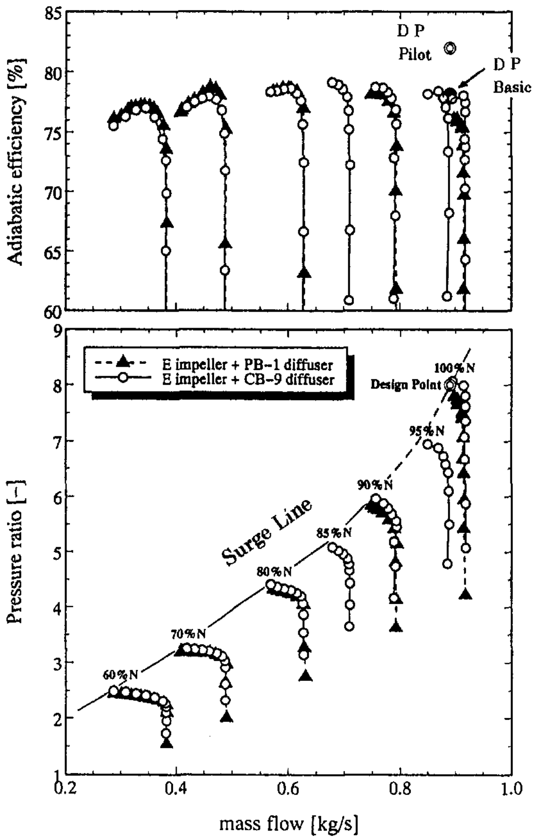

Fig. 10 Performance of type *E* with CB-9 and PB-1

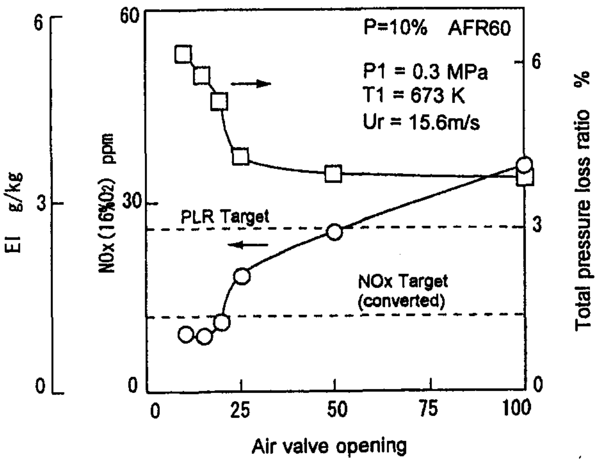

Fig. 12 Total pressure loss ratio and NO_x emissions

3 Combustor. Figure 11 is a schematic drawing of the combustor of the CGT. The ceramic liner is supported by ceramic coil springs. These springs absorb the difference in thermal expansion between the ceramic liner and the metal casing.

The combustor is equipped with the air bypass line, which has one air bypass valve. The valve is controlled to keep the air/fuel ratio (A/F) in the combustion zone within a suitable range, although the total A/F changes widely over a broad operating range.

Using this combustor, combustion rig tests at intermediate pressure were carried out. The inlet pressure and temperature were 0.3 MPa and 673 K, respectively. Results of the tests are shown in Fig. 12. In Fig. 12, the total pressure loss ratio and NO_x emissions are plotted each as a function of the air valve opening of the bypass line, while the A/F is set to a constant value of 60. As the air valve opening is closed, NO_x emissions decrease. At the range where the air valve opening was smaller than 20 percent, the NO_x target was cleared.

The engine tests were conducted with the same configuration after the rig tests. The NO_x emissions results are shown as a function of gas generator rotate speed (N1) in Fig. 13. The NO_x target of the basic CGT was also confirmed in the actual engine under the rated conditions. The value of 69.2 ppm (O_2 = 16 percent) was proved.

Current Status of Development of the CGT302 (R& D of Basic Engine System)

From the first run of the CGT302 in 1993, engine tests have been carried out. At this point, the cumulative operation time has reached about 94 hours. The engine operating time during the tests is shown in Table 3.

At the end of the fiscal year 1994, we demonstrated 30 hours of operation, against the target of over 20 hours operation at 1200°C of TIT, without disassembly at over 1200°C and proved its durability, and the operating time of over 1200°C was accumulated to 40 hours. This engine operated with the full ceramic configuration except for the power turbine blades.

In the series of engine performance tests, in 1994 we achieved its second-stage (basic CGT) target of 30 percent thermal efficiency (it was proved to be 29.2 percent). Furthermore, in 1995 the CGT302 recorded 33.1 percent successfully at 1190°C of TIT and no damage or trouble was detected in the engine sys-

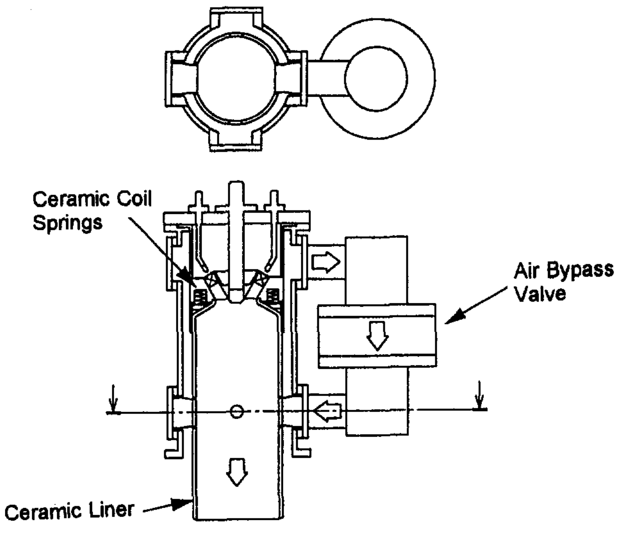

Fig. 11 Schematic drawing of combustor

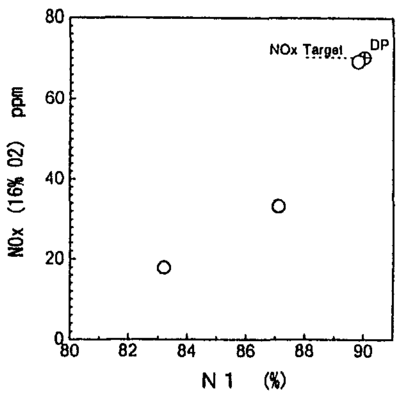

Fig. 13 NO_x emissions at engine test (basic CGT)

Table 3 Cumulative operation time

Operating TIT	Full cofig.	Except PT bld	Cumulative
1200℃~	12 min	39 hr 47 min	39 hr 59 min
1150~1200℃	1 min	2 hr 26 min	2 hr 27 min
1100~1150℃	21 min	3 hr 50 min	4 hr 11 min
1000~1100℃	58 min	15 hr 25 min	16 hr 23 min
800~1000℃	2 hr 26 min	28 hr 32 min	30 hr 58 min
Total	3 hr 58 min	90 hr 00 min	93 hr 58 min
Start/stop	19	273	292

tem. The performance curve plotted against the gas generator speed is shown in Fig. 14, and in Fig. 15 against the power turbine speed. A summary of the engine data obtained is shown in Table 4.

Throughout these durability and performance tests, the CGT302's concept and design were verified and now we are beginning to the next step to the final target (pilot CGT).

Summary

1 The CGT302 cleared the intermediate appraisal and the development for the final stage of 1350°C CGT (Pilot CGT) has started.

2 The cumulative operating time of the CGT302 has reached 94 hours and we have confirmed its 30 hours durability operation without disassembly at a TIT of over 1200°C.

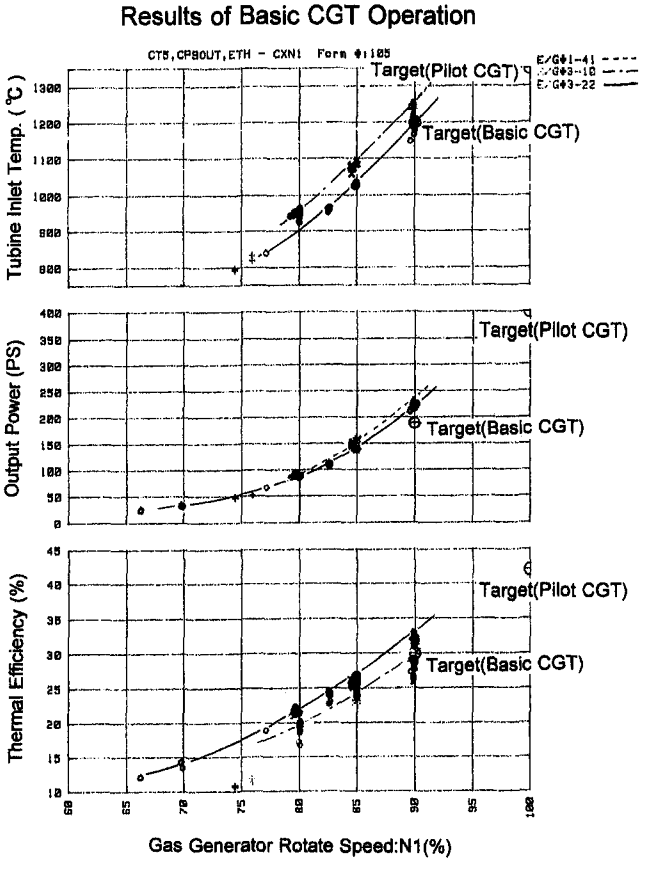

Fig. 14 Performance curve of CGT302 (basic CGT)

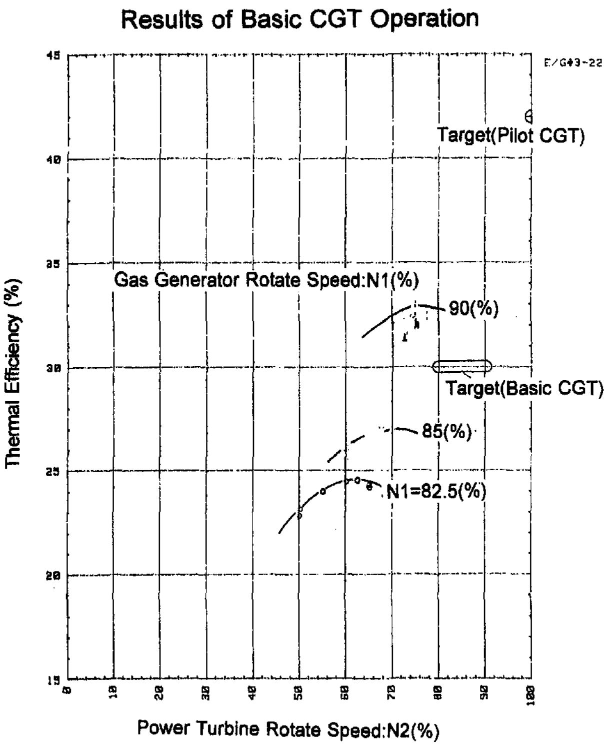

Fig. 15 Performance curve of CGT302 (#3-22)

Table 4 Summary of performance

E/G No.	N1 (%)	η th	TIT (℃)	Power(ps)	Remarks
Target	90.0	30.0	1200.0	190.0	
# 1-39	85.4	28.8	1116.5	175.7	
# 1-41	89.9	26.6	1200.0	232..0	non-steady
# 3-10	89.9	29.2	1251.7	222.4	
# 3-22	89.9	33.1	1189.6	223.1	

3 The CGT302 proved 33.1 percent thermal efficiency with 223.1 PS at a partial load under the 1200°C second-stage condition.

Acknowledgments

This study is being carried out under the Japanese CGT R&D program conducted by NEDO. The authors wish to express their gratitude to the Agency of Industrial Science and Technology of MITI and NEDO for making this study possible and permitting this paper to be published. They also wish to thank Kyocera Corporation and Sumitomo Precision Products Co., Ltd., for their cooperation in this study.

References

1 K. Nishio, J. Fujioka, T. Tatsumi, and I. Takehara, 1995, "Development of 300 kW Class Ceramic Gas Turbine (CGT302)," ASME Paper No. 95-GT-264.

2 A. Watanabe, T. Tatsumi, K. Tanimura, I. Takehara, and T. Fujii, 1994, "Development of 300 kW Class Ceramic Gas Turbine (CGT302)," ASME Paper No. 94-GT-19.

3 T. Murayama, K. Nagata, and H. Abe, 1995, "Current Status of 300 kW Industrial Ceramic Gas Turbine," ASME Paper No. 95-GT-445.

4 T. Tatsumi, I. Inobe, I. Takehara, and Y. Ichikawa, 1995, "Current Status of CGT302 Ceramic Gas Turbine," GTSJ '95 Yokohama International Congress.

D. J. Thomas
NASA Lewis Resident Research Associate;
Department of Civil Engineering,
Cleveland State University,
Cleveland, OH 44115

R. C. Wetherhold
Department of Mechanical and
Aerospace Engineering,
State University of New York,
Buffalo, NY 14260-4400

Modeling the Effective Elastic Behavior of a Transversely Cracked Laminated Composite

The solution for the stress state present in the vicinity of transverse matrix cracks within a composite laminate is typically obtained by assuming a regular crack spacing geometry for the problem and applying a shear-lag analysis. In order to explore the validity of this underlying assumption, the probability density function for the location of the next transverse matrix crack within a crack bounded region is examined. The regular crack spacing assumption is shown to be reasonable from an engineering point of view. Continuing with this assumption, a generalized shear-lag model for multilayer, off-axis laminates subjected to full in-plane loads is developed. This model is used to quantitatively evaluate the effective elastic properties of the damaged material. The results are applicable to materials such as ceramic matrix or polymer matrix unidirectional fiber systems where damage in the form of transverse matrix cracks arises.

Introduction

Composite materials typically experience damage in the form of transverse matrix cracking (i.e., through-the-thickness cracks running parallel to the fibers, which are largely brought about by the presence of the in-plane transverse stress) during the course of loading. This form of damage may be non-catastrophic; i.e., it does not necessarily result in the immediate failure of the laminate. However, transverse matrix cracking does adversely affect the mechanical response of the material and is often a precursor to additional modes of failure. As such, a significant body of research has been devoted to modeling the effects of progressive transverse cracking. Continuum damage models (Talreja, 1985; Nuismer and Tan, 1988) as well as many shear-lag approaches (Garret and Bailey, 1977; Reifsnider, 1978; Laws and Dvorak, 1988; Lee and Daniel, 1990; Tsai et al., 1990) have been proposed for analyzing cross-ply laminates. Shear-lag models implicitly assume the transverse matrix cracks occur at regularly spaced intervals. This assumption allows the solution of the stress state for the damaged laminate to be reduced to the solution for a characteristic volume element bounded by two transverse cracks and having a length equal to the average crack spacing. This permits calculation of the effective elastic constants to be made. In this paper, the validity of this assumption will be investigated qualitatively by examining the probability density function for transverse crack location. The paper proceeds to extend the method of Lee and Daniel for determining the shear-lag parameters to a general symmetric multilayer system. The elasticity problem for the region of the laminate between two parallel matrix cracks having an arbitrary off-axis orientation is set up from equilibrium considerations in terms of the average (through the thickness) stresses and solved using the newly developed generalized shear-lag (GSL) relation and the appropriate boundary conditions. Modeling of the effective elastic properties that result for the damaged layer is detailed. The analysis method is benchmarked against published results for a cross-ply laminate, and the advanced modeling capabilities of the model are demonstrated for a $[0/30/60/-30/-60]_s$ laminate.

Regularity of Crack Spacing

In a classic paper by Oh and Finney (1970), the traditional Weibull analysis was extended to model the characteristics of the location of failure for brittle materials. It was demonstrated that for cases where the stress state present in the solid can be given as the product of a far field reference stress and a function of the location, the probability density function (pdf) for the location of failure can be determined analytically. In this paper, Wetherhold's treatment (1991) of Oh and Finney's work will be followed, and combined with the solution for the stress state present in the region between two transverse matrix cracks to arrive at the pdf for the next crack (i.e., failure) location.

Derivation of Crack Location pdf. Consider a four-layer, symmetric, cross-ply laminate subjected to an applied in-plane uniaxial load. Due to symmetry, only the top half of the laminate is modeled (see Fig. 1(*a*)). Lee and Daniel (1990) have published a shear-lag solution for the stress state in such a system. Assuming that failure due to transverse cracking can be modeled using a probabilistic version of the maximum stress criterion, the critical stress that must be considered is the in-plane transverse stress. Lee and Daniel's solution for this stress term, transformed to the coordinate system of the damaged layer (see Fig. 1(*b*)) and averaged through the thickness is

$$\bar{\sigma}_{y'}(y') = \frac{E_2 P_{y'}}{(h_1 + h_2)E_o}\left[1 - \frac{\cosh(\omega s - \omega y')}{\cosh(\omega s)}\right]$$

$$= r(y') \cdot P_{y'} \qquad (1)$$

Note that the dependence on the location variable, $y' \in [0, 2s]$, has been isolated in the newly introduced function $r(y')$ as required for Oh and Finney's method. In Eq. (1), $P_{y'}$ is the force resultant (i.e., applied load per unit width) for the half structure, $2s$ is the crack spacing, and h_1 and h_2 are the layer thicknesses. Additionally, the parameters E_o, ω, and H are defined as

$$E_o = \frac{E_2 h_1 + E_1 h_2}{h_1 + h_2} \qquad (2)$$

$$\omega = \left[\frac{(h_1 + h_2)E_o}{h_1 h_2 E_1 E_2} H\right]^{1/2} \qquad (3)$$

Contributed by the International Gas Turbine Institute and presented at the 41st International Gas Turbine and Aeroengine Congress and Exhibition, Birmingham, United Kingdom, June 10–13, 1996. Manuscript received at ASME Headquarters February 1996. Paper No. 96-GT-495. Associate Technical Editor: J. N. Shinn.

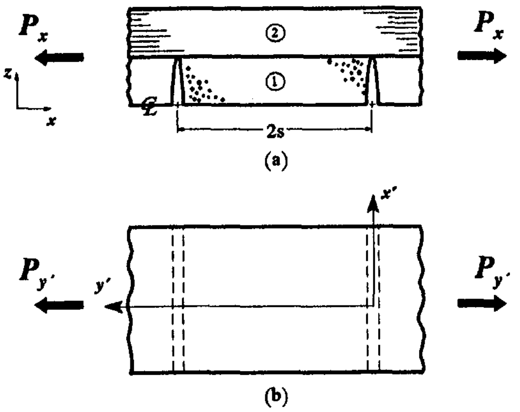

Fig. 1 (*a*) Edge view showing top half of four layer symmetric cross-ply laminate. (*b*) Top view showing transformed coordinate system for stress solution.

$$H = \frac{3G_{12}G_{13}}{h_1G_{23} + h_2G_{12}} \tag{4}$$

where E and G are the various Young and shear moduli; with the subscript 1 referring to the layer's fiber direction, subscript 2 corresponding to the transverse direction, and subscript 3 designating the out-of-plane direction.

The cracking event is a function of both the location variable, y', and the applied load, $P_{y'}$. The joint density function, $f(P_{y'}, y')$, for these variables can be expressed (Oh and Finney, 1970; Wetherhold, 1991) as

$$f(P_{y'}, y') \equiv \frac{\partial\psi}{\partial P_{y'}} \exp\left(-\int_{y'} \psi dy'\right) \tag{5}$$

where ψ is the risk of rupture per unit length. Integrating Eq. (5) with respect to $P_{y'}$ yields the marginal density function for the location of failure, $\varphi(y')$,

$$\varphi(y') = \int_{P_{y'}} f(P_{y'}, y')dP_{y'} \tag{6}$$

In evaluating the joint density function, it is assumed that the risk of rupture per unit length has a Weibull distribution,

$$\psi(P_{y'}, y') = \left(\frac{\bar{\sigma}_{y'}(P_{y'}, y')}{\sigma_L}\right)^m = \left(\frac{r(y')P_{y'}}{\sigma_L}\right)^m \tag{7}$$

where σ_L is the Weibull scale parameter based on length and m is the Weibull modulus. The following variable substitution is introduced in order to normalize the location variable,

$$y' \in [0, 2s] \Rightarrow \xi = \frac{y'}{2s}; \quad \xi \in [0, 1] \tag{8}$$

Performing the integration of the joint density function, and normalizing the result to equal one (the normalization requirement of a pdf), yields the final form for the marginal density function for location of the next transverse matrix crack between two existing matrix cracks:

$$\hat{\varphi}(\xi) = \frac{r^m(\xi)}{q} \tag{9}$$

Here, $\hat{\varphi}$ denotes the normalized pdf, and the constant q has been introduced to represent the following integral:

$$q \equiv \int_0^1 r^m(\xi)d\xi \tag{10}$$

Table 1 Material properties for SiC/RBSN and graphite/epoxy

Property	SiC/RBSN	Gr/Ep
Longitudinal modulus	193.0 GPa	144.8 GPa
Transverse modulus	69.0 GPa	10.7 GPa
In-plane shear modulus	31.0 GPa	7.2 GPa
Out-of-plane shear modulus	27.5 GPa	3.8 GPa
In-plane major Poisson's ratio	0.21	0.29
Weibull scale parameter for transverse strength	28.0 MPa $m^{1/m}$	51.7 MPa $m^{1/m}$
Weibull modulus for transverse strength	10.9	10.0
Ply thickness	0.00025 m	0.000127 m

Example. In this section, the probability density function describing the location of the next transverse crack is examined for a $[0_2/90_2]_s$ Silicon Carbide/Reaction Bonded Silicon Nitride (SiC/RBSN) laminate. Typical material properties are given in Table 1. For this example, pdf's are generated for a range of crack spacings. The evaluation of the constant q (Eq. (10)) contained in the final form of the solution requires numerical integration; all other calculations are capable of being determined in closed form.

Figure 2 contains the results of the (normalized) pdf, $\hat{\varphi}$, obtained as a function of the location, ξ, for the SiC/RBSN system. Five pdf's are depicted, each corresponding to a selected value of the crack spacing, $2s$. These values range from a minimum of 2.5 mm to a maximum of 50 mm.

The pdf's calculated for large crack spacings show large central regions of equal probability of failure. This means that the center region is far enough away from the crack face to have reloaded to a constant stress. Since there is a large area with an essentially constant pdf, the actual appearance or realization of the next crack will be very irregular. As the crack spacing gets smaller, the distribution becomes peaked. This demonstrates the tendency toward cracking in the more highly stressed central regions. Consequently, in the early stages of damage, when the matrix crack density is relatively low, it appears that the assumption of regularly spaced transverse cracks may be unrealistic (although the average crack location will always be at the midpoint, $\xi = \frac{1}{2}$). However, the global effects of the damage in these early stages are relatively minor. As damage progresses and the crack density increases, the validity of the regular spacing assumption gains credence. Therefore, the assumption of a regular spacing throughout the damage development, which in turn allows the problem to be modeled via the analysis of a characteristic volume, would appear to be justified from an engineering standpoint.

Generalized Shear-Lag Model

Continuing with the assumption that solution via a representative volume approach is valid, a generalized shear-lag (GSL)

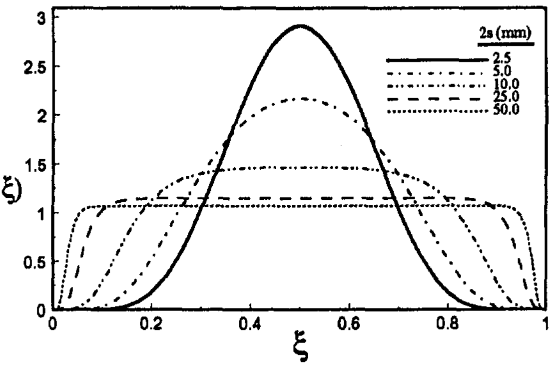

Fig. 2 pdf's for next failure location in $[0_2/90_2]_s$ SiC/RBSN

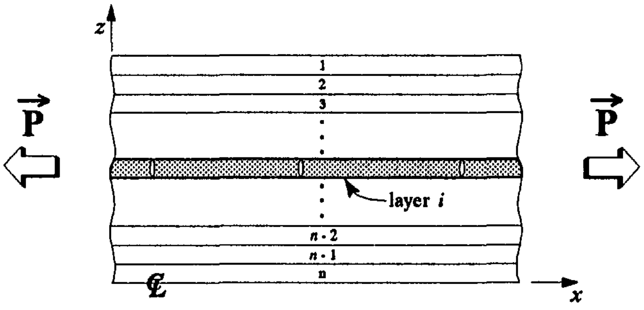

Fig. 3 Matrix cracking occurring in layer i of laminate

model is developed. A general symmetric multilayered laminate having a total of $2n$ layers with corresponding thicknesses h_j and orientations θ_j, $j = 1, 2n$ is considered. The laminate is subjected to a general in-plane loading of $(2P_x, 2P_y, 2P_{xy})$. Due to the fact that the laminate is symmetric, we can restrict our attention to half of the system (i.e., layers 1 through n). As the load is slowly applied to the laminate, consider the event of matrix cracks developing in layer i (see Fig. 3). The objective is to determine the in-plane stress state in layer i as a function of the coordinates x and y, and averaged over z (i.e., $\bar{\sigma}^{(i)}(x, y)$). The assumption is made that the damaged layer behaves effectively the same in the simpler but elastically equivalent system shown in Fig. 4. Referring to this figure, the numbers $\tilde{1}$, $\tilde{2}$, and $\tilde{3}$ designate the layers in the equivalent system, with $\tilde{1}$ corresponding to the layer undergoing damage. The undamaged layers (i.e., $\tilde{2}$ and $\tilde{3}$) have been homogenized such that

$$h_{\tilde{1}} = h_i; \quad h_{\tilde{2}} = \sum_{j=1}^{j=i-1} h_j; \quad h_{\tilde{3}} = \sum_{j=i+1}^{j=n} h_j \tag{11}$$

$$[S']_{\tilde{1}} = [S']_i \tag{12}$$

$$[S']_{\tilde{2}} = [S']_{\tilde{3}} = \frac{1}{\sum\limits_{j=1}^{n} h_j} (\sum_{j=1}^{n} h_j [S']_j); \quad j \neq i \tag{13}$$

where $h_{\tilde{1}}$, $h_{\tilde{2}}$, and $h_{\tilde{3}}$ are the new layer thicknesses, and $[S']_{\tilde{1}}$, $[S']_{\tilde{2}}$, and $[S']_{\tilde{3}}$ are the respective compliance matrices transformed to the global coordinate system of the laminate.

The solution of the problem will be more straightforward if it is carried out in the transformed coordinates corresponding to the material coordinates of layer $\tilde{1}$, see Fig. 5. Note that this is an orthogonal transformation about the z axis such that $z' = z$. From this point forward the derivation will be restricted to the equivalent (or homogenized) system and it is no longer necessary to specify this through the use of tildes (~) in the notation. Their use is thus discontinued in order to simplify the notation.

Determination of the Shear-Lag Parameters. In this section the derivation of the shear-lag parameters for a general three-layer system is presented. The approach established by Lee and Daniel (1990) is followed. No assumptions are made regarding the type of damage present or the existence of any relationship between the layer stiffnesses.

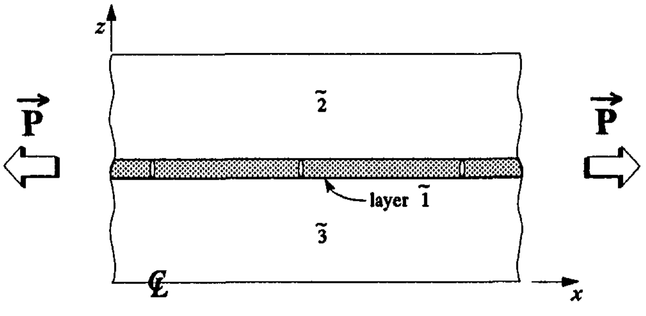

Fig. 4 Elastically equivalent three-layer homogenized system

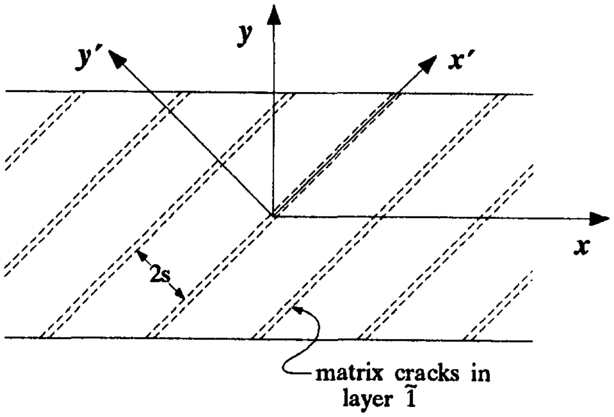

Fig. 5 Transformed system coordinates aligned with material coordinates of damaged layer

The key to this derivation is the assumption of a quadratic displacement field through the thickness direction for each layer,

$$u_i'(x', y', z) = a_i z^2 + b_i z + c_i \tag{14}$$

$$v_i'(x', y', z) = d_i z^2 + e_i z + f_i; \quad i = 1, 2, 3 \tag{15}$$

with u_i' and v_i' designating displacements in the x' and y' directions, respectively, and the coefficients a_i, b_i, c_i, d_i, e_i and f_i representing undetermined functions of x' and y'.

The constitutive relation for layer i is given below:

$$\begin{Bmatrix} \tau_{x'z} \\ \tau_{y'z} \end{Bmatrix}_i = \begin{bmatrix} Q_{55}' & Q_{45}' \\ Q_{45}' & Q_{44}' \end{bmatrix}_i \begin{Bmatrix} \gamma_{x'z} \\ \gamma_{y'z} \end{Bmatrix}_i \tag{16}$$

(No summation is implied by the repeated subscript in Eq. (16).) The primes on the stiffness terms signify that they have been transformed to the $x' - y'$ coordinate system.

The strain-displacement relations given below in Eqs. (17) and (18) allow the stresses to be related to the displacement field given above by Eqs. (14) and (15).

$$\gamma_{x'z}^{(i)} = \frac{\partial u_i'}{\partial z}; \quad \gamma_{y'z}^{(i)} = \frac{\partial v_i'}{\partial z} \tag{17, 18}$$

By considering the boundary conditions which are present: states of zero shear on the top face of the laminate and at the midplane,

$$\begin{Bmatrix} \tau_{x'z}(z = h_1 + h_2 + h_3) \\ \tau_{y'z}(z = h_1 + h_2 + h_3) \end{Bmatrix}_2 = \begin{Bmatrix} 0 \\ 0 \end{Bmatrix} \tag{19}$$

$$\begin{Bmatrix} \tau_{x'z}(z = 0) \\ \tau_{y'z}(z = 0) \end{Bmatrix}_3 = \begin{Bmatrix} 0 \\ 0 \end{Bmatrix} \tag{20}$$

as well as conditions of continuity at the two layer interfaces,

$$\begin{Bmatrix} \tau_{x'z}(z = h_1 + h_3) \\ \tau_{y'z}(z = h_1 + h_3) \end{Bmatrix}_2 = \begin{Bmatrix} \tau_{x'z}(z = h_1 + h_3) \\ \tau_{y'z}(z = h_1 + h_3) \end{Bmatrix}_1$$

$$\equiv \begin{Bmatrix} \tau_{x'z}^{(1-2)} \\ \tau_{y'z}^{(1-2)} \end{Bmatrix} \tag{21}$$

$$\begin{Bmatrix} \tau_{x'z}(z = h_3) \\ \tau_{y'z}(z = h_3) \end{Bmatrix}_3 = \begin{Bmatrix} \tau_{x'z}(z = h_3) \\ \tau_{y'z}(z = h_3) \end{Bmatrix}_1 \equiv \begin{Bmatrix} \tau_{x'z}^{(1-3)} \\ \tau_{y'z}^{(1-3)} \end{Bmatrix} \quad (22)$$

the coefficients a_i, b_i, d_i and e_i can be solved for.

Requiring u' and v' displacement continuity at the (1–2) and (1–3) interfaces, averaging the displacement equations through their respective thicknesses, and then subtracting to find the appropriate differences in the average displacements eliminates the remaining unknown coefficients, c_i and f_i. With all the coefficients either known or eliminated, the following expressions for the differences in average displacement result.

$$\begin{Bmatrix} \bar{u}_1' - \bar{u}_2' \\ \bar{v}_1' - \bar{v}_2' \end{Bmatrix} = [A] \begin{Bmatrix} \tau_{x'z}^{(1-2)} \\ \tau_{y'z}^{(1-2)} \end{Bmatrix} + [B] \begin{Bmatrix} \tau_{x'z}^{(1-3)} \\ \tau_{y'z}^{(1-3)} \end{Bmatrix} \quad (23)$$

$$\begin{Bmatrix} \bar{u}_1' - \bar{u}_3' \\ \bar{v}_1' - \bar{v}_3' \end{Bmatrix} = [C] \begin{Bmatrix} \tau_{x'z}^{(1-2)} \\ \tau_{y'z}^{(1-2)} \end{Bmatrix} + [D] \begin{Bmatrix} \tau_{x'z}^{(1-3)} \\ \tau_{y'z}^{(1-3)} \end{Bmatrix} \quad (24)$$

where

$$[A] = -\frac{h_1}{3}[Q]_1^{-1} - \frac{h_2}{3}[Q']_2^{-1} \quad (25)$$

$$[B] = -\frac{h_1}{6}[Q]_1^{-1} \quad (26)$$

$$[C] = \frac{h_1}{6}[Q]_1^{-1} \quad (27)$$

$$[D] = \frac{h_1}{3}[Q]_1^{-1} + \frac{h_3}{3}[Q']_3^{-1} \quad (28)$$

The shear stresses can be solved for as a function of the differences in average displacements from Eqs. (23) and (24),

$$\begin{Bmatrix} \tau_{x'z}^{(1-2)} \\ \tau_{y'z}^{(1-2)} \end{Bmatrix} = [H] \begin{Bmatrix} \bar{u}_1' - \bar{u}_2' \\ \bar{v}_1' - \bar{v}_2' \end{Bmatrix} + [J] \begin{Bmatrix} \bar{u}_1' - \bar{u}_3' \\ \bar{v}_1' - \bar{v}_3' \end{Bmatrix} \quad (29)$$

$$\begin{Bmatrix} \tau_{x'z}^{(1-3)} \\ \tau_{y'z}^{(1-3)} \end{Bmatrix} = [K] \begin{Bmatrix} \bar{u}_1' - \bar{u}_2' \\ \bar{v}_1' - \bar{v}_2' \end{Bmatrix} + [L] \begin{Bmatrix} \bar{u}_1' - \bar{u}_3' \\ \bar{v}_1' - \bar{v}_3' \end{Bmatrix} \quad (30)$$

The matrices $[H]$, $[J]$, $[K]$, and $[L]$ are the shear-lag parameters for the system. They are two by two matrices containing known constants. Their form is given below:

$$[L] = [[D] - [C][A]^{-1}[B]]^{-1} \quad (31)$$

$$[H] = [A]^{-1} + [A]^{-1}[B][L][C][A]^{-1} \quad (32)$$

$$[J] = -[A]^{-1}[B][L] \quad (33)$$

$$[K] = -[L][C][A]^{-1} \quad (34)$$

As a check of the derivation to this point, if layer 3 were no longer present, this three-layer model should reduce to the simpler two layer case solution in the literature. This can be verified by setting the shear stresses at the (1–3) interface equal to zero. Under these conditions, Eq. (23) becomes

$$\begin{Bmatrix} \bar{u}_1' - \bar{u}_2' \\ \bar{v}_1' - \bar{v}_2' \end{Bmatrix} = -\left[[Q]_1^{-1}\frac{h_1}{3} + [Q']_2^{-1}\frac{h_2}{3} \right] \begin{Bmatrix} \tau_{x'z}^{(1-2)} \\ \tau_{y'z}^{(1-2)} \end{Bmatrix} \quad (35)$$

and this agrees with previous solutions for the two-layer case (Tsai et al., 1990).

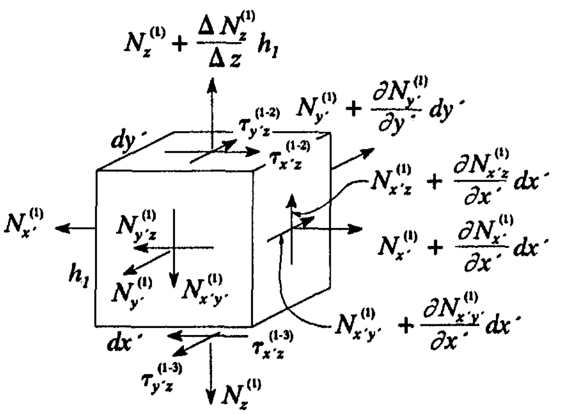

Fig. 6 Volume element from layer 1

Elasticity Solution of the Three Layer Problem. The objective is to determine the solution for the average (through-the-thickness) state of in-plane stress present in the damaged layer of the original laminate. In this paper the assumption has been made that the stress state present in this layer is equivalent to that which is found in layer 1 of the homogenized laminate. In the last section, the relation that exists between the interlaminar shear stresses and the in-plane displacements for a general three-layer system were developed. In this section, this relation will be used in conjunction with equilibrium conditions to solve for the average in-plane stresses of layer 1, $\{\bar{\sigma}(x', y')\}_1$, of the homogenized laminate.

Selecting a volume element from layer 1 having a differential size in the in-plane directions, and of finite size (corresponding to the layer thickness) in the out-of-plane direction (see Fig. 6), the following equilibrium equations are derived:

$$\tau_{x'z}^{(1-3)} - \tau_{x'z}^{(1-2)} = \frac{\partial N_{x'}^{(1)}}{\partial x'} + \frac{\partial N_{x'y'}^{(1)}}{\partial y'} \quad (36)$$

$$\tau_{y'z}^{(1-3)} - \tau_{y'z}^{(1-2)} = \frac{\partial N_{x'y'}^{(1)}}{\partial x'} + \frac{\partial N_{y'}^{(1)}}{\partial y'} \quad (37)$$

The assumption is made that the effects of the matrix cracking damage are direction specific. That is to say, the influence of the damage is seen in the y' direction moving perpendicularly away from the matrix crack; and along the x' or fiber direction, no damage influence is seen (i.e., $\partial(\cdot)/\partial x' = 0$). A direct result of this assumption is the existence of displacement continuity in the x' direction, thus $\bar{u}_1' = \bar{u}_2' = \bar{u}_3'$.

Beginning the analysis with Eq. (37) and applying the shear-lag relation from the previous section produces

$$\frac{dN_{y'}^{(1)}}{dy'} = (K_{22} - H_{22})(\bar{v}_1' - \bar{v}_2') + (L_{22} - J_{22})(\bar{v}_1' - \bar{v}_3') \quad (38)$$

Differentiating this equation with respect to y', and applying the strain-displacement relation $\bar{\epsilon}_{y'} = (d\bar{v}'/dy')$, yields

$$\frac{d^2N_{y'}^{(1)}}{dy'^2} = (K_{22} - H_{22})(\bar{\epsilon}_{y'}^{(1)} - \bar{\epsilon}_{y'}^{(2)}) + (L_{22} - J_{22})(\bar{\epsilon}_{y'}^{(1)} - \bar{\epsilon}_{y'}^{(3)}) \quad (39)$$

Equation (39) contains within it as unknowns both load and strain terms. By utilizing the constitutive relation for the individual layers, the strain can be expressed in terms of the in-plane loads:

$$\bar{\epsilon}_{y'}^{(i)} = \frac{1}{h_i}[S_{12}'^{(i)}N_{x'}^{(i)} + S_{22}'^{(i)}N_{y'}^{(i)} + S_{26}'^{(i)}N_{x'y'}^{(i)}]; \quad i = 1, 2, 3 \quad (40)$$

At this point, in examining two specific examples (one for a

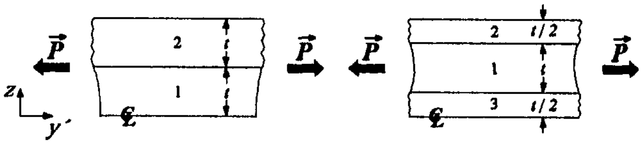

Fig. 7 Related two-layer and three-layer problems

two-layer case and one for a three-layer case, see Fig. 7) a problem can be detected. In these two related cases, layer 2 from the two-layer case has basically been "split up" into layers 2 and 3 for the three-layer case. The governing differential equation for the two-layer case is given below,

$$\left(\frac{d^2N_{y'}^{(1)}}{dy'^2}\right)_{\text{2-layer case}} = H(\bar{\epsilon}_{y'}^{(1)} - \bar{\epsilon}_{y'}^{(2)})_{\text{2-layer case}} \tag{41}$$

where H (defined in Eq. (4)) designates the shear-lag parameter for the two-layer case (Lee and Daniel, 1990).

The elastic properties are the same for the two cases, therefore the loads are related as follows,

$$(N^{(1)})_{\text{3-layer case}} = (N^{(1)})_{\text{2-layer case}}$$

$$(N^{(2)})_{\text{3-layer case}} = \tfrac{1}{2}(N^{(2)})_{\text{2-layer case}}$$

Calculation of the strains using the constitutive relations of Eq. (40) leads to the incorrect prediction that the difference between the strains of layer 1 and layer 2 are the same for both cases. In actuality, there is a thickness effect present such that as the thickness of layer 2 decreases, the difference in the strains also decreases. Thus, the relationship that needs to be predicted is:

$$(\bar{\epsilon}_{y'}^{(1)} - \bar{\epsilon}_{y'}^{(2)})_{\text{2-layer case}} > (\bar{\epsilon}_{y'}^{(1)} - \bar{\epsilon}_{y'}^{(2)})_{\text{3-layer case}}$$

and a correction term is necessary to achieve this.

In proposing the form of the thickness correction terms, the following relationship is chosen to hold true;

$$\left(\frac{d^2N_{y'}^{(1)}}{dy'^2}\right)_{\text{2-layer case}} = \left(\frac{d^2N_{y'}^{(1)}}{dy'^2}\right)_{\text{3-layer case}} \tag{42}$$

This equation may be restated using the shear-lag relationships,

$$H(\bar{\epsilon}_{y'}^{(1)} - \bar{\epsilon}_{y'}^{(2)})_{\text{2-layer}} = \delta_2(K_{22} - H_{22})(\bar{\epsilon}_{y'}^{(1)} - \bar{\epsilon}_{y'}^{(2)})_{\text{3-layer}} + \delta_3(L_{22} - J_{22})(\bar{\epsilon}_{y'}^{(1)} - \bar{\epsilon}_{y'}^{(3)})_{\text{3-layer}} \tag{43}$$

where thickness correction terms, δ_2 and δ_3, for layers 2 and 3 respectively, have been introduced to modify the appropriate strain differences. For this example case, upon evaluating the shear-lag parameters, it is found that the following condition on the thickness correction terms must be upheld:

$$\delta_2 + \delta_3 = \tfrac{1}{2} \tag{44}$$

In accordance with this condition, the proposed form for the correction terms are,

$$\delta_2 = \frac{h_2}{2(h_2 + h_3)}\,; \quad \delta_3 = \frac{h_3}{2(h_2 + h_3)} \tag{45a, b}$$

The governing differential equation for the three-layer case thus becomes

$$\frac{d^2N_{y'}^{(1)}}{dy'^2} = \psi_{22}(\bar{\epsilon}_{y'}^{(2)} - \bar{\epsilon}_{y'}^{(1)}) \tag{46}$$

where

$$\psi_{22} = \frac{1}{2(h_2 + h_3)}[h_2(H_{22} - K_{22}) + h_3(J_{22} - L_{22})] \tag{47}$$

Substituting for the strains using Eq. (40) yields a governing differential equation entirely expressed in terms of in-plane loads:

$$\frac{d^2N_{y'}^{(1)}}{dy'^2} = \psi_{22}\left\{\frac{1}{h_2}[S_{12}^{\prime(2)}N_{x'}^{(2)} + S_{22}^{\prime(2)}N_{y'}^{(2)} + S_{26}^{\prime(2)}N_{x'y'}^{(2)}] - \frac{1}{h_1}[S_{12}^{(1)}N_{x'}^{(1)} + S_{22}^{(1)}N_{y'}^{(1)} + S_{26}^{(1)}N_{x'y'}^{(1)}]\right\} \tag{48}$$

However, as it stands, this one equation contains six unknowns and therefore five additional independent equations must be found. From global equilibrium considerations, three of the necessary equations are obtained. These can be used to solve for the in-plane loads of layer 2 in terms of the in-plane loads of layer 1 and the known applied loads $P_{x'}$, $P_{y'}$, and $P_{x'y'}$:

$$P_{x'} = N_{x'}^{(1)} + N_{x'}^{(2)} + N_{x'}^{(3)} = N_{x'}^{(1)} + \left(1 + \frac{h_3}{h_2}\right)N_{x'}^{(2)} \tag{49}$$

$$P_{y'} = N_{y'}^{(1)} + N_{y'}^{(2)} + N_{y'}^{(3)} = N_{y'}^{(1)} + \left(1 + \frac{h_3}{h_2}\right)N_{y'}^{(2)} \tag{50}$$

$$P_{x'y'} = N_{x'y'}^{(1)} + N_{x'y'}^{(2)} + N_{x'y'}^{(3)} = N_{x'y'}^{(1)} + \left(1 + \frac{h_3}{h_2}\right)N_{x'y'}^{(2)} \tag{51}$$

Continuing the previously made assumption of displacement continuity in the x' direction implies that the normal strains in this direction for each layer are equal:

$$\bar{\epsilon}_{x'}^{(1)} = \bar{\epsilon}_{x'}^{(2)} \tag{52}$$

This equation can be used to solve for $N_{x'}^{(1)}$ in terms of the remaining unknown terms. Substitution of these results into Eq. (48) produces a second-order, ordinary differential equation with only two remaining unknowns, $N_{y'}^{(1)}$ and $N_{x'y'}^{(1)}$.

$$\frac{d^2N_{y'}^{(1)}}{dy'^2} = \psi_{22}(\alpha N_{y'}^{(1)} + \eta N_{x'y'}^{(1)} + \beta) \tag{53}$$

The coefficients α, η, and β are constants, which are algebraic functions of the elastic and shear-lag parameters (β also contains the applied loading terms). They are presented explicitly in the appendix.

The last necessary equation comes from local equilibrium considerations. Using Eq. (36), and applying the shear-lag relations along with the necessary thickness correction terms, a second-order differential equation for $N_{x'y'}^{(1)}$ is arrived at which is similar in form to Eq. (46). Following a similar procedure as outlined above, this equation can be reformulated such that it contains the known constants ψ_{12}, α, η, and β, and the unknown loads $N_{y'}^{(1)}$ and $N_{x'y'}^{(1)}$,

$$\frac{d^2N_{x'y'}^{(1)}}{dy'^2} = \psi_{12}(\alpha N_{y'}^{(1)} + \eta N_{x'y'}^{(1)} + \beta) \tag{54}$$

where

$$\psi_{12} = \frac{1}{2(h_2 + h_3)}[h_2(H_{12} - K_{12}) + h_3(J_{12} - L_{12})] \tag{55}$$

Thus with Eqs. (53) and (54) a system of two coupled, second-order, ordinary differential equations is arrived at. The boundary conditions for this problem are those of traction-free crack surfaces,

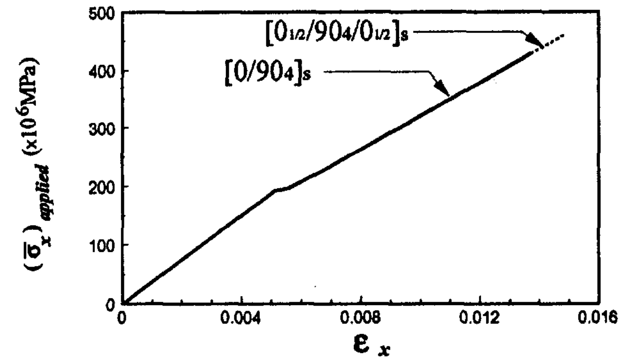

Fig. 8 Predicted stress–strain response for cross-ply laminates showing agreement between Lee and Daniel model and GSL model

$$N_{y'}^{(1)}(y'=0) = N_{y'}^{(1)}(y'=2s) = 0 \tag{56}$$

$$N_{x'y'}^{(1)}(y'=0) = N_{x'y'}^{(1)}(y'=2s) = 0 \tag{57}$$

where $2s$ is the distance between two parallel matrix cracks. This system can be uncoupled at the expense of increasing the order of differentiation, resulting in a fourth-order, homogeneous differential equation. The solution of this equation for $N_{y'}^{(1)}(y')$ then leads directly to $N_{x'}^{(1)}(y')$ and $N_{x'y'}^{(1)}(y')$ being known as well. The final forms of the solution for all three in-plane loads of layer 1 are given below:

$$N_{x'}^{(1)}(y') = B_1 \sinh(\lambda y') + B_2 \cosh(\lambda y') + B_3 \tag{58}$$

$$N_{y'}^{(1)}(y') = B_4 \sinh(\lambda y') + B_5 \cosh(\lambda y') + B_6 \tag{59}$$

$$N_{x'y'}^{(1)}(y') = B_7 \sinh(\lambda y') + B_8 \cosh(\lambda y') + B_9 \tag{60}$$

Expressions for the coefficients B_1 through B_9 and λ can be found in the appendix.

Effective Elastic Behavior. With the in-plane loads for the damaged layer completely solved within the region between two transverse matrix cracks, the next step is to determine the layer's effective macro-level behavior. In examining this behavior, in-plane-average responses (in addition to the through-the-thickness averages that have been discussed up to this point) are of interest. In order to emphasize that the averages being considered in this section are with regard to both the thickness of the layer as well as the in-plane length, a *double overbar* notation ($\bar{\bar{\cdot}}$) is introduced to signify that the average is with respect to both dimensions, and the *single overbar* notation is continued to denote averages taken with respect to thickness only.

The effective compliance of layer 1, $[\hat{S}]_1$, is defined below:

$$\begin{Bmatrix} \bar{\bar{\epsilon}}_{x'} \\ \bar{\bar{\epsilon}}_{y'} \\ \bar{\bar{\gamma}}_{x'y'} \end{Bmatrix}_1 = \begin{bmatrix} \hat{S}_{11} & \hat{S}_{12} & 0 \\ \hat{S}_{12} & \hat{S}_{22} & 0 \\ 0 & 0 & \hat{S}_{66} \end{bmatrix}_1 \begin{Bmatrix} \bar{\bar{\sigma}}_{x'} \\ \bar{\bar{\sigma}}_{y'} \\ \bar{\bar{\tau}}_{x'y'} \end{Bmatrix}_1 \tag{61}$$

by the relationship between the in-plane-average strain of the layer, $\{\bar{\bar{\epsilon}}\}_1$, and the in-plane-average stress, $\{\bar{\bar{\sigma}}\}_1$. This provides a measure of the effective ''secant'' behavior of the layer. Expressions for the in-plane-average stress can be determined by integrating the stress equations (found by dividing Eqs. (58) through (60) for the in-plane loads by the layer thickness; i.e., $\bar{\sigma}^{(i)} = N^{(i)}/h_i$) over the crack bounded region. Note that these equations are independent of x'. As a result, integration is only necessary over y'.

Remembering that it is the effective global behavior of the layer within the laminate that is being modeled, it is reasonable to assume that the average strains appearing in Eq. (4.72) are equal to the midplane strains of the laminate:

$$\begin{Bmatrix} \bar{\bar{\epsilon}}_{x'} \\ \bar{\bar{\epsilon}}_{y'} \\ \bar{\bar{\epsilon}}_{x'y'} \end{Bmatrix}_1 = \begin{Bmatrix} \epsilon_{x'}^{o} \\ \epsilon_{y'}^{o} \\ \gamma_{x'y'}^{o} \end{Bmatrix} \tag{62}$$

With this assumption, Eq. (61) relates the in-plane average stress of the layer to the strains of the laminate, all of which are known. The only unknowns are the four compliance terms.

The assumption has previously been made that the damage effects due to transverse matrix cracking are restricted to the y' direction. This implies that the effective Young's modulus in the x' direction should remain unchanged,

$$\hat{E}_1 = E_1 \tag{63}$$

and as a result we can solve for the effective compliance term $\hat{S}_{11}$.

$$\hat{S}_{11} = \frac{1}{\hat{E}_1} = \frac{1}{E_1} = S_{11} \tag{64}$$

This leaves only three remaining unknown terms in the effective compliance matrix, and these can be found using the three equations comprising Eq. (61).

Finally, the effective engineering constants (i.e., Young's moduli, shear modulus, major Poisson's ratio: all being described in the secant manner) for the damaged layer can be determined from the effective compliance matrix, and are given below:

$$\hat{E}_1 = E_1 \quad \hat{E}_2 = \frac{1}{\hat{S}_{22}}$$

$$\hat{G}_{12} = \frac{1}{\hat{S}_{66}} \quad \hat{\nu}_{12} = -\frac{\hat{S}_{12}}{\hat{S}_{11}}$$

These engineering constants describe how the damaged layer effectively behaves within the laminate system.

Examples. The examples illustrated in this section were selected to demonstrate the model's agreement with a conventional shear-lag model for simple cross-ply laminates under uniaxial load, and to demonstrate the extended capabilities of the GSL model for more general laminate geometries and loading.

In the first example, two cross-ply configurations were considered: the $[0/90_4]_s$ Gr/Ep laminate configuration examined by Lee and Daniel (1990), and additionally, a $[0_{1/2}/90_4/0_{1/2}]_s$ Gr/Ep laminate, which is examined to confirm that the condition stated in Eq. (42) is being upheld. Material properties appear in Table 1, however, the material strengths were treated deterministically to agree with Lee and Daniel. As a result, the four 90 deg layers were considered to behave as one. The analysis simulates a monotonic loading in the 0 deg direction. The resulting stress/strain curves for the $[0/90_4]_s$ (as predicted by

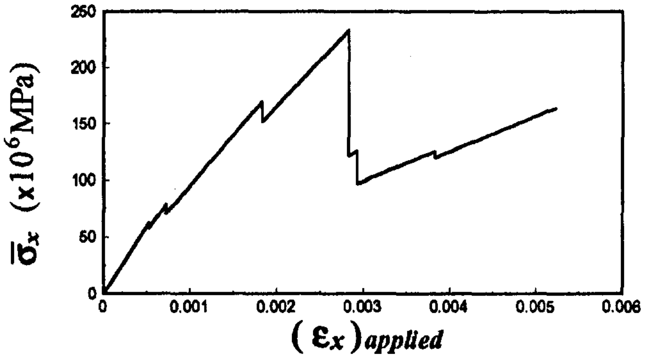

Fig. 9 Predicted global stress-strain response for $[0/30/60/-30/-60]_s$ laminate using GSL model

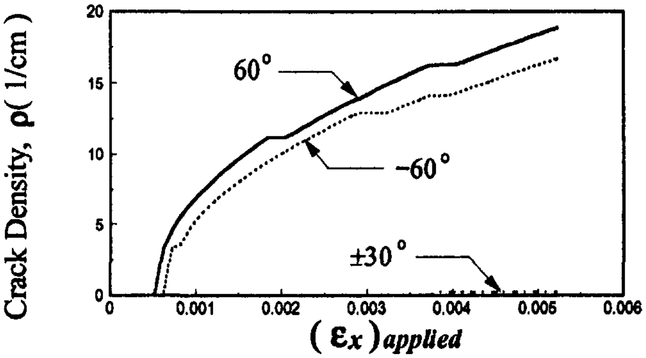

Fig. 10 Evolution of crack densities in [0/30/60/−30/−60]$_s$ laminate predicted using GSL model

both the GSL and the conventional shear-lag models) and for the $[0_{1/2}/90_4/0_{1/2}]_s$ (as predicted by the GSL model) are shown in Fig. 8. As can be seen by the nearly coincidental curves, very good agreement between the models is found.

In example two, a $[0/30/60/-30/-60]_s$ SiC/RBSN laminate was considered. Properties for this material are also given in Table 1. Figure 9 contains the predicted global strain controlled response for a specific set of realizations of material strengths. The evolution of the crack densities within each layer are presented in Fig. 10. The plateaus in each of the curves correspond to times in the analysis when other modes of damage were more active.

Summary

In this paper, the method developed by Oh and Finney for modeling the characteristics of the location of failure has been applied to a laminate with transverse matrix cracks. Using a previous solution for the stress state in the damaged layer of a cross-ply system, an analytical expression was developed for the probability density function of the next failure location in a region of the cross-ply laminate bounded by two existing transverse matrix cracks. In exercising this model, it was found that the fracture location peaks more strongly at the center of the interval as the crack spacing decreases. This shows that the assumption of regularly spaced transverse matrix cracks becomes more plausible as the crack density increases (crack spacing decreases). By assuming regularly spaced cracks, the engineer can calculate effective elastic properties for a damaged laminate.

A generalized shear-lag model has been derived to determine the average through-the-thickness stress state present in a layer undergoing transverse matrix cracking. The model is capable of considering cracking in layers of arbitrary orientation, states of general in-plane applied loading, and laminates having a general symmetric stacking sequence. The model has been shown to agree with a conventional model for the case of a simple cross-ply laminate. The model has yet to be verified experimentally for the more general cases.

Acknowledgments

This research was supported by the NASA-Lewis Research Center under Contract No. NAG3862 (technical monitor Dr. John P. Gyekenyesi).

References

Garrett, K. W., and Bailey, J. E., 1977, "Multiple Transverse Fracture in 90° Cross-ply Laminates of a Glass Fiber-Reinforced Polyester," *J. Matl. Sci.*, Vol. 12, pp. 157–168.

Laws, N., and Dvorak, G. J., 1988, "Progressive Transverse Cracking in Composite Laminates," *J. Comp. Matl.*, Vol. 22, pp. 900–916.

Lee, J. W., and Daniel, I. M., 1990, "Progressive Transverse Cracking of Crossply Laminates," *J. Compos. Matl.*, Vol. 24, pp. 1225–1243.

Nuismer, R. J., and Tan, S. C., 1988, "Constitutive Relations of a Cracked Composite Lamina," *J. Comp. Matl.*, Vol. 22, pp. 306–321.

Oh, H. L., and Finney, L., 1970, "On the Location of Fracture in Brittle Solids—I: Due to Static Loading," *Int. J. Frac. Mech.*, Vol. 6, pp. 287–300.

Reifsnider, K. L., 1978, "Mechanics of Failure of Composite Materials," *Proc. 10th Symposium on Naval Structural Mechanics*, George Washington University, Washington DC, pp. 317–331.

Talreja, R., 1985, "Transverse Cracking and Stiffness Reduction in Composite Laminates," *J. Comp. Matl.*, Vol. 19, pp. 355–375.

Tsai, C.-L., Daniel, I. M., and Lee, J.-W., 1990, "Progressive Matrix Cracking of Crossply Composite Laminates Under Biaxial Loading," *Microcracking Induced Damage in Composites*, AMDIII/MD22, G. J. Dvorak and D. C. Lagoudas, eds., ASME, pp. 9–18.

Wetherhold, R. C., 1991, "The Sensistivity of Fracture Location Distribution in Brittle Materials," *Int. J. Frac.*, Vol. 49, pp. 305–315.

APPENDIX

Parameters for GSL model:

$$\beta = A_1 P_{x'} + A_1 P_{y'} + A_3 P_{x'y'}$$

$$A_1 = \frac{1}{h_2 + h_3}$$

$$\times \left[S_{12}'^{(2)} - S_{11}'^{(2)} \left(\frac{S_{11}^{(1)}}{h_1} + \frac{S_{11}'^{(2)}}{h_2 + h_3} \right)^{-1} \left(\frac{S_{12}^{(1)}}{h_1} + \frac{S_{12}'^{(2)}}{h_2 + h_3} \right) \right]$$

$$A_2 = \frac{1}{h_2 + h_3}$$

$$\times \left[S_{22}'^{(2)} - S_{12}'^{(2)} \left(\frac{S_{11}^{(1)}}{h_1} + \frac{S_{11}'^{(2)}}{h_2 + h_3} \right)^{-1} \left(\frac{S_{12}^{(1)}}{h_1} + \frac{S_{12}'^{(2)}}{h_2 + h_3} \right) \right]$$

$$A_3 = \frac{1}{h_2 + h_3}$$

$$\times \left[S_{26}'^{(2)} - S_{16}'^{(2)} \left(\frac{S_{11}^{(1)}}{h_1} + \frac{S_{11}'^{(2)}}{h_2 + h_3} \right)^{-1} \left(\frac{S_{12}^{(1)}}{h_1} + \frac{S_{12}'^{(2)}}{h_2 + h_3} \right) \right]$$

$$B_1 = \left(\frac{S_{11}^{(1)}}{h_1} + \frac{S_{11}'^{(2)}}{h_2 + h_3} \right)^{-1}$$

$$\times \left[-B_4 \left(\frac{S_{12}^{(1)}}{h_1} + \frac{S_{12}'^{(2)}}{h_2 + h_3} \right) - B_7 \left(\frac{S_{16}^{(1)}}{h_1} + \frac{S_{16}'^{(2)}}{h_2 + h_3} \right) \right]$$

$$B_2 = \left(\frac{S_{11}^{(1)}}{h_1} + \frac{S_{11}'^{(2)}}{h_2 + h_3} \right)^{-1}$$

$$\times \left[-B_5 \left(\frac{S_{12}^{(1)}}{h_1} + \frac{S_{12}'^{(2)}}{h_2 + h_3} \right) - B_8 \left(\frac{S_{16}^{(1)}}{h_1} + \frac{S_{16}'^{(2)}}{h_2 + h_3} \right) \right]$$

$$B_3 = \left(\frac{S_{11}^{(1)}}{h_1} + \frac{S_{11}'^{(2)}}{h_2 + h_3} \right)^{-1} \left[-B_6 \left(\frac{S_{12}^{(1)}}{h_1} + \frac{S_{12}'^{(2)}}{h_2 + h_3} \right) \right.$$

$$\left. - B_9 \left(\frac{S_{16}^{(1)}}{h_1} + \frac{S_{16}'^{(2)}}{h_2 + h_3} \right) + \frac{S_{11}'^{(2)} P_{x'} + S_{12}'^{(2)} P_{y'} + S_{16}'^{(2)} P_{x'y'}}{h_2 + h_3} \right]$$

$$B_4 = \frac{\beta \psi_{22}}{\lambda^2} \frac{1 - \cosh(2\lambda s)}{\sinh(2\lambda s)}$$

$$B_5 = \frac{\beta \psi_{22}}{\lambda^2}$$

$$B_6 = -B_5$$

$$B_7 = \left(\frac{\lambda^2}{\psi_{22}} - \alpha\right)\frac{B_4}{\eta}$$

$$B_8 = \left(\frac{\lambda^2}{\psi_{22}} - \alpha\right)\frac{B_5}{\eta}$$

$$B_9 = -B_8$$

$$\lambda = +\sqrt{\alpha\psi_{22} + \eta\psi_{12}}$$

$$\alpha = \left[\left(\frac{S_{11}^{(1)}}{h_1} + \frac{S_{11}'^{(2)}}{h_2 + h_3}\right)^{-1}\left(\frac{S_{12}^{(1)}}{h_1} + \frac{S_{12}'^{(2)}}{h_2 + h_3}\right)^2 - \left(\frac{S_{22}^{(1)}}{h_1} + \frac{S_{22}'^{(2)}}{h_2 + h_3}\right)\right]$$

$$\eta = \left[\left(\frac{S_{11}^{(1)}}{h_1} + \frac{S_{11}'^{(2)}}{h_2 + h_3}\right)^{-1}\left(\frac{S_{12}^{(1)}}{h_1} + \frac{S_{12}'^{(2)}}{h_2 + h_3}\right) \times \left(\frac{S_{16}^{(1)}}{h_1} + \frac{S_{16}'^{(2)}}{h_2 + h_3}\right) - \left(\frac{S_{26}^{(1)}}{h_1} + \frac{S_{26}'^{(2)}}{h_2 + h_3}\right)\right]$$

A Mixed Lubrication and Oil Transport Model for Piston Rings Using a Mass-Conserving Algorithm

S. D. Gulwadi
Tribology Research,
Ricardo Inc.,
Burr Ridge, IL 60521

A numerical study of the interactions between hydrodynamic/boundary lubrication, oil transport, and radial dynamics of a piston ring using a mass-conserving (cavitation) algorithm is presented. The scheme outlined in this investigation facilitates the calculation of the volume of oil accumulating at the leading and trailing edges of the piston ring as it scrapes against the liner. The calculation of this oil accumulation is important in the estimation of lubricating oil consumption in engines. The numerical procedure employed in this study is capable of depicting the transition between the various modes of piston ring lubrication (hydrodynamic, mixed, and boundary) over an engine cycle, including the detachment of oil film from the ring and its subsequent re-attachment. Additionally, the effects of (a) liner lubricant availability and (b) ring face profiles on the oil accumulation are also discussed.

Introduction

A comprehensive understanding of piston ring lubrication is essential for the performance analysis of internal combustion engines. The modes of ring lubrication (hydrodynamic, mixed, or dry) determine the degree of wear in rings, which has an impact on the quality of sealing between the rings and liner. This influences the blowby and lubricating oil consumption in engines, which eventually affects the fuel economy. As a result, a vast number of studies have been conducted in the area of ring lubrication and only papers with relevance to this investigation are reported here.

The operation of rings in a piston ring pack is based on interactions between various physical phenomena such as ring axial/radial motions, ring twist, gas flows through the end-gap and lands/grooves, ring bore conformability, hydrodynamic lubrication, and transport of oil. Several studies have been conducted in the modeling of these various coupled phenomena in an integrated manner. Ting and Mayer (1973a, b) developed early models of ring lubrication and blowby with the objective of predicting cylinder wear while Dowson et al. (1979), Truscott et al. (1983), and Ruddy et al. (1979, 1981) included the effects of ring dynamics. Some recent research includes the approach used by Keribar et al. (1991), which shows the results of interaction of ring motion, gas dynamics, and ring lubrication.

Over an engine cycle the scraping of rings against the liner causes oil to accumulate at the leading and trailing edges of each ring. During the flow of gases through the land/groove regions, a fraction of this lubricant is transported by these gases toward the combustion chamber during blow-back. Additionally, a fraction of the oil accumulation above the top ring is discharged toward the combustion chamber by throw-off due to inertia. Hence, the computation of this volume accumulation of oil is imperative in obtaining a good estimate of the lubricating oil consumption.

There have been several studies related to piston ring lubrication, notably by Furuhama (1959, 1960) who considered a ring profile with a central flat region with circular arcs at either end. Other recent studies include the work by Miltsios et al. (1989) who used finite element techniques to solve the hydrodynamic lubrication equation, while Hu et al. (1994) performed a nonaxisymmetric analysis of piston ring lubrication. A one-dimensional analysis of piston ring lubrication was conducted by Jeng (1992a, b). An oil transport model was incorporated into the analysis whereby the ring could operate under the fully flooded and starved lubricating conditions depending on the lubricant availability. However, the analysis did not take into account the cavitating region in the oil film between the ring and the liner since it implemented the Reynolds boundary condition for oil film detachment but did not consider the reattachment of the oil film with the ring due to the Jakobsson–Floberg–Olsson (JFO) boundary condition.

The study conducted herein involves the implementation of a mass-conserving (cavitation) scheme in the solution of the one-dimensional hydrodynamic lubrication equation for the piston ring. This scheme, in conjunction with a boundary lubrication model and oil transport model, facilitates the computation of the volume accumulation of oil for the ring at its leading and trailing edges. The trailing height of the oil film behind the ring is also computed, which is used in the estimation of the axial oil film distribution on the liner at each instant. From this information the amount of oil available for lubricating the ring at each instant of the cycle can be calculated. An additional feature of the scheme is its capability to simulate the transition between the various modes of ring lubrication (hydrodynamic, mixed, and boundary) based on the lubricant availability including the oil film detachment from the ring and its subsequent reattachment.

Modeling Approach

In this investigation results are presented from a simulation program for a sample top ring of a piston ring pack. An axisymmetric geometry is assumed and the piston ring is treated as a reciprocating, dynamically loaded bearing. The lubrication, oil transport, and radial dynamics equations are solved over a complete engine cycle using typical cylinder, second land, and groove pressures.

Hydrodynamic Lubrication Model. A mass-conserving scheme proposed by Elrod and Adams (1974) and Elrod (1981) is applied to solve the one-dimensional hydrodynamic lubrica-

---

Contributed by the Internal Combustion Engine Division and presented at the 17th Annual Fall Technical Conference of the ASME Internal Combustion Engine Division, Milwaukee, Wisconsin, September 24–27, 1995. Manuscript received at ASME Headquarters May 1997. Associate Technical Editor: W. K. Cheng.

tion equation for a piston ring-face. Apart from the mass-conserving feature, the advantage of this scheme is the implementation of the appropriate boundary conditions for oil film rupture (Reynolds boundary condition) and the re-attachment of the oil film (JFO boundary condition). This enables the cavitating region in the oil film between the piston ring face and the liner to be determined in a more rigorous manner.

The key features of the cavitation algorithm are:

(*a*) The effect of slight compressibility of the lubricant is taken into account via the usage of the bulk modulus β, where

$$\beta = \rho \frac{\partial P}{\partial \rho}$$

and P and ρ represent the local oil film pressure and density.
(*b*) The hydrodynamic lubrication equation is expressed in terms of the variable α, where $\alpha = \rho/\rho_c$ (ratio of oil density to oil density at cavitation) in the oil filled zone, or α = fraction of the clearance height occupied by the lubricant in the cavitating zone.
(*c*) Expressions for the oil film pressures are given by

$$P = P_c + \beta(\alpha - 1), \quad \text{when} \quad \alpha \geq 1, \quad \text{and} \tag{1a}$$

$$P = P_c, \quad \text{when} \quad \alpha < 1, \tag{1b}$$

with P_c representing the cavitation pressure.
(*d*) Introduction of a switch function or cavitation index $g(\alpha)$, such that

$$g(\alpha) = 1, \quad \text{when} \quad \alpha \geq 1 \tag{2a}$$

$$g(\alpha) = 0, \quad \text{when} \quad \alpha < 1. \tag{2b}$$

The hydrodynamic lubrication equation (or mass conservation equation) is written as follows:

$$\frac{\partial \dot{m}_c}{\partial z} + \frac{\partial \dot{m}_p}{\partial z} = \frac{\partial}{\partial t}(\rho_c \alpha_n h_n). \tag{3}$$

where:

$\dot{m}_c$ = Couette (convective) mass flow rate per unit length,

$$= \rho_c \frac{V}{2}\left[\alpha_{-n} h_{-n}(1 - g_{-n}) + g_{-n} h_{-n} + \frac{g_{-n} g_n}{2}(h_n - h_{-n})\right].$$

$\dot{m}_p$ = Poiseuille (pressure driven) mass flow rate per unit length,

$$= \left[\frac{h^3}{12\mu}\right]\beta\rho_c\left[\frac{g_{-n}(\alpha_{-n} - 1) - g_n(\alpha_n - 1)}{\Delta z}\right].$$

The subscript n refers to the node about which the mass balance is performed, and the subscript $-n$ refers to the upstream node.

The hydrodynamic equation shown in Eq. (3) is solved at different nodal locations within the oil film region of the ring face. The pressure boundary conditions (using land pressures) are applied at the front and back extents of the oil film region,

$$P(z_1) = P_1; \quad P(z_2) = P_2. \tag{4}$$

from which the boundary conditions on α may be obtained using Eq. (1*a*). The oil film thickness profile $h(z)$ is based on the piston ring-face profile bounded by the front and back lubrication extent (z_1, z_2) where

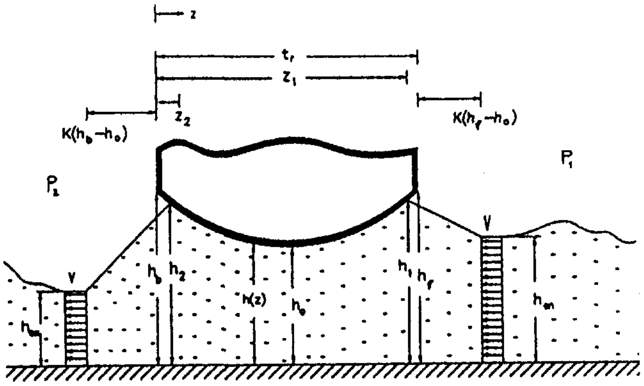

Fig. 1 Schematic for the ring lubrication model

$$h(z_1) = h_1; \quad h(z_2) = h_2, \tag{5}$$

and minimum film thickness h_0 as shown in Fig. 1. It should be noted that z_1, z_2, and h_0 are time-dependent variables.

From the solution of the hydrodynamic lubrication equation, the mass flow rates at z_1 and z_2 are obtained represented by $\dot{m}_{en}$ and $\dot{m}_{ex}$, respectively. Additionally, from the oil film pressure distribution the lineal force due to the oil pressure is calculated using

$$F_{oil} = \int_{z_1}^{z_2} P(z) dz. \tag{6}$$

Boundary Lubrication Model. The local asperity contact pressure is computed using the Greenwood and Tripp (1971) model. This model is for the contact of two nominally flat surfaces, with a Gaussian distribution of asperity heights and fixed asperity radius of curvature:

$$P_{\text{asp}} = \frac{16\sqrt{2}}{15}\pi(\sigma\gamma\eta)^2 E \sqrt{\frac{\sigma}{\gamma}} F\left[\frac{h(z)}{\sigma}\right], \tag{7}$$

$$F(x) = \frac{1}{\sqrt{2\pi}}\int_x^\infty (s - x)^{5/2} \exp(-s^2/2) ds, \tag{8}$$

where σ is the composite roughness of the ring face and cylinder $(\sigma_r^2 + \sigma_c^2)^{1/2}$, η the asperity density, γ the asperity radius of curvature, and E the composite elastic modulus of the surface materials. Since the ring face is not flat, the contact pressures are calculated at each node rather than as a single force. The lineal force due to asperity contact pressure is then calculated from

$$F_{\text{asp}} = \int_0^{tr} P_{\text{asp}}(z) dz. \tag{9}$$

Oil Transport Model. An oil transport model is coupled with the mixed lubrication model. The purposes of the oil transport model are:

(*a*) To compute the volume of lubricant accumulating at the leading and trailing edges of the ring.
(*b*) To calculate the thickness of the oil film trailing behind the ring on the liner.
(*c*) To determine the flow regimes of ring lubrication (i.e., calculation of the front and back extents of the oil-lubricated ring face) based on the availability of lubricant, ring velocity, and pressure gradient across the ring face.

Fully Flooded Ring: In this case, as seen in Fig. 2(*a*), the entire piston ring face is lubricated by the oil and the ring loads are borne by the oil/asperity forces only.

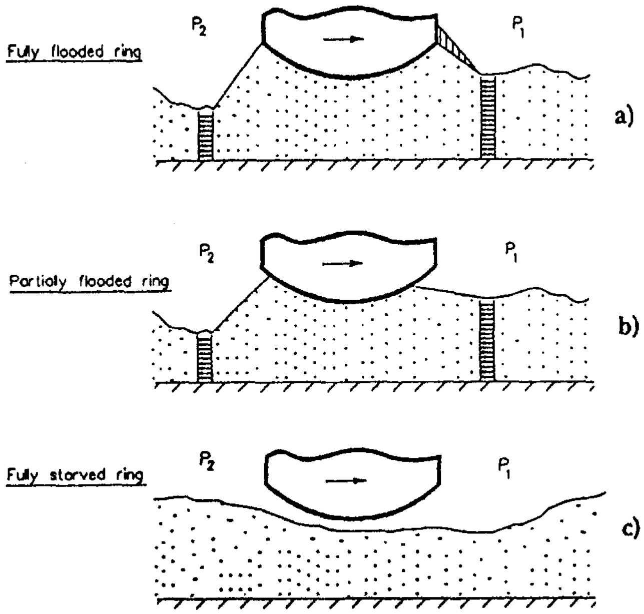

Fig. 2 Regimes of ring lubrication; (*a*) fully flooded, (*b*) partially flooded, and (*c*) fully starved

Partially Flooded Ring: As observed in Fig. 2(*b*), only a portion of the ring face is lubricated by oil, with the remaining surface of the ring face being gas lubricated. As a result, the loads are borne by oil/asperity forces and gas forces.

Completely Starved Ring: Due to low lubricant availability on the liner or a high-pressure gradient across the ring face or a combination of these two, the oil film may detach from the ring. The loads on the ring are supported by only the gases flowing below the ring (case of "ring lift" as seen in Fig. 2(*c*)), or by gas/asperity forces in the situation where the ring is in contact with the asperities.

The oil transport model involves performing mass balances on control volumes at the front and back of the oil lubricated zone of the piston ring-face, as shown in the schematic in Fig. 3. Essentially, the control volumes are fixed to the ring with the boundary of the front control volume extending to a distance $k(h_f - h_0)$, while the boundary of the back control volume is at a distance $k(h_b - h_0)$. The terms h_f and h_b are time dependent and represent the clearance heights of the leading and trailing edges of the piston ring-face from the liner, while k is the aspect ratio, which is kept at a fixed value of 100 throughout the simulation.

For the control volume in front of the oil lubricated zone, as shown in Fig. 3, the mass balance per unit circumferential length within a time interval Δt is performed, whereby

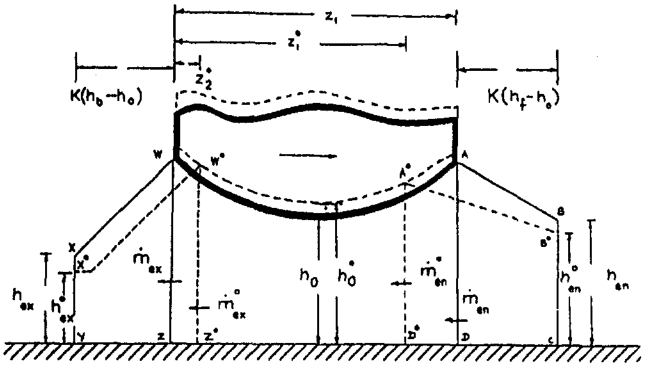

Fig. 3 Schematic for the control volumes at the leading and trailing edges of the ring

(Mass of oil entering the control volume)

− (Mass of lubricant entering the oil lubricated zone)

= (Change in oil mass in the front control volume),

or

$$\left[\rho\,\frac{Vh_{en} + V^o h_{en}^o}{2} - \frac{\dot{m}_{en} + \dot{m}_{en}^o}{2}\right]\Delta t$$

$$= [\text{Area}(ABCD) - \text{Area}(A^oB^oCD^o)]\rho \quad (10)$$

A similar mass balance is performed on the control volume behind the oil lubricated zone, shown in Fig. 3, whereby

(Mass of lubricant exiting the oil lubricated zone)

− (Mass of oil exiting the back control volume)

= (Change in mass of oil in the back control volume),

or

$$\left[\frac{\dot{m}_{ex} + \dot{m}_{ex}^o}{2} - \rho\,\frac{Vh_{ex} + V^o h_{ex}^o}{2}\right]\Delta t$$

$$= [\text{Area}(WXYZ) - \text{Area}(W^oX^oYZ^o)]\rho \quad (11)$$

The superscript o in Eqs. (10) and (11) refers to the values of parameters at the previous instant of time, $\dot{m}_{en}$ and $\dot{m}_{ex}$ are obtained from the solution of the hydrodynamic lubrication equation Eq. (3), the ring velocity V is calculated from the engine rpm and the entry height of the oil film h_{en} is dependent on the lubricant availability on the liner.

The volume of oil per unit circumferential length at any given instant of time, contained in the front control volume, is calculated from the area under the trapezoid $ABCD$ shown in Fig. 3,

$$\text{Area}(ABCD) = k(h_f - h_0)\left(\frac{h_{en} + h(z_1)}{2}\right), \quad (12a)$$

and the oil accumulation at the leading edge of the ring is computed when

$$h(z_1) > h_f; \quad V_{f,acc} = k(h_f - h_0)\left(\frac{h(z_1) - h_f}{2}\right). \quad (12b)$$

The exit height of the oil film h_{ex} is an additional variable in Eq. (11) besides h_0, z_2, and $\dot{m}_{ex}$. In lieu of a rigorous surface tension model, which can describe the surface curvature of the volume trailing the ring, a scheme is provided whereby the shape of the volume of lubricant behind the ring per unit length (i.e., Area under the trapezoid $WXYZ$) is accounted through the coupling of h_{ex} and z_2. Based on the flow rate out of the oil film zone, the volume of lubricant per unit length trailing the ring is computed depending on which regime it falls under, as shown in Fig. 4:

Regime A: $z_2 = 0$; h_{ex} is the variable such that

$$\text{Area}(WXYZ) = k(h_b - h_0)\left(\frac{h_b + h_{ex}}{2}\right), \quad \text{and} \quad (13a)$$

$$\text{if } h_{ex} > h_b; \quad V_{b,acc} = k(h_b - h_0)\left(\frac{h_{ex} - h_b}{2}\right). \quad (13b)$$

Regime B: z_2 and h_{ex} are variables subject to the condition

$$k(h(z_2) - h_{ex}) = k(h_b - h_0) + z_2, \quad \text{and} \quad (13c)$$

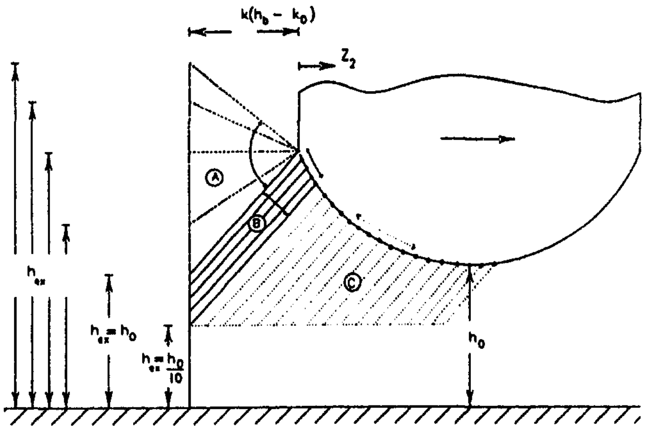

Fig. 4 Sequence of depletion or accumulation of oil behind the lubricated zone of the ring

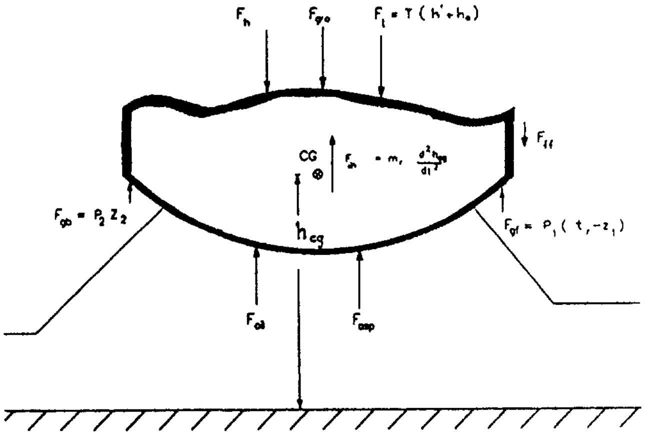

Fig. 5 Notation for radial force balance on the ring

$$\text{Area}(WXYZ) = (k(h_b - h_0) + z_2)\left(\frac{h(z_2) + h_{ex}}{2}\right) \quad (13d)$$

Regime C: $h_{ex} = h_0/10$; z_2 is the variable, and

$$\text{Area}(WXYZ) = (k(h_b - h_0) + z_2)h_{ex} + \frac{k}{2}(h(z_2) - h_{ex})^2. \quad (13e)$$

It should be noted that the hydrodynamic lubrication equation is not solved when the oil film is detached from the ring (fully starved condition). The scheme described herein is capable of detecting the conditions of detachment and the subsequent re-attachment of the oil film with the ring.

Radial Ring Dynamics. The radial motion of the ring within the groove is accounted via the radial force balance, which is expressed as

$$m_r \frac{\partial^2 h_{cg}}{\partial t^2} = F_{oil} + F_{\text{asp}} + F_{gf} + F_{gb} - F_{gro} - F_{ff} - F_t - F_h \quad (14)$$

where:

m_r = mass of the ring per unit circumferential length,
h_{cg} = radial location of center of gravity of piston ring,
F_{oil} = force due to the oil film pressure using Eq. (6),
F_{asp} = force due to the asperities using Eq. (9),
F_{gf} = force due to gas pressure acting on the front unlubricated portion of the ring face,
F_{gb} = force due to gas pressure acting on the back unlubricated portion of the ring face,
F_{gro} = force acting behind the ring due to groove pressure based on the crevice/land pressures,
F_{ff} = equivalent friction force on the ring due to asperities in the ring groove region,
F_t = ring tension force, and
F_h = an equivalent spring force activated during ring lift and to stop lift when "ring collapse" occurs.

Figure 5 shows the various components of the radial force balance. The term T in the tension force represents the radial ring stiffness per unit circumferential length while h' is the reduction in ring radius (taken as 3 percent of the bore in this study) at installation.

Numerical Technique

There are five primary time-dependent variables (h_0, $\dot{m}$, z_1, z_2, h_{ex}) associated with the phenomena whose models have been described above. The general forms of the equations are given by

Hyd. Lubrication., Eq. (3): $f_1(h_0, z_1, z_2, \dot{m})$,

Mass Balance, Eq. (10): $f_2(h_0, z_1, \dot{m})$,

Mass Balance, Eq. (11): $f_3(h_0, z_2, h_{ex}, \dot{m})$,

Back control volume, Eq. (13a–e): $f_4(h_0, z_2, h_{ex})$, and

Ring Dynamics, Eq. (14): $f_5(h_0, z_1, z_2)$.

A multi-variate form of the Newton–Raphson technique is used to solve these five coupled equations for each crank angle increment over the complete engine cycle.

The simulation is typically run using crank angle increments of 4 or 5 deg. However, when there is nonconvergence in any of the models, the crank angle increments are successively halved and there may be situations in the engine cycle when crank angle increment values of 1 or 1.25 deg are used. This helps to resolve events on a much smaller time scale, which is particularly relevant at the instant of oil film detachment from the ring and its subsequent re-attachment.

For the purposes of hydrodynamic lubrication of the piston ring face, the oil lubricated mesh is typically discretized by 51 nodes. However, simulations have also been run using 81 and 101 nodes, but hardly any variations have been observed in the basic output parameters.

Simulation Results

The results presented in this study are based on the simulation of a single ring (top ring) of a ring pack subjected to the crevice and second land pressures, shown in Fig. 6, which are acting on either sides of the ring. The basic ring/liner parameters and

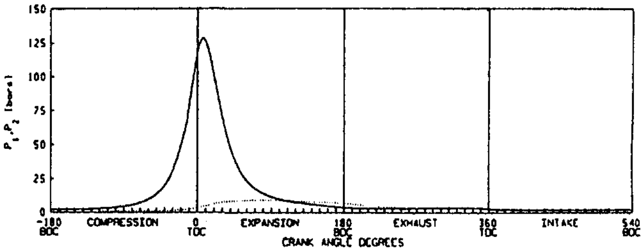

Fig. 6 Crevice and second land pressures

Table 1 Ring/liner/oil parameters and operating conditions

Ring/liner parameters:		
Thickness of ring face, t_r	0.003	m.
Lineal ring mass, m_r	0.05	kg/m
Lineal ring stiffness, T	75	N/m^2
Ring face roughness, σ_r	0.2	µm.
Liner roughness, σ_c	1	µm.
Elasticity of ring/liner, E	200	GN/m^2
Asperity radius of curvature, γ	0.005	m.
Asperity density, η	10E8	m^{-2}
Lubricant parameters:		
Viscosity, μ	0.005	Pa-s
Density, ρ	860	kg/m^3
Cavitation pressure, P_c	0.0999	MPa
Bulk modulus, β	500	MPa
Engine parameters:		
Bore,	0.125	m.
Stroke,	0.140	m.
Engine speed,	2100	rpm.
No pin offset		

the engine operating conditions used in the simulation are shown in Table 1.

Baseline Case. For the baseline case a top ring with a rectangular cross section and symmetric barrel-shaped (parabolic) face profile is selected as shown in Fig. 7(*a*). Initially, a uniform oil film thickness of 5 μm is prescribed on the liner. This implies that at the start of the simulation (150 deg BTDC) the instantaneous oil film height along the entire length of the liner is 5 μm, as is observed from Fig. 8(*a*). At other instants of the engine cycle, the entry height of the oil film is calculated based on the thickness of the oil film left behind by the ring (exit height) during the previous stroke, as depicted in Fig. 8(*b*). The exit height of the oil film has a similar qualitative behavior compared to the minimum oil film thickness in Fig. 9(*a*). The ring leaves behind a thicker oil film in the middle of the stroke where the ring velocity is high compared to the end/beginning of the stroke where the velocity is low. In particular, at the beginning of the intake and compression strokes, very low values of the exit film height are observed and this is due to the detachment of the oil film from the ring. With subsequent re-attachment of the oil film to the ring, the exit height values increase.

Figure 9(*a*) shows the plot of minimum oil film thickness. Some typical characteristics of ring behavior are observed from this plot: (*a*) low values of h_0 at the dead center locations, and (*b*) the ring being forced closer to the liner during the power stroke due to the high groove pressures acting on the ring. From Fig. 9(*b*), which displays the oil-lubricated extents of the ring face, it is observed that during the early half of the compression stroke, the latter half of the exhaust stroke, and the entire intake stroke, the ring is partially lubricated due to the relatively low groove pressure acting on the ring. In particular, during the beginning of the compression and intake strokes, the oil film detaches from the ring due to a combination of low values of ring velocity, entry height of the oil film, and groove pressures. However, as the intake and compression strokes proceed, the oil film re-attaches to the ring, as shown in Fig. 9(*b*). For those portions of the engine cycle (latter half of the compression stroke, entire expansion stroke, and early half of exhaust stroke) where there is relatively high groove pressure acting on the ring, the ring is forced closer to the liner, enabling it to operate in the fully flooded mode.

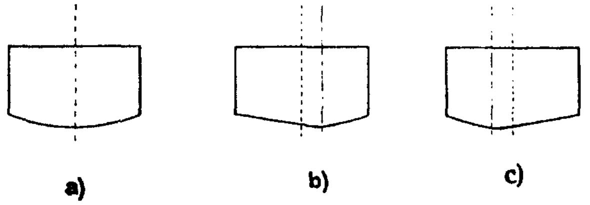

Fig. 7 Ring-face profiles: (*a*) barrel, (*b*) forward canted barrel, and (*c*) backward canted barrel

The accumulation of oil at the front and back of the ring are shown in Figs. 10(*a*) and 10(*b*). There is build-up of oil at the front of the ring through the latter half of the compression stroke and the entire expansion stroke since the leading edge of the ring is always in contact with the lubricant. At the beginning of the exhaust stroke there is an accumulation of oil, which eventually is depleted, as the leading edge of the ring loses contact with the lubricant and this can be seen from Fig. 9(*b*). Figure 10(*b*) indicates that there is no oil accumulation behind the ring during any stroke. However, at the beginning of the expansion and exhaust strokes, there is a volume of oil behind the ring, which is attributed to the oil accumulated in front of the ring during the previous stroke. The volume of oil behind the ring is eventually depleted as the ring resumes its motion.

The flow rates $\dot{Q}_{en}$ and $\dot{Q}_{ex}$ into and out of the oil lubricated zones of the piston ring are shown in Figs. 11(*a*) and 11(*b*). High values of the flow rates are observed in the middle of the strokes due to high ring velocity and these values decrease in the vicinity of the dead center locations where the ring velocity is low. At the beginning of the compression and intake strokes the flow rates are zero due to the oil film detachment from the ring but start increasing with the subsequent re-attachment of the lubricant with the ring.

Figure 12 shows the pressure distribution in the oil film between the ring face and the liner with the abscissa representing the nodes in the oil-lubricated region of the ring face. As can be observed, there is a pressure build-up in the region of the ring face, which is convergent with respect to the liner but starts decreasing in the divergent section of the ring face until the oil film detaches from the ring face. The film rupture occurs when the pressure gradient becomes zero with the local pressure having reached the cavitation pressure value (Reynolds boundary condition). The cavitating zone is one wherein the pressure is constant (cavitation pressure). In this region the lubricant is assumed to be transported in the form of striations extending to both surfaces in the oil film gap. There is an eventual reformation of the oil film, as can be seen from the increase in oil film pressures. This is due to the application of the JFO boundary conditions, which accounts for the conservation of mass for film rupture and reformation.

Effect of Ring Face Profiles. One of the features of this simulation program is that the ring face profile may be directly input to the program rather than have the profile be constructed based on input geometric parameters, which can be restrictive. In order to observe the effect of ring face profiles on the lubricant accumulation in front of the ring, the simulation is run using three different ring face profiles *A*, *B*, and *C* shown in Figs. 7(*a*), 7(*b*), and 7(*c*), respectively. All other parameters are kept constant including the initial specification of 5 μm of oil film thickness on the liner.

Figure 13(*a*) indicates that the ring with the face profile *B* (parabolic profile with an offset toward the top of the ring) leaves behind an oil film with the least thickness suggesting a strong scraping action. This is also corroborated by the minimum film thickness plot in Fig. 13(*b*), which shows the ring with the face profile *B* tends to be closer to the liner over the entire engine cycle compared to the rings with face profiles *A*

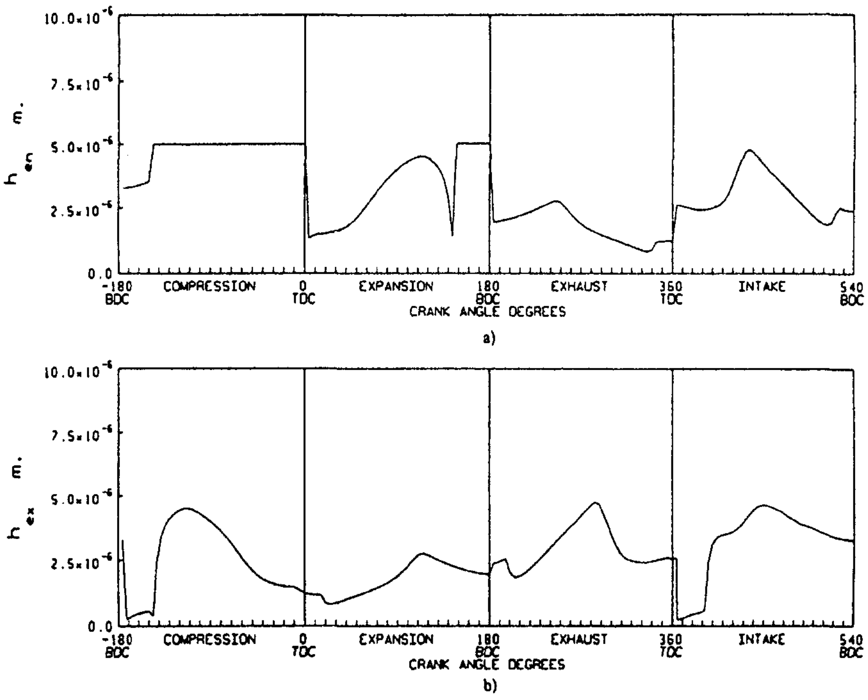

Fig. 8 (*a*) Entry height of oil film based on liner lubricant availability; (*b*) exit height of oil film trailing the ring

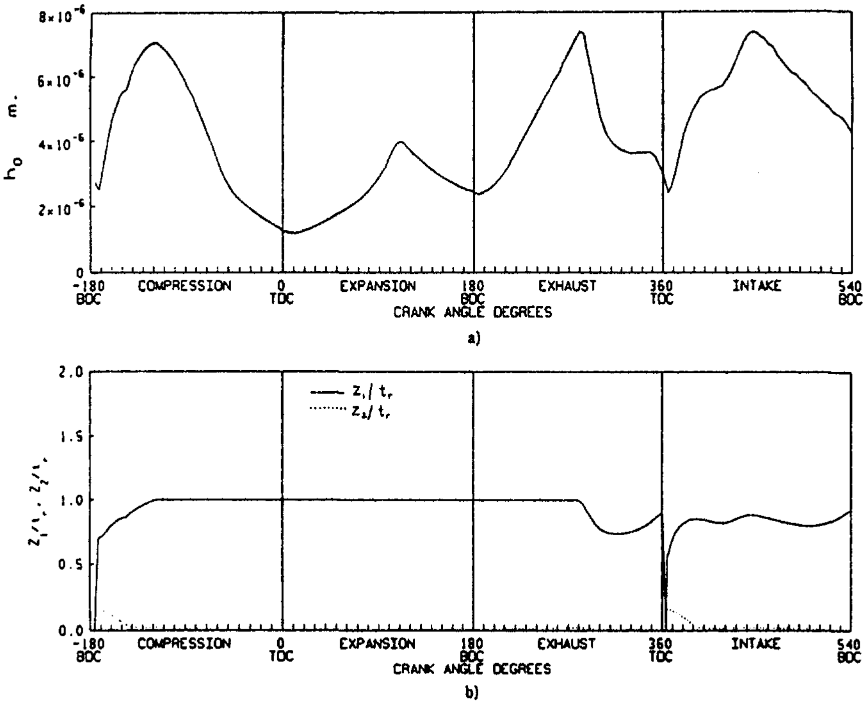

Fig. 9 (*a*) Plot of minimum film thickness; (*b*) front and back oil lubricated extents of the ring face

and C. In terms of scraping performance, the ring with the face profile C (parabolic face profile with offset toward the bottom of the ring) has the least scraping effect and leaves the thickest oil film behind.

The accumulation of oil for each ring face profile is consistent with the scraping behavior. The ring with face profile B has the maximum accumulation of oil in front of it over the whole engine cycle while the ring with face profile C has the least, as seen in Fig. 13(*c*).

Effect of Lubricant Availability on Liner. Oil film thickness on the liner has a significant influence on the radial ring motion and the volume of lubricant accumulating in front of the ring (scraping limited mode), as can be observed from Figs. 14(*a*), 14(*b*), and 14(*c*). The simulation is performed for a ring with face profile A under three conditions wherein the initial specification of constant oil film thickness on the liner is increased (5 μm, 7 μm, and 10 μm). Figure 14(*a*) shows that as the initial availability of oil on the liner is increased, the ring tends to

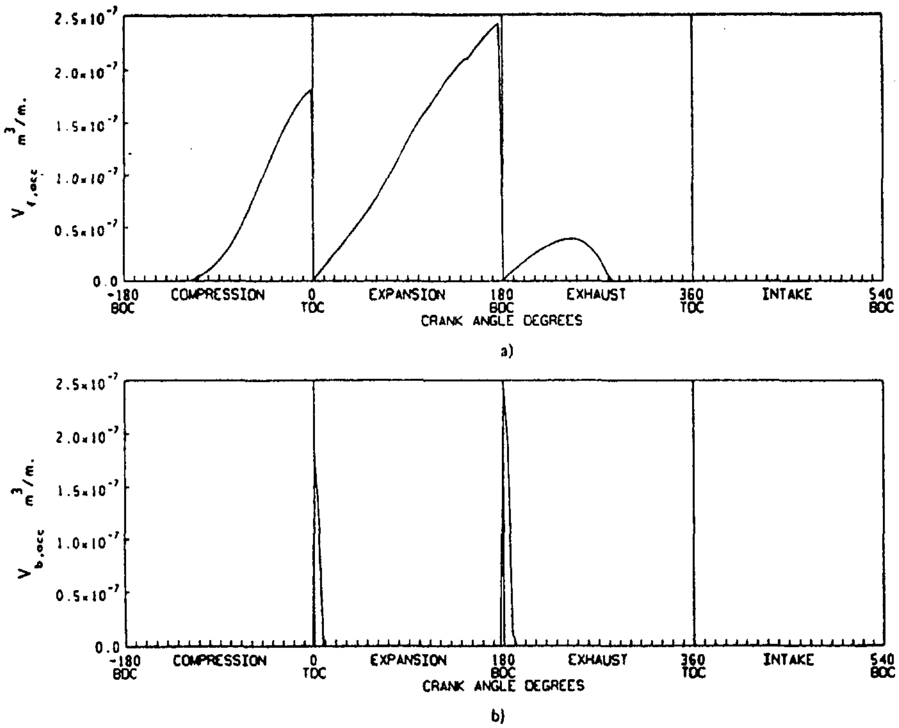

Fig. 10 (*a*) Volume of oil accumulating at the leading edge of the ring; (*b*) volume of oil accumulating at the trailing edge of the ring

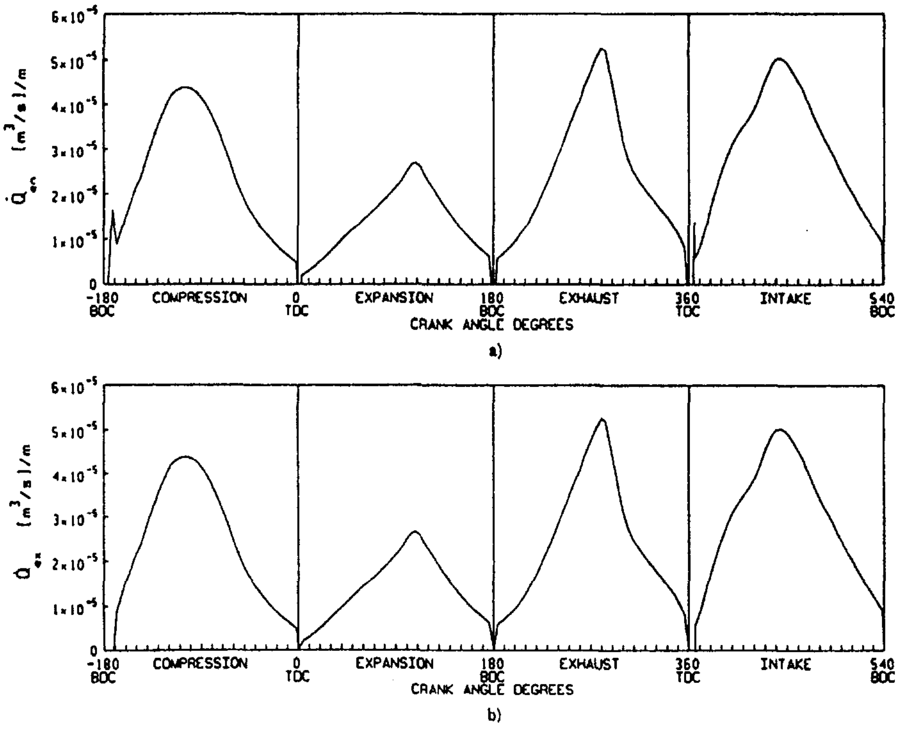

Fig. 11 (a) Flow rate of lubricant into the oil lubricated zone of the ring; (b) flow rate of lubricant out of the oil lubricated zone

leave behind a thicker oil film over the engine cycle, and this is particularly noticeable during the exhaust and intake strokes. For relatively low values of lubricant thickness on the liner, the ring operates in the partially flooded mode during portions of the compression, exhaust, and intake strokes. Increasing the oil thickness on the liner enables the ring to operate in the fully flooded lubrication mode over the complete engine cycle. This transition is clearly depicted in Fig. 14(*b*), wherein h_0 has increased over those portions of the engine cycle where the ring has moved from the partially flooded to the fully flooded lubrication mode.

The volume accumulation in front of the ring increases with increasing oil film availability on the liner, as observed from Fig. 14(*c*). For relatively lower values of oil film thickness on

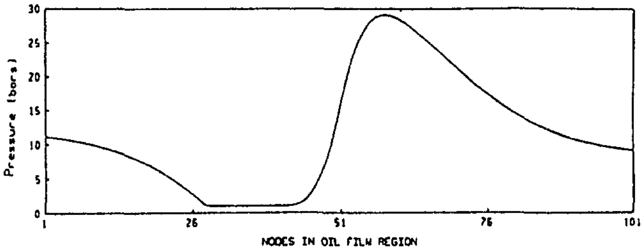

Fig. 12 Pressure distribution in the oil film between the ring and liner at the middle of the expansion stroke (90 deg ATDC)

the liner, there are portions of the exhaust and intake strokes wherein there is no volume accumulation in front of the ring as it is in the partially lubricated mode. However, by increasing the lubricant availability on the liner, there is build-up of oil in front of the ring over the complete engine cycle since the ring is operating under the fully flooded lubrication mode.

Conclusions

1 The hydrodynamic lubrication scheme adopted in this study clearly depicts the cavitating region in the oil film between the piston ring and the liner.

2 A coupled mixed lubrication and oil transport model for piston rings using a mass conserving algorithm is presented

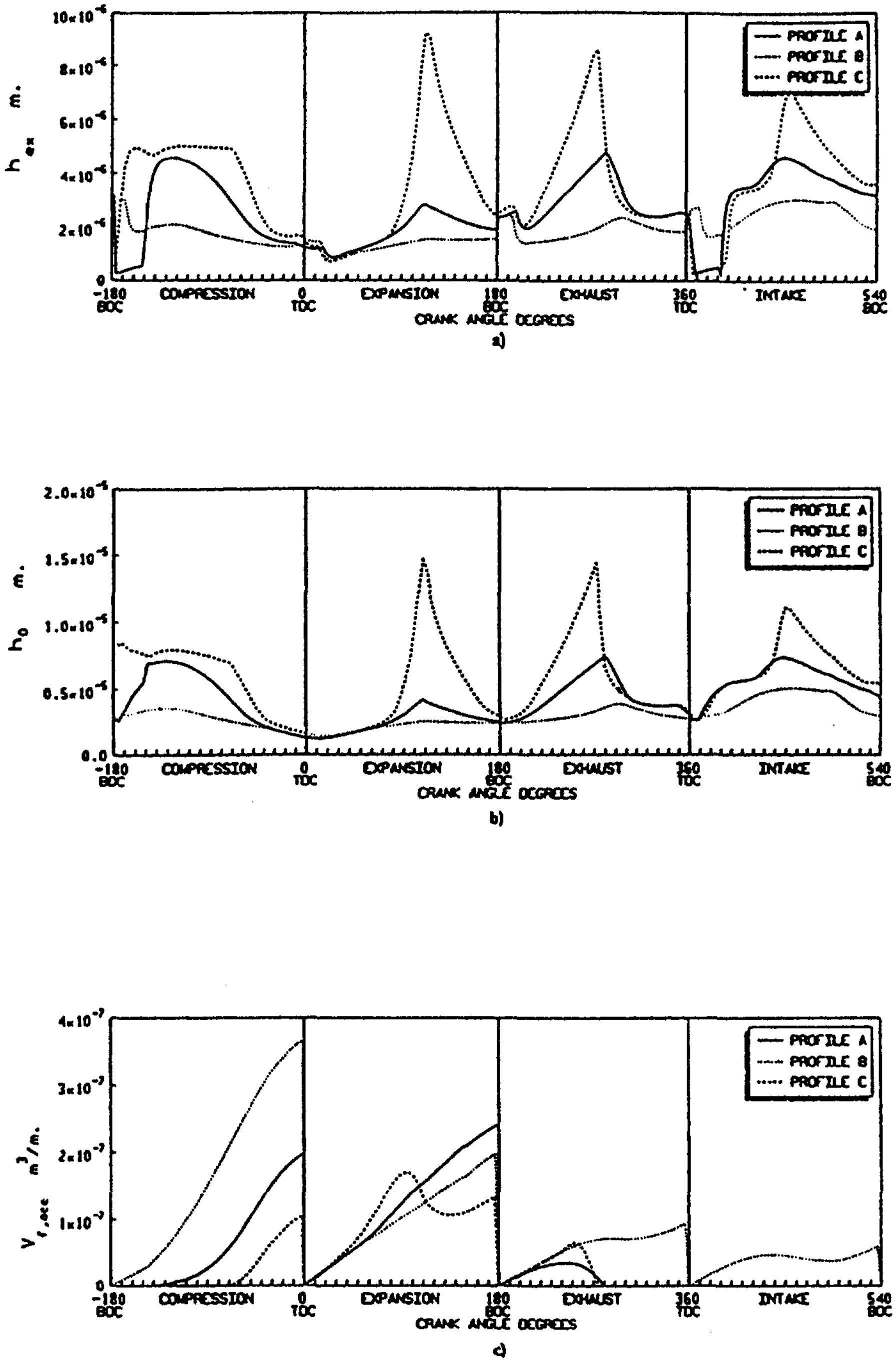

Fig. 13 Effect of ring face profiles on (a) exit height of oil, (b) minimum oil film thickness, and (c) oil accumulation at the leading edge of the ring

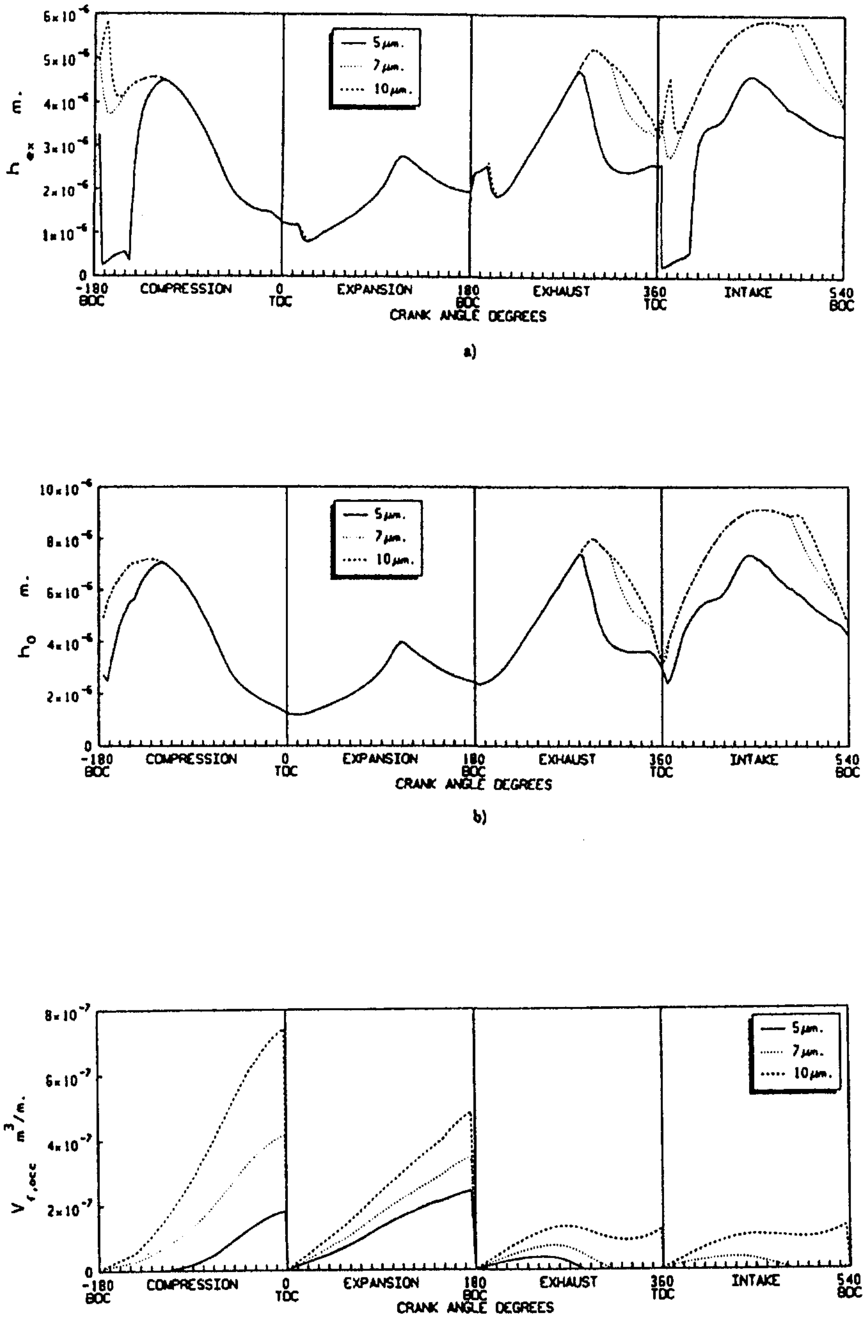

Fig. 14 Effect of lubricant availability on (*a*) exit height of oil, (*b*) minimum oil film thickness, and (*c*) oil accumulation at the leading edge of the ring

whereby the lubricant accumulation in the front and back of rings is computed in a rigorous manner. This calculation is essential in estimating the lubrication oil consumption from throw off due to inertia of the top ring. Additionally, this oil accumulation is also consumed when the gases transport this volume of oil into the combustion chamber during blow-back.

3 The mass conserving feature of the hydrodynamic lubrication equation also facilitates a robust calculation of the oil film thickness trailing the ring, which is used in obtaining the oil film distribution on the liner at any crank angle. This is relevant to the evaporative oil consumption mechanism.

4 The scheme discussed in this study has the capability to depict the transition between the various modes of ring lubrication (fully flooded, partially flooded, and completely starved).

5 This investigation displays the sensitivity of piston ring behavior to changes in ring face profiles and lubricant thickness on the liner.

Acknowledgments

This work was supported by DOE/NASA contract DEN3-374, under subcontract to Caterpillar, Inc. It was monitored by Project Managers James Wood of NASA Lewis Research Center, and Gerald Waltz of the Caterpillar, Inc., Technical Center.

References

Dowson, D., Economou, P. N., Ruddy, B. L., Strachan, P. J., and Baker, A. J. S., 1979, "Piston Ring Lubrication—Part II. Theoretical Analysis of a Single Ring and a Complete Ring Pack," in: *Energy Conservation Through Fluid Film Lubrication Technology: Frontiers in Research and Design,* ASME, pp. 23–52.

Elrod, H. G., and Adams, M. L., 1974, "A Computer Program for Cavitation and Starvation Problems," *Leeds–Lyon Conference on Cavitation,* Leeds Univ., England.

Elrod, H. G., 1981, "A Cavitation Algorithm," ASME *Journal of Lubrication Technology,* Vol. 103, pp. 350–354.

Furuhama, S., 1959, "A Dynamic Theory of Piston Ring Lubrication, 1st Report—Calculation," *Bull. JSME,* Vol. 2, pp. 423.

Furuhama, S., 1960, "A Dynamic Theory of Piston Ring Lubrication, 2nd. Report—Experiment," *Bull. JSME,* Vol. 3, pp. 291.

Greenwood, I. A., and Tripp, J. H., 1971, "The Contact of Two Nominally Flat Surfaces," *Proc. I. Mech. E.,* Vol. 185, pp. 625–633.

Hu, Y., Cheng, H. S., Arai, T., Kobayashi, Y., and Aoyama, S., 1994, "Numerical Simulation of Piston Ring in Mixed Lubrication—A Nonaxisymmetrical Analysis," ASME *Journal of Tribology,* Vol. 116, pp. 470–478.

Jeng, Y.-R., 1992a, "Theoretical Analysis of Piston-Ring Lubrication. Part 1—Fully Flooded Lubrication," *Tribology Transactions,* Vol. 35, pp. 696–706.

Jeng, Y.-R., 1992b, "Theoretical Analysis of Piston-Ring Lubrication. Part 2—Starved Lubrication and Its Application to a Complete Ring Pack," *Tribology Transactions,* Vol. 35, pp. 707–714.

Keribar, R., Dursunkaya, Z., and Fleming, M. F., 1991, "An Integrated Model of Ring Pack Performance," ASME JOURNAL OF ENGINEERING FOR GAS TURBINES AND POWER, Vol. 113, pp. 382–389.

Miltsios, G. K., Patterson, D. J., and Papanastasiou, Y. C., 1989, "Solution of the Lubrication Problem and Calculation of the Friction Force on the Piston Rings," ASME *Journal of Tribology,* Vol. 111, pp. 635–641.

Ruddy, B. L., Dowson, D., and Economou, P. N., 1979, "Piston Ring Lubrication, Part III: The Influence of Ring Dynamics and Ring Twist," in: *Conservation Through Fluid Film Lubrication Technology: Frontiers in Research and Design,* ASME, pp. 23–52.

Ruddy, B. L., Dowson, B. D., and Economou, P. N., 1981, "A Theoretical Analysis of the Twin-Land Type of Oil-Control Piston Ring," *J. Mech. Eng. Sci.,* Vol. 23, pp. 51–62.

Ting, L. L., and Mayer, J. E., 1973a, "Piston Ring Lubrication and Cylinder Bore Wear Analysis, Part I—Theory," ASME *Journal of Lubrication Technology,* Vol. 96, pp. 305–314.

Ting, L. L., and Mayer, J. E., 1973b, "Piston Ring Lubrication and Cylinder Bore Wear Analysis, Part II—Theory Verification," ASME *Journal of Lubrication Technology,* Vol. 96, pp. 258–266.

Truscott, R., Reid, T., and Ruddy, B., 1983, "Ring Dynamics in a Diesel Engine and Its Effect on Oil Consumption and Blowby," SAE Paper No. 831282.

Development and Validation of a Thermodynamic Model for an SI Single-Cylinder Engine

Y. M. Yacoub

R. M. Bata

Department of Mechanical and
Aerospace Engineering,
West Virginia University,
Morgantown, WV 26506

A multizone quasi-dimensional model that illustrates the intake, compression, combustion, expansion, and exhaust processes has been developed for a single-cylinder four-stroke spark-ignition engine. The model takes into consideration mass and energy conservation in the engine cylinder, intake and exhaust plenums, and crankcase plenum. The model calculates instantaneous variations in gas thermodynamic states, gas properties, heat release rates, in-cylinder turbulence, piston ring motion, blowby, nitric oxide, and carbon monoxide formation. The cycle simulation accounts for the induced gas velocities due to flame propagation in the turbulence model (k–ϵ type), which is applied separately to each gas zone. This allows for the natural evolution of the averaged mean and turbulent velocities in burned and unburned gas regions. The present model predictions of thermal efficiency, indicated mean effective pressure, peak values of gas pressure, ignition delay, concentrations of nitric oxide, carbon monoxide, and carbon dioxide are proven to be in agreement with experimental data.

Introduction

The processes of a four-stroke spark-ignited (SI) engine have been the subject of many experimental and theoretical studies at ever-increasing levels of sophistication. Researchers and engine designers have been considering three categories of engine combustion models (Heywood, 1980; Ramos, 1989):

- air standard cycle simulation
- zero and quasi-dimensional thermodynamic models
- multidimensional models

Thermodynamic analysis of combustion in SI engines can be classified as either diagnostic or predictive. Diagnostic models assume cylinder charge to be uniform in pressure, temperature, and composition. These models require experimentally measured in-cylinder pressure and yield heat release and fuel burn rates.

Predictive models require mass burning rates. These can be specified by using a family of functions that approximate the shape of experimentally observed burn rates, such as the Wiebe function.

Another approach is to calculate burn rates as a function of turbulent flame speed and of instantaneous flame area (Blizard and Keck, 1974; Tabaczynski et al., 1977). This approach allows the calculated burn rates to respond to cylinder geometry and flows.

In a two-zone model, the cylinder mixture is divided into burned and unburned gas zones, which are separated from each other by a surface of discontinuity (the flame). A turbulence model is required to calculate different length and velocity scales, which are fundamental for combustion rates and cylinder walls heat transfer calculations. Turbulence parameters can be calculated by solving appropriate rate equations of mean and turbulent flow kinetic energy as well as an equation for turbulent kinetic energy dissipation, which is either algebraic or differential (Ramos, 1989). If an algebraic equation for dissipation is considered, one of the following assumptions holds:

- Turbulence integral length scale is proportional to the valve lift (Blizard and Keck, 1974) or to the distance between the cylinder head and the piston (Poulos and Heywood, 1983).
- Production of turbulence kinetic energy is equal to its dissipation.

On the other hand, an ordinary differential equation for turbulence kinetic energy and its dissipation can be obtained by integrating the multidimensional counterpart throughout the combustion chamber volume. The resulting $k-\epsilon$ model can be applied separately to each gas zone during combustion. The main advantage of such an approach is the continuity in the application of the turbulence model for parts of the cycle simulation when the cylinder volume is considered as a whole (compression, expansion, and gas exchange) or divided into two zones (combustion).

During combustion, the $k-\epsilon$ turbulence model should account for the kinetic energy fluxes carried across the flame front from the unburned to the burned gas zones as well as that induced by the flame propagation. The carried energy fluxes can be estimated if the angular momentum of the burned large eddies is assumed to be conserved (Daneshyar and Hills, 1987).

The present paper describes a further extension of two-zone $k-\epsilon$ combustion models as applied to a spark ignition single-cylinder engine. It accounts for the induced gas velocities due to flame propagation in the turbulence model.

Model Development

Several subsystems, which interact with the cylinder and are considered in the present model, are shown in Fig. 1. The basic assumptions of the present model are as follows:

- The cylinder is treated as a variable volume plenum, which is spatially uniform in pressure.
- The mixture of gases is homogeneous, and they are treated as ideal gases.

Contributed by the Internal Combustion Engine Division for publication in the JOURNAL OF ENGINEERING FOR GAS TURBINES AND POWER. Manuscript received at ASME Headquarters July 1997. Associate Technical Editor: W. K. Cheng.

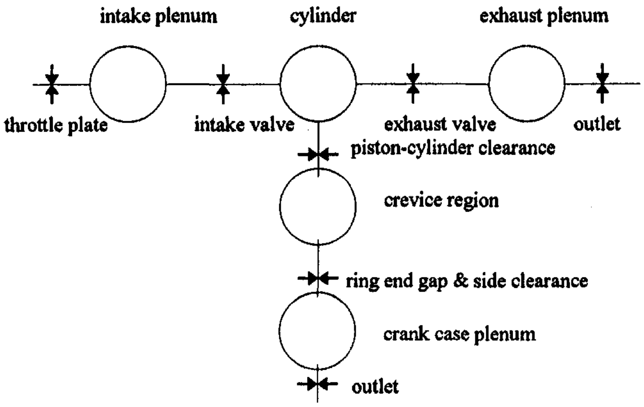

Fig. 1 Schematic of different subsystems modeled

- For the unburned cylinder gas mixture, the fuel exists in its gaseous state and the residual gas fraction is composed of the equilibrium products of a one-step reaction at the temperature and pressure of the mixture. Unburned gas region irreversibilities are negligible.
- The burned gas mixture components are the equilibrium combustion products of a one-step reaction, calculated at the mixture pressure and temperature.
- During combustion, the cylinder is divided into unburned and burned zones. Each of these zones is uniform in temperature and composition.
- The flame front is spherical with its center located at the ignition point.
- The unburned gas passes through the flame front at the entrainment speed. It is subsequently added to the burned gas at the equilibrium composition corresponding to the enthalpy and pressure of the unburned gas. In other words, combustion is assumed to be adiabatic and at constant pressure.
- Turbulence is isotropic and homogeneous.
- Quasi-steady and one-dimensional flow equations are used to predict mass flows past the valves.
- There is no heat transfer between the burned and unburned gases at the flame front.
- The reaction zone is extremely thin, so that the nitric oxide formation in the flame front is negligible. Also, the nitrogen dioxide concentration is negligible.
- When predicting pollutants, elements of the charge that are burned at different times are not mixed with each other.
- The intake and exhaust valves open and close abruptly at pre-specified crank angles, although the model could easily incorporate any desired valve lift profile.
- No account has been made for swirl and squish motions.
- No account has been made for radiative heat transfer.
- The piston rings are considered to move only axially, and any tilting due to ring rotation has been neglected.

The current model integrates various submodels and their calculations are briefly discussed as follows:

- The gas flow rates through valves, throttle plate, and plenum outlets are calculated according to the work of Benson (Benson et al., 1982) and Wallace (Wallace et al., 1986).
- A piston with two compression rings is considered. The ring motion and the mass flow rates through crevices, ring gap, and ring side clearance are calculated according to Namazian (Namazian and Heywood, 1982).
- The convective heat transfer from the burned and unburned gas zones to the combustion chamber walls is modeled by means of a Nusselt–Reynolds–Prandtl correlation similar to turbulent pipe flows[1] (Woschni, 1967). In the Reynolds number calculation, the used characteristic velocity is the sum of the mean and turbulent flow velocities in the gas zone of interest.
- The thermodynamic and transport properties of the gas mixture are calculated following the procedure outlined by Ferguson (1985). For the unburned gas mixture, the composition of the residual gas fraction is the equilibrium products (six chemical species) of a one-step reaction at the temperature and pressure of the mixture. For the burned gas mixture, the mixture components are the equilibrium combustion products (ten chemical species) of a one-step reaction, calculated at the mixture pressure and temperature.

Conservation Equations

One Zone. The equations of conservation of total mass, residual gas mass, and energy are considered. At each time step, the governing equations are numerically integrated and the state of the gas is fixed by knowing its mass intensive specific volume and internal energy.

Two Zone. During combustion, the cylinder volume is divided into unburned and burned gas zones. Four governing equations are needed to solve for trapped mass, cylinder pressure, and gas temperature in each zone. The set of equations

---

[1] Nu = $C_H \mathrm{Re}^{0.8} \mathrm{Pr}^{0.33}$, C_H in the range 0.033–0.07.

Nomenclature

A = surface area
C = constant coefficient
C_H = heat transfer correlation constant
D = gas dilatation
E = turbulence dissipation
K = kinetic energy
$\dot{K}_p$ = induced mean flow kinetic energy due to piston motion
$\dot{K}_F$ = induced mean flow kinetic energy due to flame motion
L = integral length scale
m = gas mass
$\dot{m}$ = gas mass flow rate
Nu = Nusselt number
P = turbulence production
Pr = Prandtl number
Re = Reynolds number
t = time
u = velocity
V = gas volume
$\Delta\theta$ = finite crank angle increment
Λ = model constant
Θ = model constant
ϵ = mass intensive turbulence dissipation
λ = Taylor length scale
μ = gas viscosity
ρ = gas density

Subscripts

b = burned gas
e = entrained
F = flame or burning
i = induced
ig = ignition
j = numerical index
L = laminar
m = mean flow
p = piston
t = turbulent
u = unburned
W = wall

proposed by Ferguson (1985) is considered. These are mass and energy conservation, the specific volume equation, and the entropy equation for unburned gas region. The gas state in each zone and the trapped gas mass are calculated at each time step by numerically integrating the aforementioned equations.

The resulting conservation equations are integrated in time using the explicit Runge–Kutta fourth-order method.

Turbulence Modeling

A $k-\epsilon$ model is used to predict in-cylinder turbulence. The governing equations are given as follows (Morel and Mansour, 1982):

$$\frac{dK_m}{dt} = -P - \sum_j K_m \frac{\dot{m}_j}{m} + \dot{K}_P + \dot{K}_F \tag{1}$$

$$\frac{dK_t}{dt} = P - E - \sum_j K_t \frac{\dot{m}_j}{m} \tag{2}$$

$$\frac{dE}{dt} = \frac{E}{K_t} P_E + ED - C_2 \frac{E^2}{K_t} - \sum_j E \frac{\dot{m}_j}{m} \tag{3}$$

where

$$K_m = \tfrac{1}{2} m u_m^2 \quad K_t = \tfrac{3}{2} m u_t^2 \quad E = m\epsilon \tag{4}$$

The production terms are given by:

$$P = P_0 + P_1 + P_2 + P_3 \tag{5}$$

$$P_E = C_1 P_1 + C_{11} P_2 + C_{12} P_3 \tag{6}$$

The viscous dissipation, P_0, is negligible for the high-turbulence Reynolds number compared to the turbulence dissipation (Tennekes and Lumley, 1972).[2]

The term, P_1, is modeled as follows (Mansouri et al., 1982):

$$P_1 = \mu_t V C_T \left(\frac{u_m}{L_t} \right)^2 \tag{7}$$

where C_T is a constant to be determined from model calibration.

Also,

$$P_2 = -\tfrac{2}{3} \mu_t V D^2 \quad P_3 = -\tfrac{2}{3} K_t D$$

$$C_1 = 1.44 \quad C_2 = 1.92 \tag{8}$$

The turbulence viscosity term μ_t is given by:

$$\mu_t V = C_\mu \frac{K_t^2}{E} \tag{9}$$

where the constant C_μ is equal to 0.09.

The constants C_{11} and C_{12} are chosen such that the model would satisfy certain constraint under the condition of rapid compression or expansion as follows:

$$C_{11} = 1.32 \quad C_{12} = 4.5 \quad \text{(unidirectional)}$$

$$C_{11} = 1.44 \quad C_{12} = 3.5 \quad \text{(spherical)}$$

The term K_p is the induced flux due to piston motion, which is modeled as follows:

$$\dot{K}_P = \tfrac{1}{2} \rho A_P |u_P^3| \tag{10}$$

The term K_F is the induced flux due to flame propagation, which is modeled as follows (Yacoub, 1995):

$$\dot{K}_P = \tfrac{1}{2} \dot{m}_b u_i^2 \tag{11}$$

In closed-vessel combustion, the flame propagation initiates a mass flux of unburned gas on the cold side, which is directed into the reverse direction of the burning velocity. The induced gas velocities in each region are given by (Maly and Ziegler, 1982; Yacoub, 1995):

$$u_{iu} = u_F \left(\frac{\rho_u}{\rho_b} - \frac{V_b}{V} - 1 \right) \quad u_{ib} = -u_F \frac{V_b}{V} \tag{12}$$

During combustion, the turbulence model is applied separately to the unburned and the burned gas regions. The constants C_{11} and C_{12} are set to values case of rapid spherical compression. During other cycle simulation processes, a one-zone model is adopted and the constants C_{11} and C_{12} are set to values case of rapid unidirectional compression.

The initial condition of turbulence in the burned gas region is obtained by assuming that the mass and angular momentum of the first fluid element to burn are conserved upon crossing the flame front (Ramos, 1989).

Combustion Modeling

Combustion is modeled as two simultaneous processes: entrainment followed by combustion, as discussed by Blizard (Blizard and Keck, 1974) and Tabaczynski (Tabaczynski et al., 1977). A slight modification is introduced in the rate of entrainment, m_e, which is given by:

$$\dot{m}_e = \rho_u A_F (C_w u_t + u_L) \tag{13}$$

The wall coefficient, C_w, is introduced in order to account for the fact that the rate of entrainment decreases as the flame approaches the cylinder walls; since the velocity induced by volume expansion must be zero normal to the boundary (Barr and Witze, 1988). The increased resistance to flame expansion, as it approaches the wall, leads to flattening out of the flame front. This wall effect becomes well pronounced in the final termination period of entrainment (James, 1990). In the present model, the wall effect at the final termination period of entrainment is modeled as (Yacoub, 1995):

$$C_w = 1, \quad \frac{m_e}{m} < \Lambda$$

$$C_w = \left(\frac{A_w}{A} \right)^\Theta, \quad \frac{m_e}{m} \geq \Lambda \tag{14}$$

Λ is a constant value (taken in a range between 0.8B0.9), and Θ is a constant value, which is set equal to 0.5.

It is necessary to assume a certain size of flame volume at the time of spark in order to start the calculations. Hires et al. (1978) proposed:

$$\Delta\theta_{ig} = C_{ig} \left(\frac{L_t}{u_t} \right)^{1/3} \left(\frac{\lambda}{u_L} \right)^{2/3} \tag{15}$$

where C_{ig} is an empirical value, which is unique to an engine geometry, but independent of engine operating conditions. The present model uses the procedure employed by Tomita and Hamamoto (1988). A certain volume of entrained gas exists at the time of spark, and integration of the governing equations is carried out. Then, C_{ig} is calculated from Eq. (15) and compared with the one obtained from model calibration. The initial assumed volume is readjusted until an acceptable match with the empirically determined C_{ig} is obtained.

---

[2] This assumption is not valid in the proximity of the wall boundary, where viscous dissipation is the dominant term.

Pollutant Predictions

Nitrogen Oxides: The NO concentration is calculated using the extended Zel'dovich mechanism. The reactions forward and reverse rate constants are obtained from Heywood (1988). The NO rate formation equation is integrated using the Euler implicit scheme.

Carbon Monoxide. The rate of carbon monoxide formation is calculated as proposed by Mathur et al. (1983) and Ramos (1989): The reactions' forward and reverse rate constants are obtained from the data listed by Zeleznik and Bonnie (1985). Euler's implicit scheme is used to calculate CO concentration at each time step.

The aforementioned formulation would produce realistic CO concentrations for a fuel-rich burning mixture and too low [CO] for a lean mixture. The empirical formula proposed by Benson (1977) is used to predict [CO] for the case of lean mixtures.

Model Validation

In order to evaluate the validity of the model, a comparison is made between the present model predictions and the measurements and predictions obtained by other researchers. In the next section, separate test cases are presented, where each is aiming at validating a specific submodel.

The first test case deals with calibrating the model to a specific engine geometry and operating condition. The second test case deals with evaluating the validity of the assumption that the calibration parameters, which are obtained from test case one, are independent of the engine operating conditions. The predictions are generated for the same engine, presented in case one, and running under different operating condition. The third test case is an augmentation of test cases one and two, repeated for a different engine, which is running under different operating conditions. In the fourth test case, the present model predictions of nitric oxide, for the same engine of case one, are presented and compared to the measured and predicted results of other researchers. The fifth and sixth test cases deal with validating the exhaust gas emission and turbulence predictions, respectively.

In all test cases, the fuel type is iso-octane. Relevant simulation input parameters are given in the appendix section.

Test Case 1. In order to compare the model predictions directly with the experimental data over different engine operating conditions, it is necessary to calibrate the submodels parameters with the experimental data at a specified engine operating condition. The engine geometry and operating conditions are given by Poulos and Heywood (1983).

The first step in the calibration process is to adjust the calculated mass of the charge trapped in the cylinder to that measured. This is achieved by varying the intake valve discharge coefficient and varying the throttle position, such that the pressure in the intake plenum matches the measured one. The second step is to adjust the turbulence parameter C_T such that the combustion duration and peak cylinder pressure are as close as possible to the experimental data. The third step is to adjust the convection heat transfer parameter in order to maximize agreement between predicted and measured cylinder pressure. Finally, the initial value for the entrained gas mass fraction is adjusted to minimize the phase shift between predicted and measured pressure trace.

Figure 2 shows a comparison between the present model predictions for the cylinder pressure trace and the predictions and experimental traces provided by Poulos (Poulos and Heywood, 1983). The present model predictions are in good agreement with the experimental data.

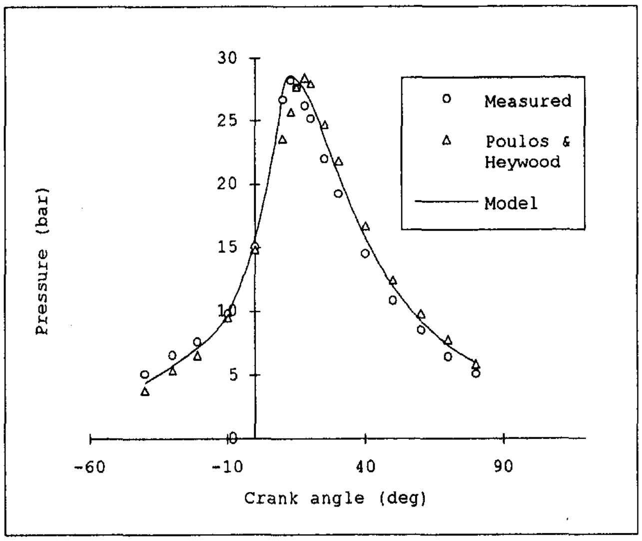

Fig. 2 Predicted and measured pressure trace for test case one

Table 1 lists a comparison between the present model predictions of different cycle parameters and those reported by Poulos. The gross indicated parameters are obtained by integrating over the power cycle, and the net indicated parameters are obtained by integrating over the full cycle (power and gas exchange). For the indicated parameters, no account is made for friction losses.

The friction work is estimated to be twice as much as the piston ring friction work. This estimate is based on the work reported by Rosenberg (1982), where it is reported that the piston assembly friction is about 60 percent of the total engine friction. The model shows agreement with the measured values.

Table 1 Predicted and measured performance for test case one

Cycle performance parameters	Measured	Predicted	
		Present	Poulos
Trapped air mass (gram/cycle)	0.412	0.428	0.412
Trapped fuel mass (gram/cycle)	0.027	0.028	0.027
Residual mass fraction	-	0.1	0.084
Pressure at IVC (bars)	1.1	0.9	0.8
Pressure at spark (bars)	7.7	7.2	6.6
Pressure @ tdc (bars)	15.1	15.9	14.8
Maximum pressure (bars)	28.3	28.7	28.5
Crank angle at maximum pressure (deg. atdc)	13	12.5	18
Duration to burn (0-10%) of charge (deg.)	16-21	15.5	18.84
Duration to burn (10-90%) of charge (deg.)	18-23	20.3	21.49
Duration to burn (0-100%) of charge (deg.)	-	52	-
Net indicated thermal efficiency	-	23.16	27.91
Gross indicated thermal efficiency	-	25.97	30.61
Brake thermal efficiency	22.79	22.66	23.72
Convection heat loss to fuel available energy	-	0.39	0.34
Nitric oxide at EVO (PPM)	4000	3999	2057

Test Case 2. In test case one, the model is fine tuned to predict the measured values. It is assumed that the turbulence parameter C_T and the ignition delay parameter C_{ig} are dependent on a given engine geometry and are independent of its operating conditions. The turbulence assumption is first proposed by Blizard and Keck (1974) and both Mansouri (1982) and Poulos and Heywood (1983) agree with this assumption. The ignition delay assumption is proposed by Hires (1978) and is supported by Tomita and Hamamoto (1988). However, to validate the present assumption, the predictions are obtained for the same

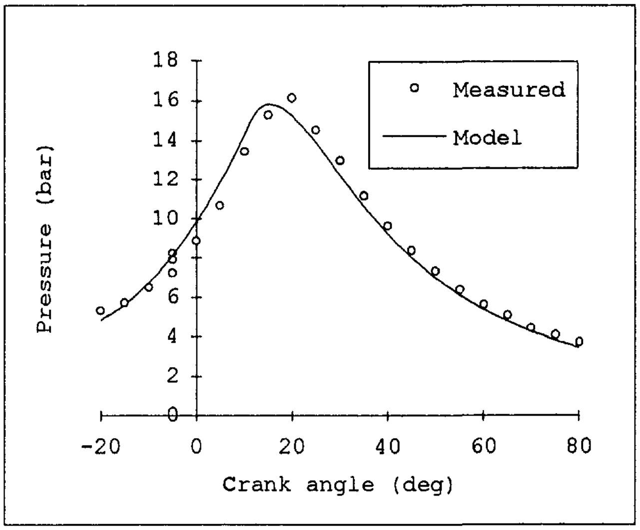

Fig. 3 Predicted and measured pressure traces for test case two

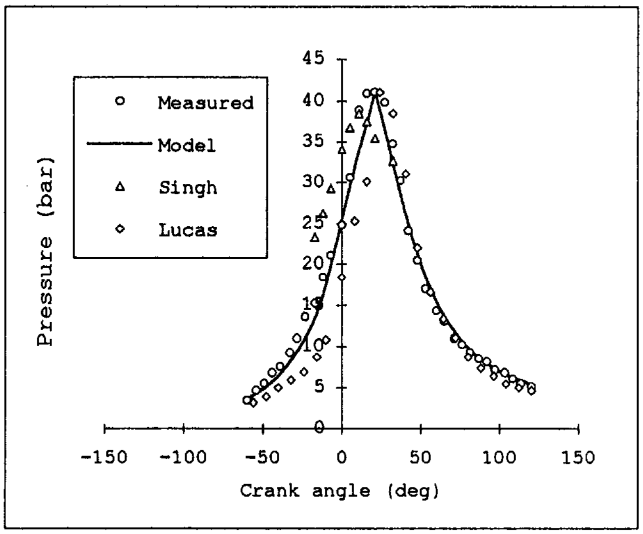

Fig. 4 Predicted and measured pressure trace for test case three, equivalence ratio equal to 1.05

engine, presented in case one, running under different operating conditions given by Heywood et al. (1979).

The only calibration needed is the adjustment of the throttle plate position, such that the mass of the charge trapped in the cylinder and the intake plenum pressure matches the measured values. Also, the initial mass fraction of entrained gas has to be adjusted in order to keep the value of C_{ig} equal to that obtained from the model calibration in test case one. Figure 3 shows the predicted pressure trace compared with what was measured by Heywood et al. (1979). The model predicts a peak cylinder pressure, which is equal to 16.01 bars @ 15.3 ca atdc. This prediction is lagging behind Heywood's value, which is equal to 16.4 @ 18.0 ca atdc. The predicted gross indicated mean effective pressure is equal to 311 kPa, compared with the measured value of 367 kPa.

Test Case 3. First, the model is calibrated in order to obtain an accurate fit to the pressure cylinder trace for a specific engine operating condition. Second, the model prediction of engine performance is computed at another operating condition and without any further tuning of the model. The engine geometry and operating conditions for the calibration step are given by Singh and Surkomol (1979). Figure 4 shows the cylinder pressure trace for the calibration step. The present model predictions are the closest to the measured trace compared to those obtained by Lucas and James (1973) and by Singh. Lucas assumed a linear dependence of the turbulent burning velocity on the engine speed. Also, the burned mass fraction of the charge, at any instant, is obtained from a three-dimensional flame propagation map, using four ionization probes, which were mounted in the cylinder. Singh considered the combustion duration only. He assumed a cylindrical flame front and used a one-dimensional unsteady analysis to determine the heat release rate. The phase lag in peak pressure, computed using Singh's model, is due to a smaller combustion duration prediction and a discrepancy in simulating an ignition delay period (Singh and Surkomol, 1979).

Figure 5 shows the pressure trace for an equivalence ratio equal to 1.42, while the other operation variables are kept the same as that used for model calibration. The present model predicts pressure trace in fair agreement with the measured. Lucas reasons that the failure in his model predictions is due to the fact that the mechanisms involved in turbulent flame propagation are not always similar to those for laminar flame propagation, which is the underlying criterion of his model.

Test Case 4. In order to validate the model's ability to predict correct nitric oxide (NO) concentration, the predictions are obtained for the same engine, presented in case one, and are compared with the measured and predicted results reported by Komiyama and Heywood (1973). The engine geometry is the same as in test case one. The calibrated parameters, obtained from test case one, are used for the present simulation. The operating conditions are 1200 rpm, spark timing 20 deg btdc, and wide-open throttle. The initial entrained mass fraction is modified (equal to 0.001) to keep the value of C_{ig} equal to that obtained from the model calibration in test case one. Figure 6 shows the variation in nitric oxide concentration with respect to the equivalence ratio for the measured predictions from the present model, and predictions from Komiyama and Heywood's model.

The present model overpredicts nitric oxide concentration on the lean side. Predictions are accurate near stoichiometric mixtures and fall sharper than the measured concentrations on the rich mixture side. The predictions provided by Komiyama and Heywood are closer to measured values compared to the present model predictions. One factor is that Komiyama and

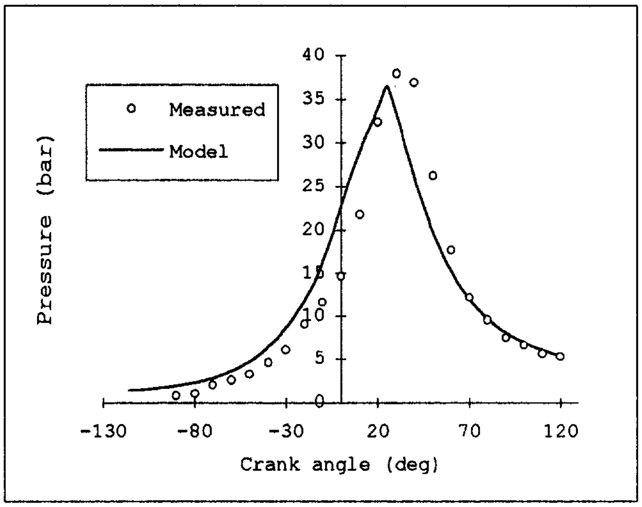

Fig. 5 Predicted and measured pressure trace for test case three, equivalence ratio equal to 1.42

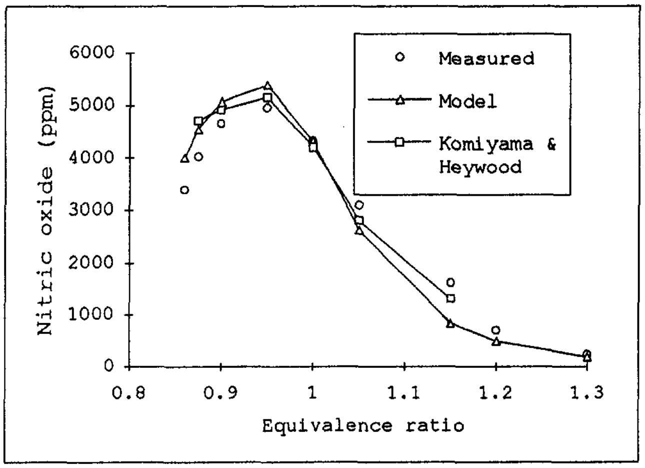

Fig. 6 Predicted and measured NO concentration for case four

Heywood fed their model with the measured cylinder pressure trace.

Test Case 5. In this test case, the model predictions of exhaust gas emissions are calculated and compared with those measured by Huls et al. (1966) for given engine operating conditions. For this test case, the only available data on the engine geometry were that it is a single-cylinder, cooperative fuel research engine. Thus, the geometry of the engine is assumed to be the same as that of test case one. The intake valve discharge coefficient is set equal to 0.23 in order to match the calculated trapped mass of charge to the experimental one. The model calibration parameters are adjusted to obtain a calculated peak cylinder pressure at a crank angle equal to 10 deg atdc, as reported by Huls for the case of stoichiometric mixture. The ratios of the intake and exhaust plenum volumes to maximum cylinder volume are set equal to 50, to match the setting reported by Huls. Figure 7 shows the variation of nitric oxide (NO) concentration with respect to the equivalence ratio. The data are obtained from measurements reported by Huls.

The variation of carbon monoxide (CO) concentration with respect to equivalence ratio is shown in Fig. 8. The trend is the same for both the predicted and measured concentrations. The empirical equation of Benson (1977) provides higher concentrations for lean mixtures and lower concentrations for rich mixtures, compared with measured values. The model CO predictions increase at a higher rate than the measured concentrations on the rich side of the mixture.

Test Case 6. This test case deals with unidirectional compression and expansion, produced by a moving piston in a right circular cylinder, of an initially homogeneous turbulent flow of zero mean kinetic energy K_m. This test case was originally proposed by Morel and Mansour (1982). Three initial values for turbulent kinetic energy are considered. These are $K_{ti} = 1.5u_P^2$, $0.15u_P^2$, and $0.0025u_P^2$. The initial value for the integral length scale of turbulence L_{ti} is equal to 0.1 h, where u_p is the mean piston speed and h is the cylinder height at bottom dead center. Figure 9 shows a comparison of the present model predictions of the integral length scale of turbulence and those of Morel and Mansour (1982). The length scale is normalized using its initial value. For the model calculations, two limiting values (0 and 1) are considered for the turbulence parameters C_T.

For the case of $C_T = 0$, i.e., the mean flow field is not supplying any energy to turbulence; agreement with Morel predictions is very good except for the case of $K_{ti} = 1.50\ u_p^2$, where the model predicts larger values of L_t at the end of expansion. For the case of $C_T = 1$, i.e., the mean flow field dissipates energy at a very fast rate to turbulence; the model predicts the same trend as that for $C_T = 0$ but with larger values of L_t. The piston motion induces mean flow kinetic energy. For the case $C_T = 1$, there is a continuous depletion of this energy to turbulence. On the other hand, for $C_T = 0$, the increase in K_m due to piston motion is maintained. The solution, provided by Morel and Mansour (1982) is obtained using a multidimensional axisymmetric computer code, which accounts for the spatial variation of the flow field inside the cylinder. On the other hand, the present model treats the flow field as a bulk and does not account for in-cylinder convection and diffusion. Bearing this in mind, the agreement between the present model predictions and those of Morel are considered to be satisfactory.

Model Sensitivity

This section discusses briefly the sensitivity of the cycle-simulation results to the values of selected submodels' constants. A series of cycle-simulations is performed where each of these constants is varied independently. The following conclusions are reached (Yacoub, 1995):

- Convection heat transfer constant C_H is investigated over the range 0.035–0.10. Decreasing its value results in an increase

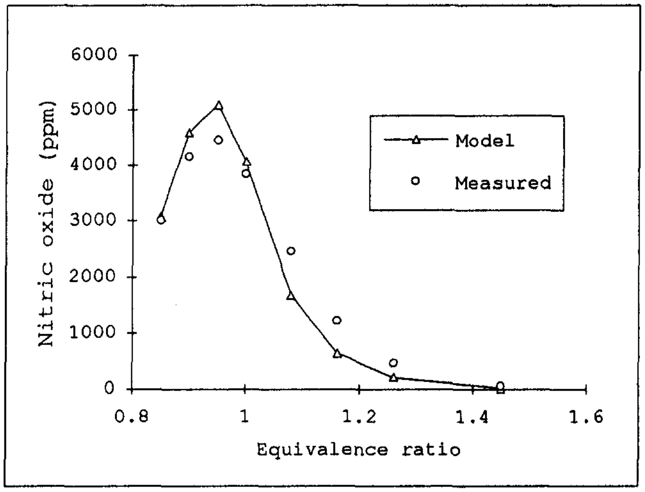

Fig. 7 Predicted and measured NO concentration for case five

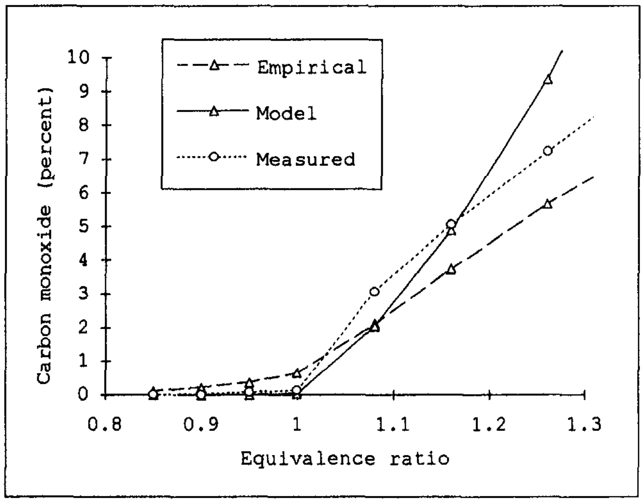

Fig. 8 Predicted and measured CO concentration for case five

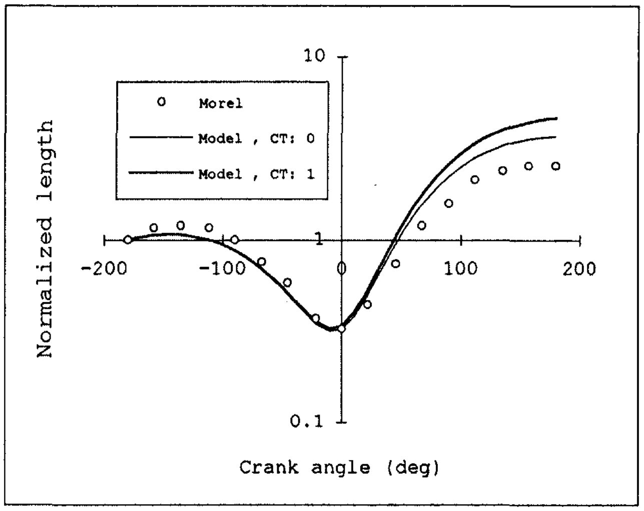

Fig. 9(*a*) Integral length scale versus crank angle, $K_{ti} = 1.5\,u_p^2$

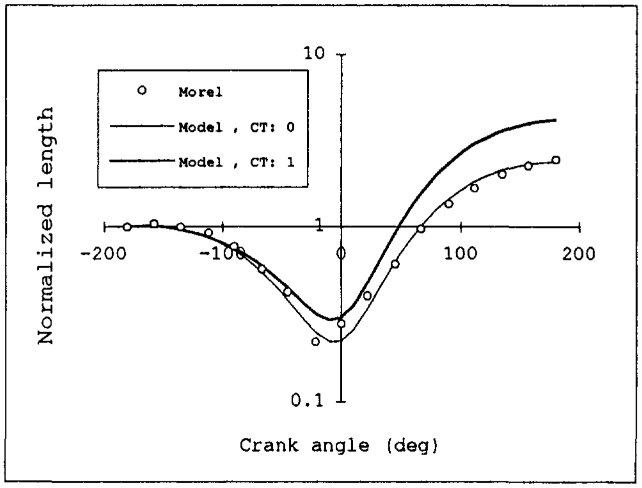

Fig. 9(*b*) Integral length scale versus crank angle, $K_{ti} = 0.15\,u_p^2$

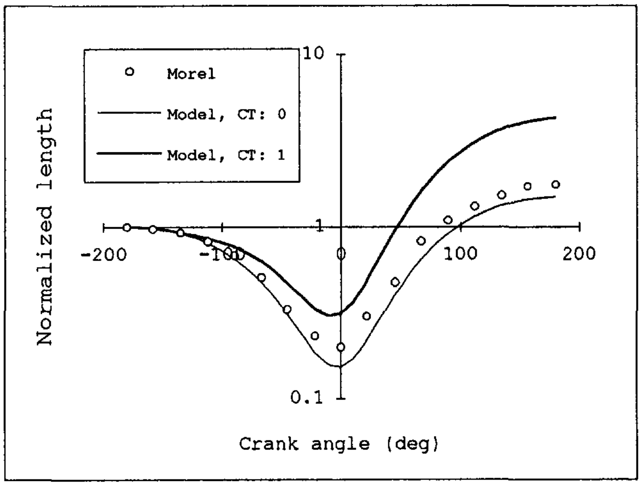

Fig. 9(*c*) Integral length scale versus crank angle, $K_{ti} = 0.0025\,u_p^2$

in thermal efficiency, increase in maximum gas temperature, decrease in convection heat loss, an increase in nitric oxide concentration, faster burning rates, and broadening of the pressure trace and an increase of its peak value, which shifts toward top dead center (tdc).

- Initial Entrained mass fraction is investigated over the range 0.00025–0.001. Increasing its value results in a slight increase in the maximum pressure, which is shifted toward tdc.
- Turbulence constant C_T is investigated over the range 0.01–0.05. Increasing its value results in faster entrainment and burning rates, higher gas pressure and temperature. For all values of C_T, angular momentum is no longer conserved at the final stage of burning, and better conservation of angular momentum is accompanied by faster burning rates for higher values of C_T.
- The coefficient Λ is investigated over the range 0.8–1.0, and Θ is kept constant, equal to 0.5. Increasing Λ results in a sharper and stronger pressure peak, which shifts toward tdc, faster final stage burning, higher convection heat loss, higher gas temperature, and lower thermal efficiency.
- The coefficient Θ is investigated over the range 0.1–0.5, and Λ is kept constant, equal to 0.8. Decreasing Θ results in a highly pronounced pressure peak, faster burning rate, higher entrainment velocity, better conservation of angular momentum, higher convection heat loss, slightly higher gas temperature, and lower thermal efficiency.

Conclusions and Discussion

The major conclusions that can be drawn from the present study are:

- The present level of modeling is capable of predicting thermal efficiency, indicated mean effective pressure, peak values of gas pressure, ignition delay, concentrations of nitric oxide, carbon monoxide, and carbon dioxide values that are in good agreement with the experimental data.
- The present algebraic turbulence model, $k-\epsilon$ type, is sufficient to predict the correct trends of turbulence. The calculated parameters are in agreement with the predictions of a multidimensional axisymmetric simulation.
- The present model predictions support the assumption that the calibrated submodels' constants are independent of the engine operating conditions and are fixed for a given engine geometry.

References

Barr, P., and Witze, P., "Some limitations to the spherical flame assumption used in phenomenological engine models," SAE Paper No. 880129, 1988.

Benson, R., and Baruah, P., "Performance and emission predictions for a multi-cylinder spark ignition engine," *Proc. Instn. Mech. Engrs*, Vol. 191, 32/77, 1977.

Benson, R., Horlock, J., and Winterbone, D., *The Thermodynamics and Gas Dynamics of Internal Combustion Engines*, Vol. 1, Clarendon Press, Oxford, 1982.

Blizard, N., and Keck, J., "Experimental and theoretical investigation of turbulent burning model for internal combustion engines," SAE Paper No. 740191, 1974.

Daneshyar, H., and Hill, P. G., "The structure of small-scale turbulence and its effect on combustion in spark ignition engines," *Progress in Energy and Combustion Science*, Vol. 13, 1987.

Ferguson, C. R., *Internal Combustion Engines, Applied Thermosciences*, Wiley, New York, 1985.

Heywood, J. B., et al., "Development and use of a cycle simulation to predict SI engine efficiency and NO_x emissions," SAE Paper No. 790291, 1979.

Heywood, J. B., "Engine Combustion Modeling C An Overview," *Proc. Symposium on Combustion Modeling in Reciprocating Engines*, Plenum Press, 1980.

Heywood, J. B., *Internal Combustion Engine Fundamentals*, McGraw-Hill, New York, 1988.

Hires, S. D., Tabaczynski, R. J., and Novak, J. M., "The prediction of ignition delay and combustion intervals for a homogeneous charge, spark ignition engine," SAE Paper No. 780232, 1978.

Huls, T., Myers, P., and Uyehara, O., "Spark ignition engine operation and design for minimum exhaust emission," SAE Paper No. 660405, 1966.

James, E. H., "Further aspects of combustion modeling in spark ignition engines," SAE Paper No. 900684, 1990.

Komiyama, K., and Heywood, J., "Predicting NO_x emissions and effects of exhaust gas recirculation in spark-ignition engines," SAE Paper No. 730475, 1973.

Lucas, G., and James, H., "A computer simulation of a spark ignition engine," SAE Paper No. 730053, 1973.

Maly, R., and Ziegler, G., "Thermal combustion modeling C Theoretical and experimental investigation of the knocking process," SAE Paper No. 820759, 1982.

Mansouri, S., Heywood, J., and Radhakrishnan, K., "Divided-chamber diesel engine, Part 1: A cycle-simulation which predicts performance and emissions," SAE Paper No. 820273, 1982.

Mathur, H., Babu, M., and Reddi, K., "A thermodynamic simulation model for a methanol fueled spark ignition engine," SAE Paper No. 830333, 1983.

Morel, T., and Mansour, N., "Modeling of turbulence in internal combustion engines," SAE Paper No. 820040, 1982.

Namazian, M., and Heywood, J. B., "Flow in the piston-cylinder-ring crevices of a spark-ignition engine: Effect on hydrocarbon emissions, efficiency and power," SAE Paper No. 820088, 1982.

Poulos, S., and Heywood, J. B., "The effect of chamber geometry on spark-ignition engine combustion," SAE Paper No. 830334, 1983.

Ramos, J. I., *Internal Combustion Engine Modeling*, Hemisphere Publishing Corporation, New York, 1989.

Rosenberg, R. C., "General friction considerations for engine design," SAE Paper No. 821576, 1982.

Singh, T., and Surakomol, K., "Mathematical modeling of combustion process in a spark-ignition engine," SAE Paper No. 790354, 1979.

Tabaczynski, R., Ferguson, C., and Radhakrishnan, K., "A turbulent entrainment model for spark-ignition engine combustion," SAE Paper No. 770647, 1977.

Tennekes, H., and Lumley, J. L., *A First Course in Turbulence*, The MIT Press, Cambridge, MA, 1972.

Tomita, E., and Hamamoto, Y., "The effect of turbulence on combustion in cylinder of a spark ignition engine-evaluation of entrainment model," SAE Paper No. 880128, 1988.

Wallace, F., Horlock, J., and Winterbone, D., *The Thermodynamics and Gas Dynamics of Internal Combustion Engines*, Vol. 2, Clarendon Press, Oxford, 1986.

Woschni, G., "A universal applicable equation for the instantaneous heat transfer coefficient in the internal combustion engine," SAE Paper No. 670931, 1967.

Yacoub, Y., "Model development and validation of an SI single cylinder engine performance and emissions," MSc. thesis, Mechanical and Aerospace Dept., West Virginia University, 1995.

Zeleznik, F. J., and MacBride, B. J., "Modeling the internal combustion engine," NASA reference publication 1094, 1985.

APPENDIX

	case 1	case 3	case 6
ENGINE DATA			
BORE (cm):	8.26	8	10
STROKE (cm)	11.43	10	9.08
HALF STROKE TO ROD RATIO:	0.225	0.225	0.3375
SPRK PLG LCTN RADIUS (cm):	4.12	3.99	4.98
EXHAUST VALVE SPECIFICATIONS			
DIAMETER (cm):	2.89	2.8	
MAXIMUM LIFT (cm):	0.29	0.28	
DISCHARGE COEFFICIENT:	0.5	0.5	
VALVE CLOSE (deg. atdc):	15	12	
VALVE OPEN (deg. bbdc):	40	64	
INTAKE VALVE(S) SPECIFICATIONS			
DIAMETER (cm):	3.3	3.2	
MAXIMUM LIFT (cm):	0.5	0.64	
DISCHARGE COEFFICIENT:	0.23	0.85	
VALVE CLOSE (deg. abdc):	34	64	
VALVE OPEN (deg. btdc):	-10	12	
THROTTLE PLATE SPECIFICATIONS			
DIAMETER (cm):	4	4	
SHAFT TO BORE DIAMETER:	0.03	0.03	
ANGLE WHEN COLSED (deg.):	5	5	
DISCHARGE COEFFICIENT:	0.8	0.8	
PISTON CYLINDER CREVICE DATA			
PSTN GROOVE HEIGHT (cm):	0.18	0.177	
PSTN CYLNDR CLRNCE (cm):	0.05	0.03	
TTL CRVC VOLUME (%VTDC):	1.66	1.81	
TOP LAND HEIGHT (cm):	0.68	0.68	
SECOND LAND HEIGHT (cm):	0.3	0.3	
RING WIDTH (cm):	0.4	0.4	
RING THICKNESS (cm):	0.175	0.175	
RING MASS (grams):	12.08	11.61	
RING END GAP (cm):	0.025	0.015	
RNG SIDE CLRNC (cm):	0.005	0.0015	
CLRNC BEHIND RING (cm):	0.05	0.05	
DSCHRG CFF.RNG END GAP:	0.8	0.8	

SIMULATION DATA	case 1	case 2	case 3	case 5	case 6
COMPRESSION RATIO:	7	7	9	8	8
SPEED (rpm):	1477	1600	2490	1000	2000
CYLNDR WLL TMPRTR (k):	425	400	400	400	
SPARK ANGLE (deg. btdc):	21	32	30	30	
EQUIVELANCE RATIO:	0.97	0.81	1.05	.85-1.45	
TURBULENCE COEFFICIENT C_T:	0.035	0.035	0.004	0.005	
CNVCTN HEAT CONSTANT:	0.07	0.07	0.03	0.07	
ENTRNED MASS FRCTN @ IGNTN:	.0015	.0002	.000015	.001	
THROTTLE POSITION (% WOT):	39.5	13.5	100	100	

The Spray Structure of Air-Shrouded Dual-Stream Port Fuel Injectors With Different Air-Mixing Mechanisms

F.-Q. Zhao[1]
Department of Mechanical Engineering,
Wayne State University,
Detroit, MI 48202

J.-H. Yoo
Hyundai America Technical Center,
Ann Arbor, MI 48419

M.-C. Lai
Department of Mechanical Engineering,
Wayne State University,
Detroit, MI 48202

An experimental study of the spray structure from air-shrouded dual-stream injectors with different air mixing mechanisms was carried out extensively to understand the spray characteristics of dual-stream port injectors for applications to four-valve gasoline engines. The injectors were tested under both steady and transient conditions at different injection pressures and air shrouding pressure differentials. The global spray structure was visualized using the planar laser Mie scattering technique and spray atomization processes were characterized by the phase-Doppler anemometry method. The experimental results showed that spray atomization characteristics are improved markedly by the air-shrouding technique and also strongly dominated by the air-mixing mechanisms. When the air flows into the injector tip mainly from the radial direction, two streams of the spray are forced to merge together and as a result a single-stream spray is formed. When the radial velocity component of the air is reduced and the air is made to mix well with the fuel inside the injector tip, however, the two streams of the spray are well separated over different injection conditions. Moreover, other spray parameters are also modified by the air shrouded into the injector, which must be optimized in order to achieve the best performance of the air-shrouded injector.

Introduction

A well-atomized spray is the basic requirement of current port-injected gasoline engines in order to meet the stringent hydrocarbon emission regulations. This is because improved spray atomization is effective in minimizing fuel wall-wetting, reducing fuel/air mixing time, and promoting a more uniform mixture for the engine. It is particularly important when fuel injection is done toward an open valve (Zhao et al., 1995a; Lai and Zhao, 1995). To date, a lot of technologies such as air-assist (Takeda and Sugimoto, 1992; Harada et al., 1992; Saikalis et al., 1993; Zhao et al., 1995e), elevated fuel pressure (Lai et al., 1994a, b), liquid–liquid impingement (Nogi et al., 1992), solid-surface impingement (Nagaoka et al., 1994; Inamura et al., 1992), swirl flow (Kashiwaya et al., 1990; Okamoto et al., 1992), director-plate compounding (Lai et al., 1994a, b; Amer and Lai, 1995; Amer et al., 1995; Parish and Evers, 1995), ultrasonic vibration (Namiyama et al., 1989), pressure modulation (Zhao et al., 1995b, c, d), and nozzle-tip heating (Saito et al., 1993; Chen and Chen, 1995) have been developed to enhance the spray atomization process of port fuel injectors. Among them, the air-assisted injector attracts much attention from automotive engineers due to its guaranteed effect on improving the spray atomization performance. However, other spray parameters such as spray targeting, fuel dispersion, and spray separation angle may also be modified when the assisting air enters the injector. This may degrade the engine performance even though the spray has good atomization characteristics. This indicates that simply adding air into the fuel system is no guarantee of an improvement in engine performance. In fact, there are numerous cases of degraded performance when air-assist was added to an existing single-fluid system. A carefully selected air mixing mechanism is strongly required to realize the full advantages of air-assisting techniques.

This paper reports an extensive study of spray breakup and atomization processes of air-shrouded dual-stream (ASDS) injectors with different air mixing mechanisms. This dual-stream (DS) injector is designed to target each of the two streams to each of the intake valves to avoid serious wall-wetting on the port divider of two-intake-valve gasoline engines (Zhao et al., 1996). Such design can not only reduce the port divider fuel wetting but also can increase fuel dispersion. The effect of the air mixing mechanism on the spray characteristics including the global spray structure, fuel dispersion, spray separation angle, and atomization performance is investigated in detail. The global spray structure was visualized under steady and transient conditions over different fuel injection pressures and air-shrouding pressure differentials (ASPD) using the Planar Laser Mie Scattering (PLMS) technique. The spray was characterized by the Phase-Doppler Analyzer (PDA).

Experimental System

Figure 1 shows a schematic of injector geometries under different air mixing mechanisms. It is a director-plate injector with two different types of vacuum-driven air-shrouding adapters retrofitted at its tip. Air is provided through an adapter connected to the engine intake manifold. Air is driven by a pressure differential between the manifold and intake port through a passage between the injector body and the adapter and the air-shrouding sleeve, and interacts with liquid fuel. Two different air-mixing methods are used to study the effect of air-mixing mechanisms on the spray characteristics. For the short-tip type injector, the radial velocity component of the shrouded air is dominant. Correspondingly, the radial component of the air velocity is reduced dramatically due to the internal design of the long-tip type injector. Moreover, the air mixes well with the liquid fuel inside the small mixing chamber at the injector

---

[1] Current address: Chrysler Corporation, CIMS 482-01-19, 800 Chrysler Dr. E., Auburn Hills, MI 48326.

Contributed by the Internal Combustion Engine and presented at the Spring Technical Conference of the ASME Internal Combustion Engine Division, Youngstown, Ohio, April 21–24, 1996. Manuscript received at ASME Headquarters May 1997. Associate Technical Editor: W. K. Cheng.

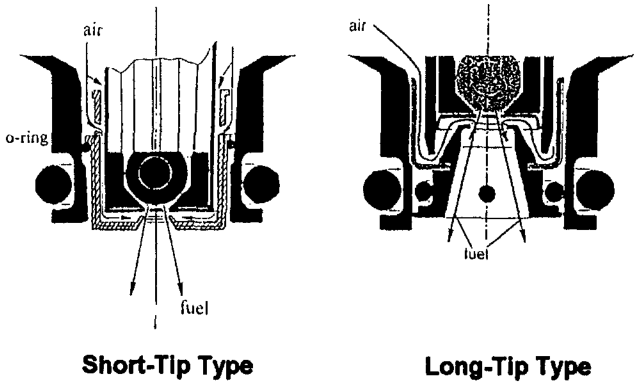

Short-Tip Type **Long-Tip Type**

Fig. 1 Schematic of ASDS injectors with two different air-mixing mechanisms

tip. A separation bar is installed at the injector tip for this long-tip ASDS injector.

Calibration fluid, VISCOR-B, was used to test the injectors. This fluid has comparable physical properties to those of gasoline and is good for studying spray breakup and atomization processes of gasoline port injectors due to its nonflammability. The PLMS technique was used to obtain the global spray structure. A Nd:YAG laser operated at its second harmonic wavelength was used as a light source, whose pulse was synchronized with fuel injection timing when the injector operated under transient conditions. A 35-mm still camera was used to record the instantaneous spray image. The spray was visualized under both steady and transient conditions. For the steady-state tests, spray visualization was conducted at 60 ms after the fuel injection start. During transient measurements, fuel injection duration was fixed at 5 ms. The spray was imaged on the base of time with respect to the fuel injection start. A two-component PDA system (Aerometrics) was used to perform the simultaneous measurements of droplet size and velocity. To simplify the experimental setup, the air was supplied to the injector from a high-pressure cylinder and liquid fuel was sprayed out into the atmospheric environment. Spray structures derived under such conditions may be slightly different from those below the atmospheric conditions due to the effect of different ambient pressures. Since the current work emphasizes the global spray breakup and atomization processes instead of the detailed characteristics, this slight difference is not considered.

Results and Discussion

Short-Tip ASDS Injector. Figure 2 shows the spray photographs of the short-tip ASDS injector over different air-shrouding pressure differentials (ASPD) under continuous injection conditions. The visualization range is 56 mm in the direction of spray development. It is found that clear dual-stream jets are produced and axisymmetrically distributed within the visualization range when the injector operates without air shrouded in (ASPD = 0). When compared with the spray produced by the regular DS injector under the same condition (Zhao et al., 1995e), ligaments between the two streams were found to decrease markedly for this ASDS injector. This is effective in reducing the percentage of liquid fuel between the two streams that will impinge on the port divider, possibly to form a liquid film. When the injector operates with the air shrouded in, spray atomization characteristics are significantly improved. However, the spray separation angle of the two streams decreases dramatically. Even at a low ASPD of 27 kPa, the separating appearance of the two streams shown in Fig. 2(*a*) cannot be observed at all. Two streams are combined to form a single-stream spray. A large velocity component along the radial direction is assumed to force the two streams toward the spray axis, and cause a marked decrease in the spray separation angle. A similar finding was also reported by Takeda and Sugimoto (1992) in their externally air-assisted DS injector, which has the fuel/air mixing region far downstream of the injector tip. From the point of spray atomization, this short-tip ASDS injector shows a great improvement over the non-air-shrouded DS injector. However, the spray separation angle shows a quick disappearance when the air flows into the injector tip, which is considered to change the spray targeting and cause a serious wall-wetting around the port divider area. This makes this type of spray lose its key feature that the DS injector is supposed to have for applications to two-intake-valve engines. When compared with other spray atomization technologies such as pressure modulation (Zhao et al., 1995b, c, d), the spray separation angle of the air-shrouded DS injector seems to be more sensitive to the atomization technology itself, even though the air-shrouded spray shows a more uniform spatial fuel distribution. Correspondingly, the pressure-modulated spray remains a constant spray separation angle over a wide range of injection conditions. However, the pressure perturbation generated inside the fuel line causes a slightly rich shift of the pressure-modulated port fuel injector. The shifting extent is dependent on the injector design and fuel flow rate.

Figures 3 and 4 show the spray photographs under transient conditions. At the beginning of fuel injection (2 ms after fuel injection start), the spray tip penetration increases linearly with an increase in the ASPD. This indicates that the droplets are accelerated by the shrouded air. Moreover, the amount of vapor cloud increases when the ASPD increases. After 4 ms of fuel injection start, the spray is well developed. The transient spray structure at this moment is quite similar to that of the steady condition. At the low ASPD of 27 kPa, two almost parallel streams are forced together but their separation can still be observed. However, at the high ASPD, this separation can not be observed at all. Only a small core jet is observed at the injector tip surrounded by the vapor cloud.

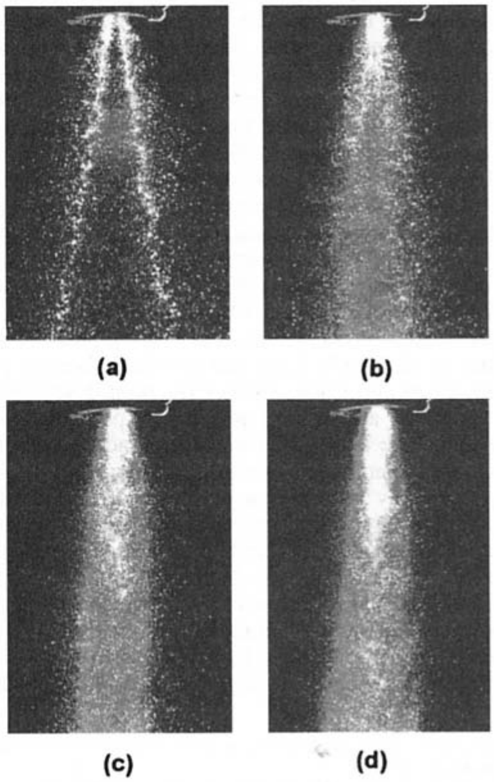

Fig. 2 Spray photographs of short-tip ASDS injector (fuel injection pressure: 290 kPa; continuous fuel injection); (*a*) ASPD = 0; (*b*) ASPD = 27 kPa; (*c*) ASPD = 54 kPa; (*d*) ASPD = 81 kPa

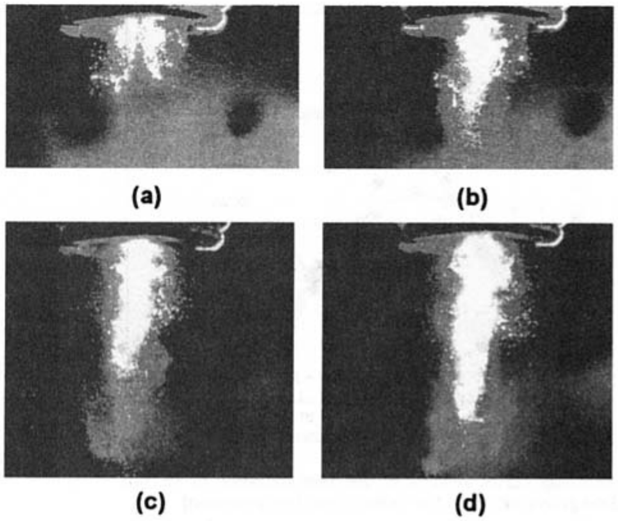

Fig. 3 Spray photographs of short-tip ASDS injector (fuel injection pressure: 290 kPa; 2 ms after fuel injection start; injection duration: 5 ms); (*a*) ASPD = 0; (*b*) ASPD = 27 kPa; (*c*) ASPD = 54 kPa; (*d*) ASPD = 81 kPa

Figure 5 shows the spray photographs of this short-tip ASDS injector at the fuel injection pressure of 810 kPa under steady conditions. When compared with the results at low fuel injection pressure in Fig. 2, it is found that the separating appearance of two streams can be observed even at ASPD = 54 kPa. An increase in the fuel injection pressure results in an increase of the spray momentum, which is considered to retain the spray separation angle up to a comparatively higher ASPD.

All these visualization results showed that the short-tip ASDS injector presents improved spray atomization performance. However, a good separation of two streams that is required for four-valve engines is degraded by the shrouded air. Further work is required to clarify whether this type of injector can meet the engine requirements. At least, improvement is needed to keep the spray separation angle while maintaining improved spray atomization characteristics.

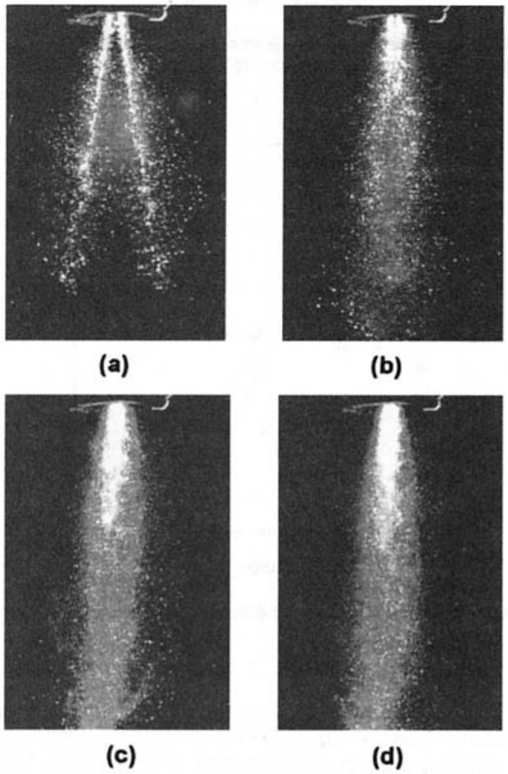

Fig. 4 Spray photographs of short-tip ASDS injector (fuel injection pressure: 290 kPa; 4 ms after fuel injection start; injection duration: 5 ms); (*a*) ASPD = 0; (*b*) ASPD = 27 kPa; (*c*) ASPD = 54 kPa; (*d*) ASPD = 81 kPa

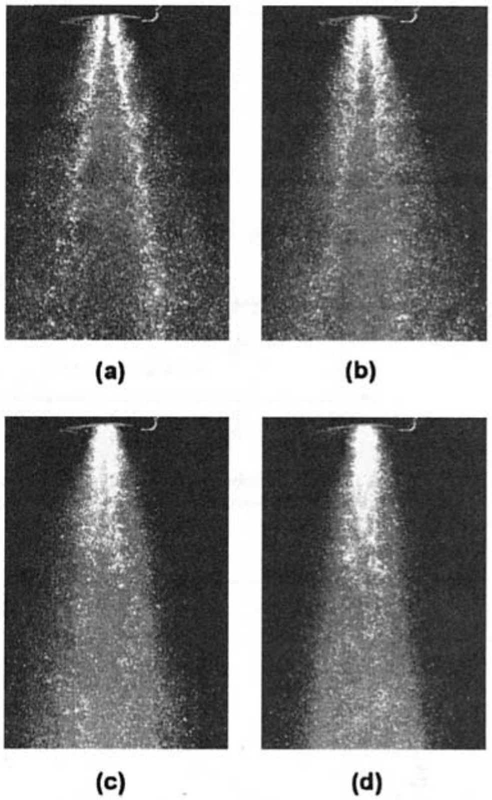

Fig. 5 Spray photographs of short-tip ASDS injector (fuel injection pressure: 810 kPa; continuous fuel injection); (*a*) ASPD = 0; (*b*) ASPD = 27 kPa; (*c*) ASPD = 54 kPa; (*d*) ASPD = 81 kPa

Figure 6 shows the radial distributions of droplet size and velocity for the short-tip ASDS injector over different ASPD. As shown in the graph, both the droplet size and velocity show a maximum at the mainstream of the spray when there is no air shrouded into the injector (ASPD = 0), which is the typical trend derived from the regular DS injector (Zhao et al., 1995e). Near the injector axis (e.g., in between the two streams), both the droplet size and velocity increase slightly. However, when the air enters the injector, the peak distribution of the droplet size disappears completely. Due to the disappearance of the two streams, droplet size increases slightly between the two original streams. However, the overall droplet size is reduced significantly because of the improved spray atomization characteristics. Moreover, the peak of the velocity shifts towards the injector axis and a great acceleration of the droplet by the shrouded air is obtained.

Figure 7 shows the droplet size and velocity distributions along the injector axis. Both the droplet size and velocity show a maximum along the axial distance at ASPD = 0. When the air is shrouded in, the droplet size is reduced markedly. Until far downstream (90 mm), the droplet size of the air-shrouded spray reaches the level of the non-air-shrouded spray. The droplet velocity of the air-shrouded spray is lower upstream (~70 mm from the injector tip). But far downstream (~70 mm) the droplet velocity is higher than that of the non-air-shrouded spray. Figure 8 shows a comparison of the spray characteristics between continuous and transient fuel injections along the injector axis. Near the injector tip, droplet size is larger for the transient spray. The droplet velocity is lower over all of the measurement locations for the transient spray due to the small spray momentum.

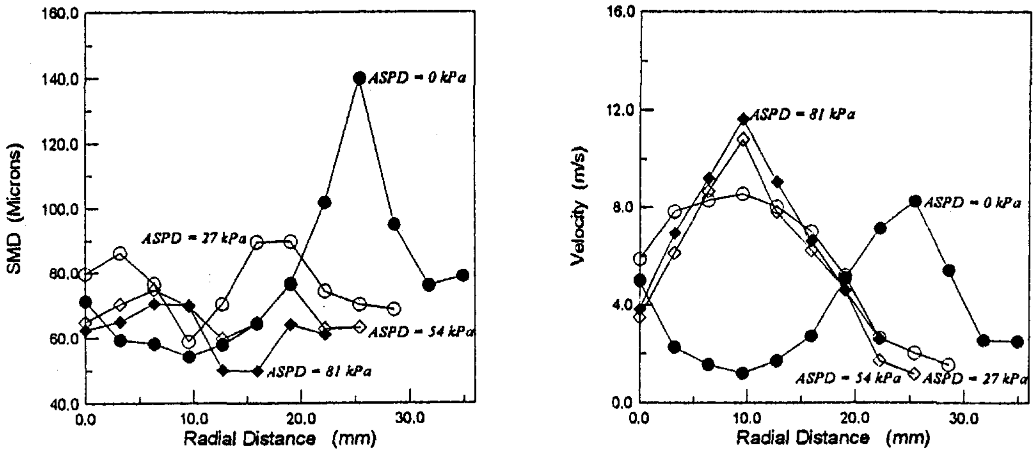

Fig. 6 Radial distributions of droplet size and velocity for short-tip ASDS injector at the axial distance of 76 mm over different air-shrouding pressure differentials (fuel injection pressure: 290 kPa; continuous fuel injection)

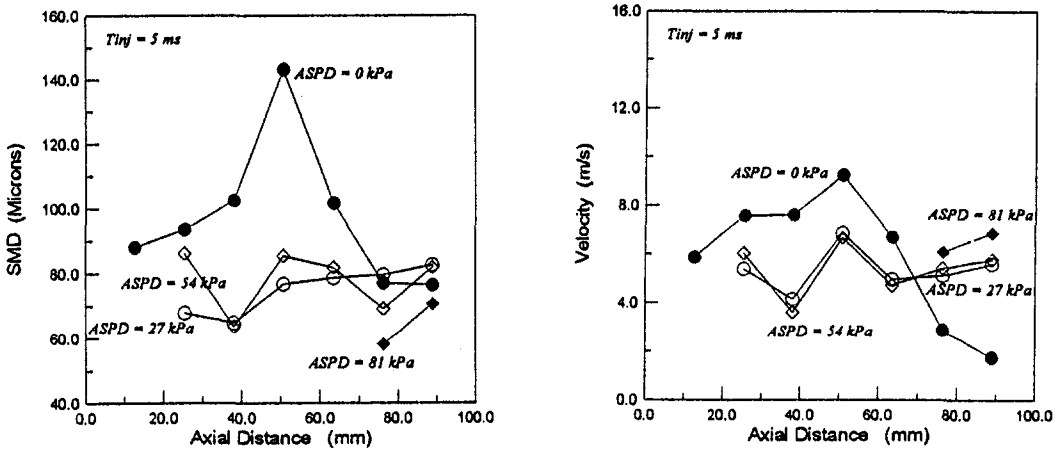

Fig. 7 Axial distributions of droplet size and velocity for short-tip ASDS injector along the injector axis over different air-shrouding pressure differentials (fuel injection pressure: 290 kPa; fuel injection duration: 5 ms)

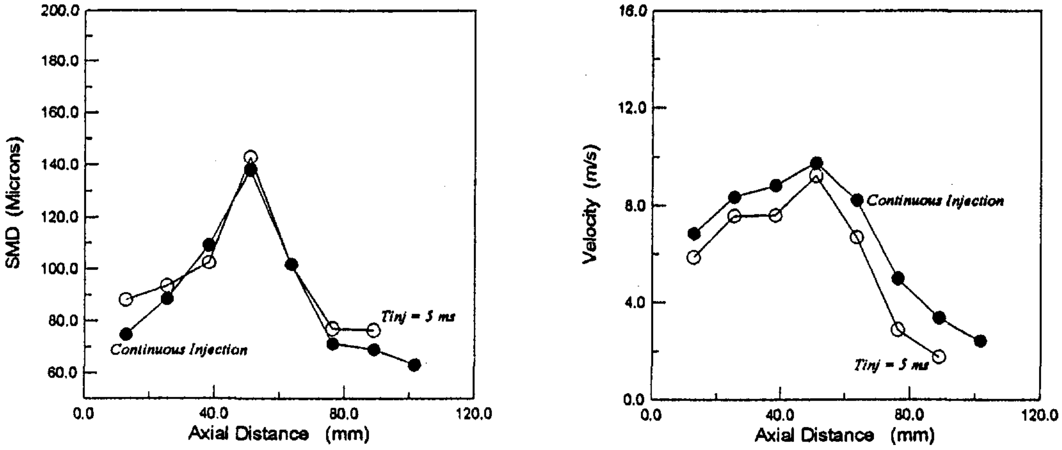

Fig. 8 Comparison of spray characteristics between continuous and pulsed fuel injections at different axial distances along the injector axis (fuel injection pressure: 290 kPa)

Long-Tip ASDS Injector. Figure 9 shows the spray photographs of the long-tip ASDS injector under steady fuel injection conditions and different ASPD. The visualization range is 30 mm in the direction of spray development. It is apparent that the two streams of the spray are well separated even at the high ASPD. There is no apparent change in the spray separation angle over different ASPD. This finding is completely different from that of the short-tip ASDS injector whose spray separation angle shows a distinct decrease even at low ASPD. The difference in the air mixing mechanism between these two injectors is assumed to cause the different spray characteristics. Since the radial velocity component of the air is reduced significantly

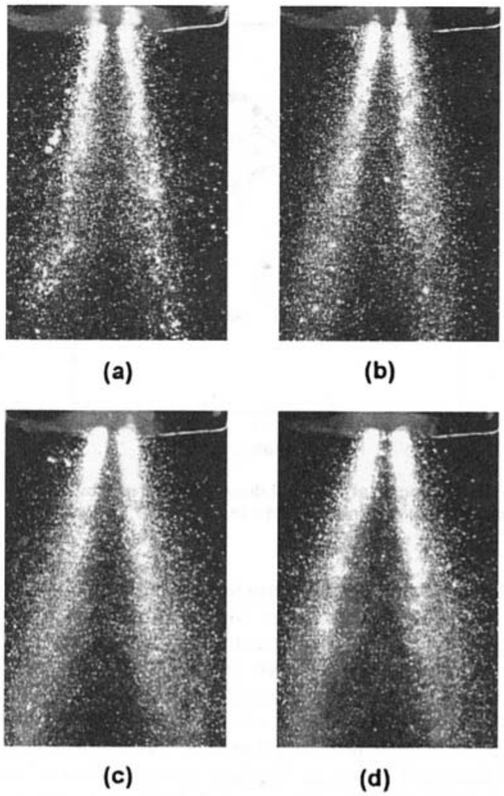

Fig. 9 Spray photographs of long-tip ASDS injector (fuel injection pressure: 290 kPa; continuous fuel injection); (*a*) ASPD = 0; (*b*) ASPD = 27 kPa; (*c*) ASPD = 54 kPa; (*d*) ASPD = 81 kPa

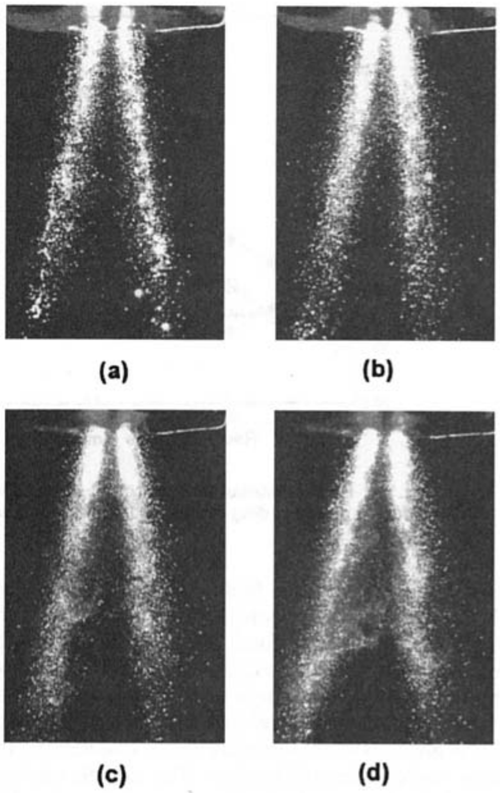

Fig. 11 Spray photographs of long-tip ASDS injector (fuel injection pressure: 290 kPa; 4 ms after fuel injection start; injection duration: 5 ms); (*a*) ASPD = 0; (*b*) ASPD = 27 kPa; (*c*) ASPD = 54 kPa; (*d*) ASPD = 81 kPa

for the long-tip injector and also the air mixes well inside the chamber near the injector tip, the trajectory of each stream is maintained to a great extent as it was developed from the original nozzle. Such a good separation of the two streams is important for the dual-stream injector. Moreover, almost no liquid fuel is observed between the two streams. All of these features show the advantages of this type of air-mixing method in fuel dispersion for reducing the wall wetting on the partition of the intake port when applied to a two-intake-valve engine. However, when compared with the spray photographs of the short-tip ASDS injector, more large droplets are observed from the spray periphery of the long-tip ASDS injector. Moreover, the liquid fuel distribution of each stream is not symmetric and large droplets concentrate around the outer edges of each stream. This observation can also be verified from the PDA results in Fig.

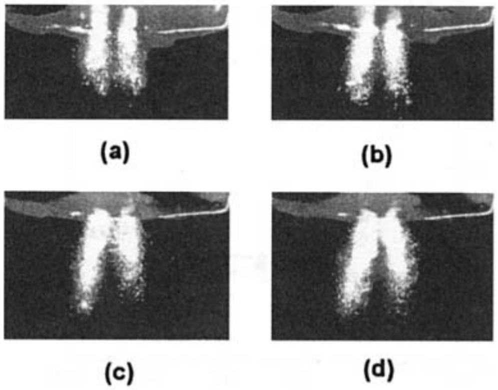

Fig. 10 Spray photographs of long-tip ASDS injector (fuel injection pressure: 290 kPa; 2 ms after fuel injection start; injection duration: 5 ms); (*a*) ASPD = 0; (*b*) ASPD = 27 kPa; (c) ASPD = 54 kPa; (*d*) ASPD = 81 kPa

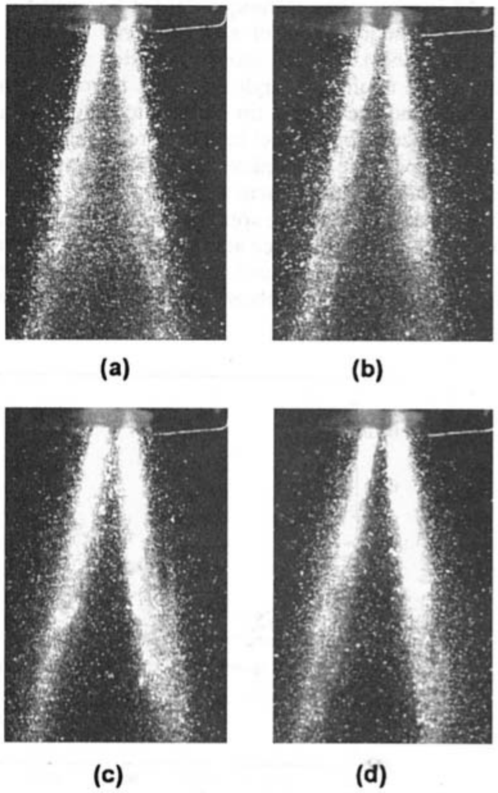

Fig. 12 Spray photographs of long-tip ASDS injector (fuel injection pressure: 810 kPa; continuous fuel injection); (*a*) ASPD = 0; (*b*) ASPD = 27 kPa; (*c*) ASPD = 54 kPa; (*d*) ASPD = 81 kPa

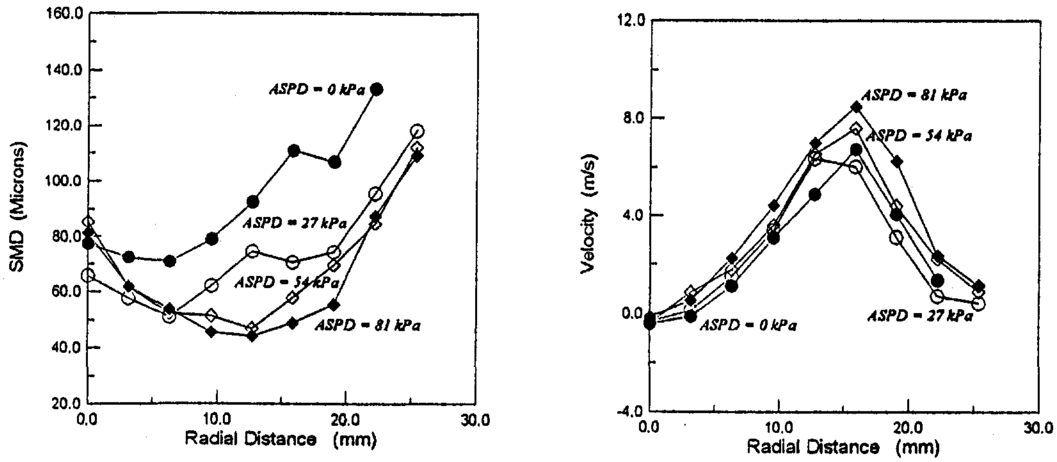

Fig. 13 Radial distributions of droplet size and velocity for long-tip ASDS injector at the axial distance of 76 mm over different air-shrouding pressure differentials (fuel injection pressure: 290 kPa; continuous fuel injection)

13. During the experiment, fuel dripping was also observed from the injector. This is possibly caused by the liquid impingement on the separation bar. Such a separation bar may be good in maintaining the spray separation angle but will cause liquid dripping, especially at the high fuel flow rate. The internally air-assisted DS injector developed by Takeda and Sugimoto (1992) was also reported to be effective in maintaining the spray separation angle of the DS injector. The fuel/air mixing region is quite near the injector tip for this type of air-assisted injector. However, at the higher ASPD (~30 kPa), the spray separation angle was reduced nearly half of the non-air-assisted spray separation angle for this internally air-assisted DS injector. From this point of view, the long-tip ASDS injector reported here is much superior. When comparing the features of different types of spray atomization technologies, it is recognized that the liquid–liquid impingement technique cannot be used for the DS injector with a requirement of a larger spray separation angle (Nogi et al., 1992). The ultrasonic vibration technique has a difficulty when applied to high flow rate injector (Namiyama et al., 1989) and the nozzle-tip heating technique takes more time than expected for the fuel temperature to reach the desired operating temperature to achieve desirable spray atomization characteristics (Chen and Chen, 1995).

Figures 10 and 11 show the spray photographs under transient conditions. It is found that even at the beginning of fuel injection (2 ms after fuel injection start), the separating appearance of the two streams is clearly observed. With an increase in the ASPD, the spray tip penetration increases monotonically. Moreover, when the ASPD is over 54 kPa, vapor is formed around the liquid core of the two streams. It can also be noticed that even though the original two streams of the spray (without shrouded air) are axisymmetrically distributed, the spray distribution becomes asymmetric when the shrouded air flows into the injector. This is probably due to the nonuniform distribution of the shrouded air inside the flow passage. At 4 ms after the fuel injection start, the spray is well developed. At low ASPD, the liquid core is dominant and many large droplets are observed from the main streams. When the injector operates under higher ASPD, the spray atomization is enhanced greatly. Especially at the ASPD of 81 kPa, a large cloud of vapor is formed between the two streams and no dominant liquid core is observed downstream of the injector. Figure 12 shows the spray photographs of the long-tip ASDS injector at the fuel injection pressure of 810 kPa. A well-separated and atomized spray is obtained under different air-shrouded conditions.

Figure 13 shows the radial distributions of droplet size and velocity at the axial distance of 76 mm downstream from the injector tip. The droplet size decreases slightly from the injector axis, and then it starts to increase again near the mainstream. Such a phenomenon is common for different injection conditions. Generally, for the DS spray as observed from the PDA measurement, it is understandable that the droplet size shows a peak at the center of each main stream (Zhao et al., 1995e). However, this is not true for the current injector. The droplet

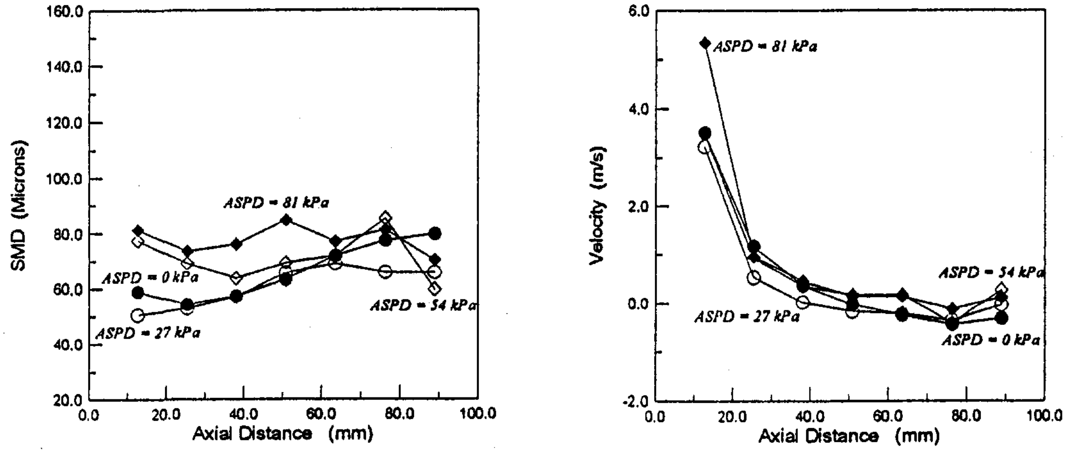

Fig. 14 Axial distributions of droplet size and velocity for long-tip ASDS injector along the injector axis over different air-shrouding pressure differentials (fuel injection pressure: 290 kPa; continuous fuel injection)

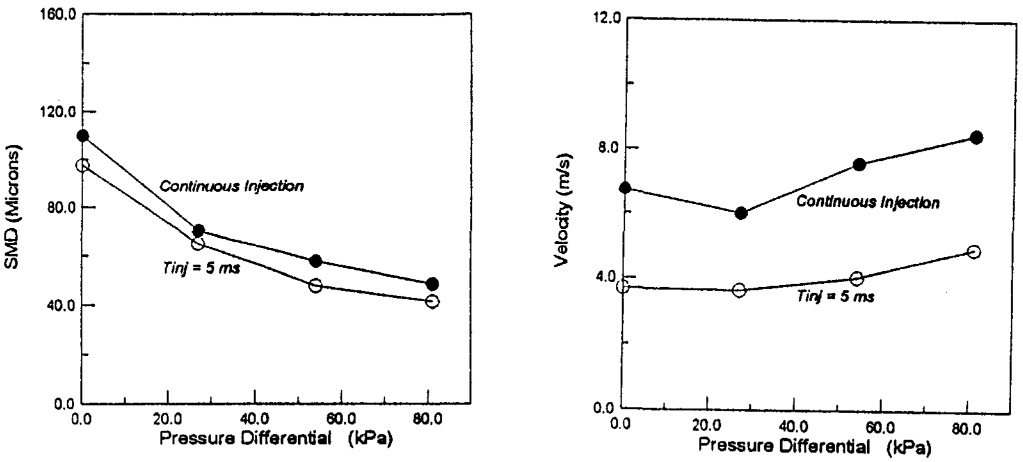

Fig. 15 Comparison of spray characteristics between continuous and pulsed fuel injections at the center location of the main stream and 76 mm downstream (fuel injection pressure: 290 kPa)

size increases with an increase of the radial distance from the center of each stream. The asymmetric liquid mass distribution of each stream is probably the reason for this finding. When the injector operates with the air shrouded in, the droplet size decreases significantly. The droplet size shows a minimum at the ASPD of 81 kPa. Such a finding matches well with the visualization result. The velocity distribution shows the same trend as that of the regular DS injector (Zhao et al., 1995e). A peak was observed at the center of each stream. Even with different ASPD, this trend remains almost the same and the peak velocity appears at the same radial location. With an increase of the ASPD, there is only a slight increase in the droplet velocity, with a maximum velocity occurring at the ASPD of 81 kPa. Around the injector axis, the droplet velocity is very low and some reversibly flowing droplets are also observed.

Figure 14 shows the axial distribution of droplet size and velocity for the long-tip ASDS injector along the injector axis. With an increase in the axial distance, the droplet size increases slightly for the low ASPD spray. At the high ASPD, the droplet size does not show any apparent change over different axial distances. The droplet velocity decreases monotonically with an increase in the axial distance over different ASPD. The difference of the droplet velocity between different ASPD is quite small, especially far downstream.

Figure 15 shows a comparison of spray characteristics between the transient and steady fuel injections. The measurement was done at the center of mainstream, namely $r/z = 0.2$ at the axial distance of $z = 76$ mm from the injector tip. It is evident that continuous fuel injection generates a larger droplet with a quite high velocity over different ASPD. However, the difference of the droplet size between continuous and steady injections is not so marked. Since continuous spray has a comparatively larger momentum, continuous injection generates droplets with high velocities. Moreover, the droplet size is comparatively small and is easily decelerated by the air resistance. As a result, the droplet of the transient injection is more easily decelerated, and the droplet velocity is only half of the continuous injection condition.

Conclusions

An experimental study was carried out to investigate the spray structure resulting from two different types of air-shrouded dual-stream port fuel injectors using PLMS technique and PDA. The injectors were tested under a range of flow conditions. It was found that the spray atomization characteristics are improved markedly by the air-shrouding technique. However, apparent separation of two streams disappears, which merge together to form a single-stream spray for the short-tip ASDS injector. For the long-tip injector, the two streams are well separated over different injection conditions. However, the liquid mass distribution of each main stream is not symmetric and the liquid core occurs a little away from the stream center. Moreover, a separation bar installed at the injector tip may be effective in enhancing the spray separation but may also cause an injector dripping problem due to the impingement of liquid fuel on the bar. This indicates that even though the spray atomization process is significantly enhanced by the air shrouded into the injector tip, the other spray parameters may also be greatly modified. If the air mixing mechanism is not optimized, the overall spray performance, and as a result the engine performance, may be degraded. A carefully selected air-mixing mechanism is definitely required in order to achieve the best performance of the air-shrouded injector.

References

Amer, A. A., and Lai, M.-C., 1995, "Time-Resolved Measurements of a Transient Gasoline Spray," SAE Technical Paper No. 950509.

Amer, A. A., Chue, T.-H., Zhao, F.-Q., and Lai, M.-C., 1995, "Modeling Turbulence Primary Breakup and Its Application in Director-Plate-Compounded Port Injectors," *Proc. 8th Annual Conference on Liquid Atomization and Spray Systems,* ILASS-America, Troy, MI, May 21–24, 1995, pp. 129–133.

Chen, J. L. and Chen, G., 1995, "Slow Heating Process of a Heated Pintle-Type Gasoline Fuel Injector," SAE Technical Paper No. 950068.

Harada, K., Shimizu, R., Kurita, K., Muramatsu, M., Makimura, T., and Ohashi, M., 1992, "Development of Air-Assisted Injector System," SAE Technical Paper, No. 920294.

Inamura, T., Nagai, N., and Sunanaga, H., 1992, "Improvement for Spray Performance of a Low-Pressure Atomizer by Conical Sheet Formation," *JSME Trans.,* Vol. 58, No. 551, pp. 2296–2301 [in Japanese].

Kashiwaya, M., Kosuge, T., Nakagawa, K., and Okamoto, Y., 1990, "The Effect of Atomization of Fuel Injectors on Engine Performance," SAE Technical Paper, No. 900261.

Lai, M.-C., Zhao, F.-Q., Amer, A. A., and Chue, C.-H., 1994a, "The Structure of Port Injector Sprays in Gasoline Engines," *Proc. of International Symposium on Advanced Spray Combustion (ISASC),* Hiroshima, Japan, July 6–8, pp. 79–89.

Lai, M.-C., Zhao, F.-Q., Amer, A. A., and Chue, C.-H., 1994b, "An Experimental and Analytical Investigation of the Spray Structure From Automotive Port Injectors," SAE Technical Paper, No. 941873.

Lai, M.-C., and Zhao, F.-Q., 1995, "The Spray Characteristics of Automotive Port Fuel Injectors—Implications to the Mixture Formation Process and Engine Performance," *Proc. 1995 KSEA International Technical Conference,* Aug. 31–Sept. 2, San Francisco, CA, pp. 112–131.

Nagaoka, M., Kawazoe, H., and Nomura, N., 1994, "Modeling Fuel Spray Impingement on a Hot Wall for Gasoline Engines," SAE Technical Paper, No. 940525.

Namiyama, K., Nakamura, H., Kokubo, K., and Hosogai, D., 1989, "Development of Ultrasonic Atomizer and Its Applications to S.I. Engines," SAE Technical Paper, No. 890430.

Nogi, T., Ohyama, Y., and Fujieda, M., 1992, "Study on the Intermittent Impinging Atomization of Fuel Injector for Gasoline Engine," *JSME Trans.,* Vol. 58, No. 552, pp. 2607–2611 [in Japanese].

Okamoto, Y., Arai, N., Nakagawa, K., Kosuge, T., and Atago, T., 1992, "Atomization Characteristics of Two-Stream Injector for 4-Valve Engines," SAE Technical Paper, No. 920705.

Parish, S. E., and Evers, L. W., 1995, "Spray Characteristics of Compound Silicon Micro Machined Port Fuel Injector Orifices," SAE Technical Paper, No. 950510.

Saikalis, G., Byers, R., and Nogi, T., 1993, "Study on Air Assist Fuel Injector Atomization and Effects on Exhaust Emission Reduction," SAE Technical Paper, No. 930323.

Saito, A., Kawamura, K., Tani, Y., and Ogiwara, Y., 1993, "Analysis of Spray Characteristics of Heated Nozzle for Gasoline Injection (1st Report, Observation of Nozzle Inside and Spray Shape)," *Proc. 2nd ILASS-Japan Symposium,* pp. 157–162 [in Japanese].

Takeda, K., and Sugimoto, T., 1992, "Development of 2-Hole Air-Assist Injector for 4-Valve Engines," *Proc. 1st ILASS-Japan Symposium,* pp. 107–112 [in Japanese].

Zhao, F.-Q., Lai, M.-C., and Harrington, D. L., 1995a, "The Spray Characteristics of Automotive Port Fuel Injection—A Critical Review," SAE Technical Paper, No. 950506.

Zhao, F.-Q., Amer, A. A., Lai, M.-C., and Dressler, J. L., 1995b, "Atomization Characteristics of Velocity-Modulated Port Injector Sprays in Gasoline Engines," *Proc. 8th Annual Conference on Liquid Atomization and Spray Systems,* ILASS-America, May 21–24, Troy, MI.

Zhao, F.-Q., Amer, A. A., Lai, M.-C., and Dressler, J. L., 1995c, "The Effect of Fuel-Line Pressure Perturbation on the Spray Atomization Characteristics of Automotive Port Fuel Injectors," SAE Technical Paper, No. 952486.

Zhao, F.-Q., Lai, M.-C., Amer, A. A., and Dressler, J. L., 1995d, "Atomization Characteristics of Pressure-Modulated Automotive Port Injector Sprays," *Atomization and Sprays,* accepted for publication.

Zhao, F.-Q., Yoo, J.-H., and Lai, M.-C., 1995e, "The Spray Characteristics of Dual-Stream Port Fuel Injectors for Applications to 4-Valve Gasoline Engines," SAE Technical Paper, No. 952487.

Zhao, F.-Q., Yoo, J.-H., and Lai, M.-C., 1996, "Spray Targeting Inside a Production-Type Intake Port of a 4-Valve Gasoline Engine," SAE Technical Paper No. 960115.

An Examination of the Ignition Delay Period in Gas-Fueled Diesel Engines

Z. Liu

G. A. Karim

Department of Mechanical Engineering,
The University of Calgary,
Calgary, Alberta, Canada T2N 1N4

Changes in the physical and chemical processes during the ignition delay period of a gas-fueled diesel engine (dual-fuel engine) due to the increased admission of the gaseous fuels and diluents are examined. The extension to the chemical aspects of the ignition delay with the added gaseous fuels and the diluents into the cylinder charge is evaluated using detailed reaction kinetics for the oxidation of dual-fuel mixtures at an adiabatic constant volume process while employing n-heptane as a representative of the main components of the diesel fuel. In the examination of the physical aspects of the delay period, the relative contributions of changes in charge temperature, pressure, physical properties, pre-ignition energy release, heat transfer, and the residual gas effects due to the admission of the gaseous fuels are discussed and evaluated. It is shown that the introduction of gaseous fuels and diluents into the diesel engine can substantially affect both the physical and chemical processes within the ignition delay period. The major extension of the delay is due to the chemical factors, which strongly depend on the type of gaseous fuel used and its concentration in the cylinder charge.

Introduction

The ignition delay period in a compression ignition engine is a very important performance parameter that influences subsequent combustion processes, engine performance, and exhaust emissions. In gas-fueled diesel engines (dual-fuel engines), the control of the ignition delay period is equally important and can display trends significantly different from those observed in the corresponding diesel engine operation. The injection of a small quantity of liquid diesel fuel is maintained in dual-fuel engine operation to ensure ignition of the charge. The length of the ignition delay, however, increases significantly with the increased admission of the gaseous fuel up to a detectable maximum value and then drops gradually, as shown typically in Fig. 1. Changes in the type of gaseous fuel used in a dual-fuel engine for the same injected quantities of liquid pilot fuel and total equivalence ratio also produce significant changes in ignition delay. For example, as shown in Fig. 1, the admission of propane increases the length of the ignition delay in dual-fuel engine operation to an extent much longer than the corresponding values observed with methane or with other gaseous fuels. For the admission of the diluents nitrogen and carbon dioxide into the intake air, however, the observed experimental values of the ignition delay in the operation of a diesel engine display yet different trends from those observed for the admission of gaseous fuel in the cylinder charge [1, 2]. Neither nitrogen nor carbon dioxide addition could produce comparable trends in increasing the ignition delay of the diesel fuel.

Some research has been carried out in the past to examine the changes in the ignition delay period during the operation of dual fuel engines. Moore and Mitchel [3] indicated that the increase in ignition delay observed in dual-fuel engines was caused by the presence of the gaseous fuels. The length of the ignition delay could be improved by increasing the pilot quantity and preheating the intake charge. Karim and Burn [2] indicated that the observed variations of the ignition delay in dual-fuel engines cannot be explained wholly on the basis of the reduction of the partial pressure of oxygen in the intake charge as a result of gaseous fuel admission. The gaseous fuel must affect in an unknown manner the pre-ignition processes of the diesel pilot fuel to bring about the observed specific variations in the length of the ignition delay. In our previous work [5], the effects of changes due to gaseous fuel admission, in mean charge temperature, external heat transfer to the surroundings, and the extent of pre-ignition energy release during the compression process on the length of the ignition delay of a dual-fuel engine have been examined while using detailed reaction kinetics for the oxidation of the gaseous fuel and air and employing an experimentally based formulation for the ignition delay of the liquid pilot. The effects of any chemical interaction between the pilot and gaseous fuels during the preignition processes could not be accounted for.

The present contribution examines further the observed changes in the physical and chemical processes during the ignition delay period of a gas-fueled diesel engine (dual-fuel engine) due to the increased admission of the gaseous fuels and diluents. In the examination of the chemical aspects of the ignition delay, the environment of the mixture of diesel pilot with the gaseous fuel is simulated by an adiabatic constant volume process while employing n-heptane as a representative of the main components of the diesel fuel. The effects of changes in the concentrations of the added gaseous fuels, such as methane, propane, and hydrogen, and the diluents carbon dioxide and nitrogen to the cylinder charge as well as the changes in intake charge temperature on the ignition delay of the fuel mixture in air are evaluated through using detailed reaction kinetics for the oxidation of the n-heptane and gaseous fuels mixture.

In the examination of the physical aspects of the delay period, the relative contributions to the ignition delay, resulting from changes in charge temperature, pressure, physical properties, pre-ignition energy release, heat transfer, and the effects of the residual gases due to the admission of gaseous fuels are discussed and evaluated. It is shown that the introduction of gaseous fuels and diluents into the diesel engine will change both the physical and chemical processes of the ignition delay period. The extension to the chemical process of the delay period with the admission of the gaseous fuel is the main rate controlling processes. Its extent, which depends on the type of the gaseous fuel used and its concentration in the cylinder charge, will be decreased with the improvement of combustion performance.

Contributed by the Internal Combustion Division for publication in the Journal of Engineering for Gas Turbines and Power. Manuscript received at ASME Headquarters May 1997. Associate Technical Editor: W. K. Cheng.

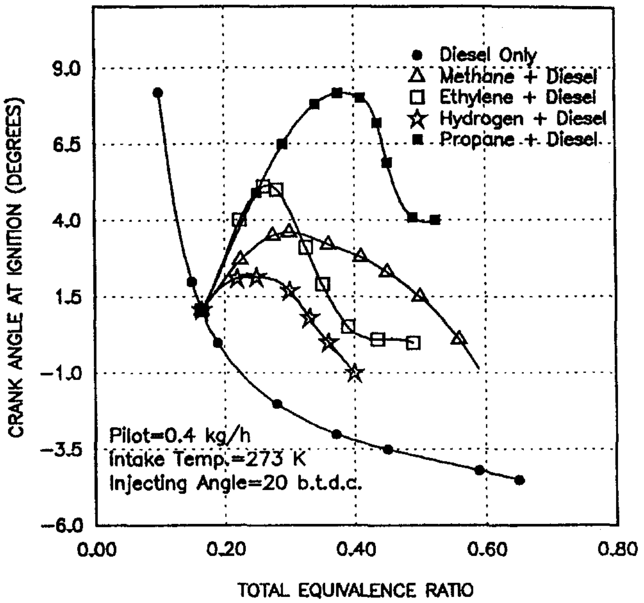

Fig. 1 Variations of ignition delay with various gaseous fuels admission over a range of equivalence ratio in a dual fuel engine operation

Analytical Considerations

The ignition delay in a diesel engine is defined as the time interval between the start of fuel injection and the commencement of rapid energy release due to combustion. The pre-ignition processes can be viewed as being initially predominantly physical, followed by overlapping somewhat later chemical processes. In the physical part of the delay process, the fuel is injected, atomized, vaporized, and mixed with the air. The associated chemical processes are controlled by the precombustion reactions of the local mixtures of the fuel, air, and residual gases. A convenient approach based on experimental observation of the delay in diesel engines is to consider the length of the ignition delay period to be a function of the charge pressure and equivalence ratio of the fuel vapour and air, and exponentially dependent on the inverse of the mean charge temperature [6, 7].

In dual-fuel engine operation, the admission of a gaseous fuel with the air will influence profoundly both the physical and chemical ignition processes of the mixture. This admission will bring about variations in the physical properties of the mixture such as the specific heat ratio and heat transfer parameters. These can lead to significant changes in the charge temperature and pressure levels at the time of fuel injection and extend the physical ignition delay period of the mixture. The presence of the gaseous fuel–air charge during the pre-ignition reaction results in changes to the energy release and the associated production of active species. Moreover, any chemical interactions that may take place between the diesel vapor and gaseous fuel will produce further changes in the chemical ignition processes of the mixture.

Some of the major effects of the introduction of the gaseous fuel on the ignition period of the dual-fuel–air engine can be expressed conveniently as a modification to the compression mean charge temperature, ΔT, and can be written as:

$$\Delta T = \Delta T_{th} + \Delta T_{re} + \Delta T_{ht} + \Delta T_{rt} + \ldots \qquad (1)$$

where ΔT_{th} is the temperature change due to any variations in the thermodynamic and physical properties of the mixture, ΔT_{re} is the change due to the contribution of residual gases, ΔT_{ht} is the change due to the heat transfer, and ΔT_{rt} is the change due to the contribution of pre-ignition energy release. Changes in the thermodynamic and physical properties of the mixture could normally bring about a decrease in the charge temperature while other changes, such as the contribution of the residual gases, could result in an increase in the charge temperature. The effects of any chemical interaction between the diesel and gaseous fuels during the preignition reactions can be accounted for empirically through a modification to the effective overall activation energy term of the mixture, which will be strongly dependent on the types and concentration of gaseous fuels involved.

Hence, when accounting for the effects of these changes, a *modified value* for the ignition delay in dual fuel engines can be produced [5]. This modified value, $\tau + \Delta\tau(s)$, in order to be compared to the corresponding value under diesel operation [6, 7], can be written as:

$$\tau + \Delta\tau = A(P + \Delta P)^a(\phi + \Delta\phi)^b \exp\left(\frac{c + \Delta c}{T_g + \Delta T}\right) \qquad (2)$$

where P and T_g represent, respectively, the mean cylinder pressure (atm) and charge temperature (K) during the ignition delay period. ϕ is the equivalence ratio of the fuel vapor–air mixture. A, a, b, and c are constants to be established experimentally for the relevant operating conditions. The values of these constants as obtained, for example, by Hiroyasu [6, 7] in a constant volume vessel are:

$$A = 4.0 \times 10^{-3}, \quad a = -2.5, \quad b = -1.04, \quad c = 6000 \qquad (3)$$

In the present work, the equivalent modifications to the charge temperature in accordance with Eq. (1) can be correlated from the results of analysis and experiment. The corresponding chemical effects on the ignition delay period of the dual-fuel–air mixture are examined on the basis of adiabatic constant volume reaction conditions while employing detailed reaction kinetics for the oxidation of the dual-fuel–air mixture. In these kinetic considerations, *n*-heptane is chosen to represent the oxidation of the diesel fuel since the chemical kinetics of the diesel fuel oxidation are currently unavailable. Moreover, the adiabatic constant volume conditions tend to be close to the environment of the diesel pilot fuel in dual-fuel engines during the delay period (for example, a charge mean temperature of 780 K and a charge pressure of 28 atm). The concentrations of the mixtures of *n*-heptane vapor and the gaseous fuel are considered in terms of their corresponding stoichiometric value, which tends to be associated with the peak value of the reaction rates for the oxidation of the mixture. The chemical reaction mechanism of the mixtures of *n*-heptane and the other gaseous fuels was based on those schemes reported by Westbrook et al. [8]. This detailed kinetic scheme consisted of 1966 elementary reaction steps and 380 chemical species. The corresponding thermochemical data were obtained mainly from JANAF tables [10].

The residual gases from the previous cycle, which were assumed to fill the clearance volume when a new cycle began, were considered to have the same composition as that for the exhaust gases at the end of expansion to atmospheric pressure. These residual gases, when the inlet valve was opened, mixed completely and adiabatically with the fresh charge at the same pressure. For heat transfer, the mean wall temperature T_w was assumed to remain constant over the cycle, while convective and radiative heat transfer was accounted for by a formulation recommended by Annand [11] following his analysis of a wide range of experimental data in engines.

Results and Discussion

When the pilot diesel fuel is injected into the combustion chamber under high injection pressures, the pilot fuel is atomized and distributed within its spray cone. The resulting axial and radial fuel concentration profiles could be calculated approximately by employing established theoretical procedures for the flow of jets [12]. Increasingly more surrounding fuel along with the air are entrained into the spray cone as the jet

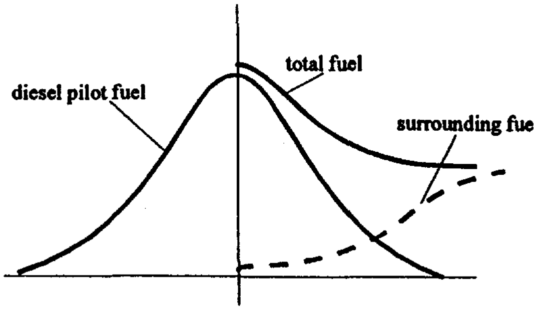

(a)
Upstream Region of the Jet

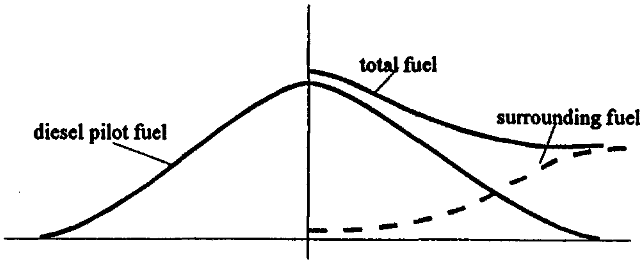

(b)
Downstream Region of the Jet

Fig. 2 Schematic representation of fuel concentration profile within a diesel fuel jet issuing in an atmosphere of gaseous fuel and air mixture

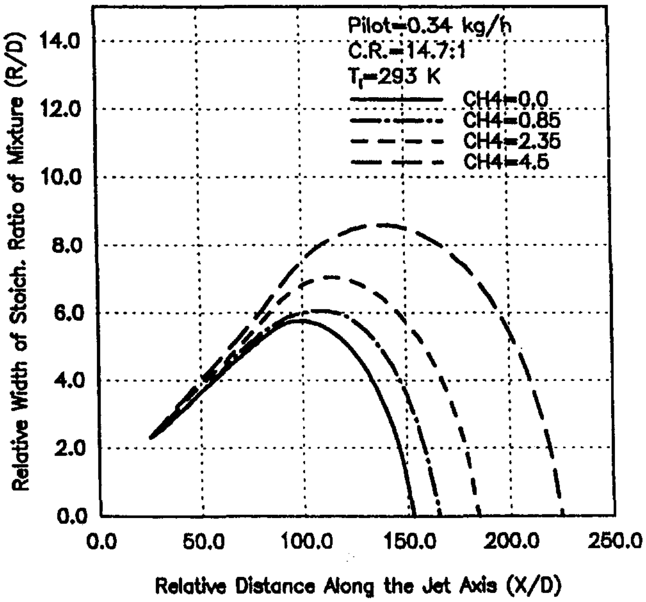

Fig. 3 Calculated relative width of the stoichiometric ratio envelopes in jet fuel mixture with changes in methane concentration in the surrounding charge

of diesel fuel moves downstream. The downstream radial fuel concentration profiles become increasingly flatter. Consequently, for the same overall fuel–air ratio in the cylinder charge, the relative concentration of the gaseous fuel at a downstream jet location, as shown schematically in Fig. 2(*a*) and 2(*b*), has a much higher value than that at an upstream jet location due to the entrainment of the surrounding gaseous fuel. The induction of more gaseous fuel into the engine cylinder will further change the local fuel composition and increase the concentration of the total fuel at any point while the concentration of the air reduced by the same amount. However, this change in the local fuel composition is not uniform for the mixture within the jet spray cone. As shown in Fig. 3, the overall size of the stoichiometric region at every section downstream of the nozzle is increased, both in width and length, as the concentration of the gaseous fuels in the surroundings is increased. However, the increase of gaseous fuel in the local fuel composition for the same stoichiometric zone tends to be prominent only at regions away from the discharge point of the jet. These changes in local fuel composition with the admission of the gaseous fuels play an important role in modifying the ignition and combustion characteristics of the engine from those of normal diesel operation.

It is expected that the most probable location for first ignition encountered will be along a stoichiometric mixture envelope of the fuel jet for the same temperature level. In the operation of a dual-fuel engine, the ignition delay period will depend not only on the concentration of the mixture but also on the local fuel composition for the same values of the stoichiometric mixture, since the admission of the gaseous fuel changes the local fuel composition, as shown in Figs. 2 and 3. It has been confirmed in Fig. 4 that for stoichiometric mixtures at mean temperature and pressure values similar to those during the delay period in engines, the calculated ignition delay period of heptane and gaseous fuel mixtures in air is gradually extended as the percentage of the gaseous fuel in the mixture is increased. For methane admission, the extension to the ignition delay period of the fuel mixture tends to be initially very slow until the percentage of the methane in the fuel mixture is substantially increased to beyond around 70 percent. The increased percentage of hydrogen in the mixture does not increase the ignition delay significantly. However, for propane admission, the ignition delay extends more rapidly with increasing the percentage of propane in the fuel mixture. These changes in the ignition delay period, which depend on the type of the gaseous fuel and its concentration in the cylinder charge, are consistent with those observed experimentally in Fig. 1 for dual-fuel engine operation. Figure 5 shows similarly the corresponding variations of the ignition delay period with increasing concentrations of gaseous fuel and the diluents carbon dioxide and nitrogen in the local stoichiometric mixture for *n*-heptane and the added gas. It can be seen that unlike with the admission of gaseous fuels, neither the presence of small amounts of nitrogen nor

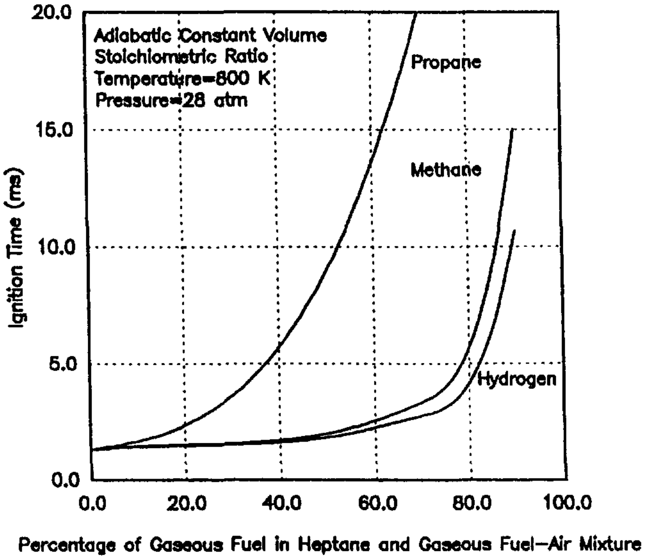

Fig. 4 Calculated ignition times of the stoichiometric dual-fuel mixture with changes in the percentage of gaseous fuel in the total mixture for an adiabatic constant volume process

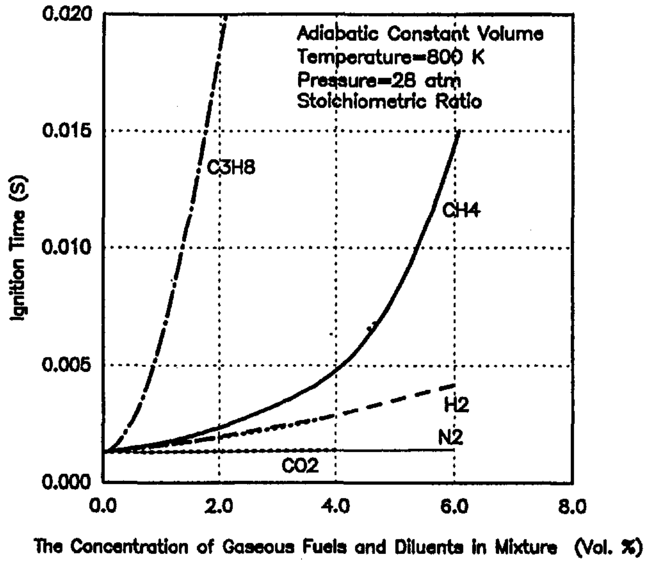

Fig. 5 Variations of calculated ignition times with changes in the concentration of gaseous fuel and diluent in the mixture for an adiabatic constant-volume process

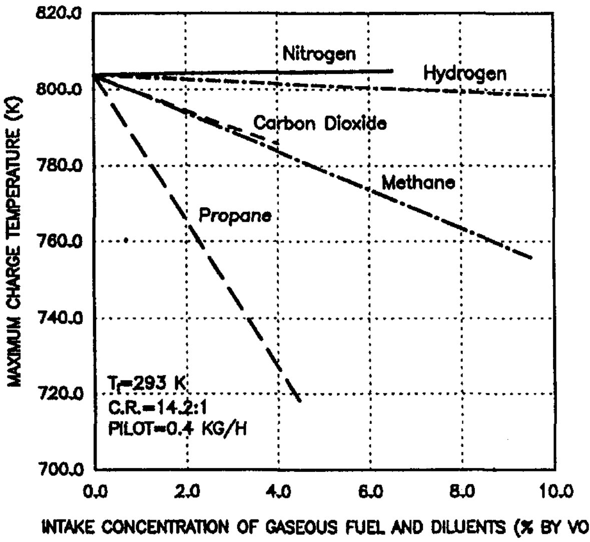

Fig. 7 Variations of calculated maximum temperatures with equivalence ratios for propane, methane, hydrogen, carbon dioxide, and nitrogen in a motored engine operation

carbon dioxide with n-heptane can produce significant increases in the ignition delay period. The small changes observed are associated mainly with the reduction of the partial pressure of oxygen in the surroundings. Figure 6 shows that the decrease in the mixture temperature extends the ignition delay period of the mixture without significantly changing the trends of ignition delay period with the increased admission of gaseous fuels.

Accordingly, on the basis of these trends, the admission of the gaseous fuel with the intake air in dual-fuel applications will result in an extension to the ignition delay period due to the chemical interactions between the diesel and gaseous fuels. This extension will be further increased, but not proportionally, with the increase of the concentration of the gaseous fuel in the cylinder charge. It can be anticipated that ignition in the dual-fuel engine will first take place within the region of the diesel pilot jet where sufficient amounts of diesel fuel vapor and air but with small concentration of gaseous fuel form the most reactive ignition elements. Those regions that are close to or far away from the discharge point of the fuel jet will tend to produce a later ignition due to either the lack of vaporized diesel fuel or a relatively high concentrations of the gaseous fuel in the local mixture.

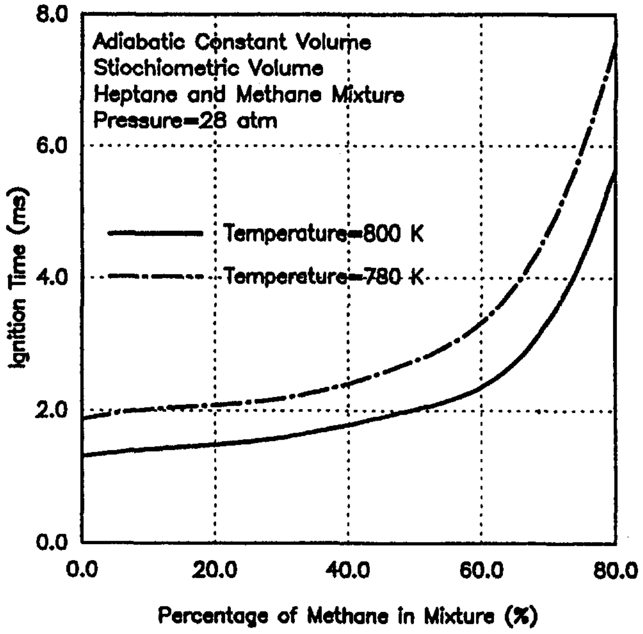

Fig. 6 Variations of calculated ignition times with changes in intake temperatures for methane admission for an adiabatic constant volume process

Another major effect of the introduction of a gaseous fuel or a diluent in the engine cylinder with the intake air is the resulting variations in the charge temperature during compression. These are due to the changes in the physical properties of the mixture, such as the specific heat ratio and heat transfer parameters, as well as any energy release arising from the pre-ignition reactions of the gaseous fuels. As shown in Fig. 7, the addition of hydrogen to the engine intake air reduces the maximum temperature level of the charge at the end of compression only relatively little. However, the corresponding values of temperature observed with the addition of methane or propane decrease markedly. With propane addition, for the typical case shown, a drop in temperature of around 90 K was observed for the stoichiometric mixture. Similarly, the mean value of the charge temperature at the end of compression decreases essentially linearly with increasing the concentrations of carbon dioxide in the cylinder charge. The addition of nitrogen to the intake air hardly changes the charge temperature.

The effect of changes in the physical properties of the mixture and heat transfer arising from the admission of the gaseous fuel on the charge temperature at the end of compression can be correlated on the basis of the type and concentration of the gaseous fuel. As shown in Fig. 8, this temperature is markedly reduced with the increased addition of methane into the air while following similar trends for wide working conditions. The values predicted by the correlated formulation agree very well with the corresponding individually calculated values according to the following relationship:

$$\Delta T_{g\max} = (T_{a\max} - T_{g\max}) = T_{a\max}\left(1 - \exp\left(-\frac{\varphi}{a}\right)\right) \quad (4)$$

where $T_{g\max}$ is the charge temperature at the end of compression with the admission of gaseous fuel, $T_{a\max}$ is the charge temperature at the end of compression with pure air admission, φ is the equivalence ratio of the gaseous fuel, a is a constant having the following values 16.61, 8.90, 55.31, and 13.56 for the addi-

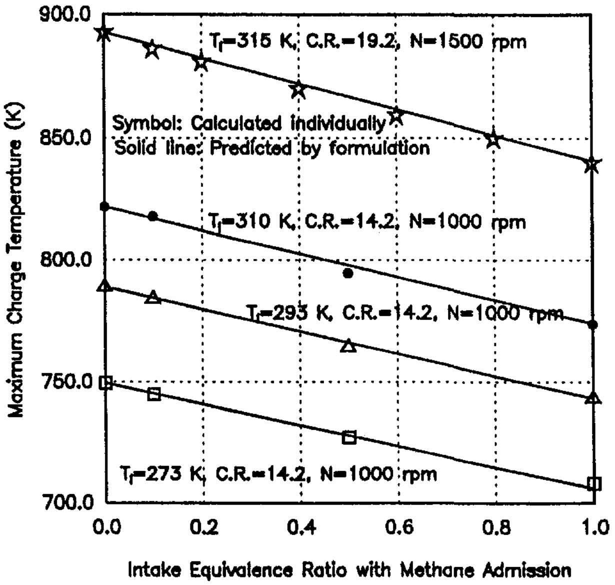

Fig. 8 Comparison of maximum charge temperatures predicted by full calculation and by the correlated formulation for methane admission of Eq. (4)

tion of methane, propane, hydrogen, and ethylene, respectively. On this basis when the charge temperature at the end of compression for pure diesel operation is known, the charge temperatures at the end of compression with the admission of different gaseous fuels can be evaluated.

With the consideration of both the physical and chemical effects of the admission of the gaseous fuels or the presence of the diluents on the ignition delay period of the mixture, the observed changes in the experimental values of the ignition delay during the operation of dual fuel engines can be diagnosed. As shown in Fig. 9, the observed experimental values of the ignition delay increase almost linearly with the extent of carbon dioxide admission to the cylinder charge. A higher intake temperature results in a relatively shorter ignition delay, while an essentially linear trend is maintained. The increase in the ignition delay period with the admission of carbon dioxide is mainly attributable to the decrease in the charge temperature due to the variations of the physical properties of the charge and the heat transfer during compression. The addition of a small amount of carbon dioxide does not significantly affect the pre-ignition reaction processes. Meanwhile, as shown in Fig. 5, the admission of a small amount of carbon dioxide into the intake air does not produce a significant extension to the chemical part of the ignition delay period of the mixture. Hence, when these factors that affect the ignition delay period due to the addition of carbon dioxide have been excluded, the modified ignition delay calculated by Eq. (2) remains, as shown in Fig. 9, at almost the same value as observed in pure diesel operation and will not change with the increased carbon dioxide concentrations.

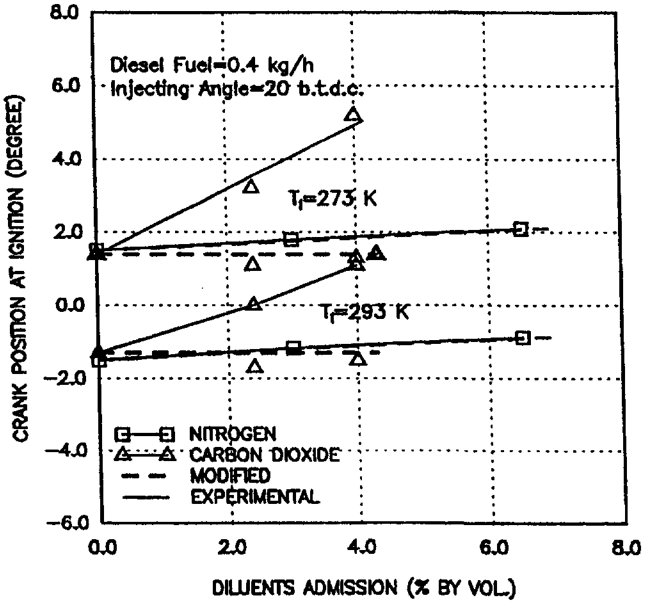

Fig. 9 Variations of experimental and modified ignition delay values with the intake concentration of carbon dioxide and nitrogen for two intake temperatures

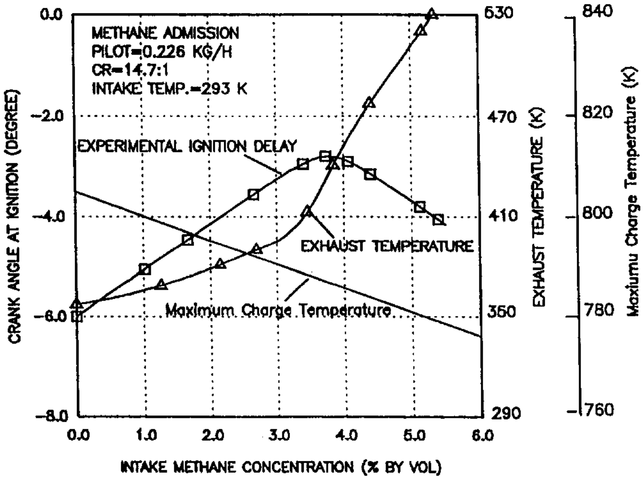

Fig. 10 Variations of experimental ignition delay, exhaust temperature and calculated maximum charge temperature with methane admission

As shown in Fig. 6, the addition of nitrogen will not change the mean charge temperature and no extension to the physical process of the ignition delay period is expected with the admission of small amounts of nitrogen. The corresponding changes in the ignition delay for nitrogen admission, as show in Fig. 9, are far less evident than those observed with carbon dioxide admission. The very small increase observed in the value of the ignition delay resulted from the small extension to the chemical process of the delay period.

Unlike with the admission of the diluents, Fig. 10 shows that the ignition delay period, measured in a direct-injection single-cylinder dual-fuel engine, initially increases significantly up to a maximum value as the methane concentration in the cylinder charge is increased. The admission of the gaseous fuel influences the length of the ignition delay not only through a possible modification of the nature of the chemical reactions of the mixture but also through changes in the charge temperature levels, heat transfer, the extent of pre-ignition energy release during compression, and the associated changes in the contribution of residual gases from previous cycles. As shown typically in Fig. 10, the increased admission of methane reduces the calculated values of the maximum charge temperature at the end of compression. The corresponding measured exhaust temperature, which is consistent with the state of the residual gases, is initially increased slowly but with a continued increase in methane concentration in the cylinder charge its value is enhanced very significantly. The marked reduction in the length of the ignition delay is accompanied by the significant increase in the exhaust temperature.

Figure 11 shows typically the variations of the charge temperatures at the commencement and end of the compression stroke with methane admission, when the effects of the changes in physical properties of the mixture, heat transfer, the extent of

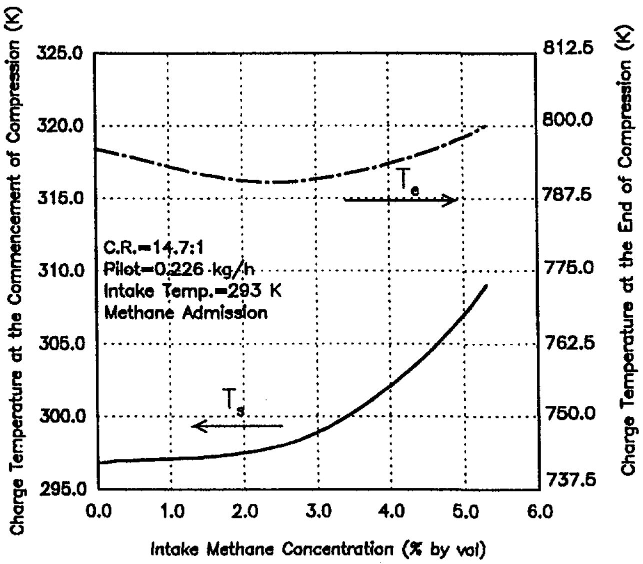

Fig. 11 Variations of calculated charge temperatures at the commencement and end of the compression stroke for methane admission

pre-ignition energy release during compression, and the associated contribution of residual gases from previous cycles on the charge temperature have been considered on the basis of the results in Fig. 10. It can be seen that at light load, which involves very lean gaseous fuel–air mixtures, the charge temperature at the commencement of the compression stroke is not increased significantly with the consideration of the contribution of the residual gases, since the combustion of the mixture at light load is confined to around the pilot fuel and cannot produce sufficiently hot residual gases. The values of the corresponding charge temperature at the end of the compression stroke are lower than the value observed for pure diesel operation due to the variations of the physical properties of the charge and external heat transfer effects. With the continued increase in the gaseous fuel concentration, the combustion process can extend gradually further into regions of the mixture made up of the gaseous fuel and air to produce higher residual gas temperatures. The values of the charge temperature at the commencement of the compression stroke, as shown in Fig. 11, is then significantly elevated through the increased contribution of the hotter residual gases. These increases in the charge mean temperature at the commencement of compression will contribute to counteracting the corresponding reduction in the charge temperature due to the admission of methane to produce eventually a higher charge temperature at the end of compression.

These changes in the charge temperature with the admission of methane influence significantly the ignition characteristics of the pilot fuel. As shown in Fig. 12, the changes in the ignition delay period of the dual-fuel engine can be considered in terms of physical and chemical extensions calculated in accordance with Eqs. (1) and (2). At light load, the decrease in the charge temperature, as shown in Fig. 11, extends the physical process of the ignition delay period. Meanwhile, the increased presence of methane with the diesel fuel charge will result in some extension to the chemical processes of the delay, as displayed in Figs. 4 and 5. Both of these extensions to the ignition period lead to the observed increase in the delay period in dual-fuel engines as the methane concentrations in the cylinder mixture are increased.

At relatively high loads, the charge temperature at the end of compression can reach high values mainly due to the increased contribution of the hotter residual gases. Hence, as shown in Fig. 12, the extension to the physical process of the ignition delay is reduced gradually as the charge temperature at the end of compression continues to increase. The corresponding extension to the chemical processes of the ignition delay is also reduced under the increased charge temperatures. Thus, the ignition delay period at relatively high load is decreased with the increased methane concentration in the cylinder charge.

These changes in the ignition delay period of the dual-fuel engine show that the extension to the chemical processes of the ignition delay with the admission of the gaseous fuel is the main rate controlling processes during the delay period of the dual fuel engine. The extent of this extension, which depends on the type of gaseous fuel used and its concentration in the cylinder charge, will be decreased with the improvement of combustion performance.

These analytical results can be used further to explain other changes in the ignition delay period observed in dual fuel engine operation. For example, the admission of propane into the dual-fuel engine results in a significant decrease in the charge temperature and a longer extension to the chemical part of the ignition delay period. The value of the delay for propane admission is higher than those values observed for methane or hydrogen admission. Moreover, an increase in the size of the pilot fuel, which improves the combustion characteristics of the dual fuel engine, reduces the relative concentration of the gaseous fuel in the fuel mixture for the same overall equivalence ratio, resulting in higher charge temperatures at the end of the compression and a shorter chemical extension to the ignition delay period. Hence, the observed values of the ignition delay are lower than those observed for small pilots [1, 2].

Conclusion

The introduction of gaseous fuels or diluents with the intake air into a diesel engine will change both the physical and chemical processes of the ignition delay period. The corresponding extension to the physical process of the delay period is related to changes in the charge temperature, pressure, pre-ignition energy release, heat transfer, and the effects of the residual gases. The extension to the chemical process of the ignition delay, which results from the chemical interactions between the diesel and gaseous fuels, is the main rate-controlling process during the delay period of the dual-fuel engine. The extent of the extension to the ignition delay period depends strongly on the type of the gaseous fuel used and its concentration in the cylinder charge.

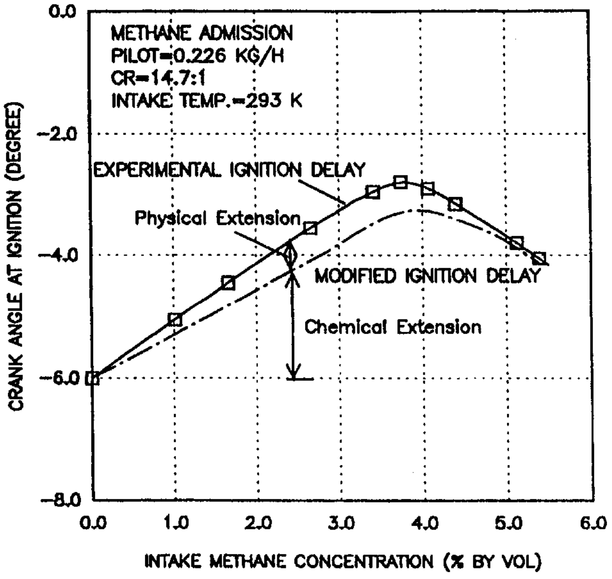

Fig. 12 Variations of experimental and modified ignition delay values with intake concentration for methane admission

Acknowledgments

The financial support of Natural Science and Engineering Research Council of Canada (NSERC) and Alternative Fuel System, Inc., is gratefully acknowledged. The contributions of Mr. K. S. Burn, Mr. E. Khalil, and Dr. C. K. Westbrook are also acknowledged.

References

1 Nielsen, O. B., Qvale, B., and Sorenson, S. C., "Ignition Delay in the Dual Fuel Engine," SAE Paper No. 870589, 1987.

2 Karim, G. A., and Burn, K. S., "The Combustion of Gaseous Fuels in Dual Fuel Engine of the Compression Ignition Type With Particular Reference to Cold Intake Temperature Conditions," SAE Paper No. 800263, 1980.

3 Moore, N. P. W., and Mitchell, R. W. S., "Combustion in Dual Fuel Engines," *Proc. Fourth Combustion Conference of ASME and I. Mech. E.*, London, 1955.

4 Karim, G. A., Jones, W., and Raine, R. R., "An Examination of the Ignition Delay Period in Dual Fuel Engines," SAE Paper No. 892140, 1989.

5 Liu, Z., and Karim, G. A., "Ignition Delay Period in Dual Fuel Engines," SAE Paper No. 95950466, 1995.

6 Hiroyasu, H., "Diesel Engine Combustion and Its Modelling," *Diagnostics and Modelling of Combustion in Reciprocation Engine*, Tokyo, 1985, pp. 20–45.

7 Hiroyasu, H., "Fuel Spray Trajectory and Dispersion in a D.I. Diesel Combustion Chamber," SAE Paper No. 890462, 1989.

8 Westbrook, C. K., Warnaze, J., and Pitz, W. J., "A Detailed Chemical Kinetic Reaction Mechanism for the Oxidation of Iso-Octane and n-Heptane Over an Extended Temperature Range and Its Application to Analysis of Engine Knock," *Proc. 22nd Symp. (Int.) on Combustion*, 1988, pp. 893–901.

9 Pitz, W. J., Westbrook, C., and Leppard, W. R., "Autoignition Chemistry of C4 Olefins Under Motored Engine Conditions: A Comparison of Experimental and Modelling Results," SAE Paper No. 912315, 1991.

10 JANAF, *Thermochemical Tables*, 3rd ed., ACS&AIp for Nation, Bureau of Standards, 1985.

11 Annand, W. J. D., "Heat Transfer in the Cylinders of Reciprocating Internal Combustion Engines," *Proc. I. Mech. E.*, Vol. 177, 1963, pp. 973–980.

12 Abramovich, G. N., *The Theory of Turbulent Jets*, M.I.T. Press, 1963.

Fast-Burn Combustion Chamber Design for Natural Gas Engines

R. L. Evans

J. Blaszczyk

Department of Mechanical Engineering,
The University of British Columbia,
Vancouver, B.C., Canada

The work presented in this paper compares the performance and emissions of the UBC "Squish-Jet" fast-burn combustion chamber with a baseline bowl-in-piston (BIP) chamber. It was found that the increased turbulence generated in the fast-burn combustion chambers resulted in 5 to 10 percent faster burning of the air–fuel mixture compared to a conventional BIP chamber. The faster burning was particularly noticeable when operating with lean air–fuel mixtures. The study was conducted at a 1.7 mm clearance height and 10.2:1 compression ratio. Measurements were made over a range of air–fuel ratios from stoichiometric to the lean limit. At each operating point all engine performance parameters, and emissions of nitrogen oxides, unburned hydrocarbons, and carbon monoxide were recorded. At selected operating points a record of cylinder pressure was obtained and analyzed off-line to determine mass-burn rate in the combustion chamber. Two piston designs were tested at wide-open throttle conditions and 2000 rpm to determine the influence of piston geometry on the performance and emissions parameters. The UBC squish-jet combustion chamber design demonstrates significantly better performance parameters and lower emission levels than the conventional BIP design. Mass-burn fraction calculations showed a significant reduction in the time to burn the first 10 percent of the charge, which takes approximately half of the time to burn from 10 to 90 percent of the charge.

Introduction

Combustion chamber design is one of the key factors affecting the performance of a spark-ignition engine. In particular, it is well known that the level of turbulence in the chamber just prior to ignition and during the combustion process has an important impact on the burning rate of the air–fuel mixture. The level of turbulence in the chamber can be influenced by the chamber design through the degree of swirl imparted to the mixture during the intake process and by the squish motion generated as the piston nears top-dead-center. High levels of turbulence generation lead to faster burning rates, which can result in improved thermal efficiency and reduced levels of exhaust emissions. It is important, however, to realize that the scale of turbulence generated in the chamber, not just the magnitude of the velocity fluctuations, is a key factor in optimizing the combustion rate.

The use of lean air–fuel ratios is another means of increasing engine efficiency and reducing exhaust emissions. The formation of nitrogen-oxide compounds is primarily a function of temperature, so that the lower combustion temperatures resulting from lean combustion lead to reduced NO_x emissions. Under lean operating conditions, there is also an excess of oxygen available to oxidize carbon monoxide and unburned hydrocarbon compounds. As the air–fuel ratio is increased toward the lean limit of combustion, however, misfire cycles may occur and incomplete combustion may result in an increase in unburned hydrocarbon emissions.

A disadvantage of lean operation is that the burning rate is reduced compared to combustion under stoichiometric conditions. This reduction in the burning rate results in an increase in the overall combustion duration, which in turn leads to increased heat transfer losses to the cylinder walls and a decrease in the overall engine thermal efficiency. The increased combustion duration under lean conditions requires the spark-timing to be advanced compared to stoichiometric operation, which may in turn lead to knock and an increase in unburned hydrocarbon formation. To successfully implement a lean-burn strategy to minimize exhaust emissions and maximize thermal efficiency, therefore, the combustion chamber should be designed to enable the fastest possible combustion rate to be achieved under all operating conditions.

The goal of the research work reported here was to develop a "fast, lean-burn" combustion system, which would enable emission regulations to be met without the use of exhaust gas clean-up equipment. A new type of combustion chamber was developed and tested over a wide range of air–fuel ratios under full-load operating conditions. The fuel used was natural gas, a slow-burning fuel compared to gasoline, which makes the use of a fast-burn type of chamber even more important.

The Role of Turbulence in SI Engines: Previous Research Review

A review of the literature shows the progression of engine investigations of turbulence from the early 1920s to the present-day computer simulation models. Semenov's (1963) studies of turbulent gas flow in piston engines is regarded as fundamental. Hot-wire anemometry (HWA) studies in a motored engine with a flat top piston showed that shear flow through the intake valve was the primary source of turbulence generation, followed by decay during the compression stroke and relaxation toward isotropic turbulence at top-dead-center.

Andrews et al. (1976) have demonstrated in combustion bomb studies that burning velocity is nearly a linear function of turbulence intensity. Turbulence in spark-ignition engines is generated by the shear-flow that occurs during the intake process, and by the squish motion as the piston approaches the cylinder head just before top-dead-center. In most cases, however, much of the turbulence generated during the intake stroke decays before the combustion process is started. Squish-generated turbulence, on the other hand, is generated during the last phase of the compression stroke, just before it is most needed to influence the combustion process. Nakamura et al. (1976) discovered that the introduction of a small diameter jet of air into the combustion chamber through a third valve just before ignition resulted in a significant increase in burning rate and

---

Contributed by the Internal Combustion Engine Division and presented at the 17th Annual Fall Technical Conference of the ASME Internal Combustion Engine Division, Milwaukee, Wisconsin, September 24–27, 1995. Manuscript received at ASME Headquarters May 1997. Associate Technical Editor: W. K. Cheng.

a substantial improvement in engine performance. The air jet evidently brought about an enhancement of the turbulence field near the spark plug, leading to a significant increase in the combustion rate.

Tri-axial HWA measurements were carried out by Lancaster et al. (1976) in a motored engine with and without swirl, which was generated by a shrouded intake valve. His studies confirmed isotropy and showed that the swirl intensity increased linearly with engine speed. Similar investigations by others (Winsor and Patterson, 1973; Witze, 1977; Bopp et al., 1986; Daneshyar and Fuller, 1986), also showed isotropy and scaling with engine speed.

Lancaster (1986) conducted one of the first correlation studies of turbulence and combustion data using HWA and heat release model techniques. Comparison of a disk chamber for a swirl and a nonswirl case showed that the normalized flame speed was a linear function of turbulence intensity, with little influence of turbulent scale within the limits of measurements. Other researchers (Dohring, 1986; Nagayana et al., 1977; Matekunas et al., 1983) also found strong effects of turbulence on combustion. Unfortunately, this intake-generated turbulence intensity decreases with the approach of the piston to top-dead-center, the point around which ignition and combustion occur in an internal combustion engine (Tippett, 1989). An extended turbulence field in the combustion chamber can be maintained by, for example, an intake jet-valve application, squish, and/or swirl in the combustion chamber (Heywood, 1988).

Studies of optimizing turbulence by combustion design with emphasis on squish have shown (Heywood, 1984) that the optimum chamber design should provide: fast–burn for high efficiency; good emission control through large valve effective areas; low wall surface areas to minimize heat loss and avoid quenching; and should be geometrically practical for manufacture.

Gruden's (1981) investigation of combustion chamber layout in modern passenger cars showed that a combustion chamber located in the piston crown was the simplest way to meet these requirements. In line with Young's (1980) optimization criterion of an open and compact chamber, Gruden concluded that the dimensions and the positions of the quench areas and the quench distance, i.e., maximum flame travel, were important.

Overington and Thring (1981), on a Ricardo Hydra engine with variable compression ratio and combustion chambers in the head and piston, showed a 2 to 5 percent improvement in fuel economy for the chamber in the crown over that of the head chamber. This improvement could result from higher turbulence during combustion induced by squish.

The squish effect, reviewed by Young (1980), and predominant in diesel configurations, gave conflicting results. Although more recent studies in diesel engines (Shimoda et al., 1985; Jane, 1988) provide information on squish and swirl interactions, and the effects of combustion chamber shape on fluid motion, only limited comparison can be made with SI engines.

Evans (1986) proposed and patented a variation of the standard bowl-in-piston squish design using channels in a bowl-in-piston chamber to enhance the squish effect through developed jets. Cameron (1985) and Evans and Cameron (1986) evaluated this design analytically with HWA and combustion pressure measurements in a CFR engine. Initial results showed increased peak pressure and reduced combustion duration compared with standard bowl-in-piston squish pistons.

Subsequent investigations carried out by Jones and Evans (1985) and Dymala-Dolesky (1986) evaluated the nature of the jets developed. These jets in general diminished the effect of the main squish motion. Indicated Mean Effective Pressure covariance calculations, and mass fraction burned analysis, indicated that the squish jet was most effective in the latter half of combustion. The most promising chamber was with eight jets angled toward the spark location toward the center of the bowl.

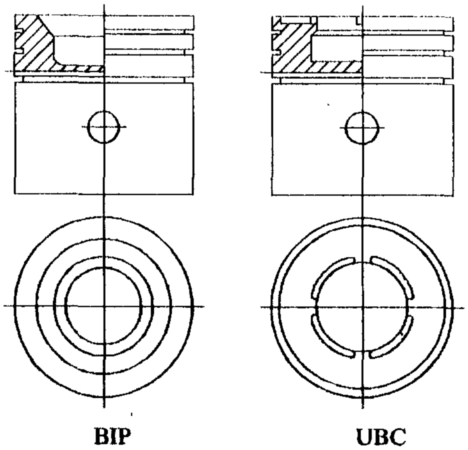

Fig. 1 "Bowl-in-piston" and UBC "squish-jet" combustion chambers

Evans et al. (1987, 1990a, 1990b), Milane et al. (1987) and Mawle (1989) published results of experiments on the influence of combustion chamber design on turbulence enhancement in a fast, lean-burning engine. Potential was found for the squish jet action to improve engine efficiency and increase the knock limit. Reduced coefficient of variance of Indicated Mean Effective Pressure and reduced ignition advance requirements were exhibited.

Evans and Blaszczyk (1991a, 1992a, b, c) completed an R&D project on fast-burn combustion chamber development and published more results of experiments on the squish-jet combustion chamber design and its influence on combustion of lean mixtures.

Combustion Chamber Design

The combustion chamber design investigated here is based on the principle of using squish motion to generate a series of jets directed toward the center of the chamber just prior to ignition. A family of chambers utilizing this concept, and referred to as "squish-jet" combustion chamber designs, have been patented by Evans (1991b). The chamber used in this study, referred to as the UBC "Squish-Jet" chamber, is shown in the piston drawing of Fig. 1 along with a conventional "Bowl-in-Piston" (BIP) chamber. The UBC combustion chamber incorporates a recess machined into the piston crown, which, in conjunction with a flat cylinder head, results in a cavity, which traps mixture as the piston nears top-dead-center. A small outlet passage from the cavity then results in the mixture being squished out as a series of jets directed toward the main bowl in the center of the piston crown as the piston nears the end of its stroke. These "squish jets" generate high levels of turbulence as they penetrate into the center of the bowl. By carefully choosing the dimensions of both the pocket in the piston crown, and the outlet passages, the scale of turbulence, as well as the intensity, can be controlled. The performance of this chamber was compared to the performance of a conventional "bowl-in-piston" chamber, which was utilized as the base case. In both cases a clearance height of 1.7 mm was used, and the piston bowl depth was machined to obtain a compression ratio of 10.2:1.

The squish area for each piston was determined as a percentage of the total surface area of the piston. For the simple bowl-in-piston, this is given by:

$$S\% = 100\%*(D^2 - d^2)/D^2$$

where D is the piston bore and d is the bowl diameter. The BIP piston squish area was 45 percent and the UBC design piston had a squish area of 75 percent. The volume of the recesses in

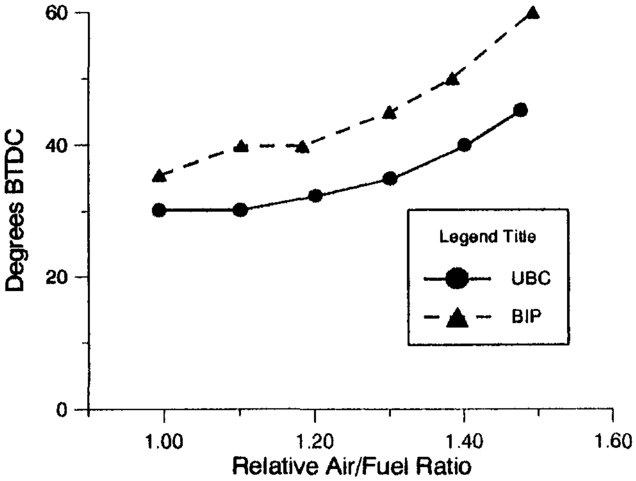

Fig. 2 MBT ignition timing

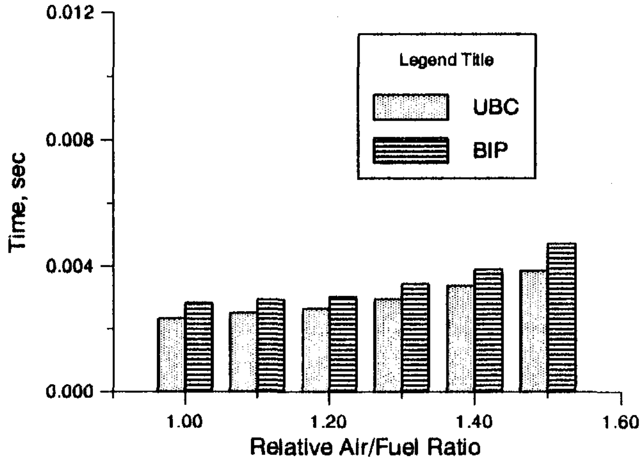

Fig. 3 Comparison of 0 to 10 percent charge burned times

the squish area was compensated for in the depth of the main (central) cavity so that the resulting compression ratio was always the same.

Test Facilities

The test engine was a Ricardo Hydra single-cylinder research engine connected to a D.C. motor/dynamometer. The Ricardo Hydra engine, described in detail by French (1983), has a displacement of 450 cc and utilizes a single overhead camshaft. The standard Hydra cylinder head, which incorporates a "bathtub" type of combustion chamber, was replaced with a flat cylinder head for use with the bowl-in-piston type of combustion chambers examined in this study. The engine is fully instrumented to obtain all standard performance measurements and is also connected to an exhaust emissions bench, which contains analyzers for measuring CO_2, CO, CH_4, THC, NO_x, and O_2. The bench also contains equipment for condensing water vapor from the exhaust gas sample.

All of the engine instrumentation is connected to a microcomputer-based data acquisition system consisting of a PC and a PCL818 data acquisition board. A software package was written to scan 16 channels of data coming from the engine and emissions bench, and to either display it or store it for further analysis. Up to 400 values are read from each channel and then averaged before being stored or updated on the computer screen. The measured torque is corrected by the program to standard SAE conditions and is then used to calculate brake-specific quantities. Up to 38 different parameters, either in the form of raw data or calculated variables, can be stored on a floppy disk for further processing or viewing following engine testing. During operation, any of these variables can be displayed and updated every few seconds on the computer screen. Due to screen-size limitations, however, only 16 variables can be displayed at one time, but these 16 can be selected or changed at any time during the test run.

Results

All of the test results reported in this paper were obtained using natural gas as a fuel. Natural gas was used since it is known to have a combustion rate significantly lower than that of gasoline (Jones and Evans, 1985), and is therefore particularly useful for testing the effectiveness of fast-burn combustion chambers. Measurements of engine performance and exhaust emissions for both the base-case BIP and UBC chambers were taken over a range of air–fuel ratios ranging from stoichiometric to the lean limit of combustion. The results are shown as a function of the relative air–fuel ratio (RAFR), where RAFR = 1.0 represents the stoichiometric air–fuel ratio, and values greater than 1.0 denote lean conditions. All of the results shown here are for an engine speed of 2000 rpm with a wide-open throttle and MBT (minimum advance for best torque) spark advance.

The relationship between minimum spark advance for best torque (MBT) ignition timing and relative air–fuel ratio (RAFR) for both pistons is shown in Fig. 2. Early ignition is usually accompanied by an increased level of exhaust emissions; therefore, an engine exhibiting a reduced MBT ignition advance is normally preferred. MBT ignition timing increases with increasing RAFR, which corresponds to decreasing flame velocities with lean mixtures. MBT timing for the BIP piston was 5 deg more advanced than that for the UBC piston at rich mixture conditions, and this difference increased to 15 deg at an RAFR of 1.5. These results indicate that the UBC chamber results in a significantly faster combustion rate than does the base case, particularly at values of the relative air–fuel ratio greater than 1.1.

The faster burning rate is confirmed by the mass-burned fraction results obtained by analyzing cylinder pressures. The time required to burn the first 10 percent of the mixture is shown in Fig. 3, and the time required to burn 10 to 90 percent of the mixture can be seen in Fig. 4. It is interesting to note that in each case it takes only twice the time to burn 80 percent of the mixture as it takes to burn the first 10 percent, indicating the importance of the early combustion period. At all air–fuel ratios the UBC chamber results in a reduction of the time to burn the

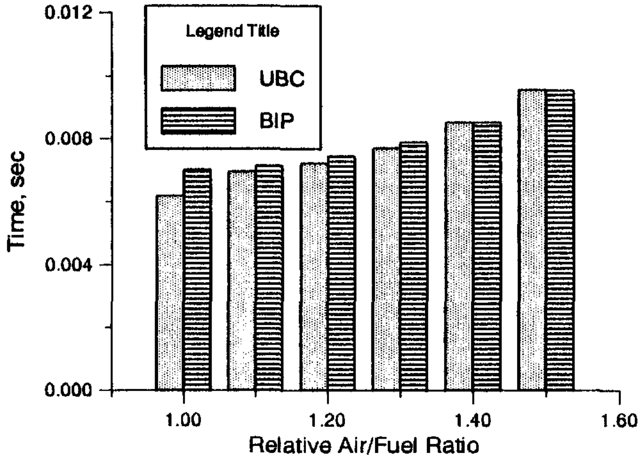

Fig. 4 Comparison of 10 to 90 percent charge burned times

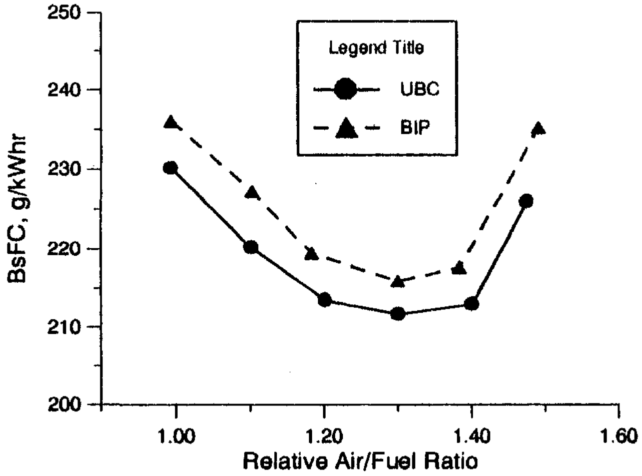

Fig. 5 Brake specific fuel consumption versus RAFR

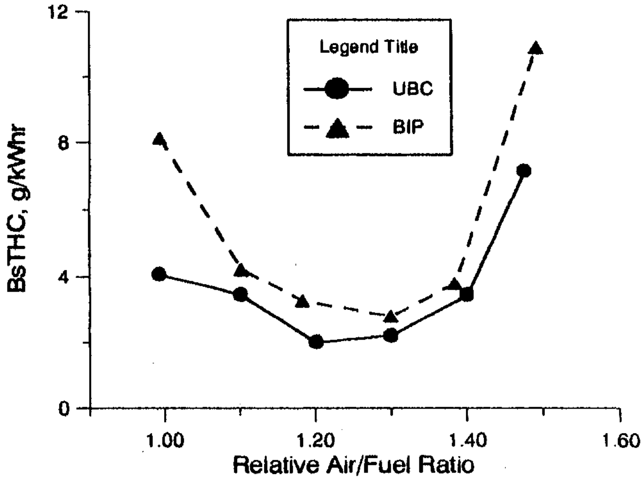

Fig. 7 Brake-specific total hydrocarbons versus RAFR

first 10 percent of the mixture as well as a reduction of the total combustion time compared to the base-case.

The brake-specific fuel consumption (BsFC) is shown for both the UBC and the base-case chambers in Fig. 5. The increased burning rate with the new chamber translates into approximately a 3 percent reduction in BsFC. The reduction is significantly greater at values of the relative air–fuel ratio around 1.5, however, evidently due to the base-case chamber approaching the lean combustion limit earlier. For both cases the minimum BsFC occurs at a relative air–fuel ratio of about 1.3, in common with results for most spark-ignition engines. The improvement in BsFC is due, at least in part, to the reduced time available for heat transfer from the hot combustion gases to the cylinder walls, and to the reduction in the MBT spark advance.

Another indication of increased thermal efficiency is shown by the BMEP values of the engine operating with Wide-Open-Throttle, as shown in Fig. 6. The BMEP values of the engine operating with the UBC chamber are approximately 5 percent higher than those for the base-case chamber at stoichiometric mixtures, and this difference increases slightly with increasing air–fuel ratio.

Figure 7 shows the brake-specific total unburned hydrocarbon (BsTHC) emissions for both chambers as a function of relative air–fuel ratio. It should be noted that the values are total hydrocarbon emissions, a large part of which are known to be methane emissions when natural gas is the fuel. As methane is not a very reactive gas, it does not contribute significantly to smog formation, and so is not considered in the emissions regulations by most authorities. The brake specific total hydrocarbons emissions are 20 to 50 percent lower for the UBC chamber than those for the BIP chamber.

Previous experience indicates that about 90 percent of the THC emissions from natural-gas-fueled engines consist of unregulated methane emissions. The emission levels of nonmethane hydrocarbons should therefore be below the U.S. EPA heavy-duty engine limit of 1.7 g/kW-h with the UBC chamber up to a relative air–fuel ratio of approximately 1.5.

The relationship between oxides of nitrogen and RAFR is shown in Fig. 8. For both combustion chamber designs the NO_x emission from the engine followed the classical relationship with maximum NO_x occurring at RAFR slightly leaner than stoichiometric. However, the NO_x emissions at their peak values are about 20 percent lower with the UBC chamber than those with the base-case chamber. With increasing air–fuel ratio this difference reached a maximum of 50 percent in favor of the UBC chamber.

There would appear to be an operating envelope between RAFR values of 1.35 and 1.5 that would result in operation with emission levels below the U.S. EPA heavy-duty engine limits of 6.7 g/kW-h without the use of a catalytic converter.

The emissions of carbon monoxide versus air–fuel ratio are shown in Fig. 9. At mixtures leaner than RAFR = 1.1, the CO emission level for both chamber designs increased by a factor

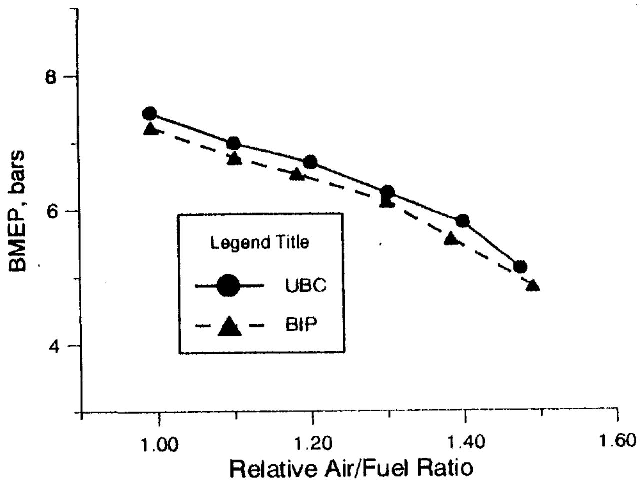

Fig. 6 Brake mean effective pressure versus RAFR

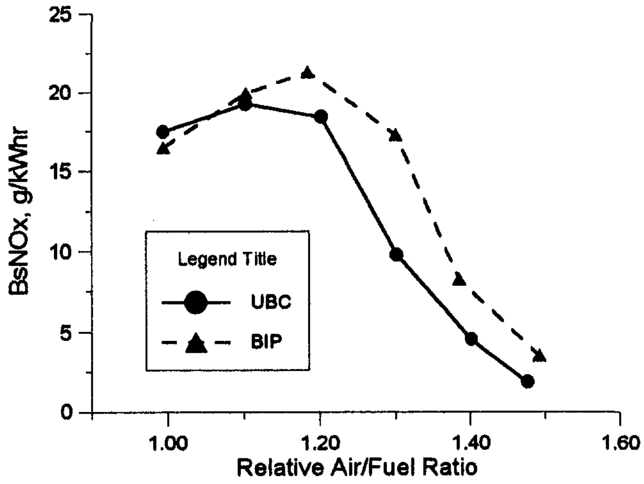

Fig. 8 Brake-specific nitrogen oxide versus RAFR

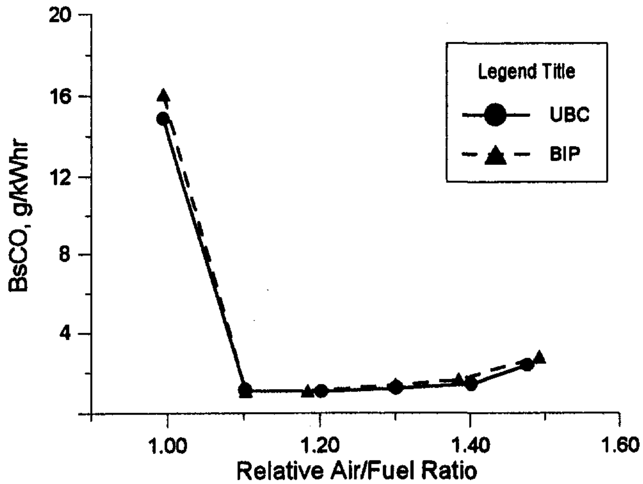

Fig. 9 Brake-specific carbon monoxide versus RAFR

of nearly three compared to the minimum value. However, as long as the air–fuel ratio is kept leaner than RAFR = 1.1, CO emissions are below the regulated limit. The UBC chamber demonstrated nearly 15 percent lower CO emissions than those of the BIP chamber at RAFR = 1.4.

Conclusions

Combustion chamber design has been shown to be an important factor in determining the thermal efficiency and exhaust emissions for a spark-ignition engine. These parameters are greatly affected by the burning rate in the combustion chamber, which is in turn controlled by both the intensity and scale of the mixture turbulence just prior to ignition and during the combustion process. A new family of fast-burn combustion chamber designs, which utilize squish-motion to create a series of turbulence-generating jets as the piston nears top-dead-center, has been found to result in increased burning rates. The faster burning rate leads to an average 3 percent reduction in brake-specific fuel consumption, 5 percent increase in BMEP, and an increase in the lean limit of combustion. The exhaust emissions were lower for the UBC chamber than those for the BIP chamber: BsTHC and $BsNO_x$ lower by 20 to 50 percent, and BsCO up to 15 percent lower. The observations based on the performance tests were confirmed by the mass-burn fraction results, which showed the UBC chamber resulted in significantly faster burning compared to the base case, particularly in the 0 to 10 percent charge-burned time. The UBC chamber design should enable an engine operating with lean air–fuel ratios to meet the U.S. EPA heavy-duty emissions regulations without the use of exhaust gas clean-up equipment.

Acknowledgments

The authors would like to express their appreciation to the Transportation Development Centre of Transport Canada for their support of the research described in this paper through the funding provided under the PERD program. In particular they would like to thank Mr. Roy Nishizaki, the Transport Canada Scientific Authority, for his continuing support and encouragement.

References

Andrews, G. E., Bradley, D., and Lwakabamba, S. B., 1976, "Turbulence and Turbulent Flame Propagation—a Critical Appraisal," *Combustion and Flame,* Vol. 24, pp. 285–304.

Bopp, S., Vafidis, C., and Whitelaw, J. H., 1986, "The Effect of Engine Speed on the TDC Flow Field in a Motored Reciprocating Engine," SAE Paper No. 860023.

Cameron, C., 1985, "An Investigation of Squish Generated Turbulence in IC Engines," M.Sc. Thesis, (AFL-85-02), University of British Columbia, Vancouver, B.C., Canada.

Daneshyar, H., and Fuller, D. E., 1986, "Definition and Measurement of Turbulence Parameters in Reciprocating IC Engines," SAE Paper No. 861529.

Dohring, K., 1986, "The Relative Effects of Intake and Compression Stroke Generated Turbulence on I.C. Engine Combustion Duration," UBC Alternative Fuels Laboratory Report, AFL-86-01, University of British Columbia, Vancouver, B.C., Canada (not published).

Dymala-Dolesky, R., 1986, "The Effects of Turbulence Enhancements on the Performance of a Spark-Ignition Engine," M.Sc. Thesis, University of British Columbia, Vancouver, B.C., Canada.

Evans, R. L., 1986, "Internal Combustion Engine Squish Jet Combustion Chamber," US Patent No. 4,572,123.

Evans, R. L., and Cameron, C., 1986, "A New Combustion Chamber for Fast Burn Applications," SAE Paper No. 860319.

Evans, R. L., and Dohring, K. W., 1987, "A Rapid Intake and Compression Machine for Fundamental Combustion Research," presented at the Energy-Sources Technology Conference and Exhibition, Dallas, TX.

Evans, R. L., and Tippett, E. C., 1990a, "The Effects of Squish Motion on the Burn-Rate and Performance of a Spark-Ignition Engine," presented at SAE Technical Paper Series, Future Transportation Technology Conference and Exposition, San Diego, CA.

Evans, R. L., Tippett, E. C., and Mawle C. D., 1990b, "Fast-Burn Combustion Chamber Design for Natural Gas Fuelled Spark-Ignition Engines," *Proc. Combustion Institute Spring Technical Meeting,* Banff, Canada, pp. 20–22.

Evans, R. L., and Blaszczyk, J., 1991a, "Fast-Burn Combustion Chamber Development," CGA R&D Project Technical Report #200-1.5, Sept. (not published).

Evans, R. L., 1991b, "Improved Squish-Jet Combustion Chamber," U.S. Patent No. 5,065,715.

Evans, R. L., and Blaszczyk, J., 1992a, "Combustion Chamber Design for a Lean-Burn SI Engine," *Proc. Spring Technical Meeting of Combustion Institute, Canadian Section,* University of Alberta, pp. 73–76.

Evans, R. L., and Blaszczyk, J., 1992b, "Low-Emission Combustion Chamber Design," 25th ISATA International Symposium on Automotive Technology and Automation, Florence, Italy, Paper #920420.

Evans, R. L., and Blaszczyk, J., 1992c, "Combustion Chamber Design for a Lean-Burn SI Engine," SAE Paper No. 921545.

French, C. C. J., 1983, "A Universal Test Engine for Combustion Research," SAE Paper No. 830453.

Gruden, D. O., 1981, "Combustion Chamber Layout for Modern Otto Engines," SAE Paper No. 811231.

Heywood, J. B., 1988, *Internal Combustion Engine Fundamentals,* McGraw-Hill, New York, pp. 326–370.

Heywood, J. B., 1984, "Combustion Chamber Design for Optimum Spark Ignition Engine Performance," *International Journal of Vehicle Design,* Vol. 5, No. 3, pp. 133–147.

Jane, P. A. H., 1988, "The Development of a Direct Injection Diesel Combustion System for Low Noise Emissions and Mechanical Loading," *C66/68 IMechE.*

Jones, A. L., and Evans, R. L., 1985, "Comparison of Burning Rates in a Natural Gas Fuelled Spark-Ignition Engine," ASME JOURNAL OF ENGINEERING FOR GAS TURBINES AND POWER, Vol. 4, pp. 908–913.

Lancaster, D. R., 1986, "Effects of Engine Variables on Turbulence in a Spark Ignition Engine," SAE Paper No. 760159.

Lancaster, D. R., Kreiger, R. B., et al., 1976, "Effects of Turbulence on Spark Ignition Engine Combustion," SAE Paper No. 760160.

Matekunas, F. A., 1983, "Modes and Measures of Cyclic Variability," SAE Paper No. 830337.

Mawle, C. D., 1989, "The Effects of Turbulence and Combustion Chamber Geometry on Combustion in a Spark Ignition Engine," UBC Alternative Fuels Laboratory Report AFL-89-02, University of British Columbia, Vancouver, B.C., Canada (not published).

Milane, R. E., Evans, R. L., and Hill P. G., 1987, "Combustion and Turbulent Structure in a Closed Chamber With Swirl," *Comb. Sci. and Tech.,* Vol. 51, pp. 1–20.

Nagayana, I., Araki, Y., and Lioka, Y., 1977, "Effects of Swirl and Squish on SI Engine Combustion and Emission," SAE Paper No. 770217.

Nakamura, H., et al., 1976, "Development of a New Combustion System (MCA-Jet) in Gasoline Engine," SAE Paper No. 790016.

Overington, M. T., and Thring, R. H., 1981, "Gasoline Engine Combustion Turbulence and the Combustion Chamber," SAE Paper No. 810017.

Semenov, E. S., 1963, "Studies of Turbulent Gas Flow in Piston Engines," *Tech. Trans.,* F97 NASA.

Shimoda, M., et al., 1985, "Effect of Combustion Chamber Configuration on In-Cylinder Air Motion and Combustion Characteristics of CI Diesel Engine," SAE Paper No. 850070.

Tippett, E. C., 1989, "The Effects of Combustion Chamber Design on Turbulence, Cyclic Variation and Performance in an SI Engine," UBC Alternative Fuels Laboratory Report, AFL-89-01, University of British Columbia, Vancouver, B.C., Canada (not published).

Winsor, R. E., and Patterson, D. J., 1973, "Mixture Turbulence—A Key to Cyclic Combustion Variation," SAE Paper No. 730086.

Witze, P. O., 1977, "Measurements of Spatial Distribution and Engine Speed Dependence of Turbulent Air Motion in an IC Engine," SAE Paper No. 770220.

Young, M. B., 1980, "Cyclic Dispersion—Some Quantitative Cause-and-Effect Relationships," SAE Paper No. 800459.

Primary Atomization and Spray Analysis of Compound Nozzle Gasoline Injectors

J. L. Chen

M. Wells

J. Creehan

Powertrain Control Systems Division,
Visteon Automotive Systems,
Ypsilanti, MI 48197

This work addresses primary atomization modeling, multidimensional spray prediction, and flow characteristics of compound nozzle gasoline injectors. Compound nozzles are designed to improve the gasoline spray quality by increasing turbulence at the injector exit. Under the typical operating conditions of 270-1015 kPa, spray atomization in the compound nozzle gasoline injectors is mainly due to primary atomization where the flow turbulence and the surface tension are the dominant factors. A primary atomization model has been developed to predict the mean droplet size far downstream by taking into account the effect of turbulent intensity at the injector exit. Two multidimensional spray codes, KIVA-2 and STAR-CD, originally developed for high-pressure diesel injection, are employed for the lower-pressure gasoline injection. A separate CFD analysis was performed on the complex internal flows of the compound nozzles to obtain the initial and boundary conditions for the spray codes. The TAB breakup model used in KIVA-2 adequately facilitates the atomization process in the gasoline injection.

Introduction

Gasoline injectors, unlike diesel injectors, are usually operated at a lower pressure drive (the pressure difference between injector inlet and outlet) of 270-1015 kPa (~40–150 psi). In this range, slow liquid jets are formed at the injector exits. The aerodynamic forces (as a result of relative motions between the jet and the surrounding air) are not strong enough to break the liquid jet into small droplets. Most of the droplets are formed from the primary atomization where flow turbulence is the dominant factor. To improve the atomization process and the spray quality, a compound nozzle is attached to a gasoline injector to increase the turbulence at the injector exit. Figure 1 shows a schematic of a typical compound gasoline injector. The compound nozzle consists of two sets of nozzles, with one top nozzle beneath the needle and four bottom nozzles to direct the flow. Four orifices are located at the top of the four bottom nozzles, where the flow areas are smallest in the compound nozzles. There are two primary objectives in this work: first, to develop a primary atomization model to estimate the mean droplet size at gasoline injector far downstream; second, to test the capability of two popular spray codes, KIVA-2 and STAR-CD, for gasoline injection.

Wu et al. (1992) examined primary atomization in turbulent jets. They believed that the droplets formed at the onset of turbulent primary atomization are the smallest droplets that can be formed. The size of the smallest droplets is comparable to the smallest size of turbulent eddies whose kinetic energy is large enough to overcome the surface energy. By assuming a constant turbulent intensity in a simple turbulent jet, they proposed a semi-empirical correlation to predict the droplet size formed during primary atomization. However, there is a major flaw in this approach: Turbulent intensity at the orifice is assumed to be constant, which is not true for comprehensive injectors. In this work, a primary atomization model is developed by including the effect of turbulent intensity in predicting the mean droplet size.

In addition to the mean droplet size, other multidimensional spray features such as spray angle, volume distribution, and droplet size distribution are important in characterizing injector performance. To predict the detailed spray structures, two multidimensional computer codes, KIVA-2 (O'Rourke and Amsden, 1987) and STAR-CD (v. 2.2.1) (Computational Dynamics LTD, 1994) were employed. Spray models in both KIVA-2 and STAR-CD codes were originally developed for diesel injection, which is operated at a much higher pressure. In the KIVA-2 code, the TAB (Taylor Analogy Breakup) model is used to predict spray breakup and in STAR-CD, the Bag and Stripping breakup models are used. Successful work using KIVA-2 in diesel injection and combustion has been reported (Liu et al., 1993; Kong and Reitz, 1993; Beatrice et al., 1995). However, little work on KIVA-2 and STAR-CD spray prediction has been done in gasoline injection, which has different spray breakup mechanisms. We need to test these two codes' capability in predicting gasoline sprays before using them extensively on gasoline injectors.

To run these two spray codes, we have to specify the boundary and initial conditions at the injector exit (orifice), such as spray velocity and angle, turbulence properties, and the initial droplet size. For a diesel injector with a simple nozzle, these boundary conditions can be estimated from the fully developed pipe flows. However, for a compound nozzle gasoline injector, the flow characteristics are complex and cannot be estimated through a simple classical analysis. A separate computational fluid dynamics (CFD) simulation on the injector internal flow is required to provide the proper boundary conditions for KIVA-2 and STAR-CD.

The processes in predicting the multidimensional spray structure and the mean droplet size far downstream are summarized in Fig. 2. To use the KIVA-2 and STAR-CD codes for multidimensional spray prediction, the appropriate spray breakup models are selected, and the initial droplet sizes and velocities assigned. On the other hand, prediction of the mean droplet size is dependent on the primary atomization model, the flow properties at the orifice, and the characteristic length. To obtain the initial conditions for the spray codes and the flow properties at the orifice, a CFD analysis in the internal flow is performed. Thus, for a comprehensive compound nozzle injector, the quality of spray and droplet prediction relies on accuracy of the injector internal flow prediction.

Model Formulation

Primary Atomization. As discussed by Lefebvre (1989), primary atomization is related to jet breakup by the action of

---

Contributed by the Internal Combustion Engine Division for publication in the JOURNAL OF ENGINEERING FOR GAS TURBINES AND POWER. Manuscript received at ASME Headquarters July 1997. Associate Technical Editor: W. K. Cheng.

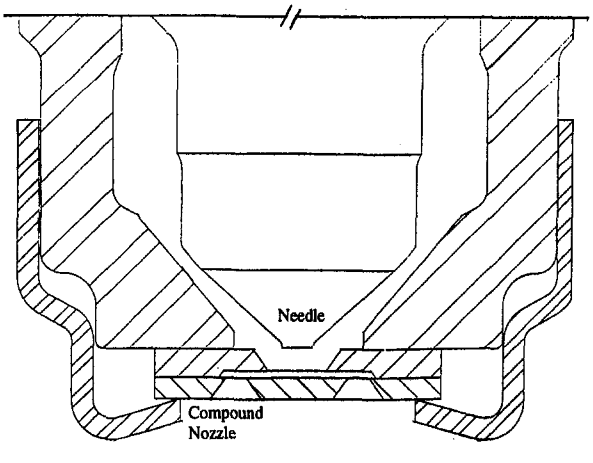

(a) Schematic diagram of a typical compound nozzle injector

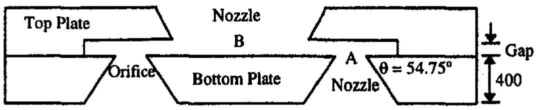

(b) Side view of the CSMM nozzle

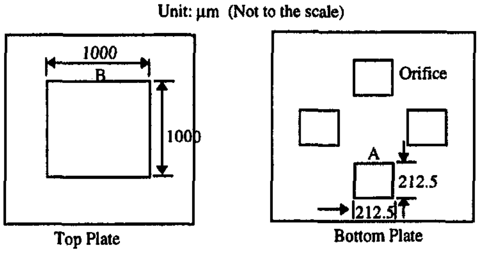

(c) Bottom view of the top plate and top view of the bottom plates of CSMM nozzle

Fig. 1 Schematic of a typical compound nozzle and dimension of the CSMM nozzle

internal forces, such as turbulence, inertial forces, and surface tension. The effects of aerodynamic forces, as a result of relative motions between the jet and the surrounding air, are much smaller.

Primary Atomization by Wu et al. (1992). Wu et al. (1992) believe the droplets produced at the onset of turbulent primary atomization are the smallest droplets that can be formed. The size of the smallest droplets is comparable to one of two scales. The first is the turbulence smallest scale, i.e., the Kolmogorov microscale. The second is related to the smallest size of turbulent eddies whose kinetic energy is large enough to overcome the surface energy and to form the smallest droplets. In their test conditions, the Kolmogorov length scale is 1–10 μm, which is much smaller than the typical smallest droplets observed experimentally. Thus, the turbulent eddy mechanism is concluded to be the only possibility and the energy balance exists as in Eq. (1) when a droplet is formed from a turbulent eddy:

$$\pi\rho_f l^3 v_l^2/12 \sim \pi l^2 \sigma$$

[kinetic energy of an eddy]

~ [surface energy required to form a droplet] (1)

where l is the characteristic size of the eddy at the initiation of the breakup and the eddy has a velocity relative to the surrounding, v_l. Due to the effect of the streamwise velocity, w_o, the eddy could be an elongated shape. The droplet formed by this eddy is assumed to have a diameter comparable to l. In order to form the droplet, l must be smaller than the largest eddies (comparable to the orifice size, Λ) and greater than the smallest dissipative eddies (comparable to the Kolmogorov length scale); therefore, it is reasonable to assume l is within the inertial spectrum. Thus, l and v_l can be related to the largest scales through the energy balance as

$$(v_l^2)(v_l/l) \sim (\overline{v_o'^2})(\overline{v_o'}/\Lambda) \Rightarrow v_l \sim \overline{v_o'}(l/\Lambda)^{1/3} \qquad (2)$$

where $\overline{v_o'}$ is the time-averaged root-mean-square fluctuating velocity at the injector orifice and Λ is the radial length scale. Combining Eqs. (1) and (2) and setting SMD (Sauter mean diameter) ~ l and assuming the turbulence properties in the liquid can be approximated by the jet exit turbulence properties, the following equation is obtained for the SMD at the onset of breakup:

$$\frac{\mathrm{SMD}}{\Lambda} = C_s\left(\frac{w_o}{\overline{v_o'}}\right)^{6/5}\left(\frac{\rho_f w_o^2 \Lambda}{\sigma}\right)^{-3/5} = C_s\left(\frac{w_o}{\overline{v_o'}}\right)^{6/5} \mathrm{We}_{f,\Lambda}^{-3/5} \qquad (3)$$

where w_o is the mean streamwise velocity at the injector exit, and C_s is the empirical breakup constant, and $\mathrm{We}_{f,\Lambda}$ is the Weber number at the orifice.

For fully developed turbulent pipe flows, the turbulent intensity ($=\overline{v_o'}/w_o$) is essentially a constant (Hinze, 1975; Schlichting, 1979). Therefore, SMD/Λ in Eq. (3) can be expressed as a function of $\mathrm{We}_{f,\Lambda}$ only. From test data obtained from a simple turbulent jet, Wu et al. proposed an empirical fit:

$$\mathrm{SMD}/\Lambda = 133\ \mathrm{We}_{f,\Lambda}^{-0.74} \qquad (4)$$

The power of $\mathrm{We}_{f,\Lambda}$ is reduced from $-\frac{3}{5}$ in Eq. (3) to -0.74 in Eq. (4) for the best correlation in test data. Note that Eq. (4) is only applicable to the sprays when the jet exit properties are similar to those of a fully developed turbulent pipe flow.

The Modified Primary Atomization Model. The modified primary atomization model is an improvement over the model developed by Wu et al. (1992). The effect of turbulent intensity on spray breakup is taken into account in this model. For a

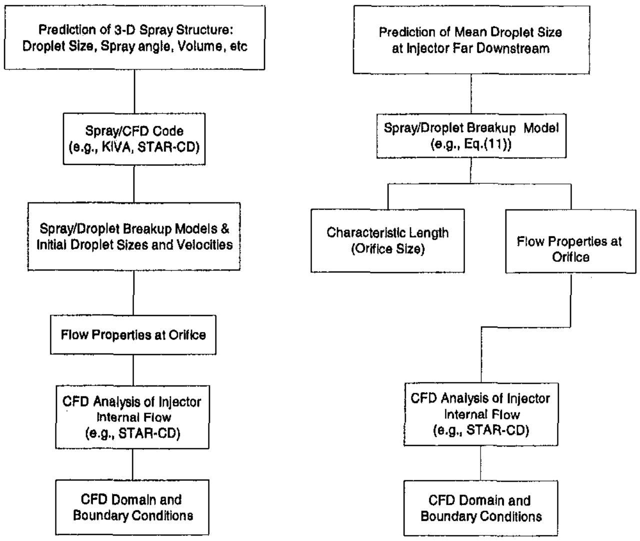

(a) Prediction of 3-D Spray Structure

(b) Prediction of mean droplet size at injector far downstream

Fig. 2 Flow charts showing processes of predicting three-dimensional spray structure and the mean droplet size at injector far downstream

comprehensive injector such as the compound nozzle gasoline injector, the turbulent intensity in the liquid jet is not constant. Equation (4), developed by Wu et al. (1992), is only valid for a simple turbulent jet and it predicts wrong droplet sizes for the compound nozzle gasoline injectors. Before modifying the primary atomization model of Wu et al. for compound nozzle gasoline injectors, we have to rule out the possibilities of (1) secondary atomization (where aerodynamic force is important); and (2) the typical droplet size in the range of the Kolmogorov length scale. The Weber number (based on gas properties, $\mathrm{We}_{g,\Lambda}$) for a typical compound nozzle injector under a pressure drive of 270 kPa is about 1.8, which is too small to initiate the secondary atomization. The critical Weber number to initiate the secondary atomization is 3.6 to 8.4 (Reitz and Diwakar, 1986). The Kolmogorov length scale ($=(\nu^3/\epsilon)^{0.25}$; ν is the kinetic viscosity and ϵ is the turbulent dissipation) of these injectors at current operating condition is several microns. This length scale is much smaller than the typical droplet size of 40–130 μm. Thus, the basic assumptions in forming the primary atomization model for a simple turbulent jet are also valid for gasoline compound injectors.

By assuming that the isotropic turbulence at the injector exit, Eq. (3) can be rearranged to

$$\mathrm{SMD} \sim \frac{\sigma^{3/5}\Lambda^{2/5}}{\rho_f^{3/5}\overline{v_o'}^{6/5}} \sim \frac{\sigma^{3/5}\Lambda^{2/5}}{\rho_f^{3/5}\bar{k}_o^{3/5}} \tag{5}$$

where $\bar{k}_o$ is the average turbulent kinetic energy at the orifice. Equation (5) indicates that a liquid jet with a large turbulent kinetic energy at the orifice will produce small droplets. If we view the droplet formation as a result of the outer layer of the jet being "peeled off," the droplets formed near the injector exit will be smaller than those formed downstream. This is because the turbulent kinetic energy at the jet edge is usually higher than that at the jet center. As the liquid jet travels downstream, the average turbulent kinetic energy is smaller after some outer layers of the jet are peeled off to form droplets. Photographs taken by Lai et al. (1994) confirm that small droplets formed at the compound nozzle exit and larger droplets at downstream.

In our approach, we assume that various sizes of droplet are formed as the liquid jet travels downstream. Unlike the assumption of one size of SMD $\sim l$ (the eddy size) at the onset of primary atomization (Wu et al., 1992), we assume the droplets produced at different downstream locations are a function of the jet property at these locations. The droplet size, d_L, formed at a downstream location, L, is assumed to be comparable to the smallest eddy size at that location. Therefore, Eq. (5) can be expressed as

$$d_L \sim \left(\frac{\sigma\Lambda^{2/3}}{r_f}\right)^{3/5}\left(\frac{1}{\bar{k}_L}\right)^{3/5} \sim \bar{k}_L^{-3/5} \tag{6}$$

where $\bar{k}_L$ is the average of turbulent kinetic energy at the downstream location L. Since the droplets formed at the expense of the liquid jet's outer edge, the fluid with higher turbulent kinetic energy is transformed into droplets. As a result, the average turbulent kinetic energy of the jet, $\bar{k}_L$, decreases as the jet travels downstream.

At the compound nozzle orifice, the turbulent kinetic energy distributes from a high value near the walls, to a low value at the center. The mean turbulent kinetic energy is dominated by the outer region because the flow area and turbulent kinetic energy of the outer region are larger than those in the inner region. Thus, at any downstream location, L, the mean turbulent kinetic energy of the jet is in proportion to that of a small layer at the jet edge, r_L. This gives an overestimate of effective turbulent kinetic energy for producing d_L and can be corrected through correlation with the test data. Thus, Eq. (6) can be expressed as

$$d_L \sim \bar{k}_L^{-3/5} \sim k_L^{-3/5}|_{r=r_L} \tag{7}$$

where r_L is a function of the location, L, and r_L decreases as L increases.

We follow the assumption used by Wu et al. (1992), that the turbulence properties of the downstream jet are approximated by those at the jet exit, i.e.,

$$k_L|_{r=r_L} \sim k_o|_{r=r_L} \tag{8}$$

where the subscript o denotes the orifice and k_o is the turbulent kinetic energy at the orifice, which is a function of the radial position. Combining Eqs. (7) and (8) and assuming SMD is the mean value of d_L in the region from the injector exit to the full atomization region, say at the downstream location of Z, one can develop the equation for SMD as

$$\mathrm{SMD} \sim \frac{\int_o^Z (d_L)dz}{Z} \sim \frac{\int_o^Z \bar{k}_L^{-3/5}dz}{Z} \sim \frac{\int_o^{r_o} k_o^{-3/5}|_{r=r_L}\, r_L dr_L}{\pi r_0^2} \sim \overline{k_o^{-3/5}} \tag{9}$$

where r_o is the orifice radius. Note that $\overline{k_o^{-3/5}}$ is the surface average of the variable $k_o^{-3/5}$, and $\bar{k}_o^{-3/5}$ is the variable $\bar{k}_o$ with a power of $-\frac{3}{5}$. Comparing Eqs. (5) and (9), we replace $\bar{k}_o^{-3/5}$ in Eq. (5) with $\overline{k_o^{-3/5}}$ to include the effects of fluid properties and orifice size. Thus,

$$\mathrm{SMD}/\Lambda \sim \mathrm{We}_{f,\Lambda}^{-3/5}\left[\frac{\overline{k_o^{-3/5}}}{w_o^{-6/5}}\right] \tag{10}$$

where the term $(\overline{k_o^{-3/5}/w_o^{-6/5}})$ indicates the effect of the turbulent intensity on SMD. By employing the measured SMD's (Lai et al., 1994) for the left-hand side of Eq. (10), and the CFD results for the right-hand side of Eq. (10), we can correlate Eq. (10) into Eq. (11) for the four comprehensive gasoline injectors, as shown in Fig. 3:

$$\mathrm{SMD}/\Lambda = 1.0322\left[\mathrm{We}_{f,\Lambda}^{-3/5}\left(\frac{\overline{k_o^{-3/5}}}{w_o^{-6/5}}\right)\right]^{0.7852} \tag{11}$$

Reduction of the power of $[\mathrm{We}_{f,\Lambda}^{-3/5}(\overline{k_o^{-3/5}/w_o^{-6/5}})]$ from 1 in Eq. (10) to 0.7852 in Eq. (11) corrects the overestimate of the turbulent kinetic energy in Eq. (7). Note that the value of $\overline{k_o^{-3/5}}$ can be calculated through the mass-flow average to reduce

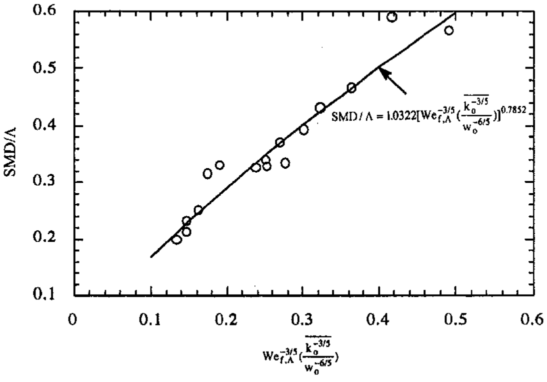

Fig. 3 Correlation between the variables SMD/Λ and $\mathrm{We}_{f,\Lambda}^{-3/5}(\overline{k_o^{-3/5}/w_o^{-6/5}})$ for four injectors

dependency of the grid sizes and numbers at the orifice, which is

$$\overline{k_o^{-3/5}} = \sum_j (\rho_j w_j A_j k_{o,j}^{-3/5}) / \sum_j (\rho_j w_j A_j) \qquad (12)$$

where the subscript j denotes the element number at the orifice and w_j is the streamwise velocity of the element j.

TAB Breakup Model in KIVA-2 Code. This model is based on an analogy suggested by Taylor (1963), in which a droplet is analogous to a spring-mass system. O'Rourke and Amsden (1987) modified Taylor's model and integrated it into the KIVA-2 code. The droplet oscillating motions analogous to a spring-mass system are governed by the following equation:

$$\begin{aligned} m\ddot{x} &= F - kx - c\dot{x} \\ &= [\text{aerodynamic force}] + [\text{surface force}] \\ &\quad + [\text{damping force due to viscosity}] \qquad (13) \end{aligned}$$

where x is the displacement of the equator of the droplet from its equilibrium position.

Droplet breakup occurs when the amplitude of oscillation of the north and south poles equals the droplet radius. After droplet breakup, the droplet sizes are determined based on the energy conservation. Before droplet breakup, the total energy is the sum of the minimum surface energy and the energy of oscillation and distortion in the fundamental mode. It can be written as

$$\begin{aligned} E_{\text{before}} &= 4\pi r^2 \sigma + \frac{8\pi}{3} \rho_l r^3 (\dot{x}^2 + \omega^2 x^2) \\ &= [\text{minimum surface energy}] \\ &\quad + [\text{energy in oscillation and distortion}] \qquad (14) \end{aligned}$$

where ω is the angular velocity. Note that the initial amplitude of oscillation is a function of the turbulent kinetic energy. After droplet breakup, the product (new) droplets are assumed not to be oscillating or distorted. Thus, the total energy is the sum of the minimum surface energy of the product droplets and the kinetic energy due to their motion normal to the path of the parent droplet. The kinetic energy is expressed in the frame of reference of the parent droplet. The total energy after breakup can be expressed as

$$\begin{aligned} E_{\text{after}} &= 4\pi r^2 \sigma \frac{r}{r_{32}} + \frac{2\pi}{3} \rho_l r^3 \dot{x}^2 \\ &= [\text{minimum surface energy}] + [\text{kinetic energy}] \qquad (15) \end{aligned}$$

where r_{32} is the Sauter mean radius of the product droplets. By equating E_{before} and E_{after}, and applying the suitable angular velocity, one can obtain the product droplet size.

The TAB breakup model includes interactions among several forms of energy such as aerodynamic, surface, damping (due to viscosity), and turbulent kinetic. Note that there are four dimensionless constants in this model that are determined through testing.

Bag and Stripping Breakup Model in STAR-CD. The Bag and Stripping breakup model used in STAR-CD, version 2.2.1 was developed by Nicholls (1972) and Reitz and Diwakar (1986). In this model, droplet breakup is a result of interfacial forces (aerodynamic and surface forces) acting on the droplet surface. In the Bag breakup regime, the nonuniform pressure field around the droplet causes it to expand in the low-pressure wave region. The droplet disintegrates when surface tension forces are overcome; typically when the Weber number slightly exceeds the critical number, C_{bl}. The Bag breakup equation can be expressed as

$$\mathrm{We}_{d,g} = \frac{\rho_g |u_g - u_d|^2 d_d}{\sigma} \geq C_{bl} \qquad (16)$$

where u_d and u_g are the droplet velocity and flow velocity near the droplet and d_d is the droplet diameter. Experimental data show this number ranges from 3.6 to 8.4 (Nicholls, 1972). In STAR-CD, $C_{bl} = 6$ is used as the default value.

In the Stripping breakup regime, the liquid is stripped from the droplet surface through the viscous force. It occurs when the Weber number is much higher than the critical number, C_{bl}. The Stripping breakup equation is written as

$$\mathrm{We}_{d,g}/\mathrm{Re}_d^{0.5} \geq C_{sl} \qquad (17)$$

with

$$\mathrm{Re}_d = \frac{\rho_g |u_g - u_d| d_d}{\mu_g} \qquad (18)$$

where Re_d is the droplet Reynolds number and a C_{sl} of 0.5 obtained from Nicholls (1972).

The Bag and Stripping breakup models demonstrate only the importance of the aerodynamic forces and surface forces in droplet breakup. There are two empirical coefficients in each model, one in Eq. (16) or (17) and another in the related time scale equation. Note that in the Bag breakup regime, the droplet size is inversely proportional to the square of the velocity difference, $d_d \sim |u_g - u_d|^{-2}$, while in the Stripping breakup regime the relationship changes to $d_d \sim |u_g - u_d|^{-3}$. The aerodynamic force effect is greater in the Stripping breakup regime.

Injector Internal Flow and Initial Conditions for Spray Codes. Injector internal flow analysis is essential in spray modeling of the comprehensive gasoline injectors. Flow properties at the orifice provide important information used to estimate the mean droplet size in the primary atomization models, and to determine the initial conditions for the multidimensional spray simulations. The computational domain covers the region from above the valve seat to the injector exit as shown in Fig. 1(*a*), instead of the whole injector, to save computational efforts. This approach worked well in related injector studies (Chen et al., 1993; Chen and Chen, 1995). Four individual internal flow analyses are carried out for four comprehensive gasoline injectors. These injectors are coded as CSMM, CSMMN, EDM, and SMM. The major differences among four injectors are the plate/nozzle dimension and the orifice size, as follows:

- CSMM: Two compound silicon plates, Fig. 1(*b*), with one square hole (nozzle) in the top plate and four divergent square holes (nozzles) in the bottom plate, as shown in Fig. 1(*c*). The gap height between these two plate is 100 μm and the orifice size, Λ, is 212.5 μm.
- CSMMN: Similar to CSMM, except the gap is 50 μm.
- SMM: Similar to CSMM, except there is no top plate and the orifice size is 195 μm.
- EDM: Four tilted straight-round holes in a metal plate and an orifice size of 218.9 μm.

Technical specifications in injector flow analysis are summarized as follows. The flow is assumed to be steady, turbulent, and isothermal. Due to symmetry in the director plate and the compound nozzle, only one quarter of the flow domain is considered as the computational domain for EDM, and one eighth for SMM, CSMM, and CSMMN. VISCOR-B is used as the working fluid with a density of 779.4 kg/m^3, a viscosity of 9.27×10^{-4} kg/m-s at room temperature, and a surface tension of 2.4×10^{-2} N/m (with air). As for boundary conditions, the injector exit is set at ambient pressure. Pressure drives of 270, 540, 810, and 1015 kPa are applied at the inlet. Relative pressure is used in the CFD calculations. Symmetric conditions are used for symmetric planes in SMM, CSMM, and CSMMN injectors, whereas cyclic conditions are used for EDM since EDM nozzles create swirl flows.

The flowfield at the orifice is used to determine the initial spray velocity and angle for the KIVA-2 and STAR-CD code. The initial spray sizes are set to the hydraulic diameters of the orifices, under the assumption that the jet is still intact at that location. The computational domain of spray is the downstream from the injector with a diameter of 6 in. and a length of 3 in. The variable, Amp0, in the TAB model of KIVA-2 is estimated based on the assumption that the initial droplet oscillation rate is proportional to the square root of turbulent kinetic energy at the orifice. Thus, for isotropic turbulence, $\dot{x}(0) = \sqrt{2k_o/3}$ and Amp0 $= (4\sqrt{2k_o/3})/(w_o\Lambda)$. It is not our intention to do a sensitivity study on the TAB model. The objective here is to test the KIVA-2 predictability in low-pressure gasoline injection with complex nozzles, since most of the KIVA-2 applications are relatively high-pressure diesel injection with simple nozzles.

Results and Discussion

Primary Atomization. In gasoline injection, the injectors are operated at a pressure much lower than for diesel injection. The pressure drive (e.g., 270 kPa in most automotive applications) is not large enough to create a powerful secondary breakup, where the aerodynamic forces are important. For example, the Weber number based on air property, $\mathrm{We}_{g,\Lambda} = \rho_g w_o^2 \Lambda/\sigma$ (with w_o the mean jet exit velocity and Λ the square orifice length), is 1.8 at a pressure drive of 270 kPa for a CSMM injector. This Weber number is smaller than the critical Weber number of 3.6–8.4 suggested by Reitz and Diwakar (1986) to initiate the secondary atomization. Thus, gasoline spray atomization is mainly controlled by primary atomization where turbulence and surface tension are more important.

The droplet sizes at injector far downstream predicted by two primary atomization models are compared with the measured droplet sizes, as shown in Figs. 4 and 5, respectively. The droplet sizes are measured at 7.6 cm (3 in.) downstream of the injectors by the PDPA (Phase-Doppler Particle Analyzer) technique (Lai et al., 1994). Their measurements also show that there is almost no variation in droplet sizes beyond 2.54 cm (1 in.) from the injector exit. The comparison for the model developed by Wu et al. (1992), i.e., Eq. (4), is shown in Fig. 4. This primary atomization model predicts an inaccurate trend of droplet sizes for the different gasoline injectors. The prediction shows that CSMM should produce the largest size of droplets and SMM the smallest droplets at a given pressure drive. However, test data show that the largest droplets are actually produced by EDM and the smallest droplets by CSMM. The result is not surprising as the gasoline injection is not a simple turbulent jet with a constant turbulent intensity.

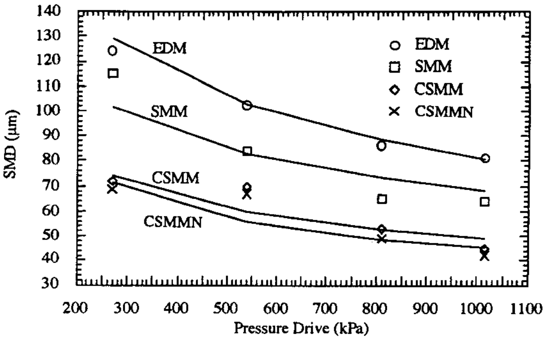

Fig. 5 Measured SMD's and predictions from the primary breakup model of this work for four injectors

In comprehensive injectors like compound nozzle injectors, turbulent intensity at the injector exit is not a constant; it is a function of nozzle geometry, size, and the pressure drive. To predict the droplet sizes produced by comprehensive injectors, the effect of turbulent intensity has to be included. The term $(k_o^{-3/5}/w_o^{-6/5})^{0.7852}$ in Eq. (11) of the modified primary atomization model represents the influence of turbulent intensity on droplet sizes. Predicted and measured droplet sizes of EDM, SMM, CSMM, and CSMMN injectors at a pressure drive of 270-1015 kPa are shown in Fig. 5. Equation (11) predicts a good pressure effect on droplet sizes for four different injectors. Test data and prediction both indicate that the CSMMN injector produces the smallest droplets and the EDM injector the largest.

Comparing the primary atomization models from Wu et al. (1992), i.e., Eq. (4), and from this work, i.e., Eq. (11), one can observe the effects of different Weber numbers on droplet sizes. In Eq. (4), $\mathrm{SMD}/\Lambda \sim \mathrm{We}_{f,\Lambda}^{-0.74}$ and in Eq. (11), $\mathrm{SMD}/\Lambda \sim \mathrm{We}_{f,\Lambda}^{-0.471}$. Equation (11) shows a weaker effect of Weber number; the power is changed from −0.74 to −0.471. This is because Eq. (4) of Wu et al. (1992) only has a single factor, the Weber number, to determine the droplet size. Here the effects of turbulent intensity and Weber number are combined; there are two factors in Eq. (11). The second factor $(k_o^{-3/5}/w_o^{-6/5})$ takes away (or shares) some effects from the first one. Some of the Weber number effect is shifted to the second factor; the parameter $(k_o^{-3/5}/w_o^{-6/5})$ could be a function of the Weber number.

Multidimensional Spray Predictions. Figure 6 illustrates a comparison of the droplet sizes predicted by the spray codes (KIVA-2 and STAR-CD) and the two primary atomization models, and the test data for the CSMM injector. Both KIVA-2 and the modified primary atomization model presented here predict good droplet sizes. At a pressure drive of 270-1015 kPa, the modified primary atomization model predicts a SMD of 74.2 to 48.8 μm and KIVA-2, 71.4 to 49.2 μm at 7.6 cm (3 in.) downstream of the injector. Both predictions are very close

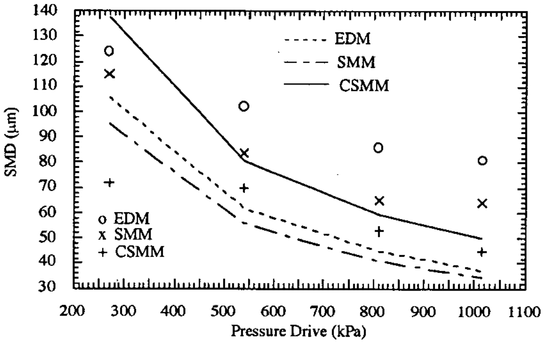

Fig. 4 Measured SMD's and predictions from the primary breakup model of Wu et al. (1992) for three injectors

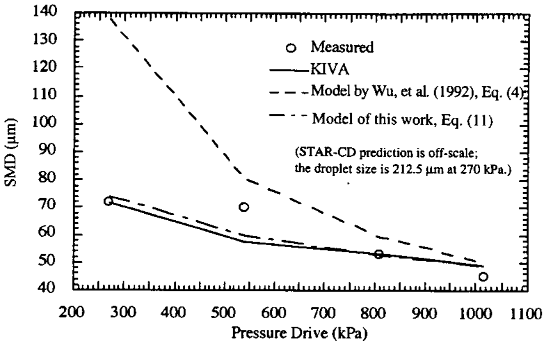

Fig. 6 Measured SMD's and predictions from KVIA, STAR-CD, and two primary breakup models for the CSMM injector

to the measured SMD's of 72 to 45 μm. The primary atomization model by Wu et al. (1992) predicts decent droplet sizes at high pressures (>810 kPa), but poor results at low pressures (<540 kPa). This limits the applications of this primary atomization model because most of today's automotive gasoline injectors are operated at a relatively low pressure, around 270 kPa. STAR-CD fails to predict any droplet breakup at a pressure drive of 270 kPa. All droplets remain at their initial size of 212.5 μm, which is the size of the square orifice. (The prediction of STAR-CD is off the scale in Fig. 6.) This is because the droplet breakup models in STAR-CD are only good for secondary atomization where both the aerodynamic forces and the fluid internal forces (surface, inertial, etc.) are important. The operating conditions of current gasoline fuel injectors make the spray breakup in the primary atomization regime. Weber number based on air property, $We_{g,\Lambda} = \rho_g w_o^2 \Lambda/\sigma$ for the CSMM injector, ranges from 1.8 to 7.0 at a pressure drive of 270–1015 kPa. The Weber number in this range is either too small or barely large enough to initiate the Bag breakup, let alone the Stripping breakup needed at a higher Weber number.

Besides droplet sizes, KIVA-2 also provides other important spray information. Spray flow rates for various pressure drives are shown in Fig. 7. Radial distance starts from the center of the injector. No spray at the injector center indicates it is a hollow spray. This is because the four nozzles are located at a distance away from the center. At higher pressures, the peak of the spray flow rate moves toward the injector center, and the spray has more axial momentum and expands less in the radial direction. By integrating the spray flow rates, the volume accumulation and the spray edge are obtained (see Fig. 8). The spray edge is defined as the location where the volume accumulation is 95 percent of the total volume (SAE, 1992). As the pressure increases, the spray edge moves closer to the injector center ($r = 0$). The spray is narrower, which is consistent with the experimental observations (Lai et al., 1994). With the radial and axial locations of the spray edge, one can determine the spray angle through simple calculations. Comparison of the predicted and measured spray angles are shown in Fig. 9. The measurements were adopted from Lai et al. (1994) where the angles were measured on the photographs of spray jets. The measured spray angles only represent the approximate values since it is not easy to get a clear-cut view of spray edges from the photographs. Even so, KIVA-2 still predicts reasonably good spray angles.

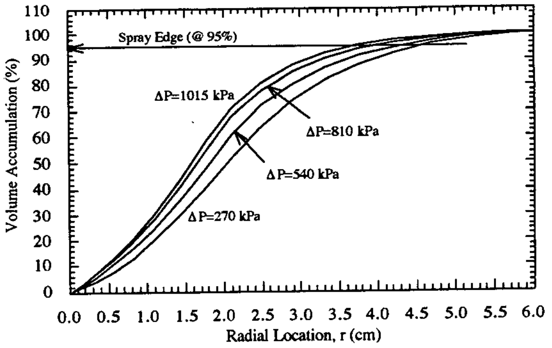

Fig. 8 Distribution of spray volume accumulation at 7.62 cm (3 in.) downstream of the CSMM injector exit. The event time is 100 ms and the pressure drive is 270-1015 kPa.

Injector Flow Performance. Several items related to the injector internal flows are of interest: first, the turbulent kinetic energy at the orifice, which is important to determine droplet sizes in the primary atomization models, and the initial droplet oscillation in KIVA-2; second, the flow rates and velocities at the orifice, which are needed to estimate the initial droplet numbers, spray angle, and velocities for KIVA-2 and STAR-CD; finally, the discharge coefficient, which defines the efficiency of the injector metering process, and is an important parameter that characterizes the metering process of the injector.

The turbulent kinetic energy distributions at the injector orifices, which have significant effects on primary atomization of gasoline injection, are shown in Fig. 10. High turbulent kinetic energy regions are located at the outer regions near the nozzle walls. This is why more fine droplets are observed, as a result of primary atomization, at the outer edges of the spray. CSMMN has the highest overall turbulent kinetic energy and is expected to have the smallest droplet sizes. Since the only difference between CSMM and CSMMN is the gap height inside the compound nozzle, this gap height is a key parameter in increasing the turbulent kinetic energy. For the EDM injector, even though it has a higher turbulent energy region at the edge, it also has a larger region of low turbulent kinetic energy. Thus, the average turbulent kinetic energy of EDM is smaller, which produces a larger droplet size.

The predicted static flow rates are reasonably good in comparison with test data to validate the CFD analysis of the injector internal flows. The uncertainty of prediction is around 10 percent. For example, the measured flow rates of EDM and CSMM at 270 kPa (~40 psi) of pressure drive are 1.76 and 1.84 g/s, and the predicted values are 1.949 and 1.833 g/s, respectively. The EDM and SMM injectors deliver almost the same flow rates under the same pressure drive, whereas the flow rates of CSMMN are much smaller. Thus, CSMMN has the lowest discharge coefficient, which is defined as the ratio of the actual mass flow to the ideal mass flow (Heywood, 1988),

$$C_d = [\text{actual mass flow}]/[\text{ideal mass flow}]$$
$$= \dot{m}_{\text{real}}/A_2\left[\frac{2\rho_f(p_1 - p_2)}{1 - (A_2^2/A_1^2)}\right]^{0.5} \qquad (19)$$

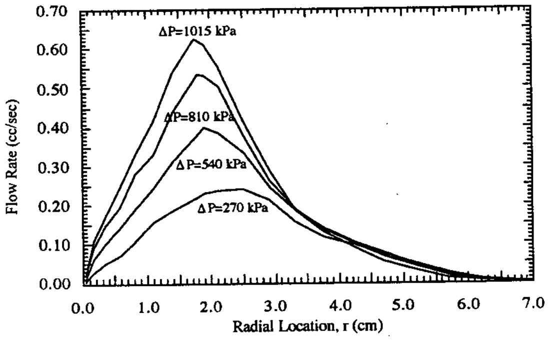

Fig. 7 Distribution of spray flow rates at 7.62 cm (3 in.) downstream of the CSMM injector exit. The event time is 100 ms and the pressure drive is 270-1015 kPa.

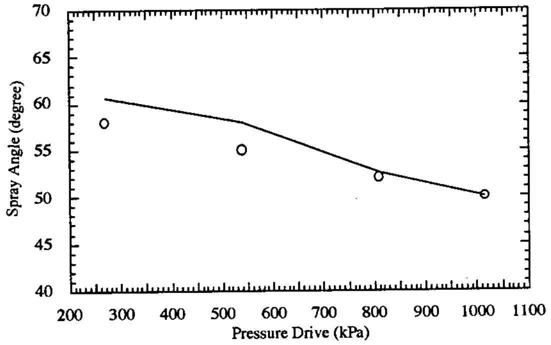

Fig. 9 Measured angles of the CSMM injector and predictions from KIVA at a pressure drive of 270-1015 kPa

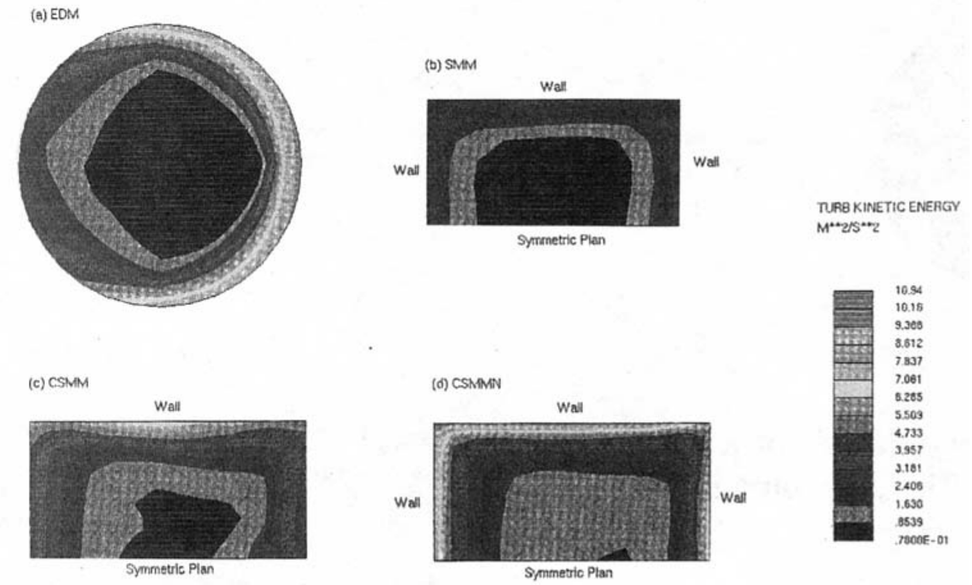

Fig. 10 Distribution of turbulent kinetic energy at the orifices of (*a*) EDM, (*b*) SMM, (*c*) CSMM, and (*d*) CSMMN injectors. The pressure drive is 270 kPa.

where the subscripts 1 and 2 denote the inlet and downstream of the orifice, respectively. In fuel injectors, the orifice area is much smaller than the inlet area (i.e., $A_2/A_1 \ll 1$). Therefore, Eq. (19) is simplified to

$$\begin{aligned} C_d &= \dot{m}_{\text{real}}/A_2[2\rho_f(p_1 - p_2)]^{0.5} \\ &\approx \dot{m}_{\text{real}}/A_o[2\rho_f(p_1 - p_{\text{exit}})]^{0.5} \qquad (20) \end{aligned}$$

where A_o is the orifice area and P_{exit} is the pressure at the exit. In the pressure drive of 270–1015 kPa (~40–150 psi), the discharge coefficients for these four injectors barely change. For example, $C_d = 0.495$–0.505 and 0.691–0.719 for CSMM and EDM injectors, respectively. The flow rates at high pressures can be estimated from C_d at low pressures without losing much accuracy.

Conclusions and Recommendations

- Spray breakup in gasoline injection is mainly in the preliminary atomization regime in most automotive applications at a pressure drive of 270–1015 kPa (~40–150 psi).
- The modified primary atomization model developed here and the KIVA-2 code predict good droplet sizes. The STAR-CD code predicts no spray breakup. The primary breakup model developed by Wu et al. (1992) is not robust enough for comprehensive injector nozzles.

References

Beatrice, X. X., P. Belardini, C. Bertoli, M. C. Cameretti, and N. C. Cirillo, 1995, "Fuel Jet Models for Multidimensional Diesel Combustion Calculation: An Update," SAE Paper No. 950086.

Chen, J. L., G. Chen, and M. Wells, 1993, "Dynamic and Static Flow Analysis of a Gasoline Fuel Injector," ASME JOURNAL OF ENGINEERING FOR GAS TURBINES AND POWER, Vol. 115, pp. 750–755.

Chen, J. L., and G. Chen, 1995, "Slow Heating Process of a Heated Pintle-Type Gasoline Fuel Injector," *Progress in Fuel Systems to Meet New Fuel Economy and Emissions Standards,* SAE SP-1084, pp. 25–34, SAE Paper No. 950068.

Computational Dynamics, LTD, 1994, *STAR-CD Version 2.2.1 Manuals,* London, United Kingdom.

Heywood, J. B., 1988, *Internal Combustion Engine Fundamentals,* Appendix C, McGraw-Hill, New York.

Hinze, J. O., 1975, *Turbulence,* 2nd ed., McGraw-Hill, New York, pp. 427 and 724–742.

Kong, S. C., and R. D. Reitz, 1993, "Multidimensional Modeling of Diesel Ignition and Combustion Using a Multistep Kinetics Model," ASME JOURNAL OF ENGINEERING FOR GAS TURBINES AND POWER, Vol. 115, pp. 781–789.

Lai, M. C., F. Q. Zhao, A. A. Amer, and T. H. Chue, 1994, "An Experimental and Analytical Investigation of the Spray Structure From Automotive Port Injectors," SAE Paper No. 941873.

Lefebvre, A. H., 1989, *Atomization and Spray,* Hemisphere Publishing Corporation, New York, pp. 35 and 45–48.

Liu, A. B., D. Mather, and R. D. Reitz, 1993, "Modeling the Effects of Drop Drag and Break-up on Fuel Sprays," SAE Paper No. 930072.

Nicholls, J., 1972, "Stream and Droplet Breakup by Shock Waves," NASA SP-194, eds. D. T. Harrje and F. H. Reardon, eds., pp. 126–128.

O'Rourke, P. J., and A. A. Amsden, 1987, "The TAB Method for Numerical Calculation of Spray Droplet Breakup," SAE Paper No. 872089.

Reitz, R. D., and R. Diwakar, 1986, "Effect of Drop Breakup on Fuel Sprays," SAE Paper No. 860469.

SAE, 1992, "Gasoline Fuel Injector," *1992 SAE Handbook,* Vol. 3, SAE J1832 NOV89, Society of Automobile Engineers, Warrendale, PA, pp. 24.246–24.262.

Schlichting, H., 1979, *Boundary Layer Theory,* 7th ed., McGraw-Hill, New York, p. 599.

Taylor, G. I., 1963, "The Shape and Acceleration of a Drop in a High Speed Air Stream," *The Scientific Papers of G. I. Taylor,* G. K. Batchelor, ed., Vol. III, University Press, Cambridge.

Wu, P.-K., L.-K. Tseng, and G. M. Faeth, 1992, "Primary Breakup in Gas/Liquid Mixing Layers for Turbulent Liquids," *Atomization and Sprays,* Vol. 2, pp. 295–317.

Journal of Engineering for Gas Turbines and Power

Technical Brief

A Stability Analysis of a Rotor System With Electromagnetic Control Forces

M. Zhu[1]

The stability analysis of a rotor system with electromagnetic control forces is investigated. The formulas for the electromagnetic forces between the stator and rotor of the electromagnetic actuator are derived with respect to the displacements of the journal center and coil currents. The minimum setting values of the controller, and the relationship between mode shapes at the positions of sensors and actuators of the system, are given by using a perturbation method and Routh–Hurwitz theory.

Introduction

In recent years, the development of electromagnetic bearing technology (Schweitzer, 1990) enables active vibration control of the rotor system to be practical, because this kind of device can effectively suppress the vibration of the system. Many studies concerning electromagnetic bearings can be found in the literature. Gondhalekar and Holms (1984) reported on the design of magnetic bearings for long flexible shafts. Salm and Schweitzer (1984), Matsumura and Yoshimoto (1986), and Youcef-Toumi and Reddy (1992) discussed the modeling and controlling of flexible rotor systems with electromagnetic bearings. Bradfield et al. (1987) investigated the performance of an electromagnetic bearing used for rotor vibration control operating in the supercritical rotor speed condition. Ulbrich and Anton (1984) studied some details about magnetic bearing applications. Hebbale (1985), and Hebbale and Taylor (1986) carried out a nonlinear theoretical analysis of magnetic bearings. Stanway and Reilly (1984) presented a state space control method and a pole assignment method for the system. Lee and Kim (1992) discussed modal test and suboptimal vibration control. Tong and Wang (1992) calculated the electric current of optimal output feedback control. Humphris et al. (1986), and Williams et al. (1991) studied the effect of control algorithms on properties of magnetic journal bearings and made a comparison of analog and digital controls. Nonami and Yamanaka (1990) and Kasarda et al. (1990) did some important experiments.

However, many of the investigators mentioned above have not accounted for the stability of a flexible rotor system with electromagnetic control forces. The stability analysis of the system with these forces is investigated in this paper.

Equation of Motion of the Rotor System

The equation of motion for n degrees of freedom of the system with electromagnetic control forces can be written as

$$[M]\{\ddot{x}\} + [C]\{\dot{x}\} + [K]\{x\} = \{F(t)\} + \{u(t)\} \quad (1)$$

where $[M]$, $[C]$, and $[K]$ are the $n \times n$ inertia matrix, damping matrix, and stiffness matrix, respectively. $\{F(t)\}$ and $\{u(t)\}$ are the $n \times 1$ external perturbation force vector and control force vector.

Electromagnetic Force

The control forces $\{u(t)\}$ in Eq. (1) are the electromagnetic forces induced by the electromagnetic actuator as shown in Fig. 1. The actuator consists of a stator and rotor. There are eight control coils and four static ones on the stator. All of the electromagnets have the same cross-sectional area, all coils have the same number of windings, that is, $S_1 = S_2 = \ldots = S_8$, $N_1 = N_2 = \ldots = N_8$. The control currents are i, and static currents are I_0. According to electromagnetic theory, the electromagnetic forces induced by every pair of electromagnets can be represented as follows:

$$f_i = \frac{\mu_0 S N^2 I_i^2}{4\delta_i^2} \cos\varphi \quad i = 1, 2, \ldots, 8 \quad (2)$$

where f_i is the attractive force between electromagnets of the stator and rotor, μ_0 is the permeability in the air gaps between the stator and rotor, S is the effective area of the cross section of one electromagnet, N is the number of windings around the core, I_i is the coil current that is equal to a control current and static current, δ_i is the radial clearance between the stator and rotor of the actuator, φ is the corresponding half angle of a radial magnetic circuit as shown in Fig. 1.

Equation (2) is derived upon the following assumptions: The magnetic fields in the air gap and core are uniformly distributed. The ferromagnetic material has the property of nonsaturation. The effects of the leakage and overflow of the magnetic flux are ignored.

When the rotor deviation from the journal center is x and y, the radial clearance for the angle α_i can be written as:

$$\delta_i = \delta_0 - x\cos\alpha_i + y\sin\alpha_i, \quad i = 1, 2, \ldots, 8 \quad (3)$$

where α_i is shown in Fig. 1.

The corresponding coil currents are

$$I_1 = I_8 = I_0 - i_x$$

$$I_2 = I_3 = I_0 - i_y$$

---

[1] Institute of Vibration Engineering Research, Nanjing University of Aeronautics & Astronautics, Nanjing, 210016, People's Republic of China.

Contributed by the International Gas Turbine Institute of THE AMERICAN SOCIETY OF MECHANICAL ENGINEERS. Manuscript received by the International Gas Turbine Institute September 12, 1994. Associate Technical Editor: R. E. Kielb.

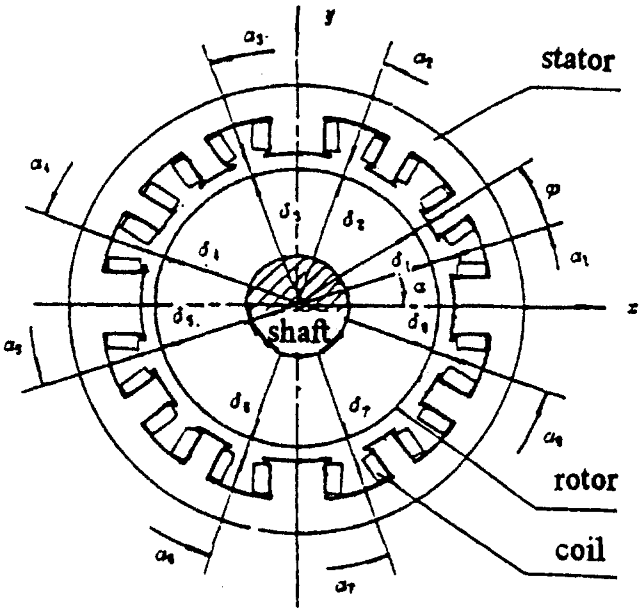

Fig. 1 Electromagnetic actuator geometry

$$I_4 = I_5 = I_0 + i_x$$

$$I_6 = I_7 = I_0 + i_y \qquad (4)$$

So the resultants of the electromagnetic forces between the stator and rotor of the actuator in the horizontal and vertical directions are, respectively, of the forms

$$f_x = (f_1 - f_4 - f_5 + f_8)\cos\varphi\cos\alpha + (f_2 - f_3 - f_6 + f_7)\cos\varphi\sin\alpha$$

$$f_y = (f_2 + f_3 - f_6 - f_7)\cos\varphi\cos\alpha + (f_1 + f_4 - f_5 - f_8)\cos\varphi\sin\alpha \qquad (5)$$

Stability Analysis

According to the literature (Saito, 1985; Jean and Nelson, 1990; Shiau et al., 1993), the steady-state solution of Eq. (1) can be approximately described by

$$\{x_s\} = \{x_0\} + \sum_{i=1}^{N_W} \{u_{ci}\}\cos\omega_i t + \sum_{i=1}^{N_W} \{u_{si}\}\sin\omega_i t \qquad (6)$$

where N_W is an integer. To examine the stability of the steady-state solution, the dynamics are perturbed and the resulting motion is expressed as

$$\{x\} = \{x_s\} + \{\delta x\} \qquad (7)$$

Assuming that the electromagnetic actuators are assigned at the points $\{x_c\}$ of the system, and the sensors at $\{x_m\}$, we can express the electromagnetic forces as

$$\{f_x\} = \{f\}_s + \frac{\partial f_x}{\partial x}\{\delta x_c\} + \frac{\partial f_x}{\partial i_x}\{\delta i_c\} \qquad (8)$$

where the subscript s denotes the steady-state solution.

Consider a general feedback control with the following equation:

$$\{\delta i_c\} = -k\{\delta x_m\} - c\{\delta \dot{x}_m\} \qquad (9)$$

where k is the proportional gain and c is the rate gain of a controller.

The corresponding electromagnetic control force is

$$\{f_x\} = \{f_s\} + \frac{\partial f_x}{\partial x}\{\delta x_c\} - k\frac{\partial f_x}{\partial i_x}\{\delta x_m\} - c\frac{\partial f_x}{\partial i_x}\{\delta \dot{x}_m\} \qquad (10)$$

Substituting Eqs. (6), (7) and (10) into Eq. (1), the perturbed equation of the system is of the form:

$$[M]\{\delta\ddot{x}\} + \left[C + c\frac{\partial f_x}{\partial i_x}E_{cm}\right]\{\delta\dot{x}\} + \left[K - \frac{\partial f_x}{\partial x}E_{mm} + k\frac{\partial f_x}{\partial i_x}E_{cm}\right]\{\delta x_m\} = \{0\} \qquad (11)$$

where the element of the cth row and the mth column in the E_{cm} matrix, and the mth row and the mth column in the E_{mm} matrix are equal to one. The other elements are equal to zero.

The corresponding eigenequation belonging to Eq. (11) is

$$\left\{\lambda^2[M] + \lambda\left[C + c\frac{\partial f_x}{\partial i_x}E_{cm}\right] + \left[K - \frac{\partial f_x}{\partial x}E_{mm} + k\frac{\partial f_x}{\partial i_x}E_{cm}\right]\right\}\{\delta x\} = \{0\} \qquad (12)$$

The eigenvectors are normalized as follows:

$$\Phi^T[M]\Phi = I$$

$$\Phi^T[K]\Phi = [\omega_i^2] = \Lambda \qquad (13)$$

where $\Phi = [\Phi_1\Phi_2 \ldots \Phi_n]$, and

$$\{x\} = \Phi\{q\} \qquad (14)$$

where $\{q\}$ is the modal coordinate, and $\{q\} = \{q_1q_2 \ldots q_n\}^T$.

Substituting Eq. (14) into Eq. (12), and premultiplying by Φ^T, Eq. (12) becomes

$$[\lambda^2 I + \lambda\bar{C} + \bar{K}]q = \{0\} \qquad (15)$$

where

$$\bar{C} = \Phi^T[C]\Phi + c\frac{\partial f_x}{\partial i_x}E$$

$$\bar{K} = \Lambda - \frac{\partial f_x}{\partial x}E_m + k\frac{\partial f_x}{\partial i_x}E \qquad (16)$$

and

$$E = \Phi^T E_{cm}\Phi = [e_{ij}]$$

$$E_m = \Phi^T E_{mm}\Phi = [e'_{ij}]$$

$$e_{ij} = \Phi_i^T(x_c)\Phi_j(x_m)$$

$$e'_{ij} = \Phi_i^T(x_m)\Phi_j(x_m) \qquad (17)$$

If the eigenvalues satisfy

$$|\lambda^2 I + \lambda\bar{C} + \bar{K}| = 0 \qquad (18)$$

and all of the real parts of eigenvalues in Eq. (18) are negative, the rotor system is stable.

Example

For one example, consider the first critical rotational speed. Taking the first mode in Eq. (14), Eq. (18) can be simplified to:

$$\lambda^2 + \left(C_1 + c\frac{\partial f_x}{\partial i_x}e_{11}\right)\lambda + \left(\omega_1^2 - \frac{\partial f_x}{\partial x}e'_{11} + k\frac{\partial f_x}{\partial i_x}e_{11}\right) = 0 \qquad (19)$$

where

$$C_1 = \Phi_1^T[C]\Phi_1 > 0$$
$$e_{11} = \Phi_1^T(x_c)\Phi_1(x_m)$$
$$e'_{11} = \Phi_1^T(x_m)\Phi_1(x_m) \qquad (20)$$

According to the Routh–Hurwitz theory, the stability conditions of the system can be obtained as follows:

$$e_{11} = \max\left[-\frac{C_1}{c\dfrac{\partial f_x}{\partial i_x}},\ \left(-\omega_1^2 + \frac{\partial f_x}{\partial x}e'_{11}\right)\Big/ k\frac{\partial f_x}{\partial i_x}e_{11}\right]$$
$$k > \left(-\omega_1^2 + \frac{\partial f_x}{\partial x}e'_{11}\right)\Big/\frac{\partial f_x}{\partial i_x}e_{11} = k_0$$
$$c > 0 \qquad (21)$$

Because the proportional gain k and rate c are both larger than zero, the sufficient conditions for a stable system are

$$e_{11} = \Phi_1^T(x_c)\Phi_1(x_m) > 0$$
$$k > \left(-\omega_1^2 + \frac{\partial f_x}{\partial x}e'_{11}\right)\Big/\frac{\partial f_x}{\partial i_x}e_{11} = k_0$$
$$c > 0 \qquad (22)$$

For another example, consider the range of the first two modes. Using the same method described above, the sufficient conditions for a stable system are

$$e_{11} = \Phi_1^T(x_c)\Phi_1(x_m) > 0$$
$$e_{22} = \Phi_1^T(x_c)\Phi_1(x_m) > 0 \qquad (23)$$
$$k > \frac{\dfrac{\partial f_x}{\partial x}}{\dfrac{\partial f_x}{\partial i_x}}\cdot\frac{\dfrac{e'_{11}}{\omega_1^2} + \dfrac{e'_{22}}{\omega_2^2}}{\dfrac{e_{11}}{\omega_1^2} + \dfrac{e_{22}}{\omega_2^2}} - \frac{1}{\dfrac{\partial f_x}{\partial i_x}\left(\dfrac{e_{11}}{\omega_1^2} + \dfrac{e_{22}}{\omega_2^2}\right)}$$
$$c > 0 \qquad (30)$$

in which

$$e'_{11} = \Phi_2^T(x_m)\Phi_2(x_m)$$
$$e'_{22} = \Phi_2^T(x_m)\Phi_2(x_m) \qquad (24)$$

References

Bradfield, C. D., Rorberts, J. B., and Karunendiran, R., 1987, "Performance of an electromagnetic bearing for the vibration control of a supercritical shafts," *Proc. Instn. Mech. Engrs.*, Vol. 201c, No. 3, pp. 201–211.

Gondhalekar, V., and Holms, R., 1984, "Design of electromagnetic bearing for the vibration control of a supercritical shafts," *Proc. Instn. Mech. Engrs.*, Vol. 198.C, No. 16, pp. 235–242.

Hebbale, K. V., 1985, "A theoretical model for the study of nonlinear dynamics of magnetic bearings," Ph.D. Thesis, Cornell University, Ithaca, NY.

Hebbale, K. V., and Taylor, D. L., 1986, "Nonlinear dynamics of attractive magnetic bearings," *Rotor Dynamic Instability Problems in High Performance Turbomachinery*, NASA Conference, pp. 397–418.

Humphris, R. R., Kelm, R. D., Lewis, D. W., and Allaire, P. E., 1986, "Effect of control algorithms of magnetic journal bearing properties," ASME JOURNAL OF ENGINEERING FOR GAS TURBINES AND POWER, Vol. 108, pp. 624–632.

Jean, A. N., and Nelson, H. D., 1990, "Periodic response investigation of large order nonlinear rotor dynamic systems using collocation," *Journal of Sound and Vibration*, Vol. 143, No. 3, pp. 473–490.

Kasarda, M. E. F., Allaire, P. E., Humphris, R. R., and Barrett, L. E., 1990, "A magnetic damper for first mode vibration reduction in the multimass flexible rotor," ASME JOURNAL OF ENGINEERING FOR GAS TURBINES AND POWER, Vol. 112, pp. 463–469.

Lee, C. W., and Kim, J. S., 1992, "Modal testing and suboptimal vibration control of flexible rotor bearing system by using a magnetic bearing," ASME *Journal of Dynamic Systems, Measurement, and Control*, Vol. 114, pp. 244–252.

Matsumura, F., and Yoshimoto, T., 1986, "System modeling and control design of a horizontal-shaft magnetic-bearing system," *IEEE Trans. on Magnetic*, Vol. 22, No. 3, pp. 196–203.

Nonami, K., and Yamanaka, T., 1990, "Vibration and control of a flexible rotor supported by magnetic bearing," JSME *International Journal Series III*, Vol. 33, No. 4, pp. 475–482.

Saito, S., 1985, "Calculation of nonlinear unbalance response of horizontal rotor supported by ball bearing with radial clearances," ASME *Journal of Vibration, Acoustics, Stress, and Reliability in Design*, Vol. 107, pp. 416–420.

Salm, J., and Schweitzer, G., 1984, "Modeling and control of a flexible rotor with magnetic bearing," *Proc. Third International Conference on Vibrations in Rotating Machinery*, pp. 553–561.

Schweitzer, G., 1990, "Magnetic bearings—applications, concept and theory," JSME *International Journal Series III*, Vol. 33, No. 1, pp. 13–18.

Shiau, T. N., Huang, J. L., and Chang, Y. B., 1993, "A study on stability and response analysis of a nonlinear rotor system with mass unbalance and side load," ASME JOURNAL OF ENGINEERING FOR GAS TURBINES AND POWER, Vol. 115, pp. 218–226.

Stanway, R., and Reilly, J. O., 1984, "State-variable feedback control of rotor bearing suspension system," *Third International Conference on Vibration in Rotating Machinery*, pp. 515–524.

Tong, S. G., and Wang, X. X., 1992, "Theoretical research on electromagnetic damper in the rotor bearing system," *J. Vibration Engineering*, Vol. 5, No. 1, pp. 17–24.

Ulbrich, H., and Anton, E., 1984, "Theory and application of magnetic bearing with integrated displacement and velocity sensor," *Third International Conference on Vibration in Rotating Machinery*, pp. 543–552.

Williams, R. D., Keith, F. I., and Allaire, P. E., 1991, "A comparison of analog and digital control for rotor dynamic vibration reduction through active magnetic bearings," ASME JOURNAL OF ENGINEERING FOR GAS TURBINES AND POWER, Vol. 113, pp. 535–543.

Youcef-Toumi, K., and Reddy, S., 1992, "Dynamic analysis and control of high speed and high precision active magnetic bearings," ASME *Journal of Dynamic Systems, Measurement, and Control*, Vol. 144, pp. 623–633.